Gold mineralisation and tectonomagmatic evolution of the Yalgoo-Singleton Greenstone Belt, Western Australia

Jamie J. Price

Submitted in partial fulfilment of the requirements for the degree of Doctor of Philosophy (PhD)

December 2020

"The mind seemed to grow giddy by looking so far into the abyss of time; and whilst we listened with earnestness and admiration to the philosopher who was now unfolding to us the order and series of these wonderful events, we became sensible how much further reason may sometimes go than imagination may venture to follow…"

- John Playfair, colleague of James Hutton,
on viewing the Siccar Point unconformity, 1788

Acknowledgements

This thesis represents the culmination of four years of work that has only been possible thanks to the support and assistance of a great number of wonderful people.

Firstly, I would like to extend my sincere thanks to my supervisors, Andrew Kerr, Tom Blenkinsop and Kathryn Goodenough. Andrew has been a steadfast supervisor who has always been on hand to answer questions (on anything from igneous petrology to genealogy), provide direction for the project and guide me through the trials and tribulations of the PhD process. The annual Kerr's Christmas Curry, meetings over a few refreshments and demonstrating the Pembrokeshire fieldtrip with Andrew are just some of the many highlights that made my time in Cardiff so very enjoyable. Tom's expert supervision on matters relating to structural geology and gold mineralisation has been invaluable and I have learnt a great deal from our discussions about Archaean rocks and tectonics. Kathryn has been instrumental in providing an unrelenting source of geological knowledge, ongoing encouragement, and meticulous feedback on any drafts or questions that were sent her way. I would also like to thank Tim Ivanic, for his practical guidance, suggestions and insights into Archaean stratigraphy and geochemistry.

I am immensely indebted to Minjar Gold and the staff at the Golden Dragon mine site, who generously hosted me for three successive field seasons, provided crucial logistical support and access to tenements, pits and drillcore. Without the support of Minjar Gold and the Exploration Manager Clint Kuehnapfel, this project would not have been possible. In particular, a resounding cheers to the 2016-2018 Exploration Crew, including Gav, Matt, Maudy, Fitzy, Rohan, Ali, Chris, Jamie, Yan, Dave and of course, Dr Boddy. Your hospitality, friendship and enthusiasm made my field seasons the most enjoyable part of the entire project, and do not get me started on those BBQs in the bush…

I am very grateful for the support of the exceptional laboratory staff at Cardiff, including Tony Oldroyd (for unrivalled preparation of polished thin sections), Duncan Muir (for his patience and assistance with SEM analysis) and Iain McDonald (for analysing whole rock geochemical samples). Special thanks to Katie Dobbie, for her friendship, shared passion for burritos and for her unrelenting work that undoubtedly keeps the department in operation. I also owe thanks to Pete Kinny, Adrian Boyce, Simon Tapster, Matt Horstwood, Riana Rossouw and Mareli Grobbelaar-Moolman for assistance with data acquisition.

Many thanks to past and present members of the PhD community at Cardiff University, for your friendship, support and encouragement – it has been a genuine pleasure to work alongside such a lovely bunch of people. A special shoutout to occupants of the 'Magma Chamber', and in particular,

to Jian and Joanna, for your companionship, provision of welcome distractions and encouragement to get this thesis written! I am extremely honoured to have learnt the art of 't-ball' (thanks Nick, Micky, Hodge, George and Bob) and I am grateful to have spent much-valued time both inside and outside of the office with Josh, Andrew, Panton and Abdul.

Last, but certainly not least, I would like to extend my heartfelt thanks to my family. My parents and sister have always provided me with unwavering support, encouragement and inspiration, for which I will always be extremely grateful. Dad – thanks for pointing out and describing the shapes in the cliffs all those years ago, perhaps I will now be able to return the favour! Mum – I hope that this finally makes those many hours of traipsing around 'crystal healing' shops worthwhile! And of course, Poppy – I cannot thank you enough for your patience, motivation and for quite literally fuelling me through the writing-up period. You all rock.

This thesis is dedicated to the memory of the late Prof. Hazel M. Prichard; an inspirational woman and geologist that I had the honour of working with prior to this project, and to whom I am utterly indebted. Thanks for everything Hazel.

Funding for this project was provided principally by a NERC GW4+ Doctoral Training Partnership studentship from the Natural Environmental Research Council [NE/L002434/1]. Additional funding for fieldwork costs was provided by a Society of Economic Geologists – Canada Foundation (SEG-CF) grant and support and funding for stable isotope analysis and LA-ICPMS geochronological analysis was provided by a NERC Isotope Geosciences Facilities Steering Committee (NIGFSC) grant [IP-1858-1118].

Abstract

The Archaean Yalgoo-Singleton greenstone belt (YSGB) represents one of the most understudied supracrustal complexes in the well renowned Yilgarn Craton, Western Australia. Despite being highly prospective for various mineral deposit types and host to several gold deposits, the stratigraphy, structure, geochemistry and ages of rocks in the YSGB remains poorly understood. This study utilises a combination of mapping, petrography, geochemistry, and geochronology to better constrain the development of rocks in the YSGB. Drillcore logging, SEM analysis and stable isotope analysis has determined the style, paragenesis and controls on lode-gold mineralisation in the belt.

Detailed mapping shows that the YSGB comprises a lower succession of mafic-ultramafic volcanic rocks, overlain by a sedimentary-dominated succession, and extensively intruded by layered, mafic-ultramafic sills. Geochemical analysis has distinguished multiple distinct volcanic and intrusive subgroups within the stratigraphy, which exhibit geochemical evidence of variable degrees of crustal contamination and fractional crystallisation. U-Pb zircon geochronology has constrained the ages of several previously undated supracrustal units and demonstrates the rapid formation of the greenstone belt over a short interval of < 15 Ma, from ca. 2825-2810 Ma. Coupled geochronology and geochemistry has enabled the correlation of units within the YSGB across the region.

This study has established a seven-stage deformational model for rocks in the YSGB, recording a progression from bulk extension that accommodated volcanism, sedimentation, and sill emplacement, to a period of extensive granitic diapirism, followed by bulk horizontal shortening and associated shearing, and successive brittle faulting episodes.

Lode-gold deposits in the YSGB are invariably structurally-controlled and were emplaced along steeply-dipping shear zones associated with fluid overpressure, during horizontal shortening. The remarkable consistency of structural style, paragenesis and stable isotope signatures at lode-gold deposits is indicative of a single, widespread mineralising event. The age of lode-gold mineralisation in the belt has been constrained at ca. 2623 Ma.

Status of Published Work

Together, Chapter 3, a significant proportion of Chapter 5 and the geological maps in Appendix A, have peen published as a Geological Survey of Western Australia (GSWA) Record. Whilst the figures, tables and text presented here are essentially the same as that published in the GSWA record, the content has been rearranged and reformatted to fit the layout of the thesis.

Price, J.J., Blenkinsop, T.G., Goodenough, K.M. & Kerr, A.C. (2020). Stratigraphy, petrography and structure of Archaean rocks in the Rothsay Mining Area, Western Yilgarn Craton. *Geological Survey of Western Australia Record 2020/13*, 109 pp.

https://dmpbookshop.eruditetechnologies.com.au/product/stratigraphy-petrography-and-structure-of-archaean-rocks-in-the-rothsay-mining-area-western-yilgarn-craton.do

Table of Contents

Notes on Appendices

This thesis includes appendices containing geological maps (**Appendix A**) and details of laboratory methods (**Appendix B**), and is also accompanied by an electronic appendix (**Appendix E**). The electronic appendix consists of two files – an excel file containing data tables (**E1-E5** and **E7-E13**) and a PDF compilation of petrographic descriptions (**Appendix E6**). The contents of Appendices are as follows:

APPENDIX A	▪ 1:25,000 Scale Surface Bedrock Geology of the Rothsay Mining Area, Western Australia (PDF) ▪ 1:25,000 Scale Interpreted Bedrock Geology of the Rothsay Mining Area, Western Australia (PDF)
APPENDIX B	▪ B1: Methods for whole rock geochemistry ▪ B2: Methods for U-Pb zircon geochronology ▪ B3: Methods for SEM analysis, stable isotope analysis and U-Pb monazite geochronology
ELECTRONIC APPENDIX (APPENDIX E1-E13)	▪ E1: Field observations in the Rothsay mining area ▪ E2: Field observations in the Yalgoo-Singleton greenstone belt ▪ E3: Lithological logs of drillcore at the Silverstone, M1, Bugeye and Winddine Well gold deposits ▪ E4: Structural logs of drillcore at the Silverstone, M1, Bugeye and Winddine Well gold deposits ▪ E5: Sample details and checklist for petrographic, geochemical and geochronological analysis ▪ E6: PDF compilation of petrographic descriptions and representative photomicrographs ▪ E7: Hydrous whole rock major and trace element geochemical data ▪ E8: Standard data for whole rock geochemical analysis ▪ E9: SHRIMP U-Pb zircon geochronological data ▪ E10: Details of samples from lode-gold deposits in the YSGB and checklist for analysis undertaken ▪ E11: Sulphur stable isotope data for sulphides at lode-gold deposits in the YSGB (and standard data) ▪ E12: Oxygen stable isotope data for quartz at lode-gold deposits in the YSGB (and standard data) ▪ E13: LA-ICPMS U-Pb monazite geochronological data

List of Figures

Chapter 4

Chapter 6

Chapter 7

Chapter 8

Chapter 9

List of Tables

Abbreviations

AFC	Assimilation-fractional crystallisation
Au	Gold
BIF	Banded iron formation
BSE	Back scattered electron
CL	Cathodoluminescence
CSZ	Chulaar Shear Zone
ESZ	Enchanted Shear Zone
EGS	Eastern Goldfields Superterrane
FC	Fractional crystallisation
Fm	Formation
GSWA	Geological Survey of Western Australia
HFSE	High field strength elements
HREE	Heavy rare earth elements
LA-ICP-MS	Laser ablation inductively coupled plasma mass spectrometry
LILE	Large ion lithophile element
LOI	Loss on ignition
LREE	Light rare earth elements
MORB	Mid-ocean ridge basalt
MREE	Middle rare earth elements
MSZ	Mougooderra Shear Zone
PPL	Plane polarised light
REE	Rare earth elements
RL	Reflected light
RSZ	Rothsay Shear Zone
SEM	Scanning electron microscope
SHMB	Siliceous high-Mg basalt
TTG	Tonalite-trondhjemite-granodiorite
WWSZ	Winddine Well Shear Zone
XPL	Cross polarised light
YSGB	Yalgoo-Singleton Greenstone Belt

CHAPTER 1

Introduction

1.1 Background

Archaean rocks provide exceptional insights into the geological processes operating during the first two billion years of Earth's history. Archaean cratons, reflecting disconnected fragments of the early Earth's crust, are distributed across all modern continents and document the time period between the end of the Hadean eon (~4.0 Ga) and the start of the Proterozoic eon (~2.5 Ga; Bleeker, 2003) (Fig. 1.1). The late stages of the Archaean, specifically the late Mesoarchaean (3.2-2.8 Ga) and Neoarchaean (2.8-2.5 Ga), are recognised as a period of significant crustal growth (e.g., Condie, 2003). Granite-greenstone terranes form a principal component of most Archaean cratons (e.g., Kusky and Polat, 1999), and typically comprise linear to arcuate greenstone belts composed of metavolcanic and metasedimentary rocks, separated by vast intrusions of felsic-intermediate compositions (Anhaeusser, 2014; Thurston, 2015).

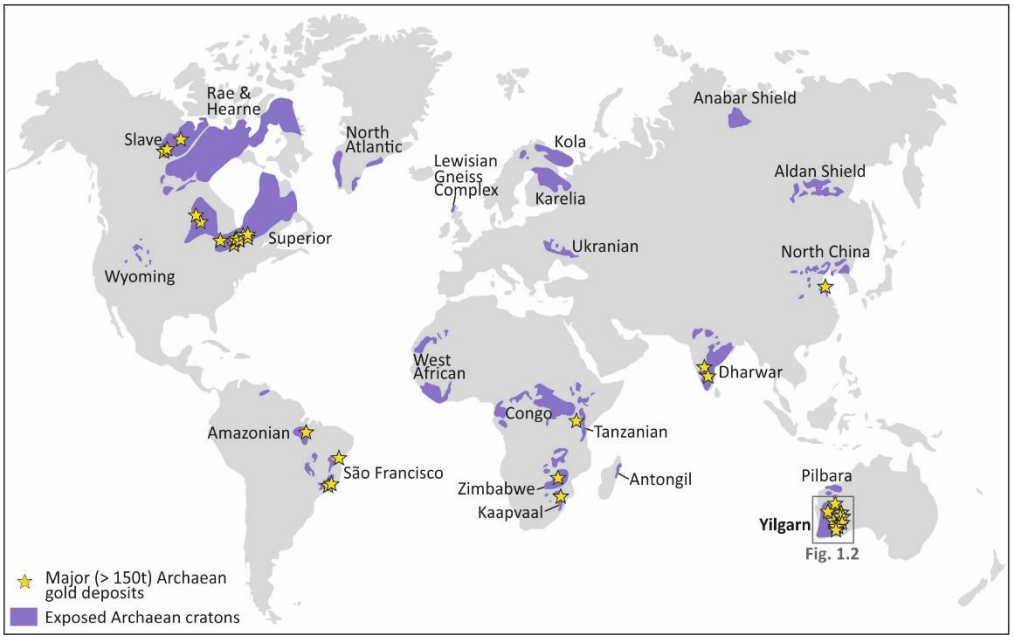

Figure 1.1: Simplified world map displaying the global distribution of exposed Archaean cratons and the locations of major Archaean gold provinces highlighted by world-class > 150t gold deposits of Archaean age. The distribution of cratons is compiled from Bleeker (2003), Pearson & Wittig (2008), Schofield et al. (2010) and Bédard et al. (2013). Archaean gold deposits with a 2004 total gold content of >150 tonnes are shown, as calculated by Gosselin & Dubé (2005).

The geodynamic setting(s) in which granite-greenstone terranes formed is enigmatic and has been the subject of long-standing controversy (e.g., Cawood et al., 2018; Palin & Santosh, 2020). Whereas some researchers support the operation of modern-style plate tectonics in the Archaean (e.g., Dilek & Polat, 2008; Shirey et al., 2008; Korenaga, 2013; Arndt, 2013; Hastie et al., 2016; de Wit et al. 2018), others reject the concept of Archaean plate tectonics and favour other, non-uniformitarian geodynamic processes (e.g., Hamilton, 1998; Stern, 2008; Ernst, 2009; Bédard, 2010; Hamilton, 2019).

Archaean greenstone belts are of major economic importance because they characteristically host an abundance of various mineral deposits (Thurston, 2015). In addition to syngenetic mineralisation, such as volcanogenic massive sulphide (VMS) deposits and komatiite-hosted Ni deposits, Archaean terranes are highly endowed with epigenetic gold mineralisation (Groves et al., 1998; 2003; Mole et al., 2015). For instance, Archaean crust is host to >25 % of current global gold resources, despite accounting for <6 % of the current continental crustal volume (Cawood & Hawkesworth, 2015). Several cratons contain major Archaean gold provinces defined by a profusion of world-class orogenic lode-gold deposits (Fig. 1.1), including the Superior Craton of western Canada and the Yilgarn Craton of Western Australia (Gosselin & Dubé, 2005).

The Yilgarn Craton is one of the largest exposed portions of Archaean crust on Earth and covers a total area of ~1 million km^2 (Ivanic et al., 2012). The craton consists of metasedimentary and metavolcanic rocks with granites, granitic gneisses and gabbroic rocks that were formed predominantly between

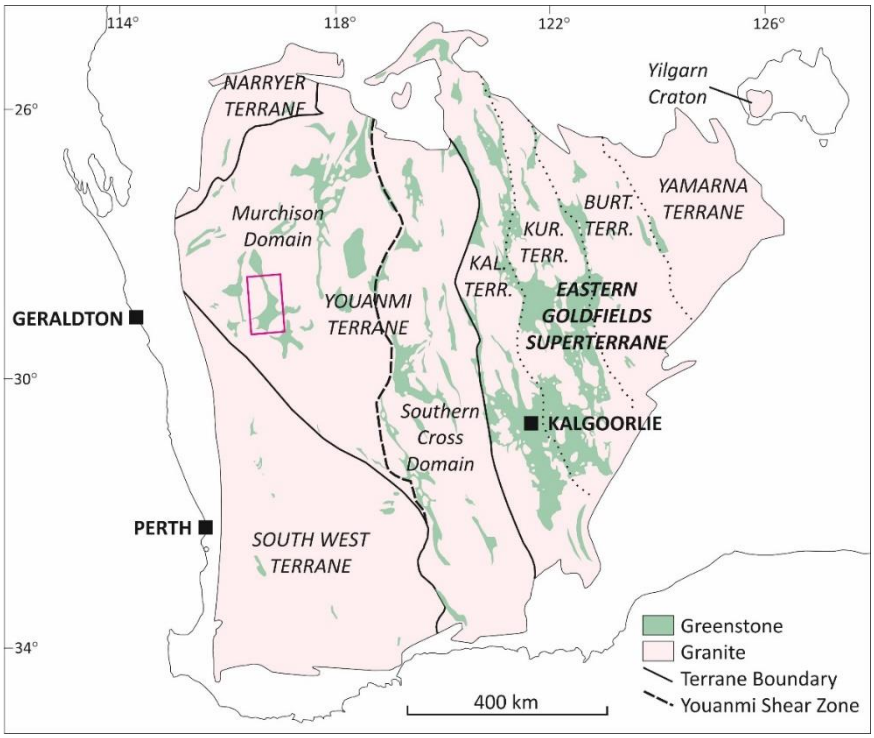

Figure 1.2: Overview geological map of the Yilgarn Craton, Western Australia, showing the distribution of greenstone belts and the location of the Yalgoo-Singleton Greenstone Belt (pink outline). Burt. Terr = Burtville Terrane; Kur. Terr = Kurnalpi Terrane; Kal. Terr = Kalgoorlie Terrane. Redrawn after Cassidy et al. (2006) & Mole et al. (2014).

3.05 Ga and 2.62 Ga, but with some components as old as ~3.7 Ga (Pidgeon & Wilde, 1990; Nelson, 1997; Pidgeon & Hallberg, 2000). The Yilgarn Craton has been divided into seven distinct terranes: the Narryer Terrane in the northwest and the highly deformed South West Terrane bound the vast, centrally-located Youanmi Terrane, which is further subdivided into the Murchison and Southern Cross domains across the Youanmi Shear Zone (Fig. 1.2; Cassidy et al., 2006). The Kalgoorlie, Kurnalpi, Burtville and Yamarna Terranes in the east constitute the Eastern Goldfields Superterrane (EGS; Cassidy et al., 2006) (Fig. 1.2), which contains an abundance of world-class Neoarchaean gold deposits, including the major mining district of Kalgoorlie (Vielreicher et al., 2016).

Geological studies in the Yilgarn Craton have long been focussed on the well-endowed EGS, commonly funded by, or in collaboration with, mining and exploration companies. Consequently, this extensive geological mapping, geochemistry and more recently, geophysical and geochronological analysis in the eastern Yilgarn Craton over many decades has resulted in pioneering research into Archaean geology, geodynamic processes, and the genesis of Neoarchaean lode-gold mineralisation (e.g., Groves et al., 1998; Czarnota et al., 2010; Mole et al., 2015; 2019). However, other highly prospective parts of the Yilgarn Craton, particularly in the west, have been the focus of very little geological study and remain poorly understood.

The Murchison Domain in the western Yilgarn Craton represents a typical Archaean granite-greenstone terrane, which despite its protracted 3.0-2.6 Ga history, distinct crustal architecture, and metal inventory, is relatively understudied compared to other terranes in the Yilgarn Craton (Watkins & Hickman, 1990; Pidgeon & Hallberg, 2000; Wyman, 2019). Supracrustal rocks cover approximately 9.5% of the exposed area of the Murchison Domain (Fig. 1.3), however, original relationships between rock units are commonly hard to decipher, owing to minimal (<5 %) outcrop and extensive transported cover in the region (Watkins & Hickman, 1990). Since the late 2000s, Geological Survey of Western Australia (GSWA) regional geological mapping, coupled with high-resolution geochronology, has been undertaken to better constrain the stratigraphy and structure of rocks in the region and develop a coherent stratigraphic framework across the Murchison Domain (Van Kranendonk, 2008; Van Kranendonk et al., 2013). Whereas this mapping has essentially been completed in the northeastern Murchison Domain, host to the mining centres of Cue and Meekatharra (Fig. 1.3), work in the southwest is ongoing and remains incomplete.

As part of this research, the GSWA have published several studies focussing on the abundant mafic-ultramafic intrusions that typify the Murchison Domain (Ivanic et al., 2010; Ivanic, 2019), including the vast (approx. 85 x 35 km) Windimurra Igneous Complex that represents one of the largest mafic-ultramafic intrusions on Earth (Ivanic et al., 2017).

Several structural and geochemical studies have recently been published based on completed GSWA regional mapping (Zibra et al., 2018; 2020; Clos et al., 2019a; Zibra, 2020). In contrast to earlier studies, which suggested the structural architecture of the Murchison Domain can be accounted for by

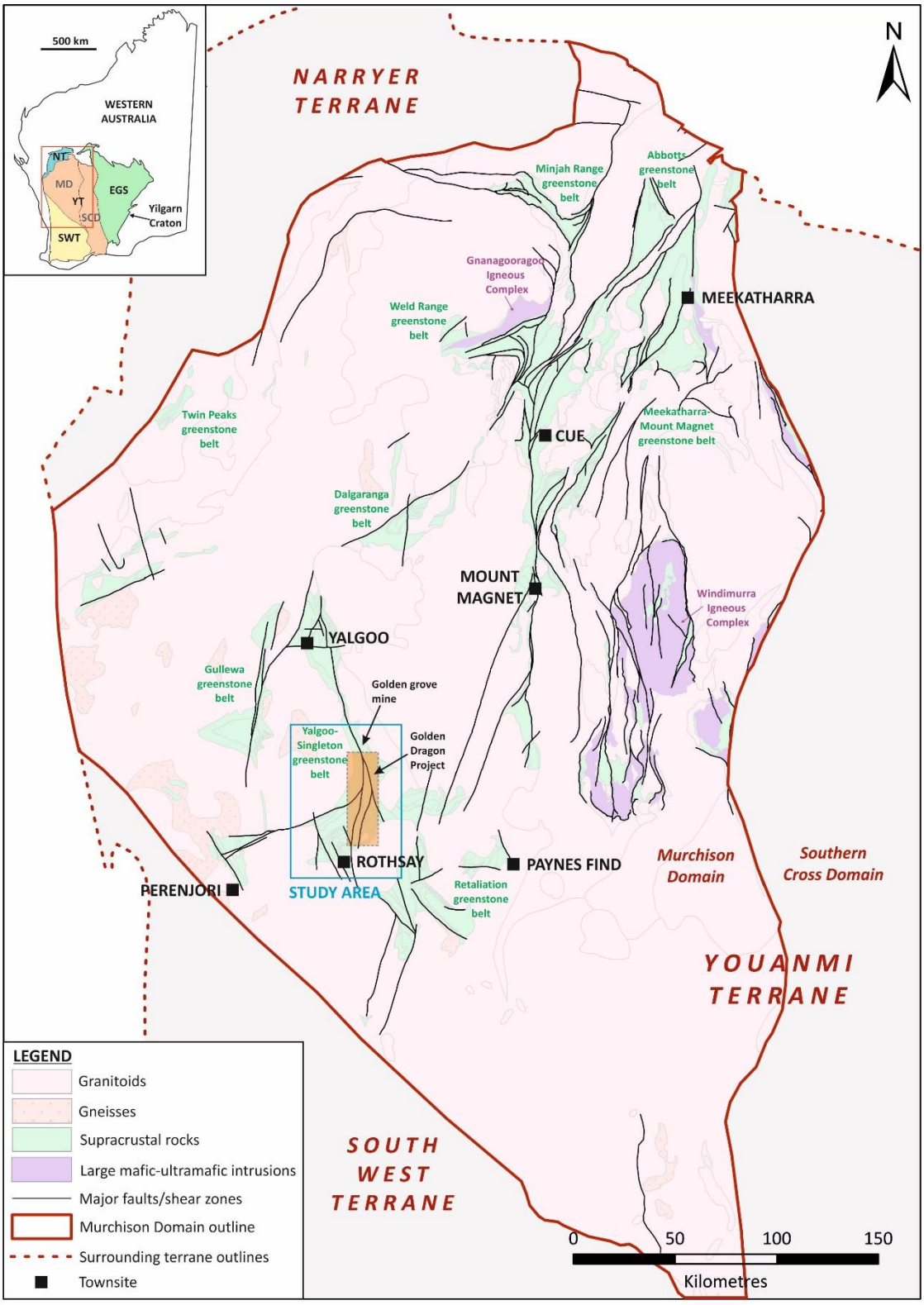

Figure 1.3: Simplified regional geological map of the Murchison Domain showing the distribution the major greenstone belts (green), granitoids (pink) and major structures. The study area is outlined in blue and the approximate area of the Golden Dragon project is shown in orange. The extent of the neighbouring terranes and the adjacent Southern Cross Domain is also shown. Inset image: NT = Narryer Terrane; YT = Youanmi Terrane; EGS = Eastern Goldfields Superterrane; SWT = South West Terrane; MD = Murchison Domain; SCD = Southern Cross Domain. Redrawn after Wyche et al. (2013).

multiple, overprinting episodes of horizontal shortening (Myers & Watkins, 1985; Watkins & Hickman, 1990; Van Kranendonk et al., 2013), recent work has advocated an early period of diapirism associated with the intrusion of large, granitic domes (Zibra et al., 2018; Zibra, 2020). The geochemistry of volcanic rocks in the northeastern Murchison Domain has previously been attributed to plume-derived volcanism and in turn, used in support of an autochthonous model of stratigraphic development (Ivanic et al., 2012; Van Kranendonk et al., 2013). In contrast, the recent identification of a new form of 'platy pyroxene' spinifex texture (Lowrey et al., 2017) and the identification of so-called boninite-like rocks in the northeastern Murchison Domain, have been used to infer the onset of Archaean subduction in the area, and to support allochthonous, plate-tectonic style geodynamic models (e.g., Wyman & Kerrich, 2012; Wyman, 2019; Lowrey et al., 2020).

Lode-gold mineralisation in the Murchison Domain is invariably structurally controlled and closely associated with major shear zones and faults (Watkins & Hickman, 1990). Most discovered lode-gold deposits in the region are situated in the northeast Murchison Domain, in the areas surrounding the Cue and Meekatharra mining centres (Fig. 1.3), although some lode gold deposits are also present in the southwest. Limited outcrop, extensive transported cover and the typically smaller size of deposits have precluded a thorough investigation of the style, characteristics and controls of lode-gold mineralisation in the southwest Murchison Domain, and so the area represents major opportunities for future mineral exploration.

Due to an absence of research, it is unclear whether the stratigraphy, structural geology and hosted gold mineralisation in the southwestern Murchison Domain differs significantly from the seemingly more endowed, well researched areas to the northeast, and elsewhere in the Yilgarn Craton. The work presented in this PhD thesis utilises detailed geological mapping, structural analysis, whole rock geochemistry and high-precision geochronology to assess the structural and geochemical development of supracrustal rocks in the understudied Yalgoo-Singleton greenstone belt (YSGB), southwestern Murchison Domain (Fig. 1.3). New data are used to constrain the features and age of major stratigraphic units in the belt, and to place the stratigraphy of the YSGB into the context of the wider Murchison Domain. Additionally, map-scale aeromagnetic interpretations, coupled with structural logging, paragenetic analysis, stable isotope analyses and radiometric dating, are used to determine the style, characteristics and age of lode-gold mineralisation in the YSGB.

1.2 Study area

The study area covers a ~60 x 50 km region in the southwestern Murchison Domain, situated ~35 km south of the Yalgoo townsite and ~50 km northwest of Paynes Find (Fig. 1.3). The study area

encompasses the southern and central portions of the Yalgoo-Singleton greenstone belt (YSGB), including the deserted mining settlement of Rothsay in the southwest, and can be accessed by sealed roads from Yalgoo and Perenjori (Fig. 1.3). The study area has a negligible magnetic declination of -0.5°. The topography of the area is largely flat, with some gently sloping ridges and occasional, steeply inclined ridges. The region is primarily prospective for gold mineralisation, in addition to base metals, W-Sn and banded iron formation (BIF) related iron ore deposits. The study area is host to several operating mine sites, most notably the world-class Scuddles and Gossan Hill base-metal deposits at the Golden Grove mine in the northeast (Fig. 1.3). The focus of this project is around the Golden Dragon Project, operated by Minjar Gold, which consists of a series of gold deposits exploited as shallow open cast pits that occur along a ~50 km length of the study area (Fig. 1.3). Over the course of this project, I was hosted by Minjar Gold at the Golden Dragon project for three field seasons between October 2016 and September 2018. During this time, I was very generously provided with accommodation, technical and logistical support, and access to tenements, pits and drillcore, without which this project would not have been possible.

Rocks in the southwestern Murchison Domain are generally poorly exposed (<5%) and are largely blanketed by superficial, transported cover up to several tens of metres in thickness. Where exposed, bedrock is commonly weathered and oxidised. Despite this, the study area contains several well exposed sections that comprise relatively unaltered rocks at various stratigraphic levels. Additionally, recent mineral exploration in the study area by Minjar Gold has provided access to exploratory drillcore intersecting fresh rocks along two unexposed shear zones, in addition to detailed geophysical datasets covering the entire study area. Regional geophysical datasets provided by the GSWA also encompass the YSGB. Even though rocks in the region have invariably been subject to at least greenschist facies metamorphism (Watkins & Hickman, 1990), primary textures and structures in igneous and sedimentary rocks are commonly preserved. For these reasons, the prefix 'meta' is not used but inferred in rock classification. The fortuitous combination of geological preservation, locally well-exposed areas and access to drillcore and geophysical data from otherwise concealed areas provides an excellent opportunity to investigate Archaean processes, petrogenesis and deformation, as well as the controls on lode-gold mineralisation, in an understudied corner of the well-renowned Yilgarn Craton.

1.3 Research objectives

The main aims of this study were to utilise a combination of detailed geological mapping, structural logging, geochronology, petrography, whole rock geochemistry and stable isotope analysis to:

- Produce a 1:25,000 scale geological map of a previously unconstrained portion of the YSGB;
- Define the stratigraphy of supracrustal units comprising the greenstone belt and assess the relationship between supracrustal rocks and mafic-ultramafic layered intrusions;
- Determine the structure and kinematics of several gold-mineralised shear zones in the belt;
- Construct a coherent, unifying structural model for rocks in the YSGB, based on field mapping, drillcore logging and interpretation of regional aeromagnetic data;
- Determine the petrographic and geochemical characteristics of volcanic, volcaniclastic and mafic-ultramafic intrusive rocks comprising the study area;
- Assess and model the extent and effects of magma chamber processes, such as fractional crystallisation and crustal contamination, upon the volcanic and magmatic suites studied and evaluate the wider tectonomagmatic implications of geochemical data;
- Constrain the ages of major supracrustal units in the YSGB, attempt stratigraphic correlations across the Murchison Domain and assess timescales for greenstone belt formation;
- Assess the style, structure, paragenesis and stable isotope characteristics of lode gold deposits in the belt and evaluate potential controls on gold mineralisation;
- Determine the age of lode-gold mineralisation in the YSGB and place this into the context of lode-gold mineralisation elsewhere in the Yilgarn Craton.

1.4 Conventions

In this study, planar structural data are recorded in accordance with the right-hand rule, in which the strike measurement is located 90° anticlockwise of the dip direction. Planar structural data are presented using the format strike/dip (e.g., a planar feature striking 170° and dipping 60° west is shown as 170/60°), and linear measurements are presented using the format plunge→trend (e.g., a linear feature plunging 60° towards an azimuth of 350° is shown as 60°→350). Way-up indicators have been symbolised using the 'inverted Y' convention of Borradaile (1976), in which the stem of the symbol **Y** points in the direction of stratigraphic younging.

Sulphur and oxygen stable isotope data are reported in standard notation ($\delta^{34}S$, $\delta^{18}O$) as per mil (‰) deviations from the Vienna Canyon Diablo Troilite (V-CDT) and Vienna Standard Mean Ocean Water (V-SMOW) standards, respectively. For example, a $\delta^{34}S_{V\text{-}CDT}$ value of +2.5 ‰ represents a $\delta^{34}S$ value that is +2.5 per mil deviations heavier than the V-CDT standard. To avoid unnecessary repetition, the subscript notation V-CDT and V-SMOW are omitted after first use in the main text.

1.5 Thesis outline

This thesis is subdivided into ten chapters, seven of which comprise results chapters that present new data (Chapters 3-9). An appendix contains geological maps, details of methods followed, and analytical instruments used. Additionally, an electronic appendix accompanies this thesis and contains data tables and detailed petrographic descriptions. Results chapters 3, 8 and 9 are self contained and can be read independently, with each containing introduction and discussion sections that investigate particular research objectives pertinent to the overarching aims of the thesis. In contrast, chapters 5-7 follow on from one another and collectively address several primary research aims, and the results presented in Chapter 4 are discussed in Chapter 10, with additional input from other chapters in this thesis.

Chapter 1 consists of an introduction to the project, comprising background material, an overview of the study area and an outline of the scope of work and research aims. A comprehensive review of previous literature and geological work undertaken in the Murchison Domain is documented in Chapter 2. Chapter 3 (adapted from Price et al., 2020) details the field relations, stratigraphy and structural geology of a well exposed and previously unstudied portion of the YSGB, the Rothsay mining area, accompanied by 1:25,000 scale geological mapping, and specifically investigates early deformation in the area. Chapter 4 expands upon the work presented in Chapter 3 and employs detailed structural mapping, interpretation of aeromagnetic data and drillcore logging to describe the structural development of the YSGB, with a particular focus on the later phases of deformation.

Chapter 5 contains petrographic descriptions of the major supracrustal units and mafic-ultramafic intrusions present in the YSGB. Chapter 6 presents whole rock major and trace element data for volcanic and volcaniclastic rocks, as well as the layered intrusive sills present in the belt. Chapter 7 comprises an interpretation of the geochemical data presented in Chapter 6 and petrographic data presented in Chapter 5, including modelling of primary magmas, fractional crystallisation and contamination processes, in addition to comparisons with geochemically similar units in the region. Chapter 8 presents new geochronological data for previously unconstrained units comprising the YSGB, assesses stratigraphic relationships based on the new dating and evaluates the timescales for greenstone belt formation. Chapter 9 uses a combination of drillcore logging, paragenetic study, stable isotope analysis and radiometric dating to determine the structural style, mineral paragenesis, stable isotope characteristics and age of lode-gold mineralisation in the YSGB, primarily along the previously unstudied Mougooderra Shear Zone. The final chapter uses new structural and geochronological data to construct a revised structural model for the YSGB, assesses the geodynamic implications of this study, provides an outline of opportunities for future work and presents the conclusions of this study.

1.6 Contributions to this study

All fieldwork related to this study, including geological mapping, lithological and structural logging of drillcore and sample collection, in addition to the digitisation of geological maps and drillcore logs, was conducted by Jamie J. Price. Prof. Tom Blenkinsop and Dr. Kathryn Goodenough each provided field support for a total of three days. Preparation of samples for petrographic work, whole rock geochemical analysis, geochronological analysis and isotope work was carried out by Jamie J. Price.

Petrographic analysis presented in Chapter 5 and **Appendix E6** was undertaken by Jamie J. Price. Analysis of prepared solutions for whole rock geochemistry (Chapter 6) was conducted by Dr. Iain McDonald, Cardiff University. Sensitive High Resolution Ion Micro Probe (SHRIMP) U-Pb zircon analysis (Chapter 8) was undertaken by Jamie J. Price under the guidance of Prof. Pete Kinny, Curtin University. Prof. Pete Kinny was involved in processing SHRIMP geochronological data and the plotting of concordia diagrams. Scanning Electron Microscope (SEM) analysis (Chapter 9) was carried out by Jamie J. Price with technical support from Dr. Duncan Muir, Cardiff University. Preparation of stable isotope samples (Chapter 9) was undertaken by Jamie J. Price, overseen by Prof. Adrian Boyce of the Scottish Universities Environmental Research Centre (SUERC) and prepared samples were analysed by Mrs. Alison McDonald (SUERC). Monazite U-Pb geochronological analysis (Chapter 9) was conducted by Jamie J. Price with technical support and assistance from Dr. Matt Horstwood and input from Dr. Simon Tapster, both of the NERC Isotope Geoscience Laboratories (NIGL). Dr. Matt Horstwood processed the monazite U-Pb data and plotted concordia diagrams. Gold assay data presented in **Appendix E10** was provided courtesy of Minjar Gold Pty.

CHAPTER 2

Literature review

2.1 Supracrustal Stratigraphy

Stratigraphic understanding of greenstone belts in the Murchison Domain has developed significantly over the last half-century, principally due to more comprehensive and systematic geological mapping being undertaken across the region, in combination with significant advancements in geochronology. Early work attributed a single stratigraphic scheme to all the greenstone belts across the entire Murchison Domain (Watkins and Hickman, 1990), whereas the most recently devised lithostratigraphic framework (Van Kranendonk, 2008; Van Kranendonk and Ivanic, 2009; Van Kranendonk et al., 2013) is primarily applicable to the northeastern Murchison Domain and many units in the southwest remain unassigned. Ongoing geological mapping in the southwest Murchison Domain (e.g., Zibra et al., 2016; Zibra et al., 2017a; Ivanic, 2018) aims to incorporate rocks in this area into the wider Murchison Domain stratigraphy. As the stratigraphy in the Yalgoo-Singleton Greenstone Belt (YSGB) is only partially incorporated into the most recent framework, this section includes a review of previous stratigraphic schemes (Section 2.1.2), in addition to an overview of the updated framework of Van Kranendonk et al. (2013) (Section 2.1.3).

2.1.1 Classification of Ultramafic Extrusive Rocks

The classification of extrusive ultramafic rocks has long been a contentious issue, and the use of varying and inconsistent terminology has led to confusion in the literature (Arndt et al., 2008). Komatiites are a type of ultramafic extrusive rock that was originally recognised by Viljoen & Viljoen (1969) in the Archaean Barberton greenstone belt of South Africa. These rocks were distinguished not only by their very high MgO content, but also large, skeletal, platy or bladed crystals of olivine, termed ‘crystalline quench textures’ by Viljoen & Viljoen (1969) and later named ‘spinifex texture’ by Nesbitt (1971). The original komatiite classification was thus based on geochemical constraints and their distinct textures (Kerr and Arndt, 2001). However, in the most recent IUGS classification of ultramafic rocks (Le Bas, 2000), a komatiite classification is based purely on chemical criteria; for rocks with > 18 wt.% MgO, < 1 wt.% TiO_2 and < 2 wt.% $Na_2O + K_2O$. Meanwhile, a picrite is defined as a rock with 12-

18 wt.% MgO for < 2 wt.% $Na_2O + K_2O$, and all rocks with > 12 wt.% MgO for samples with 2-3 wt.% $Na_2O + K_2O$.

Kerr & Arndt (2001) criticised this purely chemical classification, emphasising the original requirement of spinifex texture for a komatiitic classification and using ultramafic extrusive rocks on the Isle of Gorgona, Colombia (Kerr et al., 1996), to exemplify the shortcomings in the IUGS classification. However, in response, Le Bas (2001) reiterated that in such a classification, the chemical composition, which relates to the parental magma chemistry, is more important than textural features, which instead indicate crystallisation conditions. Consequently, a range of terminology has been used by Archaean researchers in relation to high Mg-Ni-Cr volcanic rocks, including magnesian basalt, high-Mg basalt, basaltic komatiites and komatiitic basalts, commonly assigned to rocks of the same chemistry (Arndt & Nisbet, 1982; Hallberg, 1983; Watkins & Hickman, 1990).

In light of these concerns, the following classification for high-magnesian, extrusive, ultramafic rocks is used in this thesis:

- < 12 wt.% MgO + no spinifex texture = *Basalt*
- 12-18 wt.% MgO + no spinifex texture = *High-Mg basalt*
- < 18 wt.% MgO + spinifex texture = *Spinifex-textured basalt*
- > 18 wt.% MgO + spinifex texture = *Komatiite*
- > 18 wt.% MgO + no spinifex texture = *Picrite*

2.1.2 Previous Stratigraphic Schemes

Supracrustal assemblages in the greenstone belts of the Murchison Domain were originally subdivided into a four-part stratigraphic succession, based primarily on the concept of lithological associations (Hallberg, 1976; Muhling & Low, 1977; Baxter et al., 1983; Lipple et al., 1983; Baxter & Lipple, 1985) and comprised the following:

a) An upper felsic-sedimentary association
b) An upper mafic association
c) A lower felsic-sedimentary association
d) A lower mafic association

Though it crudely satisfied the presence of multiple volcanic cycles, the lack of detail and crucially, time constraints, proved problematic and stratigraphic correlations were complicated by extensive folding and faulting of supracrustal rocks in the region. Watkins and Hickman (1990) subsequently introduced a formal stratigraphic scheme for the Murchison Domain, based on extensive regional

geological mapping and limited radiometric dating. Within their lithostratigraphic scheme, the Murchison Supergroup encompassed all supracrustal rocks in the Murchison Domain and is divided into two distinct successions, the Luke Creek Group and overlying Mount Farmer Group.

In this classification, the older Luke Creek Group contains four formations regarded as continuous throughout most greenstone belts of the domain, forming a ~10 km-thick conformable succession (Watkins & Hickman, 1990; Fig. 2.1). The lowermost formation, the Murrouli Basalt, consists of a thick pile of tholeiitic and high-Mg basalts with minor ultramafic rocks and is overlain by the Golconda Formation (Fm), a succession of quartz-hematite Banded Iron Formation (BIF) units interlayered with mafic and ultramafic extrusive rocks. These two lowermost formations were only distinguished by Watkins & Hickman (1990) north of 28° 50' latitude, thus were not identified in the far southwestern Murchison Domain. The overlying Gabanintha Formation comprises a bimodal sequence of mafic-ultramafic volcanic rocks progressing upwards into felsic volcanic, volcaniclastic and sedimentary rocks (Fig. 2.1; Watkins & Hickman, 1990). The uppermost Windaning Fm consists of a succession of jasper-bearing BIF and chert units, interlayered with felsic volcanic and volcaniclastic rocks and minor basalt. Watkins & Hickman (1990) assigned a majority of the supracrustal rocks in the YSGB to the Gabanintha and Windaning formations.

The Mount Farmer Group contains 13 broadly contemporaneous formations of limited lateral extents, which are largely restricted to single greenstone belts. Most formations represent individual volcanic centres developed on a basement of Luke Creek Group rocks and comprise variable proportions of tholeiitic and high-Mg basalt, andesite and felsic volcaniclastic rocks. In contrast, the Mougooderra Fm, which occurs over a 150 x 100 km extent of the southwestern Murchison Domain including the YSGB (Fig. 4.3), consists of a 3 km-thick, upward-fining sequence of epiclastic sedimentary rocks,

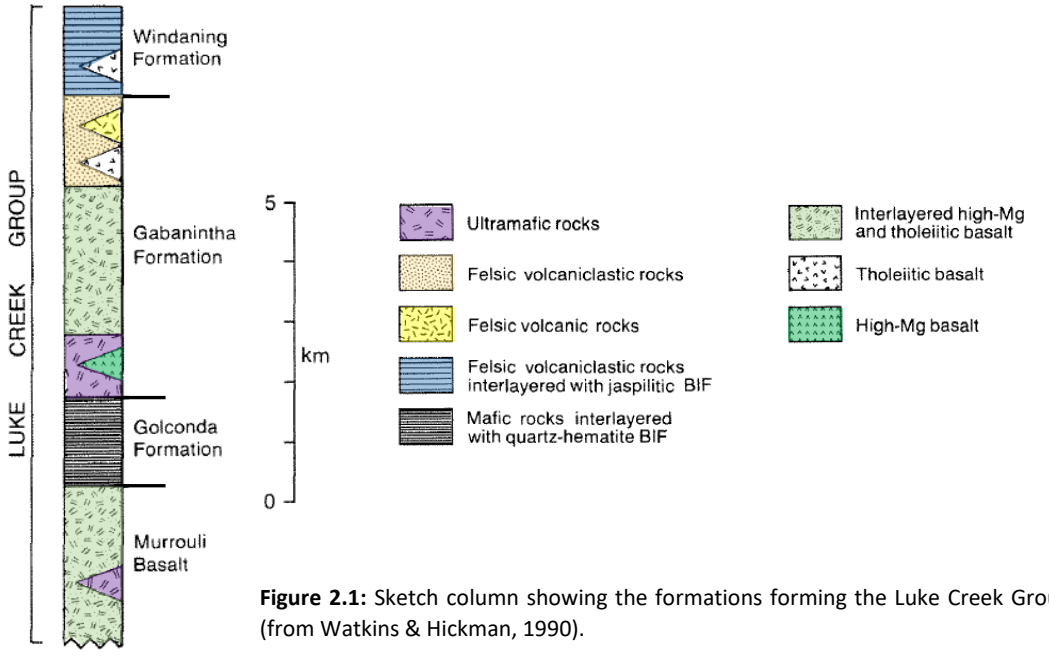

Figure 2.1: Sketch column showing the formations forming the Luke Creek Group (from Watkins & Hickman, 1990).

including conglomerate, sandstone, shale, chert and BIF, in addition to minor basalt and felsic volcaniclastic rocks (Lipple et al., 1983; Watkins & Hickman, 1990). The Mougooderra Fm unconformably overlies the Luke Creek Group and conglomerates include clasts of Luke Creek Group rocks, indicating derivation from underlying rocks. The Mougooderra Fm is largely confined to a shear-bounded basin or graben structure, typically 1-7 km in width, and represents the only significant, epiclastic sedimentary basin in the Murchison Domain (Watkins & Hickman, 1990).

In light of expanded geochronology in the region, several problems and inconsistencies have been identified with the lithostratigraphic scheme of Watkins & Hickman (1990) (Pidgeon & Hallberg, 2000; Van Kranendonk & Ivanic, 2009). Subsequently, Pidgeon & Hallberg (2000) proposed an informal scheme comprising five assemblages that were not time-equivalent across the region, and concluded it was not possible to erect a formal, unified framework for the greenstone belts of the northern Murchison Domain due to poor exposure, structural complexity, and physical separation by granitoid intrusions. However, this scheme is considered problematic for the same reasons as Watkins & Hickman (1990), with the further issue that a significant amount of rocks remain unassigned (Van Kranendonk & Ivanic, 2009).

2.1.3 Current Stratigraphic Framework

A new stratigraphic framework for the northeastern Murchison Domain was proposed by Van Kranendonk (2008) and updated by Van Kranendonk & Ivanic (2009) and Van Kranendonk et al. (2013). This framework was initially based on new GSWA geological mapping, petrography and geochronology in the northeastern part of the domain, due to better exposure and greater economic interest in this area. However, ongoing GSWA geological mapping in the southern Murchison Domain (e.g., Ivanic, 2018; Zibra et al., 2016; 2017a), including part of the YSGB, is building upon the stratigraphic framework of Van Kranendonk et al. (2013) and working to encompass rocks across the entire Murchison Domain.

In the new stratigraphic scheme, the Murchison Supergroup comprises four groups of volcano-sedimentary supracrustal rocks, comprising an unnamed group of the oldest formations in the succession that have dates of c. 2.95 Ga, in addition to the Norie Group, Polelle Group and Glen Group (Fig. 2.2). The Norie Group broadly correlates with the Murrouli Basalt and Golconda Fm of Watkins & Hickman (1990), the Polelle Group replaces the Gabanintha and Windaning formations, and the Glen Group supersedes the Mount Farmer Group. The c. 2.95 Ga Formations were not previously recognised by Watkins & Hickman (1990), and units of the group were erroneously assigned to the Luke Creek Group. Regional unconformities have been identified between the c. 2.95 Ga formations and Norie Group by Wang et al. (1998), and between the Polelle and Glen groups by Van Kranendonk

(2008). It has been suggested that this demonstrates the autochthonous development of the supracrustal rocks, supported by a lack of large thrusts recognised in the region (Ivanic et al, 2012).

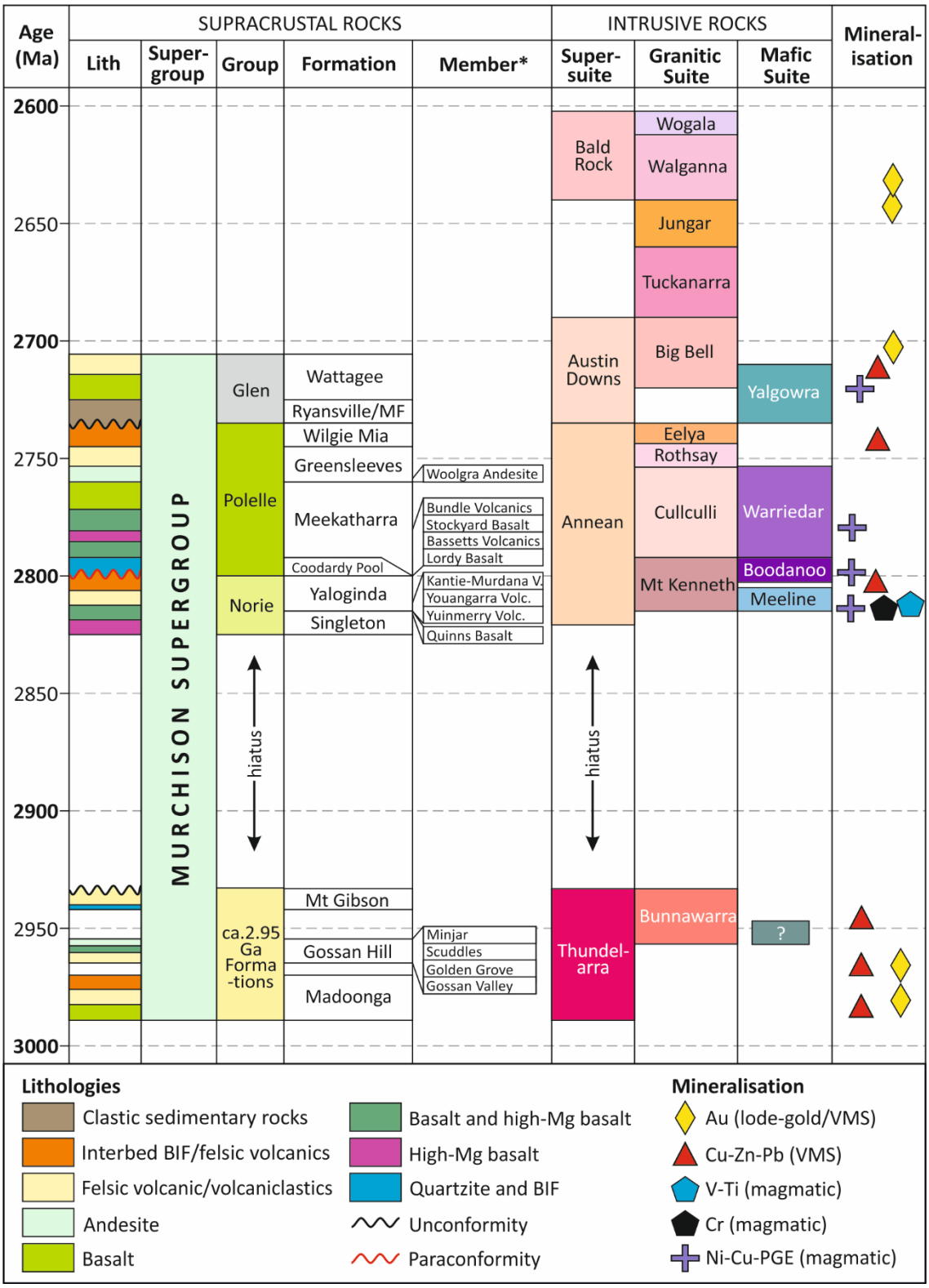

Figure 2.2: Stratigraphic framework for rocks in the Murchison Domain, including supracrustal rocks (with accompanying generalised lithological column) and intrusive rocks, divided into granitic suites and mafic-ultramafic suites. Significant mineralisation events are shown in the last column. Note the hiatus in magmatic activity from 2930 to 2820Ma and the unnamed group of 'c. 2.95 Ga Formations' reflecting less well studied rocks. *Members have been assigned principally for units in the northeastern and eastern Murchison Domain. Abbreviations; MF = Mougooderra Fm. Redrawn after Lowrey et al. (2020), Ivanic (2019) and Van Kranendonk et al. (2013).

Currently, a significant proportion of supracrustal rocks in the southwestern Murchison Domain, including the study area located in the YSGB, remain unassigned with regard to the new stratigraphic

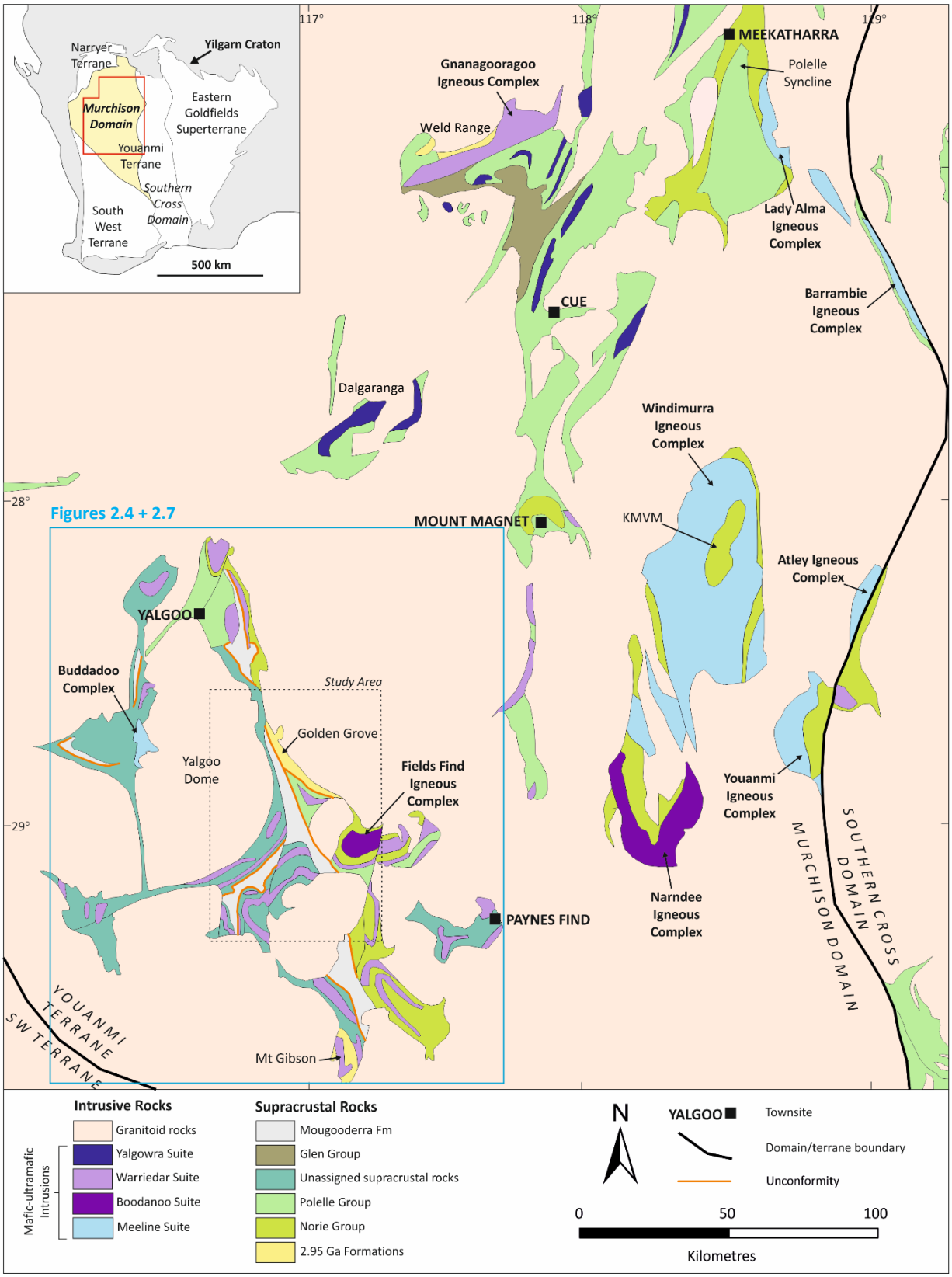

Figure 2.3: Regional geological map of the Murchison Domain showing the distribution of supracrustal rocks and mafic-ultramafic intrusive rocks. Significant mafic-ultramafic intrusions are labelled in bold. The inset image shows the location of the area within the Yilgarn Craton. KMVM = Kantie Murdana Volcanic Member. The outline of Fig. 2.4 is shown in blue. Redrawn after Ivanic et al. (2017) and Ivanic (2019). Geological data from GSWA.

framework (Fig. 2.3). In particular, the extent of the Polelle and Norie Groups in this area is not well defined; the current partial designation of some units to these groups is based on limited geochronological and geochemical data and is locally subject to change.

2.1.3.1 c. 2.95 Ga Formations (2980-2935 Ma)

The lowermost group of the Murchison Supergroup, referred to as the c. 2.95 Ga Formations, comprises the Madoonga Fm, Gossan Hill Fm and Mt Gibson Fm (Fig. 2.2). The latter two are found exclusively in the southwestern Murchison Domain, specifically at the Golden Grove and Mt Gibson mining centres, respectively, whereas the Madoonga Fm is found in the northern Weld Range (Fig. 2.3). This group does not outcrop over most of the Murchison Domain, but has been proposed to occur at depth due to the presence of inherited zircons of a similar age in overlying metasedimentary rocks (Wang, 1998). The Madoonga Fm consists of rhyolitic volcanic and volcaniclastic rocks, and currently represents the oldest rocks identified in the Murchison Domain (Wingate et al., 2012).

The Gossan Hill Fm is exposed at the Golden Grove mine in the northeast YSGB (Fig. 2.4) and consists of a 2.5 km thick sequence of felsic and intermediate volcanic and volcaniclastic rocks, with minor chert (Van Kranendonk et al., 2013), representing the oldest unit in the greenstone belts of the southern Murchison Domain (Wang et al., 1998). The Gossan Hill Fm is also host to syngenetic volcanic-hosted massive sulphide (VHMS) style Cu-Zn-Ag-Au mineralisation, at the world class Gossan Hill and Scuddles deposits (Sharpe & Gemmell, 2001). The Gossan Hill Fm is composed of four conformable members (Clifford, 1992). The lowermost Gossan Valley Member consists of quartz-porphyritic rhyolite and felsic volcaniclastic rocks and is intruded by the Gnows Nest Granodiorite (Thundelarra Supersuite; Section 2.3.2) at its base (Zibra et al., 2016). The overlying Golden Grove and Scuddles members comprise rhyolite, rhyodacite and laminated felsic volcaniclastic rocks and are both host to massive sulphide mineralisation (Clifford, 1992; Zibra et al., 2016). The uppermost Minjar Member consists of felsic volcaniclastic rocks and siliciclastic sedimentary rocks, with minor amygdaloidal basalt (Clifford, 1992).

The Mount Gibson Fm is exposed exclusively in the southernmost Murchison Domain and is composed of rhyolitic to dacitic volcanic and volcaniclastic rocks that are also host to syn-volcanic VHMS mineralisation, overprinted by lode-gold mineralisation (Yeats et al., 1996).

2.1.3.2 Norie Group (2820-2805 Ma)

The c. 2.95 Ga Formations are unconformably overlain by the more extensive Norie Group, which occurs across the Murchison Domain and is the lowest stratigraphic unit observed in the northern

Murchison Domain (Fig. 2.3). The group contains the Singleton Fm at its base, comprising mafic-ultramafic volcanic rocks commonly altered to talc-chlorite-tremolite-serpentine schists, in turn

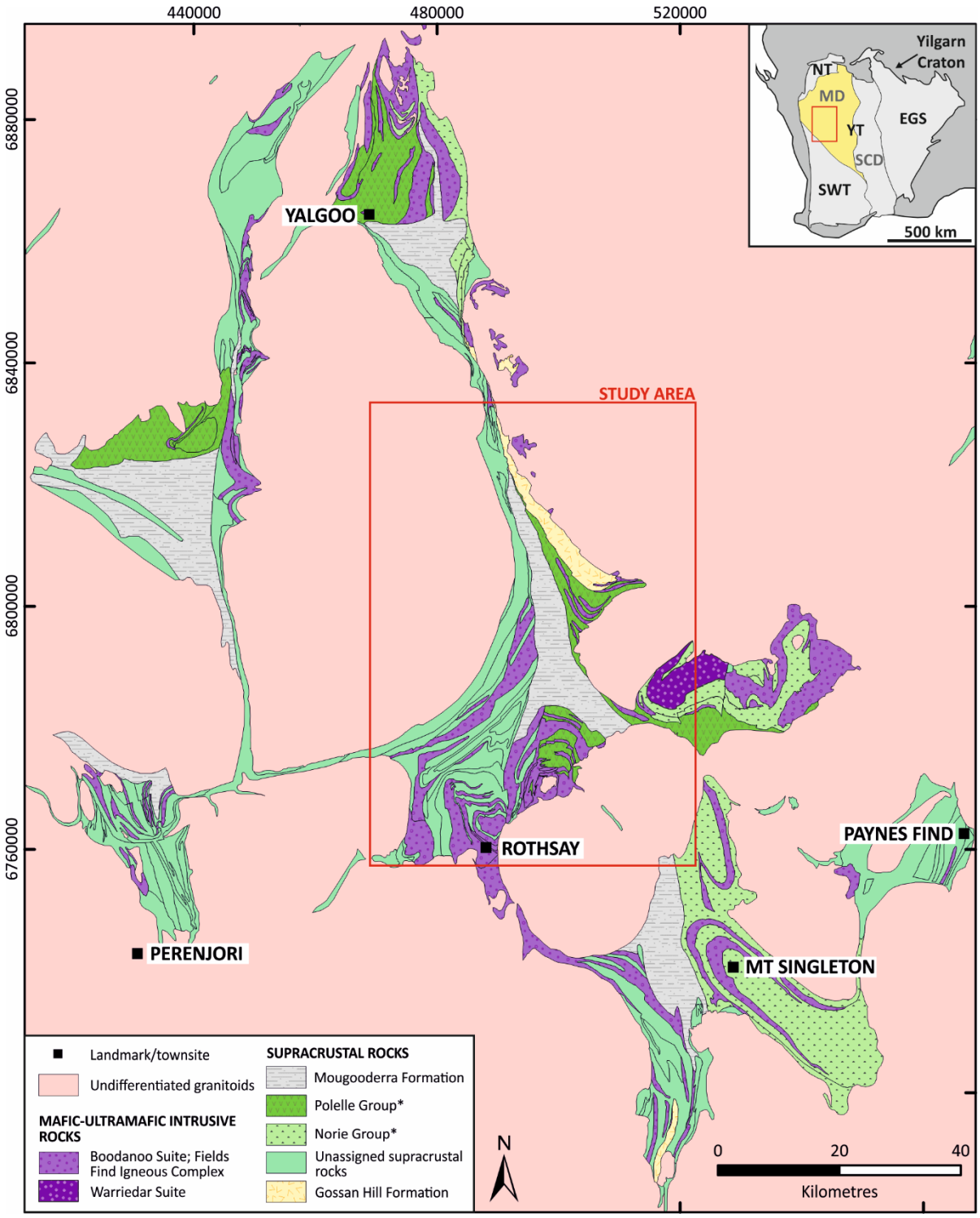

Figure 2.4: Geological map of the southwestern Murchison Domain showing the geology of greenstone belts comprising supracrustal rocks and mafic-ultramafic intrusions. The geology of intervening felsic-intermediate ('granitoid') intrusions is detailed in Figure 2,7. The extent of the displayed area is shown on the inset image of the Yilgarn Craton, in which NT = Narryer Terrane, YT = Youanmi Terrane, EGS = Eastern Goldfields Superterrane, SWT = South West Terrane, MD = Murchison Domain and SCD = Southern Cross Domain. The study area of this project is outlined in red. Geological data has been modified from the GSWA 2020 1:500,000 scale regional map of Western Australia. *The extent of the Polelle and Norie groups in the southwestern Murchison Domain is not clear – the current partial designation of these units by GSWA is based on limited geochronological and geochemical data and is locally subject to change.

overlain by the Yaloginda Fm (formerly Golconda Fm of Watkins & Hickman, 1990), consisting of intermediate volcanic rocks and sedimentary rocks including BIF, chert and shale (Fig. 2.2). The extent of these formations is not discernable on the scale of the map in Figure 2.3, and so these units are collectively symbolised as the Norie Group. Mafic-ultramafic extrusive rocks of the Singleton Fm have been interpreted to have a komatiitic association, and thus, to be indicative of mantle plume activity (Watkins & Hickman, 1990; Barley et al., 2000; Pidgeon & Hallberg, 2000; Van Kranendonk et al., 2013). Barley et al. (2000) identified a suite of ultramafic amygdaloidal and spinifex-lacking volcanic and volcaniclastic rocks in the Singleton Fm with Ti-rich, Al-depleted and incompatible element-enriched geochemical signatures. These rocks were interpreted as Karasjok-type komatiites (after Barnes & Often, 1990) and were suggested to form from interaction of plume magmatism with subduction-modified lithosphere (Barley et al. 2000). However, Wyman (2019) contended that the rocks were more comparable to picrites in Phanerozoic ophiolites and that pyroclastic ultramafic rocks resulted from magma mixing with hydrous crustal magmas. Singleton Fm rocks have been identified at the southern extremity of the YSGB, in the Mt Singleton area (Fig. 2.4; Ivanic, 2018; Wyman, 2019).

In the northeastern Murchison Domain, the Yaloginda Fm occurs a 2 km-thick sequence consisting of porphyritic basaltic andesites, volcaniclastic rocks and rhyolitic tuffs at its base, progressing upwards into a ~1.5 km-thick unit of jaspilitic BIF, shale and chert (Lowrey et al., 2020). Abundant fine-grained sedimentary rocks and BIF in the upper part of the Yaloginda Fm indicate a protracted period of volcanic quiescence between the Norie Group and overlying Polelle Group (Watkins & Hickman, 1990; Lowrey et al., 2020). The Kantie-Murdanna Volcanic Member (KMVM) is a > 1 km thick metamorphosed volcano-sedimentary succession near the base of the Yaloginda Fm in the southeastern Murchison Domain (Fig. 2.3), dominated by rhyolitic and dacitic volcanic rocks, with minor interbedded BIF and chert (Van Kranendonk et al., 2013). Volcanism of the Norie Group is understood to have been accompanied by the emplacement of vast (up to 7 km thick and 80 km diameter) layered ultramafic-mafic complexes of the Meeline and Boodanoo suites (Section 2.3.1), interpreted as the intrusive component of a large igneous province (Fig. 2.3; Ivanic et al., 2010). The KMVM is interpreted to represent a large roof pendant within the Windimurra Igneous Complex, the largest Meeline Suite intrusion (Fig. 2.3) (Section 2.3.1; Ivanic et al., 2010). The upper Yaloginda Fm in the northeastern Murchison Domain is host to prevalent sheeted mafic-ultramafic sills of the Yalgowra Suite, which split and inflate the sedimentary and volcaniclastic dominated succession. It has been proposed that these sills represent subvolcanic intrusions associated with volcanism and the emplacement of overlying Glen Group volcanic rocks (Van Kranendonk & Ivanic, 2009).

2.1.3.3 Polelle Group (2800-2730 Ma)

The Polelle Group conformably overlies the Norie Group and is widespread across much of the northern Murchison Domain (Van Kranendonk et al., 2013). In the far northeast near Cue (Fig. 2.3), the base of the group is marked by a discontinuous, thin (<100 m) unit of quartzite and BIF assigned to the Coodardy Pool Fm. This unit is overlain by the more extensive Meekatharra Fm, which is up to 2500 m in thickness and consists of variably tholeiitic, high-Mg, variolitic and spinifex-textured volcanic rocks and minor interflow volcaniclastic and sedimentary rocks (Van Kranendonk et al., 2013). Some volcanic flows display evidence of subaerial extrusions, including upper rubbly flowtop breccias consisting of irregular fragments of vesicular high-Mg basalt (Van Kranendonk et al., 2013). At the type locality for the Polelle Group, the well exposed Polelle Syncline in the northeastern Murchison Domain, detailed mapping has identified four discrete units within the Meekatharra Fm (Lowrey et al., 2017; Lowrey et al., 2020). The lowermost Lordy Basalt Member consists of high-Mg basalt with acicular pyroxene phenocrysts and locally, exhibits pyroxene spinifex textures (Lowrey et al., 2020).

The overlying Bassetts Volcanic Member comprises high-Mg basaltic andesites and basalts commonly containing fine acicular pyroxene phenocrysts and major and trace element geochemical features that have been interpreted as boninite-like (Wyman, 2019; Lowrey et al., 2020). The Stockyard Basalt Member overlies the Bassetts Volcanic Member and is dominated by massive tholeiitic basalt that is locally pillowed and vesicular, whereas the uppermost Bundle Volcanic Member is a high Mg basalt to basaltic andesite unit that contains internally zoned flows comprising pyroxene spinifex-textured flow tops and olivine-bearing cumulate bases (Lowrey et al., 2020). A new form of spinifex texture, platy pyroxene spinifex, has recently been identified within Bundle Volcanic Member volcanic rocks (Lowrey et al., 2017). Notably, some Meekatharra Fm volcanic rocks contain sheaves of metamorphic actinolite and tremolite crystals that locally mimic spinifex and can be difficult to distinguish from acicular pyroxene spinifex (Watkins & Hickman, 1990). Meekatharra Fm volcanic rocks commonly contain mm- to cm-scale varioles that have been suggested to demonstrate immiscibility between the silicate magma and exsolved, hydrous fluids, and therefore, may signify hydrous parental magmas (Ballhaus et al., 2015; Lowrey et al., 2020).

Meekatharra Fm volcanic rocks have recently been defined in the Yalgoo area, in the northern YSGB, based on field relationships and limited geochemistry (Fig. 2.4; Ivanic et al., 2015a). Furthermore, Koutsoumbis (2020) suggested that rocks in the southern YSGB northeast of Rothsay are equivalent to Meekatharra Fm rocks, due primarily to the identification of boninite-like geochemical trends. These rocks exhibit subtle differences in lava abundances and types compared to the northeastern Murchison Domain (Ivanic et al., 2015a).

The Greensleeves Fm overlies the Meekatharra Fm and consists of up to 5 km of andesitic to rhyolitic volcanic and volcaniclastic rocks, conformably overlain by felsic volcanic rocks, shale and BIF of the Wilgie Mia Fm (Fig. 2.2; Van Kranendonk & Ivanic, 2009). The base of the Greensleeves Fm in the Polelle Syncline is marked by the Woolgra Andesite Member, comprising interbedded volcanic flows, breccias and volcanogenic sedimentary rocks that range in composition from basaltic andesite to dacite (Van Kranendonk et al., 2013; Lowrey et al., 2020). Volcanic rocks are commonly porphyritic, containing phenocrysts of plagioclase, clinopyroxene and rare hornblende, and are locally amygdaloidal (Lowrey et al., 2020). A coarse-grained rhyolitic volcanic breccia near the base of the Greensleeves Fm is interpreted to represent the products of a massive, explosive eruption that formed proximal to the volcanic vent (Van Kranendonk et al. (2013). Windley (1995) proposed two generalised trends with increasing stratigraphic height in greenstone belts; a decrease in the amount of ultramafic rocks and an increase in the ratio of volcaniclastic material to flows. These trends are well illustrated by Polelle Group rocks, which display a progressive compositional change from mafic-ultramafic to andesitic and rhyolitic volcanic and volcaniclastic rocks. Condie (1997) suggests that this transition reflects a change from extensive submarine eruptions of mafic-ultramafic lavas to the development of localised stratovolcanoes and associated sedimentary basins. Significant thicknesses of shale and BIF in the stratigraphically uppermost Wilgie Mia Fm imply deposition in low energy, marine settings during periods of prolonged volcanic quiescence (Watkins & Hickman, 1990). Importantly, the generation and deposition of terrestrial sedimentary rocks, particularly quartz-rich sandstones (e.g., Coodardy Pool Fm at the base of the Polelle Group), is indicative of sub-aerial exposure and may suggest that weathering of uplifted crust was taking place in the region (Watkins and Hickman, 1990).

2.1.3.4 Glen Group (2735-2710 Ma)

The Glen Group disconformably to unconformably overlies rocks of the Polelle Group and is divided into the Ryansville Fm comprising clastic sedimentary rocks and the conformably overlying Wattagee Fm, consisting of high-Mg basalts and rhyolites (Fig. 2.2; Van Kranendonk et al., 2013). Clastic sedimentary rocks of the Mougooderra Fm (Section 2.1.2; Watkins & Hickman, 1990) in the southwestern Murchison Domain have been correlated with rocks of the Glen Group (Ivanic et al., 2015a; Fig. 2.3). However, this is yet to be corroborated by robust geochronology, despite multiple attempts at dating the Mougooderra Fm (Section 2.2).

Ryansville Fm sedimentary rocks vary in thickness between ~1 km in the north, to a <30 cm interval of poorly sorted conglomerate in the greenstone belts of the central Murchison Domain (Van Kranendonk et al., 2013), reflecting variable sedimentary basin development. In the western Weld Range, conglomerates, sandstones and shales of the Ryansville Fm lie with an angular unconformity

upon rocks of the Wilgie Mia Fm, which include a jasper-bearing chert unit. This chert unit contains many non-cylindrical folds of a type that is absent in overlying Ryansville Fm sedimentary rocks, documenting a hiatus between the Polelle Group and Glen Group (Van Kranendonk et al., 2013). Furthermore, these relationships indicate, at least locally, one earlier deformational phase prior to regional deformation, as previously discerned in the Kalgoorlie Terrane, eastern Yilgarn Craton (Tripp, 2000; Blewett et al., 2004a). Consequently, late-stage sedimentary rocks play a crucial role in understanding the concluding stages of the structural development of the Murchison Domain, in addition to lode-gold mineralisation (see Tripp, 2019). Volcanism and sedimentation of the Glen Group is proposed to have been coeval with the emplacement of widespread, thick mafic-ultramafic sills of the Yalgowra Suite into the underlying Polelle Group, particularly within felsic volcaniclastic rocks of the Greensleeves Fm (Section 2.1.3.3; Van Kranendonk & Ivanic, 2009).

2.2 Geochronology of Supracrustal Rocks

Sensitive High Resolution Ion Microprobe (SHRIMP) U-Pb zircon analysis has been the principal analytical technique used to determine the ages of volcanic and sedimentary units in the Murchison Domain (e.g., Wang, 1998; Wang et al, 1998; Pidgeon & Hallberg, 2000; Van Kranendonk et al., 2013; Zibra et al., 2018). Advances in geochronological analysis over the past 25 years have led to a significant reduction in the uncertainties associated with calculated ages, allowing a more detailed insight into greenstone belt development (e.g., Heubeck et al. 2013).

U-Pb zircon analysis is most frequently undertaken on compositionally evolved volcanic and intrusive igneous rocks that contain abundant primary magmatic zircon crystals, which can be analysed to constrain the crystallisation age of the host rock. Occasionally, these rocks may contain inherited 'xenocrystic' zircon crystals incorporated into the magma from country rocks prior to crystallisation, which can constrain the maximum crystallization age of the host rock (e.g., Lu et al., 2016c). In contrast, U-Pb zircon dating of sedimentary rocks involves analysis of detrital zircon grains, in order to assess the age distribution of contained zircon crystals and constrain a maximum depositional age for the rock (i.e., the age of the youngest detrital zircon[s]). Crucially, the actual depositional age of a sedimentary rock can be significantly younger than the maximum depositional age determined by detrital zircon geochronology. U-Pb zircon dating of volcanogenic sedimentary and volcaniclastic rocks can be more challenging, as it can be difficult to differentiate between primary zircon crystals derived from coeval volcanism (yielding the depositional age), and detrital zircon grains (giving a maximum depositional age). A single population of euhedral, angular zircon crystals yielding comparable ages typically indicates primary zircons derived from a single, proximal source, which in combination with petrographic and field relations, may be used to constrain the age of syn-sedimentary volcanism. In

contrast, an array of variably rounded zircon grains with multiple distinct age populations is indicative of a detrital zircon assemblage (e.g., Lu et al., 2016e).

Whereas the ages of supracrustal rocks in the northeast Murchison Domain have been relatively well

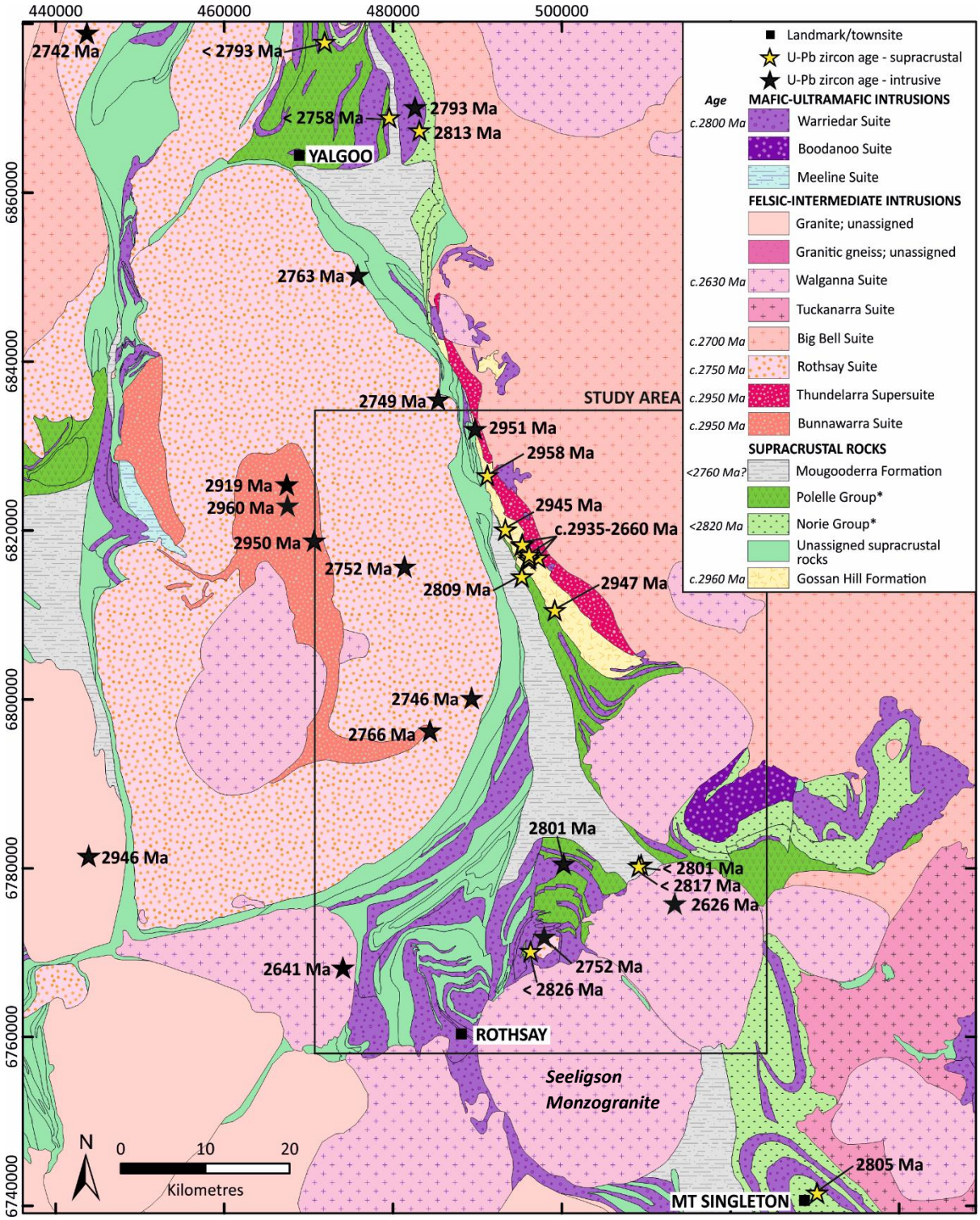

Figure 2.5: Simplified geological map of the area surrounding the Yalgoo-Singleton Greenstone Belt showing intrusive rocks, supracrustal rocks and U-Pb zircon ages from the GSWA database. Black stars represent U-Pb zircon crystallisation ages of intrusive rocks, whereas yellow stars represent the U-Pb zircon crystallisation/depositional ages of supracrustal rocks (< denotes maximum depositional ages from detrital zircons). The study area of this project is outlined in black. Geology corresponds to the GSWA 2020 1:500,000 scale map of Western Australia. *The extent of the Polelle and Norie groups in the southwestern Murchison Domain is not clear – the current partial designation of these units by GSWA is based on limited geochronological and geochemical data and is locally subject to change.

Stratigraphic unit	Location	Sample #	Rock type	Age (Ma)	Source
GLEN GROUP					
Wattagee Fm.	29.5 km N of Cue	183975	metarhyolite schist	2725 ± 4	Wingate et al. (2009a)
Ryansville Fm.	45 km NNE of Cue	185925	quartz sandstone	≤2740 ± 4	GSWA (2018)
Mougooderra Fm.	11 km NE of Yalgoo	211101	volcaniclastic mudstone	≤2758 ± 4*	Lu et al. (2016e)
Mougooderra Fm.	Warriedar Hill, YSGB	198295	metadacite	≤ 2801 ± 5	Lu et al. (2016c)
Mougooderra Fm	Warriedar Hill, YSGB	198296	quartz sandstone	≤ 2817 ± 3	Lu et al. (2018)
POLELLE GROUP					
Wilgie Mia Fm.	Weld Range	96-120	felsic crystal tuff	2752 ± 9	Wang (1998)
Greensleeves Fm.	Mount Magnet	94-117	flow-banded felsic rock	2727 ± 6	Schiøtte and Campbell (1996)
Greensleeves Fm.	Abbotts belt	93-971	felsic volcaniclastic sandstone	2734 ± 5	Wang (1998)
Greensleeves Fm.	Big Bell Mine	89-438	metarhyolite schist	2737 ± 4	Mueller et al. (1996)
Greensleeves Fm.	Mount Magnet	92-269	felsic volcanic	2739 ± 11	Schiøtte and Campbell (1996)
Greensleeves Fm.	Dalgaranga greenstone belt	W296	banded tuff	2745 ± 4	Pidgeon and Hallberg (2000)
Greensleeves Fm.	28.6 km ENE of Cue	185932	felsic volcanic	2746 ± 4	GSWA (2018)
Greensleeves Fm.	10 km NW of Cue	W373	rhyolite tuff	2761 ± 1	Pidgeon and Hallberg (2000)
Woolgra Andesite Member	30 km S of Meekatharra	178105	feldspar-phyric andesite	2755 ± 5	Wingate et al. (2008b)
Yalgoo Fm.	14km N of Yalgoo	207686	volcaniclastic metasandstone	≤ 2793 ± 8	Lu et al. (2016g)
Meekatharra Fm.	Mount Magnet mine	92-272	chert	2798 ± 8	Schiøtte and Campbell (1996)
NORIE GROUP					
Ambiguous - Norie Gp/Mougooderra Fm	Golden Grove mine	92-382	reworked volcaniclastic sandstone	2809 ± 5	Wang et al. (1998)
Yaloginda Fm.	30km S Meekatharra	93-975	amygdaloidal basalt	2810 ± 5	Wang (1998)
Yaloginda Fm.	8.5km NE Meekatharra	198953	felsic volcaniclastic rock	2814 ± 2	Wingate et al. (2011)
Yaloginda Fm.	30km S Meekatharra	93-976	amygdaloidal basalt	2815 ± 7	Wang (1998)
Kantie-Murdanna Volc. Member	56 km ESE of Mount Magnet	169003	vesicular rhyolite	2813 ± 3	Nelson (2001)
Singleton Fm	1.8km NE Mt Singleton	198228	volcaniclastic metasandstone	≤ 2805 ± 5	Wingate et al. (2013b)
Norie Group	15 km E of Yalgoo	198298	metadacite	2813 ± 3	Lu et al. (2016f)
Norie Group?	Mulgine Hill, YSGB	198293	volcaniclastic metasandstone	≤ 2894 ± 7	Lu et al. (2016a)
'c. 2.95 FORMATIONS'					
Mount Gibson Fm.	Mount Gibson mine	OR77	subvolcanic quartz porphyry	2929 ± 3	Yeats et al. (1996)
Mount Gibson Fm.	Mount Gibson mine	HN97	felsic schist	2934 ± 3	Yeats et al. (1996)
Gossan Hill Fm.	Mougooderra Hill, YSGB	211102	felsic volcaniclastic rock	2947 ± 4	Lu et al. (2016d)
Scuddles Member	Golden Grove mine	203702	metadacite	2962 ± 4	Wingate et al. (2015a)
Scuddles Member	Golden Grove mine	92-385	quartz-phyric rhyodacite lava	2945 ± 4	Wang et al. (1998)
Shadow Well Member	Golden Grove mine	92-388	quartz-phyric rhyolite	2960 ± 6	Wang et al. (1998)
Shadow Well Member	Golden Grove mine	92-386	quartz-rich lava	2953 ± 7	Wang et al. (1998)
Golden Grove Member	Golden Grove mine	203703	metarhyolite	2963 ± 6	Wingate et al. (2015b)
Golden Grove Member	Golden Grove mine	203704	metarhyolite	2959 ± 5	Wingate et al. (2015c)
Madoonga Fm.	Weld Range	155569	metarhyolite	2977 ± 3	Wingate et al. (2013a)
Madoonga Fm.	Weld Range	193972	metarhyolite clast	2979 ± 3	Wingate et al. (2012)

Table 2.1: Selected U-Pb zircon analyses published for rocks in the Murchison Domain, with those reported from the Yalgoo-Singleton Greenstone Belt (study area) highlighted in yellow. ≤ denotes maximum depositional ages determined from analysis of detrital/xenocrystic zircons. *tentative interpreted age based on field relations, despite younger zircon analyses. For a more exhaustive geochronological dataset see Van Kranendonk et al. (2013) and references therein, and the GSWA geochronology database.

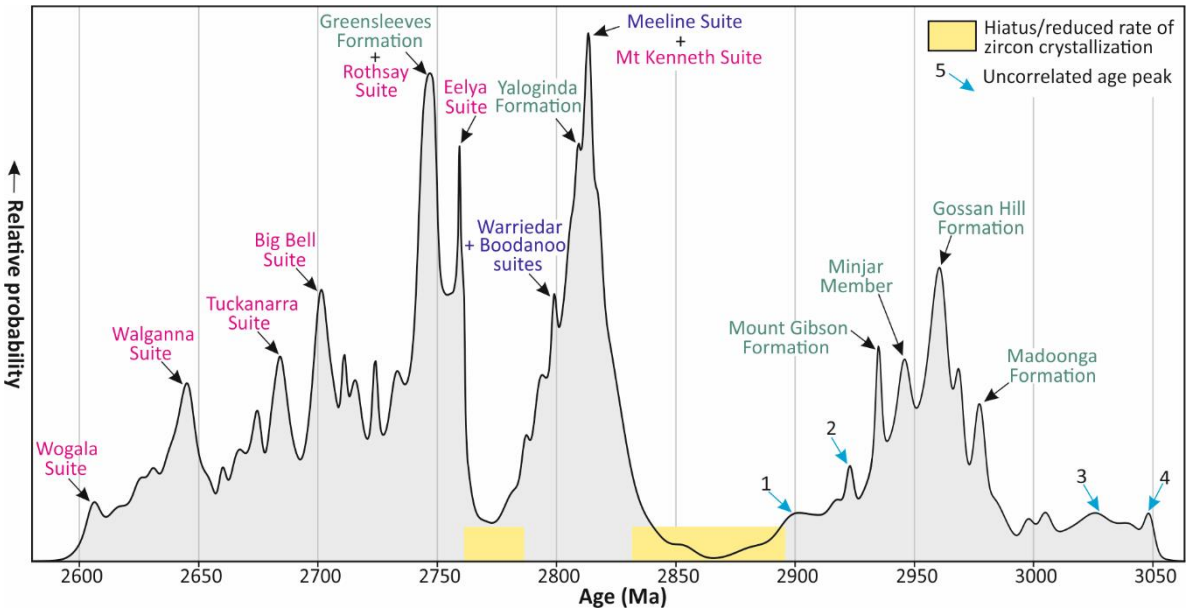

Figure 2.6: Zircon age spectra from the Murchison Domain, western Youanmi Terrane. Significant zircon crystallisation events are labelled, including supracrustal rocks (green), mafic-ultramafic intrusive suites (blue) and felsic intrusive suites (pink). Notable hiatuses are highlighted in yellow and uncorrelated peaks 1-4 are indicated. Redrawn after Ivanic (2019); data from the GSWA geochronology database.

constrained, very sparse geochronology has been undertaken on equivalent supracrustal units in the southwest. U-Pb zircon analysis has previously been undertaken on 16 supracrustal rock samples in the YSGB, the locations of which are shown in Figure 2.5. This includes five maximum depositional ages yielded from detrital zircon studies, one maximum crystallisation age yielded from zircons interpreted as xenocrystic, and ten depositional/crystallisation ages yielded from primary zircons. Of these ages, 12 correspond to samples taken from the study area, the majority of which are from the basement Gossan Hill Fm. Selected U-Pb zircon data for supracrustal rocks in the Murchison Domain, including geochronological data from the YSGB, are summarised in Table 2.1 and are described below. Ages refer to SHRIMP U-Pb zircon analyses, unless otherwise stated. A compilation of all SHRIMP U-Pb detrital and primary zircon analyses from dated rocks in the Murchison Domain exhibits distinct peaks that correspond to felsic-dominated supracrustal units in the region, including the c. 2.95 Ga Formations, Yaloginda Fm and Greensleeves Fm, in addition to felsic intrusive suites (Fig. 2.6).

The age of early felsic volcanism of the Madoonga Fm of the 'c. 2.95 Ga Formations' is constrained by U-Pb zircon ages of 2977 ± 3 Ma and 2979 ± 3 Ma, taken from a rhyolite unit and rhyolitic clast in a volcaniclastic breccia in the Weld Range greenstone belt, respectively (Wingate et al., 2012; 2013a). The latter represents the oldest published age for a supracrustal unit in the Murchison Domain. The age of felsic volcanic and volcaniclastic rocks of the Gossan Hill Fm in the YSGB is constrained by three U-Pb zircon ages of 2945 ± 4 Ma, 2953 ± 7 Ma and 2960 ± 6 Ma, taken from quartz-rich rhyolitic and rhyodacitic volcanic rocks in the Golden Grove area (Fig. 2.5; Wang et al., 1998). Recent SHRIMP U-Pb zircon dating conducted by GSWA on the Scuddles and Golden Grove members of the Gossan Hill Fm

have returned ages of 2962 ± 4 Ma, 2963 ± 6 Ma and 2959 ± 5 Ma from rhyolite and dacite samples (Wingate et al., 2015a; 2015b; 2015c). A syn-volcanic felsic quartz porphyry at Mt Gibson yielded an age of 2929 ± 3 Ma, providing an upper age bracket for the Mt Gibson Fm felsic volcanic package (Fig. 2.3; Yeats et al., 1996).

Mafic-felsic volcanism of the Norie Group is constrained by multiple U-Pb SHRIMP zircon dates from several different greenstone belts within the Murchison Domain, however, dating in the southwest is sparse and unevenly distributed (Van Kranendonk et al., 2013). U-Pb analysis of detrital zircons in a Norie Group volcaniclastic metasandstone from northeast of Rothsay, southern YSGB, yielded 64 zircon analyses with ages ranging between 3736-2882 Ma, with major age components at ca. 3300 Ma and ca. 2950 Ma, and a single zircon analysis at ~2826 Ma (Fig. 2.5; Lu et al., 2016a). The maximum depositional age of this rock was tentatively constrained at 2826 ± 7 Ma, based on the single youngest analysis, and more conservatively estimated at 2894 ± 7 Ma, based on the five other youngest analyses (Lu et al., 2016a). A felsic volcaniclastic rock of the Yaloginda Fm from the Meekatharra area (Fig. 2.3) returned a unimodal zircon age component at 2814 ± 2 Ma, interpreted as the depositional age of the rock (Wingate et al., 2011). This age is within error of the youngest detrital zircon age in a tuffaceous sandstone interbedded in the Yaloginda Fm along strike (2812 ± 7 Ma; Wang, 1998). A vesicular rhyolite from the KMVM at the base of the Yaloginda Fm yielded an age of 2813 ± 3 Ma (Nelson, 2001). Crucially, these results indicate a significant hiatus of over 100 m.y. between the deposition of the Mt Gibson Fm and Norie Group, from ~2925 to ~2820 Ma (Fig. 2.6) (Van Kranendonk et al., 2013). Wang et al. (1998) analysed a volcanogenic sandstone sample overlying the Gossan Hill Fm in the YSGB (Fig. 2.5), which yielded an interpreted depositional age of 2809 ± 5 Ma. However, the stratigraphic designation of this unit is ambiguous, as it was sampled along the sheared contact between the Mougooderra Fm and underlying supracrustal rocks (that may correspond to the Norie Group).

The age of the Meekatharra Fm in the lower part of the Polelle Group is not very well constrained. A chert sample from the Meekatharra Fm in the Meekatharra area yielded an emplacement age of 2798 ± 8 Ma (Schiøtte & Campbell, 1996). The upper portion of the Polelle Group is better constrained from U-Pb SHRIMP analysis of numerous intermediate to felsic volcanic samples. Rhyolitic tuffs of the Greensleeves Fm near Cue have been precisely dated at 2761 ± 1 Ma, with younger banded tuffs identified in the Dalgaranga greenstone belt (2745 ± 4 Ma; Pidgeon & Hallberg, 2000). Wang (1998) dated a felsic volcaniclastic sandstone from the northeastern part of the Murchison Domain, which had a significant detrital zircon age peak of 2734 ± 5 Ma. This sandstone also contained ~2.9 Ga and ~3.5 Ga zircons. The late, waning stages of felsic volcanism are marked by a flow-banded felsic volcanic unit in the Weld Range greenstone belt (Fig. 2.3), dated at 2727 ± 6 Ma (Schiøtte & Campbell, 1996). Meanwhile, a quartz diorite portion of a sill intruding supracrustal rocks in the south of the study area,

YSGB (see Warriedar Suite – Section 2.3.1; Fig. 2.5) yielded a zircon crystallisation age of 2801 ± 6 Ma (Lu et al., 2016b), implying the surrounding rocks are older than this age. An apparent ~20 Ma volcanic hiatus between the Singleton Fm and Greensleeves Fm (c. 2780-2760 Ma) is shown by a compilation of current geochronology across the Murchison Domain (Fig. 2.6), but its stratigraphic and tectonic significance is not yet clear (Lowrey et al., 2020).

The timing of late clastic sedimentation of the Glen Group is not well constrained. In the northeastern Murchison Domain, U-Pb dating of detrital zircon in a quartz sandstone from the Cue area revealed a maximum depositional age of 2740 ± 4 Ma (age of the youngest detrital zircon), likely sourced from underlying Polelle Group volcanics (GSWA, 2018). Komatiitic volcanics of the upper Wattagee Fm are interbedded with thin felsic volcanic units, including one sheared rhyolite that has been dated at 2725 ± 4 Ma (Wingate et al., 2009a). U-Pb zircon dating of Yalgowra Suite gabbroic sills in the northeastern Murchison Domain, which are geochemically comparable to Glen Group volcanic rocks, suggests that Glen Group mafic magmatism continued to at least 2710 Ma (Van Kranendonk et al., 2013).

The depositional age of the supracrustal Mougooderra Fm in the southwestern Murchison Domain is poorly constrained. In the YSGB, a Mougooderra Fm metadacite interbedded with sandstone yielded zircons that were interpreted as xenocrystic, based on stratigraphic relations and the presence of several rounded, pitted zircon grains (Fig. 2.5). The youngest 11 zircon analyses in this dacite gave a maximum crystallisation age of 2801 ± 5 Ma (Lu et al., 2016a). A Mougooderra Fm quartz sandstone sampled 300 m west yielded a detrital spectrum and a maximum depositional age of 2817 ± 3 Ma, with a pronounced age component at ca. 2820 Ma (Lu et al., 2018). In the far north of the YSGB near Yalgoo, zircons from a volcaniclastic siltstone yielded 36 near concordant analyses returning a range of ages between 2953-2612 Ma (Lu et al., 2016b). The maximum depositional age of this unit was interpreted as 2758 ± 4 Ma based on 11 analyses, and 17 analyses that yielded 2715-2612 Ma ages were considered younger than expected based on regional geological mapping and were tentatively attributed to at least three subsequent hydrothermal events (Lu et al., 2016b; Zibra et al., 2018).

In summary, SHRIMP U-Pb zircon analyses reveal an extensive ~270 Ma history of greenstone belt development in the Murchison Domain. Felsic volcanism of the c. 2.95 Ga Formations occurred at 2980-2935 Ma, followed by a >100 m.y. hiatus and ultramafic to felsic volcanism of the Norie Group at ~2820-2805 Ma. Further volcanism of the Polelle Group occurred at 2800-2730 Ma, with a progressive change from ultramafic and mafic to andesitic and felsic compositions through time, followed by epiclastic sedimentation and minor volcanism of the Glen Group at ~2735-2710 Ma. Whereas the Gossan Hill Fm in the YSGB is well constrained with multiple ages, the overlying greenstone succession remains poorly constrained and dating of the Mougooderra Fm has only yielded highly variable maximum depositional ages.

SUITE/Intrusion	Long dimension (~km)	Stratigraphic thickness (~km)	Areal extent (~km²)	Estimated volume (~ km³)	Age (Ma)	V-magnetite ?	Chromite?	Ni–Cu–PGE?	Primary hydrous phases?
Unnamed units	400	2	800	960	-	-	✓	✓	minor Hbl
YALGOWRA SUITE	250	1	900	540	2711-2735	-	✓	✓	hydrous
WARRIEDAR SUITE	300	–	–	1489	2801-2792	-	✓	✓	minor Hbl
Gnanagooragoo	63	3.5	252	529	2792	-	✓	✓	minor Hbl
BOODANOO SUITE	50	–	–	2494	2799	-	✓	✓	distinctly hydrous
Fields Find	14	2.5	60	144	~2799	-	✓	✓	abundant Hbl
Narndee	29	5	550	2350	2799	-	✓	✓	abundant Hbl, Phl
MEELINE SUITE	300	–	–	38 000	2813-2819	✓	✓	✓	nominally anhydrous
Windimurra	78	11	2500	26 000	2813	✓	✓	✓	none
Youanmi	35	5	330	1700	2819	✓	✓	✓	minor Hbl
Barrambie	50	3	150	270	2814	✓	-	-	none
Atley	25	3	110	198	~2813	✓	-	-	none
Lady Alma	20	2	35	42	~2813	✓	-	-	none
Buddadoo	11	2.5	37	56	~2813	✓	-	-	minor Hbl

Table 2.2: A summary of the characteristics of mafic-ultramafic intrusive suites and larger intrusions in the Murchison Domain. An indication of vanadiferous magnetite (V-magnetite), chromite and Ni-Cu-PGE occurrences and hydrous primary phases is also shown for each suite and intrusion. Abbreviations: Hbl; hornblende, Phl; Phlogopite. Modified after Ivanic (2019).

2.3 Intrusions and Metamorphism

In this section, the distribution, characteristics, and ages of intrusive rocks in the Murchison Domain are reviewed. The locations of significant mafic-ultramafic intrusions in the Murchison Domain are displayed in Figure 2.3 and a geological map of intrusive rocks in the southwest Murchison Domain is shown in Figure 2.7. The ages of intrusions within, and at the peripheries of, the study area are shown on Figure 2.5 and summarised in the text. In this thesis, the term 'granitoid' is used in a general sense in reference to intrusive rocks of felsic-intermediate composition, including both rocks with high-K compositions, and rocks in the tonalite-trondhjemite-granodiorite (TTG) series (Smithies et al., 2018).

2.3.1 Mafic-Ultramafic Intrusions

Voluminous mafic-ultramafic intrusions form an integral component of the geology of the Yilgarn Craton and constitute approximately 40% by volume of greenstone belt successions in the Murchison Domain (Ivanic, 2019). These intrusions typically occur as vast, tabular bodies, such as sills, laccoliths and lopoliths and larger intrusions are frequently compositionally layered (Van Kranendonk & Ivanic, 2009). Four suites of mafic-ultramafic intrusions have been identified in the Murchison Domain, namely the Meeline, Boodanoo, Warriedar and Yalgowra suites (Fig. 2.2; Ivanic et al., 2010; Ivanic, 2019). The key characteristics of these suites are summarised in Table 2.2.

The Meeline Suite consists of six large, layered and anhydrous mafic-ultramafic intrusive complexes in the Murchison Domain, which range in diameter between 12-85 km and thickness between 3-11 km

(Ivanic, et al., 2010; Ivanic, 2019). In order of size, constituent intrusions consist of the Windimurra Igneous Complex (WIC), in addition to the Youanmi, Barrambie, Atley, Lady Alma and Buddadoo igneous complexes (Fig. 2.3; Ivanic, 2019). Meeline Suite intrusions exhibit well-developed compositional layering, including olivine-bearing ultramafic bases, progressing upwards into gabbroic

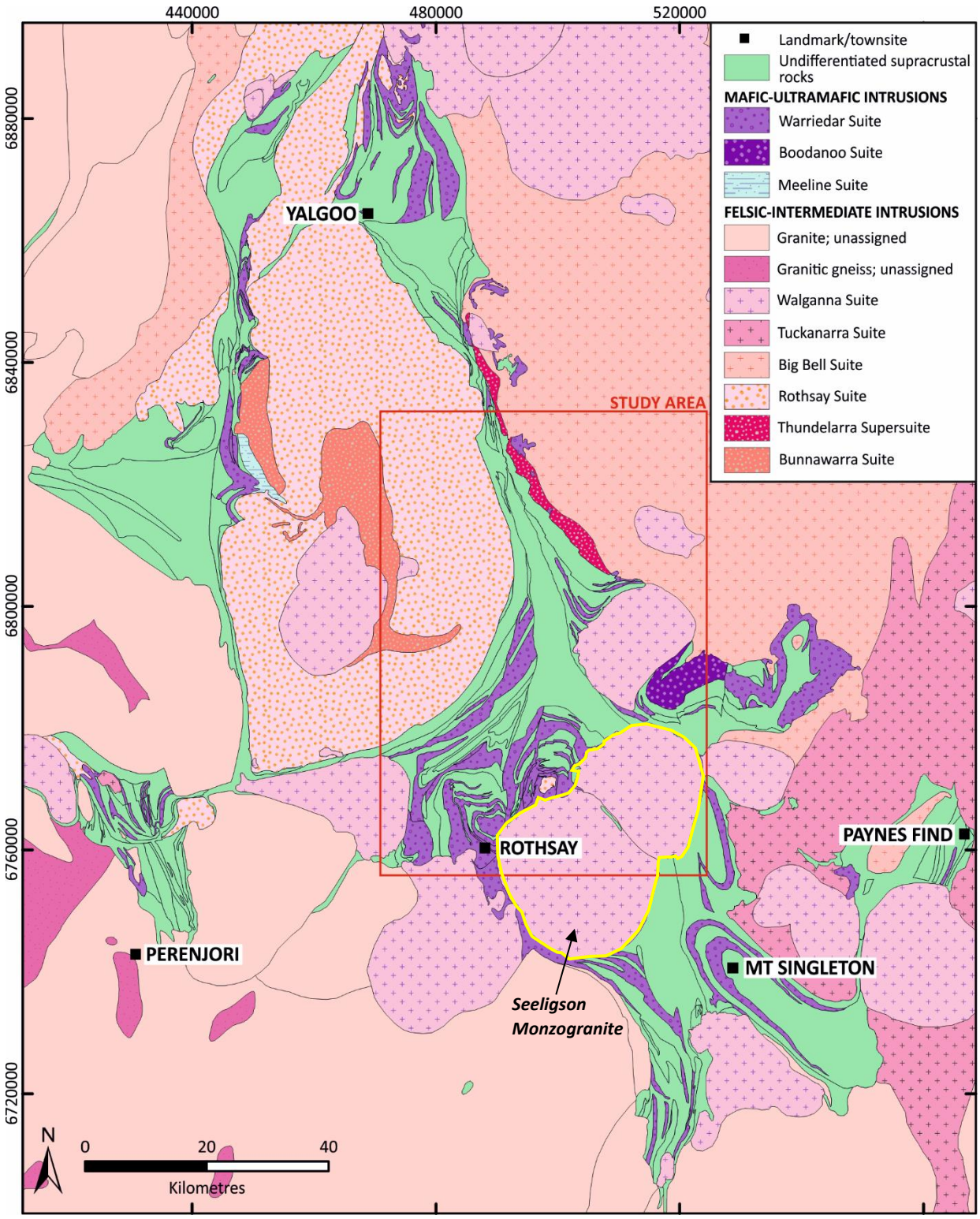

Figure 2.7: Geological map of the southwestern Murchison Domain showing the distribution of felsic-intermediate and mafic-ultramafic intrusions, and their relations with supracrustal rocks. The study area of this project is outlined in red and the Seeligson Monzogranite is outlined in yellow. Geological data has been modified from the GSWA 2020 1:500,000 scale regional map of Western Australia.

rocks and more evolved anorthosite units, in addition to thick magnetite horizons (Van Kranendonk et al., 2013). Meeline Suite intrusions do not contain primary hydrous minerals, such as hornblende (Ivanic, 2019). Discordant layering and reversals in fractionation trends with height suggest that these complexes developed through the emplacement of several pulses of magma (Ivanic et al., 2010). The 85 km x 37 km WIC is the largest single mafic-ultramafic layered intrusion exposed in Australia (Fig. 2.3; Table 2.2), and at ~11 km thickness, it is fourth largest and the thickest known mafic-ultramafic layered intrusion on Earth (Ivanic et al., 2017). Meeline Suite complexes host significant V-Ti-Fe mineralisation in upper fractionated zones, and orthomagmatic Ni-Cu-Cr-PGE mineralisation in lower ultramafic zones (Ivanic et al., 2017). The crystallisation ages of all dated Meeline Suite intrusions are within error of c. 2813 Ma, thus the emplacement of this suite is considered to be a short-lived event (Ivanic, 2019). Similar intrusions with comparable ages in the Eastern Goldfields Superterrane (EGS) suggest that this event can be correlated across the Yilgarn Craton (Ivanic et al., 2010).

The Boodanoo Suite consists of several large, primary hornblende-bearing, layered mafic-ultramafic intrusions located in the southern and central parts of the Youanmi Terrane (Table 2.2; Ivanic, 2019). The 30 km-diameter and 5 km-thick Narndee Igneous Complex represents the largest Boodanoo Suite intrusion and is located south of the WIC, approximately 70 km east of the YSGB (Fig. 2.3). The 14 km-diameter and 2.5 km-thick Fields Find Igneous Complex in the eastern part of the YSGB is also assigned to the Boodanoo Suite (Fig. 2.7; Ivanic, 2019). Rocks from this suite consist of hornblende-bearing ultramafic cumulate rocks, occasionally host to Ni-Cu-PGE mineralisation, pyroxenites and cumulate-textured gabbro containing up to 15 vol.% primary igneous hornblende, indicating hydrous parental magmas (Ivanic et al., 2010; Ivanic et al., 2015b). The presence of abundant primary hornblende and the lack of significant magnetite horizons distinguishes Boodanoo Suite intrusions from the extensive, anhydrous and approximately coeval intrusions of the Meeline Suite (Ivanic et al, 2010; Ivanic, 2019). Pyroxene barometry suggests the Boodanoo Suite was emplaced into Norie Group rocks at relatively shallow crustal depths of between 3 and 9 km (Scowen, 1991). SHRIMP U-Pb zircon dating of the Narndee Igneous Complex gives a magmatic crystallisation age of 2799 +/- 7 Ma (Ivanic et al., 2010).

The Warriedar Suite comprises numerous mafic-ultramafic sills extending across a >200 x 200 km area of the western Youanmi Terrane, principally located within supracrustal belts in the southwestern Murchison Domain (Fig. 2.3; Fig. 2.7). Warriedar Suite sills are largely found intruding upper Norie Group and lower Polelle Group rocks, and the lowermost sills intrude Gossan Hill Fm rocks in the YSGB (Fig. 2.7). The intrusions are considered to be synvolcanic with rocks of the Meekatharra Fm based on limited geochemistry (Wyman, 2019; Ivanic, 2019) and are invariably deformed with the host supracrustal rocks. The suite includes some thick sills (1-2 km thick) that are laterally continuous and

invariably layered, in addition to thinner (50-500 m thick) sills that pinch out along strike lengths of 5-10 km (Ivanic, 2019). The largest component of the suite, the 66 km-length Gnanagooragoo Igneous Complex in the northeastern Murchison Domain, has a total stratigraphic thickness of 4.5 km (Fig. 2.3; Ivanic, 2019). Thick (>500 m) sills exhibit well developed compositional layering and typically comprise ultramafic cumulate peridotitic or pyroxenitic bases that grade upwards into abundant gabbroic and doleritic rocks. The uppermost portions of sills are frequently leucogabbroic with granophyric and harrisite-like textures comprising coarse crystals occasionally reaching up to 30 cm in size, interpreted as evidence of undercooling (Ivanic, 2019). The upper portions of Warriedar Suite sills are locally host to laterally discontinuous rafts of BIF and mafic volcanic rocks. SHRIMP U-Pb zircon dating of multiple Warriedar Suite sills, including one sill in the study area, yield crystallisation ages in the range 2792-2801 Ma that are consistently within error of one another and indicate a short-lived magmatic event (Fig. 2.5; Ivanic, 2019). Notably, the ages of Warriedar Suite intrusions overlap with the age of Boodanoo Suite intrusive rocks (Van Kranendonk et al., 2013).

The Yalgowra Suite is composed of layered, tholeiitic mafic-ultramafic sills that are abundant in the northern Murchison Domain, where they imitate the distribution of Polelle Group volcanic rocks but are absent in the southwest (Fig. 2.3; Ivanic, 2019). Sills of this suite vary in thickness between 20 m and 2 km and have a bulk high-Mg basaltic composition (Van Kranendonk et al., 2013). Most Yalgowra Suite sills have intruded the upper Polelle Group and are considered to represent subvolcanic intrusions associated with the eruption of overlying Glen Group high-Mg basalts (Van Kranendonk, 2008). Whereas Yalgowra Suite rocks are largely anhydrous, primary hornblende is commonly present in chilled upper zones and is attributed to assimilation of hydrous host rocks rather than a hydrous parental magma (Ivanic, 2019). The age of Yalgowra Suite intrusions ranges between 2710-2735 Ma, indicating a c. 25 Ma intrusive episode (Van Kranendonk et al., 2013).

The presence of large mafic-ultramafic layered igneous complexes (Ivanic et al., 2010) and mafic-ultramafic sequences in the greenstone stratigraphy (Barley et al., 2000) have been interpreted to imply a significant mantle input into the Murchison Domain from 2820 to 2720 Ma. The typically tholeiitic nature of the layered complexes and association with voluminous picritic and high-MgO basaltic volcanism indicates that magmatism is likely to have been derived from impingement of one or more mantle plumes (Van Kranendonk & Ivanic, 2009; Ivanic et al., 2010). The mafic-ultramafic intrusions represent the intrusive component of a large igneous province(s), whereas the mafic-ultramafic supracrustal rocks represent their extrusive counterparts (Ivanic et al., 2017). The contemporaneous emplacement of felsic magmas and intrusion of the Meeline and Yalgowra Suites

further supports a plume origin, as Lu-Hf zircon data suggests they are derived from both primitive mantle input and older basement aged 3050 Ma and 3900 Ma (Ivanic et al., 2012).

In addition to the mafic-ultramafic intrusive suites described above, several swarms of dolerite dykes with varying orientations, most commonly east-west to northwest-southeast striking, dissect all Archaean lithologies and are interpreted to have been emplaced during extensional episode(s) in the Proterozoic (Watkins & Hickman, 1990).

2.3.2 Granitoid Intrusions

Felsic-intermediate magmatism in the Murchison Domain developed over an extensive period in association with multiple contractional and extensional deformation episodes. Consequently, granitoids comprise approximately 85% of the rocks exposed in the region (Watkins et al., 1991; Fig. 2.3). Greenstone belts in the Murchison Domain commonly exhibit deformation associated with the emplacement of granitoid plutons, resulting in several curvilinear belts broadly parallel with surrounding granitic intrusions, in contrast to other linear belts parallel to large, crustal-scale lineaments (Wang et al., 1993).

Watkins & Hickman (1990) originally subdivided plutonic granitoid rocks in the Murchison Domain into four main suites, based primarily on relative timing according to field relations and limited geochronology. These suites comprise pegmatite-banded gneiss, recrystallized monzogranite and two generations of post-folding granitoids (Watkins & Hickman, 1990). Watkins et al. (1991) presented an interpretation in which early, relatively thin, subhorizontal sheets of monzogranite and granodiorite intruded the base of the developing supracrustal greenstone sequence at c. 2900 Ma. These intrusions were later deformed and metamorphosed into pegmatite-banded gneiss, in which pegmatitic features define the gneissose banding, followed by the intrusions of several km thick, tabular monzogranite plutons into the base of the greenstone succession at c. 2700 Ma (Watkins et al., 1991). Finally, the intrusion of two compositionally distinct but contemporaneous suites of post-folding granites intruded the assemblage at ~2600 Ma, located primarily at the margins of greenstone belts and locally dissecting those belts (Watkins et al., 1991). Wang et al (1993) subsequently subdivided the 'monzogranite' grouping of Watkins & Hickman (1990) into three geochemically distinct suites. A Yilgarn Craton-wide geochemical study by Champion & Cassidy (2002) revised the Watkins & Hickman (1990) classification and defined five granitoid suites in the northern Murchison Domain, comprising high-Ca granites, low-Ca granites, 'high-HFSE' (high field strength elements) granites, syenite and mafic granites.

More recently, Ivanic et al (2012) identified a total of 10 granitoid suites in the Murchison Domain following extensive geological mapping and geochronology in the northeast (Fig. 2.7). These granitoid suites incorporate syn-volcanic, syn-tectonic and post-tectonic granitoids and consist of nine suites dated between 2815-2600 Ma, and one significantly older suite dated at ca. 2950 Ma. These granitic rocks generally become more silicic and potassic and less calcic and aluminous through time, suggesting successive remelting of granitic crust at progressively shallower levels (Ivanic et al., 2012). Furthermore, Lu-Hf zircon data identified extended periods of juvenile mantle input, with significant pulses of crustal recycling at 2750 and 2620 Ma (Ivanic et al., 2012). The granitoid suites defined by Ivanic et al. (2012) (and updated by Van Kranendonk et al. (2013)) and ongoing GSWA geological mapping (e.g., Ivanic et al., 2015a; Zibra et al., 2016; Ivanic, 2018) are described in chronological order below. Due to incomplete mapping, granitoids to the southwest of the YSGB have not yet been differentiated and largely remain unassigned.

The oldest granitic suite in the Murchison Domain, the c. 2950 Ma Bunnawarra Suite, is assigned to the Thundelarra Supersuite, and consists of migmatitic tonalite to granodiorite, commonly containing K-feldspar and hornblende phenocrysts (Zibra et al., 2016). The most extensive Bunnawarra Suite rocks occur at the margins of the YSGB, specifically intruding the base of the Gossan Hill Fm and occupying the core of the Yalgoo Dome bounding the belt to the west (Fig. 2.7; Zibra et al., 2016). Thundelarra Supersuite rocks are largely restricted to the southwestern Murchison Domain and incorporates the pegmatite-banded gneisses defined by Watkins & Hickman (1990).

Following a >100 Ma hiatus in felsic magmatism, the next oldest granitoids in the Murchison Domain are assigned to the Annean Supersuite, which consists of the Mt Kenneth, Cullculli, Rothsay and Eelya suites (Van Kranendonk et al., 2013). Notably, the Rothsay Suite is the only of these suites that has been identified as a significant component of the southwestern Murchison Domain (Fig. 2.7). The Mt Kenneth Suite (2815-2800 Ma) is granitic to tonalitic in composition, intrudes the upper margins of Meeline and Boodanoo suite intrusions and is proposed to resemble localised melts generated during the emplacement of these layered complexes (Van Kranendonk et al., 2013). The Culculli Suite comprises hornblende ± biotite TTG in the northeastern Murchison Domain and is characterised by distinctive, elliptical 1-8 cm hornblendite clots that are considered to represent mixing between contemporaneous granitic and mafic melts (Van Kranendonk et al., 2013). In contrast, the volumetrically less abundant Eelya Suite is composed of high-HFSE granites and biotite granite (Ivanic et al., 2012).

The c. 2750 Ma Rothsay Suite is composed of monzonite, granodiorite and tonalite compositions and is associated with several domal structures in the southwest Murchison Domain, including in the YSGB

(Fig. 2.7; Clos et al., 2018). The largest exposed Rothsay Suite intrusion, the Goonetarra Granodiorite, forms a principal component of the vast 100 x 50 km Yalgoo Dome situated west of the YSGB, and preserves structural features that are consistent with diapiric emplacement (Section 2.4.3; Zibra et al., 2018; Zibra et al., 2020). A less extensive and coeval Rothsay Suite intrusion, the ~3 km, ovoid Mt Mulgine Granite, is located at the exposed core of a domal structure in the southern YSGB and is also attributed to an episode of polydiapirism in the region (Zibra et al., 2020). The Mt Mulgine Granite is host to a W-Mo-Au mineralised system (Duuring et al., 2007). The Culculli, Rothsay and Eelya suites (2785-2735 Ma) are broadly coeval with volcanism of the Polelle Group and commonly intrude at the base of the Polelle Group stratigraphy (Van Kranendonk et al., 2013).

The Big Bell Suite (2735–2690 Ma), assigned to the Austin Downs Supersuite, is composed of tonalitic to monzogranitic rocks and is laterally extensive, spanning vast areas from Meekatharra in the northeast of the Murchison Domain, to the YSGB in the southwest (Van Kranendonk et al., 2013; Fig. 2.7). The Big Bell Suite includes the syntectonic Lakeside Pluton situated to the northeast of the YSGB. The younger Tuckanarra Suite (2690-2665 Ma) comprises strongly foliated granodiorite to monzogranitic compositions and locally includes felsic porphyries that intrude contiguous supracrustal sequences, such as in the Meekatharra area (Thébaud et al., 2007; Van Kranendonk et al., 2013). This suite is also laterally extensive, and intrusions of this suite are abundant in the Paynes Find area (Fig. 2.7). Subsequent intrusions of the Jungar Suite (2665-2640 Ma) have not been identified in the southwest Murchison Domain.

The youngest of the granitoids, comprising the regionally extensive Bald Rock Supersuite (2640-2600 Ma), are subdivided into two suites: the Walganna Suite of biotite and muscovite-rich monzogranites to syenogranites, and the Wogala Suite of fluorite-rich alkali granite (Van Kranendonk et al., 2013). These two suites are characteristically undeformed and so are interpreted as post-tectonic granitoids, broadly equivalent to the 'post-folding granitoids' defined by Watkins & Hickman (1990). An array of Walganna Suite intrusions is present in the southwestern Murchison Domain, typically ranging in diameter between 10-40 km and intruding both older granitoids, and greenstone belts (Fig. 2.7). One such example is the 40x20 km Seeligson Monzogranite, which intrudes the YSGB and effectively dissects the belt (Fig. 2.7). Granitic pegmatites, likely associated with the Wogala Suite plutons, locally intrude greenstone belts and are commonly enriched in Li, Be, F, Sn and Ta, and therefore are the focus of several mining projects (Van Kranendonk et al., 2013). A total of 297 tonnes of beryl ore have historically been mined from pegmatitic intrusions at Rothsay, in the southern YSGB (Fig. 2.7; Watkins & Hickman, 1990). However, Wogala Suite intrusions have not been mapped in the study area and are uncommon in the southwestern Murchison Domain.

2.3.3 Metamorphism

Greenstone belts in the Murchison Domain have predominantly been subject to greenschist facies metamorphism, with a gradation to amphibolite facies in the far southwest of the region (Watkins & Hickman, 1990). Amphibolite facies metamorphism is otherwise restricted to metamorphic aureoles surrounding post-deformation granitoids and in discrete zones at greenstone belt margins (Watkins & Hickman, 1990). In general, the distribution of metamorphic grade is similar to that observed in the eastern Yilgarn Craton, with lower grade, weakly deformed greenstone cores and higher grade, more intensely deformed granite-greenstone margins (Binns et al., 1976; Wang et al., 1993).

Regionally, the distribution of metamorphic facies is not substantially affected by major faults and shear zones, implying that rocks with significantly contrasting metamorphic histories have not been juxtaposed, unlike in some other parts of the Yilgarn Craton (Goscombe et al., 2019). Despite metamorphism, many primary textures and structures in igneous and sedimentary rocks are preserved, particularly in parts of the northeastern Murchison Domain (Watkins & Hickman, 1990; Lowrey et al., 2017; 2020). Watkins & Hickman (1990) identified three distinct generations of metamorphism in the Murchison Domain, with two earlier phases of contact metamorphism associated with intrusion of granitoid suites (M_1, M_2), and a subsequent period of regional metamorphism (M_3). However, more recent geochronology has revealed discrepancies in the intrusive history proposed by Watkins & Hickman (1990) and so this metamorphic scheme requires revision.

In the YSGB, mafic rocks contain upper greenschist metamorphic assemblages comprising albite-epidote-chlorite-actinolite(-tremolite), with a progressive transition to lower amphibolite assemblages of oligoclase-biotite-hornblende-garnet to the southwest (Watkins & Hickman, 1990). These assemblages were confirmed by geological mapping in the southern YSGB, which identified grunerite alteration of BIF and alteration of clinopyroxene to hornblende in mafic intrusions (Price, 2014). A recent study focusing on metamorphism of the metasedimentary Mougooderra Fm and underlying supracrustal rocks in the YSGB has presented garnet Lu-Hf and Sm-Nd geochronology, paired with thermobarometry and phase equilibrium modelling (Parmenter et al., 2020). Modelling and thermobarometry indicate that the Mougooderra Fm experienced P-T conditions of 545-580°C and ~2-3.5 kbar, whereas underlying rocks (assigned to the Polelle Group) experienced P-T conditions of 610-650 °C and ~4-7.2 kbar (Parmenter et al., 2020). Garnet Lu-Hf ages for the Mougooderra Fm and Polelle Group were constrained at 2686 ± 18 Ma and 2685 ± 15 Ma, respectively, and are interpreted as the timing of late prograde metamorphism (Parmenter et al., 2020). The P-T conditions and ages of metamorphism of the Mougooderra Fm are most consistent with the M2 metamorphic event proposed by Goscombe et al. (2019) in the eastern Yilgarn Craton (Parmenter et al., 2020).

2.4 Structural Geology

2.4.1 Introduction

The deformational history of the Murchison Domain involves multiple extensional and contractional phases of deformation, interrelated with early volcanism, intrusion of granitoids, uplift and erosion, sedimentary basin development, metamorphism and mineralisation (Van Kranendonk et al., 2013; Zibra et al., 2018; Zibra, 2020). Four main deformational schemes have been proposed for rocks in the Murchison Domain, two of which include rocks in the southwest including the YSGB. The deformational scheme of Watkins & Hickman (1990) is applicable to the entire Murchison Domain, whereas Van Kranendonk et al. (2013) devised a structural framework focusing on the northeastern Murchison Domain, and Zibra et al. (2018; 2020) presents a model for early deformation in the southwest. Zibra (2020) compiled a new fourfold deformational scheme for the Murchison Domain, however, this is principally applicable to rocks in the northeastern and central parts of the region, excluding the YSGB. A further structural framework for the YSGB was developed as part of an unpublished company report undertaken by SRK Australia and provided by Minjar Gold Pty (McCuaig et al., 2002). These structural schemes are summarised and correlated in Table 2.3. Whereas interpretations of the most recent deformational episodes are similar, various contrasting interpretations have been proposed for early-formed structures in the region.

2.4.2 Early Deformation

A number of studies suggest the occurrence of an early extensional phase associated with the emplacement of the supracrustal rocks (Table 2.3; Watkins & Hickman, 1990; McCuaig et al., 2002). Watkins & Hickman (1990) suggest that supracrustal rocks were emplaced into a major basin during

<table>
<tr><th>Watkins & Hickman (1990)
Murchison Domain</th><th>McCuaig et al. (2002)
YSGB</th><th>Van Kranendonk et al. (2013)
NE Murchison Domain</th><th>Zibra et al. (2018; 2020)
SW Murchison Domain</th><th colspan="2">Zibra (2020)
Murchison Domain</th></tr>
<tr><td rowspan="2">D₄ shearing</td><td rowspan="3">D₂ E-W shortening and shearing</td><td rowspan="3">D₄ E-W shortening & shearing</td><td rowspan="3">D_{OROGENIC}
E-W shortening</td><td rowspan="4">Orogenic E-W shortening*</td><td>D₄ 2660-2630 Ma</td></tr>
<tr><td>D₃ ca. 2660 Ma</td></tr>
<tr><td rowspan="2">D₃ E-W shortening</td><td>D₂ ca. 2700 Ma</td></tr>
<tr><td>D₁ ca. 2730 Ma</td></tr>
<tr><td>D₂ N-S shortening</td><td>D₁ N-S shortening</td><td>D₃ PCO</td><td rowspan="3">D₁₋₃ diapirism</td><td colspan="2" rowspan="3">‘Pre-orogenic’</td></tr>
<tr><td></td><td></td><td>D₂ tilting</td></tr>
<tr><td>D₁ slumping/faulting</td><td></td><td></td></tr>
<tr><td></td><td></td><td>D₁ tilting</td><td></td><td colspan="2"></td></tr>
<tr><td>De extension</td><td>De extension</td><td>De extension</td><td></td><td colspan="2"></td></tr>
</table>

Table 2.3: Correlation of deformational events for structural models proposed in the Murchison Domain. The area in which each model is applicable is shown in italics. PCO = Partial Convective Overturn. Note that McCuaig et al. (2002) is an unpublished company report undertaken by SRK Australia. *D_1-D_4 events in the scheme of Zibra (2020) are principally applicable to the central and northeast Murchison Domain.

this initial extensional episode, with estimated dimensions of up to 800x400 km and a depth of ~2km. McCuaig et al. (2002) proposed that greenstone formation occurred during north-south orientated extension, in successive rift basins controlled by a transform-normal fault pattern. Thickness variations in volcanic units can be accounted for by draping across transform faults, in addition to paleo-topography and proximity to source (McCuaig et al., 2002). In the YSGB, transform faults are suggested to have been initiated at this early stage (McCuaig et al., 2002).

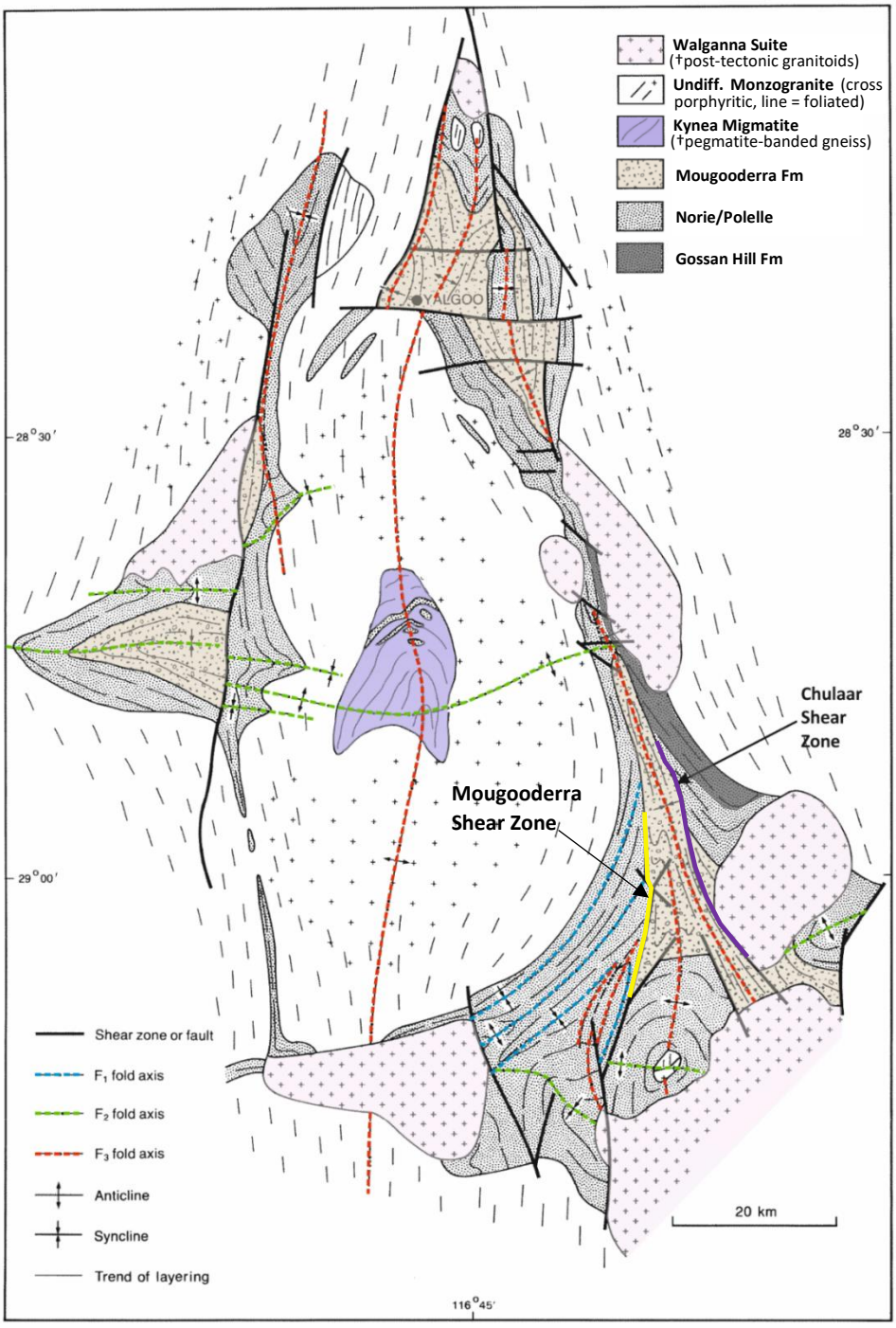

Figure 2.8: Simplified geological map of the southwestern Murchison Domain according to Watkins & Hickman (1990), showing the main geological units, F1-F3 fold axes and major structures. The location of the Chulaar Shear Zone (purple) and Mougooderra Shear Zone (yellow) is shown. Geological unit names have been updated using the new stratigraphic framework (Fig. 2.2). †original terminology used by Watkins & Hickman (1990). Modified after Watkins & Hickman (1990).

Watkins and Hickman (1990) proposed a coherent structural model for the entire Murchison Domain comprising four main deformational phases following greenstone formation (D_1-D_4; Table 2.3). After the emplacement of supracrustal rocks, Watkins and Hickman (1990) proposed that early km-scale recumbent folding and layer-parallel thrusting (D_1) resulted from horizontal tectonic movements, represented by the earliest discernable structures in supracrustal rocks. Kilometre-scale recumbent folding identified in the western YSGB was attributed to D_1 deformation by Watkins & Hickman (1990) (Fig. 2.8). Price (2014) suggested the occurrence of early thrusting in the YSGB, to account for laterally discontinuous units on aeromagnetic imagery, as previously documented in the Midlands greenstone belt, Zimbabwe (Dirks et al., 2002) and the Kalgoorlie-Kambalda region, eastern Yilgarn (Swager & Griffin, 1990). This could be attributed to the early horizontal tectonics (D_1) in the structural scheme of Watkins & Hickman (1990) outlined above.

A more recent study by Van Kranendonk et al. (2013) concluded that deformation in the Murchison Domain consists of four events (Table 2.3), the first two of which consist of successive tilting episodes recorded by major unconformities within the supracrustal succession. According to this framework, the earliest established event (D_1) involved tilting of c. 2950 Ma greenstones in the Golden Grove area, prior to being unconformably overlain by younger rocks of the Norie Group (c. 2810 Ma; Wang et al., 1998). Subsequent D_2 tilting encompassed further tilting and localised folding of Norie and Polelle Group rocks, which were later unconformably overlain by clastic sedimentary rocks of the Glen Group (tentatively including the Mougooderra Fm) (Van Kranendonk et al., 2013). It should be noted that the c. 2.95 Ga formations were not distinguished as a distinct group of supracrustal basement rocks by Watkins & Hickman (1990) based on minimal geochronology, and thus the associated unconformity was not included in their structural framework.

According to Watkins & Hickman (1990) and McCuaig et al. (2002), subsequent deformation consisted of a phase of N-S shortening (D_2; Watkins & Hickman, 1990; D_1; McCuaig et al., 2002) resulting in upright east-west trending folds, followed by E-W shortening (D_3; Watkins & Hickman, 1990; D_2; McCuaig et al., 2002) forming N-S trending and steeply plunging folds. Watkins & Hickman (1990) suggested that local D_2-D_3 interference patterns have developed and concluded that the distinctive granite-greenstone pattern in the southwest Murchison Domain resulted from map-scale fold interference (Myers & Watkins, 1985; Watkins & Hickman, 1990). This includes two outward-dipping domal structures preserved by supracrustal rocks in the southern YSGB, one of which is cored by the ~3 km Mt Mulgine Granite. Similar granite-cored domes have been identified in the Kalgoorlie Terrane, eastern Yilgarn, and display a close spatial relationship with gold mineralisation (Davis et al., 2010).

In contrast, Van Kranendonk et al. (2013) suggest that rather than superposition, these structures in the northeastern Murchison Domain formed during a period of inferred partial convective overturn

(D_3), whereby dense greenstone upper crust 'sinks' into thermally softened, granitic middle crust. In this model, the remobilised granitic material derived from partial melting of older crust rises into the upper crust as inflated domes (Van Kranendonk, 2008), following a process like that invoked for the eastern Pilbara Craton by Van Kranendonk et al. (2004). This sinking model is supported by evidence found in the Weld Range area, where foliation geometry within the limbs of a major fold supports its formation through sinking of greenstones into surrounding granitoids (Van Kranendonk et al., 2013). Furthermore, foliations and pegmatite sheets in an inequigranular monzogranite south of Weld Range define a domal geometry, thus implying that greenstone sinking is accompanied, at least in part, by either magma-assisted inflation of granitoids or diapirism (Van Kranendonk et al., 2013). D_3 structures are postulated to have formed after 2710 Ma, which is the approximate age of the Yalgowra Suite sills that are deformed by D_3 east-west trending folds in the northern Murchison Domain (Van Kranendonk et al., 2013). In the southern YSGB, de Vries (2015) attributed the development of the Mt Mulgine dome to the D_3 deformational event of Van Kranendonk et al. (2013), whereby sagging of the mafic-ultramafic volcanic and intrusive sequence was concurrent with ascent of the granite pluton. Consequently, the supracrustal sequence has been tilted into steep folded belts surrounding and plunging away from the granite core, with the development of faults along dislocation planes and between bedding (de Vries, 2015).

A recent detailed structural study undertaken by Zibra et al. (2018; 2020) in the southwestern Murchison Domain invokes an episode of diapirism to account for the formation of domal structures in the area (corresponding to D_3 of Van Kranendonk et al., 2013; Table 2.3). This work is summarised below (Section 2.4.3) prior to an overview of late deformation in the region (Section 2.4.4).

2.4.3 Diapirism in the Southwest Murchison Domain

The southwestern Murchison Domain exhibits a prominent dome-and-keel architecture that is in striking contrast to the linear, ribbon-like, upright fold belts separated by crustal-scale shear zones across much of the rest of the Yilgarn Craton (Zibra et al., 2020). This pattern is particularly evident in the area surrounding the Yalgoo Dome; a 90 x 50 km granite-migmatite dome comprising Thundelarra Supersuite and Rothsay Suite rocks, bounded by narrow, arcuate greenstone belts, including the YSGB to the east (Fig. 2.9). The geometry of the Yalgoo Dome area has previously been attributed to the superposition of broadly orthogonal, upright folds, during regional deformation (Myers & Watkins, 1985; Watkins & Hickman, 1990). Recent GSWA geological mapping in the area and structural analysis centred on the Yalgoo Dome (Zibra et al., 2018; Clos et al., 2019a; Zibra et al., 2020) has identified structural and kinematic evidence that contests fold superposition and instead, favours a diapiric origin for the Yalgoo Dome and early deformation in the area.

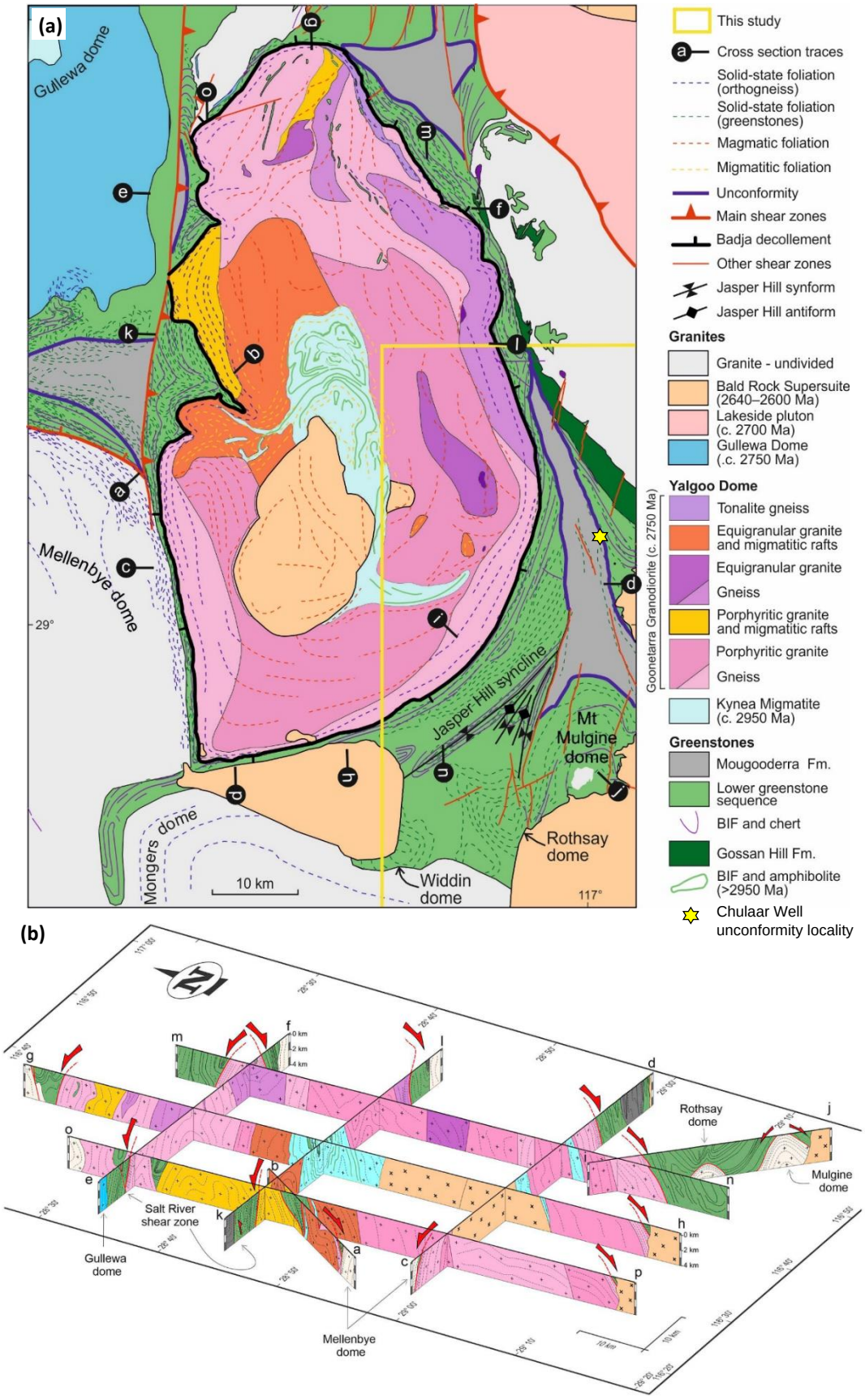

Figure 2.9: Geology of the Yalgoo Dome area. **(a)** Geological map of the area surrounding the Yalgoo Dome, highlighting the location of the three other large, deeply eroded domes (Gullewa, Mellenbye and Mongers domes) and three small domes (Mt Mulgine, Rothsay and Widdin domes). The synformal keel represented by the Jasper Hill syncline is also highlighted. The extent of the field area for this study is outlined in yellow. Modified after Zibra et al. (2018) and Zibra et al. (2020); **(b)** Composite array of cross sections demonstrating the three-dimensional geological and structural architecture of the Yalgoo Dome area. The legend is the same as in (a) and cross section lines are also indicated on the geological map in (a); From: Zibra et al. (2020).

2.4.3.1 Yalgoo Dome

The Yalgoo Dome is one of several large domes in the southwestern Murchison Domain, which, together with intervening slivers of supracrustal rocks, define the dome-and-keel architecture that typifies the westernmost Yilgarn Craton. The Yalgoo Dome is considerably better preserved and exposed than other domes, and so has been the primary focus of study (Zibra et al., 2018; 2020; Clos et al., 2019a). The patterns of foliations, lineations, folds and kinematic indicators within the Yalgoo Dome and surrounding rocks are best explained by diapirism and emplacement of partially molten, high-grade rocks into the greenstone cover (Zibra et al., 2020). In addition to diapirism, ballooning of inflated plutons of granitic magma can also account for the ascent and emplacement of large, domal structures, and the dome-and-keel pattern that typifies the area (e.g., Weinberg, 1996; 1997). However, it is commonly difficult to distinguish between diapirism and 'ballooning' mechanisms, as the resulting domal structures exhibit features that do not exclusively support either model (Weinberg, 1996; 1997; McCarthy et al., 2015). In many cases, diapirism can be taken to indicate a combination of these processes (Weinberg, 1997).

The Yalgoo Dome is post-dated by intrusion of the Lakeside Pluton in the northwest, and post-tectonic Bald Rock Supersuite intrusions. The geology of the Yalgoo Dome can be broadly subdivided into three litho-structural domains (Fig. 2.10; Zibra et al., 2018). The geology and structural characteristics of each of these domains are outlined below.

The core of the Yalgoo Dome consists of the Kynea Migmatite, a migmatitic tonalite containing rafts of older supracrustal rocks such as amphibolite and BIF (Fig. 2.10; Zibra et al., 2018). Structural analysis of outcrop-scale to map-scale dome-and-basin patterns within the Kynea Migmatite has indicated that these structures are an expression of vertical sheath folds (Clos et al., 2019a). The migmatite possesses a steeply dipping gneissic foliation (S_D; subscript D denotes doming; Zibra et al. 2020), which is axial planar to km-scale isoclinal and sheath folds and consistently oriented parallel to lithological contacts (Fig. 2.10) (Clos et al., 2019a). The foliation is frequently associated with a subvertical stretching and mineral lineation, and shear sense indicators such as mantled porphyroblasts and SC fabrics invariably demonstrate core-up sense of shear (Clos et al., 2019a). Geochemical and petrological analysis of rocks from the Kynea Migmatite are consistent with a diapiric model (Clos et al., 2019b).

The granitic domain of the Yalgoo Dome is composed of the Goonetarra Granodiorite, which exhibits various different textures and changes in mineralogy across the extent of the dome including porphyritic and equigranular-textured monzogranite, granodiorite and tonalite, and equivalent units that are host to abundant migmatite rafts (Zibra et al., 2018). The Goonetarra Granodiorite is geochemically classified as transitional TTG (Clos et al., 2018). The granitic domain preserves a primary

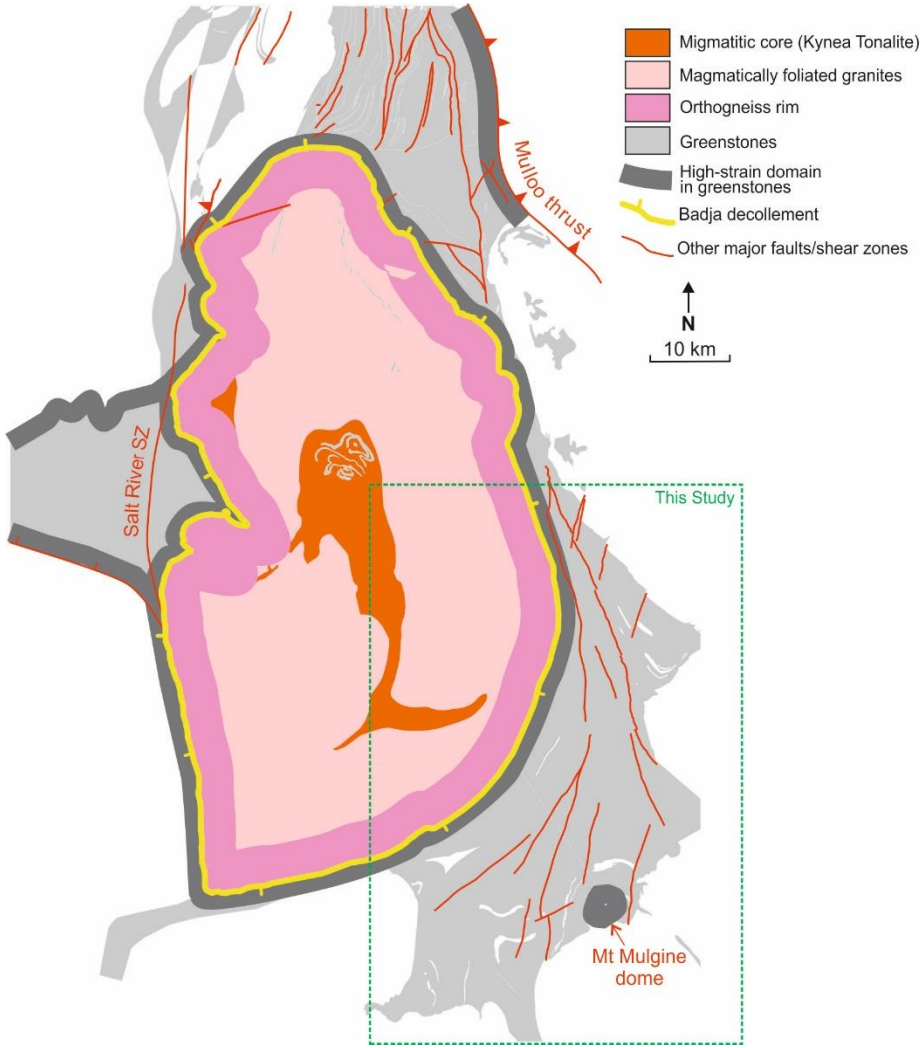

Figure 2.10: Simplified geological sketch map of the area surrounding the Yalgoo Dome, displaying each of the constituent lithostructural domains, in addition to the Badja Decollement (yellow) and other major faults/shear zones (red). The area of this study is outlined in green. Modified after Zibra et al. (2018).

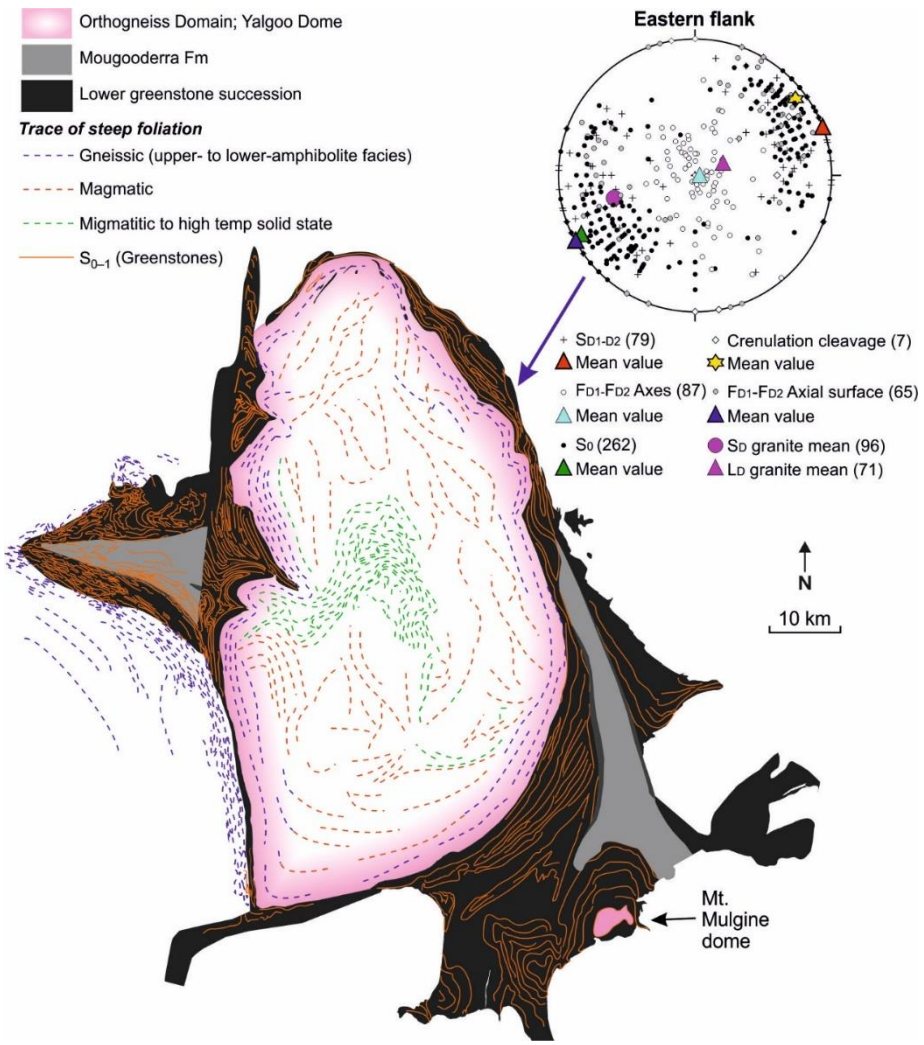

Figure 2.11: Simplified geological sketch map of the area surrounding the Yalgoo Dome, displaying the fabrics present within the lithostructural domains of the Yalgoo Dome, and an equal angle (lower hemisphere) projection plot for structures in the greenstone cover along the eastern flank of the Yalgoo Dome. Poles to planes are plotted and the number of measurements is reported in brackets. Modified after Zibra et al. (2018).

magmatic fabric, parallel to the domal S_D fabric that exhibits broadly concentric patterns on a map-scale (Fig. 2.11). Migmatites occur as large rafts (commonly >100 m) within the granitic domain and define multiple km-scale antiformal ridges parallel to granite-greenstone contacts that expose at least four subdomal structures within the Yalgoo Dome (Zibra et al., 2020). The orthogneiss domain occurs as a ~4 km-thick zone around the margin of the Yalgoo Dome, representing the deformed equivalent of granitic domain rocks (Fig. 2.10; Zibra et al., 2018). This zone is characterised by the progressive development of solid-state, outward-dipping, gneissic to mylonitic S_D fabrics, which display concentric patterns parallel to dome margins (Fig. 2.11). The S_D fabric is typically associated with a radially oriented and outward-plunging, down-dip stretching lineation. The S_D fabric intensity progressively increases towards the granite-greenstone contact, which is marked by a continuous high strain shear zone around the Yalgoo Dome defined as the Badja Decollement. Shear sense indicators in this zone display consistent granite-up, greenstone down (i.e., normal) kinematics.

2.4.3.2 Other Large Granite-Gneiss Domes

Several other large, deeply eroded domes have been identified to the south and west of the Yalgoo Dome: the Gullewa, Mellenbye and Mongers domes (Fig. 2.9). These are of a similar size as the Yalgoo Dome with comparable steep-sided margins but are poorly exposed. Each of these large domes contains domal fabrics with concentric map patterns and a transition from magmatic to solid-state fabrics at the dome margins, which frequently possess a down-dip doming lineation L_D. The Gullewa Dome also contains a migmatitic core encircled by a domal fabric, which is comparable to the Kynea Migmatite at the core of the Yalgoo Dome (Fig. 2.9). The limited data collected from neighbouring, poorly exposed domes of comparable size and geometry display structures that are fully consistent with those in the Yalgoo Dome (Zibra et al., 2018; 2020).

2.4.3.3 Small-Scale Domes

A smaller domal structure, the Mt Mulgine dome, occurs to the southwest of the Yalgoo Dome in the YSGB, and is characterised by a small (3 x 2 km) exposed core known as the Mt Mulgine Granite (Fig. 2.9). The gneissic core displays a sub-horizontal to gently outwards-dipping domal foliation, associated with a radial, outwards-plunging stretching lineation and where present, shear sense indicators demonstrate core-up kinematics (Zibra et al., 2018). Lithological contacts in surrounding supracrustal rocks display a concentric pattern and invariably dip away from the granitic core, defining a ~15 km-scale granite-cored dome. The granite-greenstone contact is host to a high-strain zone, equivalent to the Badja Décollement, and strain in greenstone cover progressively decreases away from this zone. Zibra et al. (2020) tentatively suggests that two further small domes, the Rothsay and Widdin domes,

occur southwest of the Mt Mulgine Dome and between the Yalgoo and Mongers domes, but that their inferred granitic cores remain concealed beneath greenstone cover (Fig. 2.9). In these two areas, lithological contacts display broadly concentric, outward dipping patterns and supracrustal rocks possess a layer-parallel fabric. Notably, the orientation of the long axes of these domes is inconsistent, ranging from northeast-trending for the Mt Mulgine and Widdin domes, northwest-trending for the Rothsay dome, compared to a north-trending long axis of the Yalgoo Dome (Fig. 2.9).

2.4.3.4 Structures in Greenstone Cover

In general, the strain distribution in supracrustal rocks surrounding the Yalgoo Dome mirrors that observed within the orthogneiss domain, with the highest strain occurring along the Badja Décollement at the granite-greenstone contact. The characteristics of doming-related structures in the greenstone cover varies according to the competency of supracrustal units. Competent lithologies such as gabbro and dolerite display a single, pervasive layer-parallel fabric (S_D) and radially oriented steeply-plunging L_D lineation, parallel to structures in underlying gneisses, and shear sense indicators consistently demonstrate dome-up, greenstone-down kinematics. In contrast, less competent, layered lithologies such as BIF and ultramafic rocks display up to three generations of superposed folds (F_{D1}, F_{D2}, F_{D3}), corresponding to successive stages of doming:

1. Early folds (F_{D1}) comprise isoclinal and sheath folds with steeply plunging axes coaxial to L_D and associated with the doming fabric S_D occurring within 500 m of the Badja Décollement.
2. F_{D2} folds are coaxial and coplanar to, and locally refold F_{D1} folds, are associated with a crenulation cleavage and are the oldest folds preserved >500 m from the Badja Décollement
3. F_{D3} folds are coplanar with both F_{D1} and F_{D2} but have sub-horizontal fold axes.

Figure 2.11 summarises the orientation of major doming-related structures in the YSGB, on the eastern flank of the Yalgoo Dome (Zibra et al., 2018). The Badja Decollement is poorly exposed in the southeast, so most structural data are collected from the eastern margin. In this area, S_0, the S_D fabric, F_{D1} and F_{D2} axial surfaces and the crenulation cleavage associated with F_{D2} are typically NNW-striking, parallel to the trend of the Badja Décollement, and dip steeply northeast or southwest (Fig. 2.10). F_{D1} and F_{D2} axes consistently plunge steeply to the east, parallel to L_D in supracrustal rocks and in the orthogneiss to the west (Fig. 2.10). F_{D2}-like folds - corresponding to folds with similar geometries and orientations to F_{D2} folds proximal to the Badja Decollement but located in low-strain domains - occur within Mougooderra Fm metasedimentary rocks and are associated with a steeply plunging stretching lineation. However, due to the ambiguity in correlating structures between the high-strain domain surrounding the Yalgoo Dome and distal lower-strain domains, it is not clear how these F_{D2} -like folds relate to the F_{D1}-F_{D3} development of folds close to the Badja Decollement (Zibra et al., 2018).

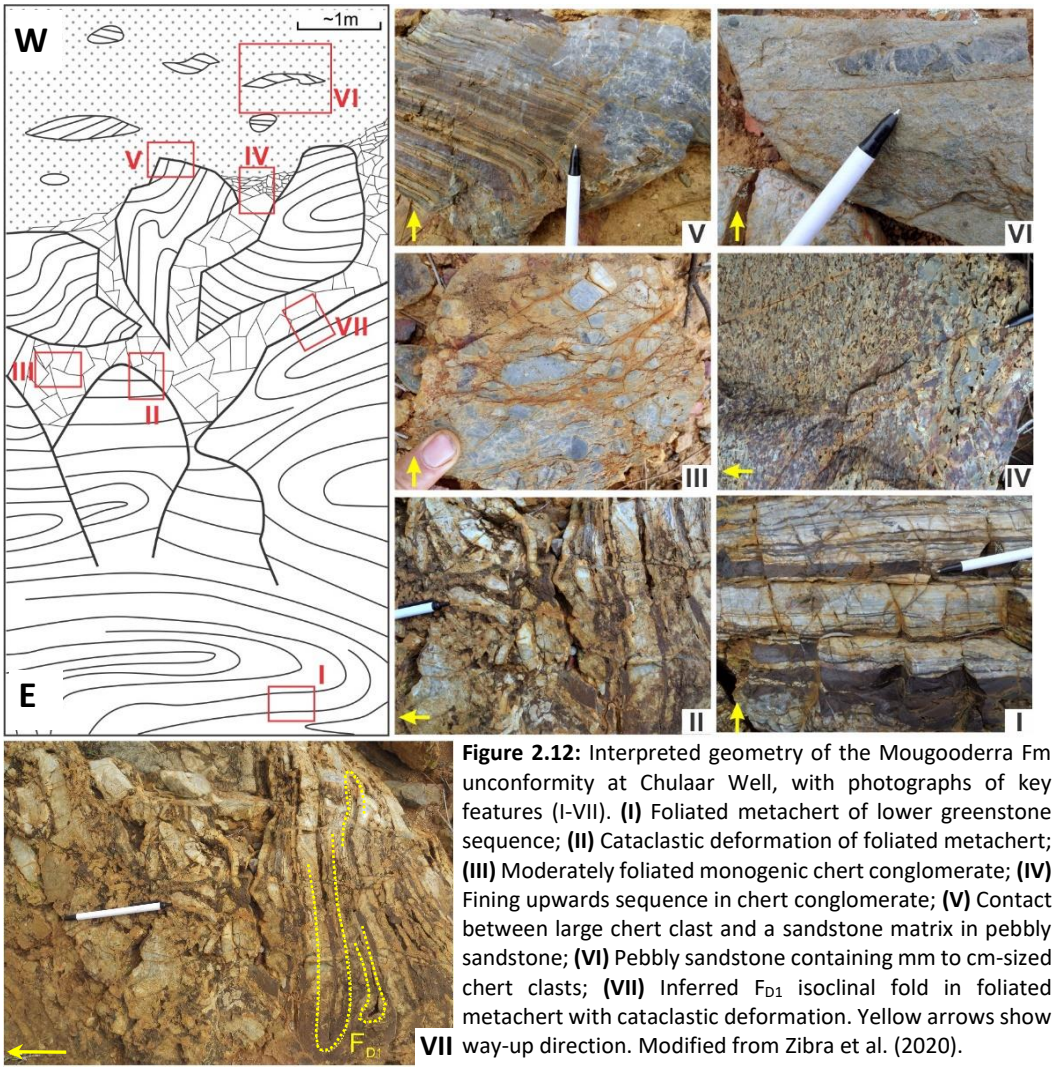

Figure 2.12: Interpreted geometry of the Mougooderra Fm unconformity at Chulaar Well, with photographs of key features (I-VII). **(I)** Foliated metachert of lower greenstone sequence; **(II)** Cataclastic deformation of foliated metachert; **(III)** Moderately foliated monogenic chert conglomerate; **(IV)** Fining upwards sequence in chert conglomerate; **(V)** Contact between large chert clast and a sandstone matrix in pebbly sandstone; **(VI)** Pebbly sandstone containing mm to cm-sized chert clasts; **(VII)** Inferred F_{D1} isoclinal fold in foliated metachert with cataclastic deformation. Yellow arrows show way-up direction. Modified from Zibra et al. (2020).

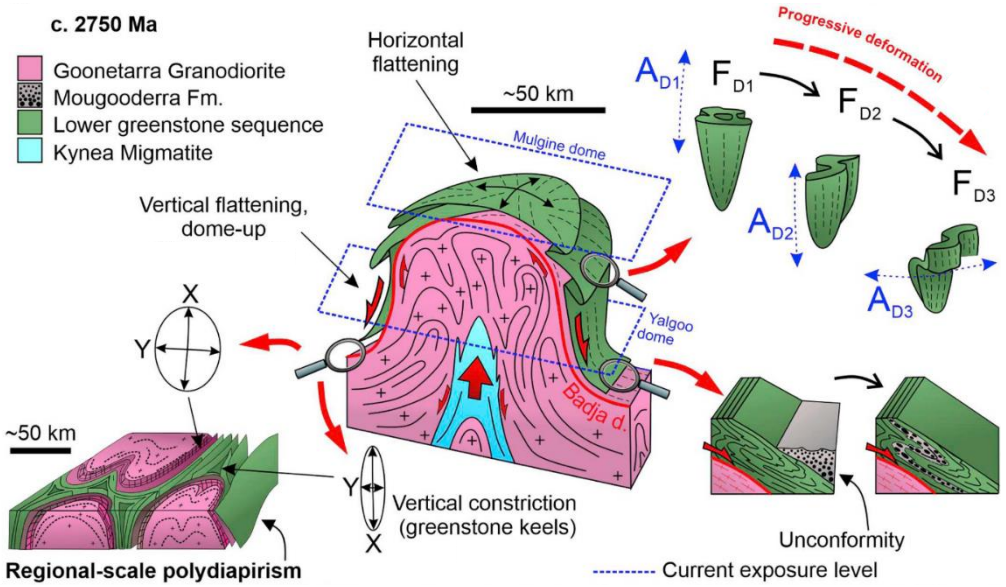

Figure 2.13: A series of schematic sketches displaying the tectonic evolution of the Yalgoo Dome area during diapirism at c. 2750 Ma. The sketches show diapiric emplacement of the Goonetarra Granodiorite into the greenstone cover, with shearing localized along the Badja Décollement at the granite-greenstone contact. In supracrustal rocks, progressive deformation resulted in: (i) syn-doming tilting of supracrustal rocks, accompanied by the deposition of a siliciclastic sequence resting on an angular unconformity; (ii) a group of coplanar cascading folds associated with subvertical stretching and the outward flow of greenstone cover, with early isoclinal and sheath folds (F_{D1} and F_{D2}) subsequently refolded by upright F_{D3} folds; (iii) shearing of Mougooderra Formation metasedimentary rocks, postdating F_{D1} folds. Modified after Zibra et al. (2020).

In addition to outcrop-scale doming-related folding, several examples of map-scale, broad synforms occupy the areas between domes in the region. These synformal structures display atypical, cuspate, often triangular geometries in which each margin is parallel with the curvilinear margins of adjacent domes. One such structure, the Jasper Hill syncline, is located in the YSGB at the triple point between the Yalgoo Dome, Mt Mulgine Dome and potential Rothsay Dome (Fig. 2.9). The overall synformal structure at Jasper Hill comprises three synforms, in addition to two minor intervening antiforms. The arcuate axial traces of these map-scale F_{D1} folds wrap around the margin of the Yalgoo Dome in the northwest, and the margin of the Mt Mulgine Dome in the east, resulting in a fan-shaped pattern (Fig. 2.9). Folding at Jasper Hill has previously been interpreted as the interaction between D_1 recumbent folding and D_3 N-S trending folding in the scheme of Watkins & Hickman (1990; Fig. 2.8).

Zibra et al. (2018) suggests that uplift of the Yalgoo Dome can be temporally and spatially correlated to angular unconformities in the greenstone cover, principally at the base of the Mougooderra Fm. Several outcrops across the unconformable base of the Mougooderra Fm are described by Zibra et al. (2018), such as at Chulaar Well, along the eastern margin of the Mougooderra Fm in the YSGB. At this locality, lithological contacts are steeply east-dipping to subvertical. The geometry and characteristics of the unconformity at Chulaar Well are illustrated in Figure 2.12 (Zibra et al., 2020). From east to west, the exposure records a progression from a foliated metachert of the lower greenstone succession (I), to foliated cataclastic metachert (II), to a fining-upwards sequence comprising monogenic conglomerate with chert clasts (III and IV), which transitions upwards into pebbly sandstone with large chert clasts (V), that decrease in size and abundance upwards (VI).

2.4.3.5 Summary

Structural analysis, coupled with regional mapping and geophysical data, indicates that the southwestern Murchison Domain contains an extensive (>100 x 100 km) granite-migmatite dome system, comprising at least seven domes separated by synformal greenstone keels (Fig. 2.13) (Zibra et al., 2020). Structural evidence including domal fabrics and outward plunging lineations within domes, outward-plunging fold axes and lineations in supracrustal cover, and ubiquitous dome-up kinematics indicate that the Badja Decollement facilitated the diapiric emplacement of the Yalgoo Dome into the greenstone cover (Zibra et al., 2018; 2020). Zibra et al. (2020) suggests that multiwavelength polydiapirism is responsible for the distinctive dome-and-keel architecture of the region, best explained by incremental igneous diapirism, combined with sagduction and erosion of the greenstone cover. Consequently, the early structural development of the area is suggested to have resulted from the interference between multiple coeval diapirs (Zibra et al., 2018; 2020), rather than fold interference (Myers & Watkins, 1985; Watkins & Hickman, 1990; McCuaig et al., 2002).

2.4.4 Late Deformation

All existing deformational schemes for the Murchison Domain encompass a phase of E-W shortening following early deformation described in sections 2.4.2 and 2.4.3, (assigned to D_3 by Watkins & Hickman, 1990; D_4 by Van Kranendonk et al., 2013) resulting in north to north-northeast trending folds and a heterogeneously developed N-S trending, steeply-dipping fabric across the region (Watkins & Hickman, 1990; Van Kranendonk et al., 2013; Zibra et al., 2018; Zibra, 2020). This fabric is referred to as the orogenic fabric (S_{OR}) by Zibra et al. (2018; 2020), which overprints the domal fabric and dome and keel architecture in the Yalgoo Dome area and is broadly parallel with the north-striking regional tectonic grain that typifies the Youanmi Terrane (Zibra et al., 2018). The orogenic fabric is locally axial planar to north-south trending folds with steeply plunging axes (Zibra et al., 2020). Ongoing E-W shortening is also considered responsible for the development of NNE- to NNW-oriented shear zones with a significant reverse component, across the Murchison Domain. Shearing is distinguished as a distinct, late-stage event (D_4) by Watkins & Hickman (1990), whereas Van Kranendonk et al. (2013) incorporates shear zone development into a prolonged D_4 E-W shortening episode. In the northeast Murchison Domain, three major north-northeast striking shear zones contain kinematic indicators that demonstrate dextral movement, whereas less common north-northwest trending shear zones exhibit sinistral kinematics (Van Kranendonk et al., 2013).

Recently, the features associated with this prolonged E-W shortening episode have collectively been attributed to the c. 2730-2650 Ma Neoarchaean Yilgarn Orogeny, comprising an ensemble of large-scale magmatic, metamorphic and deformation events that can be correlated across the Yilgarn Craton (Zibra et al., 2017a; Zibra, 2020). Using a combination of detailed mapping and new geochronology in the Murchison Domain, Zibra (2020) distinguished four locally defined, well-constrained, successive deformational events that have been dated between 2730-2630 Ma, as part of the protracted period of E-W shortening (Fig. 2.14). The first three of these events are spatially and genetically associated with the intrusion of north-south oriented, syntectonic granitic plutons along active, crustal-scale shear zones in the central and northeastern Murchison Domain, and their timings have been constrained at ca. 2730 Ma (D_1), ca. 2700 Ma (D_2) and ca. 2660 Ma (D_3) (Fig. 2.14; Zibra, 2020). Field evidence and seismic reflection data demonstrate that these plutons are wedge-shaped and east-dipping, consistent with the tectonic grain across the Yilgarn Craton, and comprise a network of syn-magmatic, east-dipping reverse shear zones (Fig. 2.14; Zibra, 2020). The D_2 event is directly associated with the emplacement of the ~150x50 km Lakeside Pluton (Big Bell Suite) located to the northeast of the YSGB, whereas the D_1 and D_3 events are spatially restricted to the Chunderloo and Cundimurra plutons, respectively, in the eastern and northeastern Murchison Domain (Fig. 2.14; Zibra, 2020). Crucially, structures associated with the D_1-D_3 events have not been identified in the YSGB,

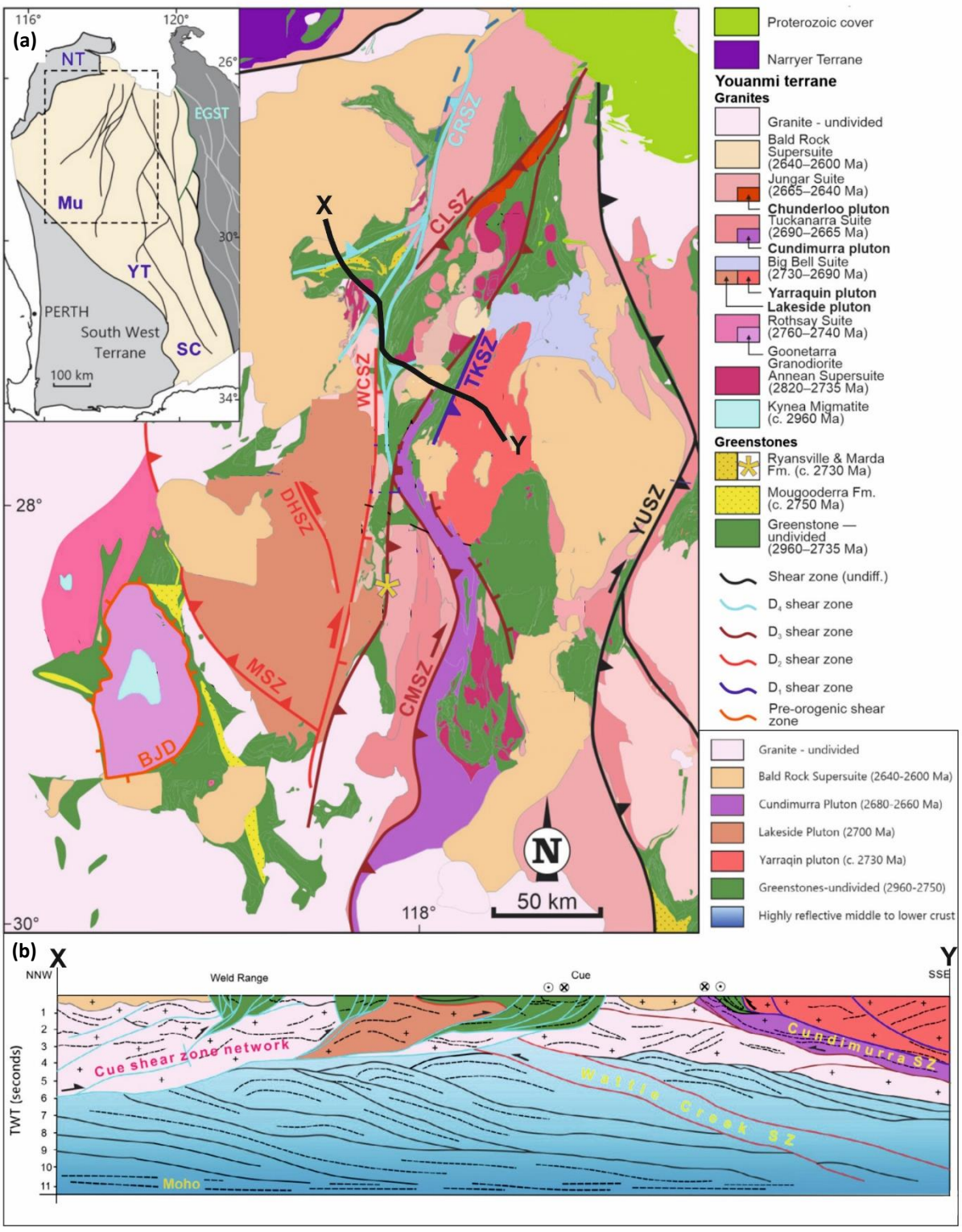

Figure 2.14: (a) Interpreted geological map of the Murchison Domain, showing major granitoid intrusions and major shear zones as defined by Zibra (2020). The black line X-Y refers to a cross section shown in (b). Abbreviations for shear zones: CLSZ: Chunderloo Shear Zone; TKSZ: Tuckabianna Shear Zone; WCSZ: Wattle Creek Shear Zone; BJD: Badja Decollement; MSZ: Mulloo shear zone; DHSZ: Daggar Hills shear zone; CMSZ: Cundimurra shear zone; CRSZ: Carbar shear zone; YUSZ: Youanmi shear zone. The inset image in the top right shows the main terranes and craton-scale shear zones in the western Murchison Domain and an outline of the extent of the geological map. The Youanmi Terrane (YT) is surrounded by the Eastern Goldfields Superterrane (EGST) and Narryer Terrane (NT) and subdivided into the Murchison Domain (Mu) and Southern Cross Domain (SC); **(b)** Interpretative geological cross section through the central portion of the Murchison Domain, along the line X-Y in (a), based on seismic and geological map data. Note that the D_1-D_3 crustal-scale fabric is truncated by D_4 structures comprising the Cue Shear Zone Network. TWT: Two-way time. Map and cross section modified after Zibra (2020).

where pre-orogenic, diapirism-related structures (Section 2.4.4) dominate (Zibra, 2020). A fourth, domain-wide deformational event between ~2660-2625 Ma (D_4; Zibra, 2020) is responsible for the development of a network of late-orogenic, upper crustal and typically west-dipping shear zones that locally truncate D_1-D_3 structures, referred to collectively as the Cue Shear Zone Network (Fig. 2.14; Zibra, 2020). The D_4 event is not associated with magmatism, indicating lower temperatures than earlier shearing events, and deformation is typically confined to narrow, high-strain and poorly exposed shear zones that frequently exploit major lithological contacts (Zibra, 2020).

Several high-strain shear zones have been distinguished in the southwest Murchison Domain. The Mulloo and Salt River shear zones are parallel to the regional 'orogenic fabric' and are situated to the northeast and west of the Yalgoo Dome, respectively (Fig. 2.10; Zibra et al., 2020). Two significant shear zones identified in the YSGB, the Mougooderra Shear Zone (MSZ) and the Chulaar Shear Zone (CSZ), are situated primarily at the western and eastern margins of the Mougooderra Fm (Fig. 2.8). The MSZ is unexposed, trends north-northwest, dips steeply to the west and is suggested to have undergone late-stage sinistral movement, though evidence is very limited (McCuaig et al., 2002; Thomas, 2003). In contrast, the CSZ is several hundred metres wide and marked by a prominent, silicified, quartz-andalusite-white mica mylonite with a ribbon-like appearance, host to a sub-vertical foliation and vertically-plunging lineation (Watkins & Hickman, 1990). The evidence suggests that the CSZ has experienced a significant component of vertical displacement (Watkins & Hickman, 1990).

McCuaig et al. (2002) suggested that the Mougooderra Fm in the YSGB was deposited either as a transpressional basin in a dilational jog, or as thrust-front molasses, during this phase of D_4 east-west shortening. These authors also discuss how the broadly parallel sub-vertical cleavage in surrounding greenstone units suggests that the MSZ and CSZ bounding the Mougooderra Fm were dominantly reverse thrust faults, and may represent reactivated, early transform faults. However, this conflicts with the scheme of Van Kranendonk et al. (2013), who advocate deposition of the Glen Group (including the Mougooderra Fm) after D_2 tilting, prior to subsequent north-south (D_3) and east-west (D_4) shortening events. McCuaig et al. (2002) imply that the MSZ and CSZ are long-lived weaknesses reactivated multiple times including a late stage of shearing. In terms of economic potential, lode-gold mineralisation tends to be focussed in regions of D_4 dextral shear and/or low-pressure domains in fold interference structures (Van Kranendonk et al., 2013). A significant majority of lode-gold deposits in the YSGB are located along the MSZ (Minjar, 2012). D_4 structures were initiated during, or soon after, the emplacement of ~2660 Ma granitoids and continued to ~2630 Ma in conjunction with gold mineralisation, thus D_4 shearing in the Murchison Domain occurred over at least 30 Ma (Van Kranendonk et al., 2013). D_3-D_4 deformation events are broadly temporally equivalent to comparable events in the eastern Yilgarn Craton (Van Kranendonk, 2008).

2.5 Archaean Geodynamics

2.5.1 The "Grand Debate"

Plate tectonics, comprising a "globally-linked system of lateral motion of rigid surface plates", is a characteristic feature of the modern Earth (Cawood et al., 2018). Since the late 1960s, the development of plate tectonic models has provided a robust framework that can be used to explain the tectonics of the Earth's crust throughout the Phanerozoic (e.g., Isacks et al., 1968; Forsyth & Uyeda, 1975; Rao & Babu, 2011), with a broad recognition that plate tectonics is essentially driven by the sinking of cold, dense lithosphere in subduction zones (Stern, 2005). The physical manifestations of plate tectonic processes on the modern Earth and in the Phanerozoic rock record (e.g., spreading ridges, ophiolites, volcanic arcs, mountain belts, subduction zones) are reasonably well-constrained (e.g., Dilek et al. 2000; Lallemand & Funiciello, 2009; Frisch et al., 2011). However, the nature and timing of the onset of plate tectonics on Earth remains equivocal and the geodynamics of the Archaean, which accounts for ~1.5 billion years of Earths history, has long been a subject of intense and prolonged debate (see Cawood et al., 2018; Johnson et al., 2019 and references therein). A better understanding of Archaean geodynamics is required to provide an essential framework in which Archaean rocks, structures and mineral deposits can be interpreted.

An ongoing discussion termed the "Grand Debate" embraces the controversy regarding the nature and evolution of Archaean crust, which has occupied the minds of Earth Scientists for many decades (Anhaeusser, 1981). The interpretation of Archaean tectonics since the early 1970s has evolved from early authors cautious to apply a uniformitarian model to the Archaean, to many recent researchers that support the existence and operation of plate tectonics throughout most, if not all, of Earth's history. In the mid-1970s, Dewey & Spall (1975) concluded that the tectonics of the Archaean were 'radically different' to plate-tectonics of recent times, with arguments given for and against the application of plate tectonic theory to the Proterozoic. At the Second International Archaean Symposium in 1980, the general consensus was that vertical tectonics was the dominant deformation mechanism during the Archaean (Glover & Groves, 1981). Gee et al. (1981) suggested that the upward diapiric movement of granitic material and concomitant sinking of greenstones occurred in the Yilgarn Craton, driven principally by density inversion. However, though Archibald et al. (1981) recognised that features of Archaean terranes were not analogous to modern tectonic settings, it was suggested that the vast volumes of granitic rocks implied the action of a process similar to subduction. In the following decades, the geodynamic models applied to the Archaean can be broadly subdivided into three main groups, corresponding largely to the predicted onset age of plate tectonics (Guice, 2019):

1. Onset of plate tectonics during the Hadean-Palaeoarchaean (>3.6 Ga), and Archaean rocks are almost entirely the products of plate tectonic processes (e.g., Dilek & Polat, 2008; Shirey et al., 2008; Korenaga, 2013; Arndt, 2013; Hastie et al., 2016; de Wit et al. 2018)
2. Onset of plate tectonics between the Palaeoarchaean-Palaeoproterozoic (3.6-2.2 Ga), with an initial pre-plate tectonic regime (>3.2 Ga) progressively transitioning to plate tectonics and Archaean rocks variably resulting from plate-tectonic and non-plate tectonic regimes (e.g., Van Kranendonk et al., 2004; O'Neill et al., 2007; Condie and Kröner, 2008; Moyen, 2010; Brown, 2010; Kamber, 2015; Johnson et al. 2017; Brown & Johnson, 2018; Cawood et al., 2018; Saji et al., 2018; Smithies et al., 2018; Condie, 2018; Wyman, 2019; Goscombe et al., 2019; Johnson et al., 2019).
3. Onset of plate tectonics during the Neoproterozoic (<1.0 Ga), and Archaean rocks are the product of pre-plate tectonic regime(s) (e.g., Hamilton, 1998; Stern, 2008; Ernst, 2009; Bédard, 2010; Hamilton, 2011; Hamilton, 2019).

A novel approach was taken by Tripp (2019), who used the abstracts from the most recent, decadal Fifth International Archaean Symposium in 2010 to gauge the recent popularity of arguments for and against the operation of plate tectonics during the Archaean. A review of the published abstracts from this symposium (Tyler & Knox-Robinson, 2010) indicates that most authors supported the existence of some form of Archaean plate tectonics. Some key pieces of evidence given in favour of Archaean plate tectonics are as follows:

- U-Pb and Hf isotope data from over 12,000 zircon analyses from the TerraneChron program suggests that most magmatic rocks represented in major periods of crustal growth were largely derived from reworking of pre-existing crust, especially since c. 2.5 Ga, indicative of recycling via subduction (Belousova et al., 2010).
- The presence of sanukitoids (TTG with elevated Mg, Ni, Cr, LILE and REE) requires an enriched mantle source, most commonly attributed to burial of hydrous, surface material, indicating a subduction-type environment (Moyen, 2010). Sanukitoids are identified in the late-Archaean, with some of the oldest dated at 2.95 Ga in the Pilbara Craton (Smithies & Champion, 2000).
- Analysis of eclogitic sulphide inclusions in diamonds from the Kaapvaal and Zimbabwe Cratons shows they contain lithospheric materials containing surficial sulphur, suggesting the onset of subduction as early as 3.9 Ga (Shirey et al. 2001; Shirey et al., 2008; Shirey & Carlson, 2010).
- Thermomechanical modelling suggest that Archaean geodynamic settings depend primarily on upper-mantle temperature, with progression from no subduction at >250-200 °C greater than present, through a pre-subduction regime, to modern one-sided subduction (whereby

one plate at a convergent margin is subducted rather than both) at <175-160 °C greater than present (Sizova et al., 2010). A combined petrological study of metamorphic assemblages indicates that the transition to one-sided subduction may have started in the Mesoarchaean-Neoarchaean and have developed globally by the Palaeoproterozoic Era (Brown, 2010).

- In the Superior Province, Canada, multiple geophysically, isotopically and chronologically unique terranes of continental and oceanic crust have been distinguished. Structural evidence indicates these terranes were juxtaposed during successive collisional events from c. 2.72 Ga to c. 2.68 Ga, supporting crustal evolution involving plate tectonics and the action of subduction (Percival, 2010).
- Boninites, LREE-enriched mafic rocks and low-Ti basalts are considered to have formed from subduction processes in a geodynamic regime akin to a modern, juvenile arc setting (Wyman & Kerrich, 2010; 2012; Wyman, 2019; Lowrey et al., 2020).

However, there are several authors who provide comprehensive arguments against the existence of plate tectonics in the Archaean, based largely on the lack of typical features exhibited at modern convergent margins, including the following:

- The critical diagnostic indicators of Phanerozoic subduction, including preserved ophiolites, high-pressure blueschist metamorphic assemblages, subduction-related batholiths and paired metamorphic belts, are not observed in the Archaean, but instead indicate modern plate-tectonics started in the Neoproterozoic Era (<1 Ga; Stern, 2008; 850 Ma; Hamilton, 2011).
- Archaean TTG-greenstone associations with typical dome and keel geometries are not found at modern convergent margins, whereas andesitic strato-volcanoes and fold-thrust belts that characterise modern convergent settings are not observed in the Archaean, showing considerable disparity in geodynamic regimes (Bédard, 2010).
- Phanerozoic island-arc associated volcanic assemblages are typically unimodal, with a single mafic peak, whereas most Archaean volcanic rocks are strongly bimodal, with distinct mafic and felsic peaks (Hamilton, 2011).
- Andesites are very common in modern arc sequences, whereas they are subordinate in Archaean volcanic successions and exhibit markedly different compositions (Hamilton, 2011).
- Rocks recognised as boninites or boninite-like in Archaean sequences generally have lower SiO_2 and higher Al_2O_3 and HREE contents compared to modern boninites (Smithies et al., 2004), and so may not reflect the same geodynamic setting of formation (Hamilton, 2011).

The timing and nature of the onset of modern-style plate tectonics remains a highly controversial issue (e.g., Kamber, 2015). Condie & Kroner (2008) noted that it is unlikely that plate tectonics on Earth was

initiated as a single, global event, during a specific interval in the Archaean, but more likely developed gradually through time. Moyen (2010) suggests that throughout the Archaean, there was a progressive transformation from an ancient tectonic style to modern-style plate tectonics. Furthermore, it is proposed that this evolution occurred on a craton-by-craton basis, possibly by 3.0 Ga in the Kaapvaal Craton but not until 2.5 Ga elsewhere, though by the early Proterozoic, the transformation was fully achieved (Moyen, 2010). Some geologists argue against plate tectonics for specific Archaean regions and times but accept it for others (e.g., Groenewald et al., 2003; Van Kranendonk et al., 2004). Other researchers suggest alternating episodes of a proto-plate tectonic regime during the late Archaean, such as stagnant-lid asthenospheric convection (e.g., Stern, 2008; Ernst, 2009), the occurrence of episodic subduction (O'Neill et al., 2007) or periods of plate tectonics interspersed with stagnant-lid episodes (Kamber, 2015).

2.5.2 Geodynamic Models for the Murchison Domain, Yilgarn Craton

Various competing geodynamic models have been proposed for the post-2820 Ma evolution of rocks in the Murchison Domain, which can be subdivided into three main models:

1. Rifting and plume-related mantle upwelling (i.e., autochthonous crustal growth; Watkins & Hickman, 1990; Ivanic et al., 2012; Van Kranendonk et al., 2013).
2. Arc magmatism, subduction and accretion (i.e., allochthonous crustal growth; Wyman, 2019)
3. Combination of plume-related and subduction-related tectonics (Wyman & Kerrich, 2012).

The general architecture of the Yilgarn Craton consists of a central nucleus, denoted by the Youanmi Terrane, with contiguous terranes to the west and east bounded by crustal-scale faults or shear zones that dip away from the central nucleus (Korsch et al., 2013). This is demonstrated by an interpreted compilation of seismic data along a 1300 km east-west traverse across the Yilgarn Craton (Fig. 2.15). Whilst some authors advocate the Youanmi Terrane has existed as a coherent crustal block since c. 3000-2900 Ma based on Nd isotopic data (Ivanic et al., 2012; Van Kranendonk et al., 2013), others argue that the Youanmi Terrane has acted as a protocraton, onto which other terranes have subsequently been accreted (e.g., Czarnota et al., 2010; Wyman & Kerrich, 2012). The three principal geodynamic models proposed for the Murchison Domain are summarised in the following sections.

2.5.2.1 Plume ('Autochthonous') Model

Van Kranendonk et al. (2013) proposed an entirely plume-driven, autochthonous development for the Murchison Domain, with no requirement for subduction or other plate-tectonic processes (Fig. 2.16). An early phase of magmatism between 2960-2930 Ma is responsible for dominantly felsic rocks of the

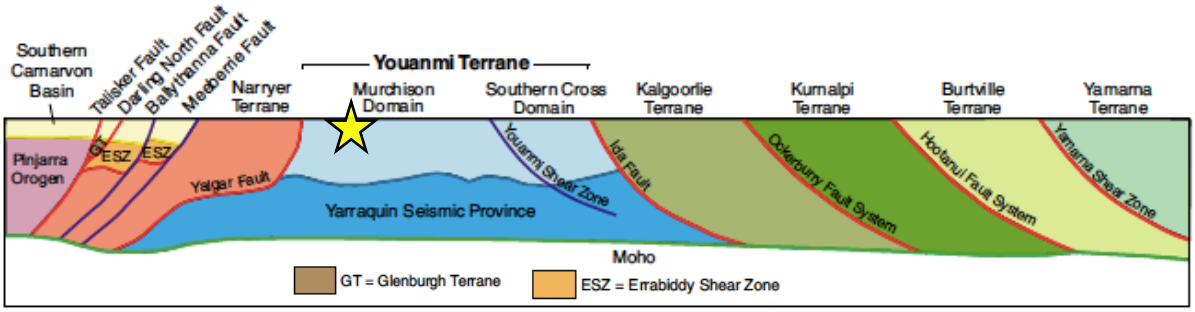

Figure 2.15: A cartoon depicting the present-day crustal architecture of an east-west transect across the Yilgarn Craton, showing the major terranes, domains and significant faults from the Narryer Terrane in the west, to the Yamarna Terrane in the east. Approximate and not to scale. The yellow star denotes the location of the YSGB. Korsch et al. (2013).

cryptic 2.95 Ga Formations, which based on detrital and xenocrystic zircons, are considered to represent the basement rocks across the entire Murchison Domain (Wang et al., 1998; Van Kranendonk + Ivanic, 2009). Following a ~110 m.y. hiatus, a major thermal event at c. 2820 Ma is consistent with the impingement of a large, craton-scale mantle plume and associated east-west extension, the consequences of which are recorded in the rock record for the following 70 m.y. (Wyche, 2010). This includes highly magnesian volcanic rocks of the lower Norie Group erupted from 2825-2800 Ma (Barley et al., 2000), in addition to large, typically anhydrous mafic-ultramafic, layered intrusions of the same age (Ivanic et al., 2010; 2017). This phase of extension is likely to have produced thin ribbons of crust with compositional and thickness variations, similar to that of modern continental rift margins (Fig. 2.17). Recent geochronology has revealed that the effects of this mantle plume event were experienced across the Yilgarn Craton, including the Kalgoorlie, Kurnalpi and Burtville terranes, and may also indicate that much of the Yilgarn Craton has been a coherent crustal block since at least 2820 Ma (Van Kranendonk et al., 2013). From c. 2790-2760 Ma, a transition from (ultra)mafic to felsic Polelle Group magmatism and increased granitoid intrusion is attributed to partial melting of older crust through conductive heating (Campbell & Hill, 1988; Van Kranendonk et al., 2013). A further consequence of such crustal interaction is contamination of magmas, which is evident in many of the Murchison Supergroup lithologies (Van Kranendonk & Ivanic, 2009).

A subsequent period of uplift and crustal tilting in the Murchison Domain resulted in the development of a regional unconformity, followed by the onset of a second phase of plume-related volcanism at c. 2720 Ma (Fig. 2.17b; Van Kranendonk et al., 2013). Consequently, crustally contaminated komatiitic and tholeiitic basalts of the Glen Group were erupted, with contemporaneous intrusion of Yalgowra Suite intrusions and subsequent deposition of sedimentary rocks (Van Kranendonk & Ivanic, 2009). High-Mg ('komatiitic') basalts are considered to represent fractionation products of komatiites derived from the hot axis of a mantle plume, whereas more widespread tholeiitic basalts are derived from magmas from the cooler plume margins (Said et al., 2012). Plume-related volcanism and extension was also experienced across the EGS from 2720-2690 Ma, during a period of voluminous mantle

melting attributed to overturn of layered mantle (Stein & Hofmann, 1994; Barley et al., 1998). At this stage, extension was most significant along the Ida Fault (Figs. 2.15, 2.17a), located at the boundary between the Youanmi and Kalgoorlie terranes.

Partial melting of pre-existing crust occurred from c. 2690-2645 Ma, ~30 m.y. after the onset of plume magmatism, replicating the postponed felsic magmatism following the previous plume impingement at c. 2820 Ma. This resulted in the widespread emplacement of voluminous high-Ca and low-Ca granitoid suites, which today account for approximately 70% of the exposed area of the craton (Van Kranendonk et al., 2013). Widespread granite emplacement is interpreted to have been broadly contemporaneous with metamorphism and upright folding of greenstones via partial convective overturn, with the heat source from granites likely responsible for metamorphism (Barnes et al., 2012;

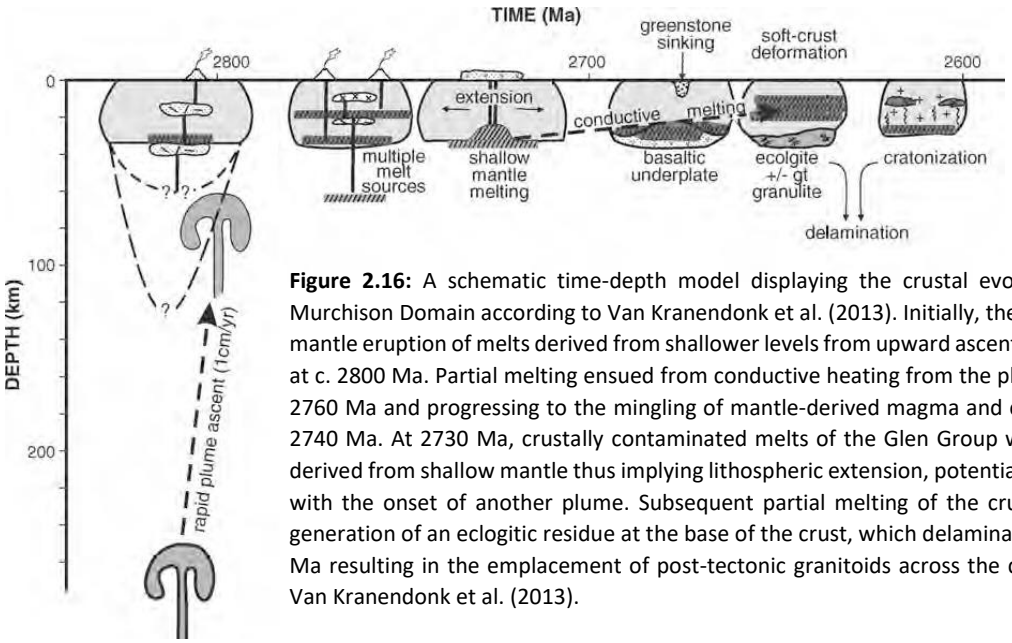

Figure 2.16: A schematic time-depth model displaying the crustal evolution of the Murchison Domain according to Van Kranendonk et al. (2013). Initially, the rise of deep-mantle eruption of melts derived from shallower levels from upward ascent of the plume at c. 2800 Ma. Partial melting ensued from conductive heating from the plume at 2785-2760 Ma and progressing to the mingling of mantle-derived magma and crust at 2760-2740 Ma. At 2730 Ma, crustally contaminated melts of the Glen Group were erupted, derived from shallow mantle thus implying lithospheric extension, potentially associated with the onset of another plume. Subsequent partial melting of the crust led to the generation of an eclogitic residue at the base of the crust, which delaminated at c. 2640 Ma resulting in the emplacement of post-tectonic granitoids across the domain. From Van Kranendonk et al. (2013).

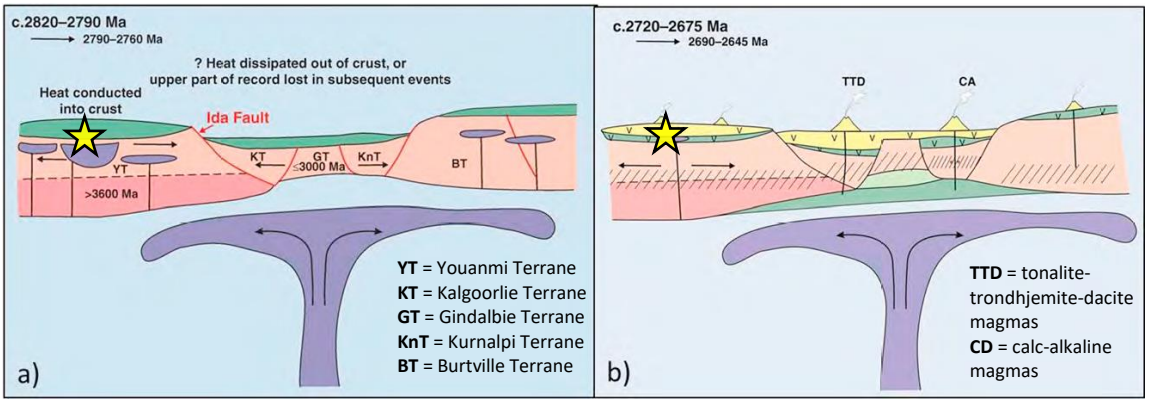

Figure 2.17: A schematic plume model for the development of the Yilgarn Craton, Western Australia. **(a)** From c. 2820-2790 Ma, a deep mantle plume undergoes melting and results in eruption of mafic volcanic rocks, emplacement of large layered igneous intrusions and lithospheric thinning of the central portion of the craton, followed by significant partial melting of older crust from c. 2790-2760 Ma; **(b)** From c. 2720-2675Ma, a second phase of plume magmatism resulted in eruption of komatiitic to basaltic volcanic rocks and underplating of previously thinned lithosphere, thus providing multiple possible sources for ensuing deep-crustal melting. From c. 2690-2645 Ma, conductive heating and ongoing input of mantle-derived melts facilitate widespread crustal melting, followed by the delamination of underplated eclogitic residual mantle according to Smithies & Champion (1999). The yellow stars denote the approximate location of the YSGB. After: Van Kranendonk et al. (2013).

Van Kranendonk et al., 2013). The peak of granitic magmatism and the onset of significant lode-gold mineralisation coincide at 2660 Ma, implying a co-genetic relationship between intrusion and gold mineralisation. Finally, the widespread emplacement of c. 2640 Ma post-tectonic granitoids across the Yilgarn Craton, including the Walganna and Wogala suites in the Murchison Domain, are credited to the delamination of an eclogitic residue that had developed at the base of the crust from further, extensive crustal melting (Smithies & Champion, 1999; Van Kranendonk et al., 2013).

The autochthonous plume-dominated model of Van Kranendonk et al. (2013) has several shortcomings. Firstly, the model cannot fully account for the occurrence of metasomatised mantle melts, the apparent hydrous parental magmas for several major mafic-ultramafic intrusive suites (e.g., Boodanoo Suite; Section 2.3.1) and the boninite-like geochemistry of some units in the Norie and Polelle groups (Wyman, 2019; Lowrey et al., 2020). The model is also inconsistent with some craton-wide observations, such as the east-west variation in the composition and age of volcanic rocks in the EGS (Czarnota et al., 2010). Furthermore, the spatial architecture of tholeiitic and komatiitic mafic-ultramafic rocks located in north-northwest trending, linear troughs at Kambalda in the EGS, is not compatible with the radial distribution expected in plume-dominated models (Czarnota et al., 2010; Wyman & Kerrich, 2012). However, this assumes a homogenous lithosphere and could plausibly be explained by the presence of pre-existing faults and other crustal weaknesses along which plume-derived magmas may have been focussed.

2.5.2.2 Subduction-Accretion ('Allochthonous') Model

Arc-accretion models proposed for the Yilgarn Craton involve allochthonous development through the accretion of successive terranes via subduction of intervening crust (Myers, 1995, Czarnota et al., 2010; Wyman & Kerrich, 2012; Wyman, 2019; Lowrey et al., 2020). Numerous pieces of evidence have been presented in support of post 2820 Ma subduction-related magmatism in the Murchison Domain. The occurrence of 2750 Ma high-HFSE sanukitoid intrusions in the Murchison Domain and andesitic-rhyolitic volcanic rocks of the 2730 Ma Marda Complex in the neighbouring Southern Cross Domain are consistent with subduction-related magmatism (Champion et al., 2002; Morris & Kirkland, 2014). In the Murchison Domain, evidence favouring a subduction-accretion model includes intermediate-felsic volcanic rocks of the 2760-2735 Ma Greensleeves Fm, which exhibit distinct calc-alkaline signatures and partly overlap with apparent subduction-related magmatism in the adjacent Southern Cross Domain at ~2735 Ma (Taylor & Hallberg, 1977; Van Kranendonk et al., 2013). Multiple large mafic-ultramafic intrusive suites in the Murchison Domain are derived from hydrous parental magmas, most notably the c. 2800 Ma Boodanoo Suite, signifying extensive hydration of mantle sources (Ivanic et al., 2015b; Wyman, 2019). Similarly, the features of Warriedar Suite intrusions are

considered to be comparable to post-Archaean, Alaskan-type intrusions that can be derived from hydrous arc magmas (Himmelberg & Loney, 1995; Yuan et al., 2017; Wyman, 2019). A compelling argument in favour of subduction-related geodynamics is the ostensible identification of boninite-like rocks within the Polelle Group at several locations in the Murchison Domain, which are considered texturally and geochemically comparable to modern boninites found in juvenile subduction zones (Wyman & Kerrich, 2012; Wyman, 2019; Lowrey et al., 2020; Koutsoumbis, 2020). These geochemical studies have found that whereas fluids and sediment-interaction played an important role in the enrichment of mantle sources for Norie Group rocks, there is no evidence of systematic crustal contamination (Wyman, 2019).

Based on this evidence, Wyman (2019) proposed a preliminary tectonic model invoking a double-slab subduction event comprising 2830-2790 Ma subduction along the west margin of the Yilgarn Craton, and possibly slightly earlier subduction along the eastern Yilgarn Margin. The ~40 Ma period recorded by volcanism of the Norie and lower Polelle Group at this time is similar to that documented in the Abitibi belt, Canada, and is considered to demonstrate short-lived subduction events regulated by slab break off (Moyen & van Hunen, 2012; Wyman, 2019). A possible scenario suggested to explain the apparent 'cratonic' location of boninite-like rocks and the rapid transition from anhydrous (Meeline Suite) to hydrous (Boodanoo Suite) mantle sources for mafic-ultramafic intrusions at ~2800 Ma, involves the propagation of an oceanic spreading ridge towards the Yilgarn Craton (Fig. 2.18; Wyman, 2019). This spreading centre would have first induced cratonic extension, followed by plate convergence and subduction once the ridge propagated to the west of the craton (Wyman, 2019). Crucially, the only komatiitic rocks previously identified in the Murchison Domain (lower Norie Group; Barley et al., 2000) used in support of a mantle plume by Van Kranendonk et al. (2013), have been reinterpreted as arc picrites derived from hydrous, subduction-modified magmas with primary liquid

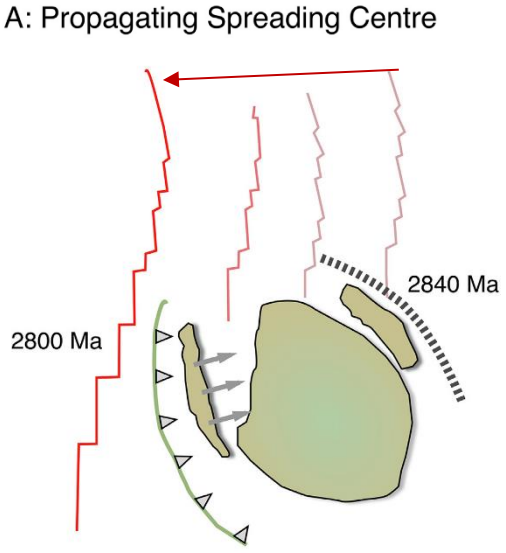

Figure 2.18: A cartoon displaying the propagating spreading centre and subduction model proposed for the Murchison Domain by Wyman (2019). A spreading centre tip (red-pink) propagates from top right to bottom left, resulting in short-lived subduction on the east and west margins of the Yilgarn Craton at ~2840-2800 Ma. At 2800 Ma, the western Yilgarn Craton setting changes from extension (rifting-related boninites and anhydrous magmatism) to subduction (subduction-related and hydrous magmatism) as the spreading centre moves away from the craton (red arrow shows movement of spreading ridge). Broad ages are inferred from the age of the dry-wet mantle transition (Ivanic et al., 2015b; Ivanic, 2019). Modified after Wyman (2019).

compositions of ~16 wt. % MgO, effectively negating the requirement for a mantle plume (Wyman, 2019). A subsequent inward-dipping double subduction event may have occurred again after 2750 Ma, consistent with geodynamic models of the eastern Yilgarn, and preceding the onset of mantle-plume-related komatiitic volcanism in the Kalgoorlie Terrane (Czarnota et al., 2010; Begg et al., 2010; Wyman, 2019). A 2780-2760 Ma volcanic hiatus in the northeast Murchison Domain, separating the lower Polelle (Meekatharra Fm) and upper Polelle Group (Greensleeves Fm), is tentatively suggested to be a local feature within the broader subduction system (Lowrey et al., 2020). Notably, the subduction-accretion model described here is based entirely on geochemical data (Wyman, 2019; Lowrey et al., 2020). This sort of approach has been criticised by some authors (e.g., Bédard, 2006; Hamilton, 2011) as geochemical fingerprinting is considered to be demonstrably equivocal and open to non-unique interpretations (Moyen & Laurent, 2018).

2.5.2.3 Combined Plume-Subduction Model

Wyman & Kerrich (2012) proposed a hybrid geodynamic model for the <2820 Ma Murchison Domain that involved both plume magmatism, and subduction-related tectonics. Models invoking a close association or coexistence of subduction zones and mantle plumes have been common since first proposed for the Abitibi greenstone belt, Canada (Wyman et al., 1999). The apparent presence of Polelle Group boninitic rocks implies that subduction tectonics played an important role in the evolution of the Murchison Domain from 2800-2735 Ma, whereas the komatiitic sequences and large,

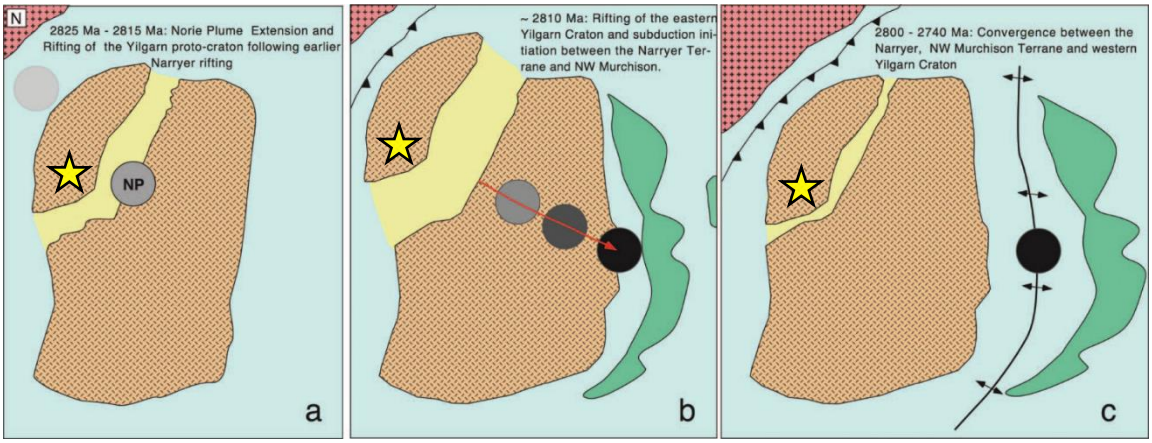

Figure 2.19: Schematic diagrams displaying the 2825-2740 Ma evolution of the Yilgarn Craton according to the subduction, plume and accretion model of Wyman & Kerrich (2012). **(a)** Rifting of the Yilgarn proto-craton following rifting and separation of Narryer Terrane continental fragment (N), from impingement of the Norie Plume (NP); **(b)** Widespread crustal extension across the Yilgarn from 2825-2810 Ma, with subsequent rifting on the eastern margin attributed to movement of the NP tail, possibly producing multiple fragments representing the precursors of EGS terranes. Komatiitic magmatism (Lower Polelle Gp) is followed by subduction zone development between the Narryer Terrane and Yilgarn Craton, leading to further rifting in the NW Yilgarn and a back-arc basin setting, with boninites emplaced in the Polelle Gp; **(c)** From 2800-2740 Ma, arc-related magmatism occurs along the western Youanmi Terrane margin, terminating in collision of the Narryer and Youanmi terranes, whilst fragments in the Eastern Yilgarn are entirely rifted from the west. Finally, convergence between the rifted fragments in the east and the Western Yilgarn from 2715-2660 Ma. The yellow star denotes the current location of the YSGB. From: Wyman & Kerrich (2012).

concomitant mafic-ultramafic intrusive complexes indicate that mantle plume activity was also a major contributor to crustal growth (Wyman & Kerrich, 2012). The tentative geodynamic model that these authors proposed thus includes a subduction event, at least for the Polelle Group, in addition to the impingement of mantle plumes (Wyman & Kerrich, 2012, Fig. 2.19). In this model, crustal formation in the Murchison Domain was initiated by extensive rifting between the Narryer and Youanmi terranes, as a consequence of impingement of the large 'Norie Plume', resulting in crustal extension from 2825-2810 Ma and the eruption of Norie Group volcanic rocks. This preceded the onset of east-dipping subduction between these two terranes, resulting in volcanism and back-arc extension, in addition to the eruption of boninites in the Polelle Group at this time (Wyman & Kerrich, 2012). Progressive convergence of the Narryer and Youanmi terranes from 2800-2740 Ma resulted in widespread subduction-related volcanism, which was terminated by the collision of these two terranes (Fig. 2.19). Finally, crustal fragments in the eastern Yilgarn were rifted from the Youanmi Terrane, before succeeding convergence from 2715-2660 Ma that resulted in the final amalgamation of the Yilgarn Craton (Fig. 2.19; Wyman & Kerrich, 2012). This model largely concurs with Czarnota et al. (2010), who proposed a hybrid geodynamic model entailing paraautochthonous development of the eastern Yilgarn Craton, comprising c. 2810 Ma mantle plume-related rifting along the eastern margin of the early Youanmi Terrane, in addition to c. 2715 Ma subduction east of the Yilgarn Craton.

Subduction-accretion models do not account for the distinct lack of structural evidence for accretion, the widespread emplacement of granitoids prior to terrane accretion, as well as a lack of high-pressure metamorphic assemblages in the foreland (Van Kranendonk et al., 2013). Czarnota et al. (2010) noted that such models also do not account for the spatial pattern of Nd depleted-mantle model ages (T_{DM}) across the craton. Furthermore, crustal contamination of many rocks in the Yilgarn Craton makes tectonic reconstructions challenging, as crustally-contaminated plume magmas are often geochemically indistinguishable from subduction-derived magmas (Wyman & Kerrich, 2012; Van Kranendonk et al., 2020). The subduction-only allochthonous model of Wyman (2019) does not account for the formation of vast c. 2820 Ma intrusions of the Meeline Suite, which have been interpreted as the products of mantle plume activity (Ivanic, 2010; Van Kranendonk et al., 2013; Ivanic et al., 2017). The Wyman (2019) model is not fully compatible with recent structural models for the Murchison Domain, which invoke diapirism and partial convective overturn to explain the 2800-2740 Ma deformational history of the region (Van Kranendonk et al., 2013; Zibra et al., 2020).

2.6 Gold Mineralisation

2.6.1 Orogenic-Lode Gold Mineralisation

Gold occurs as a primary commodity in a wide variety of geological settings and is hosted by rocks with ages that span from the Tertiary, to the Archaean. The settings in which Phanerozoic gold deposits are found include extensional regimes, such as back-arc environments, in addition to convergent margins, including oceanic arcs, continental arcs and accreted terranes (Fig. 2.20) (Robb, 2005; Goldfarb & Groves, 2015). Robert et al. (2007) defined 13 globally significant gold deposit types,

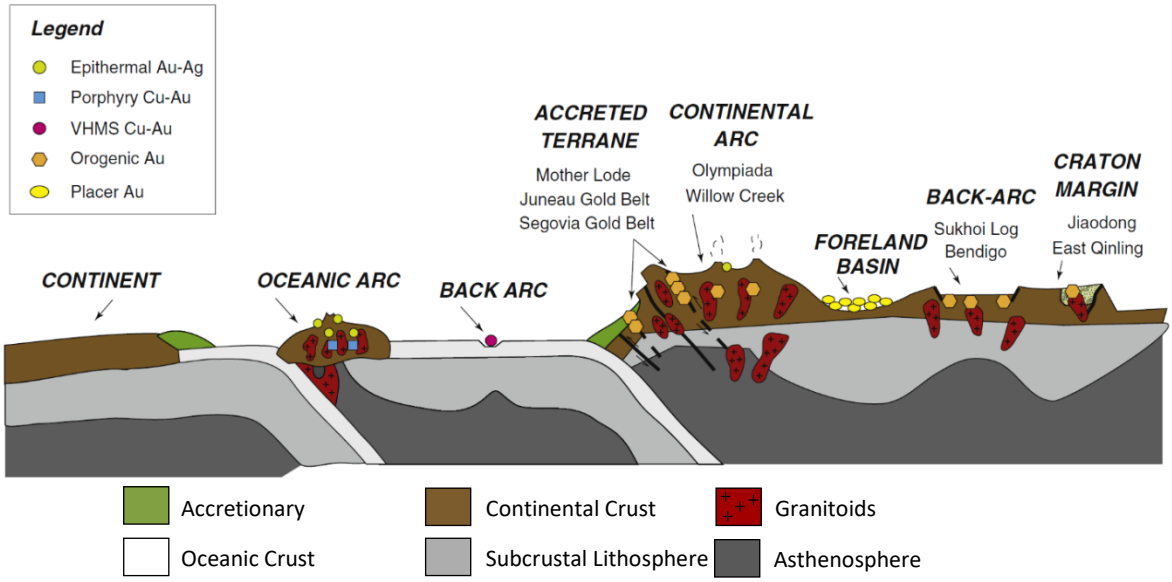

Figure 2.20: A schematic diagram showing the varied tectonic settings of epigenetic, gold-rich deposits. Orogenic gold deposits may be located in metamorphosed fore-arc/back-arc regions of continental margins, in addition to the sheared margins of continental arc batholiths. Modified from Goldfarb & Groves (2015).

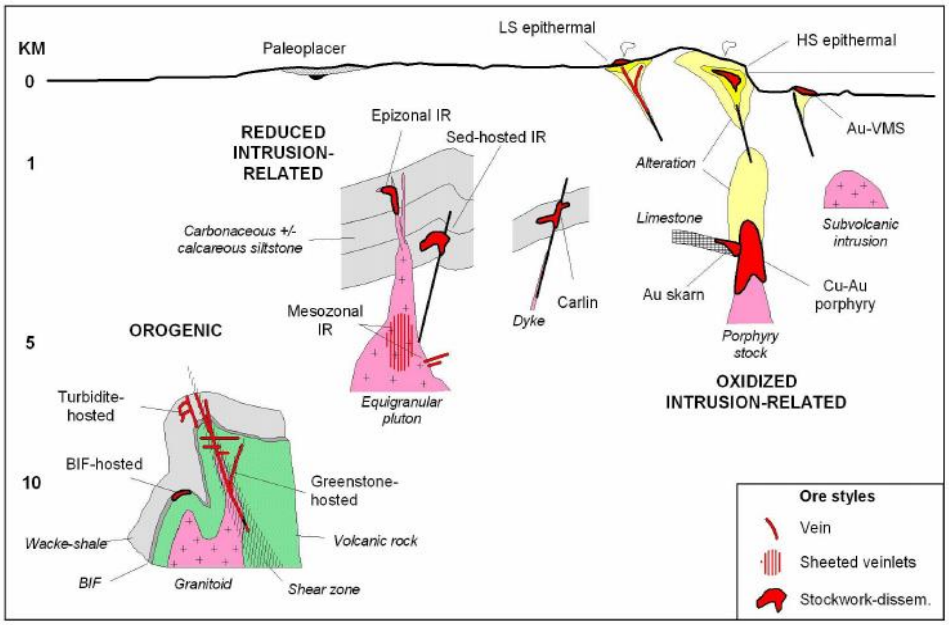

Figure 2.21: A schematic cross section showing the key geologic elements of the main gold systems and their crustal depth of emplacement (Logarithmic depth scale). From: Robert *et al.* (2007), modified after Poulsen *et al.* (2000).

which exhibit specific characteristics and form in distinct geological settings. In turn, these deposit types can be further sub-divided into four separate clans based on common features and similar formation processes, comprising orogenic, reduced intrusion-related, oxidised intrusion-related and 'other' (Fig. 2.21) (Robert *et al.*, 1997; 2007; Poulsen et al., 2000).

Orogenic gold deposits represent an estimated ~75% of the gold extracted throughout human history either through direct hydrothermal accumulation or from erosion of primary gold deposits (Phillips, 2013; Gaboury, 2019). Orogenic gold deposits are considered to have formed episodically since the mid-Archaean (i.e., over the last 3 billion years; Goldfarb et al., 2001) at depths in excess of 4 km within the crust (Fig. 2.21) (Goldfarb et al., 1991; Groves et al., 2003; Wyman et al., 2016). Some researchers have linked the genesis of orogenic gold deposits to supercontinental cycles (e.g., Bradley, 2011), as many orogenic gold deposits are considered to have developed at mid-crustal levels during intense accretional and compressional orogenic episodes (Goldfarb & Groves, 2015).

Neoarchaean-age, greenstone-hosted gold deposits have historically been interpreted in terms of a number of 'unifying' genetic models attempting to explain mineralisation processes operating during the Archaean. These include the metamorphic replacement model (Phillips & Groves, 1983; Groves & Phillips, 1987), the crustal continuum model (Groves, 1993), intrusion-related models (e.g., Duuring et al., 2007) and the widely used, all-encompassing 'orogenic' model (Groves et al., 1998; Goldfarb et al., 2001; Groves et al., 2000; Groves et al., 2003; Goldfarb & Groves, 2015). Over the last two decades, Neoarchaean gold deposits in greenstone successions have widely been referred to as orogenic lode-

Timing	Mid-Archaean to Tertiary, notable peaks at **2.7-2.5**, 2.1-2.0, 1.9-1.7 & 0.8-0.6 Ga
	Late-tectonic timing, syn- to post- metamorphism
Host Rocks	Variable, often Fe-rich rocks including mafic-ultramafic volcanics/intrusives, BIF and greywacke/slate sequences
	Typically greenschist to amphibolite metamorphic facies
Mineralisation Style	Quartz-dominant vein systems with < 5-15% carbonate content. Au found in veins and in sulphidised Fe-rich wall rocks
	< 3-5% sulphide minerals, mainly Fe-sulphides. Arsenopyrite dominant in metasedimentary rocks, pyrite and pyrrhotite in meta-igneous rocks
	Limited vertical zonation, but strong lateral zonation of wall-rock alteration phases, involving addition of CO_2, S, K, H_2O, SiO_2, Na and LILE
	Larger deposits display overprinting with multiple veining events
Ore Geometry	Strong structural control, commonly complex
	Frequently situated in 2nd or 3rd order structures, proximal to large-scale compressional structures
Ore Fluid Chemistry	Low-salinity H_2O-CO_2 ± CH_4 ± N_2 fluids, Au transported as reduced S complex
	Au-Ag ± As ± B ± Bi ± Hg ± Sb ± Te ± W metal association
	Only marginally elevated Cu, Pb, Mo, Sn & Zn
	Suggest P-T conditions of 0.5-4.5 kbar and 220-600°C, most commonly 1.5 ± 0.5 kbar and 350 ± 50°C

Table 2.4: Typical characteristics of orogenic lode-gold deposits (after Groves et al., 2003).

gold deposits, reflecting the syn- to late-deformational timing of mineralisation and common spatial and temporal relationship with orogenesis (Groves et al., 1998; Goldfarb & Groves, 2015).

However, the designation of the broad term 'orogenic' to describe Neoarchaean gold deposits has been met with controversy and criticism (e.g., Sanislav et al., 2017), as it fundamentally implies that the deposits formed in collisional or accretionary convergent margin settings related to subduction (e.g., Goldfarb et al., 2001; Groves et al., 2003; Goldfarb & Groves 2015, Groves 2019). However, there are a growing number of examples of 'orogenic gold' deposits that exhibit many characteristic traits of an orogenic gold classification but are demonstrably not associated with compressional or transpressional deformation. For example, the gold deposits of the Dolgellau Gold Belt, North Wales were historically ascribed to the orogenic classification due to diagnostic characteristics, however vein analysis has revealed that these deposits in fact pre-date orogenesis and were formed during extension (Kokelaar, 1988; Platten & Dominy, 1999). The less contentious, historical phrase 'lode-gold' is used to avoid such generalisation and is employed in this thesis. Robert et al. (2007) further subdivided the 'orogenic' group into three sub-groups based on the host lithologies, including greenstone-hosted, BIF-hosted and turbidite-hosted deposits (Fig. 2.21). However, some studies have suggested the occurrence of additional deposit styles within Archaean terranes that exhibit some diagnostic characteristics but do not conform to the broad 'orogenic' clan (e.g., intrusion-related gold; Yardley & Cleverley, 2015; Wyman et al., 2016), underscoring the ambiguity in this classification.

The key characteristics of orogenic-lode gold deposits are summarised in Table 2.4. Orogenic lode-gold deposits are characteristically formed at depths of 5-10 km (Fig. 2.21) and thus are invariably associated with deformed metamorphic terranes exhibiting sub-greenschist to amphibolite and rarely, granulite, metamorphic facies (Goldfarb & Groves, 2015; Wyman et al., 2016). Gold mineralisation is typically associated with a network of quartz-carbonate veins containing Fe-bearing sulphides, often accompanied by sulphidation of Fe-rich host rocks (Groves et al., 2003). Hydrothermal fluids responsible for mineralisation generally consist of low-salinity (0.4-0.65 wt. % NaCl), aqueous, carbonic fluids, in which gold is suggested to be transported primarily as reduced sulphur complexes at temperatures >200 °C (Groves et al., 2003; Phillips & Evans, 2004; Garofalo et al., 2014). Orogenic lode-gold deposits are characteristically structurally controlled and are commonly located within and surrounding high-strain zones, including large crustal scale shear zones and associated second and third order structures, in generally low strain supracrustal successions (Groves & Foster, 1993; Goldfarb & Groves, 2015). Gold-bearing fluids are considered to have utilised these structures as migration pathways to mid-crustal levels, prior to gold and sulphide precipitation due to changes in the physicochemical conditions of the hydrothermal fluids at depositional sites (Goldfarb & Groves, 2015; Wyman et al., 2016).

Potential depositional mechanisms are varied and include temperature changes, fluid pressure fluctuations, boiling, changes in fluid chemistry (i.e., fO_2, pH), fluid-host rock reaction and fluid mixing (Groves et al., 2003, Garafalo et al., 2014; Gaboury, 2019). Changes in these parameters, commonly coincident and operating simultaneously, reduce the solubility and complexing ability of gold, and promote precipitation from hydrothermal fluids (Mikucki, 1998; Wyman et al., 2016; Goldfarb & Groves, 2015; Gaboury, 2019). The source(s) of hydrothermal fluids (and by association, gold) involved in the formation of orogenic gold deposits is contentious (e.g., Tomkins, 2013). Whereas most authors favour fluid derivation from metamorphic devolatilization (e.g., Groves et al., 1998; Phillips & Evans, 2004; Goldfarb & Groves, 2015; Gaboury, 2019), some researchers suggest that magmatic fluids were also involved in the formation of some deposits (e.g., Yardley & Cleverly, 2015).

2.6.2 Lode-Gold Mineralisation of the Yilgarn Craton

The Yilgarn Craton is recognised as one of the best endowed geological terranes of Earth, hosting a range of world class orogenic-lode gold deposits (e.g., Golden Mile, Sunrise Dam), komatiite-hosted nickel deposits (e.g., Kambalda camp) and BIF-hosted iron deposits (Koolyanobbing, Weld Range [Mole et al., 2015]). The distribution of these deposit types can broadly be grouped into 'camps' dominated by each deposit type, as shown in Figure 2.22. Although lode-gold mineralisation occurs in

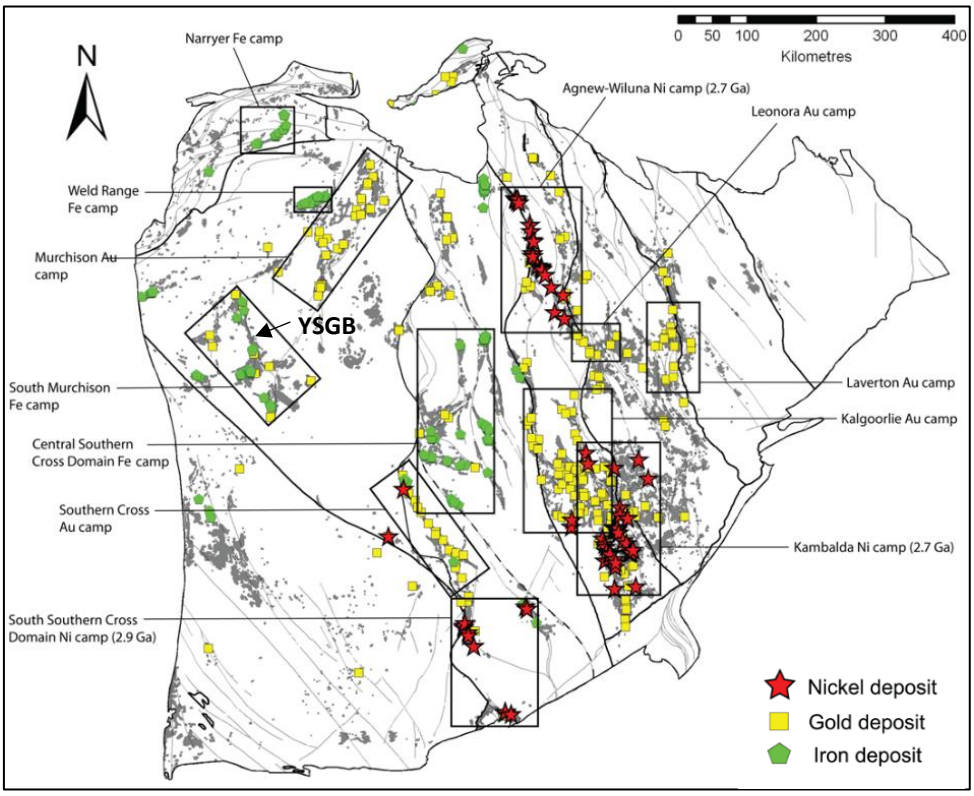

Figure 2.22: A metallogenic map of the Yilgarn Craton showing the distribution of lode-gold, komatiite-hosted nickel and BIF-hosted iron deposits. The locations of significant Au, Ni and Fe camps are outlined and labelled. The location of the Yalgoo-Singleton greenstone belt (YSGB) is also labelled. Modified after: Mole et al. (2015).

all constituent terranes of the Yilgarn Craton, a significant majority of lode-gold deposits are concentrated in the Eastern Goldfields Superterrane (Mole et al., 2015). In contrast, the western Yilgarn Craton is host to more prevalent iron deposits, predominantly BIF-related (Fig. 2.22).

Lode-gold mineralisation in the Yilgarn Craton commonly exhibits a characteristic, ubiquitous structural control (Phillips & Groves, 1983; Groves, 1998). Deposits are typically located on second or third order structures associated with large, crustal-scale shear zones, and are less commonly located on first-order structures (Groves et al., 2003). Lode-gold deposits can frequently be correlated with variations in structural parameters, such as fault perturbations (changes in dip and/or strike), restrictional bends, dilational jogs and fault intersections, which acted to increase the extent of fluid flow and facilitate the precipitation of sulphide and gold mineralisation (Tripp & Vearncombe, 2004). The crucial function of unconformably lying, late clastic successions upon the spatial and temporal distribution of lode-gold mineralisation in the Eastern Goldfields has been recognised by Tripp (2019), providing further criteria for future exploration in the region.

Geochronological analysis of accessory phases cogenetic with gold mineralisation (i.e., titanite, monazite, apatite, rutile, xenotime, zircon, molybdenite, sericite) at deposits across the Yilgarn Craton (although principally in the EGS) indicate a major period of lode-gold mineralisation between ~2665

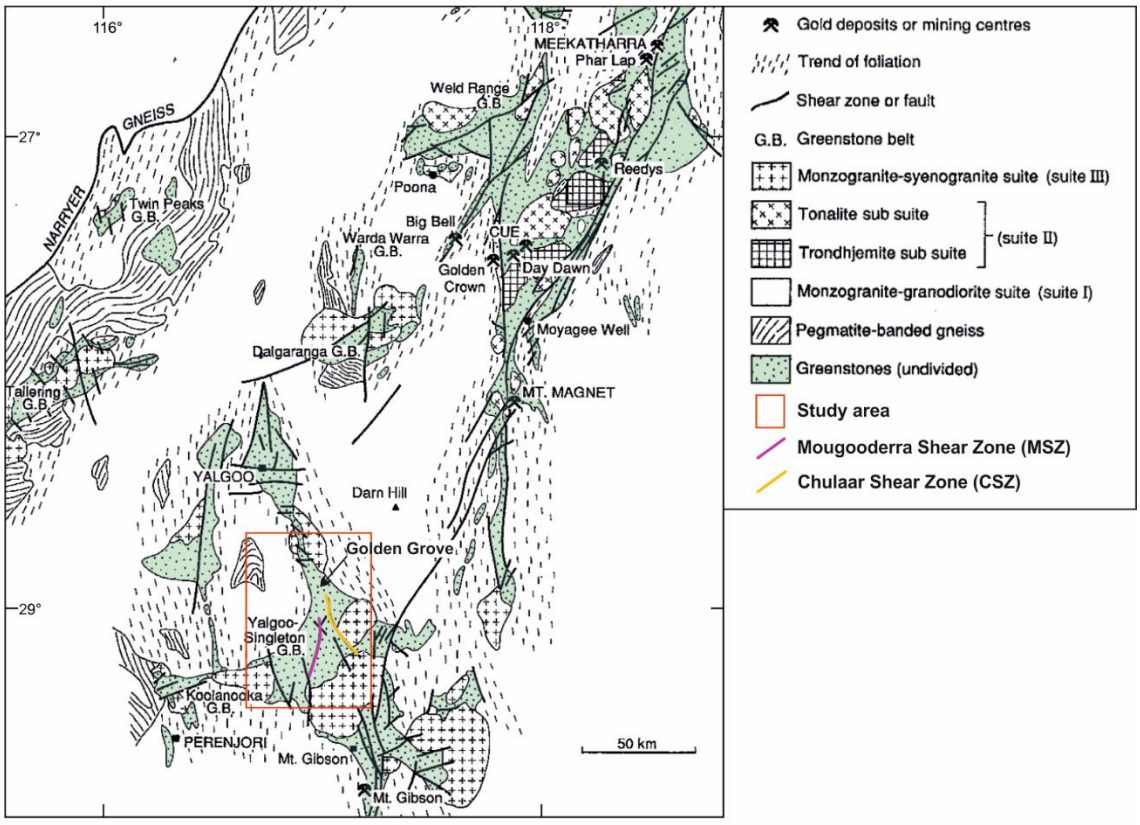

Figure 2.23: Simplified geological map of the Murchison Domain, showing the location of greenstone belts and major gold mining centres. Geology corresponds to the superceded nomenclature of Watkins & Hickman (1990). The location of the study area is outlined in red and the Mougooderra Shear Zone and Chulaar Shear Zone are shown in pink and orange, respectively. Redrawn after Wang et al. (1993) and Watkins & Hickman (1990).

Ma and ~2620 Ma (Robert et al., 2005). This is considered by some to represent multiple Yilgarn-wide mineralising events over a protracted ~45 m.y. period, possibly encompassing the formation of lode-gold deposits in successive structural settings, including early thrusting, extension and basin formation, and compression (e.g., Bateman & Hagemann, 2004; Robert et al., 2005; Czarnota et al., 2010). The identification of multiple, separate gold mineralisation events at coincident locations in the north Kalgoorlie district indicates that structures controlling early fluid flow may have been the focus of later syn-orogenic fluid flow, resulting in overprinting lode-gold mineralisation (Tripp, 2019). Others contend that lode-gold mineralisation was inextricably linked to tectonic evolution, exhibits consistent relative structural and metamorphic timing and was diachronous across the terranes of the Yilgarn Craton (Groves et al., 1993, Vielreicher et al., 2015; Wyman et al., 2016). As such, gold mineralisation is considered to have occurred over durations of less than a few million years in individual terranes, varying from ~2650 Ga in the Kurnalpi Terrane, to ~2630-2640 Ma in the Kalgoorlie Terrane (Vielreicher et al., 2015).

2.6.3 Gold Mineralisation of the YSGB, Murchison Domain

With regard to both frequency and size of lode-gold deposits, the Murchison Domain is significantly less endowed than the EGS and within the Murchison Domain, the YSGB in the southwest is host to markedly less discovered lode-gold mineralisation than the Meekatharra-Cue region in the northeast (Fig. 2.23). The historical contrast in gold endowment across the Murchison Domain is illustrated by Watkins & Hickman (1990), who calculated the pre-1990 productivity of the northeast to be 31 kg/km^2, in contrast to just 1.7 kg/km^2 in the southwest. However, the relative dearth of gold resources in the southwest may be a function of the extensive transported cover, minimal (<5%) outcrop, deep weathering profile and difficult exploration conditions present (Watkins & Hickman, 1990). Many lode-gold deposits in the western Yilgarn Craton are located within 3 km of granitoids, demonstrating an apparent spatial, but not necessarily genetic, relationship between lode-gold mineralisation and granitoids (Watkins & Hickman, 1990).

In the Murchison Domain, lode-gold mineralisation has been dated at 2639 ± 4 Ma at the Reedy mining centre, south of Meekatharra (Fig. 2.23), using the Pb-Pb isochron method on titanite and pyrite (Wang et al., 1993). At the Big Bell mining centre to the west of Cue (Fig. 2.23), gold-sulphide-scheelite mineralisation is dated at 2662 ± 5 Ma, from U-Pb analysis of almandine garnet from a low-grade contact skarn (Mueller et al., 1996). At Mount Gibson, to the south of the YSGB (Fig. 2.23), SHRIMP U-Pb dating of hydrothermal zircons directly associated with lode-gold mineralisation have been dated at 2627 ± 13 Ma at (Yeats et al., 1996). These data suggest that lode-gold mineralisation in the Murchison Domain was emplaced from ~2660-2630 Ma, coinciding with the 2665-2620 Ma ages of

lode-gold mineralisation from across the Yilgarn Craton (Bateman & Hagemann, 2004). The study area for this project, the central YSGB, contains the following four types of auriferous mineralisation.

1. Firstly, a total of 22 separate pits containing lode-gold mineralisation have been mined to date in the study area, a significant majority of which are situated along the Mougooderra Shear Zone (Fig. 2.23) (Thomas, 2003). These deposits are currently being mined by Minjar Gold as part of the Golden Dragon operations and are the principal focus of this study. As of 2012, the Golden Dragon project possessed a total gold resource in excess of 990 koz (thousand troy ounces) (Minjar, 2012). Lode-gold deposits are typically hosted by Fe-rich lithologies, such as BIF, ultramafic rocks and granophyric, magnetite-bearing dolerite (Minjar, 2012). Thomas (2003) proposed that two fundamental gold depositional mechanisms were active at the Winddine Well gold deposit in the YSGB, namely phase separation and wall-rock interaction. The style, paragenesis and age of lode-gold mineralisation in the YSGB is poorly understood.

2. The second style of gold mineralisation is the W-Mo-Au system associated with the Mt. Mulgine Granite (Rothsay Suite; Section 2.3.2) in the south of the study area. Archaean intrusion-related Au-Mo-W mineralised systems in the Yilgarn Craton are typically small in size (<10 t Au) and are both temporally and spatially associated with felsic intrusions (Duuring et al., 2007). At Mt Mulgine, W-Mo-Bi-Ag-Cu-Au mineralisation (containing ~5 t Au) is spatially associated with the fractionated, I-type Mt Mulgine syenogranite, which intruded the supracrustal sequence during peak-amphibolite facies metamorphism and is dated at 2767 ± 10 Ma, using SHRIMP U-Pb zircon dating (Oliver, 1999; Duuring et al., 2007). Molybdenite and scheelite occur as part of quartz-pyrite-fluorite stockwork veining in greisen alteration zones in the syenite, and disseminated in surrounding supracrustal rocks, whereas gold is largely hosted by shear zones west of the Mt Mulgine granite (Oliver, 1999). It is suggested that intrusion-related Mo-W mineralisation may have been overprinted by orogenic-lode gold Au ± W mineralisation (Duuring et al., 2007).

3. World class, syngenetic Cu-Zn-Au VHMS deposits are located in the study area at the Golden Grove mining centre and comprise the Scuddles and Gossan Hill deposits from which gold and silver are extracted as biproducts (Sharpe & Gemmell, 2001).

4. Anomalous gold content has been identified in conglomerate units within the Mougooderra Fm exposed in the YSGB. These gold anomalies are not clearly spatially associated with structures and have been interpreted as Archaean placers, derived from erosion of early syngenetic (VHMS) and potentially epigenetic (lode-gold) mineralisation in the area (Watkins & Hickman, 1990). As both the age of the Mougooderra Fm and lode-gold mineralisation in the YSGB are poorly constrained, the source of gold within conglomeratic units remains unclear.

CHAPTER 3

Field relations, stratigraphy and structure of the Rothsay mining area

3.1 Introduction

Archaean greenstone belts in the Yilgarn Craton, Western Australia, occur primarily as north-south trending linear features, broadly parallel with craton-scale transpressional shear zones (Gee et al., 1981; Swager et al., 1990; Fig. 1.3). However, strong linear patterns are not as prevalent in supracrustal belts in the far west of the craton. Instead, granite-greenstone contacts in the southwestern Murchison Domain display dome and keel patterns that closely resemble the archetypal patterns of the eastern Pilbara Craton (Van Kranendonk et al. 2004). These patterns and associated folding within greenstone belts have been explained in terms of superposition of upright, orthogonal folds (Myers & Watkins, 1985; Watkins & Hickman, 1990) and more recently by diapiric emplacement of granitic domes (Zibra et al., 2018; Clos et al., 2019a).

The greenstone stratigraphy comprising the supracrustal belts in the western Yilgarn Craton is also distinct from greenstone belts across the central and eastern parts of the craton. Rocks in the southwestern Murchison Domain constitute many of the oldest basement rocks (c. 2.95 Ga; Ivanic, 2019), some of the oldest metasedimentary successions (Van Kranendonk et al., 2013) and an array of mafic-ultramafic intrusions, including some of the largest on Earth (Ivanic et al., 2010; Ivanic, 2019). Despite these claims, the area has not historically received much scientific study, although in recent years, the northeastern Murchison Domain has been the focus of increased research. As such, large sections of greenstone belts in the southwest Murchison Domain remain unstudied and unmapped, other than on a regional scale.

This chapter will investigate the lithological and structural development of the Rothsay mining area, a portion of supracrustal rocks located in the southwest Yalgoo-Singleton Greenstone Belt (YSGB), southwestern Murchison Domain. Rocks in the area are better exposed than much of the rest of the belt and wider domain and are host to the historical Rothsay gold mine, in addition to multiple gold

prospects. Regional mapping (Baxter & Lipple, 1985) has indicated that the Rothsay area contains a complex fold structure, multiple shear zones and encompasses a relatively well exposed section through most of the supracrustal stratigraphy that comprises the greenstone belt. This chapter presents detailed, 1:5,000 scale lithological and structural geological mapping of a >130 km^2 area, accompanied by descriptions of lithological units, contact relations and structural measurements and observations. This comprehensive study of a well-exposed portion of the YSGB forms a geological framework for subsequent chapters in this thesis.

Following an overview of the area and the mapping techniques used, two 1:25,000 scale maps are presented, accompanied by three cross sections and a stratigraphic column. The supracrustal stratigraphy that comprises the Rothsay area is described and assigned to rock units for the first time. This is followed by a description of the intrusions in the area and an assessment of contact relations between supracrustal and intrusive units. The structural features of the Rothsay area are then described, followed by a brief comparison to structures elsewhere in the greenstone belt, to provide a more regional context. In the subsequent discussion, the emplacement of supracrustal and intrusive rocks is considered, and the structural deformation of the area is discussed. The research questions that form the basis of this chapter are as follows:

1. What is the relationship between supracrustal rocks and intrusive rocks in the Rothsay area and what does this indicate about the stratigraphic development of the belt?
2. What is the structural & deformational history of the area? Can the complex fold structure at Rothsay be explained in terms of fold superposition or granitic diapirism?
3. Is there evidence for structural repetition and early sub-horizontal deformation as recorded in other supracrustal belts in the Yilgarn Craton?

3.2 Overview of Rothsay Mapping Area

3.2.1 Location

The Rothsay Fold is located in the southwest portion of the YSGB, Murchison Domain. It contains the deserted historical mining settlement of Rothsay, situated 62 km northeast of Perenjori and 80 km west of Paynes Find (Fig. 3.1). The mapping area measures 14.2 km by 13.8 km and covers a total area of ~133 km^2, restricted to exploration and mining tenements held by Minjar Gold Pty and Egan Street Resources during the course of study. The land can be accessed from a number of exploration tracks

adjoining the Warriedar-Coppermine Road (Fig. 3.1), however, most tracks in the area are highly vegetated and inaccessible.

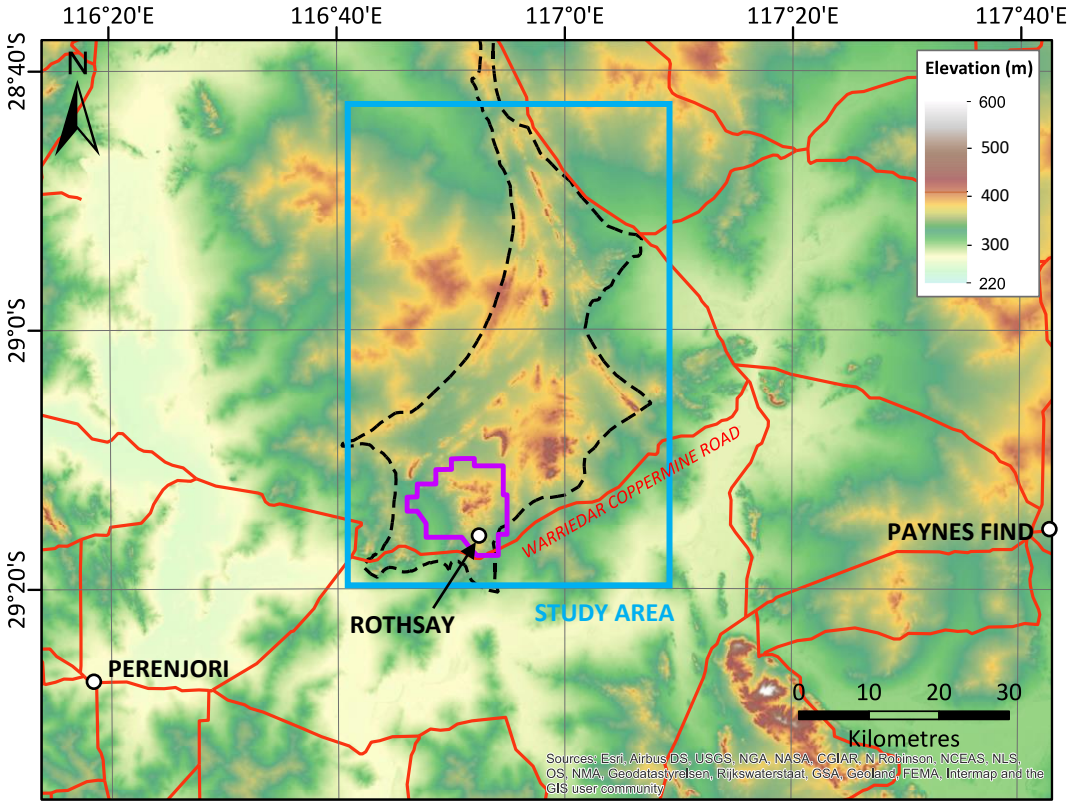

Figure 3.1: Topographic map of the southwestern Murchison Domain showing the location of the Rothsay mapping area (purple) relative to study area of this project (blue), nearby roads (red) and settlements. An outline of the central Yalgoo-Singleton greenstone belt is shown by the black dashed line. Basemap courtesy of ESRI.

3.2.2 Physiography

The topography of the area is largely flat with numerous gently sloping hills, varying in elevation from 290 m to 460 m above sea level (Fig. 3.1). Vegetation is dominated by mulga (acacia) bushes and eucalyptus trees. As is the case across the Murchison Domain, much of the bedrock is blanketed by superficial cover. During the Oligocene-Miocene, the Yilgarn Craton was subjected to tropical conditions, leading to the development of a deeply weathered lateritic layer overlying saprolite (Butt, 1981). Rock is now exposed either in watercourses that have dissected laterite and underlying saprolite, or in elevated areas that were originally above the duricrust laterite (Watkins and Hickman, 1990). Rock exposure is approximately 10% (outcrop + subcrop = 23 %), concentrated in the central part of the Rothsay mapping area and greater than that found elsewhere in the region (< 5 %). Supracrustal rocks, primarily basalts, form elongate, undulating hills, whereas prominent ridges typically consist of banded iron formations and other ferruginous metasedimentary rocks.

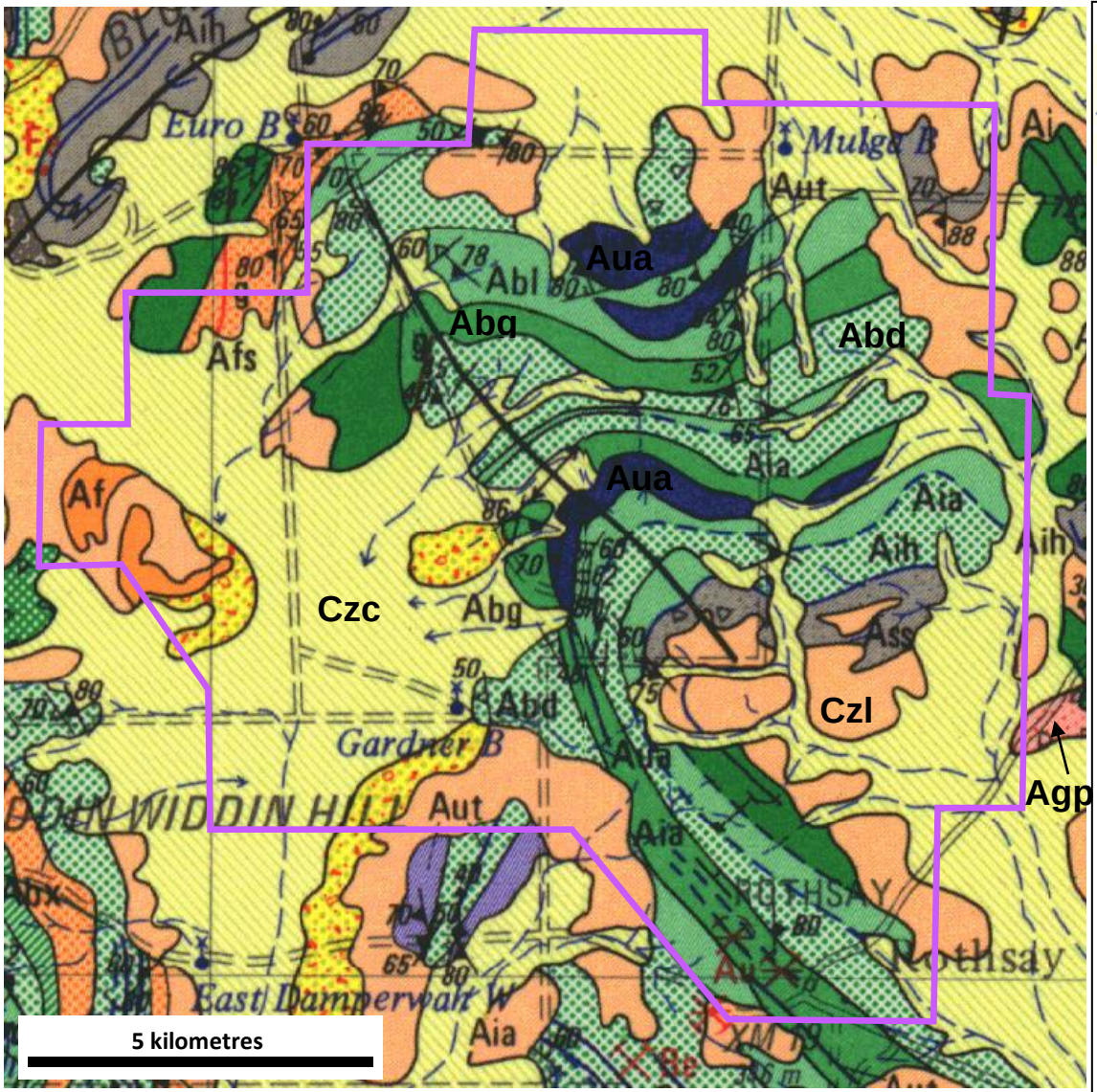

MAP SYMBOLS

- Track
- Watercourse
- Antiform fold axis, showing plunge
- Inclined bedding
- Inclined foliation (igneous rocks)
- Inclined foliation (metamorphic rocks)
- Field area (this study)

SUPERFICIAL ROCKS

- Czc — Alluvial and colluvial deposits, transported clay, sand,
- Czg — Lateritic gravel and sand
- Czl — Laterite

SUPRACRUSTAL

- Af — Felsic volcaniclastic rocks
- Afs — Unassigned felsic volcaniclastic and sedimentary rocks
- Ass — Semi-pelitic rocks, volcanogenic component present
- Asp — Pelitic quartz-sericite-kaolin rocks, siltstone, phyllite and schist.
- Aia — Magnetite-amphibole-quartz banded iron formation
- Aih — Hematite-magnetite-quartz banded iron formation
- Abl — Basalt – includes massive, variolitic, vesicular and pillowed
- Abd — Dolerite - fine-medium grained, some ultramafic differentiates
- Abg — Gabbro – medium-coarse grained, some ultramafic differentiates
- Aba — Amphibolite – developed in zones of high strain
- Aut — Talc schist, minor chlorite and amphibole
- Aua — Amphibole-chlorite-talc rocks, some serpentine/peridotite

INTRUSIVE ROCKS

- Agp — Granite-adamellite, porphyritic
- g — Granitoid vein

Figure 3.2: Geological map of the Rothsay Fold area at 1:250,000 scale, extracted from the GSWA Perenjori Map Sheet (Baxter & Lipple, 1985). The mapping area is outlined in purple.

3.2.3 Previous Work

All previously published geological work in the Rothsay area is that of Geological Survey of Western Australia (GSWA) geologists, who have worked in the region a number of times over the last century. Clarke (1925) first documented the geology of rocks hosting mineralisation at the Rothsay mining centre, with simple geological mapping undertaken around the peripheries of the mine. Baxter and Lipple (1985) mapped the area to a 1:250,000 scale as part of regional-scale reconnaissance mapping, which remains the only published geological map of the Rothsay area to date (Fig. 3.2). This work was summarised by Watkins & Hickman (1990) as part of a synthesis of the geological evolution of the Murchison Domain, including some limited geochemical sampling in the mapping area. Since 2005, the GSWA have been undertaking a regional 1:100,000 scale mapping program of the Murchison Domain, and have remapped areas including much of the YSGB (Ivanic, 2018; Ivanic et al., 2015a; Zibra et al., 2017a, 2016). However, the Rothsay area is yet to be remapped as part of this program. The undergraduate theses of Price (2014) and Wickham (2014) included some 1:5,000 scale geological mapping in the northwestern part of the Rothsay mapping area, carried out in collaboration with Minjar Gold Pty. The areas covered have been revisited and reinterpreted as part of this study.

3.2.4 Geological Overview

The geology of the Rothsay area consists of a typical Archaean supracrustal greenstone succession, comprising metavolcanic and metasedimentary rocks, intruded by a network of mafic-ultramafic layered sills (Fig. 3.2). A large 50 x 25 km granite, known as the Seeligson Monzogranite (Zibra et al., 2018), has intruded the succession in the southeast and supracrustal units typically dip away from granitoid contacts. The volcano-sedimentary stratigraphy has been deformed into an antiformal, ~12 km wavelength fold structure, referred to herein as the Rothsay Fold. The Rothsay Fold has a northwest-plunging fold axis and a broadly upright axial plane, which separates a northeast limb from a southwest limb. In the south of the mapping area, a high-strain, north-northwest trending shear zone is host to historically-exploited lode-gold mineralisation at Rothsay. A significant unconformity has been identified within the volcanosedimentary succession that forms the YSGB, at the base of the metasedimentary-dominated Mougooderra Formation (Fm) (Watkins & Hickman, 1990). Recent regional-scale geological reinterpretations have suggested the southwest part of the YSGB (within the Rothsay mapping area) contains an unconformable contact within the greenstone succession (e.g., Ivanic, 2019), however, it is unclear whether this represents the unconformity at the base of the Mougooderra Fm.

Felsic intrusive rocks

Walganna Suite[2]	Seeligson Monzogranite[2]	Biotite monzogranite, K-feldspar-quartz-biotite-muscovite-(Li-B) pegmatites

Mafic-ultramafic intrusive rocks

Warriedar Suite[1]	Damperwah Sill	Dolerite, gabbro, quartz diorite
	Gardner Sill	Peridotite, gabbro, dolerite, diorite
	Rothsay Sill	Peridotite, pyroxenite, gabbro, dolerite
	Mountain View Sill	Dolerite, gabbro, pyroxenite, quartz diorite, 'Honeycomb Gabbro'

Supracrustal rocks

?	Willowbank Clastics	Mudstone, greywacke, pebbly sandstone, felsic volcaniclastic rocks, conglomerate
Chulaar Group	Mulga Volcanics	Variolitic basalt, spinifex-textured basalt, BIF, lapilli tuff
	Beryl West Volcanics	Basalt, spinifex-textured basalt
	Two Peaks Volcanics	Basalt, porphyritic dacite, BIF
	Macs Well Clastics	Quartzite, ferruginous siltstone, BIF, felsic volcaniclastic rocks

Table 3.1: Stratigraphic nomenclature used in this study, for felsic intrusive rocks, mafic-ultramafic intrusive rocks and supracrustal rocks in the Rothsay area. The key lithologies in each unit are also outlined. [1] after Ivanic (2019); [2] after Zibra et al. (2018).

3.2.5 Nomenclature

The geology of the Rothsay area has only previously been mapped at 1:250,000 scale and ongoing GSWA geological mapping in the region is incomplete, therefore a largely informal stratigraphy is used in this study and summarised in Table 3.1. Lithological units have been grouped into assemblages based on lithological associations, field relations and distinctive macroscopic and microscopic features. Five supracrustal assemblages have been distinguished and broadly correspond with formations in a formal stratigraphy. The lower four such assemblages have been assigned to the informal Chulaar Group, whereas the uppermost assemblage has been ascribed to the informal Willowbank Clastics. Mafic-ultramafic intrusive rocks have been divided into four mafic-ultramafic layered sills and collectively assigned to the Warriedar Suite, recently defined in the central YSGB by Ivanic (2019). The only significant felsic intrusion in the area has previously been classified as the Seeligson Monzogranite of the regional Walganna Suite by Zibra et al. (2018).

The informal names ascribed to supracrustal assemblages and intrusive sills are mainly given after the names of local historical bores and wells, as well as former gold exploration targets. Several names are assigned after distinctive features exhibited by some units. Almost all rocks in the study area have been subjected to low-medium grade regional metamorphism. Where the protolith of a rock has been clearly identified, igneous or sedimentary nomenclature is used and the prefix meta- omitted. In rare instances where protoliths cannot be easily distinguished, metamorphic nomenclature is used.

3.3 Geological Mapping

3.3.1 Mapping Methods

Geological mapping was undertaken during two field seasons in July-September 2017 and July-September 2018, over a total of approximately eight weeks. The field area is divided into a total of sixteen map sheets (Fig. 3.3), which have each been mapped at 1:5000 scale. Map sheets 6, 8 and 10 have been remapped after Price (2014). Map sheets 1-5 have been remapped after Wickham (2014), using a combination of original field observations and new field observations and descriptions made at revisited localities. All field observations are assigned locality numbers, which consist of a prefix referring to the sheet number, followed by the locality number within the given sheet (e.g., loc. 8.104; locality 104 on map sheet 8). During geological mapping, the following classification was used relative to the degree of certainty that a rock was representative of the bedrock:

- **Outcrop** – rock in situ and part of the bedrock (Fig. 3.4a).
- **Subcrop** – dense boulders/blocks not in situ but considered to represent bedrock (Fig. 3.4b).
- **Float** – scattered clasts lying on superficial cover, which are less confidently representative of underlying bedrock (Fig. 3.4c). Float can be described as dense (>1 clast/m^2) or sparse (<1 clast/m^2).

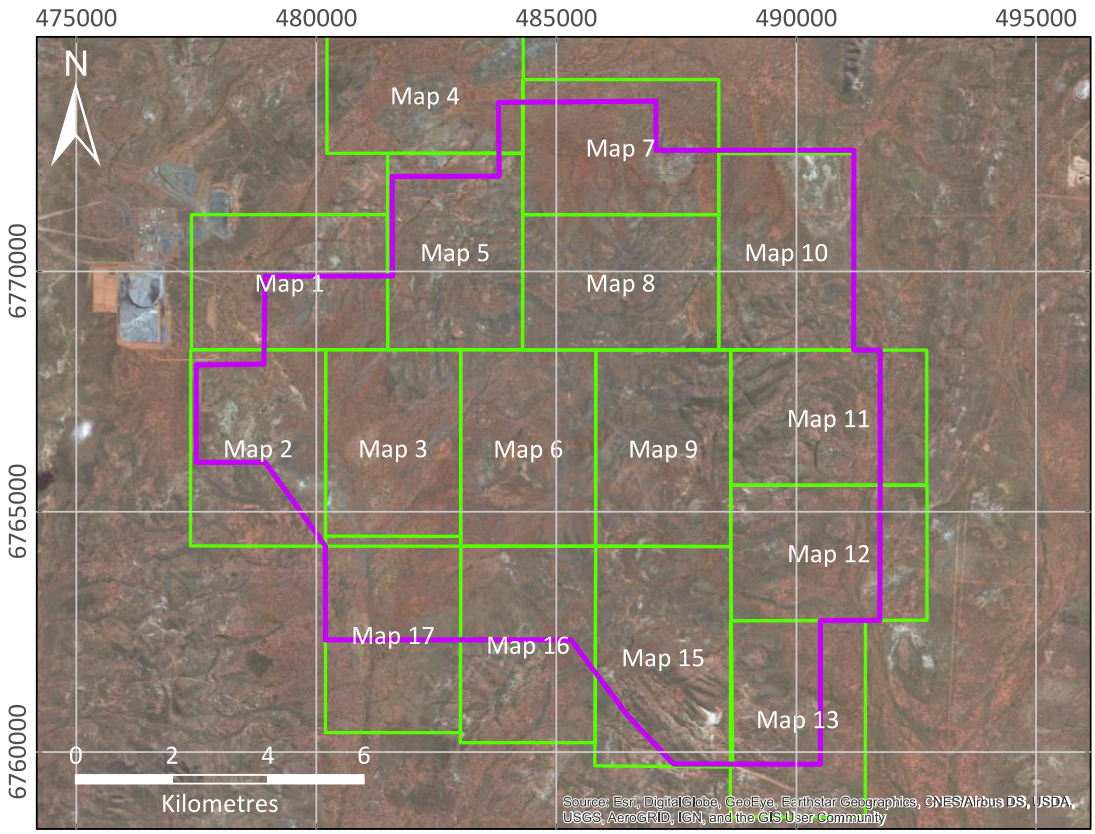

Figure 3.3: Aerial satellite imagery of the Rothsay mapping area (pink) showing the locations of map sheets used during geological mapping, and the prefix used for field localities. Aerial imagery courtesy of ESRI.

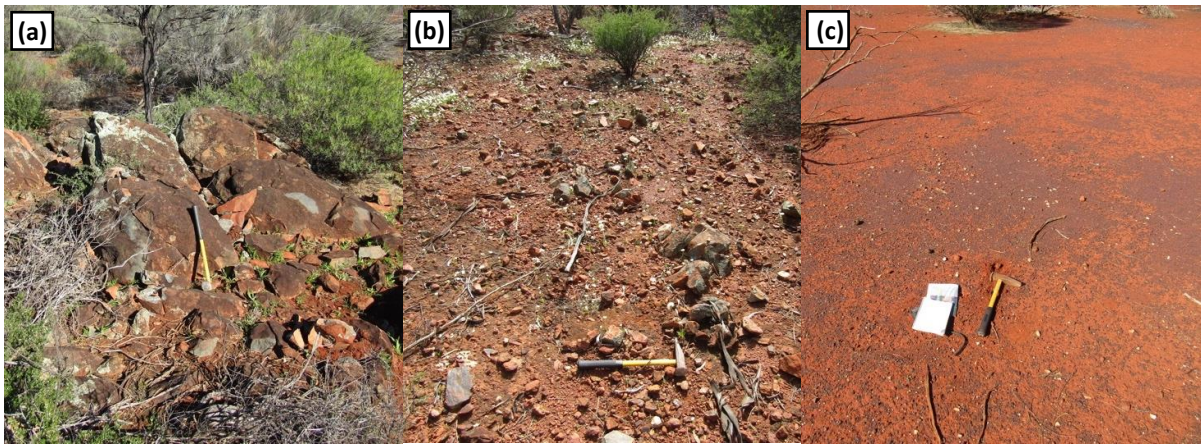

Figure 3.4: Field photographs showing the classification of rock exposure used during geological mapping with hammer for scale: **(a)** outcrop at locality 15.028; **(b)** subcrop at locality 16.032; **(c)** float at locality 17.006.

In areas of little to no outcrop, a series of traverses were undertaken, typically perpendicular to the predicted strike of units. Float mapping was assisted by the recording of changes in vegetation and regolith, which proved to be very useful. In areas of better subcrop/outcrop, traverses were less systematic and important contacts were followed. Aeromagnetic imagery was utilised for correlation of magnetic units, primarily BIF, serpentinised ultramafic units and dolerite dykes.

3.3.2 Mapping Data

A spreadsheet compiling all mapping observations and structural measurements collected in the Rothsay area can be found in **Appendix E1**. Two 1:25,000 scale geological maps of the Rothsay mining area accompany this study and can be found in **Appendix A**: I) a 1:25,000 scale surface bedrock geological map based on 1:5,000 scale geological mapping and field observations in areas of outcrop/subcrop and II) a 1:25,000 scale interpreted bedrock geological map, constructed using a combination of outcrop mapping, float mapping, changes in regolith and vegetation, aerial imagery and aeromagnetic imagery.

A simplified interpreted geological map of bedrock in the Rothsay area is displayed in Figure 3.5 and shows the extent of stratigraphic units denoted in this study. Three 1:25,000 scale cross sections have been drawn along the fence lines A-B-C (Fig. 3.6), D-E-F (Fig. 3.7) and G-H (Fig. 3.8) represented on the interpreted bedrock map in **Appendix A**, in order to illustrate the interpreted sub-surface geology. Furthermore, a 1:20,000 scale stratigraphic column constructed from the exposed stratigraphy is displayed in Figure 3.9.

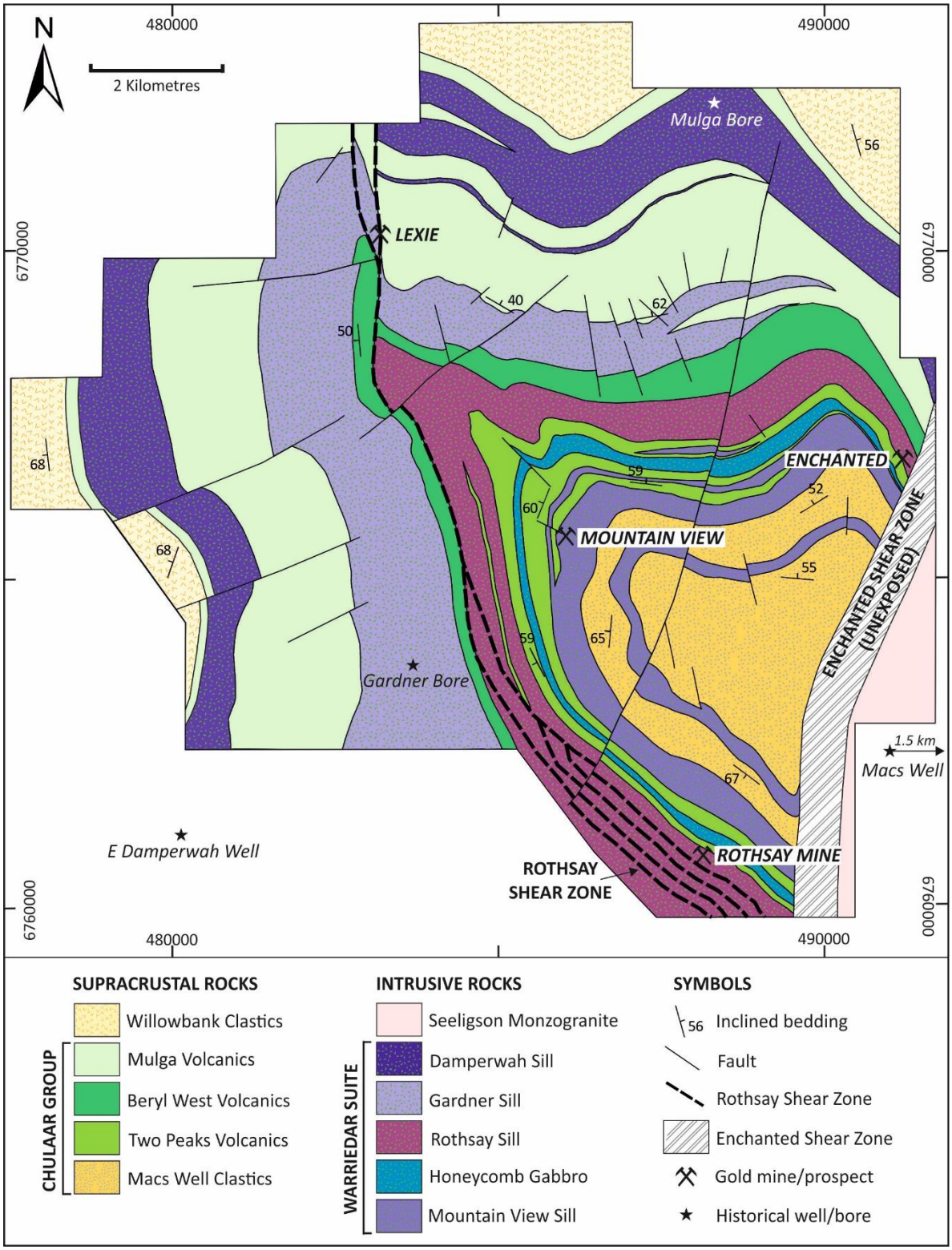

Figure 3.5: Simplified geological map of the Rothsay area showing the supracrustal units and intrusive rocks described in this study, in addition to major structures, representative bedding measurements, notable gold mines and prospects and historical wells/bores.

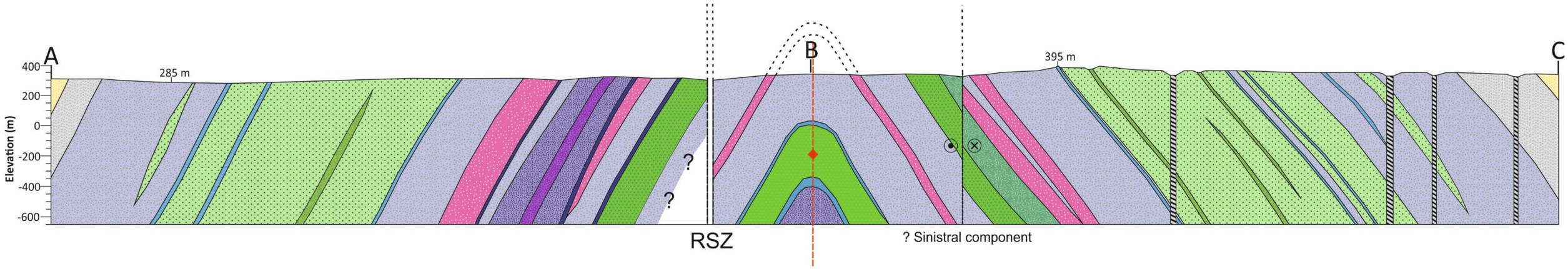

Figure 3.6: Cross section along the fence line A-B-C, drawn at 1:25,000 scale with no vertical exaggeration. RSZ = Rothsay Shear Zone. The highest and lowest topographic points along the section are labelled.

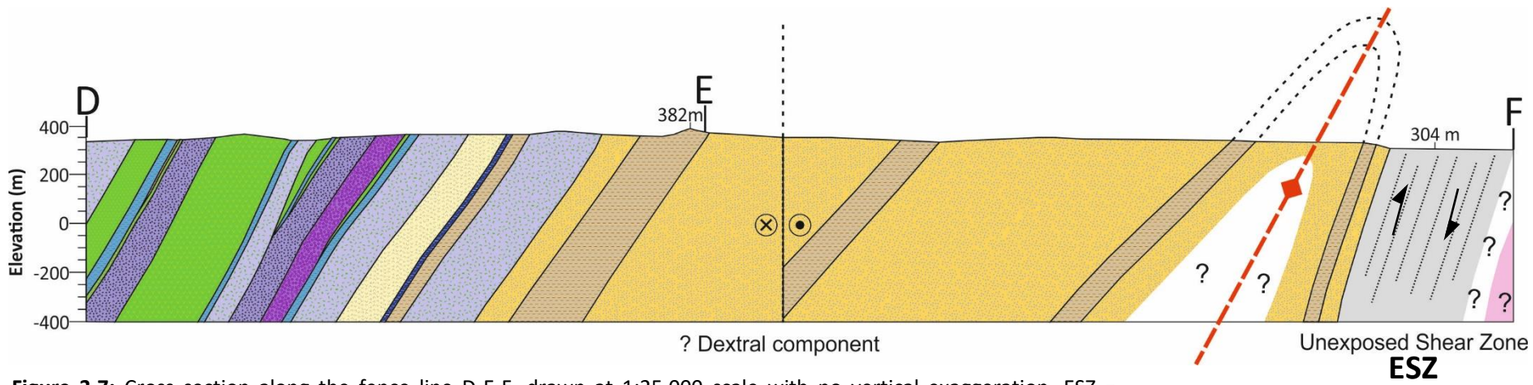

Figure 3.7: Cross section along the fence line D-E-F, drawn at 1:25,000 scale with no vertical exaggeration. ESZ = Enchanted Shear Zone. The highest and lowest topographic points along the section are labelled.

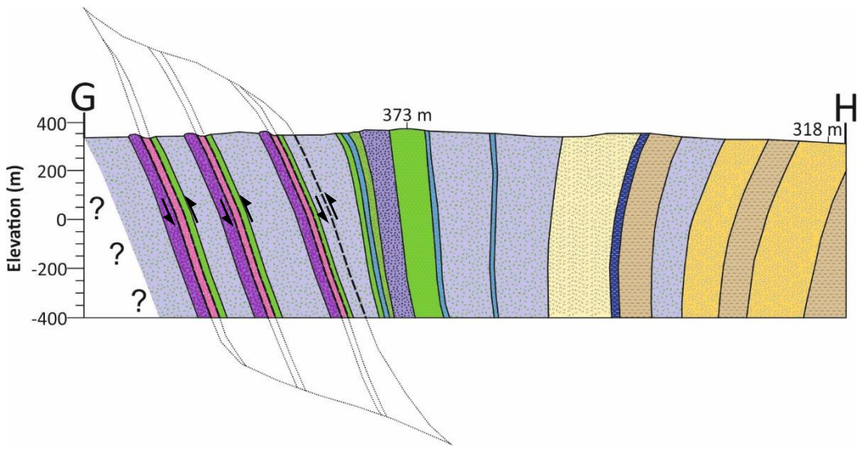

Figure 3.8: Cross section along the fence line G-H, drawn at 1:25,000 scale with no vertical exaggeration. The highest and lowest topographic points along the section are labelled.

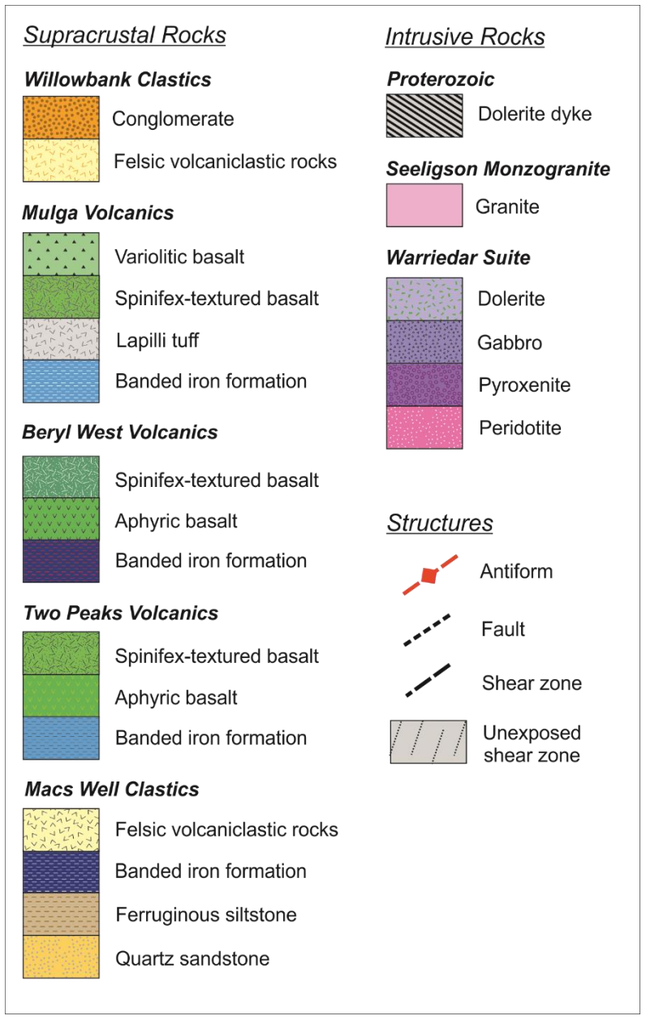

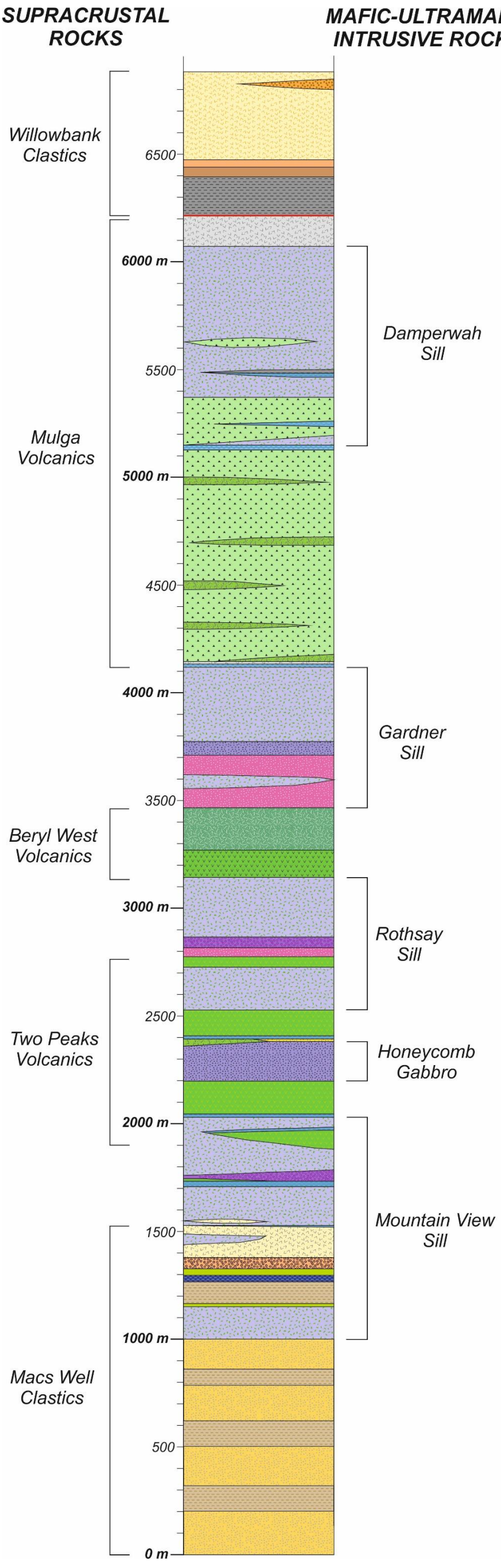

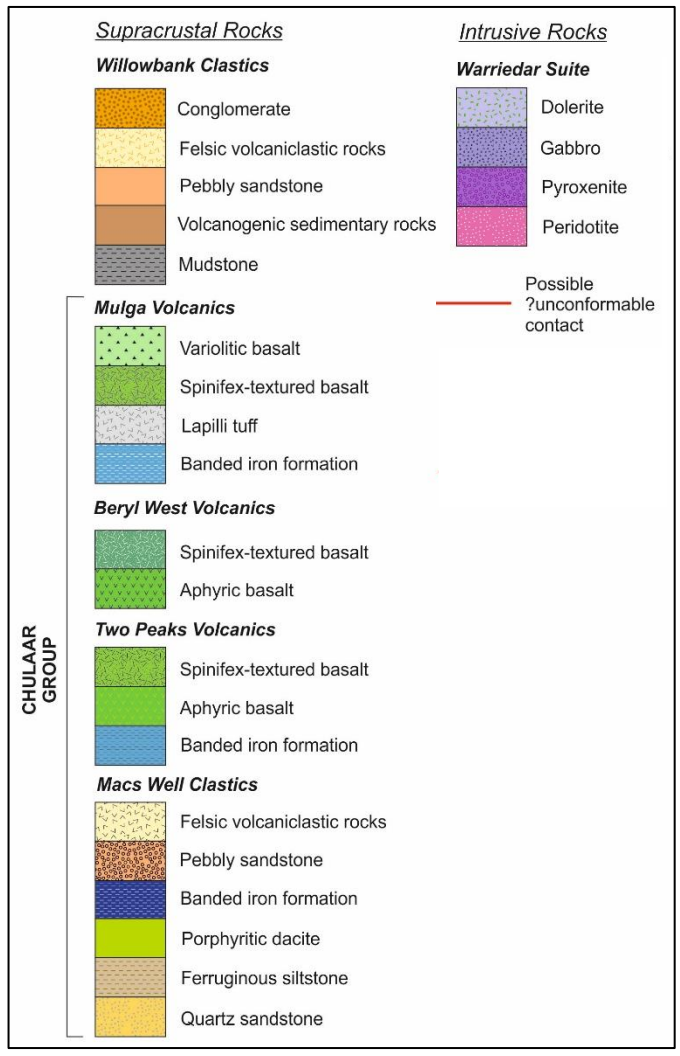

Figure 3.9: Stratigraphic column for rocks in the Rothsay area, drawn at a scale of 1:20,000 (1 mm = 20 m). The names ascribed to groups of supracrustal rocks and mafic-ultramafic intrusive rocks are shown on the left and right sides of the column, respectively. Note the different scale used here compared to accompanying 1:25,000 scale geological maps and cross sections – used in this instance to better show thin (<10 m) units. The red line denotes a potential unconformable/disconformable contact at the base of the Willowbank Clastics, which does not outcrop in the study area but is observed elsewhere in the Yalgoo-Singleton belt. The stratigraphic column has been drawn the right way-up according to multiple way-up criteria presented in section 3.5.2. Most of the stratigraphic column (all units underlying and including the Damperwah Sill) has been constructed based on a N-S transect across the northeast limb of the Rothsay Fold. The uppermost part of the column comprising the upper Mulga Volcanics and overlying Willowbank Clastics was constructed using a transect in the far western part of the field area, due to a lack of exposure elsewhere, with the exception of laterally discontinuous conglomeratic units, which were added based on units outcropping in the far northeast. The stratigraphic column has been drawn according to the true thicknesses of units, which have been calculated using apparent thicknesses from geological mapping and the average dip measurements of bedding in metasedimentary units and the layer-parallel foliation in metaigneous units along the transects described above. Features such as lenses within layered sills and units that pinch out along strike are represented on the column and the broad direction in which they pinch out has been included, with the right-hand side of the column broadly corresponding to the northeast and the left hand-side broadly corresponding to the southwest.

3.4 Stratigraphy

In this section, the supracrustal rocks and mafic-ultramafic intrusions present in the Rothsay area are described and contact relations outlined, starting at the base of the succession according to the stratigraphic column (Fig. 3.9) and stratigraphic map (Fig. 3.5). Way-up criteria supporting the described younging direction of the supracrustal succession are presented in Section 3.5.2 and include graded bedding, spinifex branching and igneous differentiation. Detailed petrography of units described in this section is presented in Chapter 5.

Figure 3.10: Photographs of rocks comprising the lower Macs Well Clastics. **(a)** Non-magnetic, fine grained ferruginous siltstone, with bedding evident (loc. 12.030); **(b)** Finely bedded ferruginous siltstone, magnetite and minor 1-2 mm quartzite bands (loc. 12.051a); **(c)** Interbedded ferruginous siltstone and 1-3 cm quartzite beds (loc. 12.019); **(d)** Typical exposure of ferruginous siltstone as a low lying ridge, facing west (loc. 12.068); **(e)** Banded unit of grey fine-grained quartzite and cream medium-grained quartzite (loc. 12.008); **(f)** Contrasting wildflower abundance on Fe-rich ferruginous siltstone (left; loc. 13.046) and Fe-poor quartzite-dominated units (right; loc. 12.040).

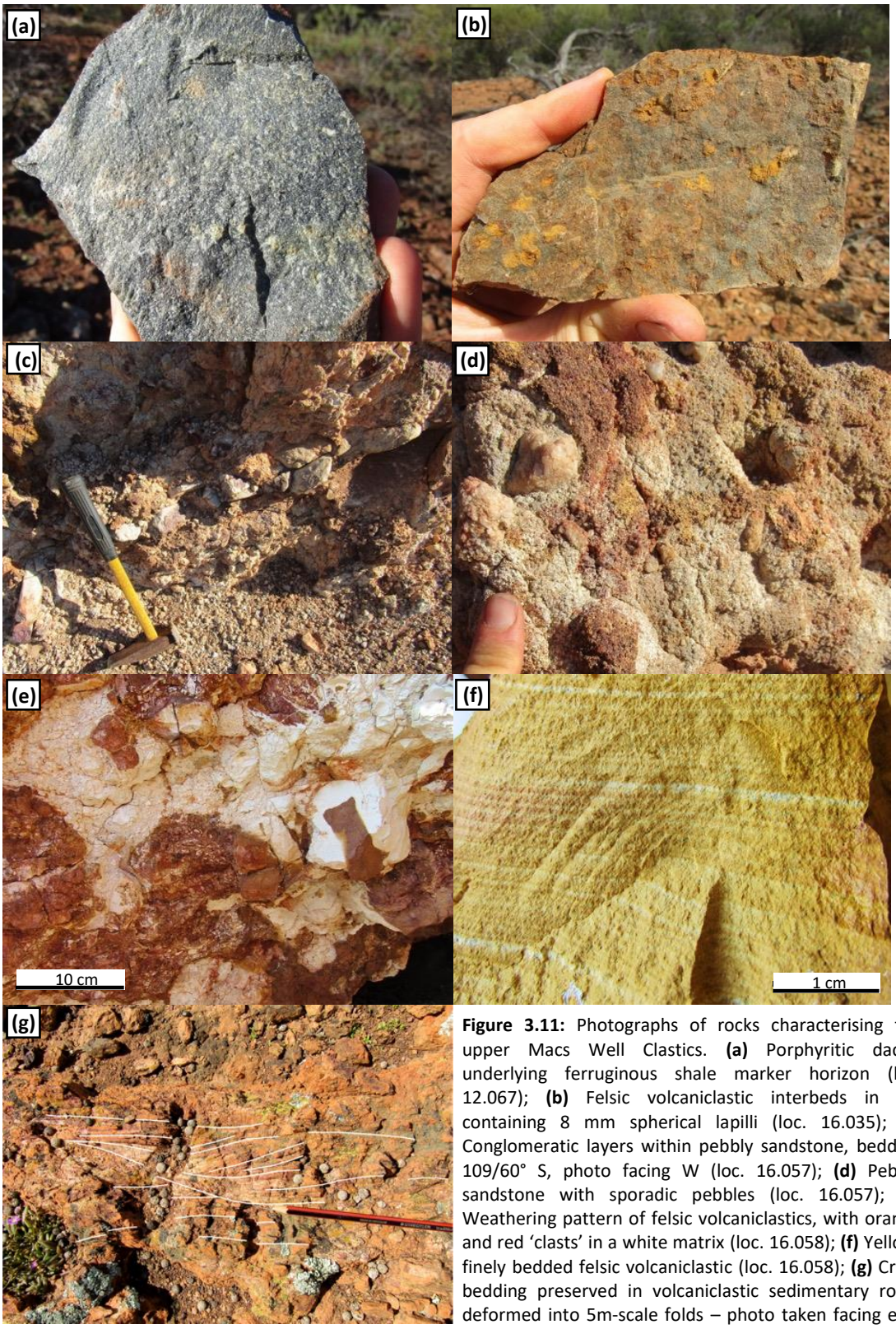

Figure 3.11: Photographs of rocks characterising the upper Macs Well Clastics. **(a)** Porphyritic dacite underlying ferruginous shale marker horizon (loc. 12.067); **(b)** Felsic volcaniclastic interbeds in BIF containing 8 mm spherical lapilli (loc. 16.035); **(c)** Conglomeratic layers within pebbly sandstone, bedding 109/60° S, photo facing W (loc. 16.057); **(d)** Pebbly sandstone with sporadic pebbles (loc. 16.057); **(e)** Weathering pattern of felsic volcaniclastics, with orange and red 'clasts' in a white matrix (loc. 16.058); **(f)** Yellow, finely bedded felsic volcaniclastic (loc. 16.058); **(g)** Cross bedding preserved in volcaniclastic sedimentary rocks deformed into 5m-scale folds – photo taken facing east and bedding oriented 350/70° E (loc. 11.082).

3.4.1 Supracrustal Rocks

3.4.1.1 Macs Well Clastics

The Macs Well Clastics are a ~1.4 km-thick package of sedimentary rocks and lesser volcaniclastic rocks, situated at the base of the supracrustal succession exposed in the Rothsay Fold area. The Macs

Well Clastics represents the lowermost formation in the Chulaar Group exposed in the area and is named after the historical locality Macs Well (Fig. 3.5), located 4 km southeast of the type locality. The lowermost ~1 km are characterised by alternations between ferruginous siltstone interbedded on a cm-scale with banded iron formation (BIF) and quartzite, and quartzite-dominated units. There are three units, 50-120 m in thickness, dominated by ferruginous siltstone, which consists of a finely laminated, dark brown, and fine-grained matrix (Fig. 3.10a). The siltstones are typically non-magnetic to weakly magnetic, however, where interbedded with BIF comprising mm-scale magnetite bands, the rocks are highly magnetic (Fig. 3.10b). Minor quartzite beds up to several centimetres in thickness are also locally interbedded (Fig. 3.10c). These ferruginous units are typically poorly exposed and where present, form low lying, deeply weathered and ferruginised platforms or ridges (Fig. 3.10d). Intervening quartzite-dominated units are largely unexposed and have only been identified from exploratory drill chips, float mapping and rare exposures along waterways. One exposure near the base of the package consists of fine-grained (<0.5 mm), grey quartzite bands alternating with medium grained (1-2 mm) light yellow quartzite on a 0.5-1 cm-scale (Fig. 3.10e). Further up sequence, quartzites are fine-medium grained (0.5-2 mm) with a sugary texture, displaying red-pink staining indicative of iron oxide content. The abundant layering, principally bedding, present in both quartzite and ferruginous siltstones has allowed preservation of folding on a decimetre to decametre scale.

Distinguishing contacts with minimal exposure available was greatly assisted by recognising changes in vegetation, particularly the wildflowers that bloom in the area in early spring. Wildflowers were found to grow preferentially on Fe-bearing units, and so were used to map the contacts between ferruginous siltstone/BIF, where the wildflowers were abundant, and quartzite, where flowers were scarce (Fig. 3.10f). These contacts closely match the trends of aeromagnetic anomalies in localities where highly magnetic BIF was interbedded with ferruginous siltstone.

The stratigraphic top of the interbedded siltstone-quartzite units is intruded by a ~150 m-thick dolerite sill (Section 3.4.2.1). This sill is overlain by a ~10 m porphyritic dacite unit, comprising a light grey, aphyric groundmass with tabular 2-4 mm plagioclase phenocrysts (Fig. 3.11a), representing the lowermost volcanic rock in the succession. Overlying the dacite is a further ~120 m-thick unit composed of interbedded ferruginous siltstone and BIF, with subordinate 1-2 mm quartzite interbeds. This unit is very well exposed, forming a near continuous, elevated ridge up to 30 m in height that can be traced along strike for over 10 km. The unit becomes more magnetic towards its top, grading into a dark red-black, magnetite-hematite-quartz BIF for the top 30 m. This is immediately underlain by interbedded orange-brown, fine-medium grained clastic units containing rounded 8 mm oxidised spherules, interpreted as lapilli-bearing felsic volcaniclastic rocks (Fig. 3.11b). In turn, the magnetic BIF is succeeded by a 30 m-thick layer of a fine grained, aphyric volcanic rock of andesitic composition.

The upper portion of the Macs Well Clastics is generally poorly exposed, however, a coherent stratigraphy can be constructed from several good outcrops. Andesite is overlain by a poorly exposed (< 100 m) thickness of non-magnetic ferruginous siltstone, above which a ~50 m broadly fining upward sequence of conglomeratic pebbly sandstone occurs. Conglomerate is concentrated near the base of the unit and occur as decimetre-scale layers of a clast-supported, poorly to moderately sorted, polymict unit that define the orientation of bedding (Fig. 3.11c). Clasts vary in size from 2 mm to 30 cm and are primarily composed of quartz, with lesser pebbly sandstone autoliths. The conglomeratic portions grade into laterally continuous poorly-bedded pebbly sandstone, comprising moderately sorted, sub-rounded to sub-angular clasts, typically 0.5-2 mm but up to 5-7 mm in size, with sporadic ~5 cm pebbles (Fig. 3.11d). Clasts are composed primarily of quartz, lesser chert of similar appearance to that in underlying BIF, and fine grained, crystalline, cream-coloured clasts, possibly felsic volcanic in origin. Bright white alteration indicates a possible volcanogenic component to the matrix.

Pebbly sandstone grades upwards into a bedded, 80-180 m-thick felsic volcaniclastic unit that marks the top of the Macs Well Clastics. This unit is typified by an orange-brown, fine grained, friable matrix, showing bedding on a 1-3 mm scale (Fig. 3.11f). It also locally shows a peculiar weathering pattern; a raised platform of bright white material contains orange-brown mottling in which a bedded volcaniclastic unit is evident and the margins of which are altering to the bright white material (Fig. 3.11e). In the far northeast, felsic volcaniclastics are interbedded with oxidised ferruginous sediment (possibly BIF) and display signs of sedimentary reworking in the form of cross bedding (Fig. 3.11g), however, the outcrop is significantly deformed and so cannot be used as a way-up criterion. This volcaniclastic unit can be traced along strike for over 8 km, however, exposure is not continuous along its strike length. This may be a consequence of the generally poor exposure or may instead signify localised deposition and accumulation of the described volcaniclastics. Dolerite intrudes this unit locally, predominantly at the fold nose and in the south. The upper margin of the Macs Well Clastics is intruded by the Mountain View Sill (Section 3.4.2.1). Minor 5 m lenses of a fine grained, orange felsic volcaniclastic unit are present as screens in the lower, doleritic portion of this intrusive sill.

3.4.1.2 Two Peaks Volcanics

The Two Peaks Volcanics are a 400-450 m-thick succession characterised by aphyric mafic volcanic rocks and interflow BIF, with minor porphyritic and spinifex-textured volcanic rocks. The group is named after the two most prominent peaks in the area, which are composed of basalt from this succession (Fig. 3.12a). The Two Peaks Volcanics conformably overlie the Macs Well Clastics, however, the contact between the two has been intruded by the Mountain View sill. As a result, multiple discontinuous horizons of Two Peaks Volcanics are preserved within this intrusive sill, including some

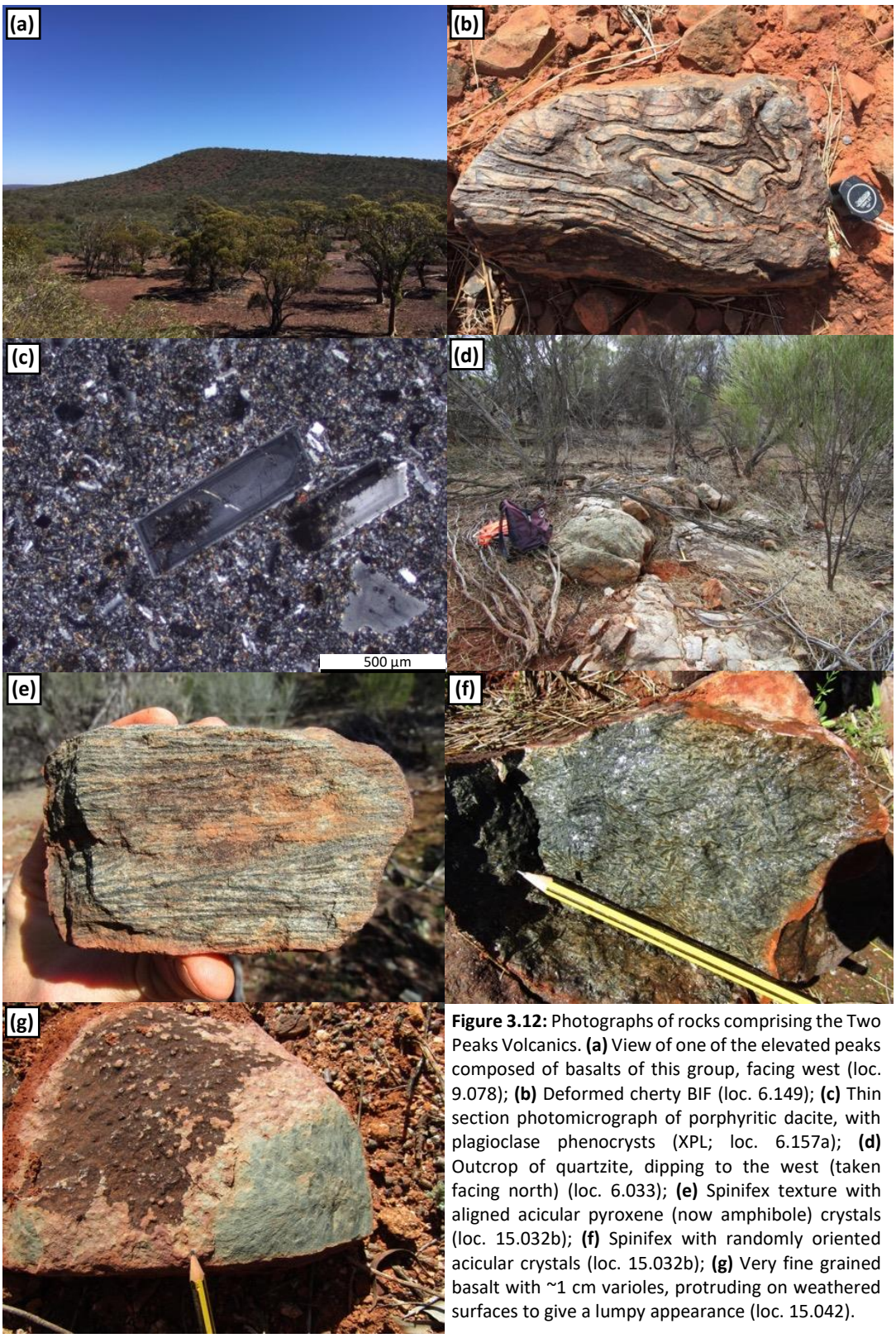

Figure 3.12: Photographs of rocks comprising the Two Peaks Volcanics. **(a)** View of one of the elevated peaks composed of basalts of this group, facing west (loc. 9.078); **(b)** Deformed cherty BIF (loc. 6.149); **(c)** Thin section photomicrograph of porphyritic dacite, with plagioclase phenocrysts (XPL; loc. 6.157a); **(d)** Outcrop of quartzite, dipping to the west (taken facing north) (loc. 6.033); **(e)** Spinifex texture with aligned acicular pyroxene (now amphibole) crystals (loc. 15.032b); **(f)** Spinifex with randomly oriented acicular crystals (loc. 15.032b); **(g)** Very fine grained basalt with ~1 cm varioles, protruding on weathered surfaces to give a lumpy appearance (loc. 15.042).

thick, very well exposed mafic volcanic units that forms the local topographic highs, elevated ~80 m higher than surrounding flat-lying areas (Fig. 3.12a). The unit thickens to ~320 m in the fold hinge and thins towards the northeast, likely a consequence of the intrusion of sills. The volcanic pile consists

mainly of aphyric, featureless and very fine to fine grained basalt, some of which break into elongate shards and make a high-pitched noise when struck with a hammer. Other portions are coarser, with crystals reaching 1 mm in size and a glittery appearance, potentially representing more slowly cooled, thicker flows. No discernible pillow structures are identified. Near the base of the unit, a thin (< 1m), more evolved porphyritic dacite is present, containing 0.2-2.5 mm euhedral phenocrysts of plagioclase and amphibole (Fig. 3.12c; Section 5.3.2).

The top of this basalt pile is intruded by the Honeycomb Gabbro, associated with the mafic-ultramafic network of sills (Section 3.4.2.2). Above this intrusive is a key stratigraphic marker horizon, consisting of two discontinuous supracrustal units overlain by a red-grey-black BIF. On the northeast limb and at the fold hinge, a thin (5 m) layer of massive quartzite is present, consisting of white-pink, medium-grained (0.5-1 mm) crystalline quartz with a sugary texture (Fig. 3.12d). The quartzite is only exposed at one locality (Loc. 6.033) but is present as subcrop and float along most of its length. The outcrop shows bedding surfaces parallel to the stratigraphy and patches of iron oxide, demonstrating contained Fe content. Thinning of this quartzite to the south coincides with the appearance of the second marker horizon on the southwest limb that is absent on the northeast limb; a poorly exposed pyroxene spinifex-bearing volcanic unit up to 25 metres in thickness (type locality: 15.032). Elongate, acicular crystals of pyroxene (now amphibole) up to 5 cm in length are strongly aligned in some parts of the outcrop (Fig. 3.12e), and randomly oriented in others (Fig. 3.12f). Outcrop is not contiguous enough to distinguish individual flows, however, this difference in alignment likely represents the various zones of spinifex-textured lava flows. This unit was originally mapped as a komatiite, but subsequent geochemistry has indicated that it is of basaltic composition (Section 6.4.1).

The overlying red-grey-black, highly magnetic BIF is 15 m in thickness and host to 0.5-1 cm bands of magnetite. Intervening chert varies from grey to red in colour, and though typically planar, this unit is significantly deformed close to the Rothsay Fold hinge. In turn, this is overlain by a further 120 m of poorly exposed aphyric basalt that forms low-lying ground and locally contains 1-2 mm tremolite needles. The top of the Two Peaks Volcanics is intruded by the Rothsay layered sill (Section 3.4.2.3). Within this sill, a thin (< 50 m), discontinuous horizon of very fine grained basalt with faint variolitic structures is present (Fig. 3.12g) and marks the top of the Two Peaks Volcanics.

3.4.1.3 Beryl West Volcanics

The Beryl West Volcanics are a ~320 m-thick sequence of aphyric and spinifex-textured volcanic rocks situated between intrusive rocks of the Rothsay and Gardner mafic-ultramafic layered sills. The sequence takes its name after a historical beryl mine located adjacent to its constituent rocks to the

south of the study area and comprises the lowermost supracrustal units to be dissected by the Rothsay Shear Zone. Rocks of the Beryl West Volcanics are generally poorly exposed and outcrops are low-lying and patchy, not elevated like other volcanic packages.

The stratigraphic base of the succession consists of aphyric and featureless basalt, which progresses upwards into a spinifex-textured volcanic rock comprising randomly oriented, needles of amphibole (pseudomorphing pyroxene) 2-6 mm in length amongst a fine-grained groundmass. This can be found across much of the strike length of the group and in turn, progresses upwards into well-developed spinifex textured rocks, with oriented acicular pyroxene crystals up to 10 cm in length (Fig. 3.13a). Furthermore, multiple units comprise another form of spinifex texture, characterised by randomly oriented sets of aligned, often skeletal crystals with a platy crystal habit (Fig. 3.13b; Section 5.3.5.4), remarkably similar to random platy pyroxene spinifex described by Lowrey et al. (2017) in similar rocks in the northeastern Murchison Domain and interpreted as evidence of undercooling. Such rocks are only found in the north of the field area and appear to be discontinuous towards the south, replaced instead by greater thicknesses of aphyric and proto-spinifex-textured basalts that contain small (<3 mm) elongate amphibole crystals. In this part of the stratigraphy, it is often difficult to distinguish between pyroxene spinifex-textured volcanic rocks and intrusive pyroxenitic rocks of the overlying

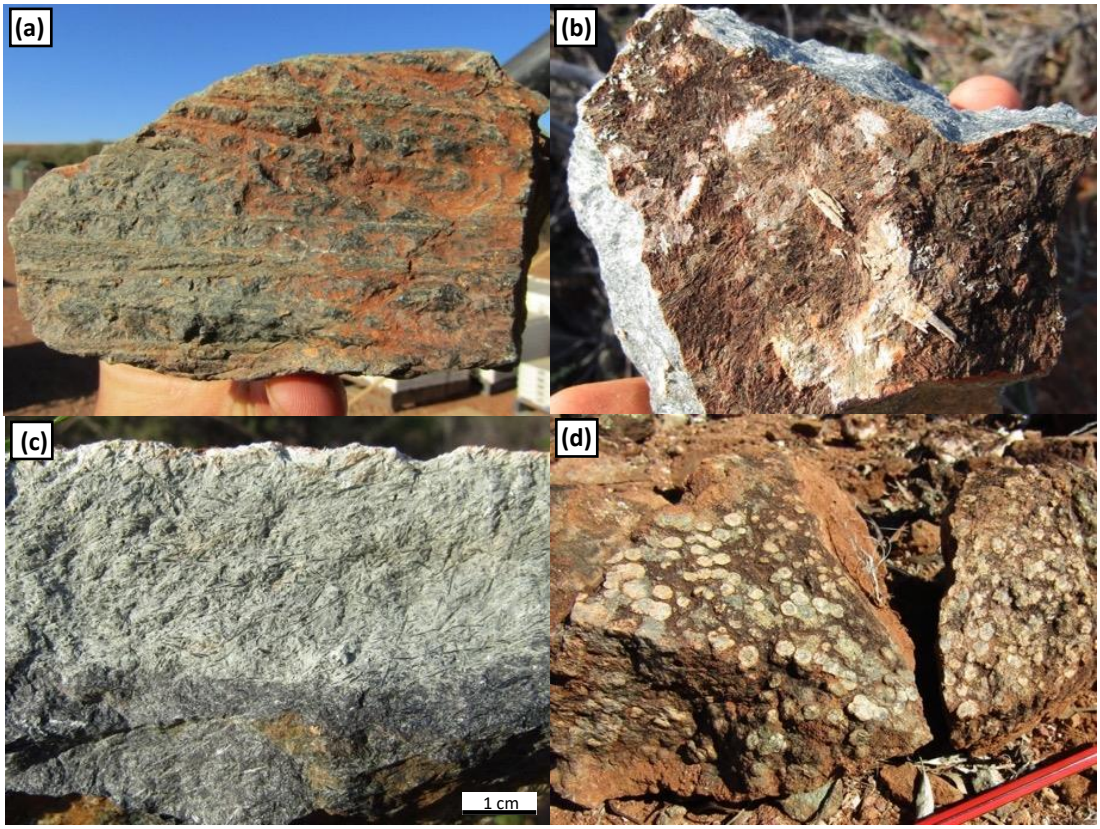

Figure 3.13: Photographs of rocks comprising the Beryl West Volcanics. **(a)** Oriented acicular pyroxene spinifex textured unit comprising ~10 cm phenocrysts (loc. 8.167a); **(b)** Weathered surface of platy pyroxene spinifex textured unit (loc. 10.046a); **(c)** Weathered margin of a pyroxene-dominated unit showing elongate needle-like nature of crystals, randomly oriented (loc. 10.034); **(d)** Spherules consisting of a white quartz core and a yellow-cream margin, in a fine-grained mafic rock (loc. 10.030).

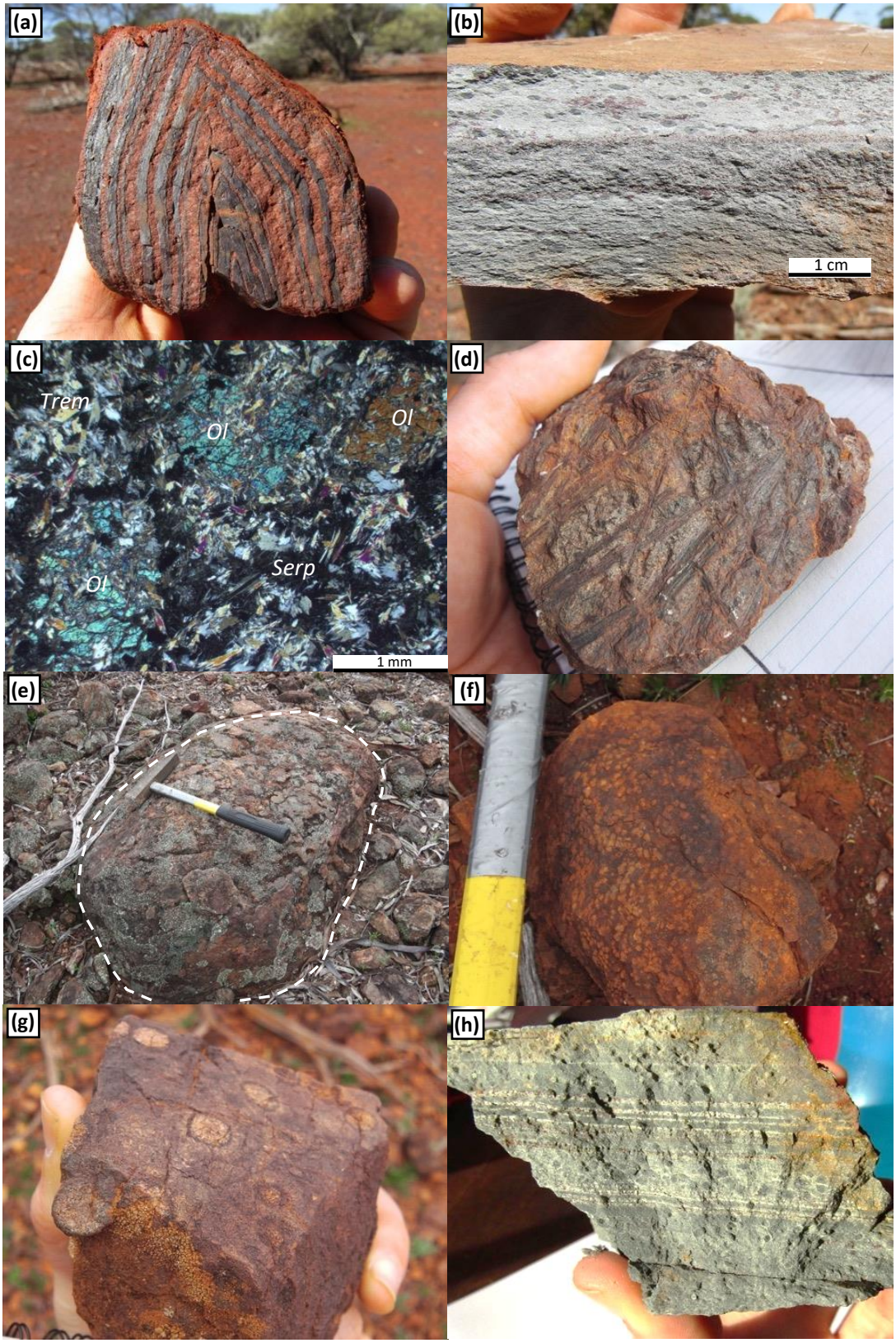

Figure 3.14: Photographs of rocks comprising the Mulga Volcanics. **(a)** Folded red-black BIF with 4-8 mm magnetite bands (loc. 8.186); **(b)** Andesitic lapilli tuff with rounded to oblate lapilli concentrated on some horizons, some of which show an angular clast at their core (loc. 8.184)**; (c)** Photomicrograph of ultramafic cumulate taken in cross polarised light, showing fragmented original olivine crystals, surrounded by serpentine, tremolite and magnetite (loc. 8.185); **(d)** Pyroxene spinifex-textured unit interleaved with basalt (loc. 8.076)**; (e)** Metre-scale pillow structure composed of aphyric basalt (loc. 8.134); **(f)** Variolitic basalt with rounded varioles 1-2 mm in size (loc. 8.116); **(g)** Variolitic basalt with 1-1.2 cm varioles, which preferentially stick out on weathered surfaces (loc. 8.116); **(h)** Finely bedded grey tuff with lapilli concentrated on some bedding horizons, and white, quartz-rich horizons (loc. 2.084);

Gardner Sill that contain elongate amphibole (after pyroxene) crystals. This is especially the case within the area of Map 10. The heavily altered margins of outcrops commonly exhibit elongate crystals of pyroxene (now pseudomorphed by amphibole) (Fig. 3.13c) and weathered surfaces also expose the elongate nature of crystals. In one instance, these units are host to unusual spherulitic structures consisting of quartz and feldspar in a finer grained groundmass (Fig. 3.13d), 0.7-1.2 mm in diameter and similar in shape to spherules in basalts of the overlying Mulga Volcanics. These spherules are associated with 1-3 cm diameter quartz veining which cross cuts host rocks.

3.4.1.4 Mulga Volcanics

The Mulga Volcanics are a 1.4 km-thick succession dominated by variolitic, pillowed and spinifex-textured basalts, with minor interflow BIF and lapilli-bearing tuff. The succession is underlain by the Gardner mafic-ultramafic layered sill and overlain by the Damperwah Sill. The Mulga Volcanics take their name from a historical local bore (Mulga Bore; Fig. 3.5) and the native mulga (acacia) bush which is often densely vegetated in areas overlying basalts of this group. Mulga Volcanics rocks are much better exposed on the northeast limb of the Rothsay Fold than they are on the southwest limb, where they are typically blanketed by transported cover occupying a large drainage channel.

The base of the Mulga Volcanics is marked by a 10 m-thick moderately well exposed cherty BIF, with a distinctive red-black to red-gold appearance (Fig. 3.14a). The unit contains magnetite bands on a 1-10 mm scale, with localised development of the fibrous Fe-amphibole grunerite. An overlying 5 m wide unit of lapilli-bearing tuff also acts as a crucial marker horizon and along with the BIF unit, characterises the base of the succession. Despite its poor exposure, it is frequently found as float and has a very distinctive spotted appearance (Fig. 3.14b). The tuff is characterised by 5-15 mm beds dominated by fine, grey ash, comprising alternations between fine to medium grained quartz-bearing units, and very fine-grained lapilli-bearing units. Lapilli are rounded, 0.2-3 mm in size, often contain an angular fragment at their centres and are concentrated on bedding horizons (Section 5.3.6). The beds also exhibit graded bedding and erosive bases to some beds, demonstrating a degree of sedimentary reworking of volcaniclastic material and acting as way-up criteria (Section 3.5.2). Overlying the tuff is a well exposed ~1.2 km mafic-ultramafic volcanic pile consisting of interleaved aphyric, variolitic and spinifex-textured volcanic rocks. On the northeast limb, the base of this pile is marked by a 20 m-thick spinifex-textured komatiitic unit comprising oriented elongate needles of amphibole (pseudomorphing pyroxene) up to 7cm in length and 1-2 mm in width, consistent with the "string-beef" spinifex classification of Arndt et al. (1977). This unit can be traced laterally along strike for 3 km and is associated with a 5 m-scale highly magnetic ultramafic cumulate, directly underlying the spinifex-textured rocks and interpreted as the cumulate base to a komatiitic flow. This ultramafic

unit contains a groundmass of serpentine, magnetite and tremolite, with preservation of 1-4 mm cumulate olivine crystals that are fragmented and partially serpentinised (Fig. 3.14c; Section 5.3.5.1). In the field, brown chalcedony is found proximal to this ultramafic unit.

The overlying 1.2 km volcanic pile consists of similar 20-30 metre acicular pyroxene spinifex-textured units interleaved with aphyric and variolitic basalt that characterise this succession; the latter volumetrically outnumbering spinifex-textured units by approximately 6:1. Due to the less resistant nature of spinifex-textured rocks, they form a series of narrow valleys concordant to the stratigraphy within the typically elevated volcanic succession. Spinifex varies in form between randomly oriented acicular pyroxene crystals (Fig. 3.14d) to strongly aligned 'sheaves' of acicular phenocrysts, defining "string-beef" spinifex textures. Basalt units occasionally exhibit pillow structures up to 1.5 metres in diameter (Fig. 3.14e) and frequently contain spherules that are spheroidal to slightly elliptical in shape and range in size from 0.5 mm to > 1 cm (Fig. 3.14f, Fig. 3.14g). Spherules are typically, but not always, concentrated around the margin of pillows. The volcanic rocks are commonly foliated and green talc-chlorite schist is developed locally, particularly close to major faults. Towards the top of the succession, a ~60 m dolerite is intruded and two thin (<10 m) cherty BIF units are distinguished by the presence of coincident float and magnetic anomalies. The upper portion of the Mulga Volcanics is intruded by the Damperwah mafic-ultramafic sill. In the far west of the area above the Damperwah intrusion, the top of the Mulga Volcanics is marked by a ~140 m-thick unit of a grey-coloured lapilli-bearing tuff with identical features to the thin tuffaceous unit present at the base of the Mulga Volcanics. The uppermost unit is finely bedded to massive and is characterised by spherical lapilli typically 2-3 mm, but rarely up to 5-6 mm in size concentrated on specific bedding horizons and often exhibiting a black angular fragment at their centres. Some parts of the unit contain lighter coloured quartz-rich horizons (Fig. 3.14h), whereas other portions consist entirely of fine grained, grey ash. This unit is poorly exposed elsewhere in the study area, but is interpreted to be present along strike based on a small amount of float material in areas of no exposure.

3.4.1.5 Willowbank Clastics

The Willowbank Clastics represents a sequence of sedimentary and volcaniclastic rocks that form the top of the supracrustal greenstone assemblage present in the Rothsay Fold area. The Willowbank Clastics are named after a local gold exploration target close to the type locality, overlie the Mulga Volcanics and have a minimum preserved thickness of 600 m. The true exposed thickness could be as much as 1 km; however, this is difficult to corroborate due to very patchy exposure and attenuation of units into the Enchanted Shear Zone in the east (Fig. 3.5).

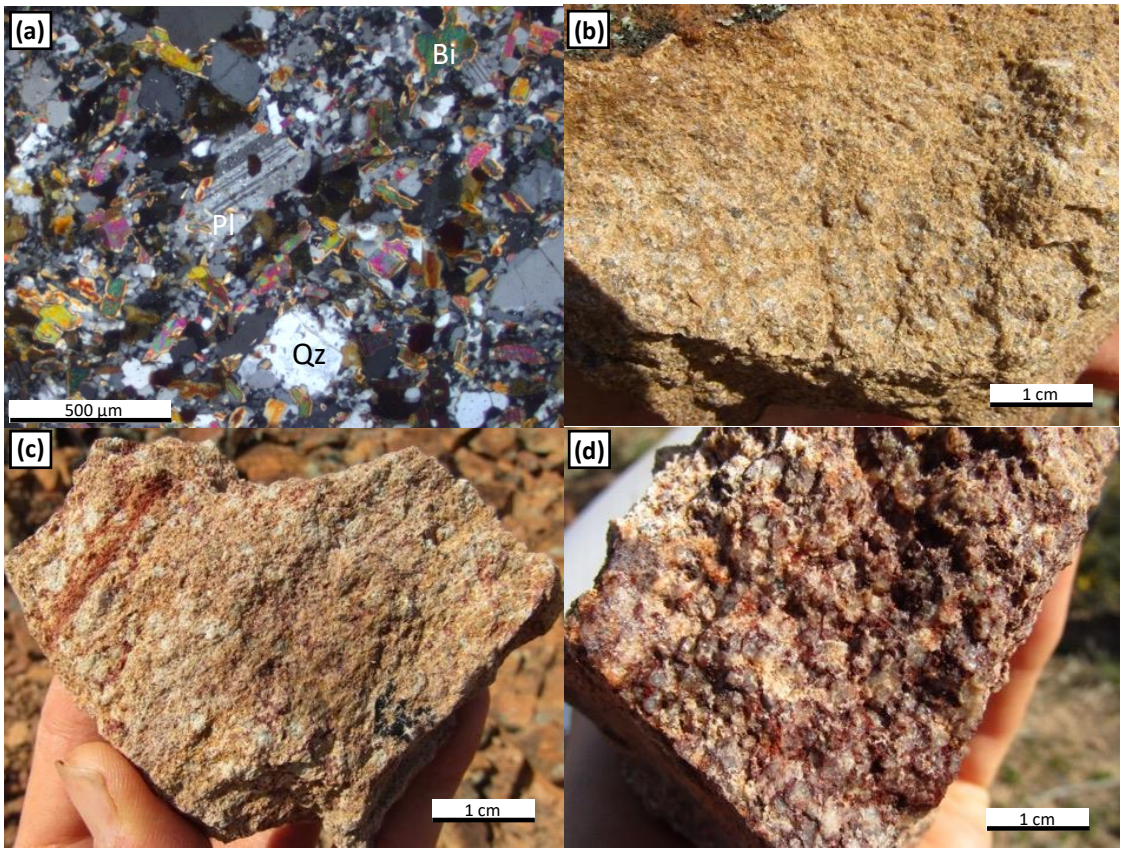

Figure 3.15: Photographs of rocks comprising the lower Willowbank Clastics exposed in the Rothsay area. **(a)** Thin section photomicrograph of a greywacke comprising anhedral grains of plagioclase, biotite and quartz (cross polarised light; loc. 2.088) **(b)** Volcanogenic quartz sandstone with 2-3 mm clasts (loc. 2.089); **(c)** Volcaniclastic unit with rounded, white 4-5 mm clasts and minor quartz in the matrix (loc. 2.089); **(d)** Pebbly quartz sandstone with a red, iron-bearing matrix (loc. 2.090).

The base of the Willowbank Clastics is very poorly exposed, however, several small m-scale outcrops of a red-brown, fine-grained and non-magnetic mudstone are present in the west. This mudstone appears to occupy a thickness of about 180 m, before progressing into a coarsening upwards sedimentary sequence. The base of this sequence is marked by a 30 m-thick unit of an immature, fine to medium grained (0.1-1 mm) micaceous greywacke, comprising clasts of muscovite, feldspar and quartz (Fig. 3.15a; Section 5.4.1). In turn, the greywacke grades into a better exposed, 15 m-thick unit of medium-grained, volcanogenic quartz sandstone, containing 1-3 mm sub-rounded quartz clasts (Fig. 3.15b). Volcanogenic content is represented by a yellow-brown, ashy matrix (Section 5.4.2). This coarsens upwards into a 5 m-thick volcaniclastic rock unit containing lithic clasts up to 8 mm in size amongst a red-grey ashy matrix, with some quartz clasts (Fig. 3.15c). Together, this unit and the underlying volcanogenic sandstone form an elevated ~5 metre ridge in an otherwise flat terrain. The thin volcaniclastic layer is overlain by a 35 m-thick unit of a clast-supported, moderately sorted, monomict pebbly quartz sandstone, containing quartz clasts 3-6 mm in size and a red-pink matrix, indicative of contained Fe (Fig. 3.15d). This unit has a similar appearance to the pebbly sandstone near the top of the Macs Well Clastics lower down in the supracrustal succession.

Overlying the pebbly sandstone, a 125 m-thick succession of intermediate to felsic volcaniclastic rocks occurs, comprising grey, bedded, lapilli-bearing tuffs, with interbedded white-cream felsic volcaniclastic rocks. The lower ~20 m of this succession is exposed as an elevated ~5 m platform of friable, grey-white ash containing clasts of multiple lithologies, demonstrating a distinctive weathering pattern similar to that of felsic volcaniclastics in the Macs Well Clastics (Fig. 3.16a). This ash bed encloses horizons containing dense lapilli (Fig. 3.16b) and another less-common clast lithology consists of a fine-grained, porphyroblastic metasedimentary rock containing euhedral, 1 cm andalusite crystals and rounded, 1-2 mm pinitized cordierite porphyroblasts (Fig. 3.16c; Section 5.4.3).

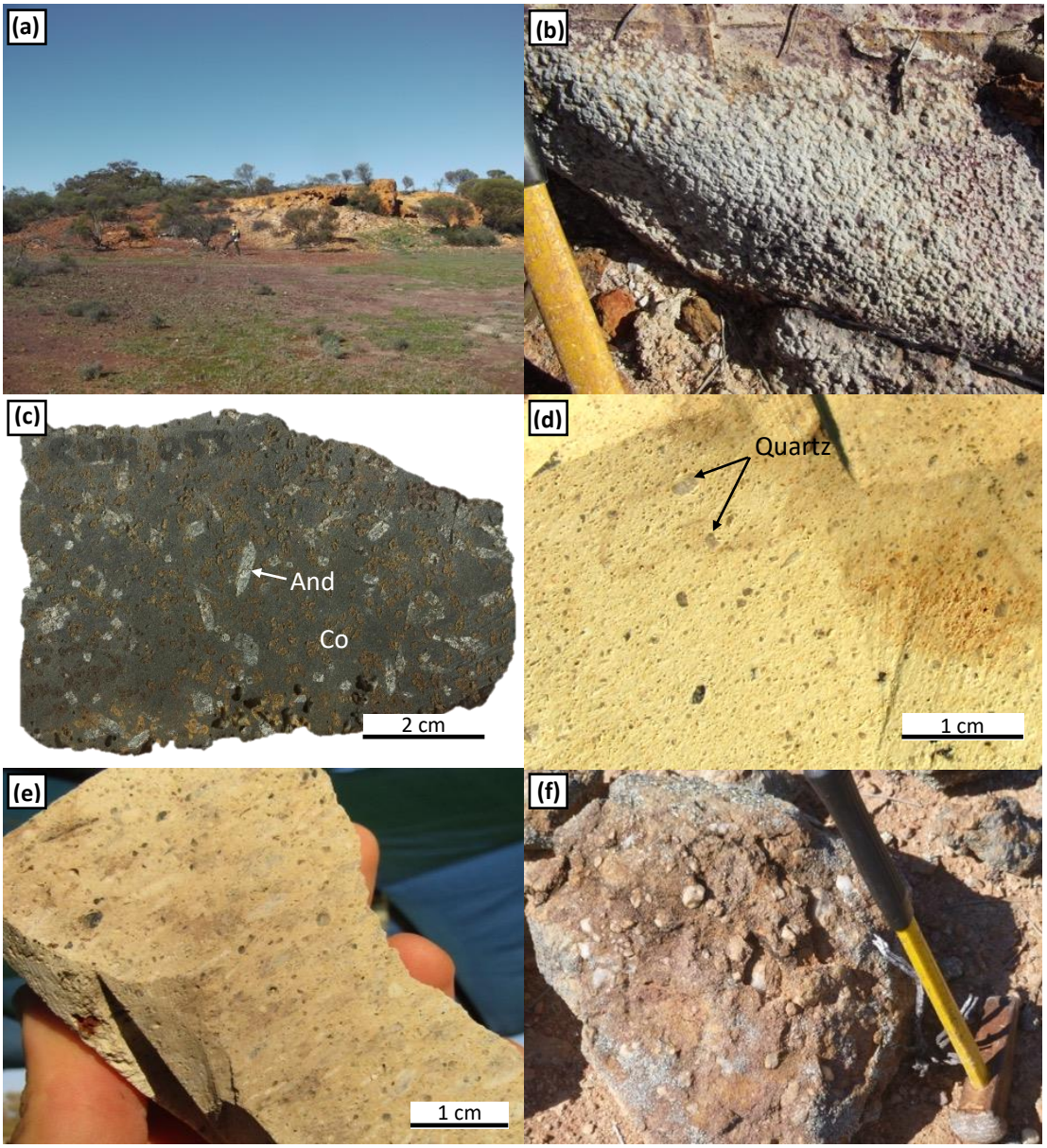

Figure 3.16: Photographs of rocks comprising the upper Willowbank Clastics in the Rothsay area. **(a)** Typical exposure of felsic volcaniclastic rocks and ash beds (loc. 2.039); **(b)** Felsic volcaniclastic unit containing dense lapilli on a 20 cm horizon – hammer for scale (loc. 2.091); **(c)** Cut surface of a porphyroblastic metapelitic rock containing andalusite and pinitized cordierite porphyroblasts – cavities around the margin of the sample representing the removal of cordierite alteration products (loc. 2.091; sample ROTH053); **(d)** Cut surface of a felsic volcaniclastic rock, containing angular quartz crystals, minor rounded lithic clasts and some black clasts (potentially volcanic glass), in a fine-grained matrix (loc. 10.093); **(e)** Cut surface of a coarser grained felsic volcaniclastic rock containing quartz crystals, and larger 4-5 mm lithic fragments. The rock possesses a fabric that could be primary (loc. 10.095); **(f)** Conglomerate outcrop containing rounded quartz pebbles up to 10 cm in size (loc. 10.107).

The upper portion of the exposed Willowbank Clastics is typified by felsic volcaniclastics, identified only in the far northeast of the study area. These rocks comprise poorly bedded clastic units composed of a white-cream coloured, fine grained quartzofeldspathic groundmass and clasts of quartz from 0.5mm to 2mm in size (Fig. 3.16d; Section 5.4.4). Some beds contain lithic clasts up to 8 mm in size that are elongate and define a fabric that may represent a primary feature (Fig. 3.16e). Rare lapilli-bearing horizons and interbeds of a darker grey ashy volcaniclastic rock are also present. This unit is characterised at the surface by milky quartz float, including in areas where the unit does not outcrop. Towards the top of the package, laterally discontinuous lenses of conglomerate occur within the felsic volcaniclastics. Conglomerates are poorly sorted, polymict and contain sub-angular to sub-rounded clasts of quartz varying in size from < 1cm to 12+ cm in size, in a grey to red, finer-grained matrix (Fig. 3.16f). At the contacts, there is a clear gradation on a 10 m-scale from volcaniclastic rocks with minor quartz clasts, to volcanogenic sandstone, to quartz sandstone and then into conglomerate. The conglomeratic lenses within felsic volcaniclastic rocks marks the top of the supracrustal stratigraphy present in the Rothsay Fold area.

3.4.2 Mafic-Ultramafic Intrusive Rocks

The Warriedar Suite of mafic-ultramafic layered intrusive sills intrudes the supracrustal stratigraphy in the Rothsay area and can be broadly separated into four sill complexes, based primarily on lithological evolution and their geometries. These intrusions comprise the lowermost Mountain View Sill, the Rothsay Sill, the Gardner Sill and the uppermost Damperwah Sill. A further distinct, relatively thin unit, the Honeycomb Gabbro, occurs at the top of the Mountain View Sill. The rocks comprising each of these mafic-ultramafic intrusions are described below:

3.4.2.1 Mountain View Sill

The Mountain View Sill is a dismembered 500 m-thick mafic-ultramafic intrusive complex intruded between supracrustal rocks of the Macs Well Clastics and Two Peaks Volcanics. It is named after a local gold exploration target (Fig. 3.5) and reflects the subdued topography of the constituent intrusive rocks relative to surrounding, elevated supracrustal units. The base of the sill is marked by a 140 m-thick unit of poorly exposed dolerite, intruded in the upper part of the Macs Well Clastics. Outcrops are rare, but where present are deeply weathered and comprise medium-grained and equicrystalline dolerite, with crystals locally reaching 3-4 mm in length. The average crystal size decreases towards the margin of the dolerite, consistent with chilled margins and an intrusive origin. Above the ~400 m-thick upper portion of the Macs Well Clastics, a 180 m-thick poorly exposed unit of equicrystalline

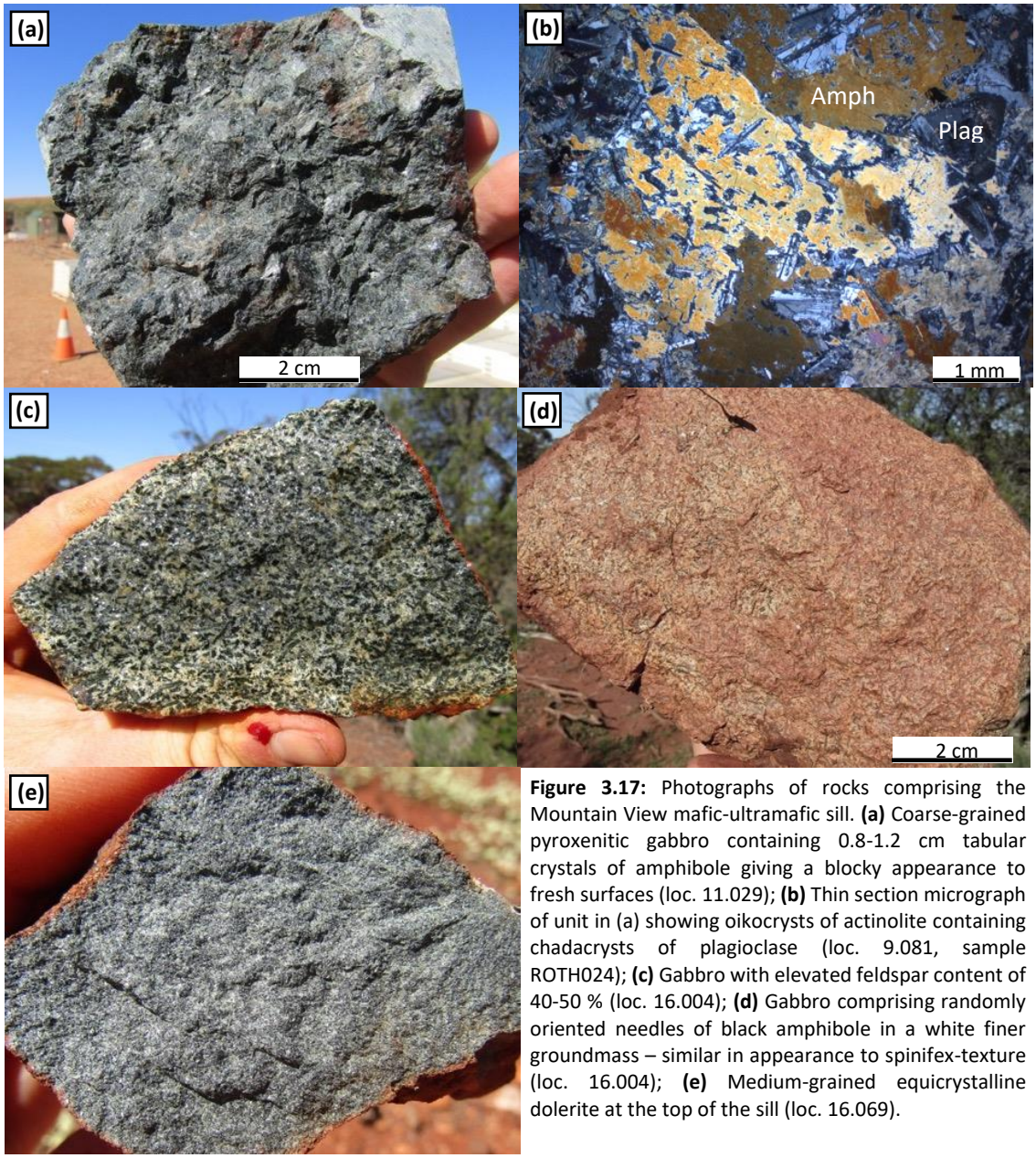

Figure 3.17: Photographs of rocks comprising the Mountain View mafic-ultramafic sill. **(a)** Coarse-grained pyroxenitic gabbro containing 0.8-1.2 cm tabular crystals of amphibole giving a blocky appearance to fresh surfaces (loc. 11.029); **(b)** Thin section micrograph of unit in (a) showing oikocrysts of actinolite containing chadacrysts of plagioclase (loc. 9.081, sample ROTH024); **(c)** Gabbro with elevated feldspar content of 40-50 % (loc. 16.004); **(d)** Gabbro comprising randomly oriented needles of black amphibole in a white finer groundmass – similar in appearance to spinifex-texture (loc. 16.004); **(e)** Medium-grained equicrystalline dolerite at the top of the sill (loc. 16.069).

dolerite is present, composed of 1-2 mm crystals of plagioclase feldspar and amphibole (replacing original pyroxene). Plagioclase crystals are often stained pink – a product of alteration and a characteristic feature of this unit. Towards the top of the dolerite, amphibole crystals increase to 4-5 mm in size and are acicular in shape. In the southwest (Loc. 16.060), a 5 m-thick lens of deeply weathered and oxidised, friable felsic volcaniclastic unit is enclosed within dolerite, close to the contact with like units in the upper Macs Well Clastics.

A laterally-continuous ~40 m-thick layer of cherty BIF and minor basalt is present above a ~180 m-thick dolerite intrusion, which in turn is overlain by a ~120 metre layer of coarser grained mafic intrusive rocks. This includes a lower ~50 m unit of coarse-grained pyroxenitic gabbro, composed of 0.8-1.2 cm tabular crystals of amphibole (actinolite) and 20-30 % interstitial crystals of plagioclase (Fig.

3.17a). Petrographic analysis shows that actinolite crystals are in fact poikilitic with inclusions of plagioclase crystals and display a sub-ophitic texture, both examples of relic igneous textures (Fig. 3.17b; Section 5.6.3). This unit occurs over 7 kilometres on the northeast limb and pinches out towards the south, and exposure is typical of that of mafic intrusive rocks in the area, occurring as mounds of large (up to 2m) rounded boulders. Pyroxenite grades upwards into a coarse gabbro, comprising 5-15 mm crystals and an increased feldspar content of 40-50 % (Fig. 3.17c). Some portions of the gabbro contain randomly orientated black amphibole crystals in a white groundmass, with a superficial appearance somewhat like spinifex texture (Fig. 3.17d). In turn, the gabbro grades upwards into a thin doleritic horizon. This dolerite is in upper contact with basalt and BIF, which is present as a discontinuous raft within the intrusive sill complex, stretching 5 km along strike and up to 100 m in thickness.

Above the basalt-BIF raft, a ~60 m-unit of equicrystalline dolerite occurs with 35-40% feldspar content (Fig. 3.17e). In some instances, crystals reach 4-5 mm in size and interstitial feldspar weathers preferentially, resulting in a blocky appearance to weathered surfaces. The top 15-20 m of the dolerite in contact with Two Peaks Volcanics supracrustal units comprises finer 0.5-1 mm crystals, indicative of a more quickly cooled, chilled upper margin

3.4.2.2 Honeycomb Gabbro

The Honeycomb Gabbro is a 110-180 m-thick unit of gabbro that intrudes the upper portion of the Two Peaks Volcanics, above aphyric basalt and below the quartzite and spinifex-textured basalt horizons. The unit represents the uppermost component of the Mountain View Sill and is composed of rounded to blocky amphibole crystals 0.8-2.5 mm in size, with finer grained interstitial plagioclase and ilmenite and minor quartz (Fig. 3.18a). Plagioclase content remains consistent at 25-30 % along strike of the unit. Weathered surfaces exhibit a honeycomb-like texture (Fig. 3.18b) that characterises

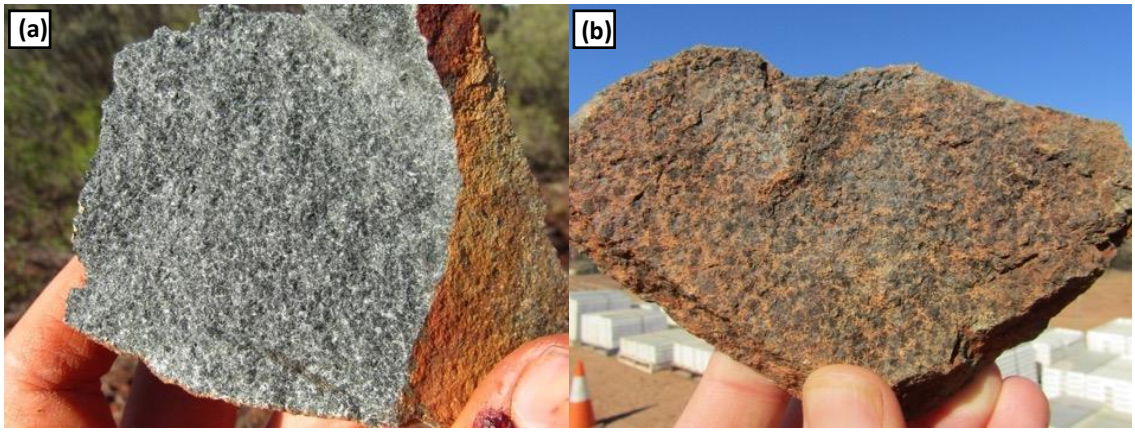

Figure 3.18: Photographs of rocks from the Honeycomb Gabbro. **(a)** Fresh surface showing rounded amphibole crystals in a finer grained groundmass (loc. 16.019); **(b)** Weathered surface displaying the characteristic honeycomb texture that typifies this unit (loc. 6.168).

and gives its name to this unit. Amphibole crystals are typically significantly deformed, and often show deformed crystallographic axes in the form of a strong undulose extinction (Section 5.6.3).

3.4.2.3 Rothsay Sill

The Rothsay Sill is a 550 m-thick mafic-ultramafic layered sill intruded at the contact between supracrustal rocks of the Two Peaks Volcanics and Beryl West Volcanics. The sill is named after the

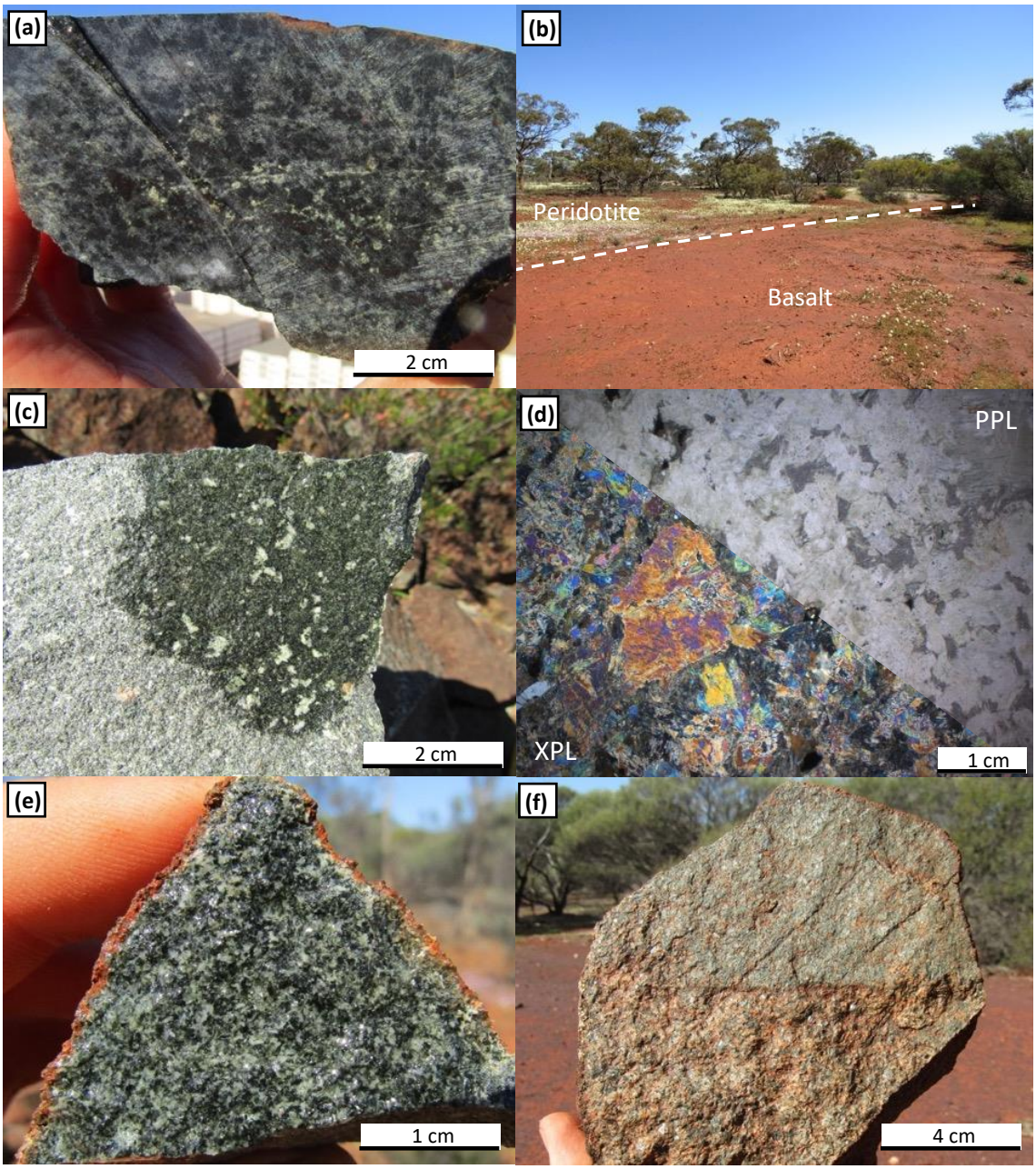

Figure 3.19: Photographs of rocks comprising the Rothsay mafic-ultramafic sill. **(a)** Serpentinised ultramafic with carbonate alteration and a relic cumulate texture (loc. 6.140); **(b)** Contact between ultramafic peridotite and basalt marked by wildflower abundance, which grow preferentially on Fe-rich ultramafic units (loc. 16.079); **(c)** Outcrop of porphyritic pyroxenite with distinctive white phenocrysts in a dark fine-grained groundmass (loc. 16.080); **(d)** Thin section photomicrograph of porphyritic pyroxenite showing tremolite crystals displaying a relic cumulate texture (loc. 9.005a, sample ROTH007); **(e)** Evolved equigranular gabbro with 50% feldspar content towards the top of the sill (loc. 16.089); **(f)** Sharp contact between two intrusives of different crystal size and feldspar-content (loc. 15.014).

historical Rothsay gold deposit that is hosted by these rocks. Exposure is good in the north and in the far south but is patchy elsewhere. The base of the Rothsay Sill consists of several metres of a poorly exposed and altered, fibrous tremolite-bearing unit that is likely the alteration product of an ultramafic precursor. This is overlain by a thick body of medium grained (2-4 mm) dolerite, with 30-40% feldspar, the top of which is marked by an incorporated < 50 m thick horizon of variolitic basalt.

A poorly exposed ultramafic unit from 25-45 m in thickness occurs above the basaltic horizon. The ultramafic rock typically comprises a dark, fine grained and highly magnetic groundmass, subject to serpentinisation and carbonate alteration, with relict cumulate textures (Fig. 3.19a). This unit is interpreted as a serpentinite, derived from a cumulate olivine-bearing ultramafic rock of peridotite composition. Weathered surfaces have a characteristic lumpy appearance and in highly altered areas, fibrous chrysotile veining and magnetite veinlets crosscut outcrops, and chalcedony occurs as float locally. The unit is largely continuous along strike but does pinch out in several locations. When under superficial cover, contacts with this unit were identified by vegetation and wildflower density, which was much greater above the ultramafic cumulate compared to surrounding lithologies (Fig. 3.19b).

A distinctive, well exposed < 40 m-thick unit of porphyritic pyroxenite overlies the ultramafic cumulate. This unit comprises a non-magnetic assemblage of 2-6 mm amphibole (tremolite) phenocrysts in an equicrystalline 1 mm-sized amphibole dominated with up to 10% interstitial altered feldspar (Fig. 3.19c) and exhibits a relict cumulate texture in thin section (Fig. 3.19d; Section 5.6.2). Notably, phenocrysts vary in colour from white in the southwest, to colourless-grey in the north. The amphibole-dominant mineralogy and cumulate textures suggests the protolith was a pyroxenitic cumulate rock, crystallised above the olivine-bearing cumulate immediately below. Outcrops in the south occur as prominent mounds of rounded boulders and are typified by a pitted appearance from preferential weathering of phenocrysts. In the north, porphyritic pyroxenite forms a prominent E-W trending, 40 m-elevated ridge. This cumulate-textured pyroxenite grades upwards into a coarser gabbro, with crystals up to 1-1.5 cm in size and a more leucocratic composition; over 50% feldspar content is observed in the southwest near the Rothsay mining centre (Fig. 3.19e). Crystal size decreases upwards to a moderately well-exposed dolerite (1-2 mm), which constitutes the upper portion of the Rothsay Sill. This distinct sequence of rocks in the upper portion of the sill – serpentinite, porphyritic pyroxenite, leucogabbro and dolerite – is fundamental for distinguishing structural repetition in the Rothsay Shear Zone (RSZ) in the far southwest, where the sequence is repeated three times. Within the upper dolerite, portions of coarser gabbroic rocks are present and some pieces of subcrop show sharp contacts between intrusions of differing crystal size (Fig. 3.19f). The Rothsay Sill represents the uppermost unit that is only found on the eastern side of the RSZ; all overlying rocks are dissected by the shear zone.

3.4.2.4 Gardner Sill

The Gardner Sill is a layered mafic-ultramafic sill intruded between the Beryl West Volcanics and the Mulga Volcanics and varies in thickness from 650 m east of the RSZ, to 950 m in the west. The Gardner Sill is the best example of a differentiated, layered mafic-ultramafic sill in the area, comprising an ultramafic, cumulate base, a gabbroic core, and an evolved leucogabbroic top. It is named after a historical bore located above constituent rocks in the southwest of the study area (Fig. 3.5). The sill is dissected by the RSZ and as a result, is thicker and more differentiated to the west.

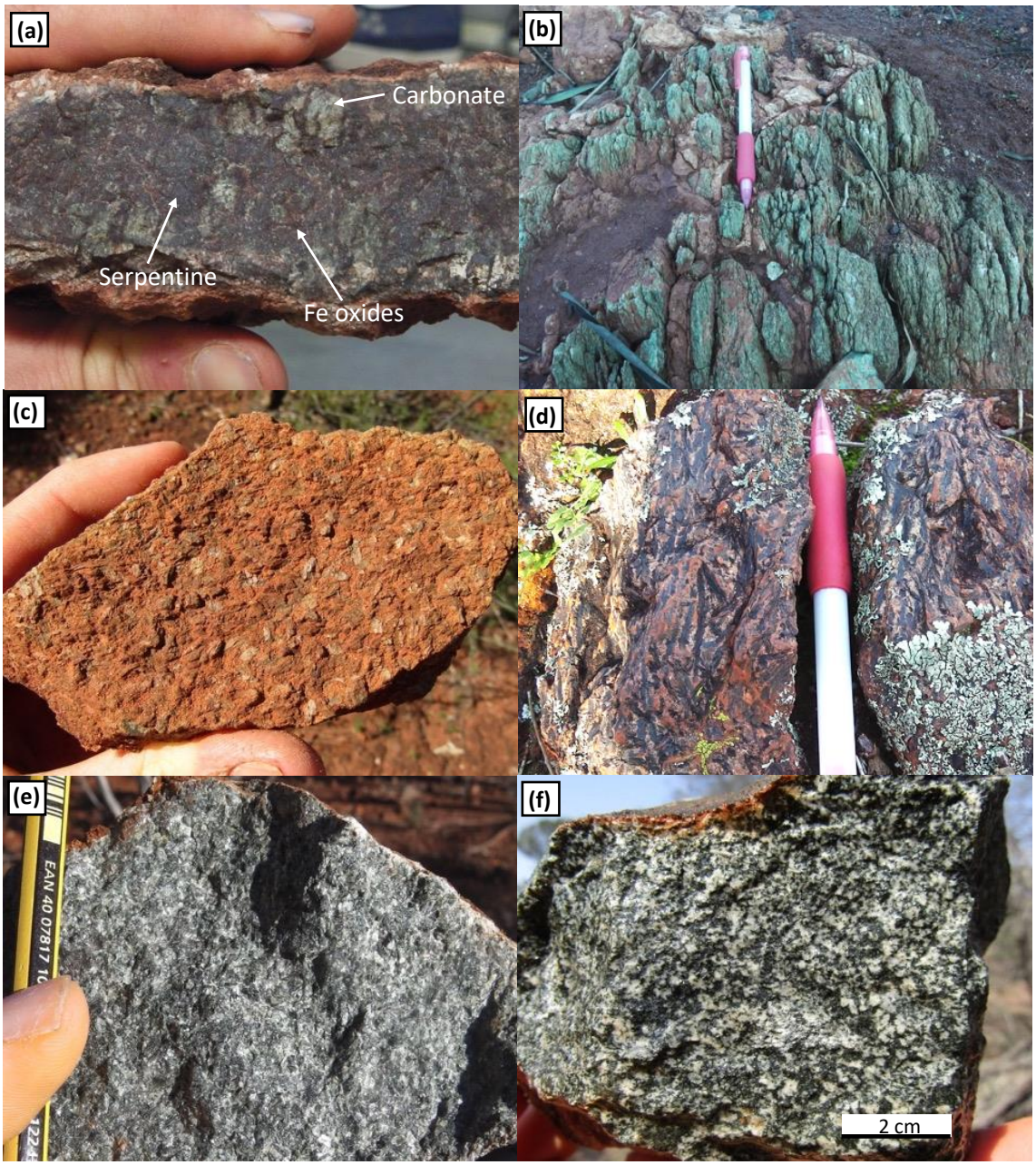

Figure 3.20: Photographs of rocks characterising mafic-ultramafic rocks of the Gardner Sill. **(a)** Carbonate altered serpentinised ultramafic, showing green carbonate, grey serpentine and red specks of iron oxide (loc. 8.122); **(b)** Bright green talc-chlorite schist derived from altered and sheared ultramafic protolith (loc. 5.122); **(c)** Weathered surface of a blocky-textured gabbro comprising coarse amphibole crystals (loc. 5.172); **(d)** Intrusive pyroxenite with feathery, elongate crystals of amphibole, after pyroxene (loc. 5.091); **(e)** Medium-grained, equicrystalline dolerite (loc. 8.041); **(f)** Coarser-grained leucogabbro from the evolved upper portion of the intrusion (loc. 8.178).

The base of the Gardner Sill is marked by a poorly exposed ~100 m-thick unit of a dark, fine-grained, highly magnetic ultramafic cumulate, typically consisting of serpentine (after olivine), tremolite, magnetite and magnesite as a consequence of hydration and carbonation reactions (Fig. 3.20a). The ultramafic protolith is interpreted as the olivine-bearing cumulate at the base of the mafic-ultramafic intrusion, of peridotitic composition. Magnetite is locally present as 1-4 mm grains and mm-scale veinlets, in addition to needle-shaped ilmenite crystals 0.1-2 mm in length (see Section 5.6.1). Fibrous chrysotile veinlets 2-20 mm in width crosscut outcrops in the far west. Weathered surfaces have characteristic lumpy appearance, as is the case for equivalent ultramafic cumulates in the underlying Rothsay Sill. Along its strike length, further ultramafic alteration products - chrysotile, talc and yellow-white chalcedony - are found as float on superficial cover. In more highly altered areas, the unit is associated with talcose, fibrous masses of tremolite – also derived from the ultramafic precursor. The ground overlying the unit is typically densely vegetated and feels unusually soft underfoot. Close to the RSZ, the ultramafic cumulate is represented by a highly foliated and magnetic, bright green talc-chlorite(-fuchsite) schist (Fig. 3.20b).

The rocks overlying this basal ultramafic unit differ on either side of the RSZ and so will be described independently below. East of the RSZ, the ultramafic unit encloses a discontinuous lens of non-magnetic dolerite up to 80 m in thickness, and is overlain by a ~60 m equicrystalline, coarse grained gabbro with crystals up to 1 cm and distinct blocky appearance (Fig. 3.20c). This unit grades upwards into a well exposed dolerite, with 1-2 mm crystals and 35% feldspar content (Fig. 3.20e). Dolerite outcrops as a series of stacks composed of large, rounded boulders subject to onion-skin weathering, the typical outcropping manner of mafic intrusive rocks in the area. The top 250 m of the intrusion reverts to a coarser grained gabbro, in which feldspar content gradually increases with stratigraphic height. The uppermost 50 m of the intrusion is leucogabbroic, with 2-5 mm crystals, ~60 % feldspar content and represents the most evolved portion of the intrusion (Fig. 3.20f). Intense epidote and chlorite alteration in some parts of this horizon are indicative of high fluid flow. The Gardner Sill thins to the east, possibly due to attenuation into the Enchanted Shear Zone.

To the west of the RSZ, the basal ultramafic layer is underlain by a poorly exposed dolerite and is overlain by a 100 m-thick unit composed largely of gabbro with tabular actinolite crystals 5-8 mm in size. Overlying this gabbro is a 70 m-thick pyroxene-rich (>75%) gabbro unit, dominated by feathery pyroxene (now amphibole) crystals up to 2-4 cm in size, separated by interstitial feldspar crystals (Fig. 3.20d). This intrusive pyroxene-dominant unit has a similar appearance to that of spinifex texture found in supracrustal volcanic rocks of the Beryl West Volcanics and Mulga Volcanics. This layer is succeeded by a further 120 m layer of equicrystalline gabbro with an average crystal size of 4-6 mm, which in turn grades upwards into a ~100 m layer of less well exposed, medium grained (1-2 mm)

dolerite. The top 20 metres of this doleritic unit, which is in upper contact with a BIF horizon, is relatively evolved and contains visible quartz crystals in one locality, thought to be primary. A second ultramafic cumulate layer is present above the dolerite and BIF, very poorly exposed but when observed, with identical characteristics and features to that of the equivalent, underlying ultramafic layer. The top of the Gardner Sill to the west of the RSZ consists of a ~300 m-thickness of medium grained dolerite, essentially unexposed other than a substantial subcrop in the far southwest. The Gardner Sill typifies a well-layered and differentiated mafic-ultramafic sill and demonstrates the lateral variation possible along strike within the individual sill complexes.

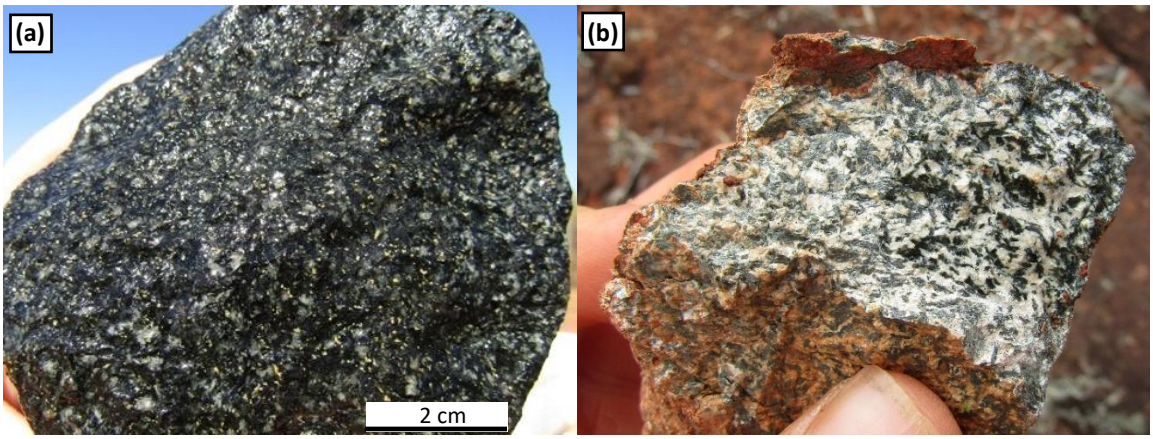

Figure 3.21: Photographs of quartz diorite that characterises the top portion of the Damperwah Sill. **(a)** Sample of quartz diorite with distinctive white-clear crystals of feldspar and quartz and yellow grains of leucoxene (loc. 11.053); **(b)** Sample of diorite from the upper Damperwah Sill in the far west of the study area, with highly elevated feldspar content and discernible yellow leucoxene (loc. 2.077).

3.4.2.5 Damperwah Sill

The Damperwah Sill is a 650-750 m-thick mafic intrusion that intrudes the upper part of the Mulga Volcanics, named after a historical well overlying constituent rocks in the southwest of the study area (Fig. 3.5). The sill is generally very poorly exposed and only outcrops in a small number of localities; it has otherwise been identified and characterised by float present above superficial cover. For this reason, the stratigraphy and features of this sill are not very well understood. The Damperwah Sill is essentially unexposed east of the RSZ, however, float is present that consists of dolerite with 1-3 mm crystals and also indicates the presence of multiple inclusions of fine-grained basalt within the lower part of the sill. A discontinuous <50 m-thick raft of BIF and shale is also present within the intrusive complex over a strike length of ~ 3km. The base of the sill is exposed in a 150-metre elevated outcrop in the northwest of the field area (loc. 1.034), an anomalous exposure of an otherwise poorly outcropping complex. Here, it comprises a medium grained (2-3 mm) dolerite with a feldspar content of approximately 40%, apparently more evolved than the lower portions of other intrusions. Elsewhere, further doleritic and occasional coarser-grained (4-5 mm) equivalents are found as float.

The upper portion of the Damperwah Sill is more evolved, consisting of a medium-grained intermediate-mafic rock with > 60% felsic mineral content and elongate amphibole phenocrysts up to 6 mm in length. One such subcropping unit that subcrops in the far east (loc. 11.053) has a mineralogy and textures consistent with a quartz diorite. The unit contains quartz crystals up to 2 mm in size, coarse and euhedral (> 0.5 mm) zircon crystals, and distinctive yellow leucoxene grains, resulting from breakdown of Ti-bearing minerals, primarily ilmenite (Fig. 3.21a). Petrographic analysis also reveals granophyric textures, comprising intergrowths of quartz in alkali feldspar crystals (see Section 5.6.4).

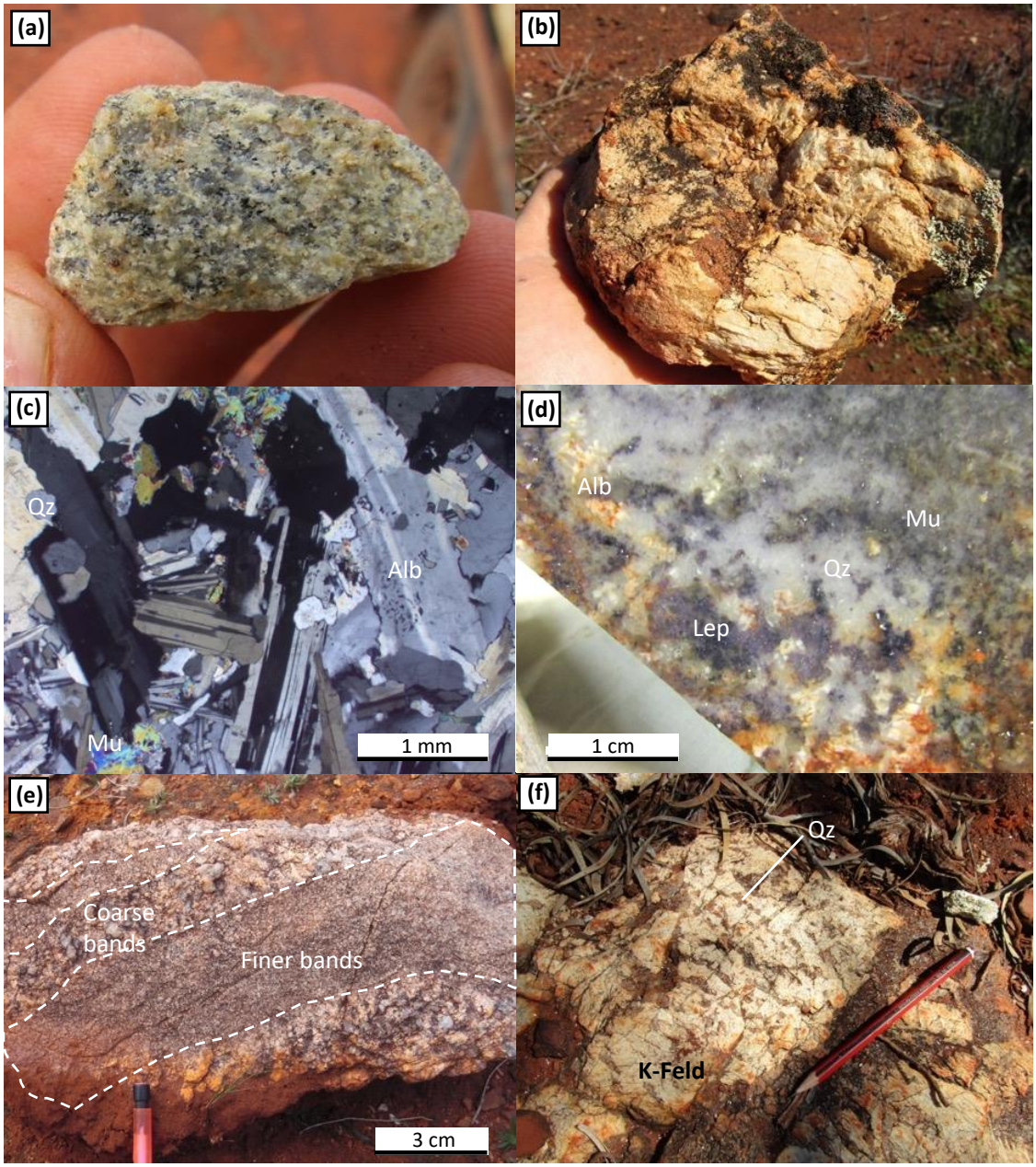

Figure 3.22: Photographs of rocks comprising granite (a) and pegmatite dykes (b-f) in the study area. **(a)** Granite identified in drill chips representing the unexposed granite in the southwest of the area (loc. 12.072); **(b)** Pegmatite sample containing large, euhedral feldspar crystals with muscovite and quartz (loc. 13.016); **(c)** Thin section photomicrograph (xpl) of a typical pegmatite sample comprising albite (Alb), quartz (Qz), muscovite (Mu) (loc. 6.052, sample ROTH014); **(d)** Cut surface of a Li-bearing pegmatite comprising purple lepidolite (Lep), quartz, muscovite and albite (loc. 6.052, sample ROTH014); **(e)** Block of pegmatite showing crystal size variation with coarser-grained bands separating finer-grained aplites (loc. 6.050); **(f)** Outcrop showing well-developed graphic textures, comprising intergrowths in quartz in a large >10 cm crystal of K-feldspar (K-Feld) (loc. 16.066).

Similar evolved quartz dioritic rocks can be found in the upper ~200 metres of the Damperwah Sill over a strike length in excess of 20 km (Fig. 3.21b). In general, the Damperwah Sill appears to be more evolved than other mafic intrusive complexes in the area.

3.4.2.6 Dolerite Dykes

Discordant dolerite dykes are very poorly exposed in the area and are often represented by highly vegetated creeks and valleys. In rare instances where float is observed at the surface, these intrusions consist of medium-grained (2-4 mm) dolerite and are undeformed and not metamorphosed. Crucially, the doleritic dykes are weakly to moderately magnetic, in contrast to the typical non-magnetic nature of most doleritic and gabbroic rocks of mafic-ultramafic sills. Consequently, the dykes are evident on aeromagnetic imagery; at least seven can be distinguished in the project area. The dykes range in thickness from a few metres to 30 m, have lengths in excess of 5-10 km and orientations typically NW-SE and NE-SW. They cross-cut both the volcano-sedimentary stratigraphy and surrounding granitoids, as well as folds, faults and shear zones, and thus are interpreted as postdating magmatism and deformation. The dykes are essentially straight along their strike length and are not affected by the topography, suggesting they are steeply dipping to vertical.

3.4.3 Felsic Intrusions

3.4.3.1 Granite

Granite is not exposed within the field area. The only evidence for the presence of felsic intrusive rocks are historical drill chips left as spoil at the surface in the far east (e.g., loc. 12.071). At these localities, a monzogranite comprising medium-grained, 1-2 mm crystals of plagioclase feldspar, K-feldspar, quartz and biotite mica is present beneath thick (>5 m) superficial cover (Fig. 3.22a). This corresponds to the margin of the 50 x 25 km granitic pluton, the Seeligson Monzogranite, to the southeast of the area. There is a distinct change to a sand-dominated regolith overlying areas of granitic bedrock in this area.

3.4.3.2 Pegmatites

Felsic pegmatite dykes discordantly intrude the supracrustal stratigraphy of the area and are well exposed in the south but only present as float and subcrop elsewhere. Pegmatites crosscut folding, faults and shear zones and invariably lack a fabric, thus are interpreted as post-deformational. Pegmatite dykes also cross-cut shear-hosted lode-gold mineralisation at the Rothsay Mining Centre.

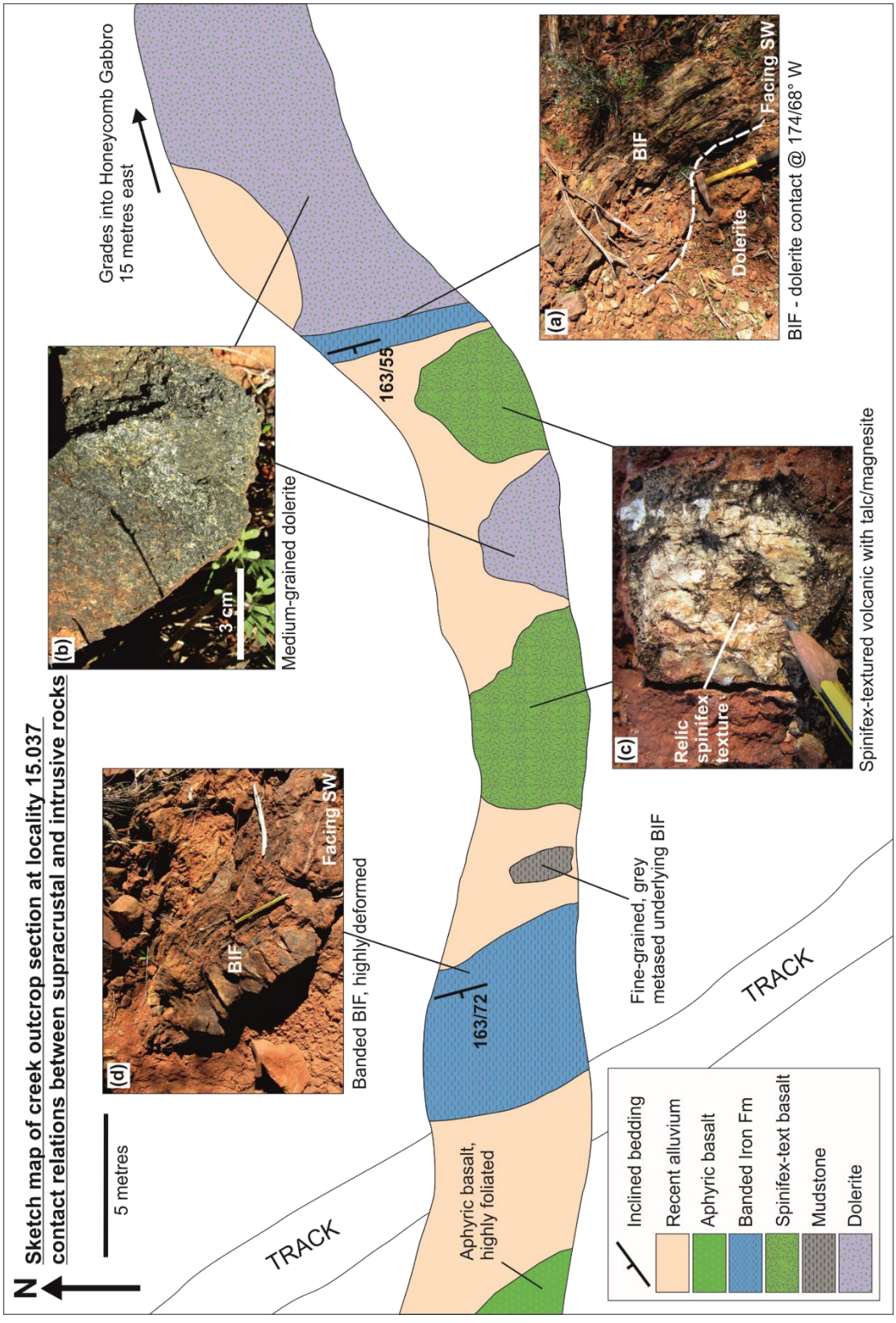

Figure 3.23: Sketch map of an outcrop section in a creek at locality 15.037, showing the contact relations between supracrustal rocks and concordant dolerite intrusive rocks.

The dykes are typically 1-5 m in width and increase in abundance towards the Seeligson Monzogranite pluton to the southwest. In this area, the pegmatites are both discordant and concordant with supracrustal units and appear to be concentrated in basalts of the Two Peaks Volcanics. The mineralogy of the pegmatites is variable but composed primarily of quartz, albite and K-feldspar with

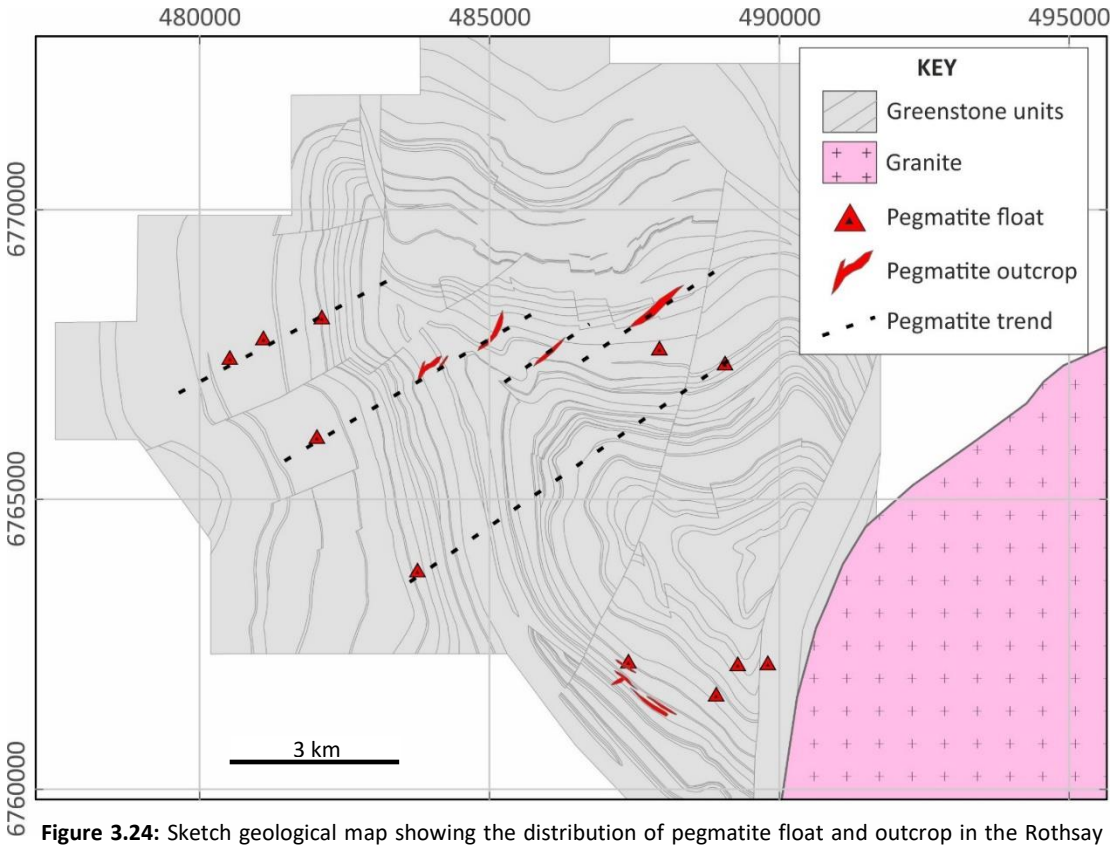

Figure 3.24: Sketch geological map showing the distribution of pegmatite float and outcrop in the Rothsay Fold area relative to the granite-greenstone contact. Pegmatites form at least 4 parallel dykes trending NE-SW up to 10 kilometres from the granite-greenstone contact.

minor muscovite and biotite (Fig. 3.22b, 3.22c). Locally, lithium-bearing lepidolite mica occurs as pink-purple rosettes (Fig. 3.22d) and light green apatite is present as 1-3 mm crystals with a greasy lustre. Rare occurrences of a dark green mineral are possibly beryl, as has been exploited historically from a pegmatite-hosted beryl mine immediately south of the study area. Crystal sizes vary considerably from 1-2 mm up to 10 cm, with some portions exhibiting a porphyritic texture, comprising coarse 1 cm+ crystals of feldspar in a finer-grained groundmass of mica, feldspar and quartz. Parallel banding of coarser-grained pegmatitic portions and aplitic finer portions are common in some dykes (Fig. 3.22e). Graphic textures are also present on a mm to 10 cm scale, comprising intergrowths of quartz in large crystals of K-feldspar (Fig. 3.22f).

3.4.4 Intrusive Relations

Contacts between supracrustal rocks and intrusive rocks are rarely observed in outcrop. However, typical contact relationships can be largely distinguished from areas of subcrop. A conspicuous feature of intrusive sills is the enclosure of multiple 'screens' of BIF observed in all mafic-ultramafic sills. These screens are often continuous for several kilometres along strike and have apparent thicknesses of up to 20 metres. Similar laterally continuous lenses of basalt are also contained within the Rothsay and

Damperwah sills and can locally be distinguished from fine-grained intrusive dolerite by spherulitic features. The composite Mountain View Sill contains two laterally discontinuous horizons of basalt and BIF up to 120 metres in thickness which thin and appear to pinch out along strike; interpreted as rafts of supracrustal units within the complex. The Mountain View Sill also contains metre scale lenses of underlying felsic volcaniclastic rocks (Macs Well Clastics) close to its base and occurs as lenses of dolerite within underlying units. These features are consistent with a pre-existing volcano-sedimentary supracrustal succession intruded by a network of mafic-ultramafic sill complexes. At one particularly good creek exposure – locality 15.037 – the contact between the Honeycomb Gabbro and overlying Two Peaks Volcanics is present in outcrop (Fig. 3.23). Dolerite of the former is directly overlain by a 1 m-thick BIF unit, which in turn is overlain by 20 m of spinifex-textured basalt and a further ~8 m BIF (Fig. 3.23). The dolerite-BIF contact is essentially parallel to bedding exhibited by both BIF units, consistent with the concordant nature of intrusions. Within the spinifex-textured unit, a 6 m-thick medium-grained dolerite is present but is not found elsewhere along strike. This ostensibly represents a minor intrusion of the more substantial Honeycomb Gabbro into overlying supracrustal rocks.

Subcrops of pegmatite dykes crosscut the volcano-sedimentary stratigraphy and are typically oriented NE-SW. When these outcrops are correlated with float occurrences, at least four parallel NE-SW trending dykes can be distinguished in the area (Fig. 3.24). These dykes are parallel to D_5 NNE-trending faults (Section 3.5.7) and increase in abundance towards the supracrustal contact with Seeligson Monzogranite, suggesting that they were emplaced during intrusion of this granitic pluton.

3.5. Structure

3.5.1 Introduction

Rocks in the Rothsay area are deformed into a broad, 12 km-wavelength, refolded, northwest-plunging antiformal fold structure, and are host to three discernible foliations, a lineation, folding on a cm- to km-scale, multiple generations of faults and two major shear zones. Collectively, these structures demonstrate that the study area has been subject to a complex and protracted deformational history. In this study, deformational events are numbered according to their relative order of occurrence and given the notation D (D_1, D_2 etc.). Folds, planar fabrics and lineations assigned to a deformational event are given the notation F, S and L respectively, followed by the corresponding deformational event number (e.g., F_3 and S_3 resulting from D_3). The structural geology of the Rothsay area can be summarised by six episodes of deformation (D_1-D_6) following emplacement of supracrustal rocks and intrusive sills (D_E). These events comprise an early inconspicuous deformational episode

Deformation Event	Setting	Features
D_6	E-W shortening	NNE-striking dextral **D_6** fault, minor N-S faulting
D_5	NE-SW shortening?	ENE-striking sinistral **D_5** faults, associated fault drag, granite and pegmatite dyke intrusion, ?oblique fabrics
D_4	Continued E-W shortening	**D_4** shear zones, duplex development, **S_4** shear fabric, oblique down-dip **L_4** lineation, **F_4** folding parallel to ESZ
D_3	E-W shortening	**S_3** N-S foliation, **F_3** N-S fold axes refolding F_2 folds,
D_2	NE-SW shortening	**F_2** NW-SE trending fold axes
D_1	?	Domal geometry, **S_1** layer-parallel foliation
D_E	Extension/rifting	Intrusion of mafic-ultramafic layered sills, screens/rafts of supracrustal units
D_E	Extension/rifting	Deposition of volcanosedimentary supracrustal succession, **S_0** bedding

Table 3.2: Table outlining the deformational framework for the Rothsay Fold area, comprising the interpreted structural setting and features observed for each event.

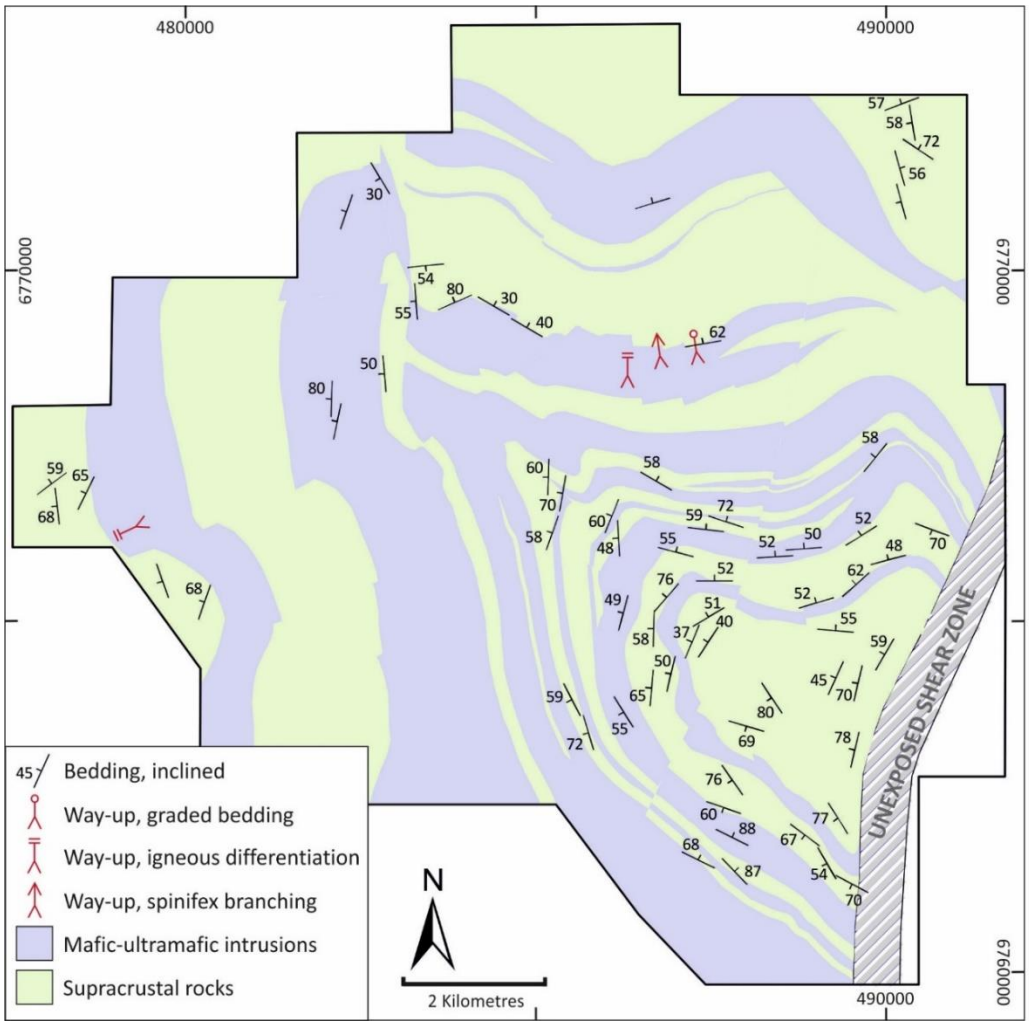

Figure 3.25: Simplified geological map of the Rothsay area showing representative bedding measurements and the locations and types of way-up indicators.

(D_1), followed by two shortening events (D_2, D_3), an episode of shearing (D_4) and two subsequent events dominated by faulting (D_5, D_6). D_4 shearing resulted in the development of two major shear

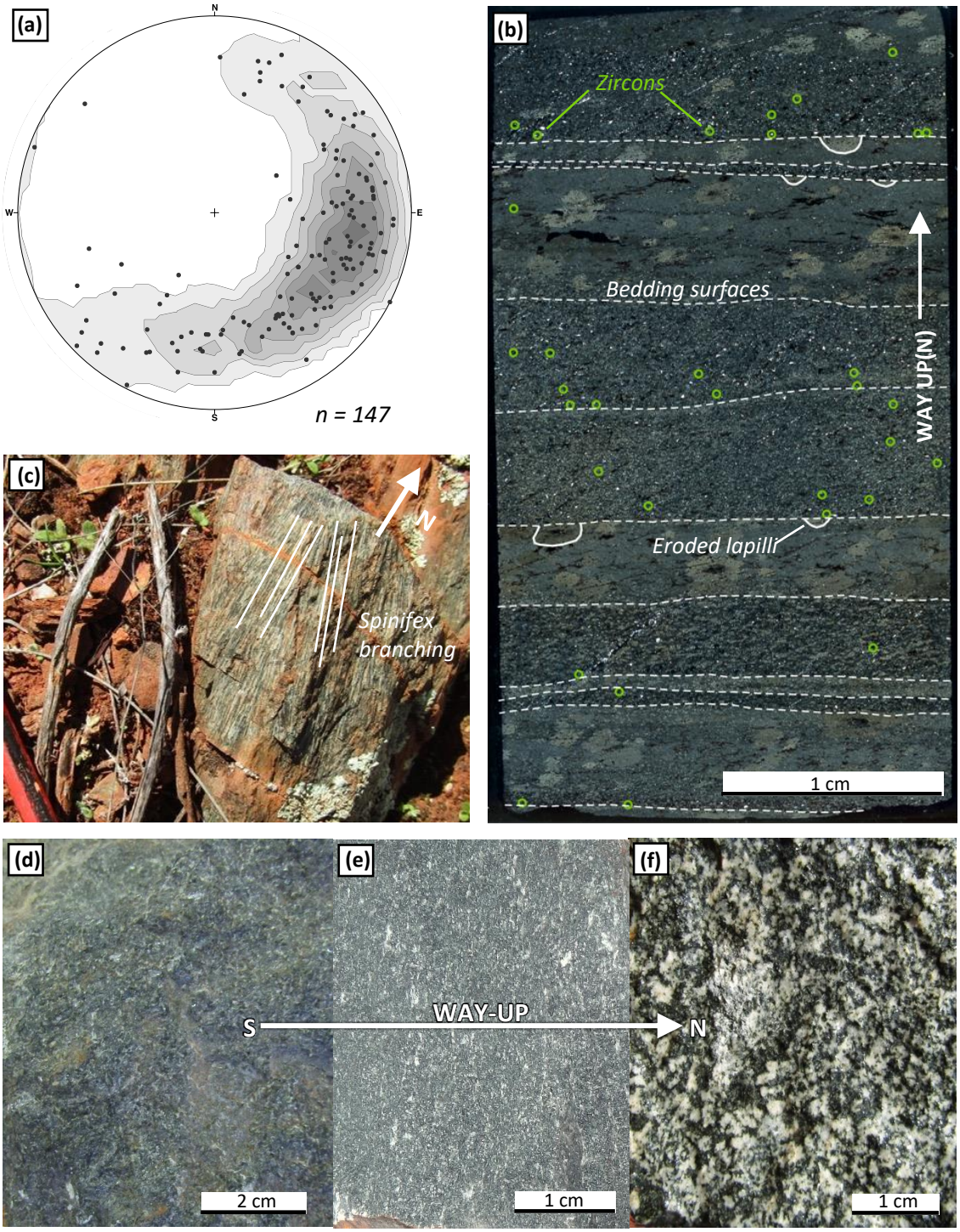

Figure 3.26: Bedding orientations and way-up criteria in the Rothsay area. **(a)** Lower hemisphere equal area stereonet of bedding orientations from the study area (n=147), with kamb contours drawn at 2σ intervals shaded in grey; **(b)** Thin section photomicrograph of lapilli-bearing tuff from locality 8.184, showing bedding surfaces and multiple way-up criteria; the distribution of zircon crystals in the section (green; largely concentrated at the base of coarser grained beds) and originally rounded lapilli (outlined in white) cut by erosive surfaces. Cross-polarised light**;** **(c)** Outcrop of spinifex-textured basalt at locality 8.188 showing branching of spinifex towards the south and thus demonstrating way-up to the north; **(d)(e)(f)** Photographs of intrusive rocks from the Gardner Sill displaying increasing feldspar content towards the north over a ~150 m stratigraphic interval from the southernmost feldspar-poor dolerite at locality 8.104a **(d)**, to dolerite at locality 8.118 **(e)**, to northernmost leucogabbro at locality 8.178 **(f)**, demonstrating way-up to the north. Note that coarser crystal size in (f) corresponds to the evolved uppermost ~10 metres of the Gardner sill, which in some instances displays harrisite-like textures.

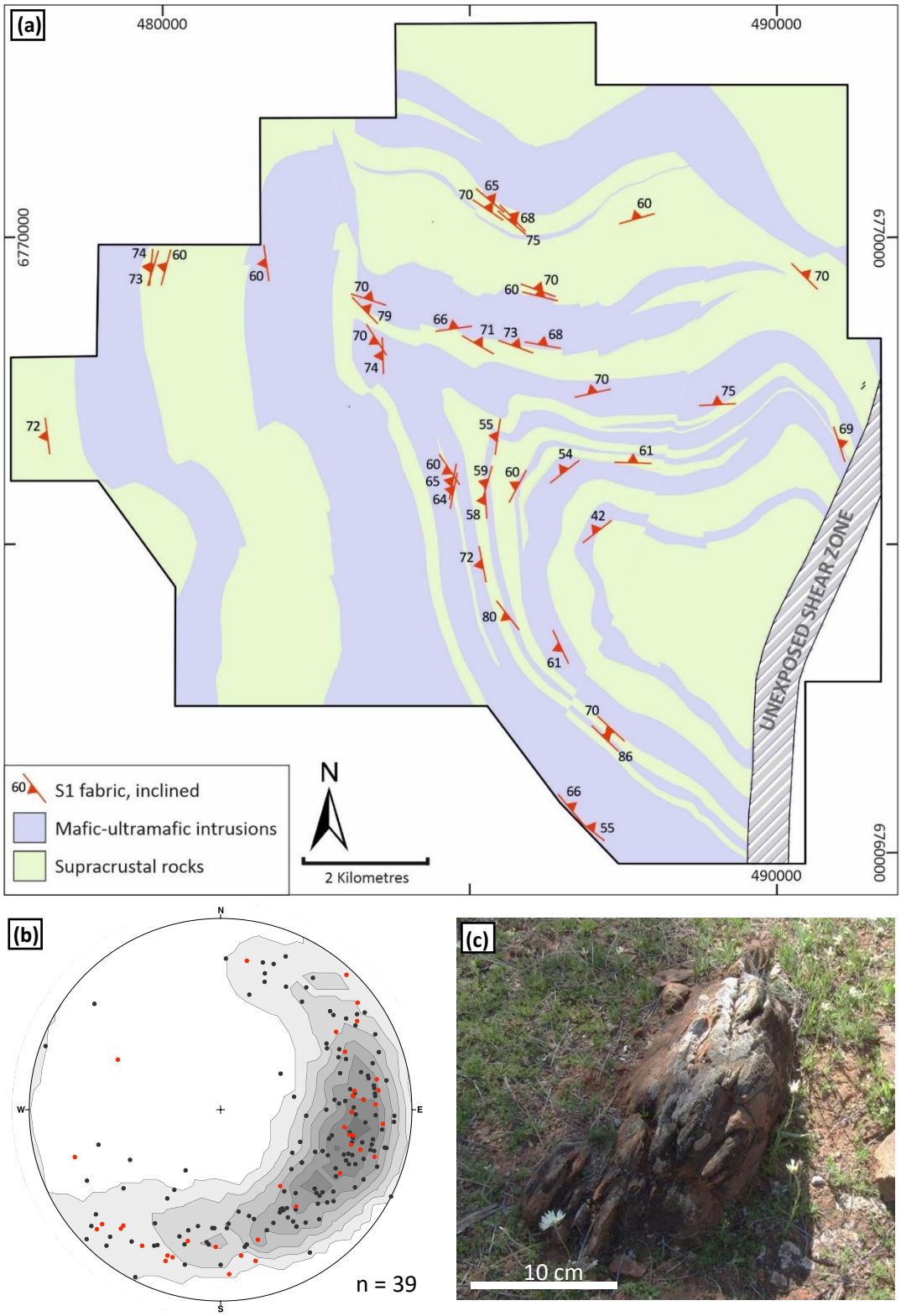

Figure 3.27: Map, stereonet and field photograph of S_1 bedding-parallel foliation. **(a)** Simplified geological map showing the orientation of S_1 foliations measured in the study area; **(b)** Lower hemisphere equal area stereonet showing orientations of S_1 bedding parallel-foliation (red) relative to bedding (grey). Kamb contours for bedding measurements are drawn at 2σ intervals; **(c)** Outcrop of fine grained metabasalt showing S_1 bedding-parallel foliation (loc. 1.029).

zones in the Rothsay area; the Rothsay Shear Zone (RSZ), host to the historically-exploited Rothsay gold deposit, and the Enchanted Shear Zone (ESZ). The structures associated with each deformational event are summarised in Table 3.2 and will be described sequentially in the sections below.

3.5.2 Bedding (S_0) and way-up criteria

Bedding in the Rothsay area is preserved by numerous metasedimentary lithologies. Most commonly, bedding orientations are recorded by the many laterally-extensive BIF units that occur throughout the supracrustal succession, including as rafts and screens within sill complexes. In these units, banding occurs on a <1 mm to ~2 cm scale and consists of highly variable proportions of chert, magnetite and hematite. In the Macs Well Clastics, bedding is well preserved by ferruginous siltstone in the form of mm-scale laminations, however, interbedded quartzite units are typically too massive to discern bedding. Lapilli-bearing tuffs of the Mulga Volcanics are locally well-bedded on a mm- to cm-scale, particularly the lowermost basal unit, and contain several sedimentary features that can be used as way-up criteria. Felsic volcaniclastic units of the Willowbank Clastics are typically poorly bedded, however, bedding orientations can occasionally be determined through the identification of minor changes in average grain size or the concentration of quartz clasts.

Bedding surfaces in metasedimentary and volcaniclastic rocks typically dip at angles between 40-80° and consistently dip in a radial direction away from the core of the Rothsay Fold, i.e. to the north on the northeast limb and to the (south)west on the southwest limb (Fig. 3.25, Fig. 3.26a). As such, bedding measurements partially define a domal pattern, although supracrustal units in the southeast are dissected and deformed by the ESZ (Section 3.5.6.1). Several way-up criteria are present in both supracrustal units and mafic-ultramafic intrusive rocks. At the base of the Mulga Volcanics in the north of the study area (Fig. 3.25), a lapilli-bearing bedded tuff is characterised by 5-15 mm beds of a grey-ash groundmass and rounded lapilli 1-3 mm in size. Petrographic analysis of an oriented sample (loc. 8.184) has identified several way-up criteria in this unit. Following sample mapping undertaken for geochronological work (see Chapter 8), zircon crystals are consistently found at the base of individual beds within the Mulga Volcanics bedded tuff, demonstrating pseudo-graded bedding (Fig. 3.26b). Coarser quartz crystals (0.3 mm) are also concentrated at the bases of beds compared to finer upper portions (< 0.05 mm). Furthermore, erosive bases are identified in several instances, distinguished by originally rounded lapilli cut by subsequent bedding surfaces (Fig. 3.26b). All criteria support the succession being the right way-up and younging away from the core of the fold. Immediately overlying the lapilli-bearing tuff, an oriented acicular spinifex-textured unit exhibits elongate crystals of amphibole (after pyroxene) up to 7 cm in length and 1-2 mm in width. At a good exposure in the north of the area (loc. 8.188; Fig. 3.25), acicular spinifex crystals consistently branch towards the south (i.e. down-sequence), consistent with the succession being the right way up (Fig. 3.26c).

The fractionation of mafic-ultramafic intrusive sills also serves as way-up criteria, best exemplified by the Gardner Sill in the north of the study area (Fig. 3.25). The base of the sill is marked by two

ultramafic units containing relic cumulate textures and invariably serpentinised olivine crystals. The central part of the Gardner Sill consists of coarse-grained gabbro and feldspar content consistently increases with stratigraphic height (Fig. 3.26d, Fig. 3.26e), with the most evolved, quartz-bearing leucogabbro occurring in the uppermost 20 m of the intrusion (Fig. 3.26f). Similar highly evolved tops are shown in the west by the Damperwah Sill (Fig. 3.25). These features demonstrate differentiation of the intrusive sills and support the succession being the right-way up.

3.5.3 D_1 Deformation

D_1 deformation comprises several features that predate all other structures in the Rothsay area. The oldest discernible fabric is a layer-parallel S_1 foliation, which is characteristically oriented parallel to the bedding of layered metasedimentary rocks (Fig. 3.27a). The orientation of this fabric consistently imitates bedding around the Rothsay Fold and correlates well with bedding orientations (Fig. 3.27b). The S_1 layer-parallel foliation is most frequently observed in fine-grained metaigneous rocks such as basalt and serpentinite, of which outcrops are typically strongly foliated and commonly aligned parallel to the strike of S_1 (Fig. 3.27c). The fabric is also found as a weak foliation or spaced cleavage

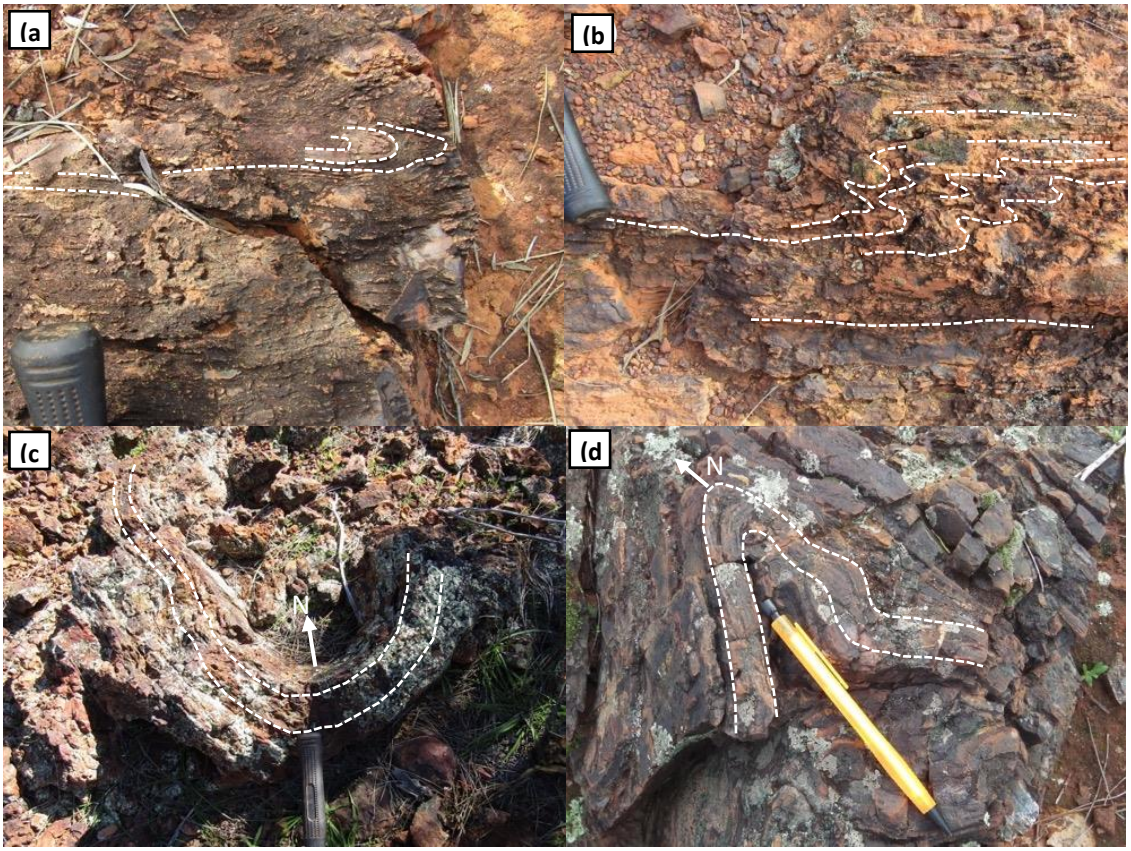

Figure 3.28: Small-scale folding in the Rothsay area. **(a)** Layer-parallel F1 isoclinal folding in banded iron formation of the Macs Well Clastics, with axial planes parallel to bedding (loc. 13.043); **(b)** Tight to isoclinal F1 folding in fine-grained metapelitic rocks (loc. 13.044); **(c)** Open, cylindrical folding of interbedded quartzite and siltstone – fold axes plunging to northwest parallel to surrounding bedding, hammer handle for scale (loc. 13.023b); **(d)** Decimetre-scale asymmetric folding of banded iron formation close to a major F2 antiformal fold hinge, plunging parallel to the major fold axes (loc. 6.098).

in coarser grained mafic intrusive rocks, such as gabbro and dolerite, and in volcaniclastic rocks. The intensity of S_1 increases towards major rheological contacts, most notably the base of the Gardner Sill (within ultramafic cumulate rocks) and the lowermost contact of the Rothsay Sill (within basaltic rocks), but occurs throughout all exposed units. No lineation has been observed with S_1 and no conclusive shear sense indicators have been identified. S_1 is crosscut by all other fabrics in the Rothsay area.

Other structures associated with D_1 include centimetre- to decimetre-scale, isoclinal, layer-parallel F_1 folding preserved in several BIF units, possessing fold hinge surfaces that are parallel to both bedding surfaces and the layer-parallel S_1 foliation (Fig. 3.28a, Fig. 3.28b). These are the earliest folds preserved in the area and have been deformed by all subsequent deformational events. The radial, outward-dipping pattern of bedding measurements in the Rothsay area define the geometry of a dome (Section 3.5.2; Fig. 3.25). Furthermore, the slight, gradual curvature of units on the southwest limb of the Rothsay Fold, most clearly demonstrated by the upper Two Peaks Volcanics, may represent an

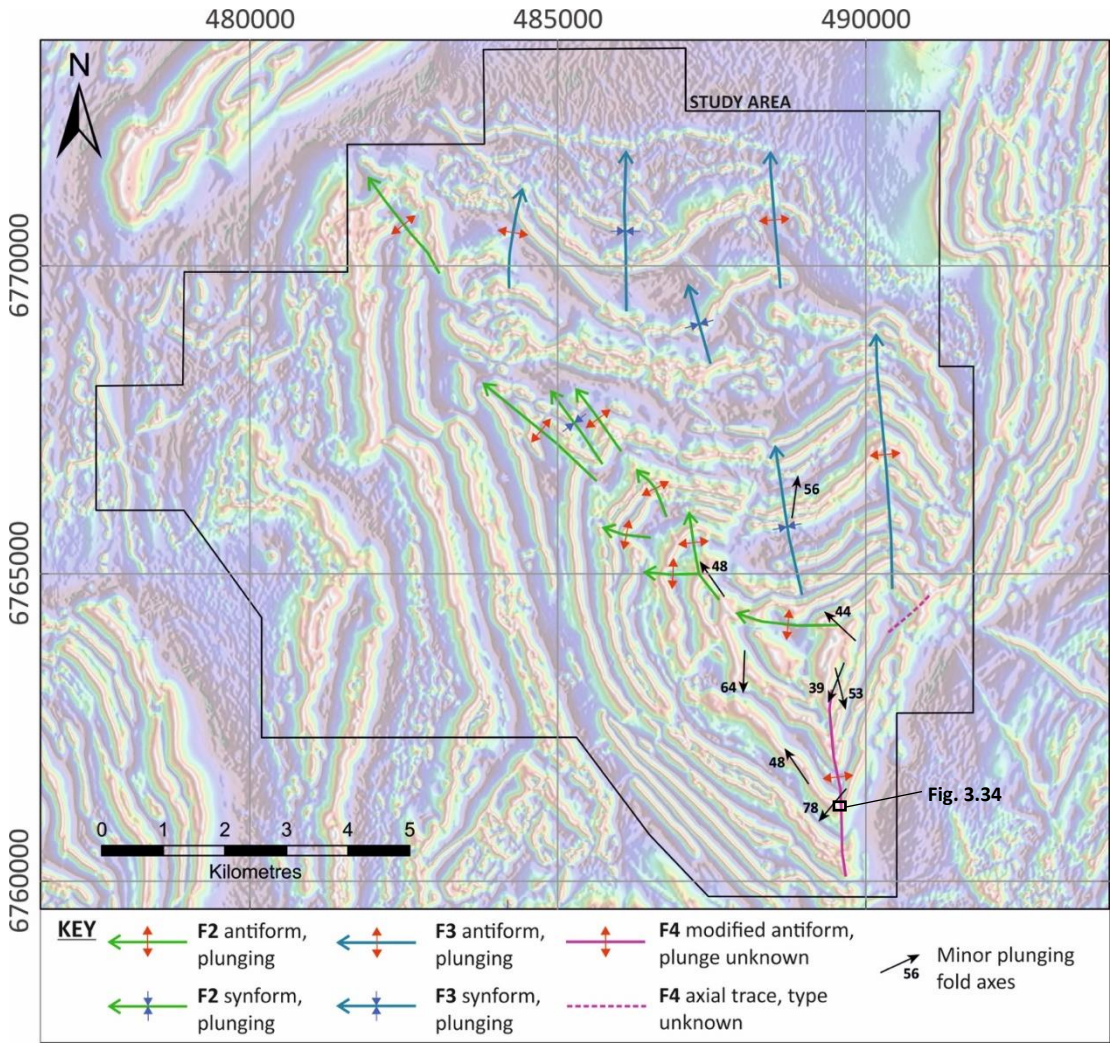

Figure 3.29: Reduced to pole (RTP) aeromagnetic map of the study area with different generations of folding symbolised, in addition to the trend of minor, outcrop scale fold axes and their plunge angles. The location of major fold axes is based on geological mapping (see Appendix A) and various aeromagnetic imagery, including that shown above (courtesy of Minjar Gold Pty.). The approximate location of Figure 3.34 is indicated in the southeast.

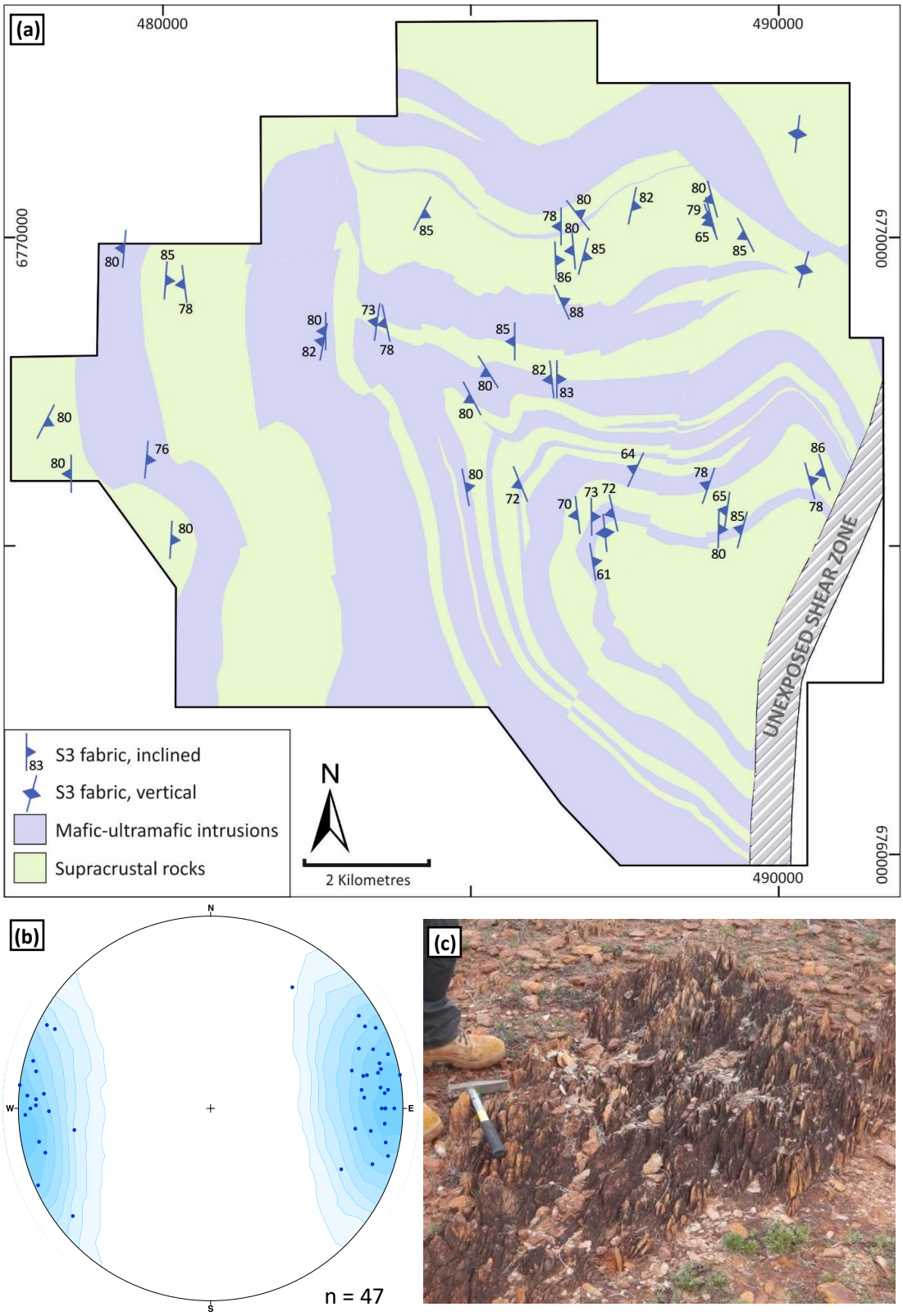

Figure 3.30: Map, stereonet and field photograph of S_3 fabric. **(a)** Simplified geological map showing the orientation of S_3 foliations measured in the study area; **(b)** Lower hemisphere equal area stereonet of S_3 N-S trending foliation, with kamb contours shaded in blue at contour intervals of 2σ; **(c)** Outcrop of metabasalt with well-developed S_3 N-S trending foliation (loc. 8.092).

expression of the original dome prior to multiple episodes of refolding (Fig. 3.25). This early dome precedes all other large-scale folds and is deformed and refolded by subsequent events in the same

manner as the layer-parallel S_1 fabric and F_1 folding. It is possible that the domal geometry and layer-parallel fabric could be attributed to separate deformation events. However, as there is no way to distinguish these features and the dome, layer-parallel fabric and layer-parallel folding predate all other structures apart from bedding, they are collectively ascribed to D_1.

3.5.4 D_2 Deformation

D_2 deformation is characterised by a group of NW-SE trending metre- to kilometre-scale F_2 folds that are focussed in the central portion of the study area, including the major ~12km-wavelength fold axis that defines the Rothsay Fold (Fig. 3.29). F_2 consists of open to tight, upright and symmetrical folds that plunge towards the northwest at angles of 35-55°. Two pairs of box folds occur within the axis of the major F_2 structure, hosted by rocks of the upper Macs Well Clastics and Mountain View Sill (Fig. 3.29). At and near the hinges of major F_2 folds, outcrops of layered units such as BIF and ferruginous siltstone are usually highly deformed and contain abundant tight to isoclinal metre-scale F_2 folding, also northwest-plunging at similar angles to the major folds (Fig. 3.28c). Several F_2 folds close to major fold hinges are asymmetric, consistent with parasitic folding (Fig. 3.28d). The F_2 group of folds are not associated with an axial planar fabric. F_2 folds deform bedding and the S_1 layer-parallel foliation and refold the D_1 dome structure, but predate shearing and faulting according to cross-cutting relations.

3.5.5 D_3 Deformation

D_3 deformation is characterised by refolding of F_2 folds into a series of N-S trending F_3 folds and the widespread development of an axial planar S_3 foliation. F_3 folds comprise several km-scale upright, symmetrical antiform-synform pairs on the northeast limb of the Rothsay Fold, with north-plunging

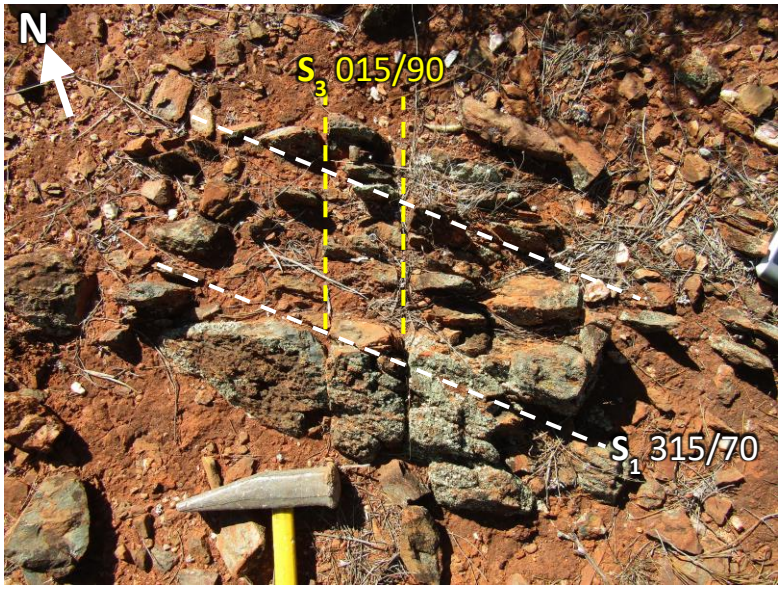

Figure 3.31: Foliated basalt outcrop comprising an S_1 foliation (315/70 NE) overprinted by an S_3 spaced cleavage (015/90). Note that this outcrop contains a less penetrative S_3 fabric than typically present (loc. 10.059).

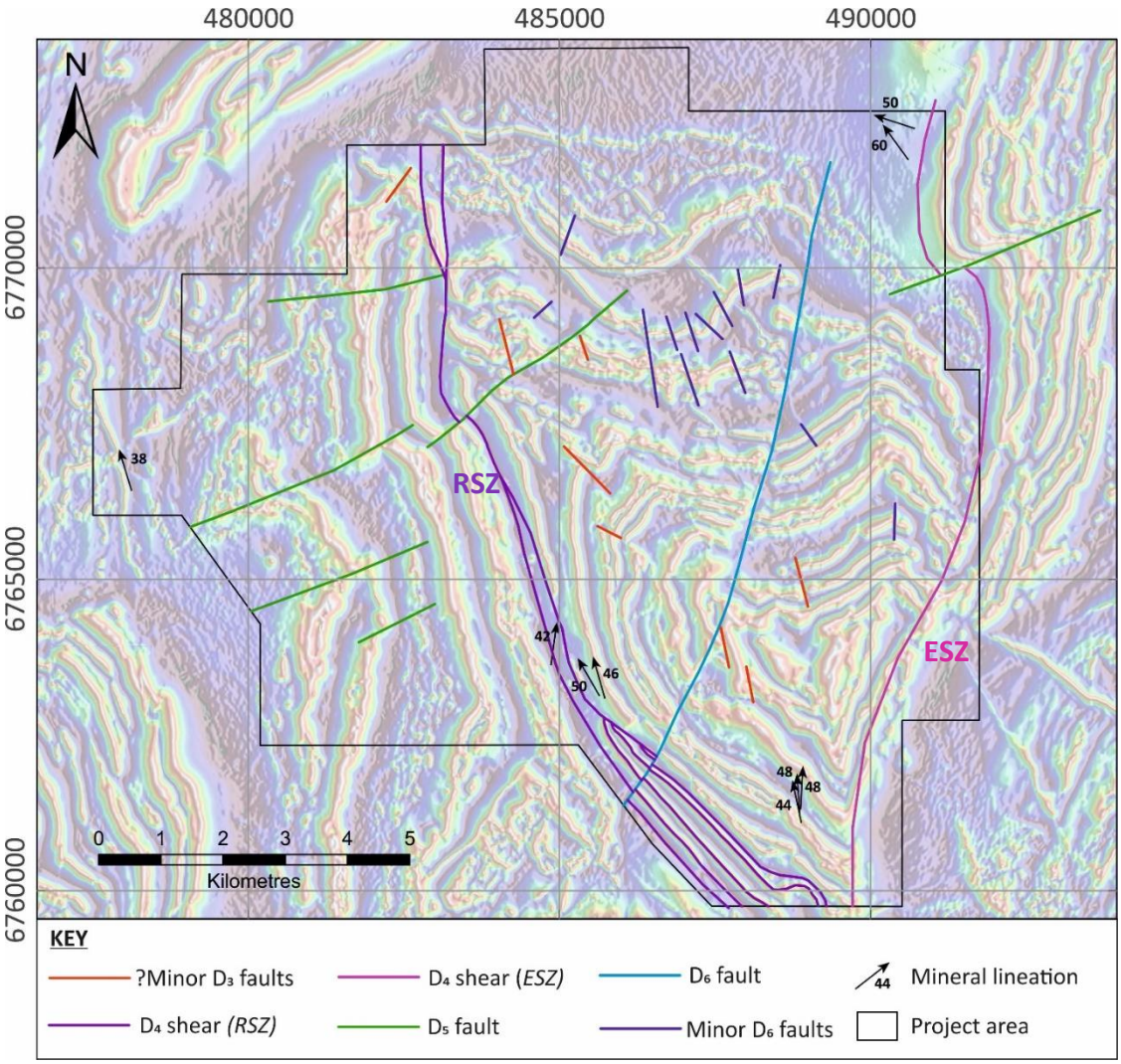

Figure 3.32: Reduced to pole (RTP) aeromagnetic map of the study area, with all major faults and shears symbolised by type and mineral lineations symbolised with plunge angles labelled. ESZ = Enchanted Shear Zone; RSZ = Rothsay Shear Zone. Aeromagnetic imagery courtesy of Minjar Gold Pty.

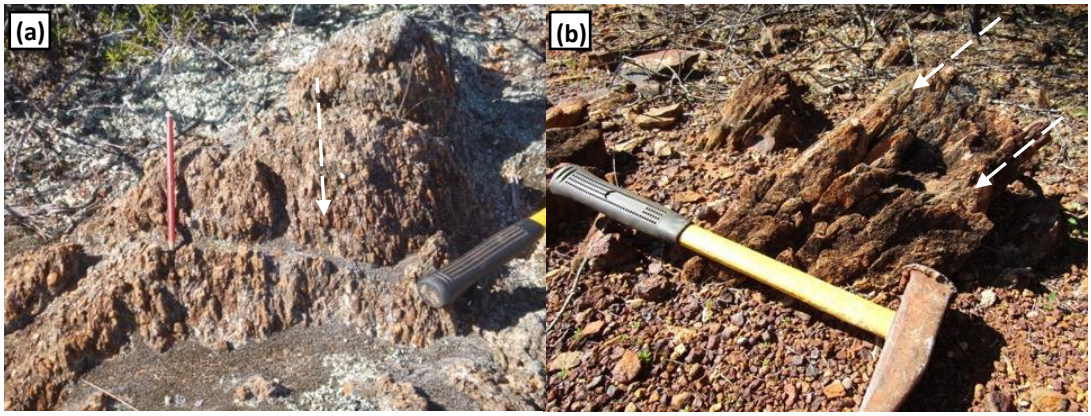

Figure 3.33: Outcrops with linear fabrics; **(a)** Conglomerate close to the Enchanted Shear Zone with elongated clasts defining the lineation (shown by pencil; hammer handle points north; loc. 10.101); **(b)** Linear fabric shown by a fine-grained basalt outcrop along the RSZ – hammer handle points north (loc. 15.045).

fold axes (Fig. 3.29). These folds refold the northeast limb of the major F_2 fold and the S_1 layer-parallel foliation, and therefore postdate D_1 and D_2 deformation. Outcrop-scale F_3 folds preserved in

metasedimentary units in the north of the study area replicate the larger F_3 folds with axes that plunge towards the north at ~55° (Fig. 3.29). Less common instances of similar metre-scale folding in the south have axes that plunge 60-65° towards the south, despite the absence of larger, km-scale F_3 folds as found in the north.

The most extensively-developed fabric in the Rothsay area is a pervasive S_3 foliation that varies in orientation from NNE to NNW and is axial planar to F_3 folds (Fig. 3.30a). S_3 typically dips steeply to the west or the east at angles of 65-85° and is occasionally vertical (Fig. 3.30b). This foliation is typically preserved in aphyric and spinifex-textured basalts, particularly well developed in rocks of the Mulga Volcanics (Fig. 3.30c), as well as serpentinite in mafic-ultramafic intrusive complexes. Less commonly, S_3 is found in coarse grained mafic intrusive rocks as a spaced cleavage. No lineations have been identified in association with S_3. In outcrops where multiple fabrics are preserved, the S_3 foliation crosscuts the layer-parallel S_1 foliation (Fig. 3.31) and also transects F_2 folds. S_3 can be most easily distinguished from the layer-parallel S_1 fabric in areas where bedding is at an oblique angle to S_3, such as the northeast limb of the Rothsay Fold, however, in areas where the strike of S_1 and S_3 is close to parallel, they are more difficult to differentiate. In contrast to the layer-parallel S_1 foliation, S_3 does not increase in intensity towards lithological contacts, but is pervasive throughout the succession. Several minor NW to NNW-trending sinistral faults with <40 m offset in the hinge zones of D_3 folds may be attributed to the late stages of D_3 shortening (Fig. 3.32).

3.5.6 D_4 Deformation

D_4 deformation is represented by two major NNE- to NNW- trending D_4 shear zones in the Rothsay area, namely the Enchanted Shear Zone (ESZ; Section 3.5.6.1) and the Rothsay Shear Zone (RSZ; Section 3.5.6.2), each described in detail below. These D_4 shear zones are continuous for at least ~15 km along strike and are characterised by strongly foliated and lineated rocks (Fig. 3.32). Foliation intensity increases proximal to and within these two shear zones, defining an S_4 fabric that overprints S_1 and S_3 foliations. The orientation of S_4 foliations are parallel to the regional trend of the respective shear zone (NNE to NNW), which is broadly similar to that of S_3 foliations. However, S_4 fabrics are typically more intense than S_3 and S_4 is commonly accompanied by a mineral lineation (L_4).

L_4 lineations within D_4 shear zones consist of mineral stretching lineations in rocks where individual crystals can be distinguished, such as coarse-grained mafic intrusions. Conglomerate outcrops proximal to the Enchanted Shear Zone possess an L_4 lineation, defined by the elongation of quartz clasts (Fig. 3.33a). In fine-grained volcanic rocks, foliated outcrops themselves can possess a linear fabric despite the grain size being too small to distinguish minerals (Fig. 3.33b). L_4 lineations for both

D_4 shear zones in the Rothsay area consistently trend towards the north-northwest to north-northeast, and plunge at angles between 38-60°, most frequently ~50°. D_4 shear zones dissect F_2 fold axes and the S_1 layer-parallel foliation, and the intense S_4 foliation associated with these shear zones consistently overprints the regionally pervasive S_3 fabric.

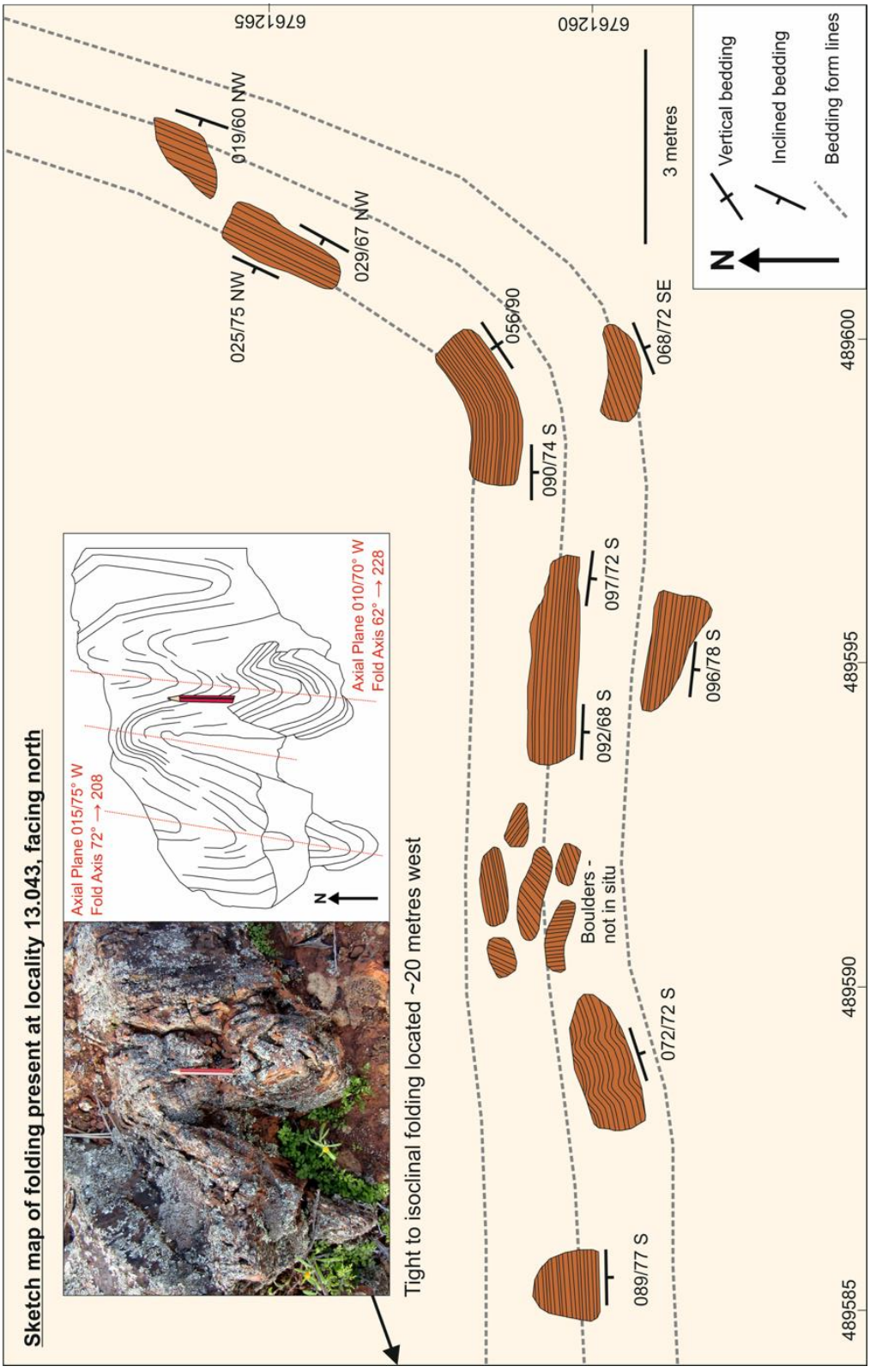

Figure 3.34: Sketch map of outcropping ferruginous siltstone and BIF at locality 13.049, showing the change in orientation of bedding on approach to the Enchanted Shear Zone. The inset photograph and accompanying sketch shows folding present in this unit 20 metres west – axial planes are marked in red and are parallel to the orientation of the transposed bedding.

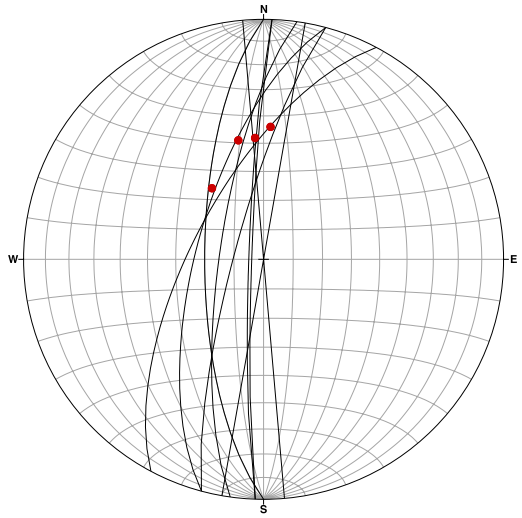

Figure 3.35: Lower hemisphere equal area stereonet showing foliation planes proximal to the Enchanted Shear Zone (black), and mineral lineation measurements taken on some of these planes (red).

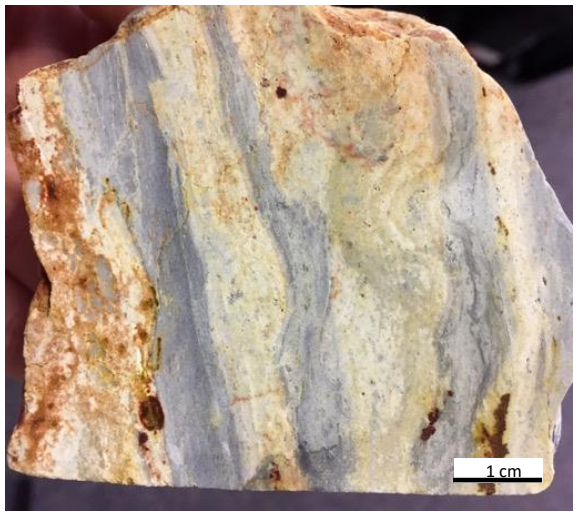

Figure 3.36: Strongly foliated banded quartzite sampled close to the Enchanted Shear Zone (loc. 12.008).

3.5.6.1 Enchanted Shear Zone (ESZ)

The ESZ is a NNE-trending D_4 shear zone situated at the eastern margin of the study area that is largely unexposed, covered along its length by superficial cover (Fig. 3.32). S_4 foliation measurements in rocks exposed along the shear zone are steeply west-dipping at 65-80° to vertically-dipping in some outcrops. L_4 mineral lineations are prevalent in strongly foliated outcrops close to the shear zone, and consistently plunge towards the north-northwest at angles of 44-60° (Fig. 3.35). The orientation of this lineation suggests an oblique sense of movement along the shear zone, and the presence of a vertical component of movement. Unfortunately, no shear sense indicators have been observed within the ESZ; a consequence of the generally poor exposure.

Multiple 100 m-scale fold structures present at the western margin of the ESZ are visible on aeromagnetic imagery, and represent folding associated with deformation along the ESZ. Furthermore, these folds also give an indication of the original geometry of the D_1 dome in this part of the area, which has since been subject to multiple refolding events and shearing. In the far south of the study area, several southeast striking magnetic anomalies deflect towards the northeast on approach to the ESZ, ostensibly defining an additional southeast limb (Fig. 3.29). Unfortunately, outcrop is generally poor in this part of the area, however, a small exposure is present at locality 13.043, located on the hinge of one of these folds (Fig. 3.29). At this locality, a 5 m-thick unit of bedded ferruginous siltstone can be traced across one such fold, from the southwest limb to the apparent southeast limb (Fig. 3.34). The orientation of bedding changes significantly across the outcrop: to the west, bedding is southeast-striking and dips 60-70° southwest, consistent with the outward-dipping pattern of bedding elsewhere in the area. Bedding in the western part of the outcrop is rotated such

that it is E-W striking and dipping 70-80° south. Over the course of 20 metres towards the east, the orientation of bedding progresses to ENE-striking and vertical to NNE-striking and dipping 60-75° northeast (Fig. 3.34), matching the trend of magnetic anomalies (Fig. 3.32). This supports the presence of a southeast limb and indicates that the units comprising this limb are overturned, dipping steeply to the northwest (Fig. 3.7; Cross Section 2).

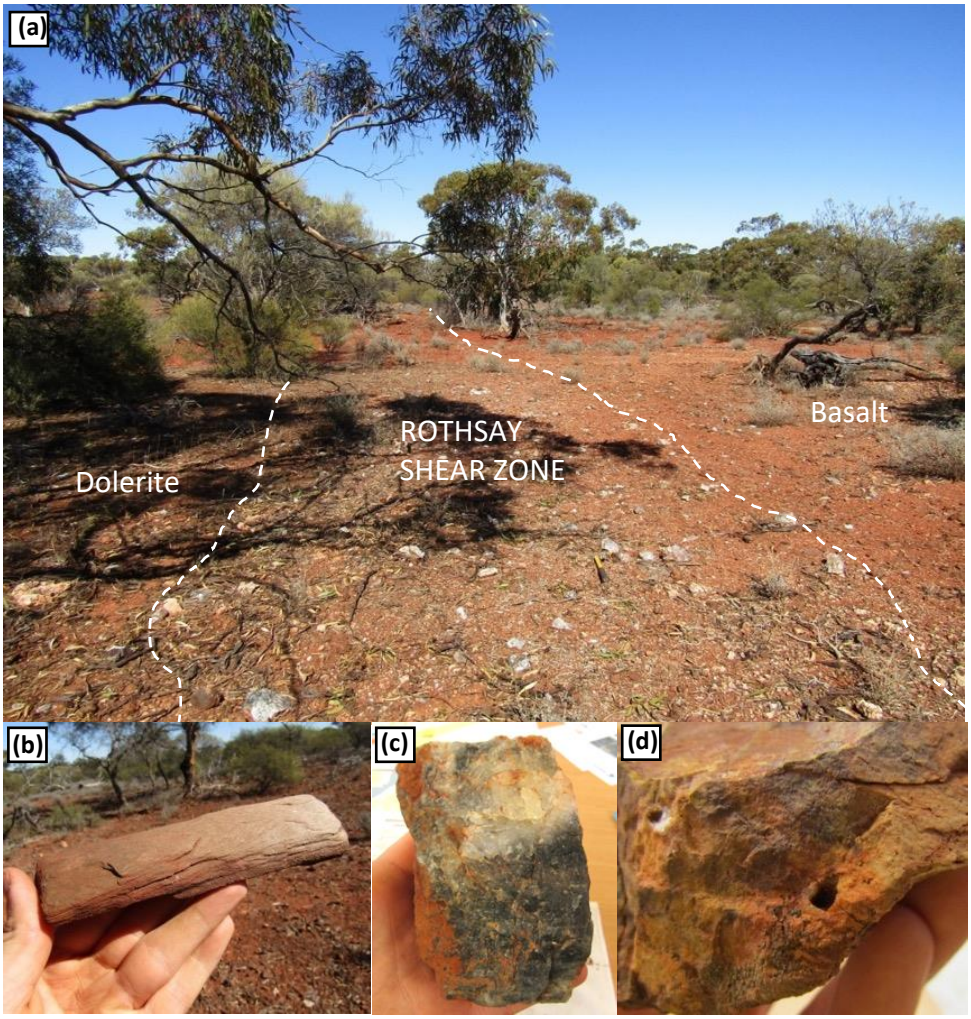

Figure 3.37: Features observed along the Rothsay Shear Zone at locality 6.124. **(a)** View facing south showing the change in subcrop from dolerite (E) to basalt (W) across the shear zone and quartz and highly foliated material along the contact trending at 350°; **(b)** Sheared material; **(c)** Grey/white quartz from the contact; **(d)** Leached material and mouldic cast, possibly after pyrite.

Elsewhere along this southeast limb (e.g., loc. 12.008), an outcrop of bedded quartzite is also NNE-striking and dips towards the northwest at 77°. This quartzite outcrop comprises yellow and grey banding, which in places is intensely folded (Fig. 3.36). Foliation measurements along the margins of the shear zone also dip steeply to the northwest, suggesting that bedding has been deformed into the shear. Occurrences of 50 cm-scale folding are present at locality 13.043, near the ESZ (Fig. 3.34). The axial planes of these folds are parallel to the bedding on the southeast limb and parallel to foliation measurements close to the shear zone. Therefore, these folds are interpreted as minor F_4 folds formed

during D_4 shearing. The coincidence of overturned bedding and axial planes of outcrop-scale folding, both of which are parallel to the northwest-dipping S_4 fabric along the ESZ, is indicative of shortening and supports a reverse component of shearing along the ESZ.

3.5.6.2 Rothsay Shear Zone (RSZ)

The RSZ is a north to NNW-striking D_4 shear zone located in the western part of the study area (Fig. 3.32). The shear zone is parallel to the supracrustal stratigraphy along much of its length, focused along the contact between the Rothsay Sill and overlying Beryl West Volcanics. The exposure and geometry of the RSZ is different in the northern and southern portion of the Rothsay area. In the north, the shear zone is generally poorly exposed, rarely outcropping as strongly foliated talc-chlorite schist, but usually concealed by superficial cover. In areas of cover, the position of the RSZ can be distinguished from changes in float lithology (Fig. 3.37a), usually accompanied by strongly foliated and occasionally lineated float (Fig. 3.37b), dense quartz float (Fig. 3.37c) and leached, oxidised rocks (locally containing sulphide mouldic casts; Fig. 3.37d). The shear zone appears to be relatively narrow (<50 m) based on float mapping. The few foliation measurements taken from sporadic outcrops are inconsistent, dipping to the west or east at 65-85°. An L_4 mineral lineation close to the RSZ plunges north at 42°.

The southern extent of the Rothsay Shear Zone is markedly different to that in the north (Fig. 3.32). A striking feature in the south is the repetition of a distinctive 200-250 m-thick sequence of rocks three times, as opposed to once elsewhere along strike. These rocks comprise serpentinite, porphyritic pyroxenite and gabbro of the intrusive Rothsay Sill, and host at least six discrete shears located along lithological contacts, primarily at the margins of serpentinite units. The rock units within the RSZ and between individual shears are overturned and dip towards the northeast at 68-78° (Fig. 3.8; Cross Section 3). An S_4 foliation that dips ~65° northeast is consistent with the orientation of the shears. On aeromagnetic imagery, there is a lack of horizontal displacement along shear zones, suggesting a significant vertical component to movement. Further to the northeast of the shear zone, rocks in the underlying succession that dip to the southwest gradually become more steeply dipping, to vertical, to overturned and dipping ~65° northeast on approach to the RSZ (Fig. 3.8; Cross Section 3). This geometry is consistent with the development of a duplex structure along the southern extent of the RSZ and supports a significant reverse component to D_4 shearing.

3.5.7 D_5 Deformation

D_5 deformation is represented by a series of ENE-striking, sinistral, brittle D_5 faults. As is the case with shear zones, faults are very poorly exposed in the Rothsay area, largely as a consequence of prolonged weathering. These structures are most easily identified on aeromagnetic imagery as offset magnetic anomalies. Field evidence also confirms the presence of faults and shear zones. In the field, these structures are typically characterised by several distinctive features: linear valleys in areas of outcrop, thick transported cover dispersed with large eucalyptus trees, waterways following the trend of the structure, and an increase in quartz float on the surface, signifying hydrothermal activity. Due to the lack of sufficient outcrop, little is known about the sub-surface orientation of most of these structures.

D_5 sinistral faults have apparent offsets on the order of 120-250 m, and step towards the northwest (Fig. 3.32). One such D_5 fault outcrops at locality 8.164, where it comprises a narrow (<10 m) outcrop of green talc-chlorite schist and exhibits ~200 m sinistral offset of a BIF unit. Gentle folding of supracrustal units adjacent to D_5 faults is consistent with fault drag associated with synchronous D_5 faulting and demonstrates both brittle and ductile deformation during this episode of deformation. The occurrence of several oblique fabrics with similar orientations on outcrops proximal to D_5 faults may be attributed to D_5 deformation, however these fabrics have not been fully characterised due to a limited dataset. D_5 faults and their associated fault drag transect F_2 and F_3 fold axes and deform both D_4 shear zones, thus D_5 faults post-date D_4 shearing. Notably, pegmatite dykes mapped in the area are also ENE-trending and broadly parallel to D_5 structures (Section 3.4.4).

3.5.8 D_6 Deformation

D_6 deformation, signifying the most recent deformation observed in the Rothsay area, is represented by a major NNE-striking dextral D_6 fault that is continuous for over 10 km and cross cuts all other structures, including the RSZ and D_5 faults (Fig. 3.32). The apparent offset along this D_6 fault varies from 75 m in the north, to 150 m in the south, based on offset aeromagnetic anomalies (Fig. 3.32). In contrast to D_5 faults, no fault drag is associated with this D_6 structure. There is very little exposure along its length, and it is instead typified by thick transported cover and increased density of vegetation. Minor N-S striking dextral faults located in the north of the study area are not laterally continuous and commonly correspond to minor valleys in the field (Fig. 3.32). As these faults have similar orientations and similar apparent offsets (typically 50-80 m, but up to 140 m) to the major D_6 fault, these may represent minor D_6 faults developed during this late deformational event.

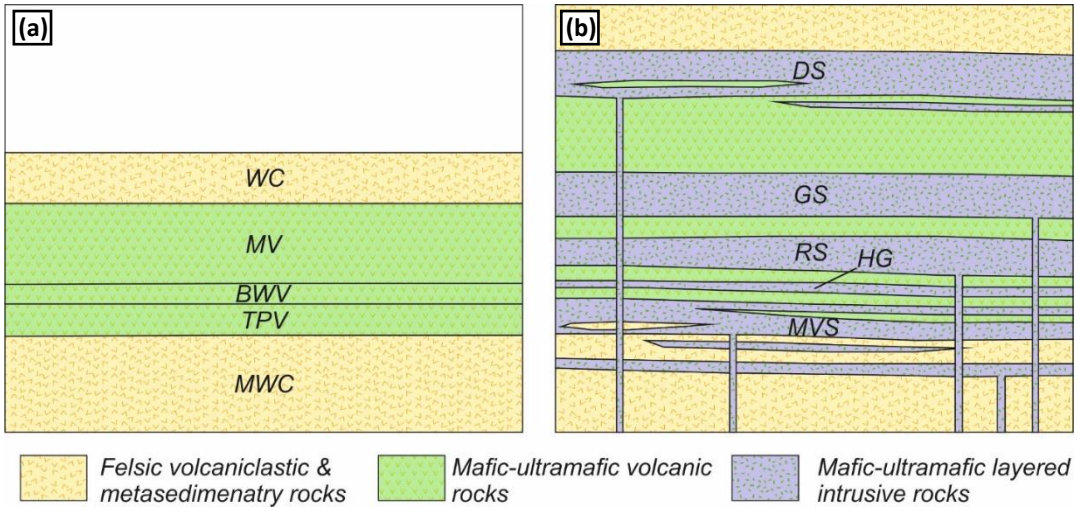

Figure 3.38: Schematic diagrams for the stratigraphic development of the Rothsay area. **(a)** Emplacement of the supracrustal succession comprising a lower sequence of felsic volcaniclastics and metasedimentary rocks (MWC; Macs Well Clastics), an overlying mafic succession (TPV; Two Peaks Volcanics, BWV; Beryl West Volcanics, MV; Mulga Volcanics), and an upper felsic/metasedimentary sequence (WC; Willowbank Clastics); **(b)** Subsequent intrusion of a network of mafic-ultramafic layered sills (MVS; Mountain View Sill, HG; Honeycomb Gabbro, RS; Rothsay Sill, GS; Gardner Sill, DS; Damperwah Sill).

3.6. Discussion

3.6.1 Supracrustal History

The ~4.2 km-thick volcano-sedimentary stratigraphy in the Rothsay area comprises a broadly bimodal succession, akin to other supracrustal greenstone successions in the Murchison Domain and elsewhere in the Yilgarn Craton (e.g., Watkins and Hickman, 1990; Van Kranendonk et al., 2013). A lower ~1.4 km-thick package of felsic volcaniclastic and metasedimentary rocks (Macs Well Clastics) is overlain by a ~2 km-thick mafic volcanic-dominated succession (Two Peaks Volcanics, Beryl West Volcanics, Mulga Volcanics), representing the Chulaar Group. In turn, these rocks are succeeded by further (>750 m-thick) felsic volcaniclastic and lesser metasedimentary rocks (Willowbank Clastics; Fig. 3.38a). Contrasting lithologies and features of the two felsic successions, as well as a lack of structures indicative of structural repetition, demonstrate that the upper and lower felsic packages are distinct and form separate components of the bimodal succession. Together, the supracrustal units at Rothsay form part of two volcanic cycles, as has previously been described for the northeastern Murchison Domain by Van Kranendonk and Ivanic (2009). These cycles record a change from effusive mafic and ultramafic volcanism, to more explosive felsic volcanism, separated by intervals of sedimentation.

Metasedimentary rocks of the lower Macs Well Clastics are representative of a marine depositional environment and a period of broad volcanic quiescence. Fluctuations in the depositional energy in the system resulted in alternations between deposition of quartz sandstone-dominated units and finer-grained ferruginous siltstone. The increasing occurrence of felsic volcaniclastic interbeds with stratigraphic height reflect the onset of felsic volcanism in the region, coincident with the minor

eruption of porphyritic dacitic lavas in the Rothsay area. The upper Macs Well Clastics record a coarsening of metasedimentary units, consistent with increasing depositional energy that likely reflects shallowing of the water column. Pebbly sandstone units with conglomeratic horizons are succeeded by thicknesses of bedded felsic volcaniclastic rocks, which contain evidence for sedimentary reworking in the form of cross-bedding. Volcaniclastic units are significantly thicker in some areas than in others, potentially signifying closer proximity to volcanic vents.

After this episode of felsic volcanism, the minor deposition of BIF during volcanic quiescence was followed by the eruption of a significant ~750 m pile of largely aphyric basalt, represented by the Two Peaks Volcanics and Beryl West Volcanics. Occasional, thin flows of porphyritic dacite near the base of this pile represent more fractionated lavas and multiple thin (5-15 m) horizons of BIF and quartzite within the mafic succession represent sedimentation during interruptions in volcanism. A single ~30 m unit of pyroxene spinifex-bearing volcanic rocks towards the top of the Two Peaks Volcanics denotes the first such komatiitic rock of the succession, which increase in both abundance and thickness with stratigraphic height. A further cessation in mafic volcanism is represented by the deposition of a laterally-continuous magnetite-chert BIF unit across the area (>20 km). This is immediately followed by a thin 5 m horizon of lapilli-bearing bedded tuff, recording ongoing distal volcanism. The presence of erosive bases and graded bedding indicate that these tuffs were at least partly affected by sedimentary reworking.

Tuff deposition was followed by the resumption of extensive mafic volcanism, resulting in the development of a 1250 m-thick lava pile comprising variolitic, pillowed and spinifex-textured basalts. This period of volcanism commenced locally with the eruption of a thick (~20 m) unit that cooled to form pyroxene spinifex-textured volcanic rocks and allowed the development of an ultramafic olivine-bearing cumulate. Similar spinifex-textured units are interspersed amongst the dominantly mafic succession, signifying pulses of komatiitic volcanism during the overall mafic volcanic episode. The lateral continuity of individual spinifex-bearing flows reflects the development of extensive lava plains (e.g., Watkins and Hickman, 1990) and pillow structures exhibited by some basalt flows are indicative of extrusion in a submarine setting. The prevalence of spinifex-textured pyroxene rather than olivine is a feature of many greenstone belts in the Murchison Domain (Lowrey et al., 2017; Van Kranendonk et al., 2013). The textures observed in the Rothsay area are consistent with the acicular, platy and string-beef pyroxene spinifex-textures described by Lowrey et al. (2017) in the northeastern Murchison Domain. Mafic volcanic rocks are overlain by a further, more extensive 140 m-thickness of lapilli-bearing tuff. These rocks are almost identical in appearance to the thin tuff horizon at the base of the Mulga Volcanics and demonstrate ongoing distal volcanism following the end of local volcanism,

albeit for a significantly longer period. The top of the bedded tuff signifies the cessation of mafic volcanism.

Overlying poorly-outcropping black mudstone of the Willowbank Clastics represents deposition in a low-energy, environment with little volcanic input, such as a deep marine or an anoxic lake setting. The upwards transition from mudstone to increasingly coarse, more mature and volcanogenic sedimentary rocks, including greywacke and pebbly sandstone, documents increasing energy and closer proximity to felsic volcanism. Proximal felsic volcanism is represented by overlying lapilli-bearing volcaniclastic rocks and ash beds that show a progressive compositional evolution up sequence. Ongoing felsic volcanism has resulted in several hundred metres of fine-grained felsic volcaniclastic rocks, minor felsic volcanic interbeds and welded tuffs, the latter retaining primary flow fabrics. Towards the top of this sequence, laterally-discontinuous lenses of quartz conglomerate containing large (10 cm+) clasts bound by volcanogenic sandstone represent subaerial exposure, and the movement of rivers reworking largely volcaniclastic material at the surface, marking the top of the stratigraphy exposed in the study area.

The mapping undertaken in this study is considerably more detailed than that by Baxter and Lipple (1985). As such, a multitude of new units have been identified, some of which form important components of the stratigraphy, for example the felsic volcaniclastic rocks near the base of the succession. The application of float mapping in areas of little exposure has also allowed the correlation of distinctive marker horizons across a greater extent of the area than in previous, large-scale mapping. As a consequence of more detailed mapping, the relationship between supracrustal rocks and mafic-ultramafic intrusive rocks has been much better constrained (Section 3.4.4). Recent regional-scale synthesis geological mapping has suggested that a significant unconformity is present in the northern and western margins of the study area, marking the unconformable contact between the main greenstone supracrustal succession and overlying metasedimentary rocks of the Mougooderra Fm (Ivanic, 2019). Elsewhere in the YSGB, this contact is exposed as a sheared angular unconformity (Watkins & Hickman, 1990), which is proposed to represent an interval of up to 60 Ma (Zibra et al., 2018). It is not clear whether the Willowbank Clastics form part of the Mougooderra Fm based on the geological mapping presented in this study. Further, the contact between the Willowbank Clastics and the underlying Chulaar Group rocks is not exposed in the Rothsay area and so the presence of an unconformable contact cannot be fully established. In this study, no clear supporting evidence has been identified in favour of such an unconformity; bedding measurements remain consistent either side of the contact and deformation is consistent throughout the stratigraphy. However, it must be noted that the northern and western peripheries of the study area suffer from poor exposure, so it is possible that superficial cover is obscuring evidence. Very similar

features are shown by the upper Macs Well Clastics and upper Willowbank Clastics, whereby fine grained metapelites are overlain by increasingly mature and coarse metasedimentary rocks (pebbly sandstone, conglomerate), prior to felsic volcaniclastic units. This likeness suggests that the units are part of a repeated volcanic cycle. Similar repeated volcanic cycles are demonstrated by Norie Group and Polelle Group rocks in the northeastern Murchison Domain (Van Kranendonk et al., 2013).

3.6.2 Intrusion of Mafic-Ultramafic Rocks

Mafic-ultramafic intrusive rocks comprise a significant component (2.6 km; ~39%) of the stratigraphic succession exposed in the Rothsay area. This is consistent with the northeastern Murchison Domain, where several generations of mafic-ultramafic layered intrusive rocks comprise approximately 40% by volume of the greenstones present (Van Kranendonk and Ivanic, 2009). Mafic-ultramafic intrusive complexes also form an integral component of greenstone belts in other cratons, such as the Kaapvaal Craton of South Africa (Anhaeusser, 2006).

At Rothsay, five distinct sills are present at different stratigraphic levels, all of which display compelling evidence for a concordant intrusive relationship with supracrustal rocks (Fig. 3.38b). This is best exemplified by the lowermost Mountain View Sill, which shows upward chemical evolution, decreasing grain size towards its top, an upper, finer-grained chilled margin, rafts of supracrustal units (BIF and basalt) within the intrusion and lenses of underlying supracrustal rocks (felsic volcaniclastics) near its base. These features are consistent with the intrusion of a network of mafic-ultramafic sills of variable thickness following emplacement of the volcano-sedimentary stratigraphy (Fig. 3.38b). It is not clear whether the sills were intruded progressively, coeval with the emplacement of supracrustal rocks, or intruded subsequently. Mafic-ultramafic intrusive complexes have been deformed and metamorphosed in the same manner as surrounding supracrustal rocks, thus were intruded horizontally prior to deformation and metamorphism of the succession. Some of the intrusions are focussed at significant rheological boundaries, such as the contact between felsic volcaniclastic and mafic volcanic successions, and their upper and lower boundaries are frequently in contact with BIF units.

Dolerite and gabbro are the dominant lithologies present in the intrusions. In-situ differentiation of thick (up to 700 m) sills has led to well-developed magmatic layering, comprising cumulate olivine-bearing peridotite bases, coarse-grained pyroxenite and gabbroic centres, which grade upwards into dolerite and variably leucogabbroic and granophyric tops. Some of the intrusive complexes display a single differentiation trend, thus represent a single, thick pulse of magma into the crust, which has subsequently differentiated (e.g., Gardner Sill, Rothsay Sill). In contrast, the Mountain View Sill shows

ambiguous differentiation trends and lacks any significant cumulate ultramafic layer(s), suggestive of multiple thinner, overprinting pulses of magma. The Damperwah Sill has a highly evolved quartz dioritic upper portion, including the presence of primary quartz, however, little else can be ascertained about its structure due to extremely poor exposure. In the northeastern Murchison Domain, mafic-ultramafic complexes are interpreted as having been the emplaced as shallow-level subvolcanic sills during eruption of the overlying supracrustal units (Van Kranendonk and Ivanic, 2009). The older, lowermost intrusions show evidence of multiple magmatic pulses and complex layering, in contrast to younger sills which are typically thinner and resemble a single pulse of magma (Ivanic et al., 2010). This same trend is observed in the Rothsay area, with the lowermost Mountain View Sill comprising multiple overprinting intrusions, and overlying Rothsay and Gardner sills more closely resembling a single pulse of magma.

A notable characteristic of the layered mafic-ultramafic sills at Rothsay is the significant lateral continuity of component lithologies. The distinctive Honeycomb Gabbro can be traced along strike for at least 15 km, and a thin (<30 m) ultramafic cumulate portion of the Rothsay Sill is present over a strike length of > 19 km. Such extensive continuity of layering is indicative of the relatively rapid intrusion of large volumes of magma into the crust. With the assumption that the other horizontal direction at least equals the observed strike length, the ~550 m thick Rothsay Sill represents the emplacement of magma with a volume of at least 198 km^3. Other intrusions, most notably the Gardner Sill, pinch out towards the east, marking the margins of the intrusive complex.

The typical characteristics described above are remarkably consistent with rocks of the ~2800-2790 Ma Warriedar Suite, mapped in the western Youanmi Terrane, including the northern part of the YSGB (Zibra et al., 2017a, 2016). The Warriedar Suite consists of mafic-ultramafic intrusive rocks, present largely as sills as well as a number of large intrusive complexes, including the ~66 x 4.5 km Gnanagooragoo Igneous Complex (Ivanic, 2019). Rocks of this suite are typified by well-developed magmatic layering, ultramafic cumulate bases, evolved often granophyric tops, and geometries that are laterally extensive for thicker sills, and that wedge out along strike for thinner sills (Ivanic, 2019). All these features are exhibited by the sills in the Rothsay area, suggesting that they are equivalent to intrusions of the Warriedar Suite.

3.6.3 Intrusion of Felsic Rocks

Felsic intrusions exposed in the Rothsay area are limited to several narrow (< 5 m) felsic, post-deformational pegmatite dykes that crosscut all stratigraphic units, major structures and lode-gold mineralisation in the area. Pegmatite dykes are ENE-oriented and increase in abundance towards an

unexposed granitic intrusion present in the southeast; part of the 50 x 25 km Seeligson Monzogranite (Bald Rock Supersuite) that dissects the YSGB (Zibra et al., 2018; Fig. 2.5). The close association of felsic pegmatites with the Seeligson Granite supports a genetic relation between the two, and suggests they were emplaced as part of the same intrusive episode, following folding, shearing and emplacement of lode-gold mineralisation. These observations are consistent with the 'post-tectonic granitoid' classification ascribed to the Seeligson Monzogranite by Watkins and Hickman (1990). The Seeligson Monzogranite has since been assigned to the Walganna Suite of low-Ca felsic intrusions, comprising biotite ± muscovite monzogranites to syenogranites (Van Kranendonk et al., 2013; Zibra et al., 2018). As is the case in the Rothsay area, Walganna Suite intrusions are known to host pegmatites enriched in LILE elements (Fetherston et al., 2017). Where pegmatites have intruded through Cr-enriched ultramafic rocks, they have been known to crystallise green beryl (emerald), such as at Poona, near Yalgoo (Ivanic, 2019). This explains the occurrence of emerald to the south of the Rothsay mine, where pegmatites intrude ultramafic cumulate portions of the Rothsay and Gardner sills.

3.6.4 Deformational History

The structural geology of the Rothsay area records a complex history comprising at least six discrete deformational episodes. Several features formed early during the deformational sequence, namely the layer-parallel S_1 fabric and the D_1 domal geometry, can be explained in terms of several different deformational mechanisms. D_1 doming could be explained in terms of fold superposition or alternatively, granitic diapirism, whereas the layer-parallel S_1 fabric could signify an early episode of layer-parallel shearing, or a manifestation of diapirism. The evidence supporting each of these mechanisms is evaluated in the following sections, with comparisons drawn to deformation in other Archaean terranes. A structural model for the Rothsay area is then presented in Section 3.6.5.

3.6.4.1 Layer-Parallel Shearing

The layer-parallel S_1 fabric observed in the Rothsay area could be interpreted as evidence of an early episode of layer-parallel shearing. Minor metre-scale layer-parallel folding may also be attributed to this early layer-parallel deformation. Early sub-horizontal, layer-parallel fabrics are a feature frequently observed in supracrustal belts in many Archaean cratons (e.g., Swager & Griffin, 1990; Kwelwa et al., 2018). Detailed structural mapping in several greenstone belts has identified low-angle structures associated with layer-parallel fabrics within supracrustal assemblages, which are interpreted to represent early layer-parallel tectonism. In the eastern Yilgarn Craton, Swager & Griffin

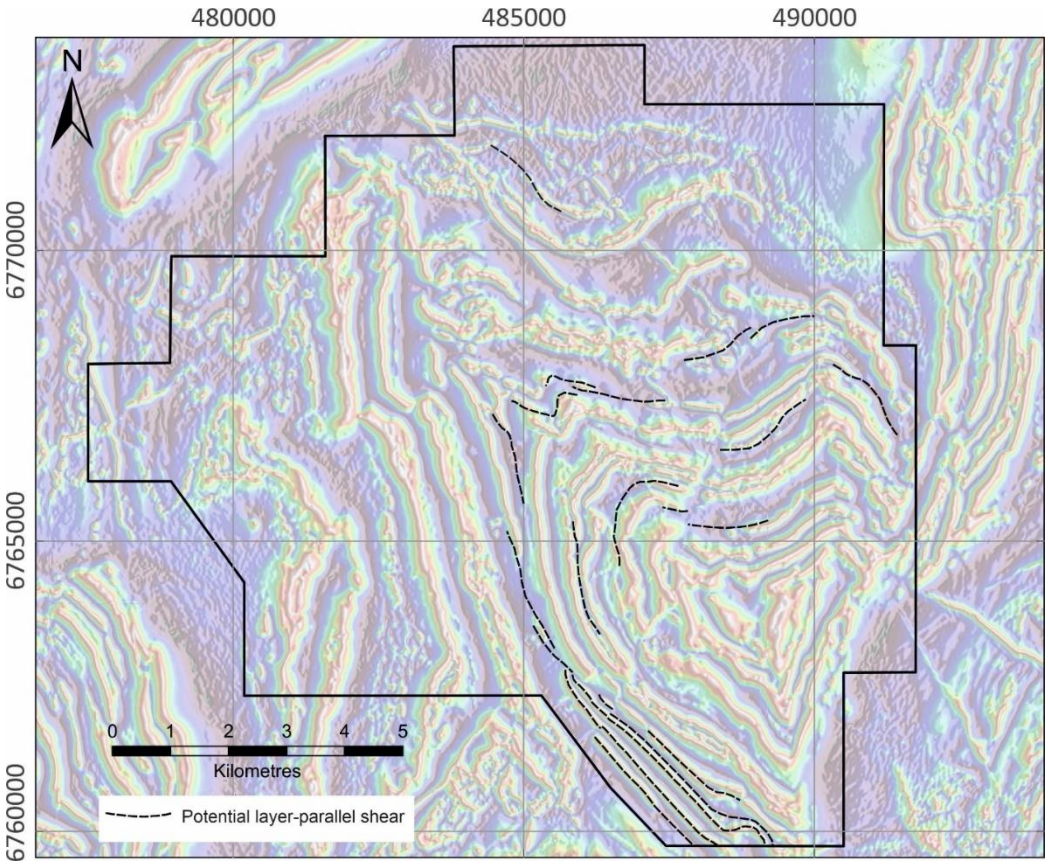

Figure 3.39: Reduced to pole (RTP) aeromagnetic map of the study area outlining the potential location of layer-parallel shears based on discontinuous magnetic anomalies or structural repetition of units.

(1990) recognised early subhorizontal thrust faults that resulted in significant thickening of the supracrustal sequence and stratigraphic repetition in duplex structures. Imbricate stacking of supracrustal units in the Zimbabwe Craton has also been attributed to an early episode of layer-parallel shearing (Dirks & Jelsma, 1998; Hofmann et al., 2001). This deformation was preserved as a layer-parallel D_1 foliation associated with an anastomosing network of narrow shear zones (Dirks & Jelsma, 1998).

In the Rothsay area, no layer-parallel shears have been observed, although the intensity of the layer-parallel S_1 fabric does increase at particular stratigraphic levels. Unlike many areas in which layer-parallel shears have been identified (e.g., Swager & Griffin, 1990; Hofmann et al., 2001), there is no significant repetition of the supracrustal stratigraphy at Rothsay, other than that present along the Rothsay Shear Zone (Section 3.5.6.2). Although no layer-parallel shears have been mapped, it could be argued that the many instances of laterally discontinuous or intermittent units are representative of attenuation of the stratigraphy against layer-parallel structures. These discontinuities are most clearly illustrated on aeromagnetic imagery, whereby magnetic units such as ferruginous siltstone, BIF and peridotite pinch out along strike, sometimes multiple times (Fig. 3.39). Furthermore, the structural repetition of units along the southern portion of the Rothsay Shear Zone (Fig. 3.39) could

be interpreted as having formed during an early period of layer-parallel thrusting, then subsequently reactivated during D_4 shearing. In the Geita greenstone belt, Tanzanian Craton, early sub-horizontal shears within the succession can be very thin and inconspicuous, despite the widespread and pervasive nature of associated layer-parallel fabrics (Sanislav et al., 2017). For this reason, the generally sparse outcrop in the Rothsay area is not good enough to preclude the presence of early layer-parallel shears.

Conversely, most of the laterally discontinuous units present in the Rothsay area can be suitably explained in terms of magmatic processes and relationships (Section 3.4.4), such as the prevalent screens and rafts of BIF and basalt within intrusive sill complexes. Similarly, structural repetition along the RSZ could be wholly attributed to D_4 shortening (Section 3.5.6) in the absence of early layer-parallel deformation. The identification of the S_1 layer-parallel fabric in parts of the study area where all units appear to be continuous for many kilometres (even 10's of km) also disputes the occurrence of significant sub-horizontal, layer-parallel structures in the area.

3.6.4.2 Fold Superposition

The general outward-dipping pattern of bedding measurements in the Rothsay area (Section 3.5.2), together with the identification of a deformed southeastern limb at the margin of the ESZ (Section 3.5.6), are consistent with the former presence of a dome, which precedes D_2 and all subsequent deformation. The origin of domal geometries in granite-greenstone terranes have long been a subject of controversy (e.g., Snowden & Bickle, 1976). One of the principal dome-forming mechanisms proposed to explain such structures is fold interference, whereby superposition of folds from at least two broadly orthogonal horizontal shortening events results in the development of a domal structure, commonly in the form of a doubly plunging anticline. It has been postulated that fold interference is responsible for the archetypal granite-greenstone pattern of the Pilbara Craton, in which most domes are dominated by vast granitic batholiths (Blewett, 2002). Fold superposition has also been suggested for the development of the greenstone-dominated North Pole Dome of the Pilbara Craton, which is cored by a ~5 km-wide granitic stock at the current erosional level (Blewett et al., 2004b) and closely resembles the geometry of the Mt. Mulgine Dome, to the northwest of the study area (Fig. 2.9). Similarly, Myers & Watkins (1995) suggested fold interference was responsible for the dominant granite-greenstone pattern in the southwestern Murchison Domain of the Yilgarn Craton, and in particular, the ovoid geometry of the Yalgoo Dome, situated immediately northwest of the study area. The Yalgoo Dome was attributed to superposition of upright folds from an earlier period of N-S shortening and subsequent E-W shortening (Myers & Watkins, 1995).

Superposition of multiple fold generations has undoubtedly played a role in the later stages of the structural development of the Rothsay area, as evidenced by multiple F_3 folds within the northeast limb of the major northwest-plunging F_2 fold. However, the role of fold interference in forming the initial domal structure is less clear. It is possible that such a dome-shaped structure could have resulted from superposition of two broadly orthogonal, upright folding events, as suggested locally by Myers & Watkins (1995). Fold interference would have to have occurred after the development of the layer parallel S_1 fabric, as this fabric is deformed in the same manner as the dome. A similar sequence of events has been documented in the Geita greenstone belt, Tanzania, in which an early layer-parallel S_1 fabric was subsequently affected by D_2-D_3 interference folding of the succession (Kwelwa et al., 2018). However, considering that F_2 folds in the Rothsay area developed during an episode of NE-SW shortening, this would require a preceding or subsequent shortening episode to have been oriented approximately NW-SE, in order to form a dome. Crucially, no structural evidence (i.e., fabrics, folds) supporting an episode of NW-SE shortening in the early stages of deformation have been observed in the Rothsay area.

3.6.4.3 Diapirism

An alternative explanation for the early domal geometry observed in the Rothsay area is that it developed during a period of granitoid diapirism and/or partial convective overturn and was subsequently refolded and deformed by multiple shortening events. Doming of supracrustal material can be achieved through the diapiric emplacement of granitic material and the outward movement of overlying rocks, resulting from gravitational instability (Collins, 1989; Collins et al., 1998; Van Kranendonk et al., 2002). These diapiric processes have been proposed for the formation of domes and the characteristic dome-and-keel regional patterns in the Pilbara Craton (Van Kranendonk et al., 2004) and in the Zimbabwe Craton (Jelsma et al., 1993). Furthermore, granite-cored domes in the eastern Yilgarn Craton have also been attributed to granitic diapirism (Davis et al., 2010). Recently, diapirism has been proposed for the development of the Yalgoo Dome (Zibra et al., 2018; Zibra et al., 2020) (Fig. 2.9), in contrast to previous models invoking fold superposition (Myers & Watkins, 1985; Watkins & Hickman, 1990). Zibra et al. (2018) also suggested that the structural framework of the areas surrounding the Yalgoo Dome were affected primarily by interference between roughly coeval diapirs.

If diapirism is considered responsible for the development of the initial dome in the Rothsay area, then modification of the structure through NE-SW shortening (forming plunging F_2 folds) and E-W shortening (forming F_3 folds) can suitably account for the present, refolded domal architecture. The Rothsay area would therefore comprise a diapiric dome refolded by at least two superposed groups

of folds. An episode of granite diapirism could also sufficiently explain the layer-parallel S_1 fabric in the Rothsay area, which could have developed during layer-parallel shearing between units as a consequence of diapiric uplift (e.g., Zibra et al., 2018). Such shearing would likely have been focussed in weaker units (i.e., basalt, peridotite) and at contacts between units with significant competency contrasts, accounting for the apparent increase in intensity of S_1 fabrics at major lithological contacts. Furthermore, and perhaps most compelling, is the presence of an analogous domal structure 15 km to the northeast of the study area, where the Mt. Mulgine Dome is composed of outward dipping supracrustal units and is cored by a granitic intrusion (Fig. 2.9). This granite, known as the Mt. Mulgine granite, is genetically related to the Yalgoo Dome, for which there is extensive structural evidence in favour of diapirism (e.g., Zibra et al., 2018; Clos et al., 2019a). The Mt. Mulgine Granite and granitic rocks comprising the Yalgoo Dome have been dated at ca. 2750 Ma (Champion & Cassidy, 2002; Zibra et al., 2018), consistent with regional polydiapirism at this time (Zibra et al., 2020). Supracrustal units deformed around the Mt. Mulgine Dome also preserve a layer-parallel foliation and host radially-oriented faults (Fig. 2.9); both attributed to doming associated with diapirism (Zibra et al., 2018).

During the geological mapping undertaken as part of this study, no granitic intrusion has been observed at or near the core of the dome at Rothsay, as would be expected for a diapiric dome (e.g., Van Kranendonk et al., 2004; Davis et al., 2010). Furthermore, no evidence of contact metamorphism or hydrothermal alteration has been observed in supracrustal rocks comprising the core of the fold, and metasedimentary units are relatively unaltered, albeit very poorly exposed. A plausible explanation is that the granitic core is concealed at the current level of erosion and remains at depth, in contrast to other neighbouring diapiric intrusions which are exposed at the cores of structures such as the Yalgoo and Mt. Mulgine domes (Fig. 2.9).

On balance, deformation associated with granite diapirism sufficiently explains both the early domal architecture and the layer-parallel fabric and is also consistent with regional geological studies in the southwestern Murchison Domain (e.g., Zibra et al., 2018; Clos et al., 2019a; 2019b; Zibra et al., 2020), which provide compelling evidence in favour of a major episode of granitic diapirism in the region at c. 2750 Ma. For these reasons, granitic diapirism is considered the favoured mechanism for the early structural development of the Rothsay area according to this study. However, in the absence of further detailed structural mapping and with limited exposure, early layer-parallel shearing and formation of a dome through fold interference cannot currently be fully discounted.

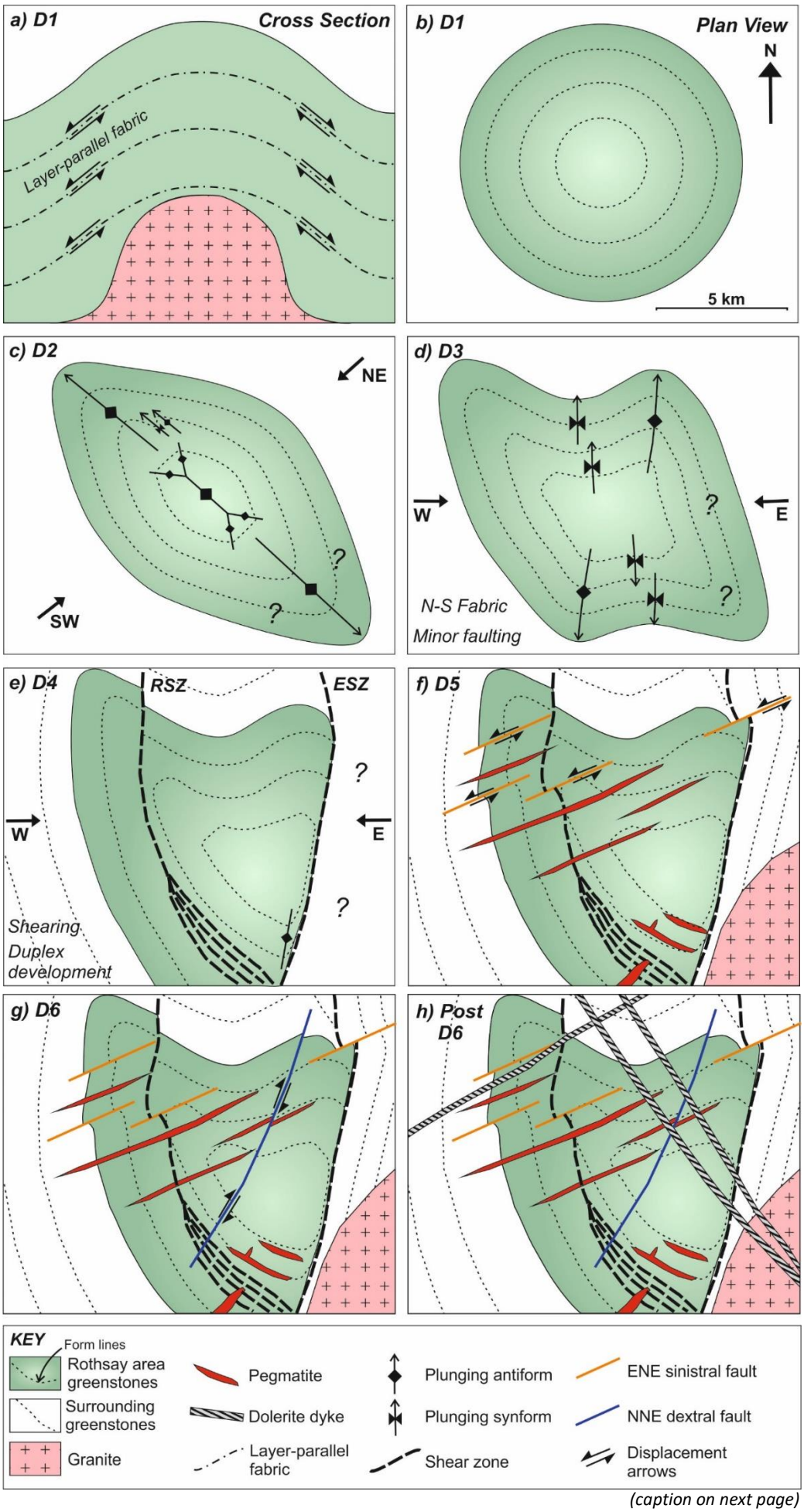

(caption on next page)

Figure 3.40 (previous page): Schematic diagrams illustrating the structural development of the Rothsay Fold. **(a)** D1 – Cross section illustrating granite diapirism forming a domal structure in overlying supracrustal units. Layer-parallel shearing developed the layer-parallel foliation, focused in fine grained units and at contacts between units of high competency contrast; **(b)** D1 – Plan view of dome structure, consisting of a radial pattern of outward dipping units; **(c)** D2 – NE-SW shortening, leading to deformation of the domal structure and the formation of a major NW-plunging antiform and associated box fold axes, in addition to minor NW-SE trending fold axes; **(d)** D3 - E-W shortening resulting in the development of overprinting N-S trending fold axes on the northeast limb of the structure (possibly replicated on the southern limb) and a pervasive N-S striking foliation; **(e)** D4 – Localisation of strain during continued E-W shortening leads to the development of two major shear zones (ESZ; Enchanted Shear Zone, RSZ; Rothsay Shear Zone), which both show evidence of a significant vertical component of movement. The RSZ displays duplex development in the south and the southeastern limb of the dome is inverted by the ESZ; **(f)** D5 - ENE-oriented sinistral faulting and associated folding (fault-drag) that deform shear zones, coeval with the intrusion of parallel ENE-striking pegmatite dykes, directly related to the intrusion of the Seeligson Monzogranite to the southeast; **(g)** D6 – Late-stage, brittle, dextral fault dissecting the area including shear zones; **(h)** Post-D6 – Intrusion of (near)-vertical doleritic dykes discordant to all units and structures in the area, marking the final stage of crustal development.

3.6.5 Structural Model

In this section, a model for the structural deformational framework of the Rothsay area is presented, based on the structural observations and measurements described in this study. The model comprises six deformational episodes (D_1-D_6). The earliest deformation, for which evidence is the most ambiguous, occurred subsequent to the emplacement of a thick succession of supracrustal units and laterally extensive, voluminous mafic-ultramafic intrusions, attributed to a period of broad extension (D_0). The details and features associated with each of these deformational episodes are outlined in Table 3.2 and illustrated schematically in Figure 3.40.

The first deformational event (D_1) distinguished in the Rothsay area is relatively well-preserved as a layer parallel S_1 fabric and the original domal geometry of the area (which has since been significantly modified). Doming is suggested to have developed during a period of granitic diapirism, in association with several other diapirs in the surrounding areas including the Yalgoo Dome and the Mt. Mulgine Dome (Zibra et al., 2020) (Fig. 3.40b). As a consequence, supracrustal rocks overlying a granitic diapir were uplifted, and layer-parallel shearing occurred along lithological contacts, primarily focussed in weaker rock types and resulting in a conspicuous S_1 layer-parallel fabric (Fig. 3.40a). The discontinuity of some units, primarily basalt and BIF, can be fully explained in terms of magmatic processes relating to the intrusion of a network of mafic-ultramafic sills prior to deformation.

The second deformational event, D_2, consisted of a period of NE-SW shortening, resulting in the constriction of the domal structure and the formation of a northwest-plunging antiform in the northwest, associated with other minor, parasitic F_2 folding (Fig. 3.40c). Some box-folding also developed during this shortening episode. It is possible that an equivalent southeast-plunging antiform developed in the southeast, however evidence is obscured by subsequent deformation and granite intrusion. No discernible fabric is associated with D_2 deformation.

The third episode of deformation (D_3) comprised a period of E-W shortening, resulting in refolding of the northern part of the dome into a series of north-plunging and north-south striking open F_3 folds (Fig. 3.40d). The major F_2 fold axes may also have been slightly deformed towards the north during D_3. This event is also responsible for the pervasive N-S striking, steeply-dipping foliation (S_3) frequently preserved in rocks of the area, broadly axial-planar to F_3 folding. This fabric is equivalent to the regional tectonic grain present across much of the Murchison Domain (Van Kranendonk et al., 2013; Watkins and Hickman, 1990).

Subsequent D_4 deformation is attributed to the localisation of strain during ongoing E-W shortening, resulting in the development of the two major NNE- and NNW-trending shear zones in the area, the Rothsay Shear Zone and the Enchanted Shear Zone (Fig. 3.40e). Both shear zones display evidence for a significant vertical component of shear. For example, the RSZ exhibits a complex duplex structure consisting of overturned supracrustal units, an oblique down-dip stretching mineral lineation and the thickness of mafic-ultramafic sills differs considerably on either side of the shear. Furthermore, abundant sub-horizontal ladder veins observed in the Rothsay mine along the RSZ also support a vertical component of shear, considering that mineralisation was concomitant with shearing (de Vries, 2015). The ESZ also possesses an oblique down-dip mineral lineation, exhibits small scale F_4 folding with axial surfaces parallel to the shear plane and is responsible for overturning the south-eastern limb of the original domal architecture of the Rothsay Fold (Fig. 3.40e). The orientation of the RSZ and ESZ matches that of other major shear zones in the belt (Fig. 2.8), indicating they formed as part of the same sustained episode of E-W shortening. It is possible that the ESZ is the southernmost extension of the Mougooderra Shear Zone, located to the north (Fig. 2.8). The RSZ and ESZ also broadly match the NNE to NNW-striking shear zones present in the northeastern Murchison Domain (Van Kranendonk et al., 2013; Watkins and Hickman, 1990). Seismic reflection profiles across the Murchison Domain and neighbouring Southern Cross Domain display listric NW-dipping crustal-scale thrust systems (Wyche et al., 2013). These structures are thought to be responsible for shortening across the region (Wyche et al., 2013) and likely correspond to the D_3 and D_4 deformation events described above.

The fifth phase of deformation, **D_5**, consisted of NE-SW shortening and resulted in the development of a series of ENE-trending, sinistral faults offsetting the two major D_4 shear zones in the area, the RSZ and the ESZ, as well as all pre-existing folds (Fig. 3.40f). Supracrustal units are deformed towards these structures, consistent with fault drag. This event may also be responsible for the development of some oblique late-stage fabrics near these structures that are not consistent with S_1 or S_3 orientations. Felsic pegmatite dykes cross cutting the supracrustal stratigraphy are also ENE-trending, parallel to the D_5 faults, and also crosscut earlier folding and D_4 shearing (Fig. 3.40f). Further, emplacement of these

ENE-striking dykes is consistent with NE-SW shortening and an approximate NW-SE σ_3 direction. For these reasons, it is suggested that pegmatites were intruded during D_5 deformation, and by extension, the emplacement of the Seeligson Monzogranite with which pegmatites are directly associated. The intrusion of the 50 x 25 km Seeligson Monzogranite dissected the greenstone belt and may have caused minor tilting of units and structures in the study area to the northwest, enhancing the plunge of F_2 and F_3 folds.

A minor subsequent deformation event, **D_6**, involved NNE-oriented dextral faulting that cross cuts the RSZ (Fig. 3.40g). The lack of folding associated with this fault suggests it occurred during late-stage deformation in the brittle regime. Unfortunately, the subsurface orientation of this fault is not constrained, however, the board continuity of the stratigraphy on either side tentatively suggests the lack of a significant vertical component of movement. Furthermore, other minor N-S to NNW-SSE trending faults in the north of the study area with similar offsets to the major D_6 fault, likely represent minor D_6 faults developed during this episode. Finally, a period of regional extension resulted in the intrusion of several orientations of near-vertical dolerite dykes. These dykes crosscut all lithologies and structures, are principally oriented NW-SE but also NE-SW and mark the final stage of the lithological and structural development of the area (Fig. 3.40h). These dykes are prevalent across much of the Murchison Domain and wider Yilgarn Craton and are widely regarded to be Proterozoic in age (e.g., Watkins and Hickman, 1990; Ivanic et al., 2010; Ivanic, 2019).

3.7 Summary

The geology of the Rothsay area consists of a ~6.8 km-thick stratigraphic succession, comprising 4.2 km of supracrustal rocks and 2.6 km of mafic-ultramafic sills. The supracrustal stratigraphy comprises a bimodal sequence of felsic volcaniclastic rocks accompanied by metasedimentary rocks, and mafic-ultramafic volcanic rocks. Components of two bimodal sequences are present: a lower felsic association, an overlying mafic-ultramafic association, and an uppermost felsic association. Many units have been recognised that have not previously been identified by larger-scale regional mapping (Baxter and Lipple, 1985). Supracrustal rocks have been divided into the Chulaar Group, which comprises the lowermost Macs Well Clastics, Two Peaks Volcanics, Beryl West Volcanics and Mulga Volcanics, in addition to the stratigraphically uppermost Willowbank Clastics. Although structural measurements indicate that the basal contact of the Willowbank Clastics does not appear to represent an angular unconformity as previously suggested (e.g., Ivanic, 2019), a lack of exposure prevents the true nature of the contact from being fully established.

A suite of four mafic-ultramafic layered intrusive sills have intruded the supracrustal succession. Each sill complex is distinct; lower sills represent multiple overprinting episodes of magmatism whereas upper sills document a single pulse of magma. Most of these sills show remarkable lateral continuity over distances in excess of 20 km, signifying rapid emplacement of magma, followed by in-situ differentiation. A granitic pluton, the Seeligson Monzogranite, intruded the succession in the southwest and is directly related to a set of parallel ENE-striking pegmatite dykes, locally identified as Li-bearing, in addition to the previously known B-enrichment (Fetherston et al., 2017).

A deformational model is proposed to account for the structural development of the Rothsay area. The model invokes an early phase of granite diapirism (D_1) as responsible for the domal architecture of the area. This is consistent with previous structural studies of neighbouring areas (e.g., Clos et al., 2019a; Zibra et al., 2020), however the Rothsay dome is interpreted as not unroofed and a concealed granitic core is interpreted at depth. Diapirism was followed by subsequent NE-SW shortening (D_2) and E-W shortening (D_3), which caused refolding of the dome in multiple orientations and the latter imparted a regional N-S tectonic grain across the area. Diapiric doming and fold interference are typically considered to be exclusive processes; however, this study demonstrates an example of a diapiric dome that has been subjected to fold interference on a similar scale to that of the original dome. During ongoing E-W shortening, two major NNE to NNW-striking shear zones (D_4) formed, including the gold-mineralised RSZ, and consistently display a reverse component of shear. A subsequent episode of NE-SW shortening (D_5) led to further smaller scale faulting, coeval with the intrusion of the Seeligson Monzogranite pluton and associated pegmatitic dykes, followed by localised brittle faulting (D_6). The intrusion of cross-cutting doleritic dykes marks the final stages of development in the Rothsay area.

CHAPTER 4

Structural geology of the Yalgoo-Singleton greenstone belt

4.1 Introduction

Greenstone belts in Archaean terranes are commonly host to a diverse range of structures that record protracted and complex deformational histories and thus, are generally considered to be highly deformed. Whilst this is true for much of the southwestern Yilgarn Craton and parts of the Murchison Domain, rocks in the Yalgoo-Singleton greenstone belt (YSGB) include locally well-exposed sections through the supracrustal stratigraphy that preserve primary textures, depositional features and deformational structures (Chapter 3). Preservation of these features is assisted by relatively low metamorphic grade, typically upper greenschist-lower amphibolite facies, in addition to the heterogeneous distribution of strain. Although the outcrop situation is mostly poor in the southwestern Murchison Domain, the integration of geophysical datasets and oriented drillcore with surface observations allows a detailed assessment of the structural geology of rocks in the area. A thorough understanding of the deformational history of Archaean greenstone belts not only provides key constraints on geodynamic models but is also crucial for understanding the formation and distribution of mineral resources in a terrane that is prospective for lode-gold, base metal, Fe, W-Sn and Li mineralisation.

This chapter documents the structural geology of the YSGB, encompassing a summary of early (D_1) deformation in the region, and new field data focussing on the later deformation across the belt (D_2-D_6). This chapter compliments Chapter 3, which focussed on a better exposed, previously unmapped portion of the greenstone belt and attempted to improve constraints on the early phases of deformation. These two chapters provide a holistic view of the structural geology and deformational history of the YSGB.

The first part of this chapter consists of an introduction to the stratigraphic framework adopted by this study and a brief review of early deformation in the southwestern Murchison Domain, following

recent structural studies that have concentrated on the structural evolution of the Yalgoo Dome, situated immediately west of the YSGB (Zibra et al., 2018; Zibra et al., 2020). This is followed by a summary of methods and presentation of new field data focussing on the later structural history of the belt, including an interpretation of aeromagnetic data, lithological and structural mapping of several well-preserved stratigraphic sections, and logging of oriented drillcore intersecting two shear zones. The sedimentology of the Mougooderra Formation is described, following geological mapping at several exposures within this unit. Additionally, the geometry, structure and kinematics of three shear zones in the YSGB are described for the first time. The structural geology of the YSGB is then summarised at the end of this chapter. In combination with new geochronological data (Chapter 8), a new, unifying structural model for the YSGB is presented in Section 10.2, based on the structural features observed in the Rothsay area (Chapter 3) and structures observed elsewhere in the YSGB (this chapter).

4.2 Stratigraphic Framework

4.2.1 Supracrustal Rocks

The geology of the YSGB consists of several folded limbs of supracrustal rocks, surrounded and intruded by granitic batholiths (Watkins and Hickman, 1990) (Fig. 4.1). The base of the exposed volcano-sedimentary succession in the YSGB is marked by a ~2.5 km thick package of felsic and intermediate volcanic and volcaniclastic rocks and minor chemical sedimentary rocks, ascribed to the Gossan Hill Fm (Van Kranendonk et al., 2013; Ivanic, 2019). The Gossan Hill Fm is only exposed in the northeast of the study area, adjacent to the Golden Grove mining centre (Fig. 4.1). Rocks equivalent to this group are thought to represent the basement to the greenstone succession across the Murchison Domain (Wang, 1998; Wang et al., 1998).

Rocks of the Gossan Hill Fm are unconformably to disconformably overlain by a ~8 km-thick succession of mafic-ultramafic volcanic rocks interlayered with BIF and other interflow metasedimentary units (Watkins and Hickman, 1990). Parts of this succession have been ascribed to the Polelle and Norie groups during ongoing stratigraphic mapping (e.g., Ivanic, 2018; Zibra et al., 2017a, 2016), however, a significant proportion of the succession is yet to be assigned to a formal stratigraphic division. For this reason, the succession of predominantly mafic-ultramafic volcanic rocks overlying the Gossan Hill Fm will be informally referred to in this study as the Chulaar Group. The Chulaar Group is exposed in the YSGB as four detached supracrustal limbs: the Badja, Chulaar, Mt. Mulgine and Rothsay limbs (Fig. 4.1).

The Chulaar Group is unconformably overlain by rocks of the metasedimentary Mougooderra Fm; a shear-bounded, 2-3 km-thick fining upward siliciclastic sequence, containing conglomerate, quartz

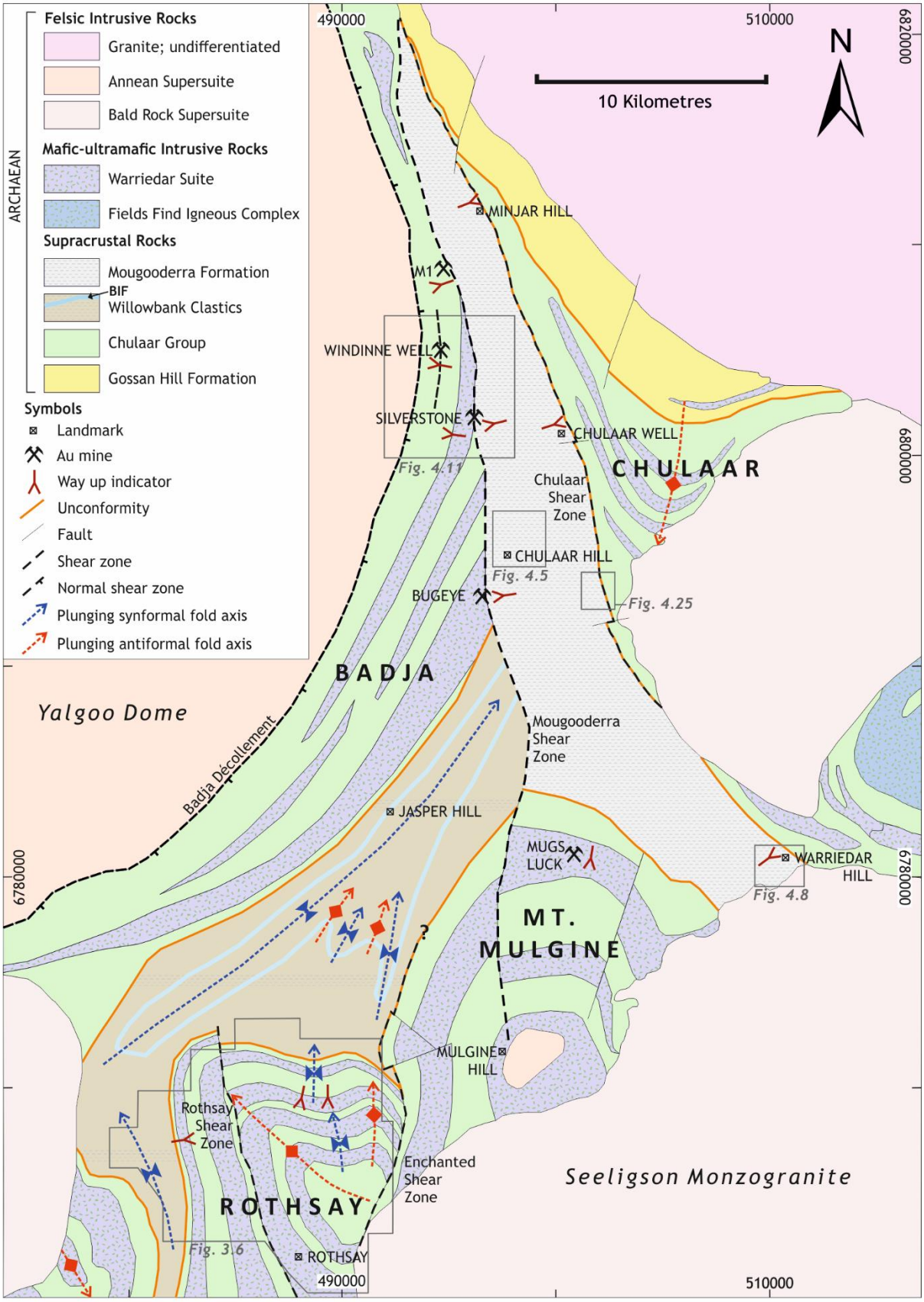

Figure 4.1: Simplified geological map of the central Yalgoo-Singleton greenstone belt, showing major structural features including fold axes, shear zones and granitoids. Way-up indicators are described in Section 4.5.3. Also shown are the extents of other geological maps included in this chapter. Geology modified after Baxter & Lipple (1985), Zibra et al. (2016), Zibra et al. (2017a) and Ivanic (2018). Grid provided in the GDA94/MGA Zone 50 co-ordinate system.

sandstone and shales, with minor chert, BIF, intermediate volcanic rocks and felsic volcaniclastic rocks (Ivanic, 2018; Watkins and Hickman, 1990). The Mougooderra Fm occupies a north-south trending, basin-like geometry in the centre of the YSGB that typically varies in width between 1-7 km (Fig. 4.1). The Mougooderra Shear Zone (MSZ) and Chulaar Shear Zone (CSZ) form the western and eastern margins of the Mougooderra Fm, respectively.

The Willowbank Clastics are an informally named, unassigned succession of felsic volcaniclastic rocks, shale and BIF situated in the southwestern part of the study area, which overlies the Chulaar Group on the Rothsay and Badja limbs of the greenstone belt (Fig. 4.1). The nature of the contact between the Chulaar Group and Willowbank Clastics is poorly constrained due to a lack of exposure (Section 3.4.1.5). The Willowbank Clastics is in sheared contact with rocks of the Mougooderra Fm, separated by the MSZ in the east (Fig. 4.1). The Willowbank Clastics occur at a similar stratigraphic level and consists of similar rock types as present in the Mougooderra Fm. However, in the absence of geochronological or geochemical data, it is unclear whether the Willowbank Clastics are equivalent to the Mougooderra Fm, or represent an intermediate assemblage between the underlying Chulaar Group and overlying Mougooderra Fm that is only locally preserved. Due to this uncertainty, the Willowbank Clastics is maintained as a separate, informal unit in this study. In subsequent chapters, petrographic (Chapter 5), geochemical (Chapter 6) and geochronological analysis (Chapter 8) is used to assess whether the Willowbank Clastics are comparable to the Mougooderra Fm.

4.2.2 Intrusive Rocks

Rocks of the Gossan Hill Fm and Chulaar Group are intruded by a suite of thick mafic-ultramafic sills, occasionally in excess of ~1 km thickness, which are typically layered and comprise ultramafic basal cumulates, gabbroic centres and more highly evolved sill tops (Ivanic, 2018; Zibra et al., 2016). These sills are considered to be cogenetic and have been assigned to the intrusive Warriedar Suite (Section 2.3.1). A further major mafic-ultramafic intrusion in the far east of the YSGB is represented by the Field's Find Igneous Complex (Fig. 4.1; Ivanic, 2019).

The YSGB is surrounded by multiple generations of granitoid intrusions, many of which post-date major deformation in the belt ('post-tectonic granites'; Watkins & Hickman, 1990). The Yalgoo Dome to the west of the YSGB is composed principally of Goonetarra Granodiorite and is considered coeval with the 2x3 km Mt Mulgine Granite, situated at the core of a domal structure in the Mt Mulgine area (Fig. 4.1). Several post-tectonic granites of the Bald Rock Supersuite are present at the margins of the study area, most notably the Seeligson Monzogranite, which dissects the belt in the south (Fig. 4.1).

4.3 Review of Early Deformation in the Southwestern Murchison Domain

A comprehensive investigation of the early structural development of the southwestern Murchison Domain has recently been undertaken by GSWA geologists (Zibra et al., 2018; Clos et al., 2019a; Zibra et al., 2020). This work is described in detail in Section 2.4.3 and is summarised here. Structural analysis, coupled with regional mapping and geophysical data, indicate that the southwestern Murchison Domain contains an extensive (>100 x 100 km) granite-migmatite dome system, comprising at least seven domes separated by synformal greenstone keels (Zibra et al., 2020). The domes are of variable size (5-50 km) and are exposed at different structural levels; the Yalgoo Dome represents a large, deeply eroded dome, the Mt Mulgine Dome exhibits a small granitic core, and the Rothsay and Widdin domes may represent buried domes, with concealed granitic cores (Zibra et al., 2020).

Previous models that invoked superposed folds for the formation of the Yalgoo Dome (Myers & Watkins, 1985; Watkins & Hickman, 1990) are not supported by structural and kinematic data, which lack evidence of the necessary upright, orthogonal folding events required by this model (Zibra et al., 2018). Structural evidence such as prevalent domal fabrics and outward plunging lineations within domes, outward-plunging fold axes and lineations in supracrustal cover, and ubiquitous dome-up kinematics indicate that a normal shear zone around the margin of the Yalgoo Dome, the Badja Decollement, facilitated diapiric emplacement into the greenstone cover (Zibra et al., 2018; 2020). Zibra et al. (2020) suggests that multiwavelength polydiapirism is responsible for the distinctive dome-and-keel architecture of the region, best explained by incremental igneous diapirism, combined with sagduction and erosion of the greenstone cover. Consequently, the early structural development recorded by rocks in the area has resulted from the interference between multiple coeval diapirs (Zibra et al., 2018; 2020).

Detailed geological mapping presented in this study (Chapter 3) has led to a new structural model for rocks in the Rothsay area. The earliest stage in this model invokes a period of diapirism (D_1) to explain the original domal geometry and conspicuous layer-parallel foliation in the area (Section 3.6.5). This new data indicates that the Rothsay area is host to a 15 km-scale diapiric dome, likely associated with a concealed granitic core, which has subsequently been refolded during multiple shortening episodes.

4.4 Methods

4.4.1 Aeromagnetic Imagery

Images of aeromagnetic data are an essential tool for regional mapping of Archaean terranes such as the Yilgarn Craton and are used by government surveys as well as mining and exploration companies.

Aeromagnetic imagery of the southwestern Murchison Domain, processed from regional airborne surveys at 100-200 metre line spacing and ~50 metre ground clearance, is accessible as part of publicly available geophysical datasets from GSWA and Geoscience Australia. As part of this study, aeromagnetic imagery from these datasets have been used to assist structural interpretations, in combination with field evidence collected from drillcore and disconnected exposures across the YSGB.

Aeromagnetic imagery shows the distribution of magnetic minerals in rocks, principally magnetite, titanomagnetite and ilmenite. These minerals may be primary contents of a rock, or secondary minerals either derived from alteration or associated with mineralisation. Consequently, the supracrustal lithologies that are most readily distinguished on aeromagnetic imagery are BIF, serpentinite (derived from serpentinisation of olivine-bearing ultramafic rocks), and dolerite containing elevated magnetite and/or ilmenite. Primary magnetic signatures can be modified by magnetite destructive alteration commonly associated with Archaean lode-gold mineralisation, such as chlorite, sericite, carbonate and silica alteration. Alternatively, the emplacement of hydrothermal magnetite and/or pyrrhotite in some lode-gold deposits can result in an elevated magnetic response (Tripp, 2013). Offset magnetic anomalies are very useful indicators of structures such as faults and shear zones, which are characteristically very poorly exposed or unexposed in the region.

4.4.2 Lithological and Structural Mapping

Lithological and structural mapping has been carried out at selected areas of interest within the YSGB. Unfortunately, outcrop is generally limited within the study area (< 5%; Watkins & Hickman, 1990), with some geological units, such as the Mougooderra Fm, suffering from even less exposure. In order to identify areas of outcrop, a combination of satellite imagery and radiometric imagery has been utilised. Two localities in which Mougooderra Fm rocks are exposed, Chulaar Hill and Warriedar Hill, and an exposure along the Chulaar Shear Zone, have been mapped as part of this study. As was the case for geological mapping in the Rothsay area, the outcrop-subcrop-float classification has been used (Section 3.3.1). Surface geological maps represent the extent of subcropping and outcropping units, whilst float is used alongside geophysical data, satellite imagery and other observations for interpretive geological maps of bedrock. A spreadsheet compiling mapping observations across the YSGB can be found in **Appendix E2**, including co-ordinates, observations, lithologies and structural data for all field localities visited.

4.4.3 Logging of Oriented Drillcore

As part of this study, lithological and structural logging of oriented drillcore from eleven drillholes in the central YSGB has been undertaken. These drillholes intersect four gold deposits along two shear zones in the study area: the Mougooderra Shear Zone (MSZ; host to the M1, Bugeye and Silverstone camp deposits) and the Winddine Well Shear Zone (WWSZ; host to the Winddine Well deposit). Access to drillcore has been generously provided by Minjar Gold Pty. Details for each of the drillholes used in this study including collar locations, hole lengths, inclinations and azimuths are given in Table 4.1. A compilation of lithological and structural logs of each drillhole are provided in **Appendix E3** and **Appendix E4**, respectively. Lithological logs are illustrated in Figures 4.12, 4.17 and 4.19.

Structural analysis of oriented drillcore has been carried out using an EZ-logger kenometer and following the unified approach presented by Blenkinsop et al. (2015). Planar features such as bedding and foliations have been measured using the α-β method and lineations have been measured using the β_L method (e.g., Marjoribanks, 2010). To determine shear direction, the concept of the vorticity vector has been utilised, defined as the axis about which internal rotation occurs in a shear zone (Means et al., 1980; Blenkinsop et al., 2015). Vorticity vectors can be identified in drillcore as the axis perpendicular to the shear sense observation plane, in which shear sense indicators display maximum asymmetry, and have been measured using the β_V method (Blenkinsop et al., 2015). Where folding is observed in drillcore, fold hinge surfaces are measured using the α-β method for planes and fold hinges are measured using two β angles, β_D and β_U, and a length measurement on the core, UD (Blenkinsop et al., 2015). Structural measurements obtained from drillcore have been combined with orientation data from downhole surveying to calculate the true orientation of structures. This has been undertaken using the Cor! program (provided by T.G. Blenkinsop), which implements the

Drillhole ID	Deposit	Shear Zone	Collar Location		Total length (m)	Initial Inclination (°)	Initial Azimuth	Final Inclination (°)	Final Azimuth	Depth to fresh rock (m)
			Eastings	Northings						
SSDD013	Silverstone	MSZ	494889	6802574	375.0	60.9	088	51.7	087	94
SSDD014	Silverstone	MSZ	494902	6801940	375.4	59.6	089	59.0	088	54
SSDD015	Silverstone	MSZ	495056	6803126	300.3	59.9	092	60.4	090	135
SSDD017	Silverstone	MSZ	494811	6802197	498.9	71.8	090	68.1	084	85
SSDD018	Silverstone	MSZ	494925	6802197	354.8	70.8	090	63.9	087	68
SSDD019	Silverstone	MSZ	494800	6802250	501.9	70.6	089	52.3	087	130
M1DD026	M1	MSZ	493465	6810783	501.1	59.6	089	49.8	083	92
BEDD002	Bugeye	MSZ	495990	6793197	317.7	60.1	088	57.1	086	124
WWDD031	Winddine Well	WWSZ	493863	6805936	280.4	59.7	267	61.3	279	146
WWDD038	Winddine Well	WWSZ	493911	6805957	330.0	60.0	270	48.4	276	135
WWDD040	Winddine Well	WWSZ	493867	6806036	299.1	59.8	273	62.7	272	146

Table 4.1: Details for drillcore used in this chapter, including the location of drillhole collars, the length of each hole, initial and final inclination and azimuth measurements for each hole and the depth along each hole to fresh rock, as established during logging. Drillhole collar locations are displayed on Figure 4.13.

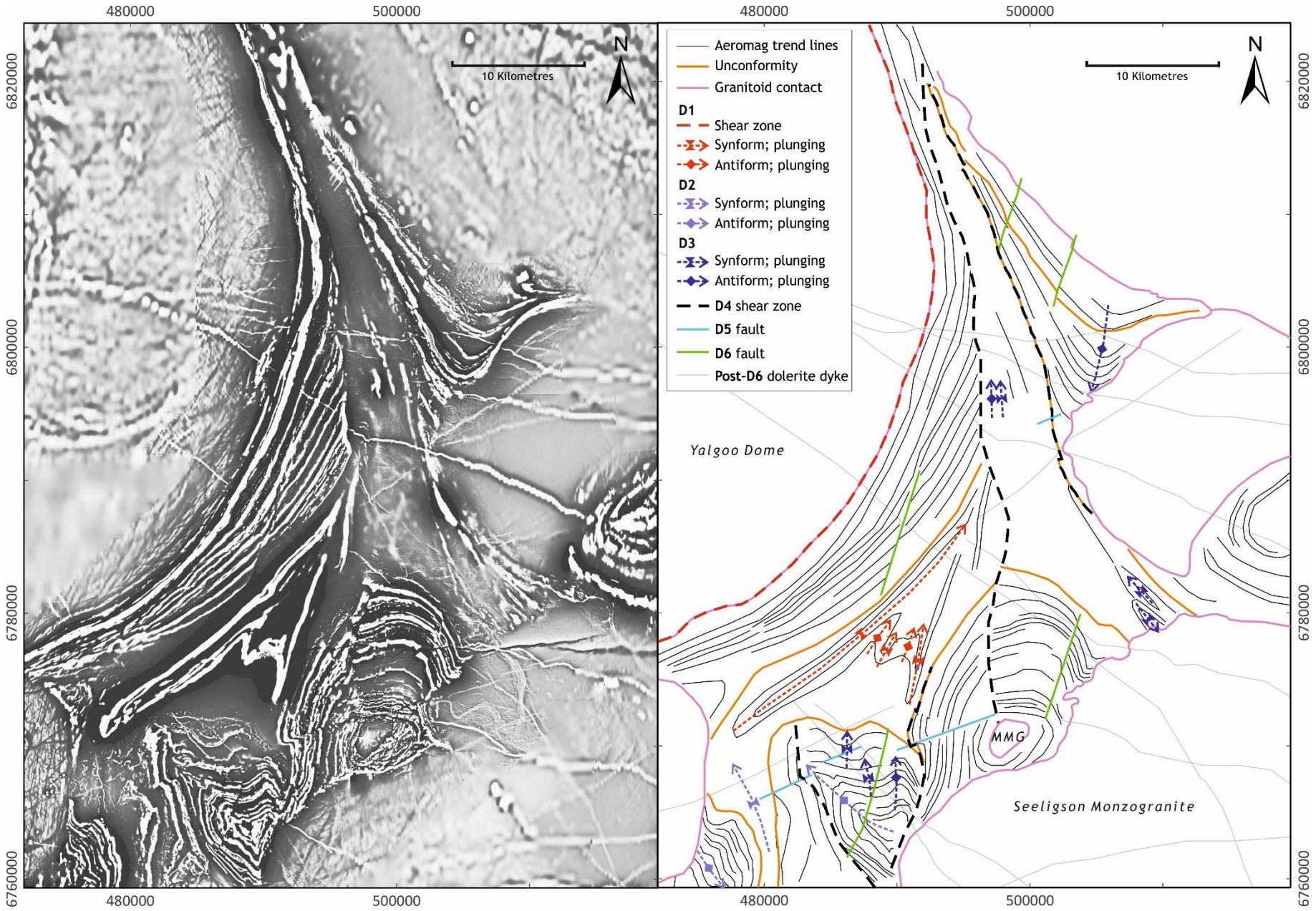

Figure 4.2: Aeromagnetic map of the central Yalgoo-Singleton greenstone belt, displaying the first vertical derivative of reduced to pole total magnetic intensity (Source: GSWA). An interpretive sketch of structural features based on aeromagnetic imagery and mapping undertaken in this study is also shown MMG: Mt Mulgine Granite.

Deformation Event	Zibra et al. 2018; 2020 structures	Setting	Intrusions	Features
Post-D_6		~N-S extension	Dolerite dykes (Proterozoic?)	Dykes dissect all structures, minor deflection/intrusion along D_4 shear zones
D_6		E-W shortening		NNE-striking dextral **D_6** fault, minor N-S faulting
D_5		NE-SW shortening?	Seeligson Monzogranite, associated Li-B pegmatite dykes	ENE-striking sinistral **D_5** faults, minor associated fault drag, granite and pegmatite dyke intrusion, **D_5** fabrics/fractures
D_4		Continued E-W shortening		**D_4** shear zones (MSZ, CSZ, WWSZ, ESZ, RSZ), duplex development, **S_4** shear fabric, (oblique) down-dip **L_4** lineation, **F_4** folding
D_3	**S_{OR}** 'orogenic' fabric	E-W shortening		**S_3** N-S foliation, **F_3** N-S fold axes refolding F_2 folds, tight to isoclinal **F_3** folding in Mougooderra Fm rocks
D_2		NE-SW shortening/ diapirism?		**F_2** NW-SE trending fold axes in southwest
D_1	**F_{D1} -F_{D3} , S_D, L_D,** Badja Decollement	Diapirism	Annean Supersuite; Yalgoo Dome, Mt Mulgine Dome, Rothsay Dome	**D_1** domes, **S_1** layer-parallel foliation, **D_1** shearing along Badja Decollement
D_E		Extension/rifting	Warriedar Suite	Intrusion of mafic-ultramafic layered sills, screens/rafts of supracrustal units, **S_0** lithological contacts
D_E		Extension/rifting		Deposition of Mougooderra Fm rocks, **S_0** bedding
D_E		Extension/rifting		Emplacement of Gossan Hill Fm and Chulaar Group rocks, **S_0** bedding

Table 4.2: Table summarising the deformational framework for the Yalgoo-Singleton greenstone belt, including structural features, intrusions and tectonic settings associated with each deformational event. Structures observed by Zibra et al. (2018; 2020) have also been included for context – the subscript $_D$ refers to doming.

methods described in Blenkinsop et al. (2015). It should be noted that orientation lines drawn on drillcore used in this study are drawn along the bottom of the core.

4.5 Results

4.5.1 Introduction

In this section, new field data relating to the structural geology of supracrustal rocks in the YSGB is presented. This includes interpretation of aeromagnetic imagery (Section 4.5.2), geological mapping at Chulaar Hill (Section 4.5.5.1) and Warriedar Hill (Section 4.5.5.2), structural analysis of oriented drillcore from the Mougooderra Shear Zone (Section 4.5.6.1) and Winddine Well Shear Zone (Section

4.5.6.2) and geological mapping along an exposure of the Chulaar Shear Zone (Section 4.5.6.3). An overview geological map of the YSGB is shown in Figure 4.1. The structural geology of spatially restricted basement Gossan Hill Fm rocks is beyond the scope of this study.

The notation for structures and deformational events used in this chapter is consistent with that used in Chapter 3, in which folds, foliations and lineations assigned to a deformational event are given the notation F, S and L respectively, followed by the corresponding deformational event number (e.g., F_3 and S_3 resulting from D_3). The structural geology of the YSGB can be summarised by six episodes of deformation (D_1-D_6) following emplacement of supracrustal rocks and intrusive sills (D_E). The D_1 deformational episode is summarised in Section 4.3. Subsequent deformation consists of two shortening events (D_2, D_3), an episode of shearing (D_4) and two subsequent events dominated by faulting (D_5, D_6). The most recent features in the YSGB are dolerite dykes, which cross cut all other structures and units. The structures associated with each deformational event are summarised in Table 4.2. Following interpretation of aeromagnetic data and an assessment of bedding and way-up criteria in the belt, the structures associated with D_2-D_6 events are described sequentially.

4.5.2 Aeromagnetic Interpretation

A structural interpretation of publicly available aeromagnetic data from GSWA has been carried out as part of this study. The aeromagnetic imagery displayed in Figure 4.2a signifies the first vertical derivative of reduced to pole total magnetic intensity, in which values from high to low are represented in greyscale from white to black. Structural features in the YSGB distinguished on aeromagnetic imagery are displayed in Figure 4.2b.

The contacts between the greenstone belt and surrounding granitic intrusions can be readily discerned and mapped using the aeromagnetic imagery. The lower part of the greenstone succession can also be distinguished from the metasedimentary-dominated Mougooderra Fm, on the basis that the former contains abundant magnetic BIF and serpentinite units that are generally absent in the latter. The earliest deformational structures in the belt, assigned to D_1, that can be discerned on the aeromagnetic map include the Yalgoo Dome, Mt Mulgine Dome and the refolded Rothsay Fold domal structure in the southwest (Chapter 3). Additionally, the intervening fan-shaped distribution of F_1 folds with axes parallel to dome margins hosted by rocks of the Willowbank Clastics can also be readily distinguished (Fig. 4.1). D_2 structures consist of multiple NW-SE oriented folds limited to the southwestern portion of the belt, whereas D_3 structures comprise N-S to NNE-SSW trending folds on a range of scales across the belt, including refolding F_2 folds in the southwest (Fig. 4.1). D_4 shear zones are oriented broadly NNE-NNW and are partially distinguished on aeromagnetic imagery, particularly

where units on either side of the shear zone intersect at an oblique angle. D_5 and D_6 structures are distinguished from offset magnetic anomalies and are characterised as ENE-trending sinistral and NNE-trending dextral faults, respectively. A further conspicuous feature on the aeromagnetics consist

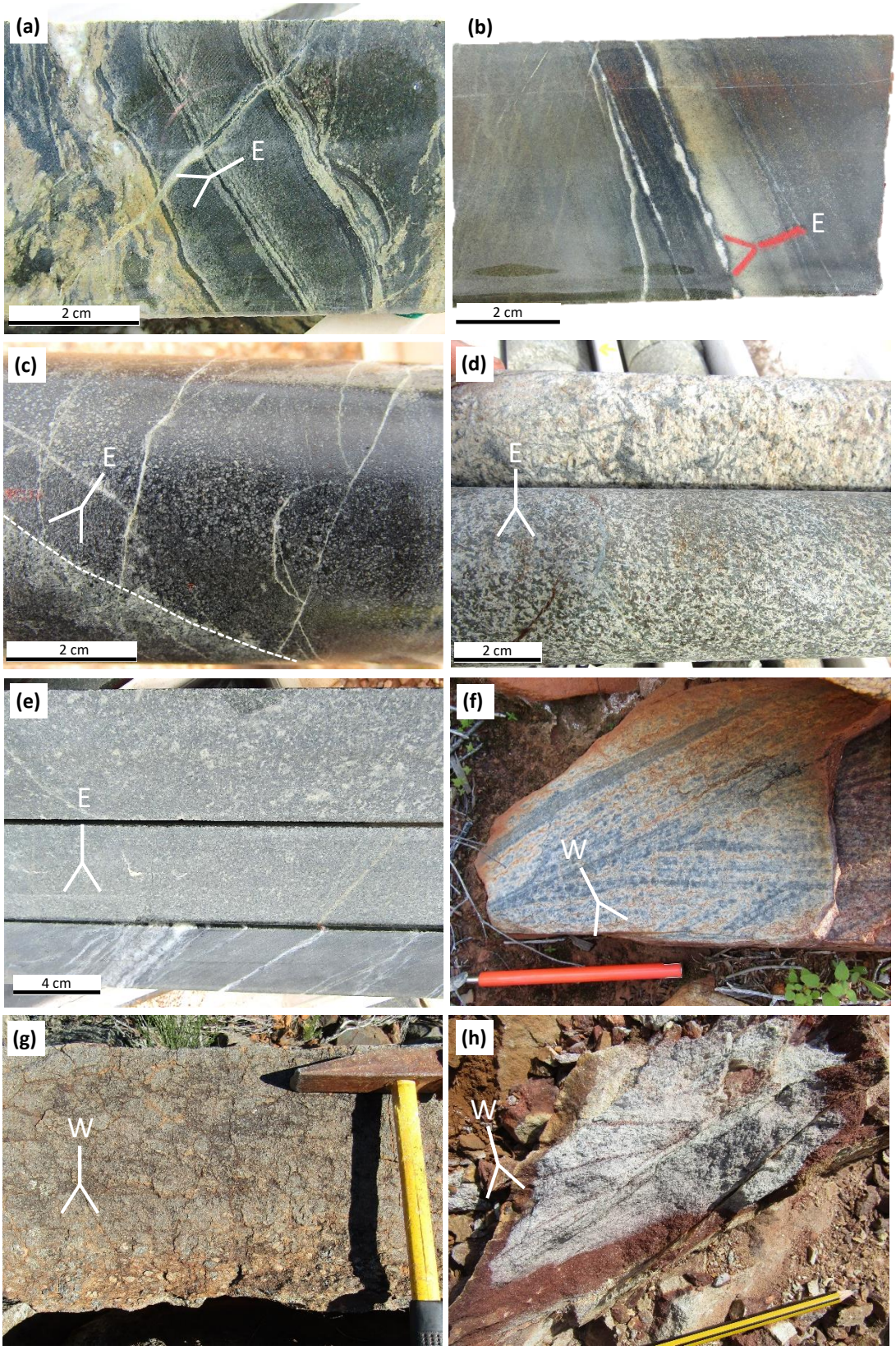

(continues on next page)

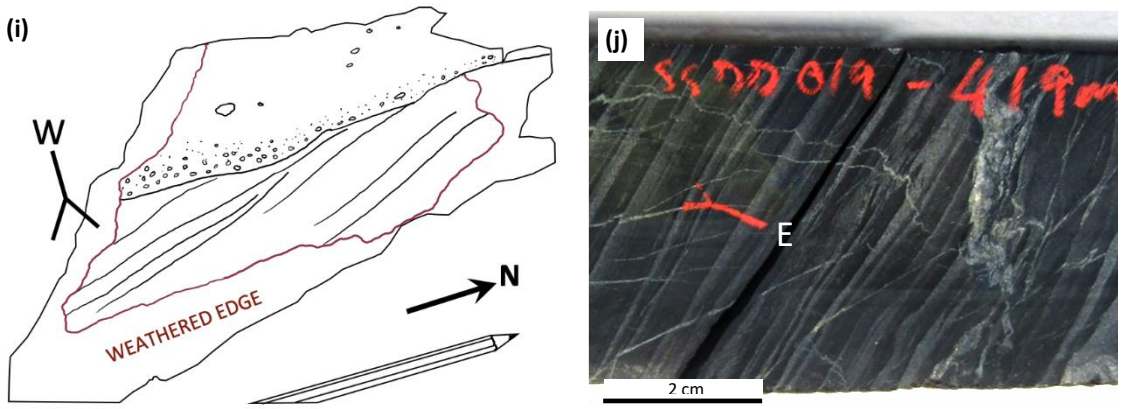

Figure 4.3: Photographs of selected way-up indicators identified in supracrustal and mafic-ultramafic intrusive rocks in the Yalgoo-Singleton greenstone belt. Way-up directions are labelled on each image and the locations of way-up indicators are displayed on Figure 4.5. **(a)** Graded bedding in cm-scale volcaniclastic units interbedded with Chulaar Group variolitic basalts at the Silverstone deposit, displaying way-up to the east (drillhole SSDD014, depth 217.1m); **(b)** Graded bedding in a Chulaar Group quartz sandstone unit interbedded with volcaniclastic units west of the Winddine Well deposit, demonstrating younging towards the east (drillhole WWDD040, depth 295.3m); **(c)** Serpentinised cumulate basal portion of a Chulaar Group high-Mg basalt flow from the M1 deposit, containing relict olivine crystals and magnetite grading upwards into non-magnetic, aphyric basalt and with a sharp basal contact on an underlying flow, indicating way-up towards the east (drillhole M1DD026, depth 283.1m); **(d)** Dolerite grading upwards into a coarse-grained, harrisitic-textured quartz dioritic sill top in a Warriedar Suite intrusion situated west of the Bugeye deposit, demonstrating way-up towards the east (drillhole BEDD002, depth 141.3m); **(e)** Representative core samples of a lower section through a Warriedar Suite intrusion situated west of the Silverstone deposit, displaying increased feldspar content and increasing crystal size from the fine-grained, altered, weakly-magnetic base, towards the centre of the sill, supporting way-up towards the east (drillhole SSDD017, depth 332.1m); **(f)** Decimetre-scale cross bedding in an outcropping Mougooderra Formation quartz sandstone unit, Warriedar Hill, displaying way-up towards the west; **(g)** Graded bedding in a Mougooderra Formation quartz sandstone unit, Warriedar Hill, comprising clasts up to 2cm in diameter grading upwards into ~1mm clasts and displaying way-up towards the west; **(h)** An outcrop of Mougooderra Formation pebbly sandstone at Minjar Hill displaying cross bedding, an erosive base and graded bedding, collectively demonstrating way-up towards the west; **(i)** Sketch of the outcrop in (h); **(j)** Graded bedding of finely bedded, vertically-dipping shales of the Mougooderra Formation observed in drillcore east of the Silverstone deposit and showing way-up towards the east (drillhole SSDD019, depth 419.0m);

of a network of cross cutting dolerite dykes, which, as they cross cut all other structures and lithologies, post-date D_6 deformation.

4.5.3 Bedding and Way Up Criteria

Various way-up criteria have been identified in metasedimentary and metavolcanic rocks of the Chulaar Group and Mougooderra Fm, as well as intrusive sills of the Warriedar Suite (Fig. 4.3). Way-up structures have been observed in outcrop, in the better exposed areas of the belt, and identified in drillcore from the very poorly exposed western part of the belt.

Tuffaceous volcaniclastic units interbedded with Chulaar Group basaltic rocks commonly display graded bedding but are seldom exposed at the surface. Drillcore from rocks located west of the Silverstone deposit contain graded interflow volcaniclastic units that consistently exhibit younging towards the east, away from the greenstone contact with the Yalgoo Dome (Fig. 4.3a). Similarly, cm-scale quartz-rich volcaniclastic units observed in drillcore west of the Winddine Well deposit also contain graded bedding that demonstrate way-up towards the east (Fig. 4.3b). Elsewhere on the Badja

limb, individual high-Mg basalt units observed in drillcore west of the M1 deposit contain serpentinised olivine-bearing cumulate bases that rest on sharp contacts with underlying flows (Fig. 4.1). The orientation of these flow bases is consistent with way-up towards the east (Fig. 4.3c). In the Rothsay area, graded bedding and erosive bases in a Chulaar Group volcaniclastic unit and spinifex branching in volcanic units demonstrate the units are the right way-up and young away from the Seeligson Monzogranite (Section 3.5.2).

Differentiation of Warriedar Suite sills serves as important way-up criteria in the YSGB. At the Bugeye deposit on the Badja limb, several doleritic Warriedar Suite sills exhibit evolved, harrisitic-textured quartz dioritic sill tops (Fig. 4.1). These units are typically <2 m in thickness, comprise coarse feathery amphibole (pseudomorphing pyroxene) crystals up to 3cm in length and primary quartz, and demonstrate way-up towards the east (Fig. 4.3d). Similar features are observed in drillcore from the Silverstone deposit, which contains Warriedar Suite intrusions progressing from dark, weakly magnetic, heavily altered bases to coarser-grained, feldspar-rich centres that represent way-up towards the east (Fig. 4.3e). At the Mugs Luck mine on the Mt Mulgine limb of the belt (Fig. 4.1), outcropping quartz diorite represents the uppermost portion of thick (>200 m) Warriedar Suite intrusions, and support the succession being the right way-up and younging away from the Mt Mulgine Granite. These observations are replicated in the Rothsay area (Section 3.5.2), where magmatic differentiation of the Damperwah and Gardner sills confirm the succession is the right-way up.

Metasedimentary rocks of the Mougooderra Fm exhibit abundant sedimentary structures, many of which can be used as way-up criteria. At Warriedar Hill, in the far southeast of the study area (Fig. 4.1), a well exposed, steeply west-dipping succession of quartz sandstone, conglomerate, shale and BIF exhibits various structures including cross-bedding (Fig. 4.3f), graded bedding (Fig. 4.3g), erosive contacts and outcrop-scale fining upwards sequences. These structures unequivocally demonstrate the succession is the right way-up and is younging to the west, away from the contact with Chulaar Group rocks to the east. Similarly, an exposure of pebbly sandstone at Minjar Hill preserves cross-bedding, in which bedding is defined by high concentrations of iron oxide minerals, in addition to scoured bases and graded bedding (Fig. 4.3h, Fig. 4.3i). All these features collectively demonstrate younging towards the west, as along strike at Warriedar Hill. Although exposure is minimal along the western margin of the Mougooderra Fm, shale and sandstone have been observed in drillcore east of the M1, Silverstone and Bugeye deposits (Fig. 4.1). At these locations, shales are bedded on a 1-10 cm-scale and frequently exhibit graded bedding, which is used to distinguish isoclinal folding proximal to the MSZ (Section 4.5.6.1). However, with increasing distance from the MSZ in undeformed shales, graded bedding consistently indicates younging towards the east (Fig. 4.3j).

In summary, way-up structures in the YSGB indicate that the succession is the right way-up and the way up criteria observed in Warriedar Suite intrusives are comparable to those in Chulaar Group host rocks. Furthermore, way-up directions are consistently oriented away from granite-greenstone contacts towards the centre of the belt. This also includes rocks of the Mougooderra Fm, which young towards the centre of the exposed formation.

4.5.4 D_2 deformation

D_2 deformation is characterised by the development of several folds in the southwestern YSGB, with NW-SE trending fold axes (Fig. 4.1). F_2 folds are not associated with a fabric. In the Rothsay area, a northwest-plunging F_2 fold refolds the D_1 domal structure (Section 3.5.4). Further southwest, a southeast-plunging F_2 fold is present, which may also have refolded a pre-existing dome in this area (Zibra et al., 2020). Between these two antiformal structures, a northwest-plunging F_2 synform occurs, trending north-northwest and containing Willowbank Clastics lithologies within its core (Fig. 4.1). Notably, F_2 axes are broadly parallel with the margin of the Mongers Dome further south (Fig. 4.1). D_2 deformation has not been identified in the northern part of the study area.

4.5.5 D_3 deformation

D_3 deformation in the YSGB occurs as metre- to kilometre-scale, NNW to north-trending F_3 folds, associated with a pervasive, steep to vertical axial planar S_3 foliation. These structures occur in the

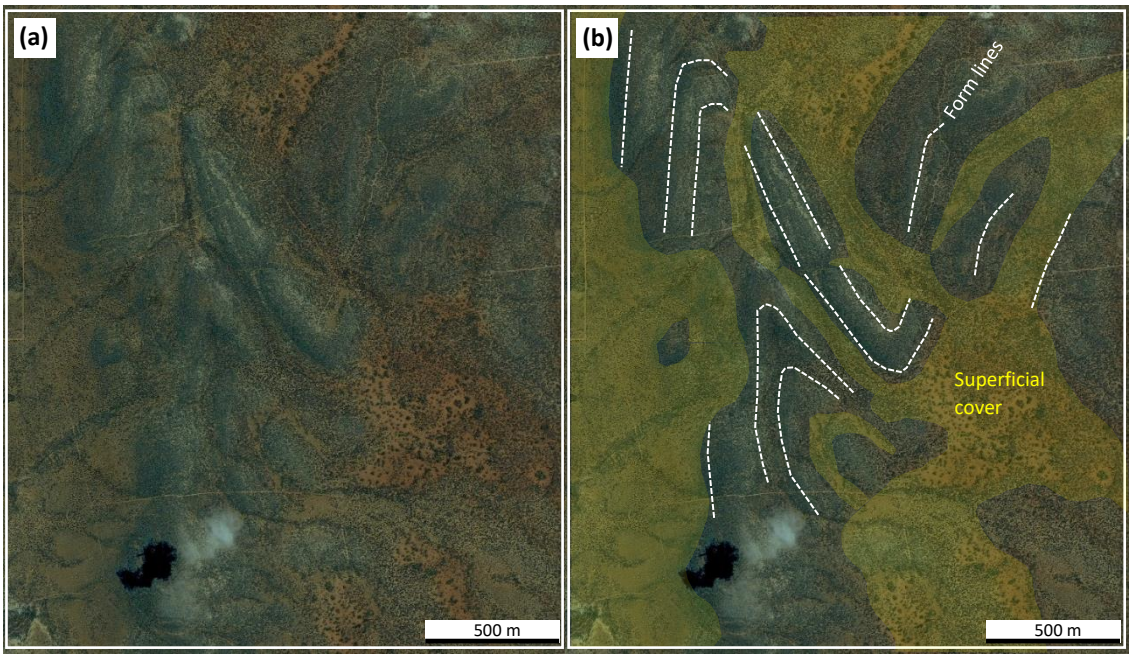

Figure 4.4: Satellite imagery of Mougooderra Formation rocks exposed in the Chulaar Hill area. **(a)** Kilometre-scale folding evident on satellite imagery; **(b)** Annotated satellite imagery highlighting the distribution of superficial cover (yellow) and form lines denoting km-scale folding of Mougooderra Formation rocks (white dashed lines). Satellite imagery is courtesy of Google Earth and is dated March 2006.

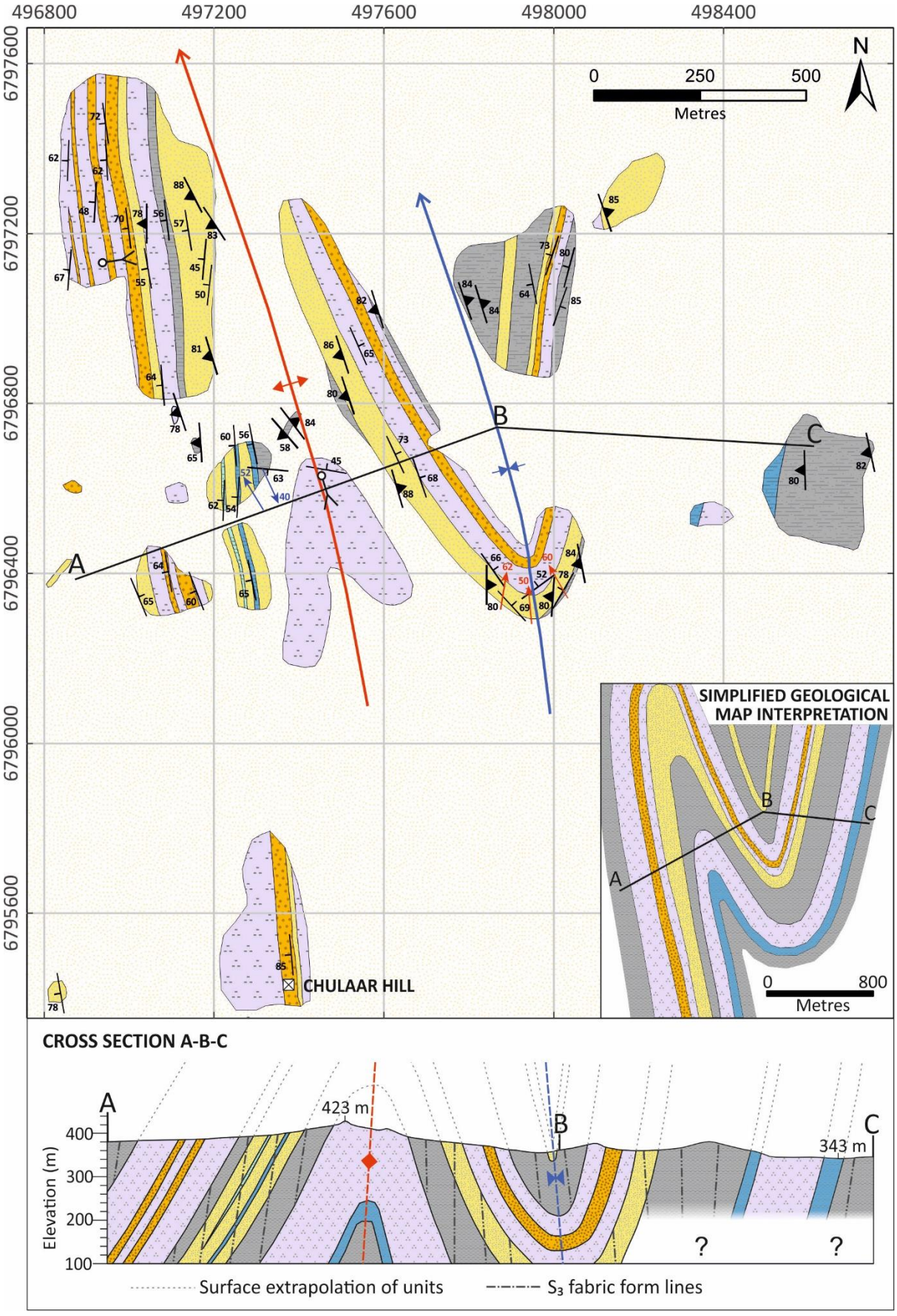

(caption on next page)

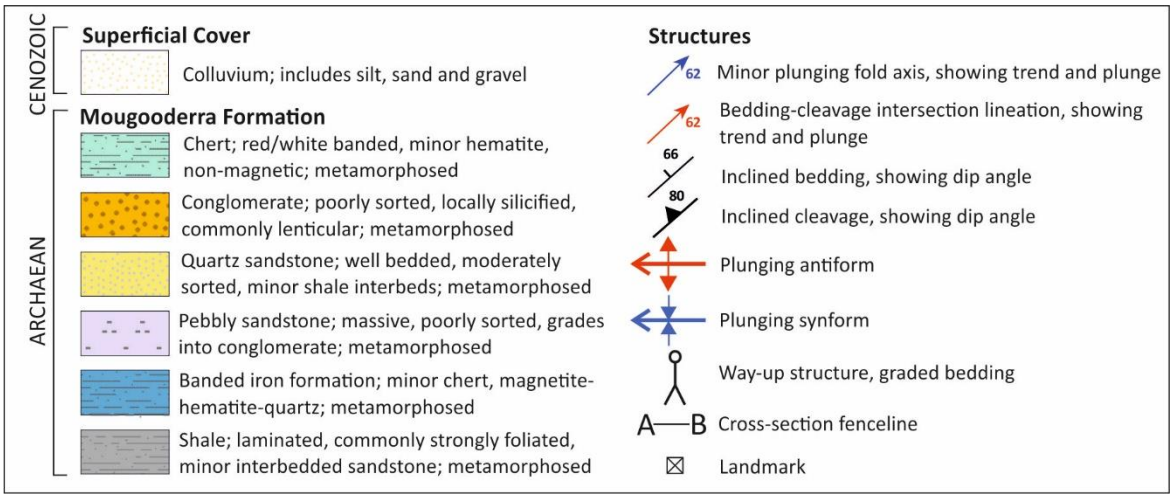

Figure 4.5: Surface geological map of Mougooderra Formation rocks exposed in the Chulaar Hill area, drawn at 1:12,000 scale. The inset map in the bottom right is an interpreted bedrock geological map of the Chulaar Hill area and an interpreted cross section along the fence line A-B-C is shown at the bottom, drawn at 1:12,000 scale with no vertical exaggeration and also displaying surface extrapolation and form lines for the S_3 cleavage, based on structural measurements. Coordinates specified in the MGA Zone 50 coordinate system.

lower greenstone succession, in rocks of the Chulaar Group and Warriedar Suite, as well as the overlying Mougooderra Fm. Rocks in the Rothsay area in the southwest of the belt (Chapter 3) preserve multiple north-plunging F_3 folds, which refold D_1 and D_2 structures, and contain a widespread, steeply inclined, axial planar S_3 cleavage. The map pattern of the YSGB displays a further regional scale fold with a north-south trending fold axis, located in supracrustal rocks in the Chulaar area (Fig. 4.1). Unlike the Mt Mulgine Dome, this fold does not appear to be associated with a granitoid or parallel to a granite-greenstone contact, and thus is not considered to be related to early diapirism. Rather, based on the ~N-S orientation of the fold axes, and the fact that an S_3 fabric has been observed in this area, this fold is tentatively assigned as an F_3 fold.

Mougooderra Fm rocks are typically poorly exposed and are instead largely concealed beneath superficial cover. Consequently, little is known about the stratigraphy comprising the Mougooderra Fm and the structures contained within these rocks. However, two isolated, abnormally well exposed, elevated areas of Mougooderra Fm rocks occur within the study area at Chulaar Hill and Warriedar Hill (Fig. 4.1). Geological and structural mapping has been undertaken at each of these localities and has identified several structures attributed to D_3 deformation. The stratigraphy and structure at Chulaar Hill and Warriedar Hill are described in the following sections.

4.5.5.1 Chulaar Hill

Chulaar Hill is located in the central part of the Mougooderra Fm, approximately 1.5 km east of the MSZ (Fig. 4.1). Rocks in the elevated area surrounding Chulaar Hill consist of a sequence of metasedimentary rocks, folded into a tight, north-northwest-plunging F_3 antiform-synform pair with

a well-developed axial planar S_3 cleavage. Kilometre-scale folding at Chulaar Hill is evident on satellite imagery (Fig. 4.4a) and is defined by the trends of elevated ridges of outcropping metasedimentary rocks, principally pebbly sandstone and conglomerate. These ridges are surrounded by subdued

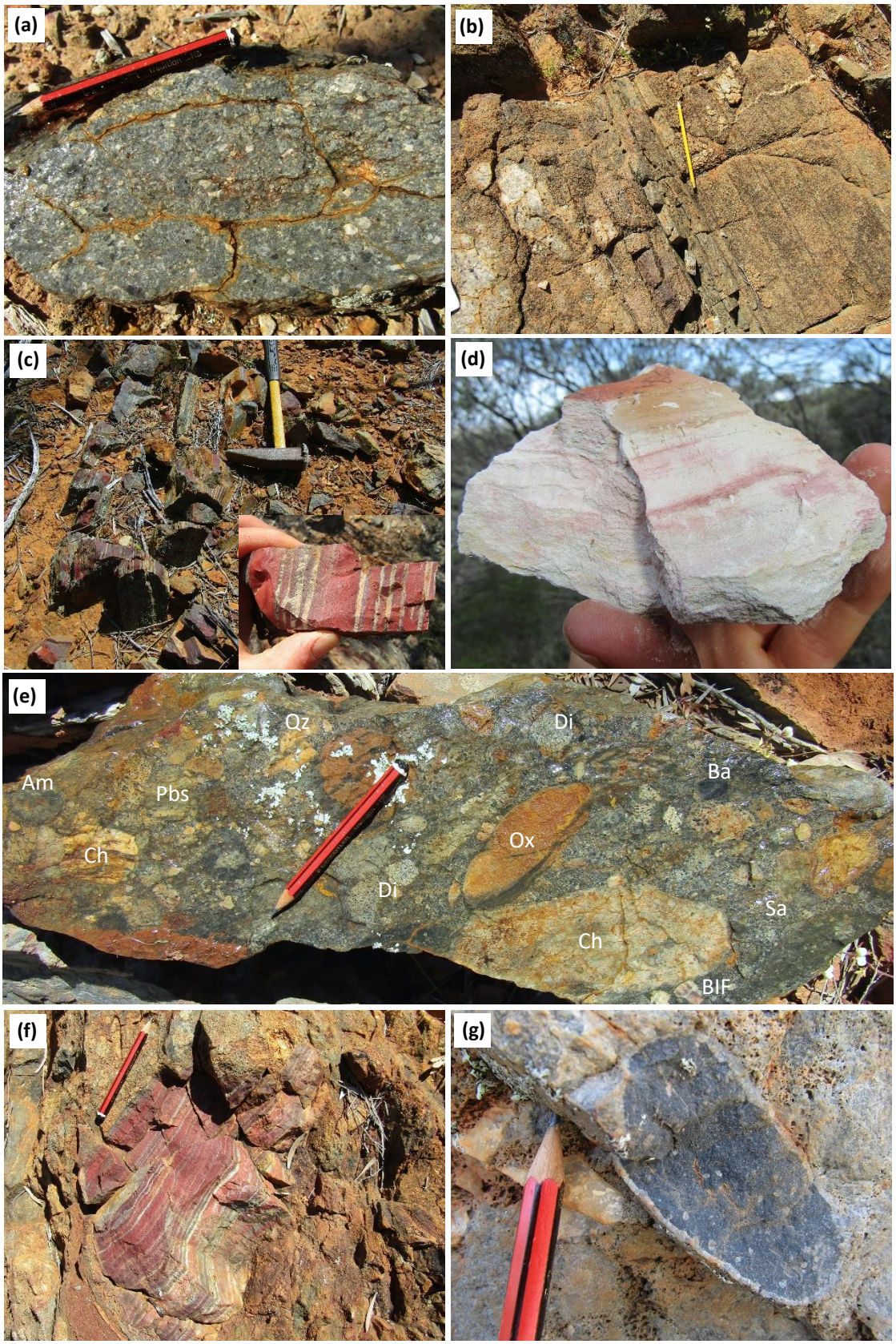

(caption on next page)

Figure 4.6: Photographs of Mougooderra Formation rocks exposed in the Chulaar Hill area. **(a)** Exposure displaying the typical texture of pebbly sandstone, containing clasts of chert, quartz and sandstone and minor pebbly sandstone autoliths (loc. JP18269); **(b)** Exposure of well bedded quartz sandstone dipping towards the northeast, pencil oriented towards north (loc. JP18227); **(c)** Exposure of jasperlitic BIF with distinctive red white banding (inset), dipping towards the west (hammer handle pointing north; loc. JP18219); **(d)** Grey-white siltstone with suspected volcanogenic content and minor red banding, and a weak cleavage (loc. JP18276); **(e)** An example of a polymictic conglomerate interleaved with pebbly sandstone, containing a variety of clast lithologies including chert (Ch), quartz (Qz), amygdaloidal basalt (Am), pebbly sandstone (Pbs), sandstone (Sa), BIF, an intermediate-felsic intrusive (likely diorite; Di), and highly oxidised clasts (Ox) – note that the pencil is aligned in the approximate bedding orientation, sample not in situ (loc. JP18255); **(f)** Sub-rounded boulder of red-white jasperlitic BIF present as a clast within a conglomeratic layer, with an identical appearance to the underlying jasperlitic BIF unit (c) (loc. JP18256); **(g)** Clast within conglomeratic layer of pebbly sandstone comprising amygdaloidal basalt (loc. JP18267).

outcrops of finer-grained metapelitic rocks, in addition to significant amounts of superficial cover (Fig. 4.4b). A geological map of the surface exposure, an interpreted geological map and a cross section of the Chulaar Hill area are shown in Figure 4.5. In this section, the stratigraphy at Chulaar Hill is first outlined, followed by a detailed description of structures observed in the area.

Stratigraphy

The geology at Chulaar Hill comprises a ~900 m-thick succession of Mougooderra Fm metasedimentary rocks. The younging direction of the stratigraphy has been constrained using several fining upwards sequences, which indicate the succession is the right way-up and that the lowermost rocks occur in the southeast (Fig. 4.5). The base of the succession consists of several hundred metres of poorly exposed, fine-grained pelitic rocks, predominantly siltstone, some of which contain minor andalusite porphyroblasts. In some outcrops, pelitic rocks are interbedded with decimetre-scale intervals of quartz sandstone and although basalt has been observed as float in this part of the succession, it does not outcrop. Metapelitic rocks grade upwards into a ~40 m-thick unit dominated by red-black, magnetic BIF, interbedded with minor mudstone and quartzite. In turn, BIF is overlain by a locally well-exposed, ~80 m-thick unit of pebbly sandstone (Fig. 4.5). Pebbly sandstone is characteristically poorly bedded and poorly sorted and contains sub-rounded clasts that are composed principally of quartz, with lesser chert, BIF, sandstone and occasional autoliths of pebbly sandstone (Fig. 4.6a). Clast size is typically in the range 1 mm-1 cm, although the unit contains multiple decimetre-scale conglomeratic horizons with clasts up to 10 cm in diameter.

Pebbly sandstone is overlain by a poorly exposed siltstone similar to that at the base of the succession, which in turn is overlain by a well exposed and well bedded ~80 m-thick unit of quartz sandstone, containing ~1mm quartz clasts, with minor cm-scale interbeds of siltstone (Fig. 4.6b). In the west of the area, multiple 5-15 m-thick horizons of distinctive red-black BIF and red-white chert are interbedded with quartz sandstone (Fig. 4.6c). The upper portion of this quartz sandstone-dominated unit is characterised by an increase in the frequency and thickness of siltstone interbeds, and the top of the unit is marked by a ~15 m-thick white volcanogenic siltstone, with red-banding, a friable ashy groundmass and relict lapilli (Fig. 4.6d).

A sequence comprising alternations between pebbly sandstone, quartz sandstone and conglomerate occurs above the volcanogenic siltstone, ranging in thickness between 200 m in the west and ~120 m in the east and forming topographic highs in the area, including Chulaar Hill (Fig. 4.5). Pebbly sandstone

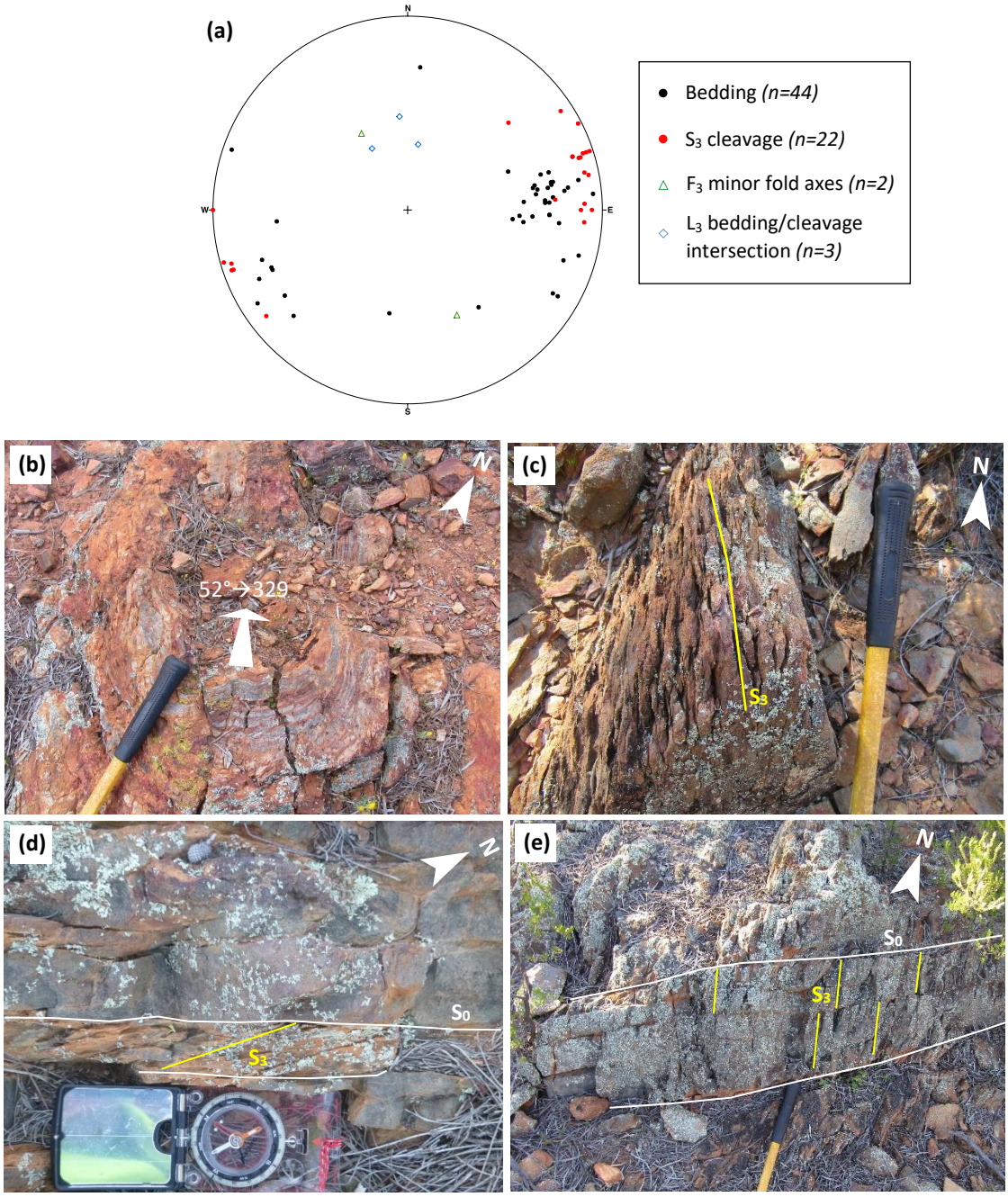

Figure 4.7: Structures identified in Mougooderra Formation rocks exposed in the Chulaar Hill area. **(a)** Lower hemisphere equal area stereonet of planar (bedding and cleavage) and linear structures (fold axes and bedding-cleavage intersection lineations) identified in the Chulaar Hill area. The poles to planes of planar structures are plotted; **(b)** Outcrop-scale synformal fold in banded BIF plunging 52° → 329 - photograph taken looking down the fold axis towards the northwest (loc. JP18291); **(c)** Outcrop of fine-grained sandstone with a well developed vertical cleavage, oriented axial planar to folding – hammer handle oriented north (loc. JP18273); **(d)** Bedding-cleavage relationship observed in interbedded sandstone and siltstone on the eastern limb of the km-scale synform (bedding-cleavage intersection lineation 60° → 330) (loc. JP18105); **(e)** Bedding-cleavage relationship preserved in fine grained sandstone at the hinge of the km-scale synform, with cleavage almost perpendicular to bedding. Bedding-cleavage intersection lineation 50° → 355, hammer handle pointing north (loc. JP18109).

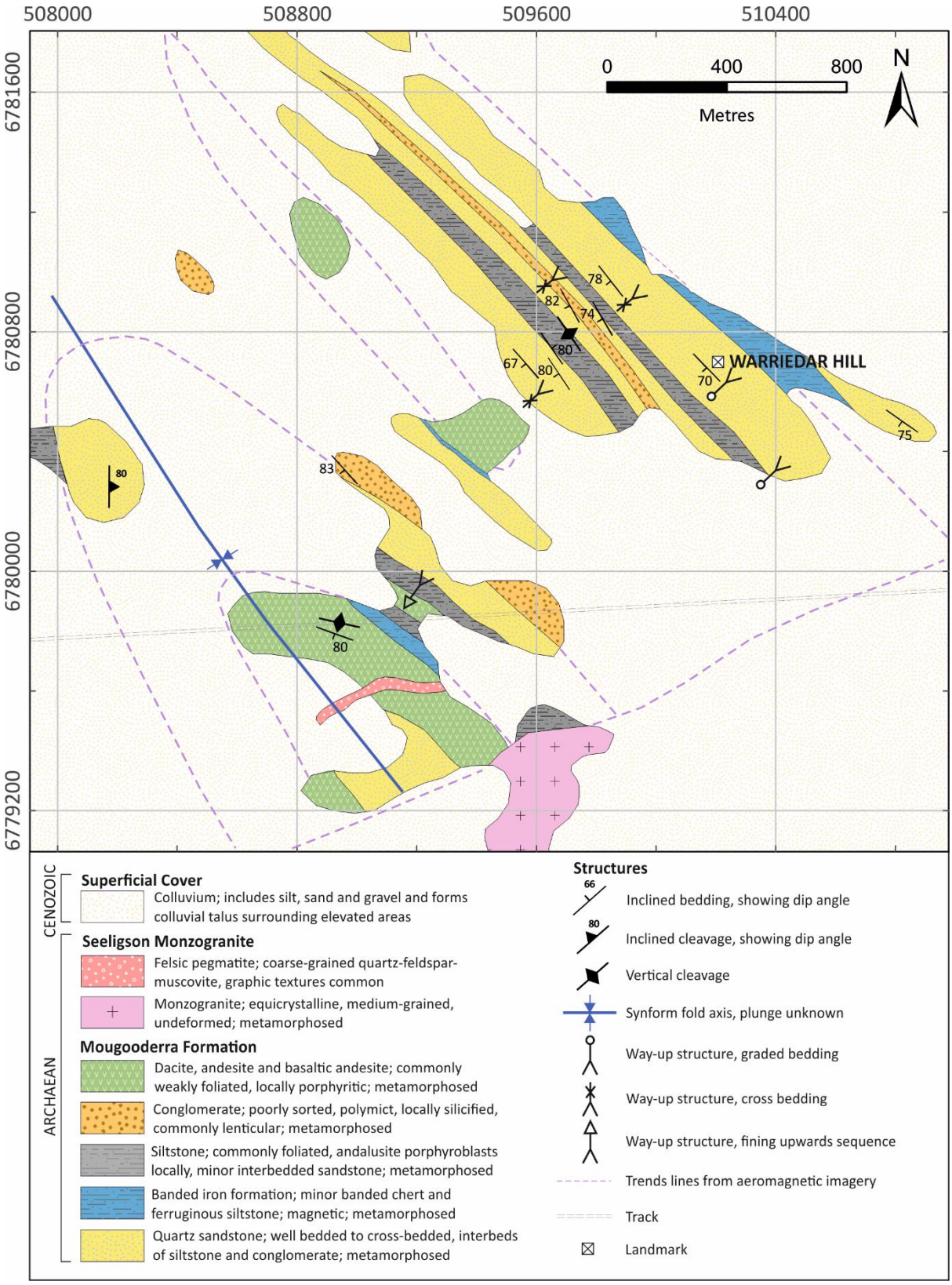

Figure 4.8: Surface geological map of Mougooderra Formation rocks exposed in the Warriedar Hill area, drawn at 1:18,000 scale. Purple dashed lines represent trend lines from aeromagnetic imagery. Several localities from the GSWA WAROX database were used in addition to geological mapping undertaken by this study to correlate units along strike. Satellite imagery, aeromagnetic data and a geologic interpretation of the area is shown in Figure 4.10. Coordinates provided in the MGA Zone 50 coordinate system.

typically grades into decimetre to metre-thick conglomeratic horizons that define bedding orientations and are laterally discontinuous. Furthermore, multiple thicker conglomerate units are interbedded with pebbly sandstone and decrease in thickness upwards from ~30 m to < 5 m. Conglomerates are typically poorly sorted and polymictic, with considerable variation in clast size between 1 mm and ~30 cm. In order of frequency, clast lithologies in conglomeratic units comprise quartz, chert, sandstone, basalt, an oxidised unit and rare clasts of an intermediate intrusive rock, likely diorite (Fig. 4.6e). Notably, several large clasts of the distinctive red-white chert observed down sequence occur in conglomerate lenses (Fig. 4.6f), in addition to amygdaloidal basalt (Fig. 4.6g) similar in appearance to Chulaar Group volcanic rocks located to the east (Section 5.3.3). Crucially, clasts in conglomerate units do not show internal deformation fabrics. The top of the Chulaar Hill stratigraphy is marked by a > 120 m-thick poorly exposed unit of red siltstone outcropping in the northwest, containing thin intervals of well bedded quartz-rich sandstone.

Structure

Mougooderra Fm rocks in the Chulaar Hill area are deformed into a kilometre-scale, tight, north-northwest plunging F_3 synform-antiform pair, with interlimb angles of approximately 20-30°. These folds can be partially observed on satellite imagery, due to the prominent elevated ridges formed by pebbly sandstone and conglomerate units. The F_3 folds are marginally asymmetric and display significant hinge thickening, particularly evident in fine grained pelitic units. Bedding in the Chulaar Hill area is most readily identified in well-bedded quartz sandstone (Fig. 4.6b), as well as interbedded sandstone and siltstone and the conglomeratic portions of pebbly sandstone, which are otherwise poorly bedded. Bedding dips at angles of 45-85°, most frequently 65-80° (Fig. 4.7a). Bedding at fold hinges dips towards the north-northwest at ~50°.

Smaller, metre-scale F_3 folds are preserved by thin BIF and chert units interbedded with sandstone in the west of the Chulaar Hill area (Fig. 4.5). These F_3 folds have axes that are parallel to km-scale folds and plunge towards the north-northwest at ~52° (Fig. 4.7a, Fig. 4.7b). A single fold has an axis that plunges towards the south-southeast at 40°. A well developed S_3 cleavage is commonly preserved by fine-grained rocks such as siltstone and mudstone (Fig. 4.7c). This cleavage is steeply dipping at 78-90°, most commonly west-dipping but is locally east-dipping and is consistently axial planar to F_3 folds (Fig. 4.7a). As such, the angle of intersection between bedding and the S_3 cleavage varies systematically around F_3 folds, from ~20° along limbs (Fig. 4.7d) to near perpendicular at fold hinges (Fig. 4.7e). Bedding-cleavage intersection lineations (L_3) identified close to the hinge of the km-scale synform plunge north-northwest at 50-62°, parallel to outcrop-scale and map-scale F_3 fold axes (Fig. 4.7a).

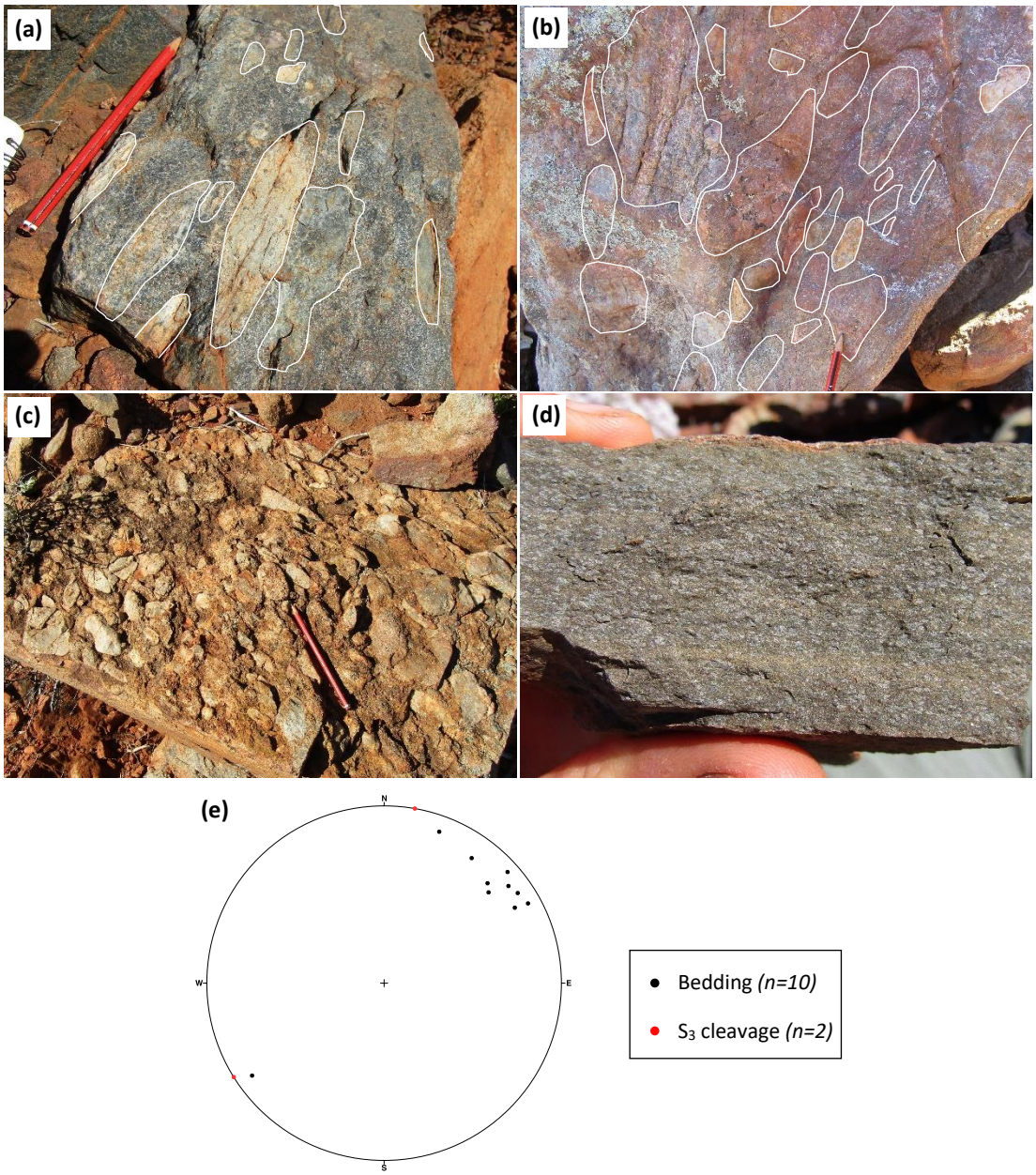

Figure 4.9: Field photographs of selected stratigraphic units and structures in Mougooderra Formation rocks exposed at Warriedar Hill. **(a)** Photograph of an along strike section of a conglomerate outcrop, displaying alignment of various clast lithologies including chert, quartz, sandstone and rare clasts of a felsic unit. Pencil is oriented towards north (loc. JP18080); **(b)** Photograph of a down-dip section through an outcrop of clast-supported conglomerate containing sub-angular to sub-rounded clasts up to 15 cm in diameter, including banded chert, BIF, quartz, sandstone and an oxidized lithology, taken facing north (loc. JP18080); **(c)** Block of clast-supported conglomerate (not in situ) displaying preferred alignment of elongate clasts (loc. JP18077); **(d)** Siltstone containing mm-scale porphyroblasts of cordierite that are not aligned parallel to the S_3 cleavage observed in most outcrops (loc. JP18079); **(e)** Lower hemisphere equal area stereonet of bedding and S_3 cleavage measurements at Warriedar Hill.

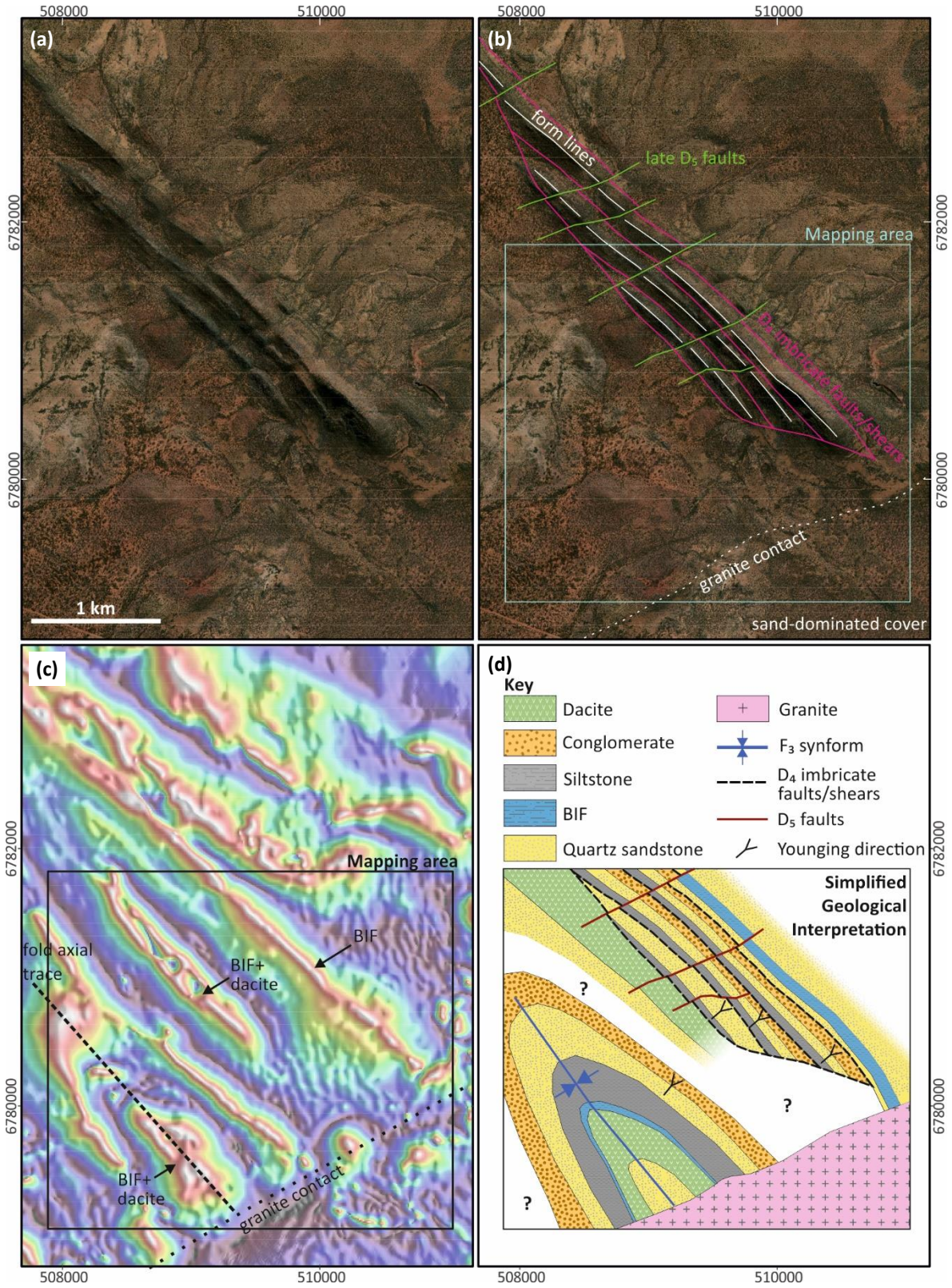

Figure 4.10: (a) Satellite imagery of the Warriedar Hill area; **(b)** Structural interpretation of satellite imagery, corroborated with field observations. Form lines correspond to elevated ridges of quartz sandstone and conglomerate; **(c)** Aeromagnetic imagery of the Warriedar Hill area, with notable features labelled including BIF and BIF interleaved with dacitic volcanic rocks, a NW-SE trending fold axial trace and an intrusive contact dissecting aeromagnetic anomalies; **(d)** Geological interpretation of the Warriedar Hill area, based on field mapping (Fig. 4.8), satellite imagery (b) and aeromagnetic data (c). Areas of uncertainty that lack outcrop and geophysical anomalies are denoted by '?'. Satellite imagery is courtesy of Google Earth and is dated September 2018.

4.5.5.2 Warriedar Hill

Warriedar Hill is located in the southeast of the YSGB, close to the eastern margin of the Mougooderra Fm and the northern contact of the Seeligson Monzogranite (Fig. 4.1). The metasedimentary-dominated stratigraphy at Warriedar Hill is partly deformed into a km-scale tight to isoclinal, upright F_3 fold and is also host to an imbricate structure attributed to D_4 deformation (Fig. 4.8).

Stratigraphy

The stratigraphy at Warriedar Hill consists of a ~1000 m-thick succession of Mougooderra Fm rocks, including quartz sandstone, conglomerate, BIF, siltstone and dacitic volcanic rocks. Abundant sedimentary structures such as graded bedding and cross bedding indicate that the succession is the right way-up and that the stratigraphically lowermost rocks occur in the far northeast (Fig. 4.8). The base of the succession is marked by a poorly exposed magnetic BIF, which grades upwards into a well bedded quartz sandstone interbedded with 50 cm to 2 m-thick conglomeratic units. These rocks form a topographically prominent ridge elevated ~150 m relative to the surrounding area, including the local topographic high, Warriedar Hill. Clasts in conglomerates are typically 1-5 cm diameter, rarely up to 15 cm, and consist of chert, quartz, sandstone, rare BIF and suspected mafic volcanic clasts (Fig. 4.9a). Clasts are typically sub-angular to sub-rounded and although some exhibit bedding, clasts do not display internal deformation fabrics (Fig. 4.9b, Fig. 4.9c). Quartz sandstone is typically white to grey in colour, well sorted and medium grained, with dark bands comprising elevated concentrations of an iron-rich mineral defining bedding and locally, cross bedding. These rocks are overlain by a poorly exposed, 30 m-thick recessive siltstone unit that in some instances contain mm-scale cordierite porphyroblasts (Fig. 4.9d), which in turn is overlain by a further ~120 m-thick, elevated package of quartz sandstone grading into laterally continuous units of conglomerate up to 30 m in thickness (Fig. 4.8).

In turn, conglomeratic sandstone grades upwards into poorly exposed interbedded sandstone and mudstone, which are also interbedded with a minor (<30 m-thick) dacitic unit in the southwest. The top of the exposed succession comprises a thin (10-15 m) BIF unit and a ~120 m-thick package of porphyritic and locally amygdaloidal dacitic volcanic rocks, overlain in the far southwest by further well bedded quartz sandstone (Fig. 4.8). Dacitic rocks are characterised by 0.5-1 mm plagioclase microphenocrysts and mm-scale quartz amygdales (Section 5.5.3). Quartz sandstone units in direct contact with dacitic volcanic units contain sub-rounded 2-5 mm black clasts that are interpreted as volcanic lithic clasts.

Structure

Bedding orientations at Warriedar Hill typically dip towards the southwest at 65-82°, apart from a single locality where bedding dips towards the northeast at 80° (Fig. 4.9e). A steep to vertical northwest-striking S_3 cleavage is present in mudstone units, typically oriented parallel to bedding although few measurements have been taken due to the lack of sufficient outcrop (Fig. 4.9e). Notably, porphyroblasts in pelitic rocks are not deformed into the S_3 cleavage (Fig. 4.9d). In conglomeratic units, clasts are commonly flattened in the orientation of the local S_3 fabric (Fig. 4.9b). In several instances in subcrop, clasts in are elongated and define a lineation, although it is not clear whether this is a sedimentary or a deformational feature (Fig. 4.9c).

Rocks in the Warriedar Hill area are host two map-scale structural features; a km-scale F_3 fold and a sequence of broadly layer-parallel shears that are interpreted as a D_4 imbricate structure. Although folding is not distinguished by field mapping or observed on an outcrop-scale, kilometre-scale folding is exhibited on aeromagnetic imagery of the Warriedar Hill area, defined primarily by BIF units interleaved with dacitic volcanic rocks (Fig. 4.10c). Based on aeromagnetic map patterns and way-up criteria, the observed folding consists of a single km-scale tight to isoclinal, upright synform with a north-northwest-trending fold axis, approximately parallel to the sparsely measured S_3 cleavage (Fig. 4.8). The plunge of this fold has not been constrained, although it is most likely southeast-plunging considering the lack of demonstrably overturned rocks in the area. Porphyritic dacite occurs in the cores of the synform (Fig. 4.8). As similar fold geometries with northwest-trending fold axes have been identified in Mougooderra Fm rocks to the northwest at Chulaar Hill, folding at Warriedar Hill is also attributed to D_3 deformation. An D_4 imbricate structure interpreted in the northeastern Warriedar Hill area based on field mapping and satellite imagery is displayed in Figure 4.10 and described in Section 4.5.6.3.

The Seeligson Monzogranite is not exposed in the Warriedar Hill area, although granite occurs as float, displays a change to quartz sand-dominated superficial cover and truncates Mougooderra Fm units and F_3 folding on aeromagnetic imagery. Furthermore, a ~30 m-wide, ENE-trending, graphic-textured pegmatite dyke comprising large (up to 15 cm) crystals of K-feldspar, quartz and minor biotite is exposed ~400 metres from the Seeligson Monzogranite contact. This pegmatite dyke dissect all other lithologies and an F_3 synform (Fig. 4.8).

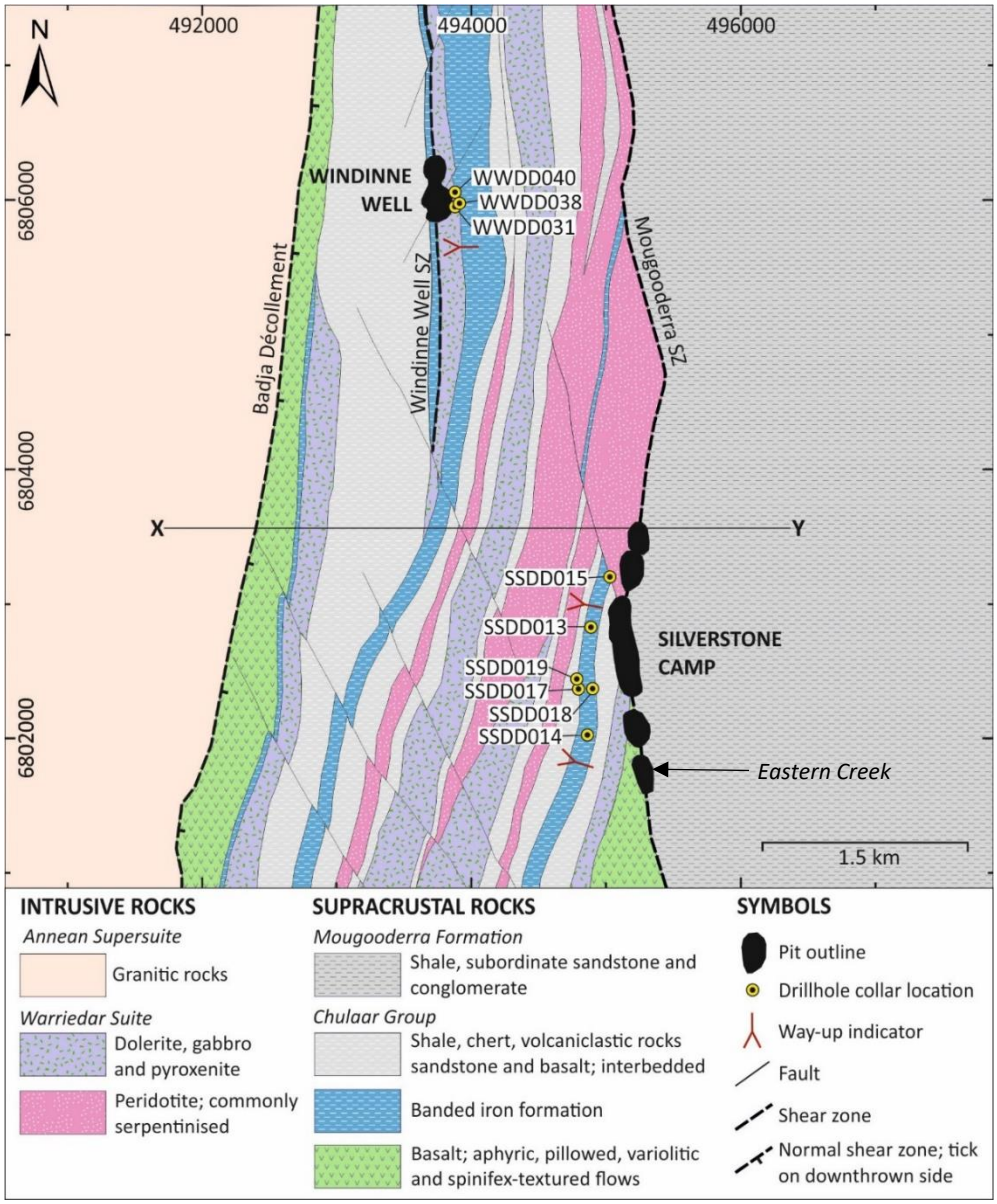

Figure 4.11: Geological map of the area surrounding the Silverstone camp and Winddine Well gold deposits, displaying collar locations of drillholes utilised in this study. The cross section along the fenceline X-Y is shown in Figure 9.21. Geology courtesy of Minjar Gold Pty. Grid is MGA Zone 50.

4.5.6 D_4 deformation

D_4 deformation in the YSGB is characterised by multiple NNE- to NNW-striking shear zones, several of which are host to lode-gold mineralisation. In the Rothsay area, D_4 deformation is represented by the mineralised Rothsay Shear Zone and the Enchanted Shear Zone (Section 3.5.6). Elsewhere in the YSGB, the Mougooderra Shear Zone (MSZ) and the Chulaar Shear Zone (CSZ) are D_4 structures located at the western and eastern margins of the Mougooderra Fm respectively (Fig. 4.1). Another D_4 structure, the Winddine Well Shear Zone (WWSZ), has been identified in the greenstone succession to the west of the MSZ and is also host to a lode-gold deposit (Fig. 4.1). The geometry, structure and kinematics of the MSZ, WWSZ and CSZ are described below.

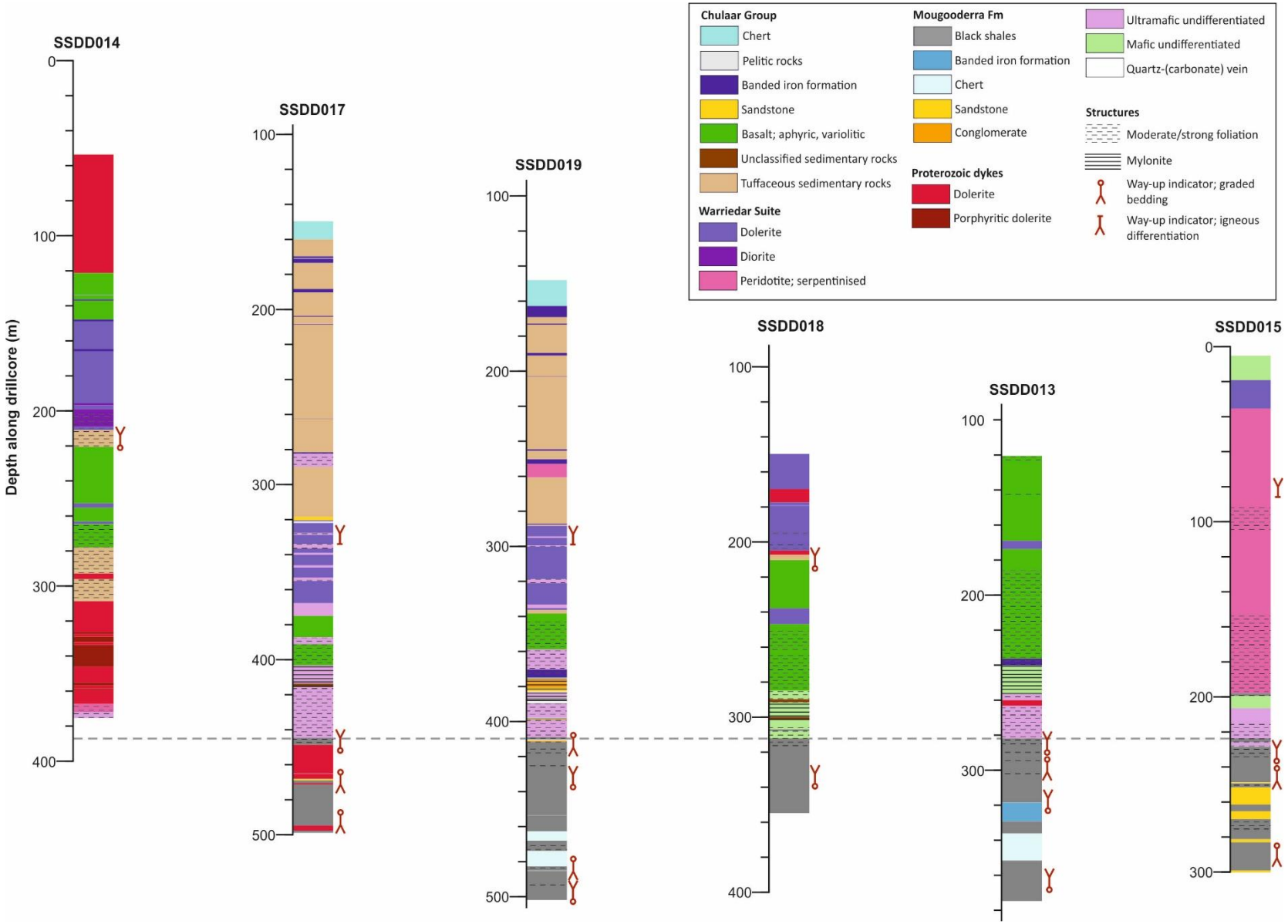

Figure 4.12: Drillhole logs for the Silverstone deposit, constructed from lithological and structural logging undertaken in this study. Collar locations are displayed on Figure 4.11 and details are shown in Table 4.1. Drillholes are arranged from south (left) to north (right) and have been drilled towards the east at an initial inclination of ~60° (SSDD013-15) and ~70° (SSDD017-19). The drillholes are aligned along the basal contact with Mougooderra Fm rocks (dashed). Way-up indicators are displayed in red alongside each drillhole.

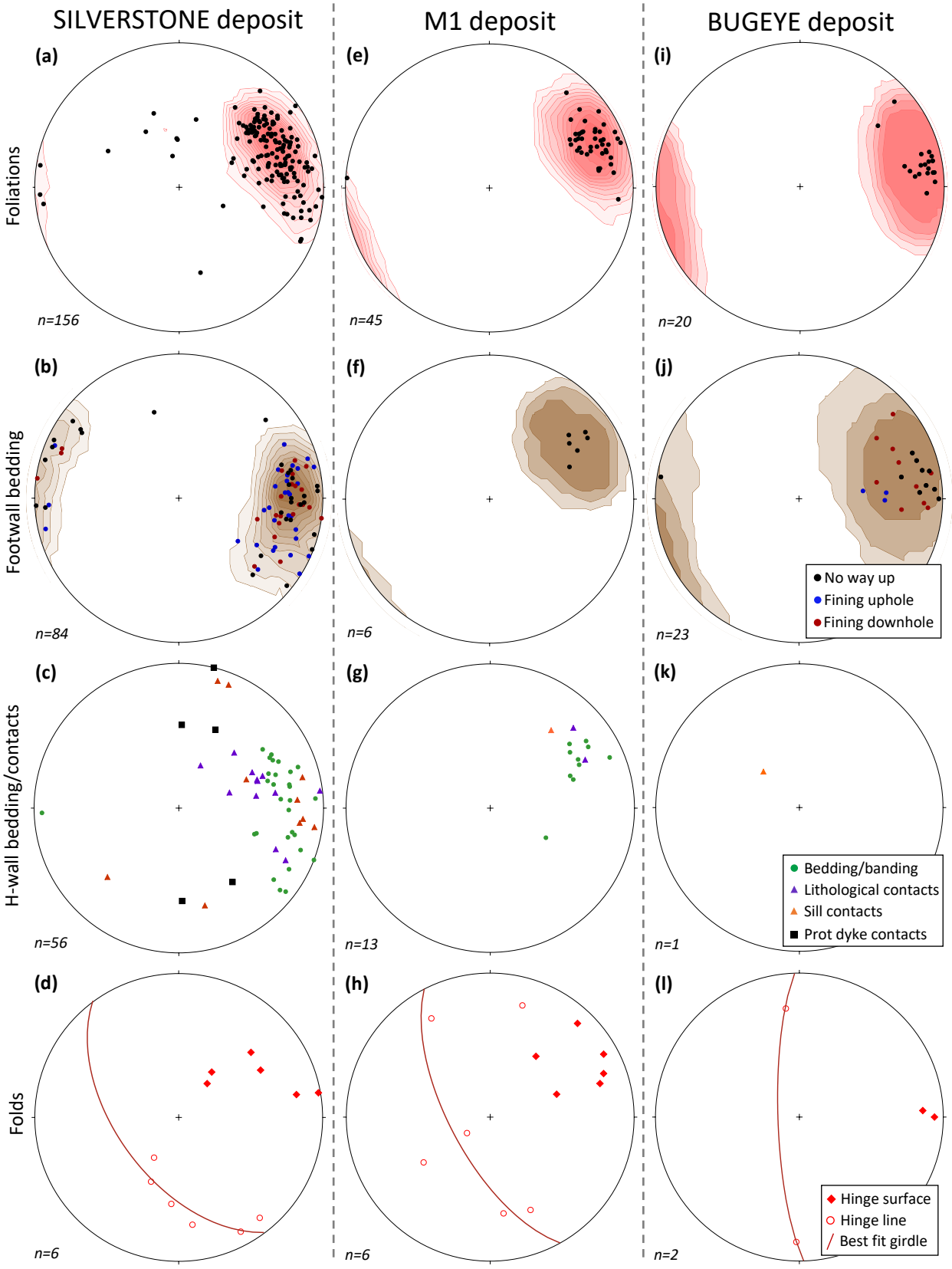

(caption on next page)

Figure 4.13 (previous page): Lower hemisphere equal area stereonets summarising structures observed along the Mougooderra Shear Zone, in oriented drillcore from the Silverstone (a-d), M1 (e-h) and Bugeye (i-l) deposits. In all stereonets, the poles to planes are displayed. Kamb contours are shown in (a-b), (e-f) and (i-j) and are drawn at 2σ intervals. **(a)** Foliation measurements at the Silverstone deposit; **(b)** Bedding in Mougooderra Fm metasedimentary footwall rocks at the Silverstone deposit – separated into those with no graded bedding, those with fining uphole graded bedding and those with fining downhole graded bedding; **(c)** Structures in hangingwall rocks at Silverstone comprising bedding (including banding observed in BIF), lithological contacts between supracrustal rocks, intrusive contacts between supracrustal rocks and Warriedar Suite intrusive sills and contacts of Proterozoic dykes; **(d)** Hinge surfaces and hinge lines of folding observed in drillcore at Silverstone. A best fit girdle for hinge lines is shown in red and is oriented parallel to the shear plane. Stereonets (e) to (h) for the M1 deposit and (i) to (l) for the Bugeye deposit are equivalent to stereonets (a) to (d) for the Silverstone deposit.

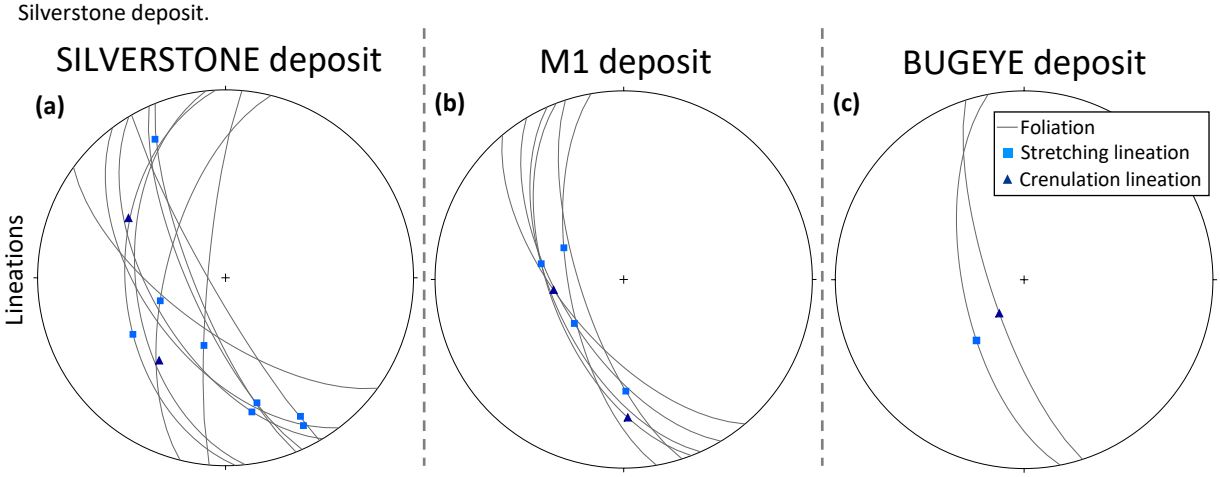

Figure 4.14: Lower hemisphere equal area stereonets of lineations observed in drillcore along the Mougooderra Shear Zone, from the Silverstone (a), M1 (b) and Bugeye (c) deposits. Both mineral stretching lineations and crenulation lineations are shown with corresponding foliation planes.

4.5.6.1 Mougooderra Shear Zone (MSZ)

The MSZ is a ~50 km, north-striking, unexposed D_4 shear zone located primarily along the western margin of the Mougooderra Fm, but also extending into the underlying greenstone succession at Mt Mulgine (Fig. 4.1). The MSZ is host to numerous lode-gold deposits and possesses a current gold resource of ~800 koz. Over the last 20 years, a total of 20 shallow pits have been mined along the MSZ, providing limited access to outcrop along the shear that is otherwise concealed by 10-15 m of superficial cover. Unfortunately, due to an extensive, deep weathering profile, pit exposures are invariably highly oxidised and altered and as such, are of limited use for identifying lithologies and structural features. Oriented drillcore has recently been obtained from fresh rock beneath three deposits along the MSZ: Silverstone, M1 and Bugeye (Fig. 4.1).

Lithological and structural logging of oriented drillcore from six drillholes at the Silverstone camp, and single drillholes at the M1 and Bugeye deposits, have been undertaken as part of this study. The structural characteristics of the MSZ at Silverstone, Bugeye and M1 are described successively below.

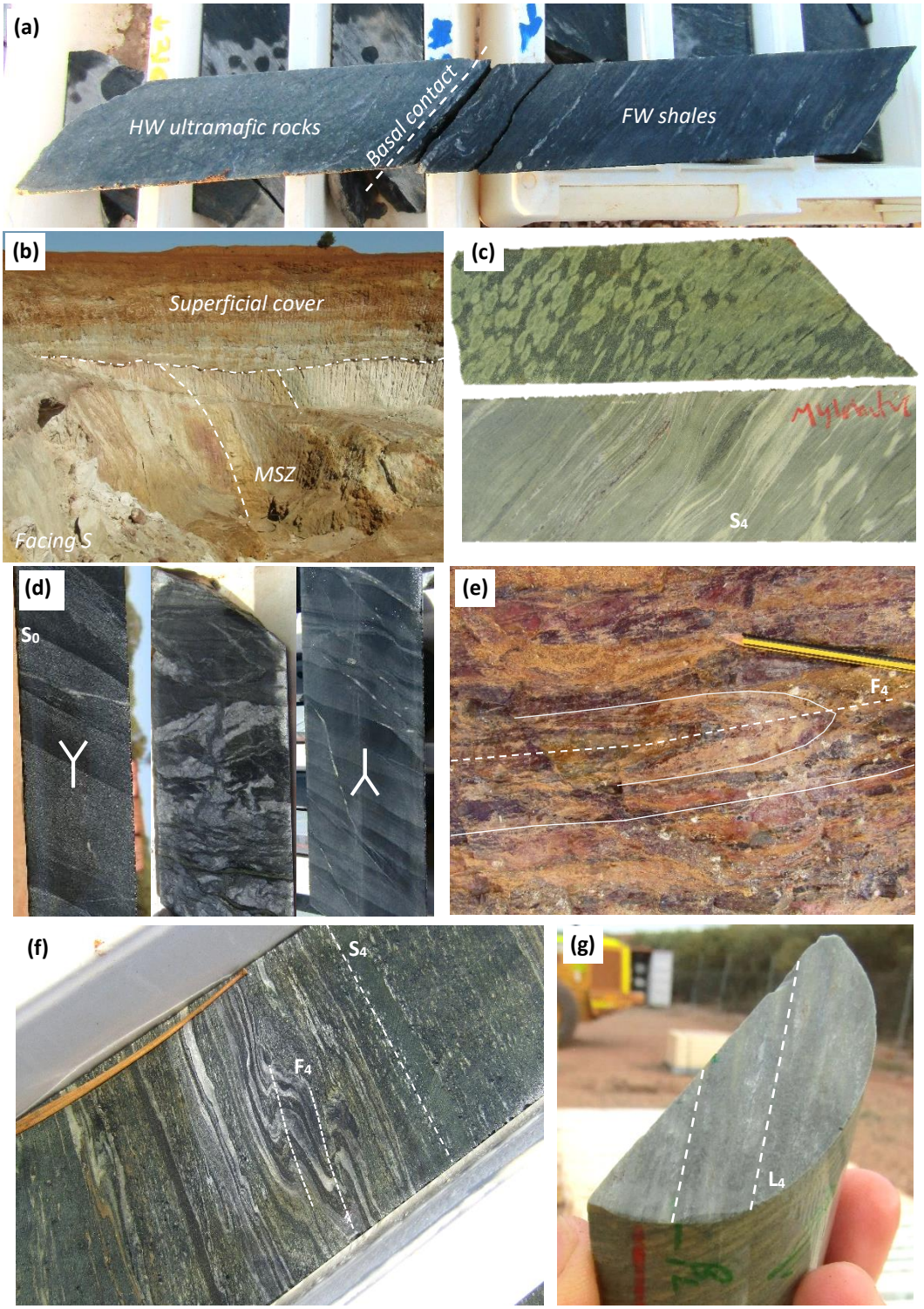

Figure 4.15: Photographs of structures along the Mougooderra Shear Zone at the Silverstone deposit, both in drillcore and in open cast pits. NQ-sized (diameter ~50 mm) drillcore is displayed in photographs. **(a)** The basal contact between hangingwall ultramafic rocks and footwall metasedimentary rocks (SSDD018; 312.1 m); **(b)** Photograph of the Mougooderra Shear Zone in the Eastern Creek pit, taken facing south; **(c)** An example of a weakly foliated variolitic basalt that has been deformed into a mylonite in the hanging wall of the shear zone (SSDD018; 255-287 m); **(d)** An example of reversal in the orientation of graded bedding in footwall shales proximal to the shear zone, separated by a highly deformed and veined interval (SSDD019; 405-419 m); **(e)** Isoclinal layer-parallel F_4 fold in hangingwall BIF on the western wall of the Eastern Creek pit, facing west; **(f)** Centimetre-scale F_4 folding of veined, chlorite-epidote altered basalt, with hinge surfaces parallel to the S_4 foliation (SSDD019; 364.9 m); **(g)** Down-dip L_4 stretching lineation in hanging-wall variolitic basalt (SSDD013; 202.8 m).

Silverstone deposit

The Silverstone deposit consists of six oxide pits along a 1.6 km length of the MSZ (Fig. 4.11). Lithological logs of six drillholes collared along the strike length of the Silverstone deposit (drilled from west of the MSZ towards the east; details shown in Table 4.1) are displayed in Figure 4.12. The geology to the west of the MSZ at Silverstone consists of Chulaar Group aphyric and variolitic basalt, tuffaceous volcaniclastic rocks, BIF and chert, intruded by Warriedar Suite mafic-ultramafic sills, primarily composed of dolerite and serpentinite. These units intersect the MSZ at an angle of ~20°, such that there is a progression from mafic volcanic and tuffaceous rocks in the south, to ultramafic-dominated units in the north (Fig. 4.11; Fig. 4.12). Rocks to the east of the MSZ consist principally of Mougooderra Fm shales, with lesser BIF, chert and subordinate sandstone and conglomerate (Fig. 4.12). The MSZ is intruded by Proterozoic dolerite dykes, which are undeformed, unaltered and particularly abundant in the southern part of the Silverstone deposit (Fig. 4.12; Section 4.5.8).

Structural analyses at Silverstone has identified a principal north-northwest striking S_4 foliation that consistently dips towards the west at 55-80°, most frequently ~65° (Fig. 4.13a). This matches the orientation of the main shear zone contact observed both in drillcore (Fig. 4.15a) and in oxide pits (Fig. 4.15b) and confirms the west-dipping nature of the MSZ to depths of at least ~200 m below the surface. Consequently, Chulaar Group and Warriedar Suite rocks to the west of Silverstone comprise the hanging wall of the MSZ, and Mougooderra Fm rocks to the east form the footwall. The slight variation in strike of S_4 corresponds to the change in orientation of the MSZ towards the north of Silverstone (Fig. 4.13).

S_4 fabric intensity increases towards the centre of the MSZ and is most intense in a 10-18 m-thick mylonitic zone, situated in the hangingwall ~10-40 metres above the basal contact (Fig. 4.12). The mylonite occurs as a banded, fine grained and veined unit with abundant ductile structures acting as shear sense indicators. In some instances, distinctive units such as variolitic basalt can be traced into the mylonitic zone (Fig. 4.15c). This mylonite appears to be best developed in mafic volcanic and sedimentary protoliths, and is not as evident in ultramafic rocks, such as those in the north (Fig. 4.12). In several drillholes, the core of the shear zone comprises one or more alternations between footwall units and hangingwall units, up to several metres in thickness and separated by narrow shears (Fig. 4.12). Narrow zones of increased foliation intensity also occur in hanging-wall units up to 150 m from the centre of the shear zone, commonly at rheological contacts such as the margins of Warriedar Suite intrusions.

Bedding and lithological contacts in hangingwall units dip ~50-80° west at orientations that partially overlap with the S_4 fabric (Fig. 4.13c). This is largely replicated by the intrusive contacts of Warriedar

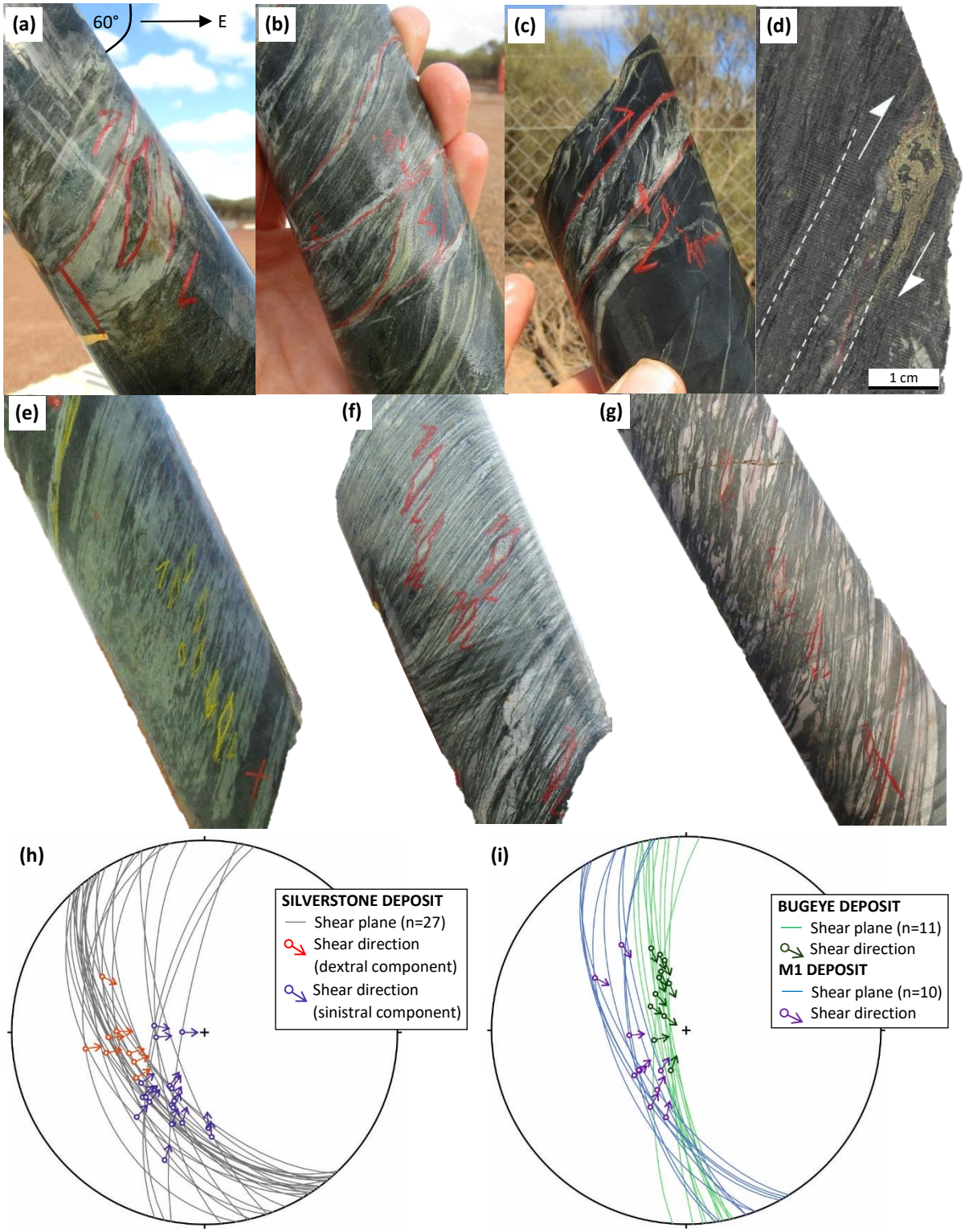

Figure 4.16: Shear sense indicators observed in oriented core along the Mougooderra Shear Zone, from the Silverstone (a-d), M1 (e-f) and Bugeye (g) deposits, all displaying ubiquitous west-side-up movement. All photographs contain NQ drillcore with a diameter of ~50 mm. Drillcore photographs are oriented according to the inclination and azimuth of the respective drillholes, facing north, as indicated in (a). **(a)** Sheared spherules in variolitic basalt (SSDD014 266.0 m); **(b)** SC fabric in sheared variolitic basalt in the hangingwall of the shear (SSDD017, 405.25 m); **(c)** Sheared quartz-carbonate veining in footwall shales (SSDD019, 443.6 m); **(d)** Pyrite σ clast in footwall shales with tails showing west-side up movement (SSDD018, 315.45 m); **(e)** Deformed varioles in basalt at M1 (M1DD026, 184.24 m); **(f)** Quartz σ clasts in footwall volcaniclastic rocks at M1 (M1DD026, 422.1 m)**; (g)** Sheared BIF at the Bugeye deposit with multiple chert σ clasts (BEDD002, 224.2 m); **(h)** Lower hemisphere equal area stereonet of shear planes and shear directions calculated from vorticity vector measurements at Silverstone; shear directions are separated into those with minor dextral (red) and sinistral (blue) components and arrows denote the direction of hangingwall movement; **(i)** Lower hemisphere equal area stereonet of shear planes and shear directions calculated from vorticity vectors in oriented drillcore at Bugeye and M1, arrows denote direction of hangingwall movement.

Suite sills. However, the orientations of hangingwall units distal to the shear zone become progressively northeast-southwest striking, matching the regional strike direction of these units (Fig. 4.11). This, along with way up criteria that indicates that hanging-wall units are consistently overturned (Section 4.5.3), indicates the gradual transposition of hanging-wall units into an S_4 orientation on approach to the MSZ.

Bedding orientations in footwall metasedimentary rocks are consistent along the length of the Silverstone deposit; typically steeply west-dipping at 65-85°, and occasionally steeply east-dipping (Fig. 4.13b). Footwall shales are characteristically finely bedded on a centimetre to decimetre-scale and contain abundant graded bedding, which can be used as a reliable way-up indicator. Footwall shales close to the shear zone contact display systematic reversals in the fining direction exhibited by graded bedding over intervals of 5-30 m, separated by narrow (< 1 m) intervals of highly deformed, foliated and veined shales (Fig. 4.15d). Bedding orientations are consistent regardless of fining direction in shales (Fig. 4.13b), ostensibly defining isoclinal folding in footwall sedimentary rocks. These folds are frequently observed proximal to the MSZ but are seldom present >60 m from the shear zone contact, suggesting that they are F_4 folds related to D_4 shearing, rather than pre-existing structures. The narrow, highly deformed zones in shales separating graded bedding reversals are likely expressions of isoclinal F_4 fold hinges that have accommodated shear.

Conspicuous layer-parallel F_4 folds are present in drillcore from both hangingwall and footwall units, most commonly in banded lithologies such as BIF and chert. These folds are typically layer-parallel, isoclinal folds, with hinge surfaces that are parallel to the local S_4 (Fig. 4.13d). Fold hinges consistently lie within a steeply southwest dipping plane that is parallel to S_4 and the orientation of the shear zone (Fig. 4.13d). Isoclinal F_4 folds have also been identified in several pit exposures at Silverstone (Fig. 4.15e), and as centimetre-scale folded quartz-carbonate veins in mafic rocks (Fig. 4.15f).

Several lineation orientations have been identified in Silverstone drillcore. On S_4 foliation planes, including units which contain abundant shear sense indicators, a steep, down-dip L_4 stretching lineation is occasionally defined by alignment of albite and chlorite in mafic rocks (Fig. 4.15g) and serpentine in ultramafic rocks and plunges to the west-southwest (Fig. 4.14a). In metasedimentary rocks, a rare crenulation lineation has a similar orientation. A further group of lineations plunge towards the southeast at 10-25° and are primarily identified in deformed ultramafic units (Fig. 4.14a).

A variety of shear sense indicators have been identified in all six drillholes at Silverstone. Shear sense indicators in hangingwall rocks include sheared varioles in variolitic basalt (Fig. 4.16a), and SC fabrics in sheared mafic and ultramafic units (Fig. 4.16b), whilst footwall rocks contain sheared veining (Fig. 4.16c) and occasionally, SC fabrics in deformed shales. Proximal to the mineralised zones, sulphide

aggregates are commonly deformed as sigma clasts with distinct tails that can also be used to determine shear sense (Fig. 4.16d). In all instances, shear sense indicators at Silverstone display ubiquitous west-side up sense of movement, in which the hangingwall units to the west have moved up relative to footwall rocks in the east. Shear directions (determined from vorticity vector measurements; Section 4.4.3) consistently show a principal vertical component, with only a minor lateral component (Fig. 4.16h). The lateral component of shear is variable, but most commonly sinistral (Fig. 4.16h).

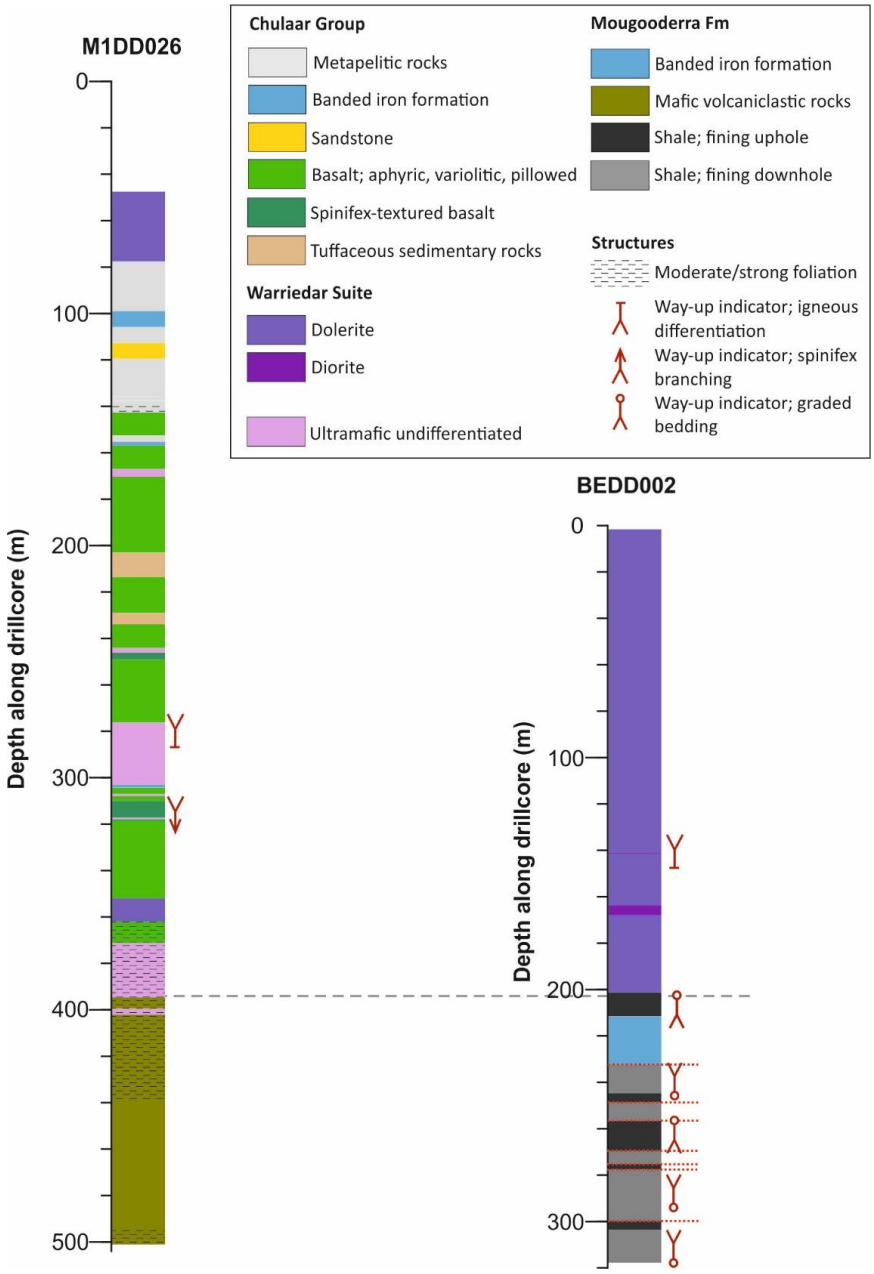

Figure 4.17: Drillcore logs from the Bugeye and M1 deposits, constructed from lithological and structural logging undertaken in this study. Drillholes have been drilled towards the east at an initial inclination of ~60° (see Table 4.1). The drillholes are aligned along the basal contact with Mougooderra Fm rocks. Way-up indicators are displayed in red alongside each drillhole.

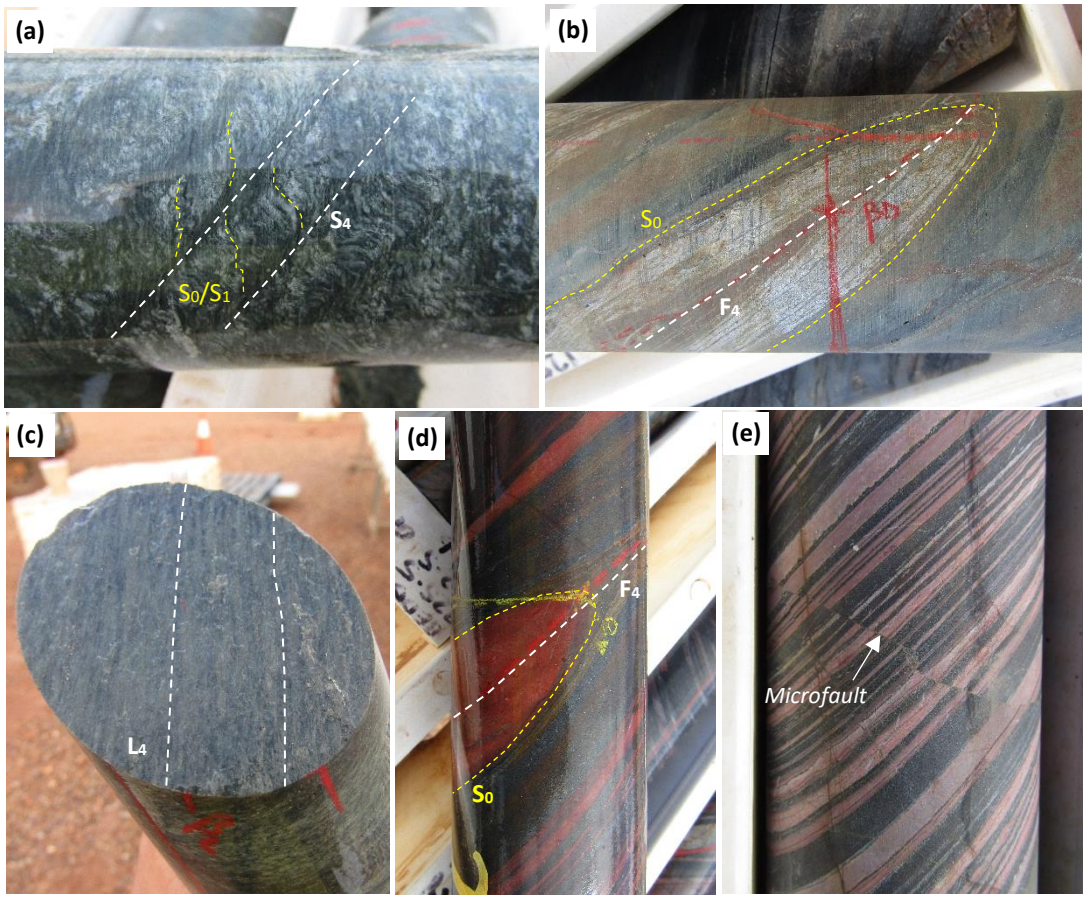

Figure 4.18: Photographs of structures along the Mougooderra Shear Zone from drillcore at the M1 (a-c) and Bugeye (d-e) deposits. NQ-sized (diameter ~50 mm) drillcore is displayed in photographs. **(a)** Spinifex-textured basalt deformed by an S_4 spaced crenulation. The deformed fabric may reflect the original orientation of aligned spinifex-textured crystals, or an S_1 layer-parallel foliation (M1DD026; 247.2 m); **(b)** Isoclinal F_4 fold of quartz-carbonate veining and S_0 bedding in hangingwall shales, with a hinge surface parallel to the S_4 fabric (M1DD026; 130.8 m); **(c)** L_4 stretching lineation on an S_4 foliation plane in sheared variolitic basalt in the hangingwall of the MSZ at M1 (which are used as a shear-sense indicator – Fig. 4.16e) (M1DD026; 171.7 m); **(d)** F_4 isoclinal fold in BIF at the Bugeye deposit (BEDD002; 213.0 m); **(e)** Late-stage brittle microfault displacing banding in BIF at Bugeye, showing a displacement of ~5 mm (BEDD002; 220.0 m).

M1 deposit

The M1 deposit is located on the MSZ, approximately 9 km north of the Silverstone deposit (Fig. 4.1). A lithological log of a drillhole intersecting the MSZ at M1 is displayed in Figure 4.17. At M1, rocks to the west of the MSZ consist of Chulaar Group aphyric, variolitic and spinifex-textured basalts, in addition to lesser BIF, sandstone and pelitic rocks. These rocks are intruded by Warriedar Suite doleritic rocks and serpentinised ultramafic units are likely derived from either the ultramafic portions of intrusive sills or high-Mg volcanic units (Fig. 4.17). In contrast, rocks to the east of M1 are comprised of mafic volcaniclastic rocks with variable sedimentary quartz content, which, based on structural relations, are tentatively ascribed to the Mougooderra Fm (Fig. 4.17). At M1, bedrock is extensively weathered to depths of at least 90 m below surface.

Structural analysis has been undertaken on drillcore at M1 for comparisons to be made with the structural features of the MSZ at Silverstone. At M1, the orientation of the S_4 fabric and shear planes is equivalent to that at Silverstone, dipping to the west-southwest at 55-85° (Fig. 4.13e) and demonstrating a mafic-ultramafic hanging-wall to the west (Fig. 4.17). S_4 foliation intensity increases towards the centre of the shear zone, where a ~3 m-thick ultramafic hangingwall unit is sheared with footwall rocks (Fig. 4.17). Unlike Silverstone, there is limited development of banded mylonitic rocks at M1. In hanging-wall spinifex-textured basalts, S_4 occurs as a spaced crenulation and deforms an earlier planar fabric that may represent the original orientation of aligned spinifex-textured crystals, or an S_1 layer-parallel foliation (Fig. 4.18a).

Lithological contacts and bedding in both footwall (Fig. 4.13f) and hangingwall rocks (Fig. 4.13g) are consistently parallel to S_4. Way-up criteria such as spinifex branching and basal cumulates of high-Mg basalt units demonstrate that hangingwall units are overturned on approach to the MSZ. F_4 isoclinal folding occurs in various lithologies towards the centre of the MSZ, including folded quartz-carbonate and epidote-carbonate veins (Fig. 4.18b). The hinge surfaces of these folds are invariably parallel to S_4, and fold hinges broadly lie within a steeply west-dipping plane parallel to the shear zone (Fig. 4.13h). An L_4 stretching lineation is occasionally defined by chlorite and albite on S_4 surfaces (Fig. 4.18c), plunging towards the south to west and typically oriented with a significant down dip component relative to S_4 (Fig. 4.14b). Shear sense indicators including sheared variolitic basalt (Fig. 4.16e), sheared quartz-carbonate veining, SC fabrics and sigma clasts in sheared footwall volcaniclastic rocks (Fig. 4.16f) show unanimous west-side up movement. Shear directions are remarkably similar to those at Silverstone, with a principal vertical component of movement, supporting reverse shear (Fig. 4.16i).

Bugeye deposit

The Bugeye deposit is located on the MSZ, approximately 10 km south of Silverstone and 19 km south of M1. A lithological log of a drillhole through the MSZ at Bugeye is displayed in Figure 4.17. The rocks to the west of Bugeye consists of dolerite and diorite comprising Warriedar Suite intrusions, whereas rocks to the east are predominantly Mougooderra Fm shales, BIF and subordinate sandstone and chert (Fig. 4.17). The S_4 foliation at Bugeye dips towards the west at 63-83°, broadly consistent with the orientation of the MSZ at Silverstone and M1, with a slight variation in strike (Fig. 4.13i). The intensity of the S_4 fabric increases in dolerite towards the shear zone. However, within BIF in the centre of the MSZ, strain is localised in 10 cm – 1 m intervals of highly deformed, brecciated BIF, separated by

relatively undeformed, laminar units. Shear is also localised along dolerite-BIF and BIF-shale contacts.

Bedding in footwall metasedimentary units dips towards the west-southwest, principally between 55-80°. Footwall shales exhibit 5-20 m-scale F_4 isoclinal folding as observed at Silverstone, characterised by reversals in graded bedding orientations without a discernible change in the orientation of bedding, separated by narrow, highly deformed intervals that correspond to fold hinges (Fig. 4.17). These inconspicuous F_4 folds decrease in abundance away from the MSZ, where bedding reverts to fining towards the east (Fig. 4.17). Tight to isoclinal F_4 folds are also observed in BIF within the shear zone (Fig. 4.18d), with hinge surfaces parallel to S_4 and sub-horizontal fold axes (Fig. 4.13l).

Shear sense indicators including sigmoidal chert fragments in deformed BIF and sheared veins in footwall shales consistently demonstrate west side up movement (Fig. 4.16g), and shear directions contain a dominant vertical component (Fig. 4.16i). Furthermore, a steep down-dip stretching lineation is defined by albite on S_4 foliation planes (Fig. 4.14c). These observations are entirely consistent with structures observed along strike at Silverstone and M1. At Bugeye, BIF and chert units contain sub-horizontal faults that displace all other structures and have displacements on the order of 3-20 mm (Fig. 4.18e).

4.5.6.2 Winddine Well Shear Zone (WWSZ)

The WWSZ is a north-striking D_4 shear zone situated within the lower greenstone succession in the western part of the YSGB, approximately 1.5 kilometres west of the MSZ (Fig. 4.11). The WWSZ is host to the ~100 koz Winddine Well lode-gold deposit, which has been exploited as an open cast oxide pit. As is the case along the MSZ, pit exposures are typically highly altered, oxidised and difficult to access. Oriented drillcore has recently been obtained from fresh rock underlying the Winddine Well pit and intersecting a mineralised segment of the WWSZ. Lithological and structural logging of oriented drillcore from three such drillholes has been undertaken as part of this study (Fig. 4.19). Collar locations are displayed on Figure 4.11 and further details for each drillhole are shown in Table 4.1.

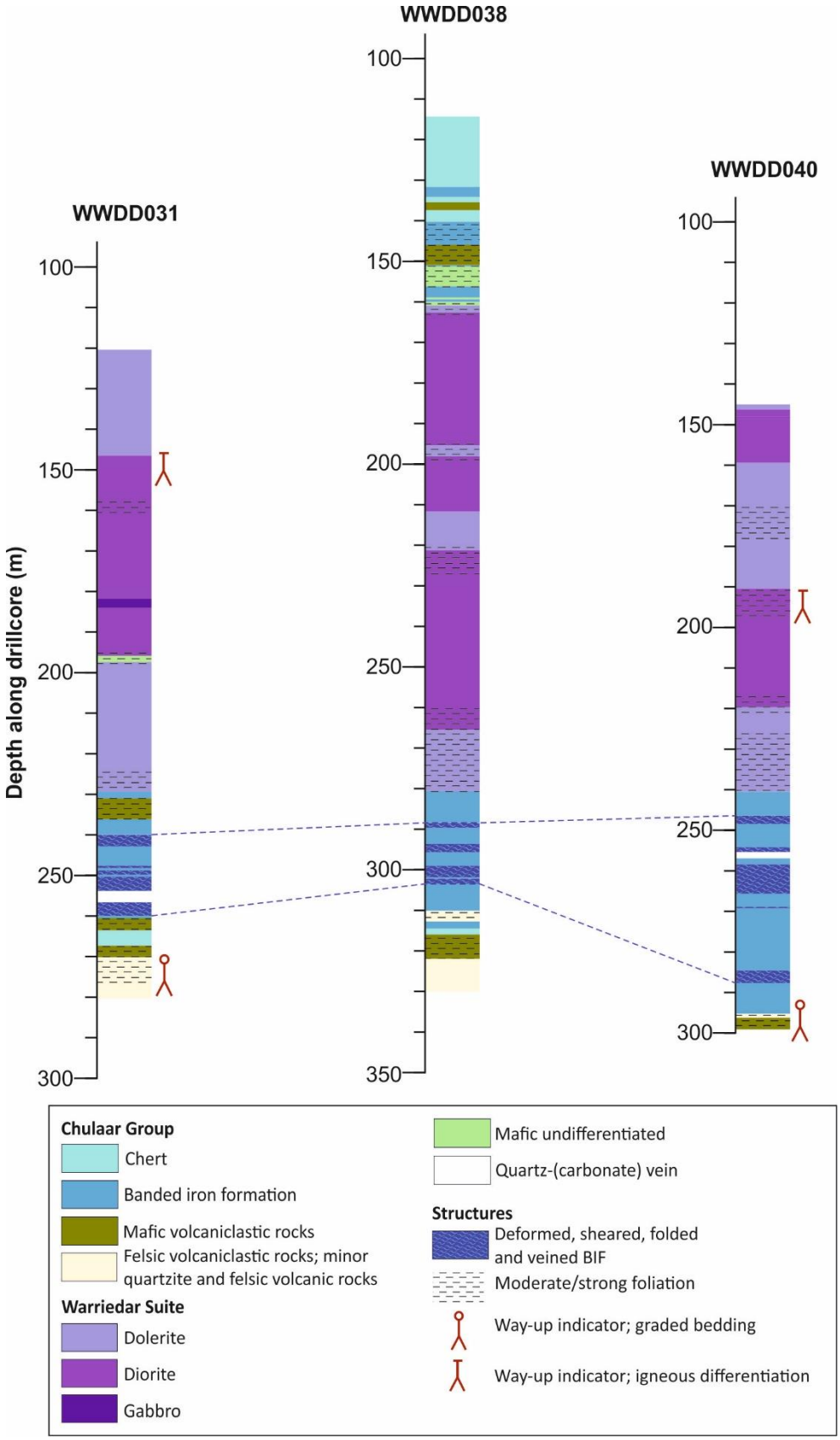

Figure 4.19: Drillcore logs from Winddine Well deposit, constructed from lithological and structural logging undertaken in this study. Drillholes are arranged from north (left) to south (right) and have been drilled towards the west at an initial inclination of ~60° (see Table 4.1). The margins of sheared, mineralised zones in BIF are correlated between drillholes. Way-up indicators are displayed in red alongside each drillhole.

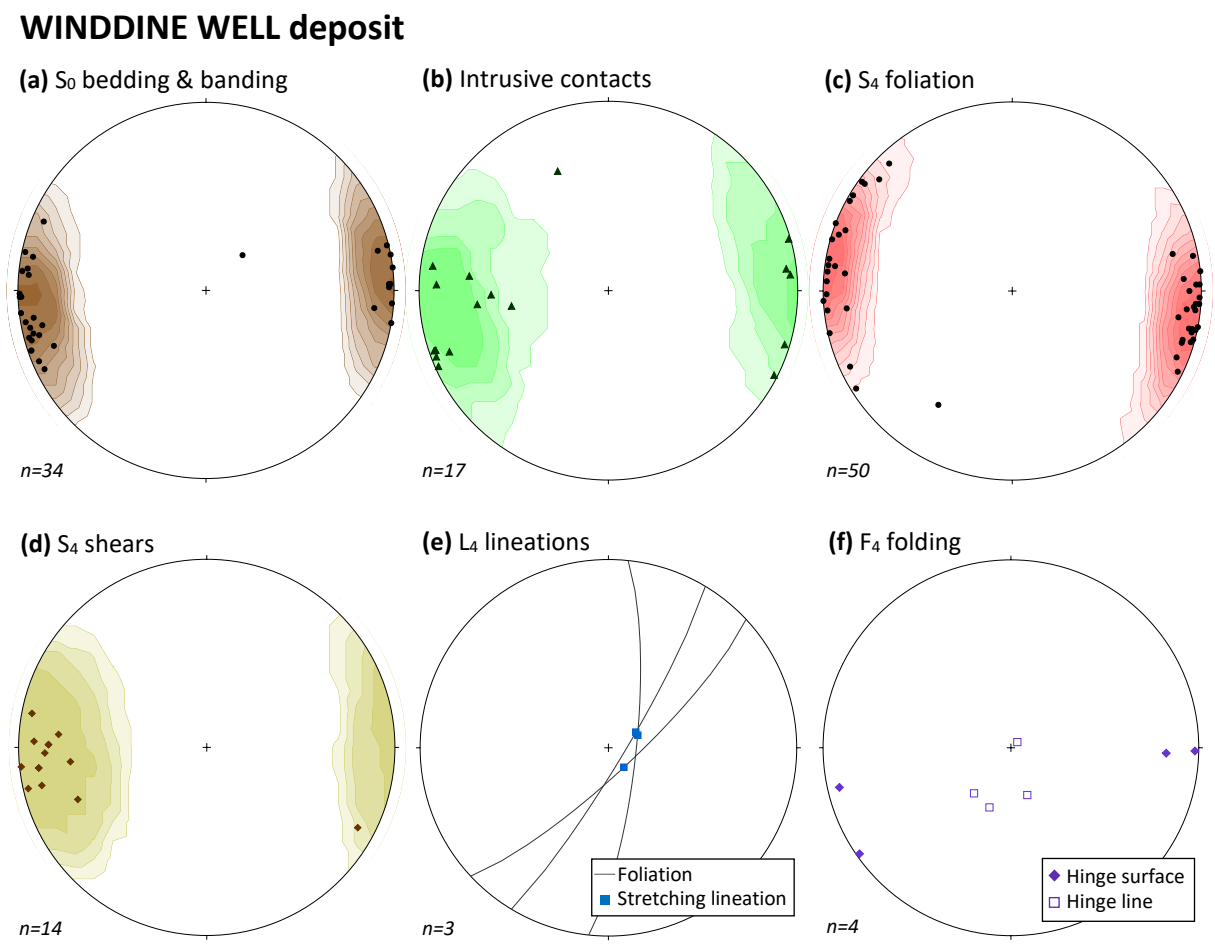

Figure 4.20: Lower hemisphere equal area stereonets of structural data from oriented drillcore intersecting the Winddine Well Shear Zone at the Winddine Well deposit. The poles to planes are shown in (a) to (d). Kamb contours are shown in (a)-(d) and are drawn at 2σ intervals. **(a)** S_0 bedding in volcaniclastic units and banding in BIF; **(b)** Intrusive contacts between Warriedar Suite intrusions and supracrustal rocks; **(c)** S_4 foliation measurements proximal and within the WWSZ; **(d)** Mineralised sheared contacts within BIF at the Winddine Well deposit; **(e)** Mineral stretching lineations and corresponding foliation planes; **(f)** Folding observed in drillcore – the poles to hinge surfaces are shown for comparison to foliation and bedding orientations.

The geology at Winddine Well consists of a steeply east-dipping to vertical, north-striking, ~20 m-thick unit of BIF interbedded with minor volcaniclastic rocks (Fig. 4.20a). These rocks are bound to the west by felsic and mafic volcaniclastic rocks and minor beds of chert, and bound to the east by a ~100 m-thick succession of Warriedar Suite dolerite, gabbro and diorite (Fig. 4.19). Warriedar Suite intrusions are broadly intruded parallel to the supracrustal stratigraphy (Fig 4.20b). Further chert, BIF and volcaniclastic rocks occur ~100 metres to the east of the BIF unit at Winddine Well. The WWSZ occurs principally within and at the margins of the ~20 m-thick BIF unit at Winddine Well.

Structural analysis of drillcore reveals that the S_4 fabric at Winddine Well is oriented approximately parallel to bedding and intrusive contacts; striking north-south and variably dipping to the east or west at greater than 80° (Fig. 4.20c). The foliation intensity is greatest at the western and eastern margin

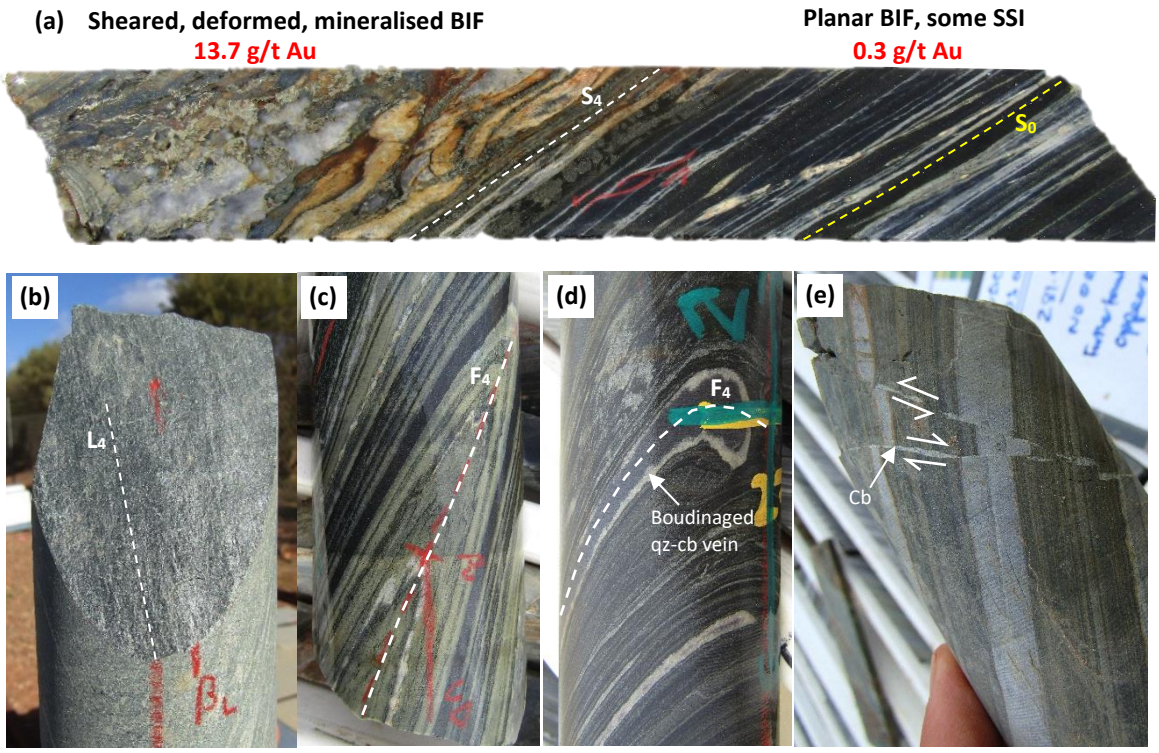

Figure 4.21: Photographs of structures from the Winddine Well Shear Zone, in drillcore from the Winddine Well deposit. NQ-sized (diameter ~50 mm) drillcore is displayed in photographs. **(a)** Drillcore illustrating the margin between highly deformed, folded, veined and mineralised BIF, containing abundant sulphides and visible gold, and relatively undeformed laminar BIF with minor boudinage of chert horizons/veining and significantly lower gold grade (WWDD031; 248.2 m); **(b)** Steep down-dip L_4 stretching lineation defined by micas in a fine grained metasedimentary rock (WWDD031; 231.3 m); **(c)** Isoclinal F_4 folding of BIF, of which the hinge surface is parallel to S_4 (WWDD040; 287 m); **(d)** Isoclinal F_4 folding of BIF and a layer-parallel, boudinaged quartz-carbonate vein. Note that the apparent curved appearance of the F_4 hinge surface is due to the curvature of the core (WWDD040; 274m); **(e)** Extensional, sub-horizontal faulting displacing banding in BIF, with minor carbonate infill along the fault planes – the orientation of the core is approximately as in situ (WWDD040; 281.5 m)

of the BIF at Winddine Well. S_4 is also observed over intervals within mafic intrusive rocks to the east, primarily at lithological contacts and sill margins (Fig. 4.19), and is distinguished from the S_1 layer-parallel foliation observed elsewhere in the belt based on consistent shear sense indicators. Within the Winddine Well BIF unit, shearing is localised in three to four highly deformed, brecciated, veined and mineralised intervals ranging between 30 cm and 5 m in thickness, hosting elevated gold grades of up to 40 g/t (Fig. 4.21a). These zones can be broadly correlated along strike between drillholes and the orientation of the margins of these shear zones is typically steeply east-dipping at > 60° (Fig. 4.20d). Notably, these orientations are marginally distinct from the dominant S_4 fabric in surrounding rocks. Highly deformed zones are separated by relatively undeformed, laminar BIF, which typically lack quartz veining and sulphide mineralisation and consequently, contain lower gold grades (Fig. 4.21a).

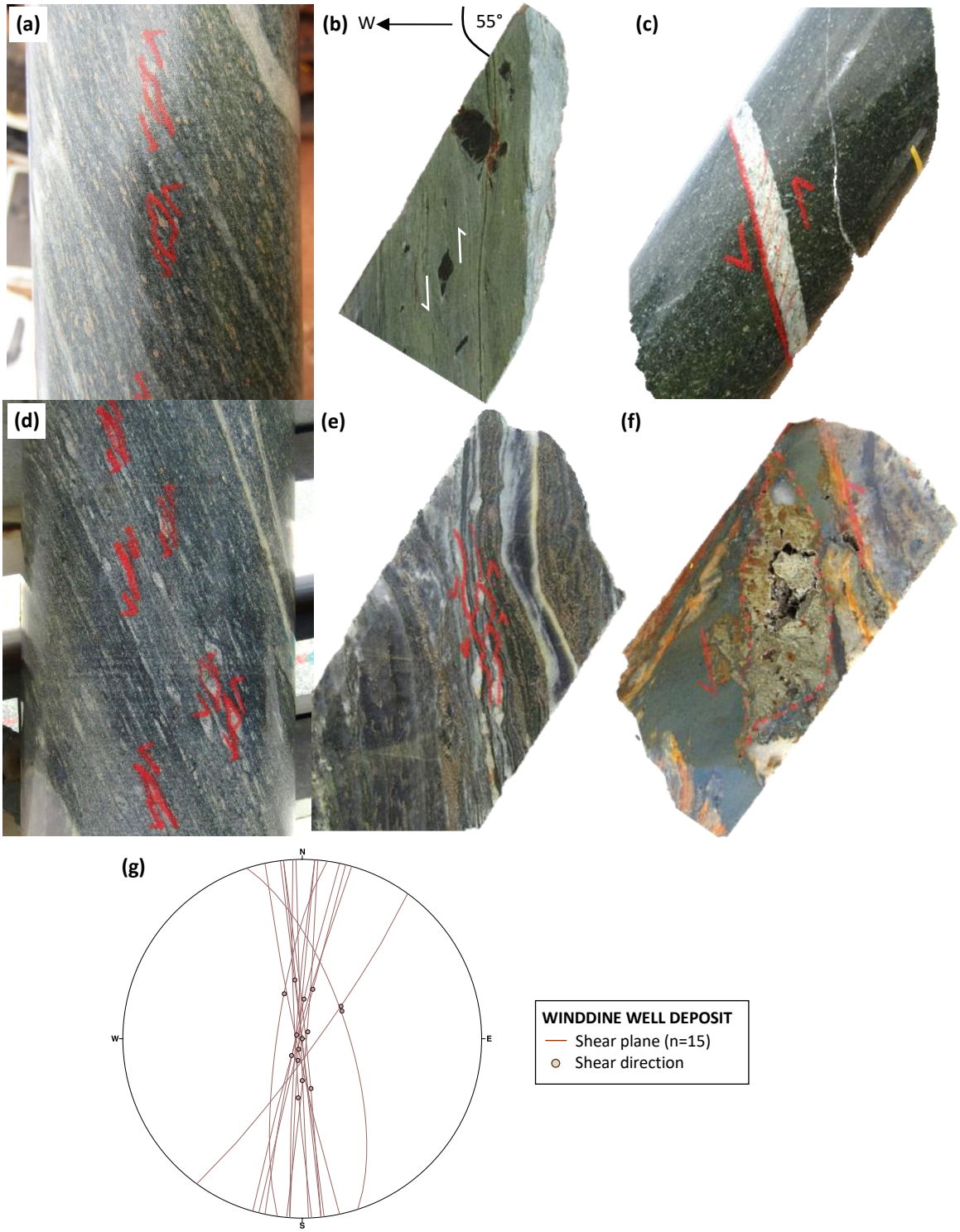

Figure 4.22: Shear sense indicators in oriented drillcore from the Winddine Well deposit, Winddine Well Shear Zone, observed in the shear sense observation plane and all displaying east side up movement. In all instances, NQ drillcore is displayed with a diameter of ~50 mm. Photographs in (b) (c) (e) and (f) contain drillcore oriented according to the inclination and azimuth of the respective drillholes, facing north, as indicated in (b). **(a)** Deformed sigma-shaped grains of yellow-brown leucoxene in diorite located east of the WWSZ (WWDD040, 170.15 m); **(b)** Sheared sigma rip-up clasts of magnetic BIF in the fine grained chilled margin of a dolerite sill (WWDD038, 160.5 m); **(c)** Oblique fabric in a carbonate vein (WWDD031, 169.05 m); **(d)** Quartz sigma-clasts in a highly foliated volcaniclastic situated west of the WWSZ (WWDD031, 272.5 m); **(e)** Deformed chert horizons and pyrrhotite veinlets in mineralised BIF (WWDD031, 252.7 m); **(f)** ~5 cm deformed pyrite assemblage within BIF close to the centre of the WWSZ (WWDD040, 254.9 m); **(g)** Lower hemisphere equal area stereonet of shear planes and shear directions calculated from the measurement of vorticity vectors in oriented drillcore at Winddine Well.

A steep down-dip L_4 lineation plunging towards the west at 76-79° is associated with the S_4 fabric along the WWSZ (Fig. 4.20e), defined by leucoxene and chlorite in foliated dolerite and by mica in fine-grained metapelitic rocks (Fig. 4.21b). Isoclinal F_4 folds occur in metasedimentary rocks and are particularly prevalent in sheared intervals within BIF, with hinge surfaces parallel to S_4 and sub-horizontal fold axes (Fig. 4.20f; Fig. 4.21c). Frequently, boudinaged quartz-carbonate veins parallel to layering in BIF are deformed into F_4 folds (Fig. 4.21d).

A diverse range of shear sense indicators associated with D_4 shearing have been observed in drillcore at Winddine Well. In mafic intrusive rocks, abundant mm-scale leucoxene grains (Fig. 4.22a) and fragments of BIF at the margins of sills (Fig. 4.22b) are deformed as sigma clasts, and calcite veins frequently contain oblique fabrics (Fig. 4.22c). Volcaniclastic rocks west of the WWSZ contain quartz sigma clasts (Fig. 4.22d). Shear sense indicators are also displayed by sulphides in mineralised BIF, including pyrrhotite bands deformed as sheared asymmetric microfolds (Fig. 4.22e), and a sigmoidal ~5 cm sulphide assemblage, both associated with gold mineralisation (Fig. 4.22f). In every instance, all shear sense indicators unequivocally show east-side up sense of movement and shear directions calculated from vorticity vector measurements are consistently steeply plunging (> 70°) to vertically-plunging (Fig. 4.22g).

The most recent structures at Winddine Well are a set of sub-horizontal microfaults with displacements of several mm to 3 cm, which crosscut all other structures (including S_4 and F_4). These structures are most readily identified in BIF and are commonly infilled by carbonate minerals that exhibit extensional textures. The geometry of some faults is also indicative of extension (Fig. 4.21e).

4.5.6.3 Chulaar Shear Zone (CSZ)

The Chulaar Shear Zone (CSZ) is a D_4 structure situated along the eastern margin of the Mougooderra Fm, in contact with the underlying greenstone succession. The total length of the CSZ is not known, although shearing has been observed over a length of at least ~30 km. Along part of the CSZ, evidence has been identified in favour of an unconformable contact (Section 2.4.3.4), albeit sheared. Contrary to other D_4 shear zones in the YSGB, the CSZ is partially exposed at several locations along its length. Watkins & Hickman (1990) recorded a "topographically prominent, silicified, recrystallised, quartz-andalusite-white mica mylonite" along the CSZ. Exposures of the CSZ situated to the southeast of Chulaar Hill and at Warriedar Hill have been mapped as part of this study and are described below.

<u>*Southeast of Chulaar Hill*</u>

The largest exposure across the shear zone is a ~2 km^2 area situated ~4 km southeast of Chulaar Hill

(Fig. 4.1). Surface 1:8,000 scale geological mapping has been undertaken on this exposure and is displayed in Figure 4.23. Due to the general lack of magnetic lithologies, aeromagnetic imagery was not utilised during geological mapping along the CSZ. The lithologies and structural features encountered during mapping this exposure, both within and adjacent to the CSZ, are summarised below.

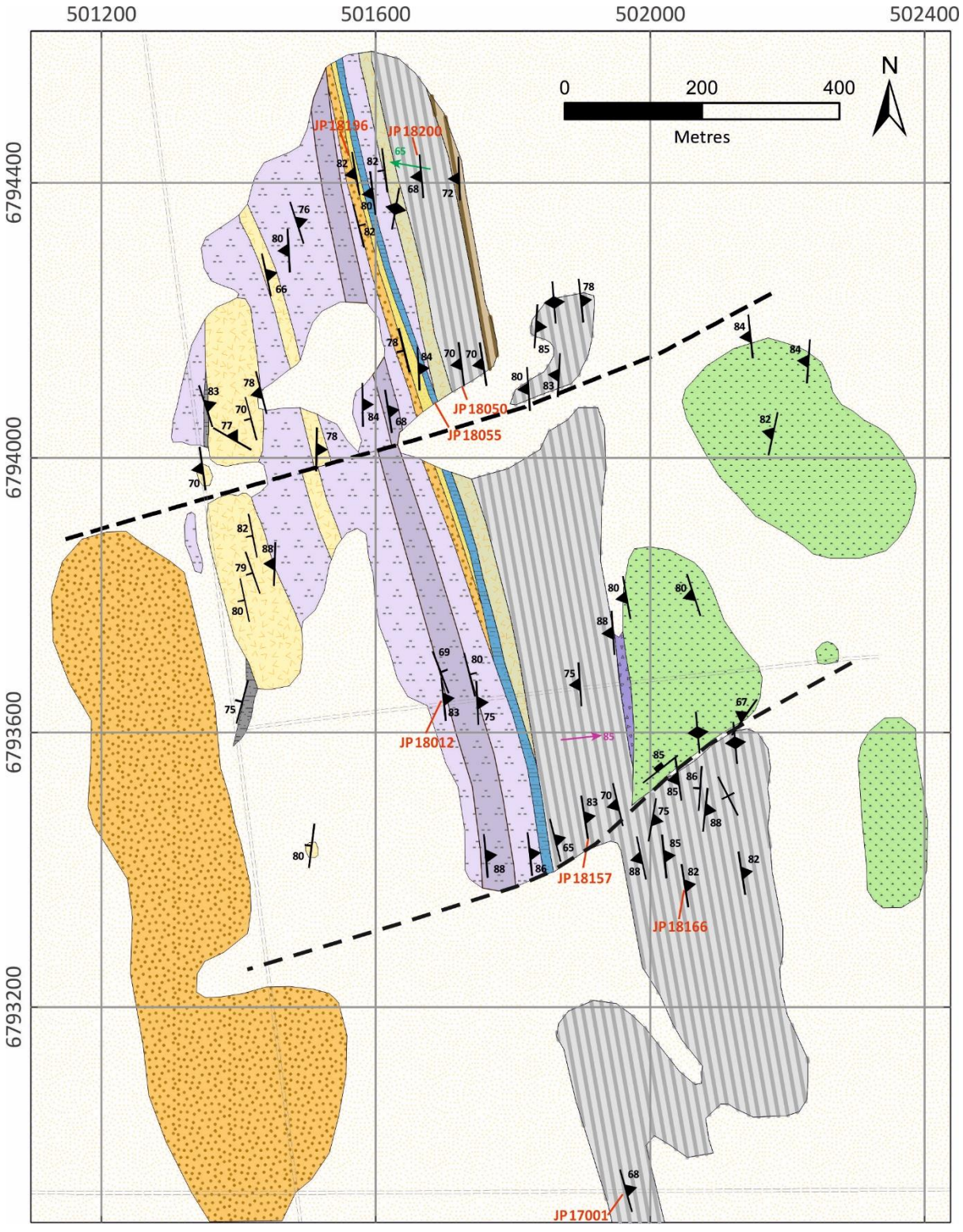

(continued on next page)

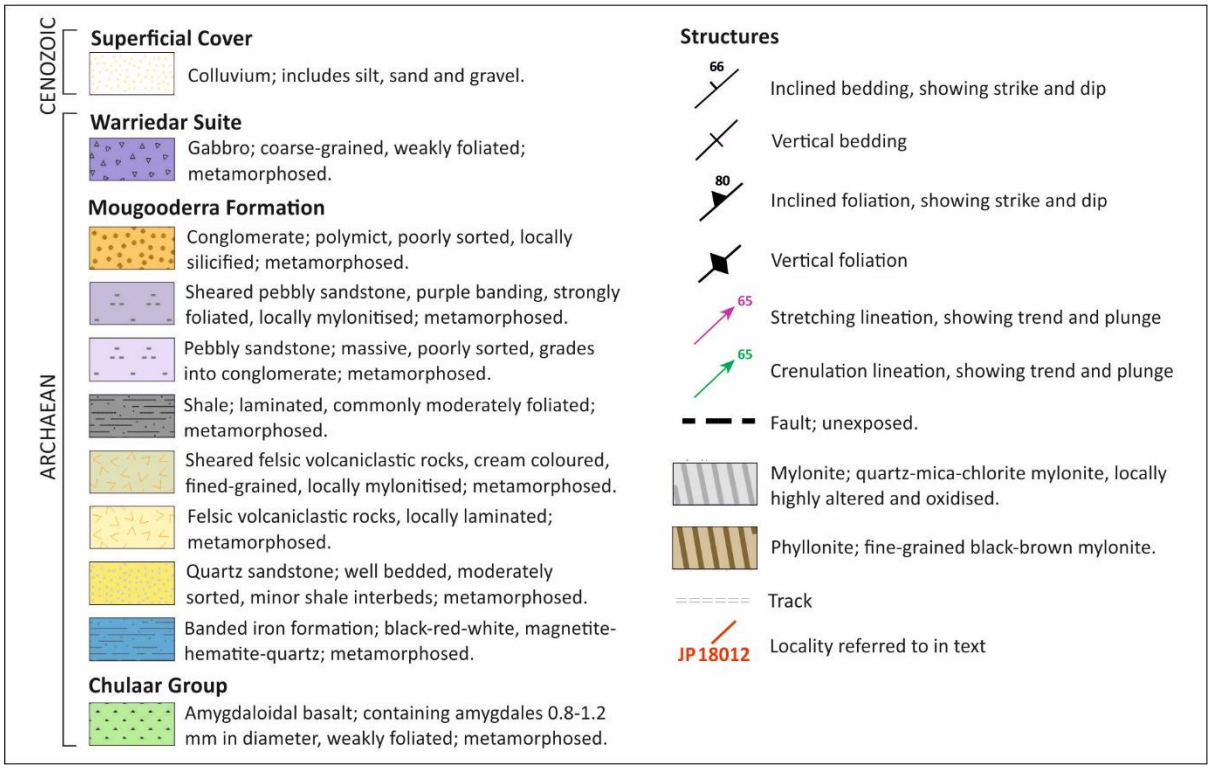

Figure 4.23 (previous page): Geological map of an exposure along the Chulaar Shear Zone located ~4 km southeast of Chulaar Hill, drawn at 1:8,000 scale. The geology displayed represents outcrop and subcrop based on geological mapping undertaken as part of this study. Grid used is MGA Zone 50. Localities referred to in the text and in Figs. 4.24 and 4.25 are labelled in red.

Rocks to the east of the CSZ are principally comprised of Chulaar Group amygdaloidal basalt, characterised by 0.8-1.2 mm amygdales of quartz and carbonate (Section 5.3.3). Further, a ~15 m-thick unit of Warriedar Suite gabbro occurs along the eastern margin of the CSZ (Fig. 4.23). In contrast, rocks to the west of the CSZ comprise a succession of Mougooderra Fm metasedimentary rocks similar to rocks exposed at Chulaar Hill (Section 4.5.5.1) and Warriedar Hill (Section 4.5.5.2), including pebbly sandstone, conglomerate, lesser quartz sandstone, interbedded mudstone and rare BIF. The succession also contains several interbedded 20-80 m-thick units of felsic volcaniclastic rocks, composed of a fine grained, cream-white, weakly bedded quartzofeldspathic groundmass with minor mm-scale quartz clasts and felsic lithic clasts (Section 5.5.2). Bedding in Mougooderra Fm rocks west of the CSZ is consistently steeply west-dipping at 70-82° (Fig. 4.24a). Rocks either side of the CSZ are host to a N-S striking S_3 foliation that dips variably to the east and west at angles of 70-88° (Fig. 4.24b). S_3 occurs as a moderately developed cleavage in metasedimentary rocks and a weak-moderate foliation in mafic volcanic and intrusive rocks.

The CSZ has a total exposed width of approximately 340 m and is characterised by a subvertical, N-S striking S_4 foliation (Fig. 4.23). S_4 variably dips towards the east and west at angles between 68-90°

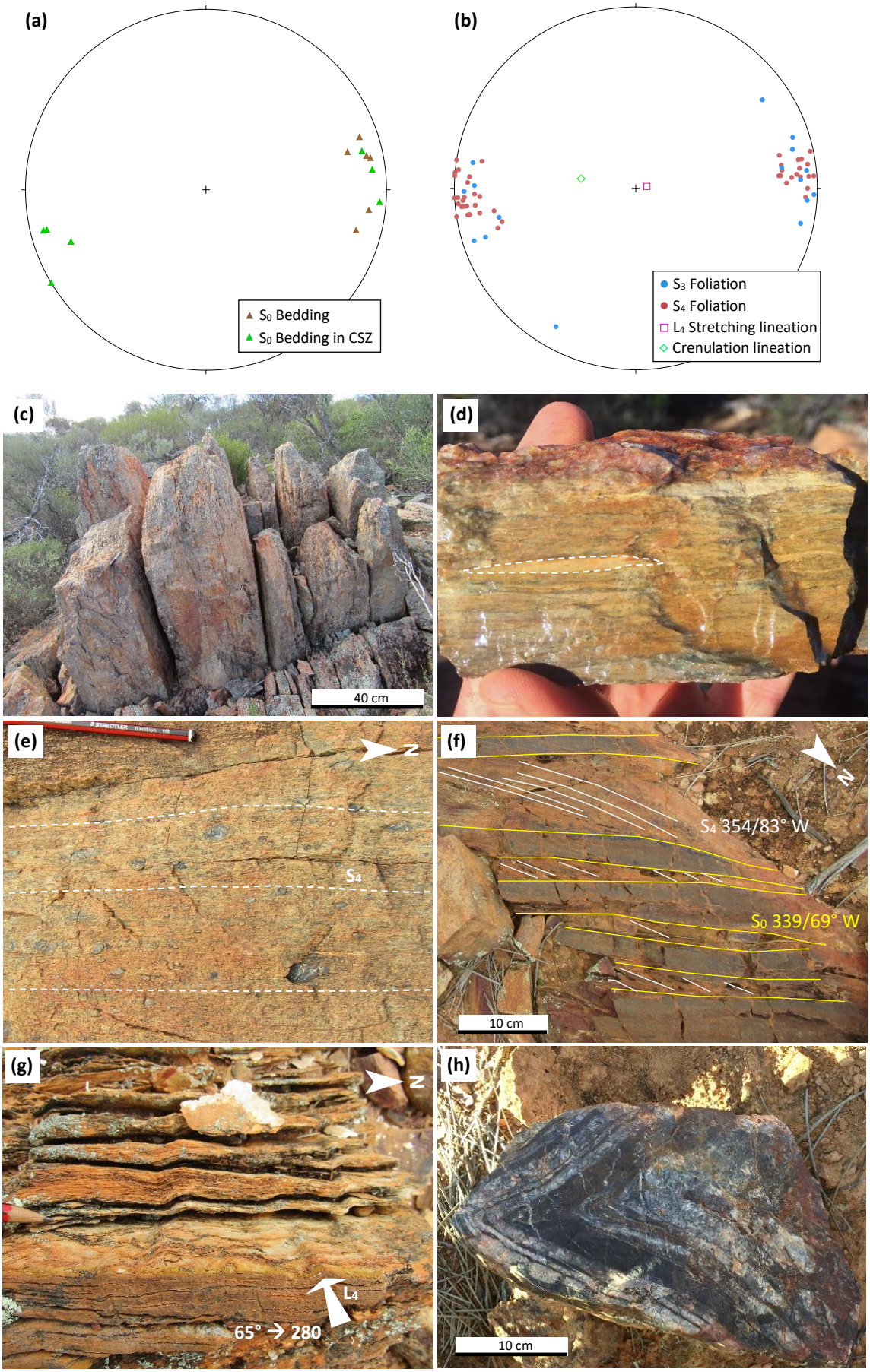

(caption on next page)

Figure 4.24 (previous page): Structures along an exposure of the Chulaar Shear Zone ~ 4 km southeast of Chulaar Hill. **(a)** Lower hemisphere equal area stereonet of foliation and lineations within and proximal to the CSZ. The S_3 fabric is distinguished in rocks to the west and east of the shear zone, whereas the S_4 fabric is identified within the CSZ; **(b)** Lower hemisphere equal area stereonet of Mougooderra Fm bedding measurements, both within the CSZ and to the west of the CSZ; **(c)** Prominent outcrop of quartz-mica mylonite exposed along the CSZ, facing north. Thin section photomicrographs and shear sense indicators in an oriented sample from this unit are displayed in Figure 4.25c (loc. JP17001); **(d)** Photograph of mylonitic pebbly sandstone, displaying elongation of quartz clasts (loc. JP18050); **(e)** Outcrop of sheared conglomeratic pebbly sandstone, with larger quartz clasts concentrated on particular horizons – photograph taken from above (loc. JP18196); **(f)** Outcrop of interbedded sandstone and siltstone displaying the relationship between cleavage and bedding (loc. JP18012); **(g)** Outcrop of laminated quartz-mica mylonite with a down dip crenulation lineation plunging steeply west – photograph taken looking down dip (loc. JP18200); **(h)** Folded, highly magnetic BIF that occurs as a discontinuous lens within the CSZ (loc. JP18055).

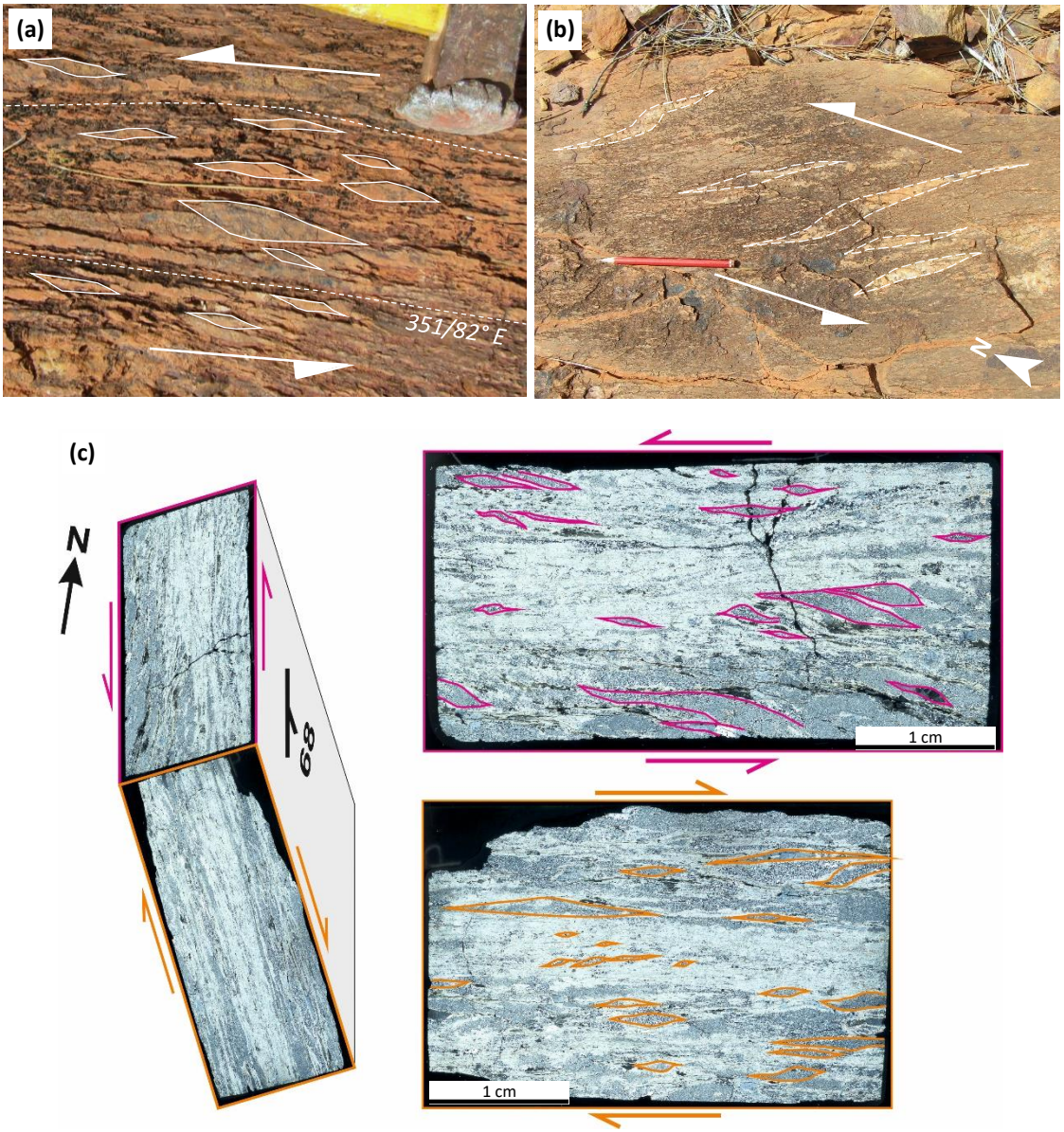

Figure 4.25: Examples of shear sense indicators along the Chulaar Shear Zone. **(a)** Outcrop of mylonitic pebbly sandstone with sheared sigma clasts defining a sinistral component of shear (loc. JP18166); **(b)** Outcrop of quartz mylonite with deformed en echelon quartz veins at orientations signifying a sinistral component of shear (loc. JP18157); **(c)** Thin section photomicrographs of an oriented quartz-mica mylonite sample taken from the centre of the Chulaar Shear Zone (loc. JP17001; 348/68° E). The upper photomicrograph is taken looking down dip and facing west, and granoblastic sigma clasts of quartz display a sinistral component of movement. The lower photomicrograph is taken along strike facing north, and deformed sigma clasts display a vertical component of movement comprising east-side down movement. The relative orientation of the two samples is represented on the block diagram.

and consequently, occurs at orientations that are indistinguishable from the regional S_3 foliation in surrounding rocks (Fig. 4.24b). The intensity of the S_4 fabric increases towards the centre of the shear zone, which is marked by the extensive development of mylonitic rocks. Mylonites have a banded, ribbon-like appearance, are typically dominated by quartz and mica, and are topographically pronounced, forming a ridge that extends along the exposed CSZ (Fig. 4.24c). Quartz clasts within some mylonitic rocks display aspect ratios in excess of 10:1 (Fig. 4.24d). Locally, micaceous phyllonites with a schistose texture are present within the mylonitic sequence. The protolith of several mylonitic units can be discerned on the basis of colour and remnant textural features, including sheared pebbly sandstone that contain conglomeratic horizons transposed into S_4 orientations (Fig. 4.24e), and sheared felsic volcaniclastic rocks (Fig. 4.23). The CSZ also includes several laterally-discontinuous lenses of less deformed rocks, however, bedding orientations in these units are consistently parallel to S_4 present in surrounding foliated and mylonitic rocks (Fig. 4.24a). At the western margin of the CSZ, interbedded sandstone and mudstone displays an angular relationship between the S_4 fabric and bedding in Mougooderra Fm rocks (Fig. 4.24f).

A steep, down-dip crenulation lineation is exhibited by some finely laminated mylonitic rocks along the CSZ (Fig. 4.24g) and a sub-vertical L_4 stretching lineation is defined by elongation of clasts in conglomerate and coarse pebbly sandstone units (Fig. 4.24b). Folding along the CSZ has not been observed in situ, although a distinctive BIF marker horizon within the shear zone frequently exhibits tight decimetre-scale folding in subcrop (Fig. 4.24e), potentially analogous to F_4 folds observed in drillcore along the MSZ and WWSZ.

Shear sense along the CSZ is demonstrated by several features observed in outcrop and thin section (Fig. 4.25). Highly sheared rocks in the core of the shear zone frequently contain sigma-shaped clasts and SC fabrics that consistently display a sinistral shear sense (Fig. 4.25a). Multiple sets of en echelon quartz veins overprinting mylonitic fabrics in the CSZ display stepping that is also consistent with a sinistral component of movement (Fig. 4.25b). Two thin sections from an oriented sample of banded quartz-mica mylonite sampled from the core of the CSZ have been analysed for shear-sense indicators; one section oriented along the strike of S_4 and one section oriented parallel to the dip of S_4 (Fig. 4.25c). Deformed quartz in these sections supports the occurrence of a sinistral strike-slip shear component, and also demonstrates a west-side up component of movement (Fig. 4.25c). Shear sense indicators and lineation orientations are consistent with oblique displacement comprising a significant vertical component, in addition to a sinistral component. The features observed along the CSZ are compatible with transpressional shear, comprising a large component of pure shear and a lineation approximately parallel to the vorticity vector.

The mapped exposure of the CSZ at the locality southeast of Chulaar Hill is crosscut by two ENE-striking faults, assigned to D_5 deformation (Section 4.5.7).

Warriedar Hill

Geological mapping in the Warriedar Hill area (Section 4.5.5.2) has identified a sequence of Mougooderra Fm metasedimentary-dominated rocks, part of which are deformed into a km-scale, tight, synformal structure in the southwest (Fig. 4.8). To the northeast, multiple parallel, northwest-striking, topographically-prominent ridges composed of quartz sandstone and conglomerate are separated by subdued valleys of poorly exposed and invariably foliated siltstone (Fig. 4.8; Fig. 4.10a). Abundant way-up criteria in these rocks consistently indicate younging towards the southwest (Section 4.5.3).

On satellite imagery, the geometry of the elevated ridges at Warriedar Hill are indicative of an imbricate structure attributed to D_4 deformation, composed of successive layer-parallel shears located between ridges (Fig. 4.10b). This interpretation is consistent with field observations, as the interpreted shears separate three repetitions of the mapped stratigraphy that display consistent younging directions and although largely unexposed, the shears are represented by an increased fabric intensity in poorly exposed, intervening siltstone units (Fig. 4.8). This D_4 imbricate structure is considered to represent the southern extent of the CSZ, along strike from the well exposed locality southeast of Chulaar Hill. Unfortunately, due to the lack of outcrop and absence of drillcore, the sub-surface geometry of this structure cannot currently be constrained. However, the occurrence of an imbricate structure along the CSZ is consistent with a significant vertical component of movement, as indicated further north. The stratigraphy and imbricate shears at Warriedar Hill are dissected by ENE-striking faults, attributed to D_5 deformation (Section 4.5.7). Notably, the geometry and orientation of the imbricate structure at Warriedar Hill is remarkably similar to the duplex structure mapped along the D_4 Rothsay Shear Zone, in the southeast of the Rothsay area (Fig. 3.9; Section 3.5.6.2).

4.5.7 D_5 deformation

D_5 deformation is characterised by a set of ENE-striking faults that deform D_4 shear zones and all pre-existing structural features. D_5 faults typically have a sinistral separation and display apparent offsets of 100-300 m. In the Rothsay area, three D_5 faults are present and dissect the RSZ and ESZ (Section 3.5.7). D_5 faults are also observed elsewhere in the YSGB, including the mapped exposure along the CSZ (Section 4.5.6.3; Fig. 4.23). At this locality, a D_5 fault dissects the CSZ with a sinistral offset of ~170 metres (Fig. 4.23). Basalt outcropping immediately north of this sinistral D_5 fault possesses conspicuous fractures oriented parallel to the fault and dipping steeply to the northwest at 70-85°. A

parallel, unexposed fault ~800 metres north has a minor dextral apparent offset of ~20 metres (Fig. 4.23). Similarly, multiple ENE-oriented faults dissect the interpreted D_4 imbricate structure at Warriedar Hill, and typically display dextral offsets of 50-150 m (Fig. 4.10). On aeromagnetic imagery, a major D_5 fault is distinguished west of the Mt Mulgine Granite (Fig. 4.2). This fault displays a sinistral offset of ~ 400 m and is associated with significant fault drag, like D_5 faults to the southwest.

In the Rothsay area, a suite of ENE-trending felsic pegmatite dykes are principally oriented parallel to D_5 faults and dissect all pre-existing structures, thus are cautiously attributed to D_5 deformation. The spatial association between pegmatite dykes and the Seeligson Monzogranite suggests that this body was also intruded at this time. At Warriedar Hill, a ~30 m-thick ENE-trending pegmatite dyke dissects F_3 folds in Mougooderra Fm metasedimentary rocks (Fig. 4.8), and exhibits similar characteristics to pegmatites at Rothsay, including distinctive graphic textures. Approximately ~400 metres south, the Seeligson Monzogranite also truncates F_3 folded metasedimentary rocks, consistent with intrusion post-D_3.

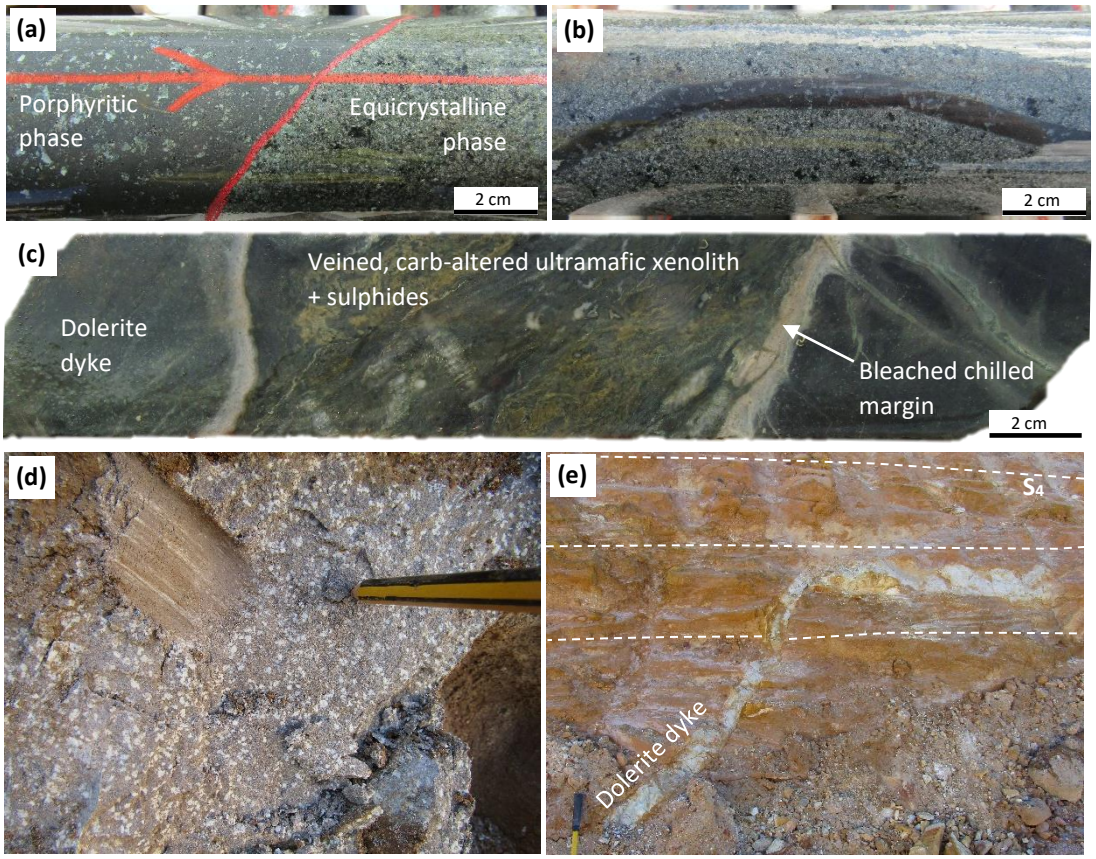

Figure 4.26: Typical features of dolerite dykes observed in drillcore and in oxide pits at the Silverstone deposit, Mougooderra Shear Zone. **(a)** Two phases comprising dolerite dykes in drillcore, including a fine grained porphyritic phase and a dominant equicrystalline phase (SSDD014, 318.0 m); **(b)** Two phases comprising dolerite dykes in drillcore, with the porphyritic phase cross cutting the equicrystalline phase (SSDD014, 357.0 m); **(c)** A xenolith of ore zone carbonate altered and mineralised ultramafic rock within a dolerite dyke, displaying bleached chilled margins (SSDD017, 465.0 m); **(d)** Highly altered and oxidized dolerite dyke intruded along the basal contact of the MSZ in the Eastern Creek pit, displaying a relict porphyritic texture; **(e)** A thin dolerite dyke offshoot cross cutting and then intruding parallel to the S_4 fabric in hangingwall rocks, on the western wall of the Eastern Creek pit (Silverstone deposit), facing west.

4.5.8 D_6 deformation

D_6 deformation in the YSGB is characterised by multiple brittle, north-northeast striking faults with dextral separations, which dissect all other structures apart from dolerite dykes. These faults are not exposed and instead have been identified by offset units on aeromagnetic imagery. One such D_6 fault occurs at Rothsay where it crosscuts the RSZ and exhibits a variable offset of between 75 m in the south and 150 m in the north (Section 3.5.8). Other D_6 faults have been identified on the Badja and Chulaar limbs of the belt and to the west of Mt Mulgine and exhibit dextral offsets of 250-300 m (Fig. 4.2).

4.5.9 Post-D_6 deformation

The most recent basement rocks in the YSGB are a network of dolerite dykes, which dissect all supracrustal rocks, intrusive rocks and structures. Dykes consist of weakly to moderately magnetic dolerite, and consequently are visible on aeromagnetic imagery. Most dolerite dykes are oriented NW-SE to E-W, although less commonly they are oriented NE-SW (Fig. 4.2). As is the case in the Rothsay area (Section 3.4.2.6), dolerite dykes are seldom exposed at the surface in the YSGB. However, dykes have been observed in oxide pits and oriented drillcore at the southern end of the Silverstone deposit, along the MSZ (Section 4.5.6.1; Fig. 4.12).

The strike of dolerite dykes observed in oriented drillcore at Silverstone is typically E-W, matching the local trends on aeromagnetic imagery. Dolerite dykes cross cut Chulaar Group supracrustal rocks and Warriedar Suite sills, and exhibit metre-scale chilled margins. As drillholes at Silverstone have been drilled parallel to the strike of dolerite dykes, it is not possible to determine their thickness. Dolerite dykes proximal to the Silverstone deposit comprise two phases: a dominant phase consisting of medium to coarse grained, moderately magnetic, equicrystalline dolerite, and a less abundant phase consisting of fine grained, weakly magnetic, porphyritic dolerite with 1-5 mm blue-white plagioclase phenocrysts (Fig. 4.26a). Porphyritic dolerite invariably occurs within equicrystalline dolerite and exhibits cross cutting intrusive relations (Fig. 4.26b). In one drillhole, a ~20 cm xenolith of a veined and gold-mineralised ultramafic unit occurs within a dolerite dyke, close to the basal shear zone contact (Fig. 4.26c). In the southernmost pit of the Silverstone deposit, Eastern Creek, a porphyritic dolerite dyke intrudes along the basal contact of the MSZ (Fig. 4.26d). Furthermore, 10-30 cm-thick doleritic dyke offshoots occur in the hangingwall and are oriented parallel to the principal S_4 fabric of the shear zone, approximately perpendicular to their regional trend (Fig. 4.26e). These features demonstrate the partial intrusion of dolerite dykes along major pre-existing D_4 structures such as the MSZ, which crucially, includes the mineralised ore zone at the southern extent of the Silverstone deposit.

4.6 Summary of Structural Data

In this chapter, the integration of new geological mapping, structural analysis of oriented drillhole and aeromagnetic interpretation in the YSGB has constrained six distinct deformational episodes (D_1-D_6), following the emplacement of supracrustal rocks and mafic-ultramafic sills (D_E). Crucially, these deformation events are wholly consistent with the structural events described on a more local scale in the Rothsay area (Chapter 3).

The earliest (D_1) structures discerned in the YSGB comprise multiple 10-50 km-scale domal structures, including the Mt Mulgine, Yalgoo and Rothsay Domes, in addition to a conspicuous layer-parallel S_1 foliation. Detailed structural mapping at Rothsay advocates an early phase of granite diapirism and associated layer-parallel shearing to account for the domal architecture of the area. This is compatible with regional structural analysis of the Yalgoo Dome, which indicates a crucial role for diapirism in the early structural development of the YSGB (Zibra et al., 2018; 2020). The early-formed D_1 structures are refolded by multiple km-scale D_2 folds, which are only observed in the southwest of the YSGB and are particularly prevalent in the Rothsay area. Overprinting D_3 deformation has imparted a regional S_3 tectonic fabric that is pervasive across the study area, in addition to metre- to kilometre-scale, tight folding in Chulaar Group and Mougooderra Fm rocks, to which the S_3 foliation is axial planar. This is consistent with a regional episode of E-W shortening. The geometry and kinematics of three major NNE- to NNW- striking D_4 shear zones have been described, which are invariably steeply inclined (>60°) structures that demonstrate a significant reverse shear component. The MSZ and CSZ are principally focussed along lithological contacts between the Mougooderra Fm and underlying Chulaar Group rocks. D_4 shear zones are post dated by two distinct, widespread brittle faulting episodes: I) D_5 faulting resulted in the development of an array of ENE-striking faults that typically exhibit a sinistral offset, and II) A subsequent D_6 faulting event is demonstrated NNE-striking faults that typically show dextral offsets. Unfortunately, little is known about the geometry and sub-surface orientation of D_5 and D_6 faults. A network of dolerite dykes dissects all other structures and lithologies in the YSGB, are locally deflected along D_4 shear zones, and are considered to be Proterozoic age.

New geochronological results for supracrustal rocks and lode-gold mineralisation along the MSZ are presented in Chapter 8 and Chapter 9, respectively, providing additional temporal constraints on the formation and deformation of rocks in the YSGB. A revised structural model for the YSGB is outlined and discussed in Section 10.2, integrating the structural and geochronological data presented in this study.

CHAPTER 5

Petrography of supracrustal and mafic-ultramafic intrusive rocks

5.1 Introduction and Sampling Strategy

A suite of 134 samples used in this study were collected over the course of three field seasons between October 2016 and September 2018 and have been used for petrographic, geochemical and geochronological analysis. These samples are representative of the major formations comprising the Yalgoo-Singleton greenstone belt (YSGB), namely the Chulaar Group, Willowbank Clastics, Mougooderra Fm and Warriedar Suite. Samples have not been collected from the basement Gossan Hill Fm, as this is beyond the scope of this study. Petrographic analysis has been undertaken on polished thin sections from 71 representative samples from this suite (this chapter), whole rock geochemical analysis has been undertaken on 111 samples (Chapter 6) and radiometric dating has been carried out on 3 samples (Chapter 8). Full details, descriptions and locations of all samples and a checklist of the analysis undertaken on each sample, are collated in **Appendix E5**.

Due to the scarcity of outcrop across much of the belt, radiometric imagery was utilised to target the better exposed parts of the study area and multiple traverses were made across each of the major limbs of the greenstone succession. Samples were invariably collected from outcropping rocks and were selected on the basis of showing as little alteration as possible. In several areas of very poor to non-existent surface exposure, samples were taken from diamond drillcore, courtesy of Minjar Gold Pty. In total, 81 samples were collected in the better exposed Rothsay area, 20 samples were collected in the Mt Mulgine area, 17 samples were collected in the Chulaar area, 13 samples were collected in the Badja area and 3 samples were collected from Warriedar Hill (Fig. 5.1).

In this chapter, the petrography of supracrustal rocks and mafic-ultramafic intrusive rocks in the YSGB is described. A compilation of petrographic descriptions and modal mineralogy for each petrographic sample can be found in **Appendix E6**. The locations of petrographic samples across the YSGB are displayed on Figure 5.1 and the locations of samples in the Rothsay area are shown on Figure 5.2.

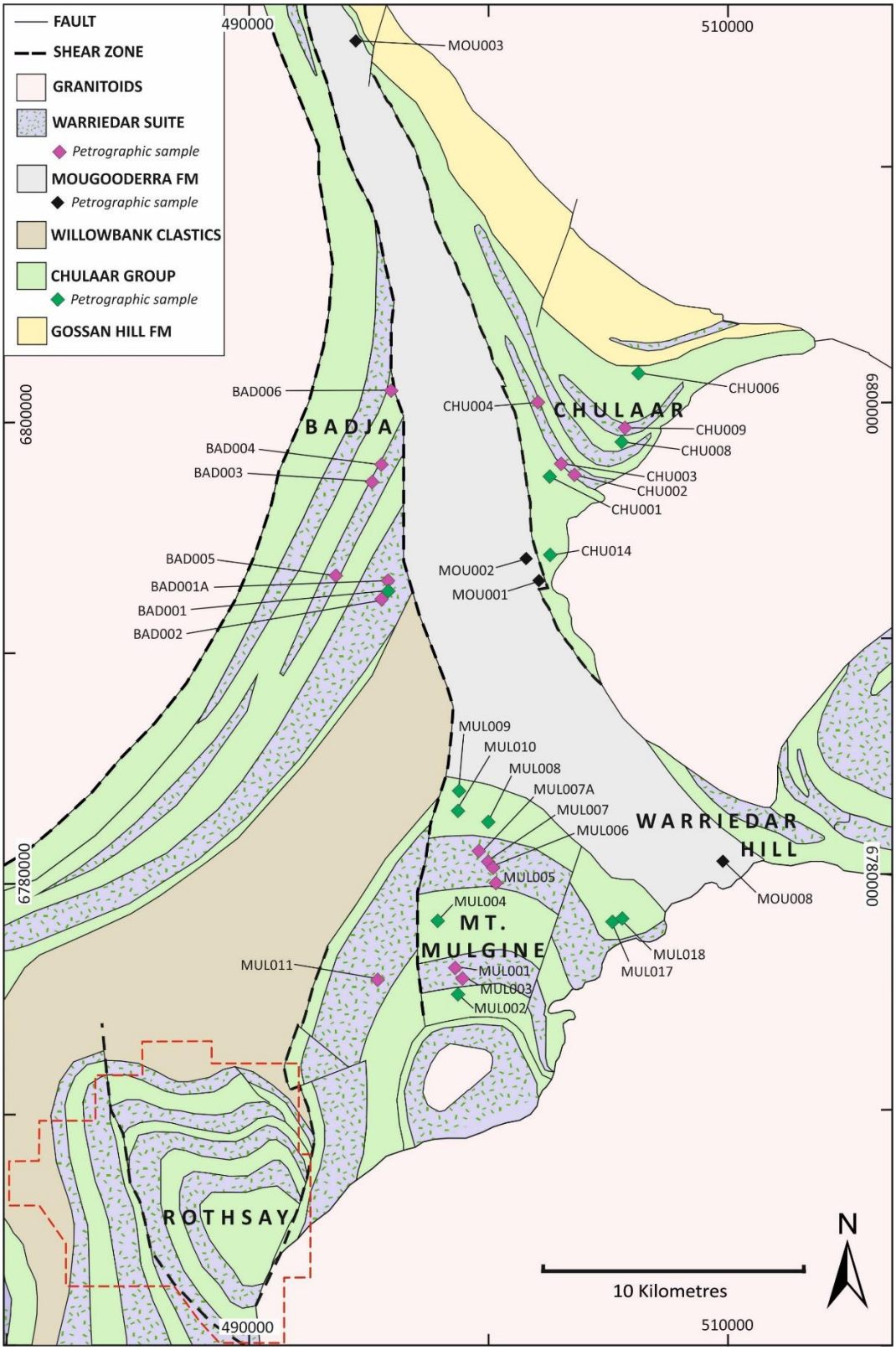

Figure 5.1: Simplified geological map of the central Yalgoo-Singleton greenstone belt showing the locations of petrographic samples analysed in this study, except for those in the far southwest (extent of Fig. 5.2 outlined in dashed red). Petrographic samples are symbolised by stratigraphic formation and labelled by sample number. Geology modified after Baxter & Lipple (1985), Zibra et al. (2016), Zibra et al. (2017a) and Ivanic (2018). Grid provided in the GDA94/MGA Zone 50 co-ordinate system.

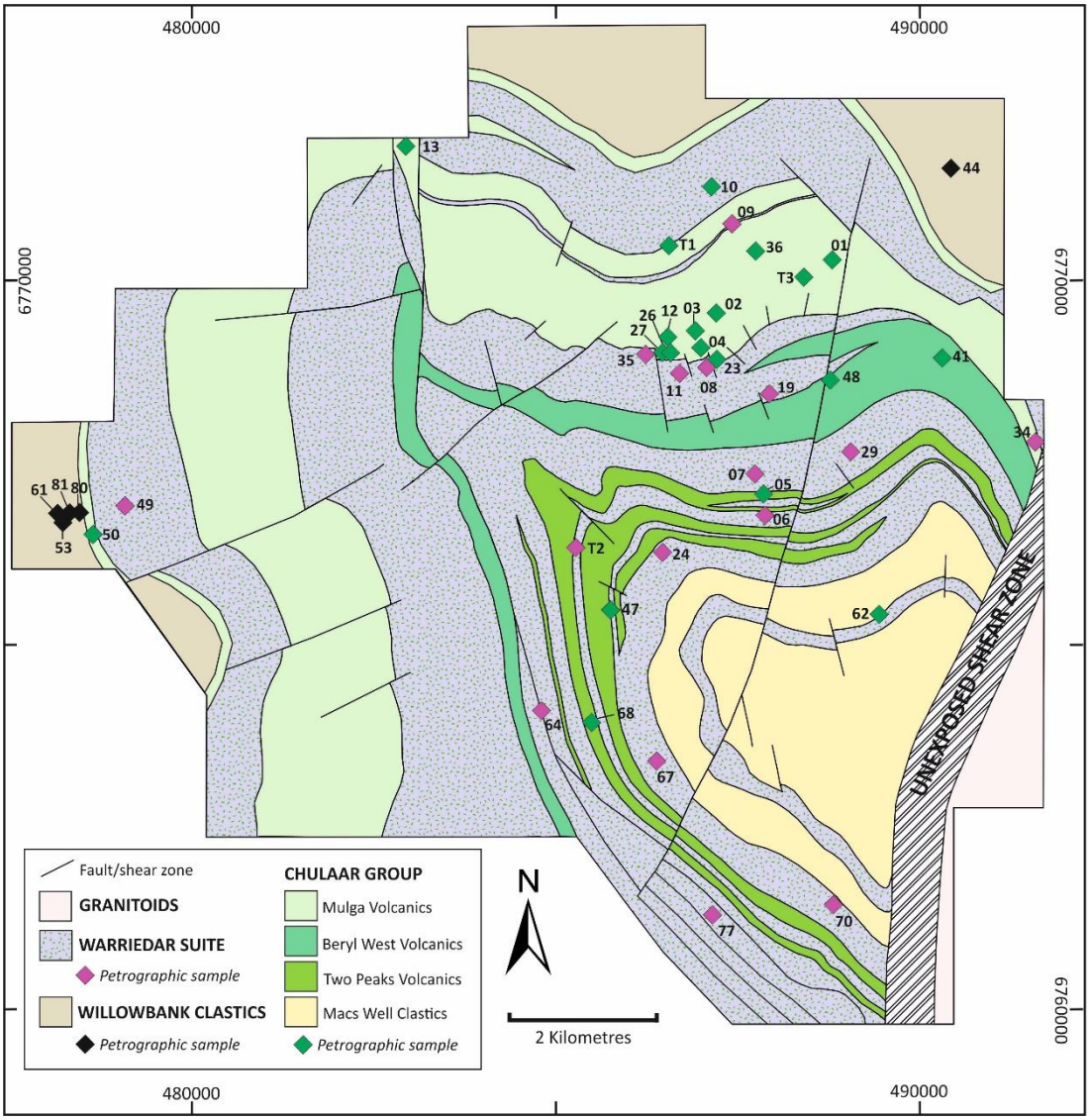

Figure 5.2: Simplified geological map of the Rothsay area in the southwest of the study area, showing the locations of petrographic samples analysed in this study. Samples are symbolised by the stratigraphic unit to which they are assigned and labelled by sample number (prefix ROTH0 omitted for all samples). Grid provided in the GDA94/MGA Zone 50 co-ordinate system. Geology from Chapter 3.

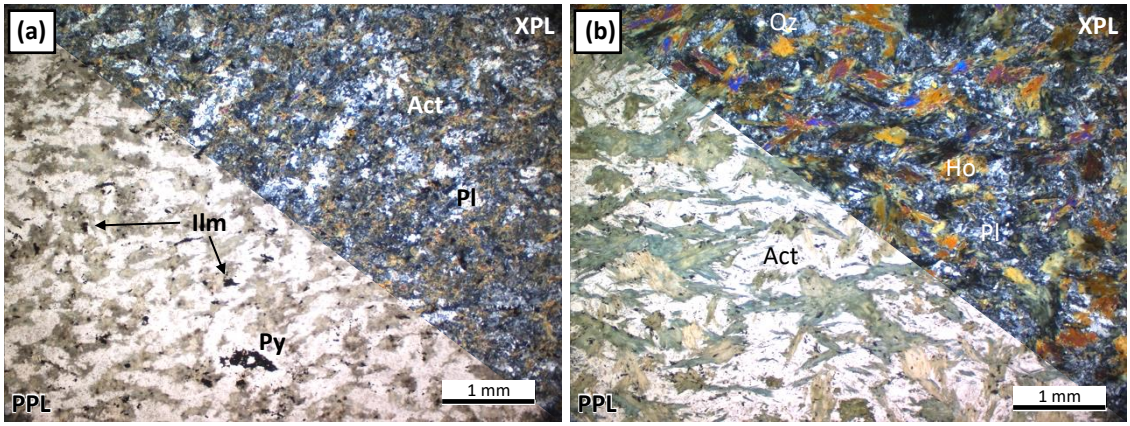

Figure 5.3: Photomicrographs of Chulaar Group aphyric volcanic rocks. **(a)** PPL/XPL view of the typical texture and mineralogy of fine-grained basalt, comprising mottled plagioclase, actinolite laths, minor quartz and disseminated ilmenite (sample ROTH013); **(b)** PPL/XPL view of a slightly coarser-grained basalt with mottled plagioclase, hornblende laths, acicular actinolite crystals and minor anhedral quartz, preserving a moderate planar fabric defined by amphibole laths (sample ROTH002).

5.2 General Overview of Metamorphic Features

All supracrustal and mafic-ultramafic intrusive rocks in the YSGB have been affected by regional metamorphism (Watkins & Hickman, 1990). Consequently, the original mineralogy of many rocks has been modified and primary minerals are frequently replaced by metamorphic minerals. In mafic extrusive and intrusive igneous rocks, metamorphic assemblages vary from actinolite-chlorite-epidote-albite to hornblende-actinolite-albite, demonstrating upper greenschist to lower amphibolite-grade metamorphism. Primary pyroxene in mafic volcanic and intrusive rocks is frequently pseudomorphed by metamorphic amphibole; most commonly actinolite although hornblende and tremolite are present in some units. Several Warriedar Suite intrusive samples contain relict primary clinopyroxene and orthopyroxene, however, pyroxene is no longer present in most intrusive samples and all Chulaar Group volcanic rocks. This includes pyroxene spinifex-textured volcanic rocks of the Chulaar Group, in which pyroxene phenocrysts are invariably replaced by metamorphic actinolite ± hornblende ± chlorite. In this chapter, the term pyroxene-spinifex will be used in reference to the original mineralogy and distinct texture of these volcanic rocks, despite pyroxene no longer being part of the mineral assemblage. Intrusive and volcanic rocks with olivine-bearing protoliths have all been subject to serpentinization and primary olivine is seldom preserved within the serpentinised alteration assemblage.

5.3 Chulaar Group

5.3.1 Aphyric volcanic rocks

Volcanic rocks of the Chulaar Group include basalts and basaltic andesites that are typically fine-grained, dark grey, massive, and aphyric in hand specimen. The petrographic samples studied come from the Two Peaks Volcanics and Mulga Volcanics. They are commonly weakly to moderately altered and are characterised by a fine-grained alteration assemblage of plagioclase, actinolite, quartz and ilmenite ± epidote ± chlorite ± tremolite ± anthophyllite ± biotite ± titanite. The rocks are predominantly aphanitic and comprise an equicrystalline groundmass dominated by interlocking crystals of lath-shaped amphibole (<0.3 mm) and tabular, often mottled, plagioclase (<0.5 mm) (Fig. 5.3a). The coarsest volcanic flows are marginally phaneritic and contain crystals up to 1 mm in length (Fig. 5.3b). In most basaltic and andesitic rocks, the dominant amphibole pseudomorphing primary pyroxene is actinolite, however, high-Mg volcanic rocks also contain variable amounts of tremolite and anthophyllite. The ratios of amphibole relative to plagioclase range between 67:33 and 48:52 and very fine-grained interstitial material often includes single acicular needles of actinolite (Fig. 5.3b).

Quartz is regularly present as 0.1-0.2 mm anhedral crystals in aphyric volcanics and varies in abundance between 1 and 6%, typically occurring in close association with chlorite, epidote, biotite and variably saussuritised Ca-rich plagioclase crystals in more highly altered samples. In several instances, elevated quartz content (up to 15%) corresponds to units crosscut by abundant mm-scale quartz veinlets, signifying increased hydrothermal alteration. Disseminated oxides are ubiquitous within the groundmass (up to 1%), occurring predominantly as 0.1-0.2 mm needles of ilmenite, with lesser anhedral magnetite grains (Fig. 5.3a). A disseminated sulphide assemblage of pyrite ± chalcopyrite ± pyrrhotite is observed in a minority of units. Aphyric rocks proximal to faults and shear zones often exhibit nematoblastic textures, in which both linear and planar fabrics are preserved by actinolite laths (Fig. 5.3b).

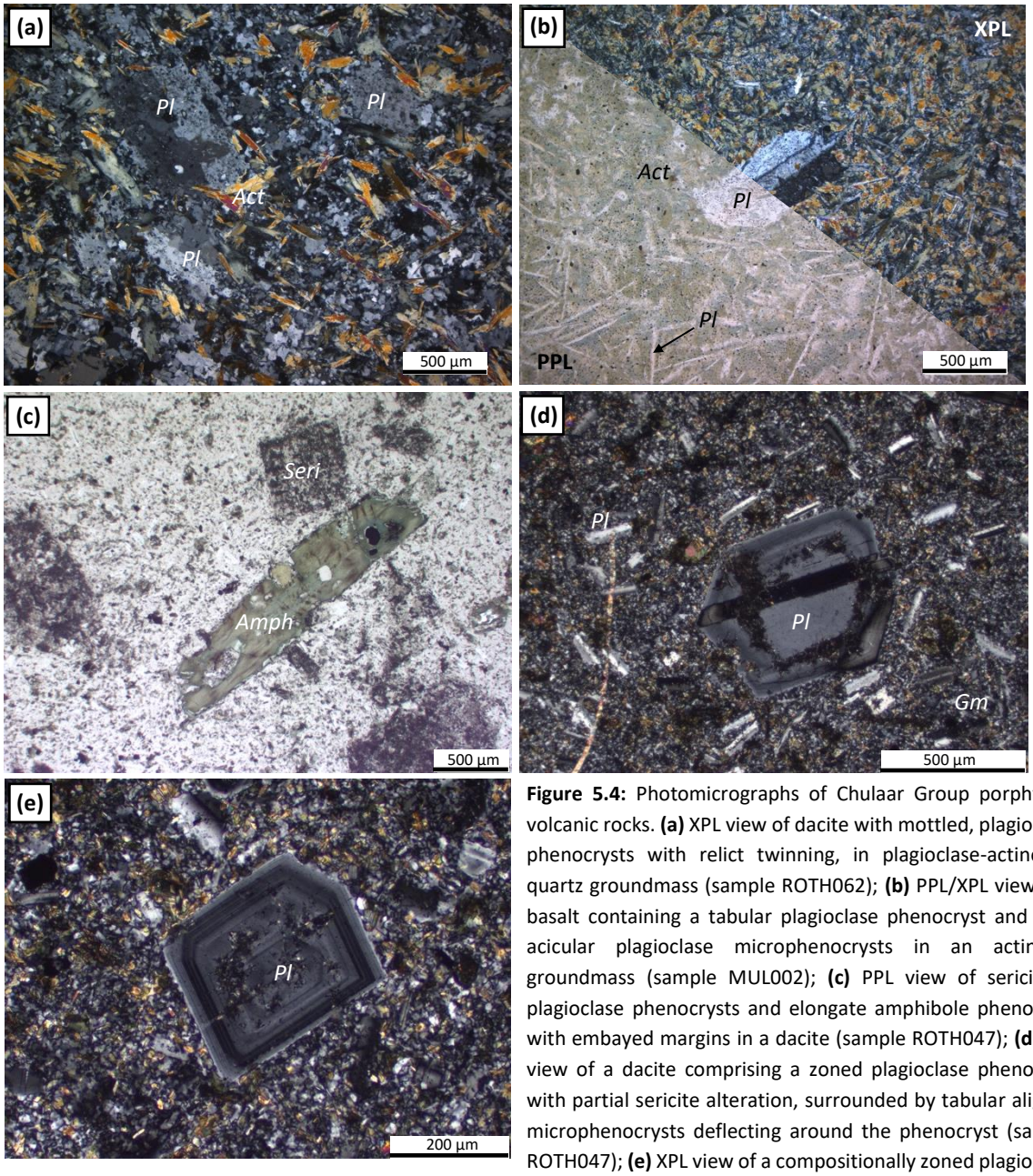

Figure 5.4: Photomicrographs of Chulaar Group porphyritic volcanic rocks. **(a)** XPL view of dacite with mottled, plagioclase phenocrysts with relict twinning, in plagioclase-actinolite-quartz groundmass (sample ROTH062); **(b)** PPL/XPL view of a basalt containing a tabular plagioclase phenocryst and thin, acicular plagioclase microphenocrysts in an actinolite groundmass (sample MUL002); **(c)** PPL view of sericitized plagioclase phenocrysts and elongate amphibole phenocryst with embayed margins in a dacite (sample ROTH047); **(d)** XPL view of a dacite comprising a zoned plagioclase phenocryst with partial sericite alteration, surrounded by tabular aligned microphenocrysts deflecting around the phenocryst (sample ROTH047); **(e)** XPL view of a compositionally zoned plagioclase phenocryst with a rounded core (sample ROTH047).

5.3.2 Porphyritic volcanic rocks

Porphyritic volcanic rocks of the Chulaar Group consist of basalts, andesites and dacites characterised by the occurrence of tabular plagioclase phenocrysts in a finer-grained holocrystalline groundmass of actinolite and plagioclase. These rocks are volumetrically less abundant than aphyric and spinifex-textured rocks and are most commonly found near the base of the Chulaar Group, at the base of the Two Peaks Volcanics (Section 3.4.1.2) and within the upper Macs Well Clastics (Section 3.4.1.1) in the Rothsay area. Phenocryst abundances vary from 1% to ~20% of the units and crystal sizes range between 0.5 and 3.5 mm, but most frequently are ~1 mm. In most units, plagioclase exhibits euhedral-subhedral shapes and preserves well-developed polysynthetic twinning, however, volcanic units containing anhedral plagioclase phenocrysts with mottled appearances and only weak traces of twinning are also present (Fig. 5.4a). Occasionally, plagioclase phenocrysts are present as both acicular crystals (up to 0.8 x 0.1 mm) and the more typical tabular phenocrysts, randomly oriented in a very fine (<0.1 mm) groundmass (Fig. 5.4b). The groundmass of porphyritic Chulaar Group rocks is essentially equivalent to that of aphyric volcanic rocks described above.

Porphyritic volcanic units are generally more prevalent in the lower part of the Chulaar Group, including rocks assigned to the Two Peaks Volcanics in the Rothsay area and equivalent rocks elsewhere in the YSGB. One such dacitic unit from the lower Two Peaks Volcanics (sample ROTH047) contains two phenocryst phases occupying ~20% of the rock. Plagioclase phenocrysts are most abundant (~75%) and occur as subhedral-euhedral 0.6-2 mm crystals, exhibiting moderately to well-developed compositional zoning and polysynthetic twinning. Approximately half of plagioclase phenocrysts have been completely sericite-altered, such that only crystal outlines and faint relic twinning remains (Fig. 5.4c). In other crystals, either the core or a specific compositional zone within a phenocryst is sericite-altered (Fig. 5.4d), suggesting that Ca-rich zones or crystals are preferentially altered relative to Ca-poor areas. Several plagioclase phenocrysts comprise rounded homogenous cores surrounded by euhedral, compositionally zoned margins, indicative of magmatic resorption (Fig. 5.4e). The remaining (~25%) phenocrysts consist of elongate, subhedral amphibole crystals up to 3.5 mm in length and showing green-brown pleochroism (Fig. 5.4c). Basal sections are hexagonal with characteristic 120° cleavage intersections and phenocrysts frequently have irregular, embayed margins consistent with resorption (Fig. 5.4c). Multiple glomerocrysts composed of three to five crystals of plagioclase and amphibole occur in some parts of the unit.

The <0.1 mm holocrystalline groundmass surrounding phenocrysts also contains 0.1-0.15 mm tabular plagioclase microphenocrysts that display a trachytic texture; crystals are typically oriented and deflect around the larger phenocrysts, preserving the lava flow direction (Fig. 5.4d). This suggests that

phenocrysts and microphenocrysts crystallised prior to eruption, likely in two stages due to the bimodal size distribution of crystals. Biotite, quartz and accessory zircon occur in the holocrystalline groundmass. Spinifex-textured porphyritic volcanic rocks are described separately below.

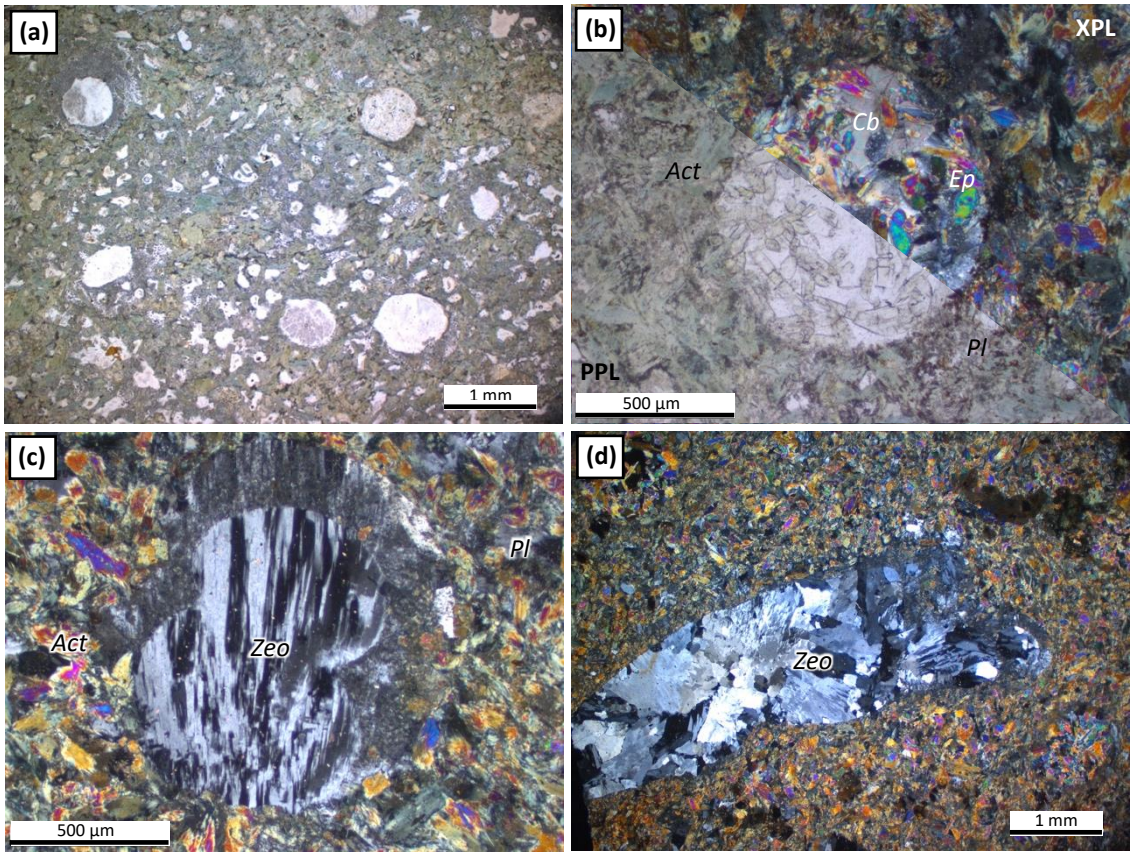

Figure 5.5: Photomicrographs of Chulaar Group amygdaloidal volcanic rocks. **(a)** PPL/XPL view of the typical texture of amygdaloidal basalt, comprising rounded ~0.7 mm amygdales in an actinolite-plagioclase-quartz-bearing groundmass (sample CHU014); **(b)** PPL/XPL view of a spherical amygdale composed of elongate epidote crystals and interstitial carbonate, in a groundmass of actinolite and plagioclase (sample CHU014); **(c)** XPL view of two conjoined amygdales composed of zeolite with abundant twinning, partially surrounded by a ~200 µm altered margin in a groundmass of actinolite and plagioclase (sample CHU014); **(d)** XPL view of large irregular ~4 mm amygdale infilled by zeolite with abundant twinning (sample CHU014).

5.3.3 Amygdaloidal volcanic rocks

Amygdales are rare in Chulaar Group volcanic rocks and have only been observed in one basaltic unit in the Chulaar area, in the northeast of the study area (sample CHU014; Fig. 5.1). In this unit, amygdales are evenly distributed (~20% abundance), rounded, typically 0.8-1.2 mm in diameter and occur in a fine-grained, light grey basaltic groundmass (Fig. 5.5a). The amygdales display a varying mineralogy: approximately ~75% of comprise of zeolite with common, irregular twinning (Fig. 5.5b). Many of these amygdales are surrounded by an altered rim, indicating that the original secondary infilling mineral(s) has been replaced by zeolite. The remaining ~25% of amygdales are composed of elongate epidote crystals and interstitial carbonate (Fig. 5.5c). Some amygdales are conjoined reflecting the amalgamation of the original vesicles (e.g., Fig. 5.5b) and uncommon irregularly shaped

amygdales up to 4 mm in diameter represent further, more significant integration of vesicles (Fig. 5.5d). Epidote has been identified as a filling in vesicles in mafic volcanic rocks elsewhere in the Yilgarn Craton (e.g., Fetherston et al., 2017). The holocrystalline groundmass around amygdales is composed of 0.1-0.6 mm blocky to fibrous actinolite crystals, 0.2-0.4 mm plagioclase and minor epidote and quartz (Fig. 5.5a).

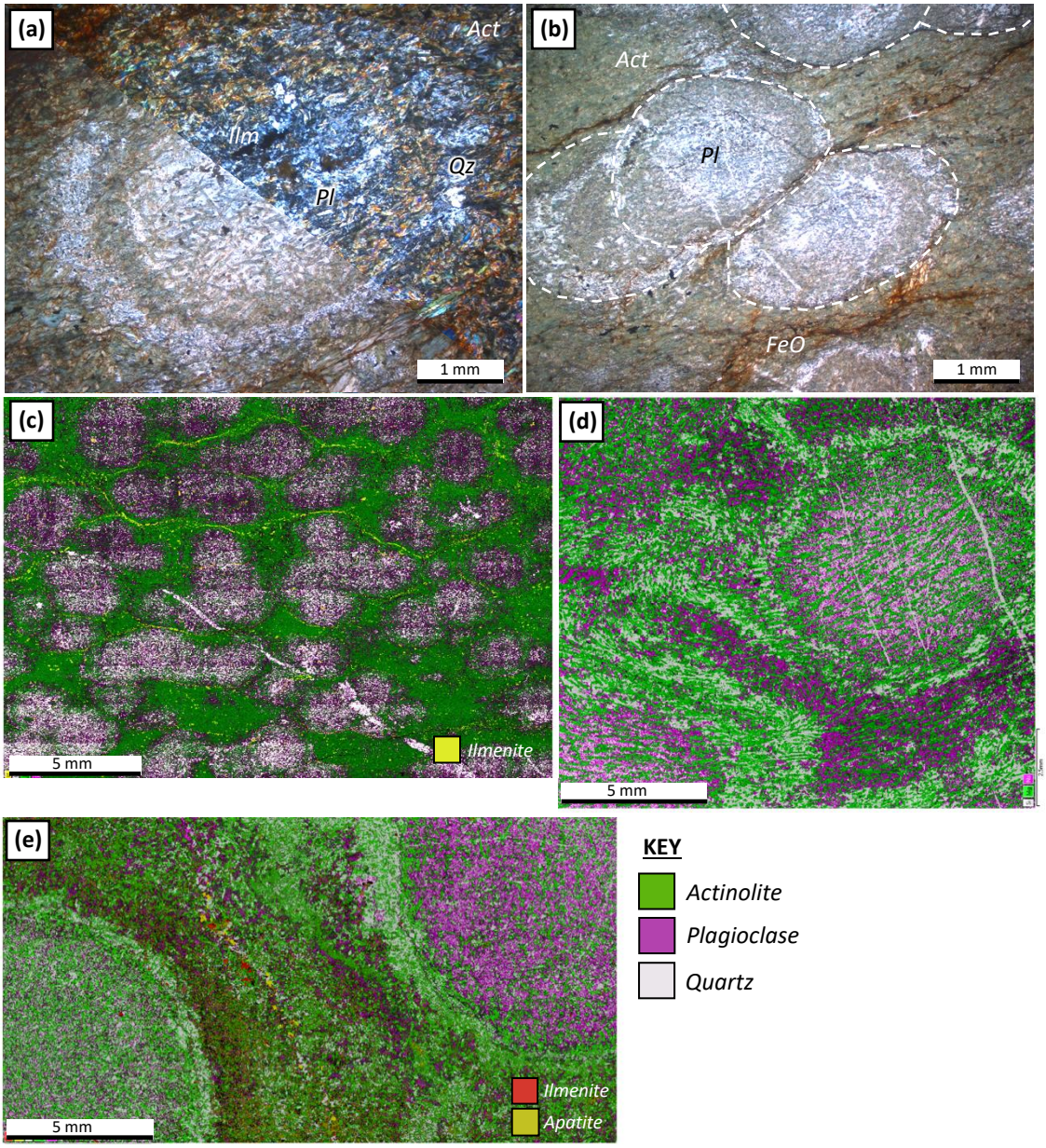

Figure 5.6: Photomicrographs and element maps of Chulaar Group variolitic rocks. **(a)** PPL/XPL view of a spherule comprising a plagioclase rich core and quartz-rich rim, with an intervening amphibole-rich band (sample ROTH012); **(b)** Smaller spherules with sharp concavo-convex contacts and higher plagioclase content than the surrounding groundmass (sample ROTH012-2); **(c)** Element map of ~2 mm spherules (sample ROTH012-2); **(d)** Element map of ~8mm spherules with plagioclase-rich cores and quartz-rich/plagioclase-poor rims (sample ROTH012); **(e)** ~12 mm spherules comprising plagioclase-rich cores and quartz-rich rims (sample ROTH012-1). The colour scales are broadly the same on each element map – green corresponds to actinolite, pink/purple corresponds to plagioclase and grey corresponds to quartz. In (c), yellow corresponds to ilmenite, whereas in (e), yellow corresponds to apatite and red corresponds to ilmenite.

5.3.4 Variolitic volcanic rocks

Basalts and rare andesites towards the top of the Chulaar Group include some units with abundant spherulitic structures referred to as varioles (Fowler et al., 2002). Variolitic volcanic rocks are particularly prevalent in the lower portion of the Mulga Volcanics in the Rothsay area (Section 3.4.1.4). The rocks are dominated by 0.1-0.3 mm actinolite laths and 0.1-0.2 mm mottled plagioclase crystals, with lesser amounts of quartz and disseminated ilmenite and accessory apatite and pyrite. Varioles are spherical to oblate in shape and range in diameter between 0.5 mm and 12 mm but are of consistent size within a given sample (Fig. 5.6a). These varioles consist of increased concentrations of plagioclase ± quartz (typically 60-75%) relative to the surrounding groundmass (~10-25%), which is dominated by actinolite (Fig. 5.6b). Varioles are frequently zoned, with plagioclase-rich (albite) cores grading outwards into the actinolite-dominated groundmass (Fig. 5.6c). Many of the larger varioles also exhibit a quartz-rich halo around their margins (Fig. 5.6a), also illustrated by element mapping (Fig. 5.6d). Further, ilmenite grains are often present near the centre of the varioles.

The contacts between overlapping varioles are sharp and concavo-convex (Fig. 5.6b, Fig. 5.6c). In some samples, aligned, elongate phenocrysts of amphibole up to 2 mm in length occur in the varioles and the groundmass, but do not show a consistent orientation and appear to be influenced by the varioles (Fig. 5.6e). Variolitic features in Archaean mafic rocks have been suggested to form through several mechanisms, including devitrification, liquid immiscibility, magma mingling and from undercooling (Fowler et al., 2002; Arndt & Fowler, 2004). The varioles comprising the Mulga Volcanics and shown in Figure 5.6 are similar to plagioclase spherulites described in the Abitibi greenstone belt, Canada, where they are attributed to the nucleation of plagioclase crystals during undercooling of superheated basaltic lavas (Arndt & Fowler, 2004). This is also consistent with the localisation of varioles at the margins of pillow structures in some Chulaar Group volcanic units (Section 3.4.1.4; Fowler et al., 2002).

5.3.5 Pyroxene spinifex-textured rocks

Pyroxene spinifex-textured rocks are prevalent in the upper parts of the Chulaar Group (e.g., Mulga Volcanics). Petrographic descriptions of these rocks have been separated into the following geometries of pyroxene spinifex-texture observed in hand specimen and thin section; random-acicular, oriented-acicular, random-platy and oriented-platy (Arndt et al., 2008; Lowrey et al., 2017), in addition to cumulate basal units associated with thicker spinifex-textured volcanic units.

5.3.5.1 Cumulate basal unit

The basal portion of a spinifex-textured flow sampled at the base of the Mulga Volcanics in the Rothsay area (Section 3.4.1.4; Sample ROTH026) is characterised by the presence of ~28% partially

serpentinised olivine in a groundmass comprised of serpentine (~30%), tremolite (~35%) and magnetite (~7%). Olivine phenocrysts are typically 1-4 mm in size, highly fragmented and anhedral and in several instances, crystals have been serpentinised to the extent that only a single 0.3 mm olivine fragment remains (Fig. 5.7a). Several olivine glomerocrysts comprising 3-4 crystals are representative of a primary igneous texture. Fibrous tremolite occurs as randomly oriented 0.1-0.7 mm crystals, whereas serpentine forms the fine-grained mesh-textured groundmass between tremolite and remnant olivine (Fig. 5.7a). An apparent sub-poikilitic texture consisting of tremolite enclosed within olivine crystals is probably a metamorphic effect. Subhedral 0.1-0.25 mm magnetite grains are associated with olivine, either enclosed within or at the margin of crystals (Fig. 5.7b).

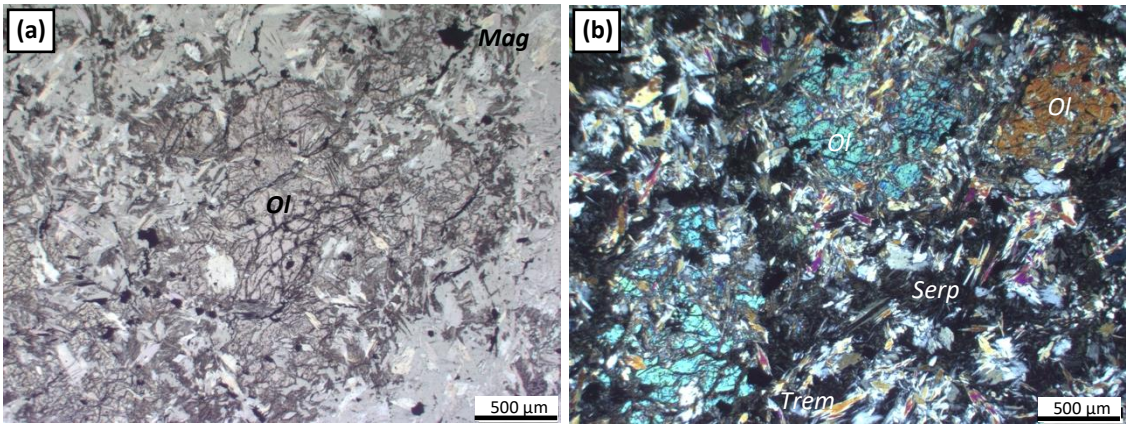

Figure 5.7: Photomicrographs of cumulate basal portions of spinifex-bearing units. **(a)** PPL view of a fragmented olivine crystal surrounded by tremolite and serpentine with magnetite along fractures and at crystal margins (sample ROTH026); **(b)** XPL view of three fragmented olivine crystals in a groundmass of serpentine, tremolite and magnetite (sample ROTH026).

5.3.5.2 Random acicular pyroxene spinifex

These spinifex-textured rocks exhibit porphyritic to vitrophyric textures that are characterised by randomly oriented acicular phenocrysts of amphibole (Fig. 5.8a). The abundance of phenocrysts varies between 15 and 50 %, most commonly ~35%, and the predominant amphibole across much of the study area is actinolite. However, in some high-Mg units tremolite is prevalent and in the far southwest near Rothsay, hornblende is the dominant phenocryst phase (Fig. 5.8b). The size of phenocrysts varies considerably between units; lengths typically range between 1-14 mm but seldom reach up to 25 mm and widths range from 0.2-1.2 mm (Fig. 5.8c). Phenocryst size also varies within units, albeit to a lesser degree. For example, average phenocryst length doubles from ~1 mm to ~2.5 mm over the length of 4 cm in sample ROTH033 (Fig. 5.8a). Many of the phenocrysts display simple twinning and intermittent cruciform-shaped phenocrysts also occur (Fig. 5.8d). The basal sections of phenocrysts are frequently subhedral-euhedral and are typically zoned with amphibole rims and altered cores replaced by chlorite and/or plagioclase (Fig. 5.8e). Rarely, basal sections are euhedral, skeletal with hollow cores, demonstrative of rapid cooling (Fig. 5.8f).

The groundmass surrounding phenocrysts is most commonly very fine grained and exhibits a plumose texture, consisting of fine (<0.1 mm) acicular crystals of actinolite intergrown with plagioclase (Fig. 5.8d). In high-Mg basalts, typically in the uppermost portion of the Chulaar Group, the groundmass is

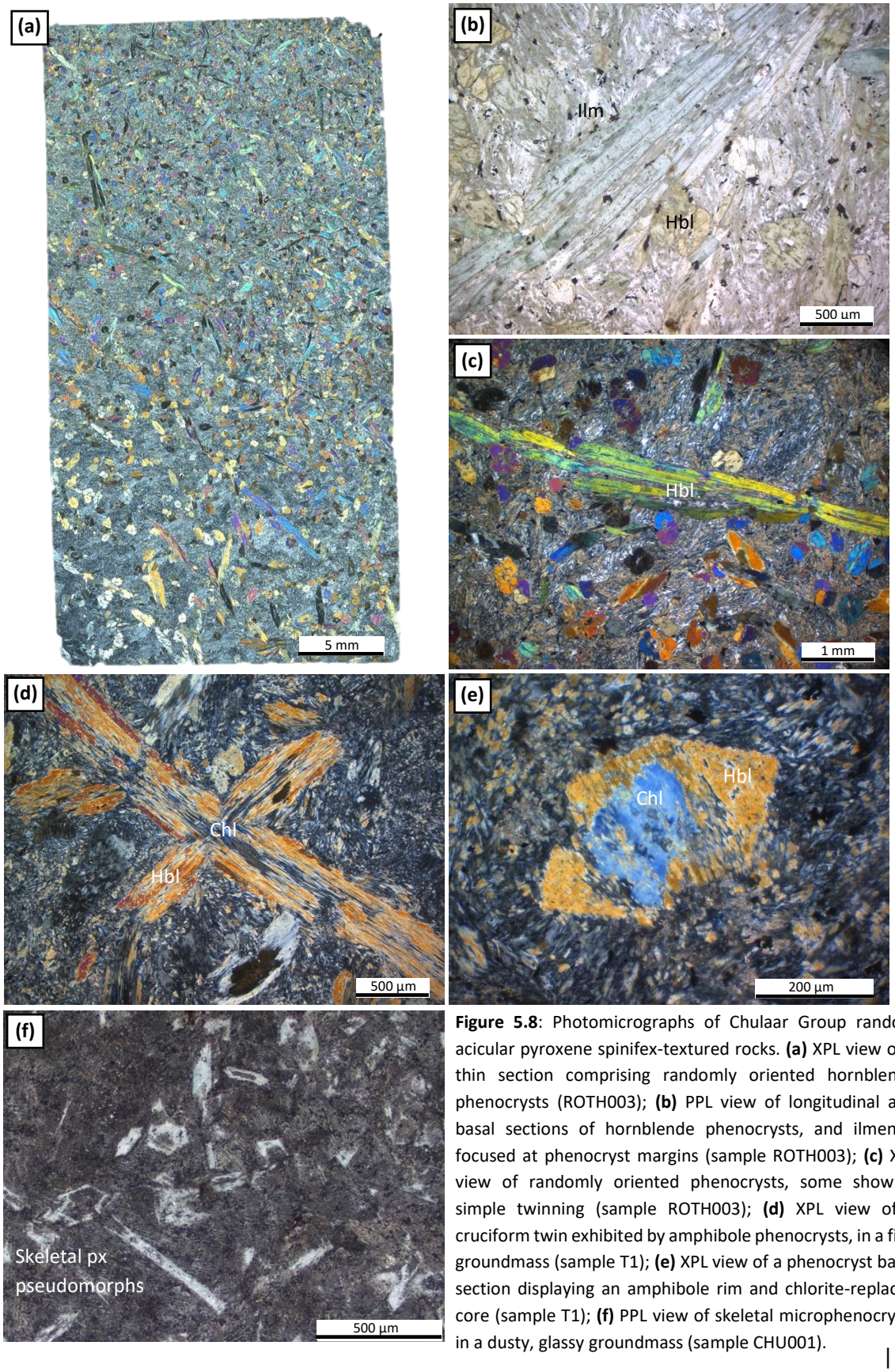

Figure 5.8: Photomicrographs of Chulaar Group random acicular pyroxene spinifex-textured rocks. **(a)** XPL view of a thin section comprising randomly oriented hornblende phenocrysts (ROTH003); **(b)** PPL view of longitudinal and basal sections of hornblende phenocrysts, and ilmenite focused at phenocryst margins (sample ROTH003); **(c)** XPL view of randomly oriented phenocrysts, some showing simple twinning (sample ROTH003); **(d)** XPL view of a cruciform twin exhibited by amphibole phenocrysts, in a fine groundmass (sample T1); **(e)** XPL view of a phenocryst basal section displaying an amphibole rim and chlorite-replaced core (sample T1); **(f)** PPL view of skeletal microphenocrysts in a dusty, glassy groundmass (sample CHU001).

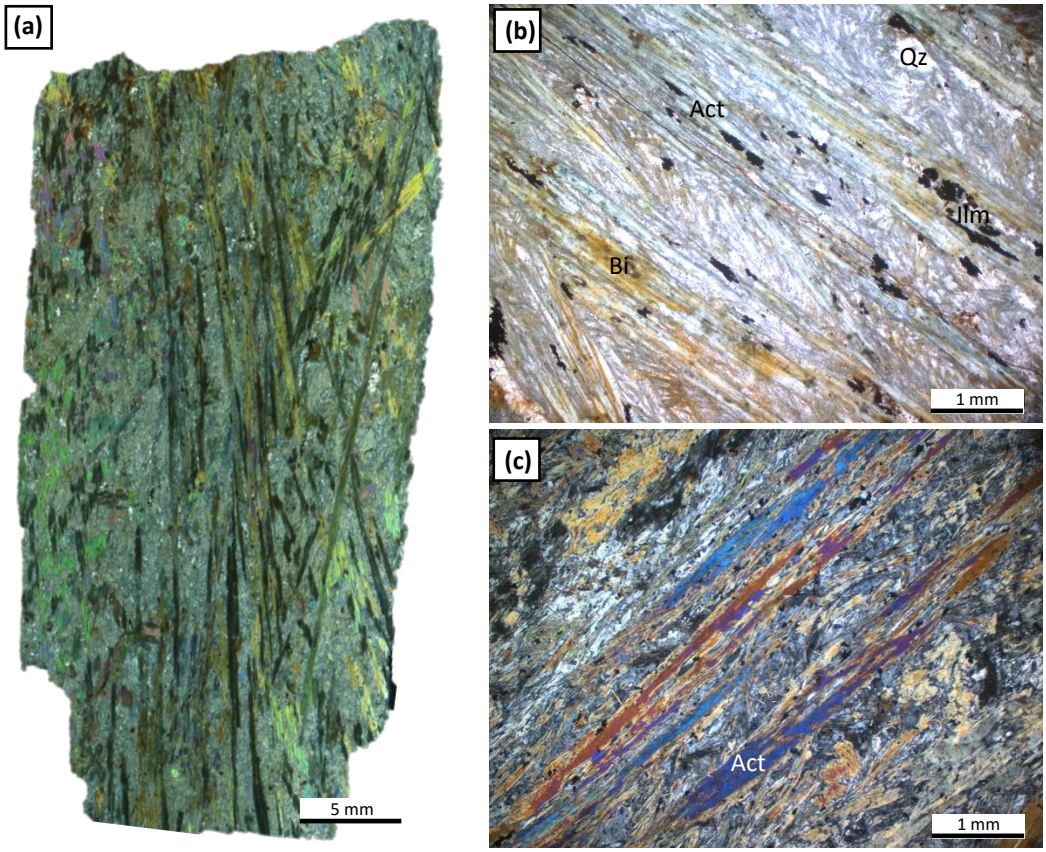

Figure 5.9: Photomicrographs of Chulaar Group oriented acicular pyroxene spinifex-textured rocks. **(a)** XPL view of a thin section comprising oriented elongate phenocrysts of amphibole up to 35 mm in length (sample T3); **(b)** PPL view of oriented acicular amphibole phenocrysts with oxides, primarily ilmenite, located at crystal margins and minor biotite and quartz derived from hydrothermal alteration (sample T3); **(c)** XPL view of oriented acicular amphibole phenocrysts surrounded by a very fine, plumose-textured groundmass (sample ROTH027).

instead composed of fine (<0.1 mm) tremolite, chlorite and minor plagioclase. In slightly coarser-grained basalts, such as those in the lower Two Peaks Volcanics in the Rothsay area (Section 3.4.1.2), the groundmass is holocrystalline and composed of 0.1-0.6 mm mottled plagioclase, quartz crystals and single acicular crystals of actinolite up to 0.5 mm in length (Fig. 5.8f). Ilmenite is disseminated as <0.1-0.3 mm anhedral-subhedral grains with characteristic needle-like shapes and are often concentrated around the margins of amphibole phenocrysts. Many of the larger ilmenite grains possess a fine-grained, non-reflective halo of leucoxene derived from alteration.

5.3.5.3 Oriented acicular pyroxene spinifex

Oriented acicular spinifex-textured rocks display a variation of spinifex texture typified by aligned elongate, acicular phenocrysts of amphibole (commonly actinolite, pseudomorphing pyroxene) that range in length from 1-35 mm and width from 0.5-1 mm (Fig. 5.9a). This form of spinifex is less common than randomly oriented acicular spinifex and is best exemplified by rocks in the Rothsay area, particularly as several units close to the base of the Mulga Volcanics (Section 3.4.1.4). Actinolite phenocrysts constitute 40-65% of the rocks and are typically subhedral with ragged, irregular crystal margins. Basal sections are frequently zoned and comprise actinolite rims and irregular cores replaced

by quartz or chlorite and long axes occasionally display simple twinning (Fig. 5.9b). The oriented acicular phenocrysts branch outwards in one direction and intersect each other at angles of <25°. A minority of phenocrysts are present as composite sets of up to 4 crystals in crystallographic continuity, both in long section and in basal section (Fig. 5.9c). The surrounding plumose-textured groundmass consists of intergrown plagioclase (< 0.3 mm) and acicular actinolite crystals (< 0.2mm) (Fig. 5.9b). Up to 7% anhedral quartz is present in the groundmass, typically <0.3 mm in size, and as minor

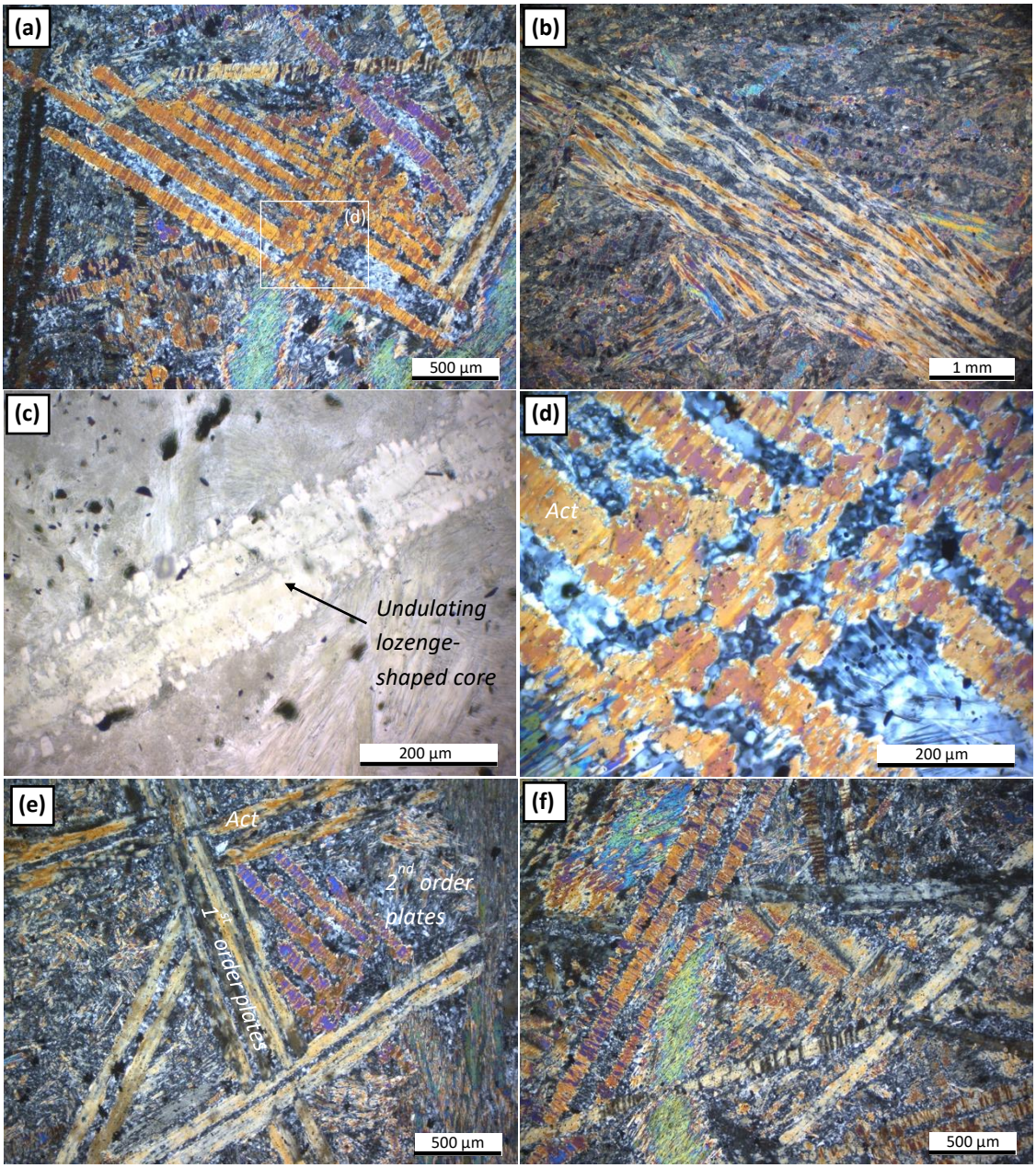

Figure 5.10: Photomicrographs of Chulaar Group random platy pyroxene spinifex-textured rocks. **(a)** XPL view of multiple randomly-oriented sets of parallel actinolite crystals, representing platy pyroxene precursors (sample MUL017); **(b)** XPL view of a set of 9 parallel plates of actinolite (after pyroxene) reaching >10 mm in length (sample ROTH041); **(c)** PPL view of a plate with undulating lozenge-shaped skeletal core and irregular crystal margins (sample ROTH041); **(d)** XPL magnified view of platy phenocrysts in (a) showing acicular basal sections between plates and a fine grained glassy groundmass including single acicular actinolite crystals (sample MUL017); **(e)** XPL view of smaller second order plate set interstitial to larger first order sets (sample MUL017); **(f)** XPL view of dendritic crystal patterns in the fine-grained groundmass interstitial to plate sets (sample MUL017).

discontinuous 4 mm veinlets, signifying hydrothermal alteration. Biotite occasionally occurs in association with quartz, including in the altered cores of actinolite phenocrysts. Oxides are abundant in interstices (~5%), particularly at the margins of actinolite crystals, and needle-like geometries suggest they are predominantly ilmenite. These characteristics are consistent with the 'oriented acicular pyroxene spinifex' classification described elsewhere in Archaean terranes (e.g., Wilson & Versfeld, 1994; Lowrey et al., 2017), also known as '*String Beef*' spinifex texture (Arndt et al., 1977).

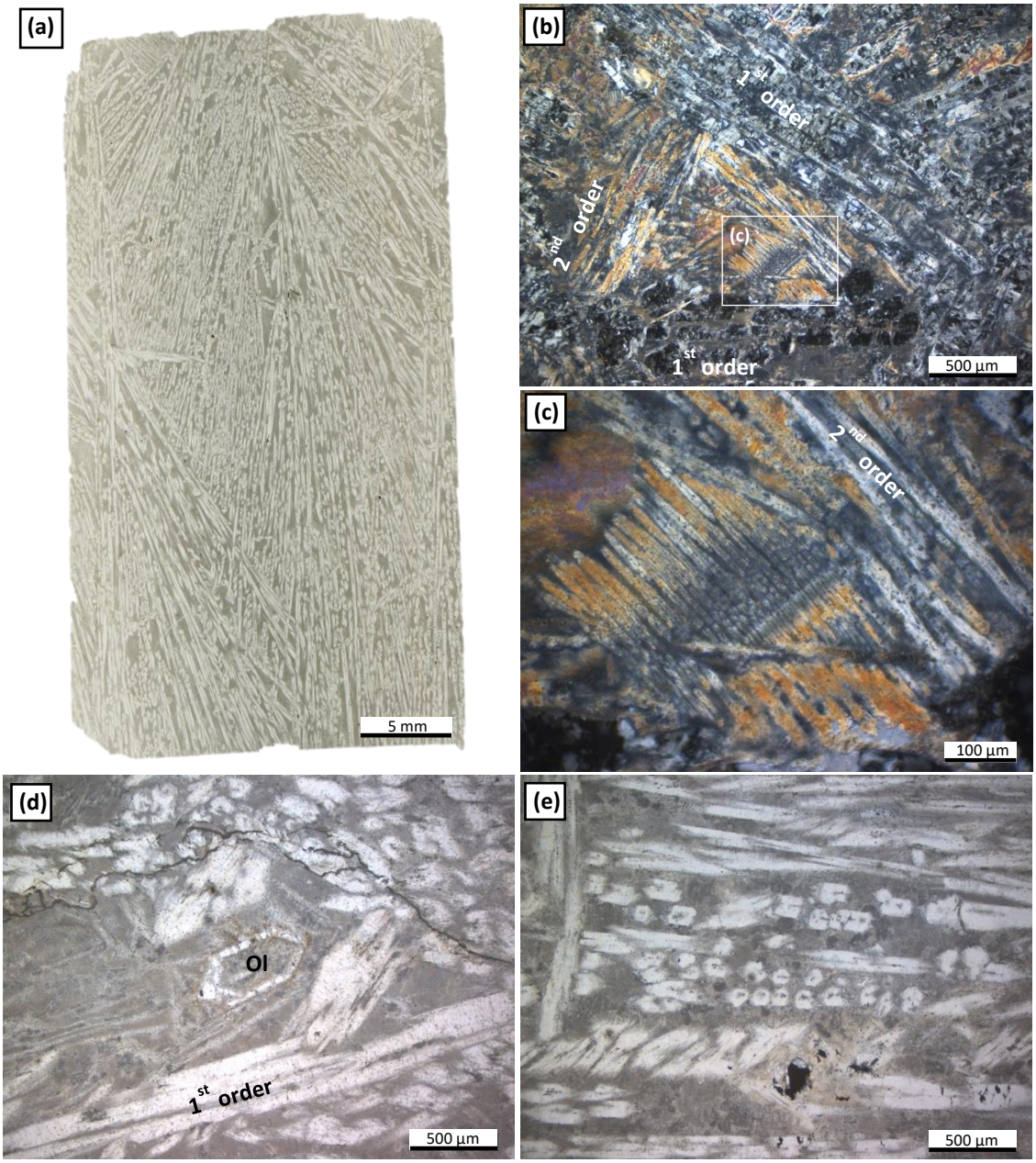

Figure 5.11: Photomicrographs of a Chulaar Group oriented platy pyroxene spinifex-textured unit (sample BAD001A). **(a)** PPL view of a thin section comprising oriented platy pyroxene crystals, branching outwards from top to bottom of the section; **(b)** XPL view of two sets of first order phenocrysts intersecting at ~40°, smaller interstitial second order crystals and third order dendritic patterns (magnified in (c)); **(c)** XPL view of branching dendritic patterns in the glassy groundmass between platy phenocrysts; **(d)** PPL view of a skeletal olivine crystal pseudomorphed by serpentine in the glassy interstices between platy phenocrysts; **(e)** PPL view of aligned basal sections of acicular crystals also aligned with platy crystals.

5.3.5.4 Random platy pyroxene spinifex

These spinifex-textured rocks contain randomly oriented sets of pseudomorphed platy pyroxene phenocrysts akin to 'random platy pyroxene' (A2 zone) described for spinifex-textured rocks in the NE Murchison Domain by Lowrey et al. (2017). In general, these rocks exhibit vitrophyric textures comprising 30-65% actinolite phenocrysts (pseudomorphing pyroxene) in a very fine glassy groundmass. The apparent elongate actinolite crystals occur on several scales. The largest 'first order' phenocrysts typically occur as sets of 2-6 parallel, closely spaced plates in crystallographic continuity, with lengths ranging between 0.5 and 13 mm and widths from 50-200 µm (Fig. 5.10a). These plate sets are randomly oriented and usually terminate against other first-order sets at angles of up to 90°, although some large plates crosscut one another in places. Rarely, up to 16 parallel plates occur in a single set and individual plates in a set are more widely spaced at up to 0.5 mm apart (Fig. 5.10b). At high magnification, the largest plates contain undulating, 'lozenge-shaped' skeletal core features along their long axes, as previously described for similar rocks by Lowrey et al. (2017) (Fig. 5.10c). Acicular actinolite phenocrysts are also present and of variable abundance relative to plates, suggesting a transition between platy-dominated units and acicular dominated-units. These acicular phenocrysts have euhedral-subhedral basal sections and do not cross first order plates, but occasionally are either aligned with them, or between them, and in crystallographic continuity (Fig. 5.10d). Random platy pyroxene spinifex is best exemplified in several units in the upper Chulaar Group in the eastern Mt Mulgine area (Fig. 5.1), although less well-preserved examples are found in the Beryl West Volcanics in the Rothsay area (Section 3.4.1.3).

In interstitial areas between first-order plates, smaller second-order sets of 2-7 plates are often present and ubiquitously terminate against the larger plates (Fig. 5.10e). In other interstices that do not contain platy crystals, dendritic, branching patterns are sometimes found, surrounded by a very fine groundmass (Fig. 5.10f). These dendritic patterns appear to be best preserved in the least altered units and are not found in others subject to high degrees of alteration. The very fine groundmass is typically plumose-textured, comprising single acicular needles of actinolite up to 0.2 mm in length intergrown with glassy material (Fig. 5.10d). Infrequent patches of recrystallised quartz up to 0.8 mm are dispersed throughout the groundmass. Irregular <0.2 mm aggregates and needles of ilmenite are disseminated through the groundmass and often focussed at the margin of actinolite phenocrysts, in addition to the minor occurrence of Cr-spinel.

5.3.5.5 Oriented platy pyroxene spinifex

A variation of platy pyroxene spinifex comprising aligned phenocrysts is observed in one sample (BAD001A) sampled in the Badja area, which displays strikingly similar features and characteristics to

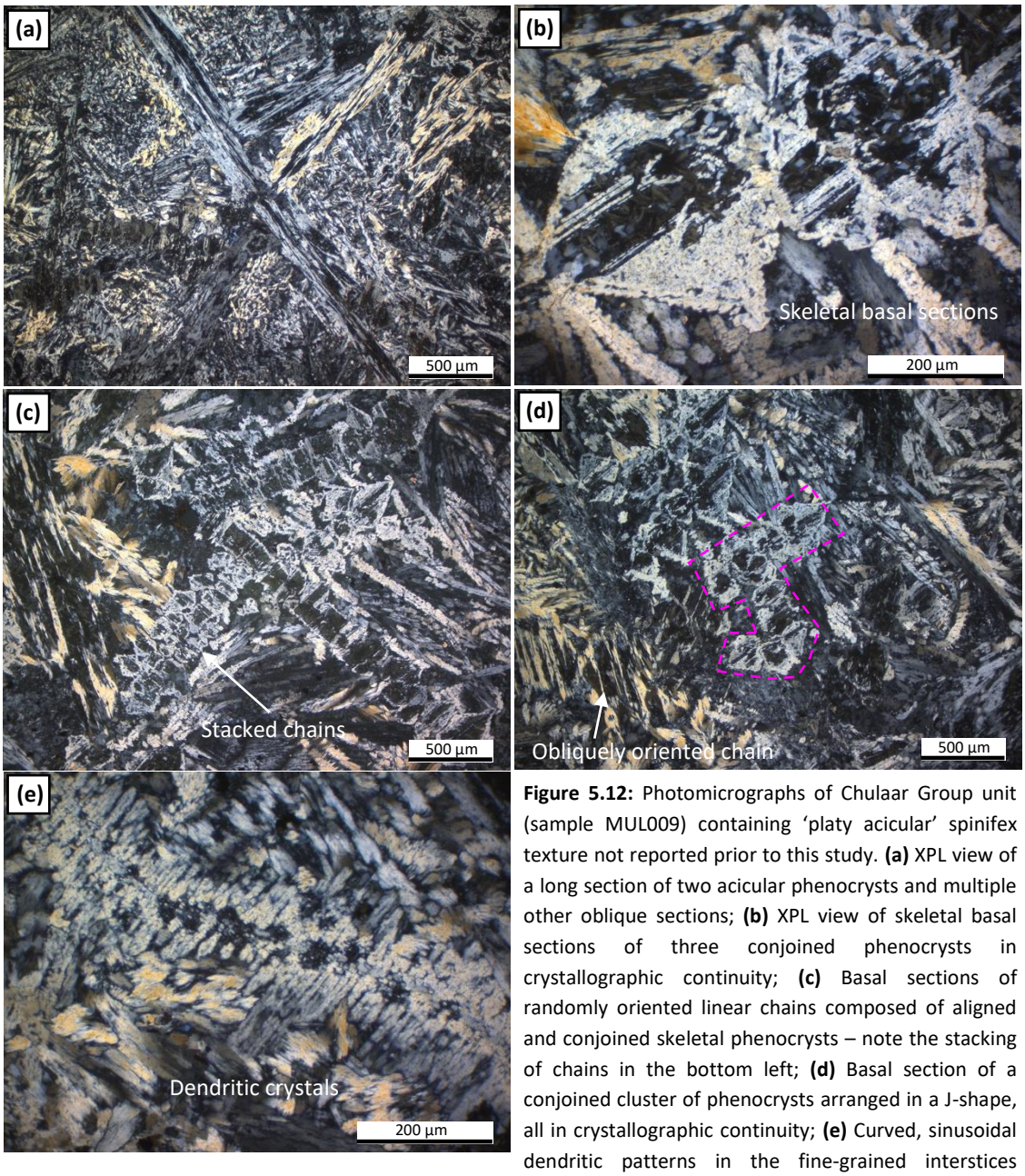

Figure 5.12: Photomicrographs of Chulaar Group unit (sample MUL009) containing 'platy acicular' spinifex texture not reported prior to this study. **(a)** XPL view of a long section of two acicular phenocrysts and multiple other oblique sections; **(b)** XPL view of skeletal basal sections of three conjoined phenocrysts in crystallographic continuity; **(c)** Basal sections of randomly oriented linear chains composed of aligned and conjoined skeletal phenocrysts – note the stacking of chains in the bottom left; **(d)** Basal section of a conjoined cluster of phenocrysts arranged in a J-shape, all in crystallographic continuity; **(e)** Curved, sinusoidal dendritic patterns in the fine-grained interstices between phenocrysts.

oriented platy pyroxene (A3 zone) spinifex-textured rocks described in the NE Murchison Domain by Lowrey et al. (2017). This rock displays a distinctive vitrophyric texture in which apparently elongate, aligned crystals of pyroxene (largely pseudomorphed by secondary minerals) constitute ~70% of the unit and are separated by an interstitial, very fine, glassy groundmass (Fig. 5.11a). The thin, elongate phenocrysts occur in sets of 2-5 parallel crystals in crystallographic continuity, interpreted as crystals with a platy habit based on their textural similarity to those recorded by Lowrey et al. (2017). In general, two scales of plate are present: I) The largest first-order plates have widths of 0.1-0.2 mm and lengths of 1-30 mm, intersect one another at angles of <40° and are totally replaced by secondary minerals, primarily serpentine (Fig. 5.11b) and II) Considerably less abundant, smaller second-order plates are 0.4-1.0 mm in length and 50-100 µm in width, confined to interstitial areas between first-

order plates and are composed of clinopyroxene (Fig. 5.11b). The second-order plates do not crosscut the first-order plates; however, first order plates do crosscut one another in some instances. In general, the plates define a branching pattern whereby first-order plate sets diverge in one direction (Fig. 5.11a). The interstices between both first and second order plates display complex, dendritic patterns (Fig. 5.11c), which appear to be smaller-scale (third order) equivalents of the large plates. These dendrites are surrounded by dusty, very fine material interpreted as quenched glass. Multiple euhedral, skeletal crystals 0.5-1 mm in diameter located in the interstitial glass are composed of quartz and other secondary minerals and may represent rapidly cooled olivine crystals trapped in interstices between plates, which have since been pseudomorphed (Fig. 5.11d). Less abundant acicular pyroxene phenocrysts are also pseudomorphed by secondary minerals and do not crosscut first-order plates. In several instances, multiple basal sections of acicular crystals are aligned with first order plates and may represent the 'acicular protrusions' into finer-grained glassy areas described by Lowrey et al. (2017) (Fig. 5.11e).

5.3.5.6 Random 'platy acicular' spinifex

A variation of spinifex-texture is observed in one unit (sample MUL009) near the top of the Chulaar Group in the Mt Mulgine area (Fig. 5.1). This unit displays a vitrophyric texture that consists of ~50% phenocrysts now composed of serpentine minerals. Phenocrysts are acicular and randomly oriented, ranging in length from 1.5-9 mm and width from 0.3-0.5 mm (Fig. 5.12a), and basal sections are consistently euhedral and skeletal (Fig. 5.12b). Phenocrysts occur in clusters of 2-10 parallel crystals in crystallographic continuity. These clusters are systematically arranged either as linear chains (sometimes stacked; Fig. 5.12c), or as crystals stacked along various longitudinal faces (including J-shaped clusters in basal section; Fig. 5.12d). These geometries appear to represent an intermediate-stage between 'acicular pyroxene' and 'platy-pyroxene' spinifex textures, in which plates are composed of conjoined acicular, skeletal phenocrysts. The variety of apparent crystal shapes present in a 2D section are a consequence of the oblique orientation of clusters of acicular skeletal phenocrysts at angles between their longitudinal sections and basal sections (e.g., Fig. 5.12d).

The fine-grained interstices between phenocrysts are dominated by dendritic patterns (Fig. 5.12e, including sinusoidal central chains with perpendicular, branching growth of crystals away from central chains (Fig. 5.12f). These patterns are like the dendritic patterns observed in platy pyroxene spinifex-textured samples, however, no 'platy pyroxene' as described by Lowrey et al. (2017) is identified in this unit. The dendritic crystals are surrounded by a very fine, glassy groundmass and occasionally, smaller acicular phenocrysts 0.3-0.4 mm in length and <0.1 mm wide also occur interstitial to clusters of large phenocrysts. Disseminated ilmenite and minor magnetite occur as <0.15 mm anhedral grains.

5.3.6 Lapilli tuff

Lapilli-bearing tuffs of the Chulaar Group occur as fine-grained, friable, light grey, finely bedded to massive, ash-dominated units in hand specimen that are characterised by abundant rounded 1-3 mm volcanic clasts, interpreted as lapilli. A 5 m-thick unit that represents the base of the Mulga Volcanics in the southwest part of the belt consists of 5-15 mm thick beds of grey ash, comprising alternating layers of fine- to medium grained quartz-bearing units, and very fine-grained lapilli-bearing units (Fig. 5.13a; Section 3.4.1.4). The grey groundmass consists of a fine grained (<0.1 mm) Fe, Mg-bearing aluminosilicate matrix containing abundant laths of feldspar in addition to quartz. Coarser beds are poorly sorted, contain angular to sub-angular <0.05 to 0.3 mm quartz clasts (30%), fine grained ash groundmass (60%), granular iron oxide (8%), and rare 0.2 mm sub-rounded cherty lithic clasts (2%). These quartz-rich layers typically have erosive bases, including the erosion of originally rounded lithic clasts (Fig. 5.13a), suggesting a degree of sedimentary reworking of volcanic material.

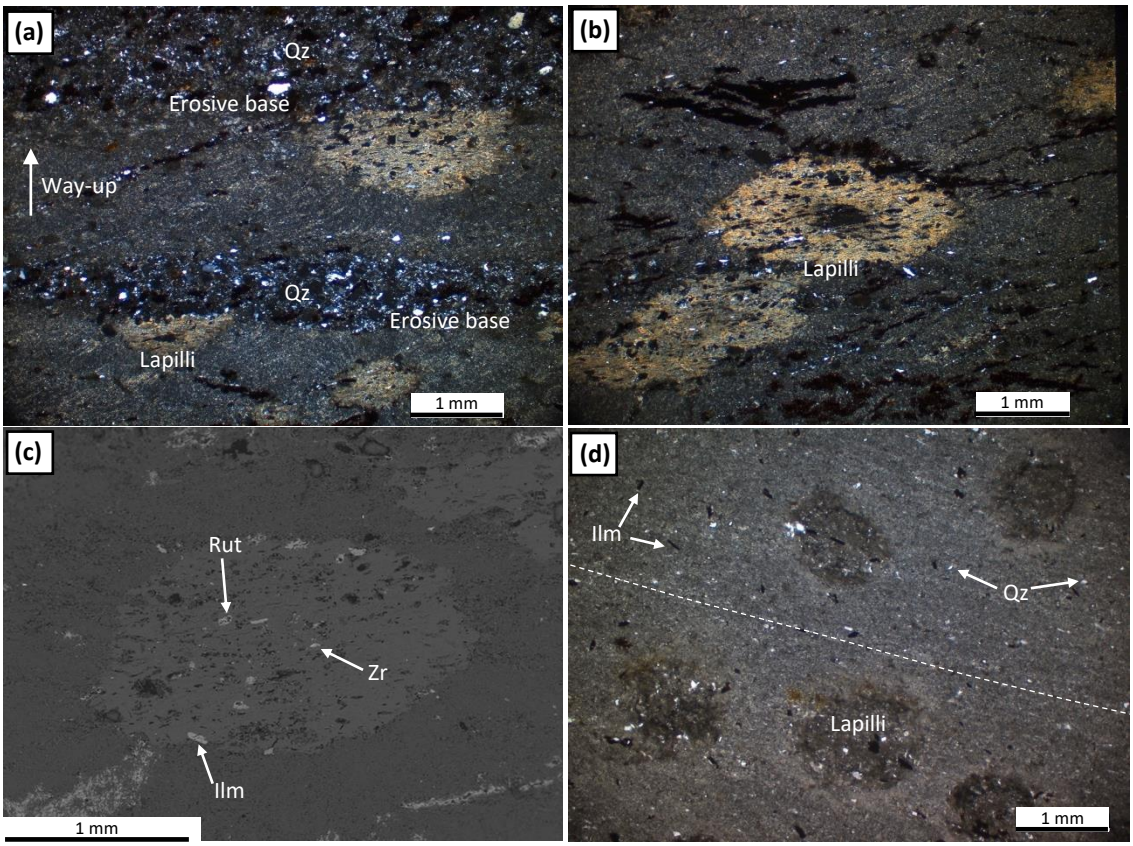

Figure 5.13: Photomicrographs of Chulaar Group lapilli tuff. **(a)** XPL view of ash-bearing units containing mm-scale quartz-rich beds with erosive bases that dissect lapilli and show way-up (sample ROTH023); **(b)** XPL view of oblate lapilli with a central, altered core, in a fine grained matrix containing minor quartz (sample ROTH023); **(c)** Back scattered electron (BSE) image of a lapilli clast containing crystals of ilmenite, zircon and a groundmass of different composition to the surrounding matrix (shown by difference in contrast) (sample ROTH023); **(d)** PPL view of massive ash-bearing unit with very weak bedding (parallel to dashed line) and rounded lapilli (sample ROTH050).

Fine grained intervals are moderately to well sorted, consist of ash (70%) and rare <0.05 mm angular quartz clasts (2%), opaque iron oxide (8%) in addition to rounded volcanic lithic clasts (20%) (Fig. 5.13b). These lithic clasts are typically 1-3 mm in size and comprise quartz crystals, sericitized feldspar

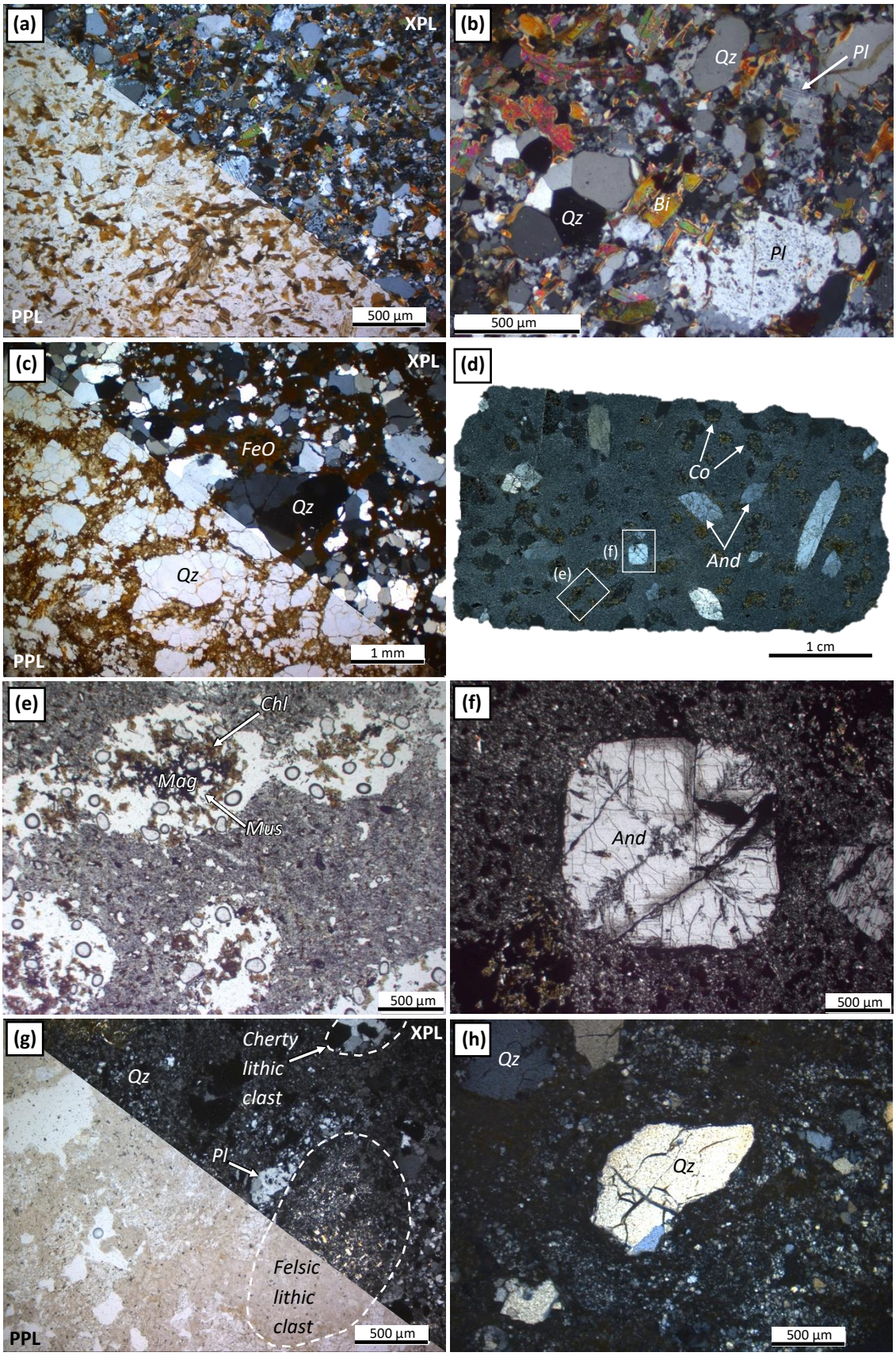

(caption on next page)

Figure 5.14 (previous page): Photomicrographs of Willowbank Clastics metasedimentary and metavolcaniclastic rocks sampled in the Rothsay area. **(a)** PPL/XPL view of the typical texture and mineralogy for greywacke (sample ROTH080); **(b)** XPL magnified view of a greywacke groundmass comprising clasts of plagioclase, biotite, quartz and cherty lithics (sample ROTH080); **(c)** PPL/XPL view of volcanogenic pebbly sandstone consisting of subrounded-subangular quartz clasts amongst a fine volcanogenic groundmass containing iron oxide and smaller quartz clasts (sample ROTH081); **(d)** XPL view of a thin section of a porphyroblastic mudstone comprising porphyroblasts of rounded cordierite (pinitized) and randomly oriented prismatic andalusite crystals, in a finer quartz-rich matrix (sample ROTH053); **(e)** PPL view of pinitized cordierite porphyroblasts now comprising iron oxide, yellow-brown chlorite and minor muscovite – note that much of the clear areas represent holes in the section, likely due to loss of clays during preparation (sample ROTH053); **(f)** XPL view of the euhedral basal section of an andalusite porphyroblast, surrounded by fine-grained quartz-rich matrix. **(g)** PPL/XPL view of felsic volcaniclastic rock comprising rounded cherty and felsic lithic clasts, subhedral plagioclase and anhedral quartz crystals in a quartzofeldspathic groundmass (sample ROTH060); **(h)** XPL view of a felsic volcaniclastic rock comprising angular, fractured quartz clasts within a fine-grained quartzofeldspathic groundmass (sample ROTH044).

crystals, fine ash and minor magnetite, rutile and ilmenite (Fig. 5.13c), though smaller 0.2-1 mm equivalents are observed in one layer. These clasts are concentrated along specific bedding horizons, are slightly elongate in the direction of bedding, often exhibit a relict crystal/cavity at their core and display fining upwards graded bedding. These features are interpreted as lapilli, and likely represent eruptive episodes between periods of reworking. Accessory minerals present in the matrix include 0.2 mm rutile crystals, 0.1 mm ilmenite grains and <0.1 mm zircons crystals and fragments. Several rod-shaped shards of quartz about 0.2 mm in length are found, that may represent relic shards of volcanic glass. The unit is crosscut by secondary quartz veinlets up to 0.3 mm in width, and minor iron oxide, probably hematite.

Thicker units of lapilli-bearing tuff at the top of the Chulaar Group are massive and display very similar characteristics to the fine-grained intervals described for the thin, basal tuff above; these units are dominated by fine-grained Fe, Mg aluminosilicate ash and contain identical 1-3 mm lapilli structures (Fig. 5.13d). Consequently, there is no evidence of sedimentary reworking and significantly less quartz clasts (< 5%) compared to the thin tuff at the base of the Mulga Volcanics (Section 3.4.1.4).

5.4 Willowbank Clastics

The base of the Willowbank Clastics in the Rothsay area, in the southwestern part of the YSGB, is marked by a sequence of coarsening upwards metasedimentary rocks, including siltstone, greywacke and pebbly sandstone, conformably overlain by felsic volcaniclastic rocks (Section 3.4.1.5).

5.4.1 Greywacke

The greywacke unit near the base of the Willowbank Clastics is a fine-grained, immature, poorly sorted clastic metasedimentary rock composed of clasts of quartz (30%), biotite (25%), plagioclase (15%) and lithic clasts (4%), surrounded by a finer grained matrix (Fig. 5.14a). Quartz clasts are typically angular

to sub-angular and vary in size between 0.1 and 0.5 mm, whereas plagioclase occurs as 0.2 mm anhedral grains that exhibit clear polysynthetic twinning. Biotite is present as 0.1-0.2 mm randomly oriented laths evenly distributed throughout the unit. Less common lithic clasts up to 0.6 mm in diameter are composed of granoblastic quartz (Fig. 5.14b). The fine-grained (<< 0.1 mm) matrix accounts for ~25% of the sample and consists of quartz, lesser feldspar and minor biotite. Minor amounts of an opaque iron oxide phase are present as anhedral aggregates. The unit is both compositionally and texturally immature, suggesting it was deposited relatively close to the source region of the sediment.

5.4.2 Pebbly sandstone

The pebbly sandstone directly overlying greywacke represents a medium-grained, moderately well sorted quartz-rich clastic metasedimentary rock. Quartz clasts dominate the unit (~75%) and are subrounded with a bimodal distribution; larger clasts are typically 1 mm in diameter (but up to 3 mm) and exhibit a granoblastic texture which may have been induced by metamorphic recrystallisation, in contrast to finer (0.1-0.2 mm) sub-angular quartz clasts (Fig. 5.14c). The unit is broadly clast-supported, with interstices between clasts accommodated by a very fine-grained, light coloured volcanogenic matrix, which includes orange-brown iron oxide discolouration (possible limonite/goethite; Fig. 5.14c). This unit records upwards increases in average grain size, maturity and volcanogenic content relative to the underlying greywacke unit.

5.4.3 Porphyroblastic mudstone

A porphyroblastic mudstone unit near the base of the Willowbank Clastics in the Rothsay area contains two porphyroblast phases accounting for approximately 25% of the unit (Fig. 5.14d; Section 3.4.1.5). The most abundant phase comprises rounded, anhedral 1-2mm aggregates of muscovite, yellow-brown chlorite and iron oxide, representing pinitization of cordierite crystals (Fig. 5.14e). Further euhedral and prismatic porphyroblasts of andalusite are randomly oriented and up to 1 cm in length (Fig. 5.14f). The surrounding matrix comprises subrounded to rounded clasts of quartz, minor plagioclase and muscovite, and randomly oriented needle-shaped crystals of ilmenite, in addition to predominant silt-sized material.

5.4.4 Felsic volcaniclastic rock

Willowbank Clastics felsic volcaniclastic rocks are typically fine-grained, cream-white, weakly bedded to massive and friable in hand specimen. They are characterised by variable abundances of quartz clasts and lithic clasts in a fine grained quartzofeldspathic groundmass. The microcrystalline

groundmass accounts for 45-50% of these units and comprises fine grained (<0.1 mm) angular to sub-angular quartz crystals and relict feldspar crystals with elongate crystal shapes and traces of complex twinning, likely plagioclase (Fig. 5.14g). The groundmass also contains sericite, in addition to localised

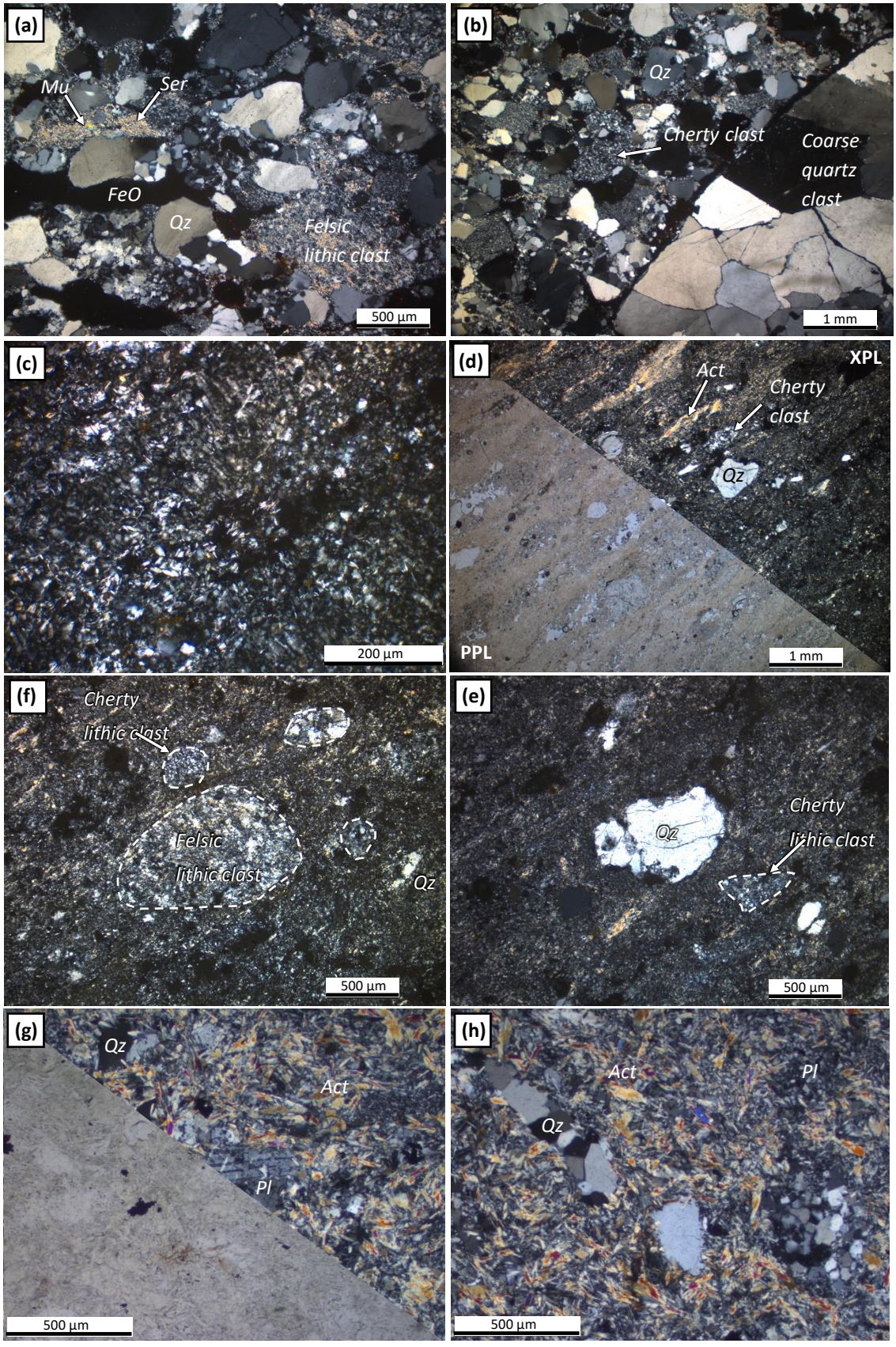

(caption on next page)

Figure 5.15 (previous page): Photomicrographs of Mougooderra Formation rocks. **(a)** XPL view of pebbly sandstone displaying subrounded-subangular, poorly sorted quartz clasts, subrounded felsic clast and interstitial sericite, muscovite and iron oxide (sample MOU003); **(b)** XPL view of pebbly sandstone containing a large >1 cm 'pebbly' quartz clast and finer subrounded quartz and cherty lithic clasts (sample MOU003); **(c)** XPL magnified view of the fine-grained quartzofeldspathic groundmass that characterizes many felsic volcaniclastic rocks (sample MOU002); **(d)** PPL/XPL view of foliated volcaniclastic unit containing quartz and cherty lithic clasts in a fine quartzofeldspathic groundmass with minor actinolite (sample MOU002); **(e)** XPL view of subrounded felsic and cherty lithic clasts up to 1 mm in diameter, in a felsic volcaniclastic rock (sample MOU002); **(f)** XPL view of angular quartz clasts and a sub-angular cherty lithic clast (sample MOU002); **(g)** PPL/XPL view of the typical texture and mineralogy of a Mougooderra Formation volcanic rock, comprising plagioclase phenocrysts with relict twinning, in a groundmass of actinolite and quartz (sample MOU008); **(h)** XPL view of a metadacite comprising elongated recrystallized quartz patches and mottled plagioclase phenocrysts in an actinolite-dominated groundmass (sample MOU008).

fibrous crystals of actinolite (0.1-0.2 mm). In some more highly altered samples, the matrix has been subject to kaolinitic alteration. Quartz clasts account for 20-25% of these units and consist of angular to sub-angular grains up to 1.2 mm in size dispersed throughout the matrix (Fig. 5.14h). In contrast, lithic clasts (25-30%) are sub-rounded, 0.5-2 mm in size and predominantly comprise microcrystalline quartz, reflecting clasts of chert. Less common (up to 5%) sub-rounded lithic clasts up to 1.4 mm in size consist of an aluminosilicate groundmass, randomly oriented plagioclase crystals and secondary actinolite crystals, interpreted as felsic volcanic lithic clasts (Fig. 5.14g). Quartz, chert and lithic clasts are frequently elongated and aligned in the local fabric direction. The microcrystalline groundmass contains sparse 0.2 mm opaque iron oxide crystals, probably secondary limonite, in addition to accessory rutile and barite. Abundant euhedral zircon crystals and fragments are present in the matrix and in felsic volcanic lithic clasts and are up to 0.2 mm in size with oscillatory zoning evident.

5.5 Mougooderra Formation

The base of the Mougooderra Fm in the eastern part of the belt is marked by a sequence of metasedimentary rocks including conglomerates and pebbly sandstones (Zibra et al. 2018), which are locally overlain by a poorly exposed felsic volcaniclastic unit. In the far southeast, multiple volcanic rock units are present within metapsammite-dominated succession (Ivanic, 2018). Petrographic descriptions of representative samples from the pebbly sandstone, felsic volcaniclastic and volcanic units of the Mougooderra Fm in the eastern part of the belt are given below:

5.5.1 Pebbly Sandstone

Pebbly sandstone units of the Mougooderra Fm are poorly sorted, clast-supported and texturally immature, consisting of 50% detrital quartz clasts, 28% lithic clasts, 5% opaque minerals and 17% fine-grained matrix. Quartz grains are typically sub-angular to sub-rounded, often elongate in shape and range in size from 0.2-2 mm (average ~1 mm; Fig. 5.15a). The largest quartz clasts are more well-rounded and commonly show undulose extinction. Approximately 60% of lithic clasts consist of

microcrystalline quartz, are typically subrounded and vary in diameter between 0.5 and >8 mm, consistent with chert lithic clasts (Fig. 5.15b). The remaining 40% of lithic clasts are subrounded, up to 1.5 mm in diameter and comprise fine grained (<0.1 mm) quartz, sericite, feldspar and a fine grained, cream coloured matrix, interpreted as probable felsic volcanic clasts (Fig. 5.15a). The intervening matrix is dominated by quartz, with minor sericite associated with patches of fine-grained (0.1-0.2 mm) muscovite crystals, in addition to rare euhedral zircon crystals and fragments. Opaque phases (5%), consisting primarily of iron oxides including hematite, limonite and goethite, in addition to rutile, are concentrated along specific horizons that are interpreted as relict bedding surfaces. Truncation of these surfaces against one another defines decimetre-scale cross bedding and way-up directions are corroborated by graded bedding present in some cm-scale beds.

5.5.2 Felsic volcaniclastic rock

Felsic volcaniclastic rocks of the Mougooderra Fm are typically fine-grained, friable, light yellow to white and weakly bedded in hand specimen. They are commonly moderately altered and foliated and are dominated by a fine-grained microcrystalline quartzofeldspathic groundmass, typically accounting for ~60% of the rocks (Fig. 5.15c). The groundmass contains fine grained (<0.1 mm) quartz, relict feldspar crystals (probably plagioclase) and sericite, likely derived from alteration of primary feldspar, in addition to fibrous actinolite crystals (up to 0.8 mm) and very fine chlorite (Fig. 5.15d). Sub-angular quartz clasts 0.5-1 mm in size are pervasive and concentrated along specific horizons (Fig. 5.15d). Two types of lithic clast are present: I) 0.5-1.5 mm sub-rounded clasts containing euhedral 0.2-0.4 mm laths of plagioclase, in addition to quartz, sericite and accessory barite, rutile and zircon, representing felsic volcanic lithic clasts (Fig. 5.15e), and II) 0.5-2 mm, sub-angular to sub-rounded, predominantly cherty clasts that comprise microcrystalline quartz, and may represent quartz-rich or recrystallized glassy volcanic lithic clasts (Fig. 5.15f). Opaque iron oxide minerals are 40 μm in size, with other accessory phases including rutile, barite and zircon. A moderately developed foliation is defined by elongate actinolite crystals, and the preferred alignment of elongate lithic clasts.

5.5.3 Dacitic volcanics

Volcanic rocks of the Mougooderra Fm include andesites and dacites that are typically porphyritic, comprising phenocrysts of plagioclase and quartz in a fine-grained crystalline groundmass. The groundmass is dominated by randomly oriented fibrous crystals of actinolite up to 0.2 mm in size and fine grained (< 0.1 mm) feldspar and lesser quartz (Fig. 5.15g). Opaques, primarily magnetite and ilmenite, account for 1% of the units and occur as anhedral to subhedral crystals and aggregates up to

0.25 mm in size, distributed throughout the groundmass. Phenocrysts typically occupy ~8% of the units and primarily comprise 0.2-1 mm, anhedral rounded to ovoid phenocrysts of quartz (6%) and 0.2-0.6 mm subhedral phenocrysts of feldspar (2%) characterised by a mottled appearance and

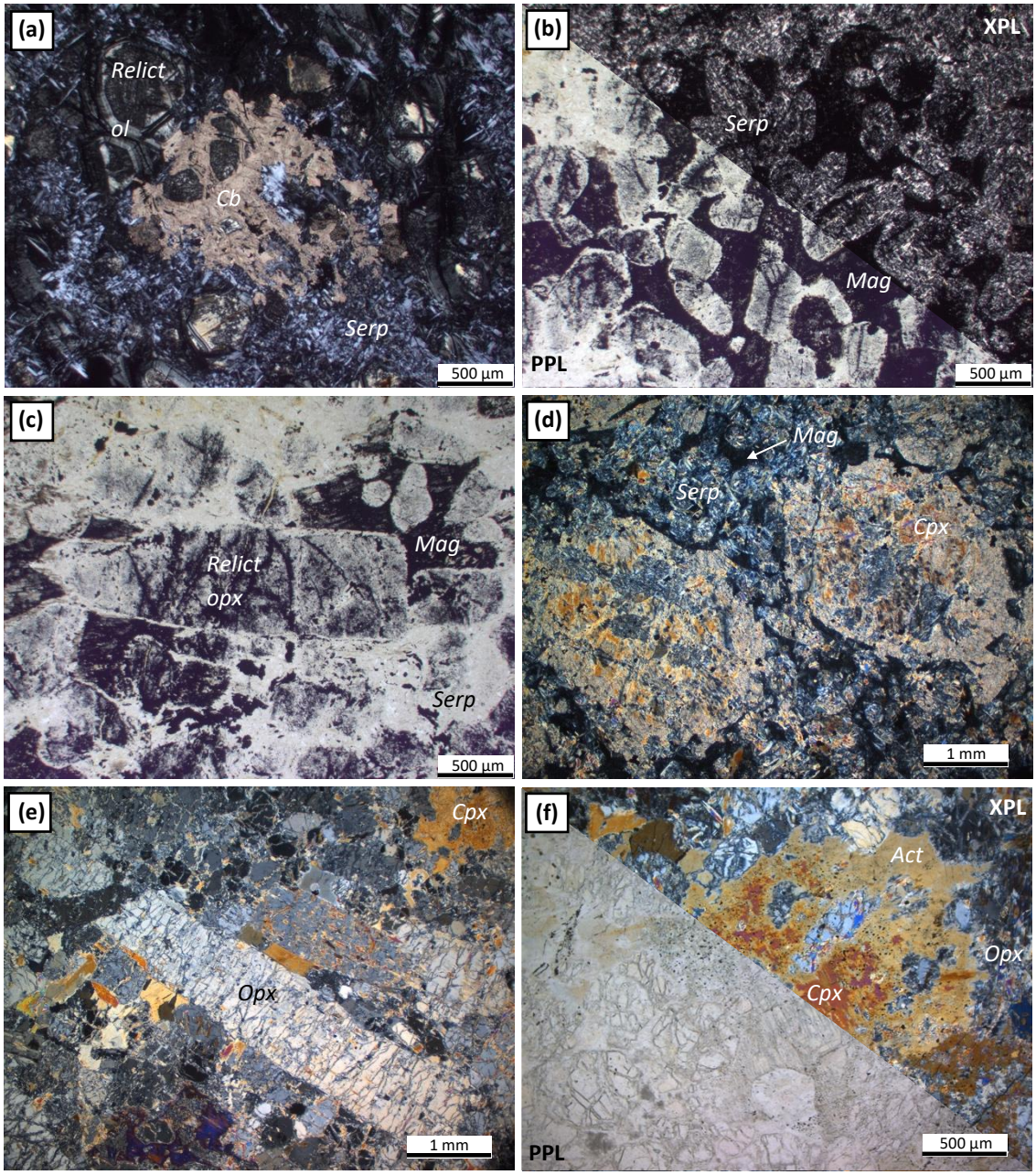

Figure 5.16: Photomicrographs of Warriedar Suite ultramafic cumulate rocks. **(a)** XPL view of a carbonate altered serpentinite comprising poikiloblastic carbonate patches enclosing and surrounded by serpentine and relict olivine crystals (sample CHU003); **(b)** PPL/XPL view of a serpentinite containing serpentinised olivine crystals surrounded by magnetite-bearing interstices preserving an primary igneous orthocumulate texture (sample CHU009); **(c)** PPL view of serpentine pseudomorphs of cumulate olivine surrounded by magnetite, and uncommon larger, tabular crystals interpreted as pseudomorphs of pyroxene, possibly orthopyroxene (sample CHU009); **(d)** XPL view of an olivine-pyroxene cumulate rock containing subhedral, prismatic phenocrysts of clinopyroxene enclosing and surrounded by smaller, serpentinised relict olivine crystals and interstitial magnetite (sample BAD002); **(e)** XPL view of an orthocumulate-textured orthopyroxenite dominated by subhedral orthopyroxene crystals, occasionally elongate, in addition to interstitial clinopyroxene (partially pseudomorphed by actinolite) and minor serpentinised olivine (sample MUL006); **(f)** PPL/XPL view of a pyroxene cumulate rock consisting of poikilitic interstitial crystals of clinopyroxene partially pseudomorphed around their margins by actinolite and containing orthopyroxene cumulate crystals (sample MUL006).

tabular crystals, albeit lacking abundant twinning (Fig. 5.15g). Furthermore, elongate ovoid to lenticular patches of recrystallised quartz 0.5-1.0 mm in diameter display a granoblastic texture and are typically oriented in the same direction (Fig. 5.15h). This orientation is not displayed by fibrous actinolite crystals in the groundmass, suggesting that these are primary features, either recrystallised quartz phenocrysts or more likely, recrystallised amygdales.

5.6 Warriedar Suite

Stratigraphic subdivision of Warriedar Suite intrusions is based primarily on mineralogical and textural variations corresponding to well-developed magmatic layering. For example, many of the thickest sills can be subdivided into a basal cumulate ultramafic unit, overlying pyroxenitic rocks, massive gabbroic/doleritic rocks and an uppermost quartz dioritic unit. As the petrographic characteristics of the individual Warriedar Suite intrusions are generally similar and to avoid unnecessary repetition, petrographic descriptions will be given for the main rock types observed throughout the suite.

5.6.1 Cumulate ultramafic rocks

The ultramafic rocks present at the bases of many Warriedar Suite intrusions are dominated by serpentine (65-70%) with up to 10% tremolite and 5-10 % iddingsite, in addition to magnetite and Cr-spinel, which together constitute ~10% of the samples. Spots of poikiloblastic magnesite 1-3 mm in size enclose serpentine and account for up to 15% of some samples (Fig. 5.16a), demonstrating partial carbonation of the ultramafic protolith. Complete serpentinization of olivine is typical, with the extensive development of mesh-textured serpentine that preserves ortho- to meso-cumulate primary igneous textures (Fig. 5.16b). Abundant rounded crystal shapes from 0.25-2 mm in diameter are pseudomorphed and highlighted by alteration phases, and display the characteristic anhedral, fractured appearance of olivine. Less common subhedral, tabular crystals often exhibiting a bastite texture indicate the presence of orthopyroxene in the cumulate assemblage (Fig. 5.16c). Based on relict crystal morphology, cumulate olivine and orthopyroxene account for approximately 70-75% and 5-10% of the ultramafic protoliths, respectively. Relict olivine is seldom preserved and only occurs as isolated fragments within a matrix of serpentine and magnetite. Towards the top of basal ultramafic cumulates, the proportion of pyroxene relative to olivine increases and clinopyroxene joins the fractionating cumulate assemblage. In one such unit, euhedral-subhedral prismatic clinopyroxene crystals (partially pseudomorphed by actinolite) 1.5-3.5 mm in size enclose abundant 0.2-0.3 mm olivine crystals pseudomorphed by serpentine and magnetite (Fig. 5.16d). The surrounding groundmass is dominated by fine grained acicular actinolite and serpentine.

An orthopyroxene-dominated cumulate ultramafic horizon outcrops in a Warriedar Suite intrusion in the Mulgine area (MUL006; Fig. 5.16e). This unit comprises ~65% subhedral orthopyroxene crystals typically 1-1.5 mm in diameter and less common (~10%) <0.5 mm serpentinised olivine crystals, which together define an orthocumulate texture. In rare instances, orthopyroxene crystals are elongate and

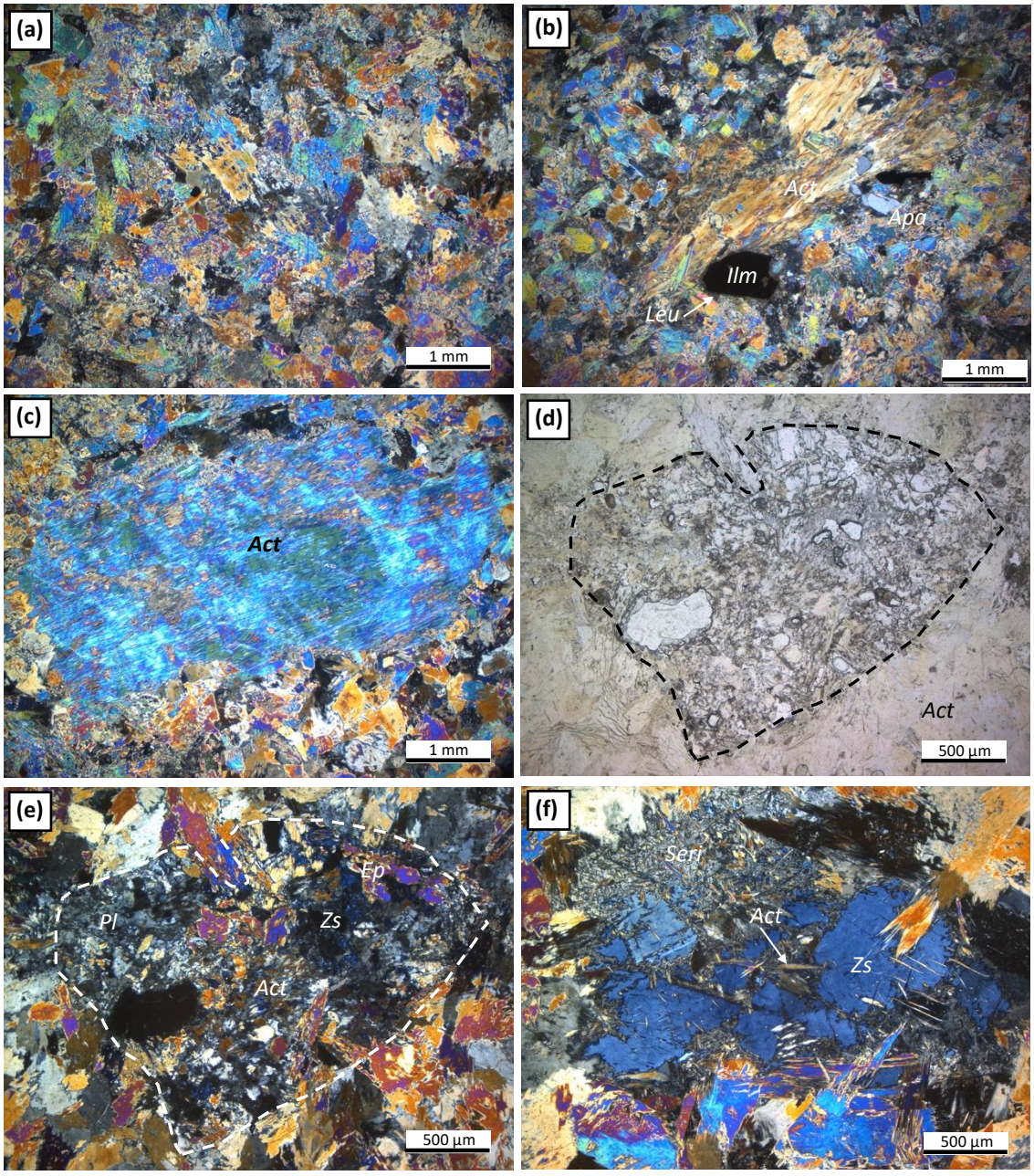

Figure 5.17: Photomicrographs of Warriedar Suite (originally) pyroxenitic rocks. **(a)** XPL view of the typical texture of a pyroxenite, now composed of anhedral, equicrystalline tremolite and actinolite laths (sample MUL005); **(b)** XPL view of pyroxenite displaying an original porphyritic texture comprising elongate actinolite phenocrysts (after pyroxene), surrounded by minor apatite, ilmenite with leucoxene halo and interlocking amphibole laths (sample ROTH007); **(c)** XPL view of a porphyritic pyroxenite comprising a subhedral, tabular ~6 mm actinolite phenocryst (after pyroxene) in a finer grained amphibole-dominated groundmass (sample MUL005); **(d)** PPL view of a saussuritised plagioclase phenocryst with relic tabular crystal shape in an actinolite groundmass, in a porphyritic pyroxenite from the Rothsay Sill (sample ROTH077); **(e)** XPL view of (d) displaying the products of saussuritisation of plagioclase; epidote, zoisite, actinolite and minor remnant plagioclase (sample ROTH077); **(f)** XPL view of saussuritised plagioclase phenocryst replaced by zoisite, acicular actinolite crystals and fine grained sericite, surrounded by actinolite laths (sample MUL005).

up to 7 mm in length. Clinopyroxene is present as an intercumulus phase, occurring as 1.5-2 mm oikocrysts enclosing both orthopyroxene and olivine; those hosting relict olivine have pervasive opaque inclusions along cleavage planes, likely derived from serpentinization. Most primary

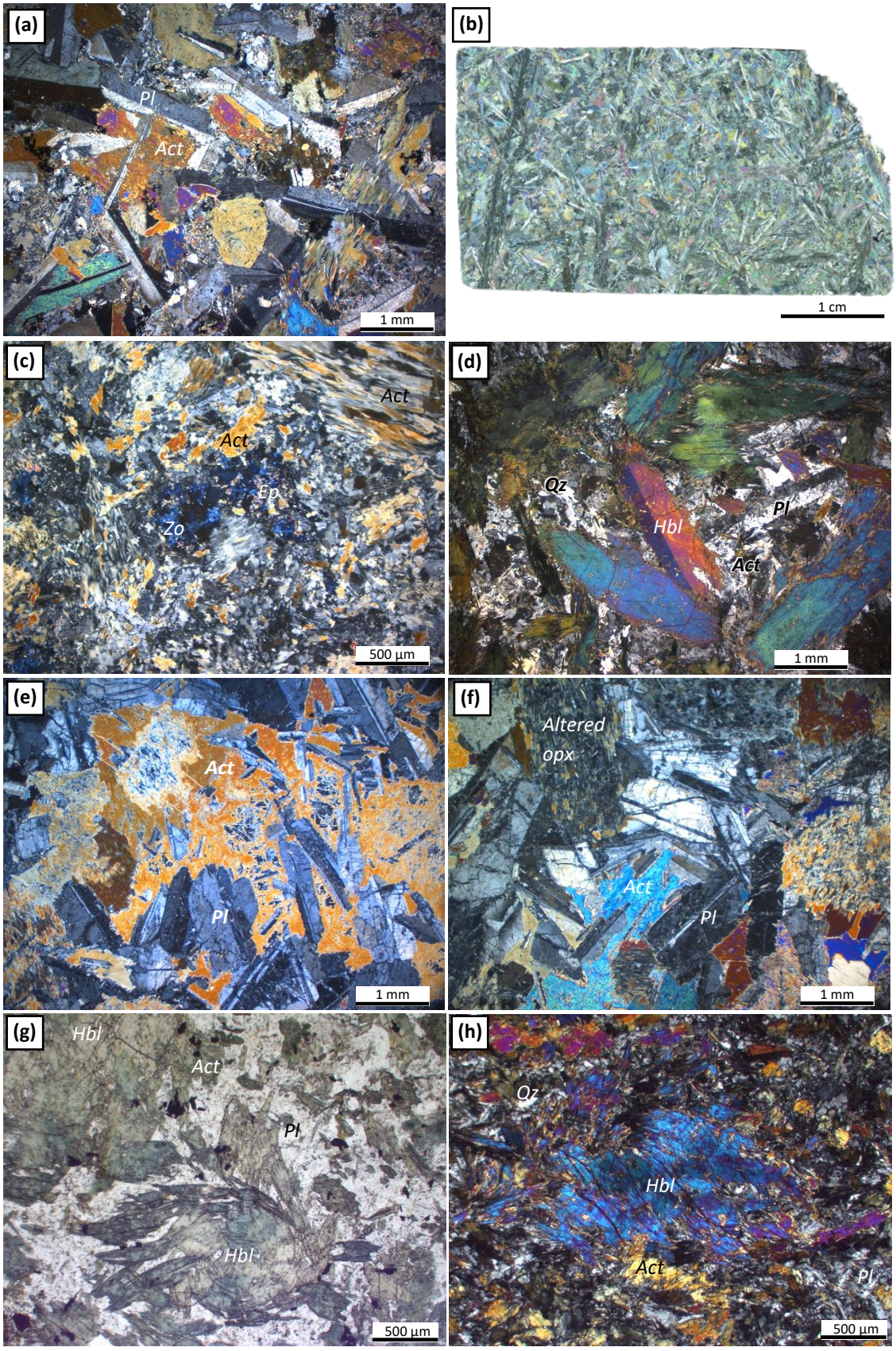

(caption on next page)

Figure 5.18 (previous page): Photomicrographs of Warriedar Suite gabbroic rocks. **(a)** XPL view of typical texture and mineralogy of equicrystalline dolerite – crystals are cross-cutting one another due to metamorphism (sample ROTH008); **(b)** XPL thin section view of feathery, interlocking crystals of plagioclase and amphibole that can mimic spinifex texture (sample ROTH019); **(c)** XPL view of a gabbro comprising moderately altered and saussuritised plagioclase, replaced by fine grained zoisite, epidote, actinolite and quartz (sample MUL011); **(d)** XPL view of porphyritic gabbro comprising simple twinned hornblende phenocrysts in a plagioclase and quartz-bearing groundmass (sample ROTH029); **(e)** XPL view of poikilitic-textured gabbro comprising large actinolite oikocrysts (after clinopyroxene) and chadacrysts of plagioclase – some portions of this unit are sub-ophitic (sample MUL007); **(f)** XPL view of cumulate plagioclase and altered orthopyroxene crystals with interstitial oikocrysts of actinolite (pseudomorphing clinopyroxene) (sample MUL007); **(g)** PPL view of the typical texture of Honeycomb Gabbro, typified by rounded, deformed amphibole porphyroblasts in a plagioclase-quartz-actinolite groundmass (sample T2); **(h)** XPL view of Honeycomb Gabbro containing a large, deformed porphyroblast of hornblende (sample ROTH006).

clinopyroxene has been pseudomorphed by secondary actinolite (~18%), with only the cores of large crystals preserved (~5%; Fig. 5.16f). Furthermore, multiple 1.5 mm-thick tremolite veinlets cross-cut the unit and signify secondary alteration. In addition to disseminated opaques (magnetite and Cr-spinel; 2%), fine grained (<0.1 mm) interstitial sulphides include chalcopyrite, pyrrhotite and pyrite.

5.6.2 Pyroxenitic rocks

Originally pyroxenitic rocks, commonly overlying ultramafic cumulate units in Warriedar Suite intrusions, are typically equicrystalline and dominated by ~80% of interlocking lath-shaped amphibole crystals ranging between 0.4 and 0.8 mm in size. In some instances, this amphibole is actinolite (pale green-dark green pleochroism), but in other units, the dominant amphibole is tremolite (colourless-light green pleochroism). In both cases, the amphiboles are pseudomorphs after pyroxene. The interlocking amphibole crystals often exhibit a relic cumulate texture (Fig. 5.17a), with interstitial phases consisting of acicular needles of actinolite and variably altered plagioclase crystals, commonly present as mottled/cloudy crystals or even sericite in more altered samples.

Pyroxenitic rocks are often porphyritic, with phenocrysts of plagioclase or amphibole occupying up to 20% of the units and giving outcrops a distinctive mottled appearance, particularly evident in the Rothsay Sill. Amphibole phenocrysts generally occur as subhedral laths 1-8 mm in length (Fig. 5.17b, c). Plagioclase phenocrysts 1-3 mm occur as anhedral crystals that have invariably been subject to saussuritisation, and now comprise a fine-grained assemblage of zoisite, sericite, actinolite ± carbonate ± epidote ± quartz (Fig. 5.17d, e, f). In some units, relict crystals of twinned plagioclase forms part of the saussurite assemblage. Intergrowths of ilmenite and magnetite are frequently present as 0.1-0.2 mm anhedral grains in the groundmass, surrounded by a leucoxene halo, derived from breakdown of ilmenite (Fig. 5.17b). Accessory apatite and sphene are common and pyroxenitic rocks in some intrusions contain sulphide mineralisation; for example, pyroxenites of the Rothsay Sill in the Rothsay area (Fig. 5.2) contain disseminated pyrite, chalcopyrite and bornite.

5.6.3 Gabbro/doleritic rocks

Warriedar Suite gabbroic rocks (and finer grained equivalents – described as dolerite) display varied modal mineralogy and a variety of textures, due to them forming the most voluminous component of all Warriedar Suite intrusions. The predominant metamorphic amphibole in Warriedar Suite gabbroic rocks is actinolite, however intrusions in the far southwest near Rothsay also contain hornblende. Disseminated needles of ilmenite (± magnetite) are invariably present, principally focussed at the margins of amphibole crystals and often possess secondary haloes of leucoxene, which in some instances, replace the oxides entirely. Gabbroic rocks can be broadly separated into three groups based on textural features: equicrystalline gabbro, porphyritic gabbro and cumulate gabbro.

- Equicrystalline gabbroic rocks typically consist of medium to coarse (0.5-8 mm), randomly oriented and interlocking euhedral crystals of amphibole and plagioclase feldspar (Fig. 5.18a), with proportions of amphibole:plagioclase varying between 72:28 and 49:51 (including plagioclase alteration products). Locally in some intrusions, most notably the Gardner Sill, elongate, feathery interlocking crystals of plagioclase and amphibole up to 30 mm in length mimic a spinifex-textured volcanic rock (Fig. 5.18b). In some units, plagioclase has been variably altered and this takes the form of either sericitisation or more commonly, saussuritisation, resulting in partial to complete replacement of plagioclase by a fine-grained assemblage of zoisite, actinolite, chlorite, quartz, epidote and carbonate (Fig. 5.18c). Such alteration is frequently localised along cleavage planes and at crystal margins, but also forms randomly oriented assemblages within crystals. Minor amounts of scattered secondary quartz are locally disseminated and associated with fractures or veinlets, occasionally accompanied by secondary biotite.
- Porphyritic gabbro exhibits very similar characteristics to the previously described porphyritic pyroxenites in that they are typified by 1-2.5 mm anhedral, altered plagioclase phenocrysts, but with increased groundmass plagioclase content (up to 34%) interspersed with actinolite crystals (Fig. 5.18d).
- Cumulate-textured gabbroic rocks are characterised by poikiloblastic textures, consisting of randomly oriented, euhedral, tabular plagioclase crystals 0.5-1 mm in length enclosed within 3-8 mm oikocrysts of actinolite (after pyroxene) (Fig. 5.18e). Less commonly, 1-10 mm subhedral and elongate crystals of actinolite are also present, representing the addition of a cumulate pyroxene phase (Fig. 5.18f). In these instances, plagioclase crystals are aligned around the margins of cumulate pyroxene (now amphibole) crystals, indicating that the order of crystallisation is cumulate plagioclase → cumulate pyroxene → interstitial pyroxene. Sub-ophitic textures are commonly preserved, with plagioclase crystals penetrating the margins of actinolite oikocrysts (Fig. 5.18e). Minor amounts of a fine-grained (<0.5 mm) groundmass occurs interstitial to

cumulate phases and oikocrysts, comprising acicular actinolite needles and plagioclase laths, the latter frequently saussuritised.

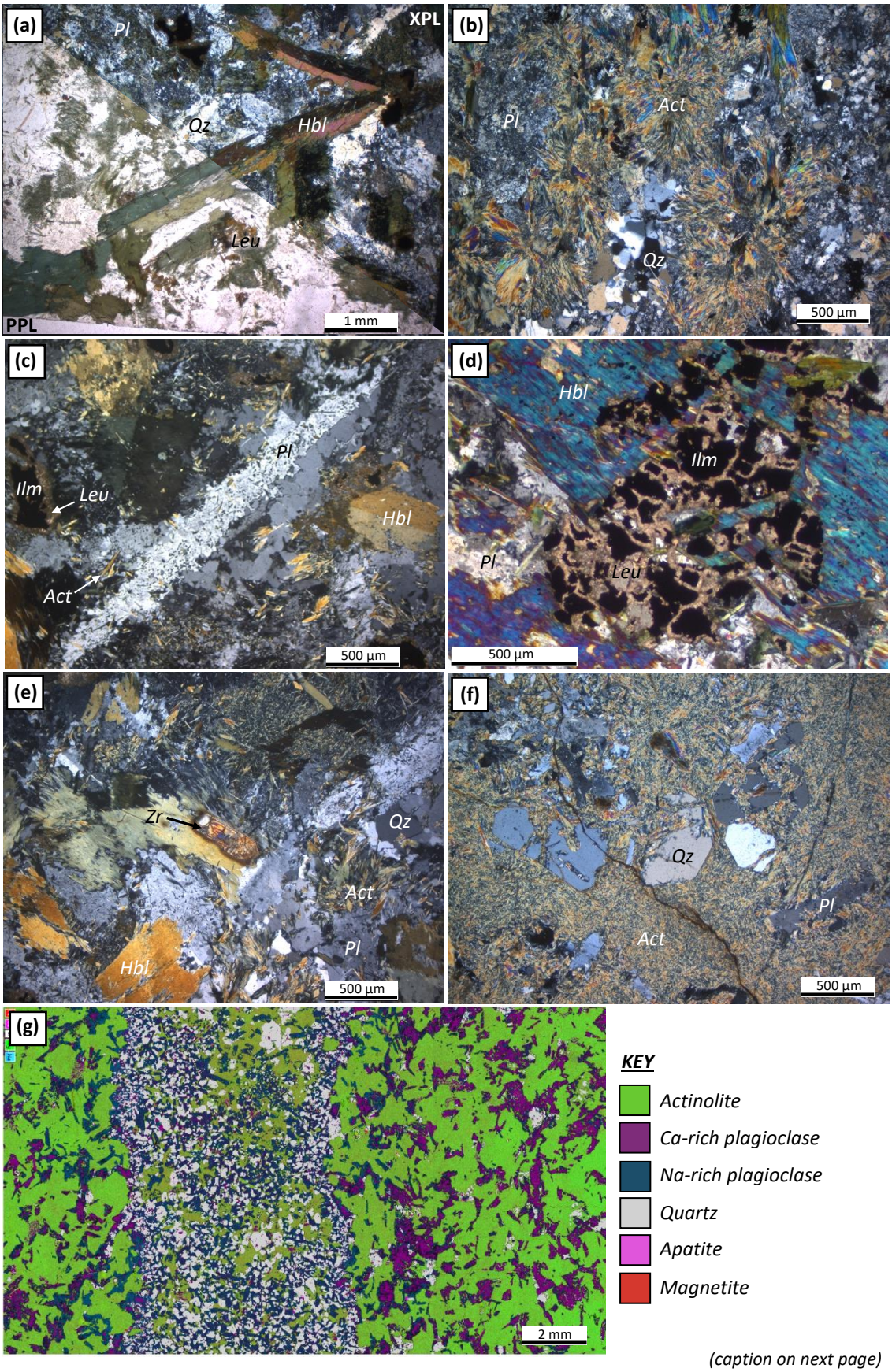

(caption on next page)

Figure 5.19 (previous page): Photomicrographs of Warriedar Suite leucogabbroic and quartz dioritic rocks. **(a)** PPL/XPL view of porphyritic quartz diorite comprising elongate phenocrysts of hornblende (after pyroxene) exhibiting simple twinning in a groundmass of quartz and mottled plagioclase (sample ROTH034); **(b)** XPL view of radiating acicular crystals of actinolite with mottled plagioclase and patches of recrystallized quartz (sample ROTH035); **(c)** XPL view of elongate granophyric-textured feldspar containing inclusions of quartz in crystallographic continuity (sample ROTH034); **(d)** XPL view of an ilmenite aggregate surrounded by a halo of fine grained leucoxene, adjacent to feldspar and hornblende (sample MUL007a); **(e)** XPL view of a large ~500 µm euhedral zircon crystal interstitial to hornblende, acicular actinolite, plagioclase and quartz (sample ROTH034); **(f)** XPL view of subhedral, embayed crystals of quartz and plagioclase within a fine-grained actinolitic groundmass (sample BAD003a); **(g)** Element map showing the texture and mineralogy of a late ~1 cm-thick quartz diorite sill (sample BAD003A).

The Honeycomb Gabbro (Section 3.4.2.2), situated at the top of the Mountain View Sill near Rothsay, exhibits a distinctive texture and mineralogy not commonly observed in other Warriedar Suite intrusions. Blocky amphibole crystals 0.8-2.5 mm in size occupy ~65% of the unit and define a porphyritic texture. Interstices between these amphibole crystals consist of fine grained (<0.5 mm) plagioclase (labradorite), quartz, acicular actinolite and ilmenite crystals. The combination of blocky amphibole phenocrysts and interstitial felsic minerals give this unit its characteristic honeycomb texture (Fig. 5.18g). Amphibole crystals invariably consist of two phases; cores consist of anhedral, fragmented grains of hornblende in crystallographic continuity, whereas the rims and intervening areas comprise actinolite (Fig. 5.18g). These relations imply the partial conversion of hornblende to actinolite during metamorphic retrogression. Further, these phenocrysts are strongly deformed, displaying undulose extinction with some crystals shaped as σ-clasts (Fig. 5.18g, h).

5.6.4 Quartz dioritic rocks

Quartz dioritic rocks are present at the tops of many Warriedar Suite sills and are typified by approximately equal proportions of plagioclase and amphibole (either hornblende or actinolite, 35-40%) and ubiquitous quartz content (~15%). In general, these horizons comprise increased feldspar content relative to the underlying intrusive units, consistent with them being the uppermost, most evolved portion of the intrusions. In several instances, these units exhibit porphyritic and harrisitic textures that consist of elongate, subhedral hornblende crystals 0.5-20 mm in length with green-brown pleochroism and simple twinning along their long axes (Fig. 5.19a). In contrast, quartz dioritic rocks of the Gardner Sill contain amphibole in the form of fibrous, acicular actinolite crystals 0.2-1 mm in length, which radiate outwards radially to define star-shaped patterns (Fig. 5.19b; Section 3.4.2.4). The surrounding groundmass is generally comprised of 0.5-4 mm plagioclase laths of andesine composition, a minority of which display granophyric textures (Fig. 5.19c) and in some intrusions, is subject to moderate sericite alteration. Quartz generally occurs as 0.2-2 mm, frequently granoblastic, anhedral aggregates of crystals in the groundmass interstitial to plagioclase, occasionally displaying a

slight undulose extinction. Oxides generally constitute 4-5 % of quartz dioritic units. The most abundant oxide, ilmenite, occurs as subhedral 0.1-1 mm grains that are typically located at the margins of amphibole crystals. Most ilmenite grains are surrounded by a halo of fine grained, granular leucoxene, an alteration product of ilmenite, and several are entirely converted to leucoxene (Fig. 5.19d). This is best exemplified by the quartz diorite from the uppermost Damperwah Sill in the Rothsay area (Section 3.4.2.5). Less frequently, magnetite also forms part of the oxide assemblage, and occurs as 0.5-3 mm fragmented grains with <0.1 mm exsolution lamellae of ilmenite. Furthermore, numerous large (up to 450 µm), euhedral zircon crystals are commonly found in these quartz dioritic rocks (Fig. 5.19e).

In one instance in the Badja area (sample BAD003a; Fig. 5.1), quartz diorite occurs as a 1 cm-thick intrusive feature within a gabbroic unit, rather than the more typical >5 m-thick evolved upper portions of intrusions. This cm-scale sill displays a porphyritic texture comprising subhedral phenocrysts of quartz (0.1-1 mm; 19%), plagioclase (0.1-1 mm; 40%) and actinolite in a fine-grained (<0.1 mm) groundmass of acicular actinolite crystals (Fig. 5.19f). The sill is quartz-rich and contains Na-rich plagioclase (albite), in contrast to predominantly Ca-rich plagioclase in the surrounding, coarser-grained host (Fig. 5.19g). Some plagioclase phenocrysts have been partially saussuritised to zoisite and chlorite and minor Fe staining is present along cleavage planes in actinolite laths. The margins of the sill are diffuse and undulating rather than sharp, indicating it is a late-stage magmatic feature (Fig. 5.19g). The fine-grained groundmass combined with ~0.5 mm skeletal ilmenite crystals indicate that this intrusion cooled rapidly and that phenocrysts likely crystallised elsewhere.

5.7 Summary of Petrographic Analysis

This chapter has presented the petrography of supracrustal rocks comprising the central YSGB. A total of 71 thin sections have been examined from lithologies throughout the belt to characterise mineral assemblages and textures.

Petrographic analysis has confirmed that all supracrustal rocks have been affected by metamorphism. In mafic extrusive and intrusive igneous rocks, metamorphic assemblages vary from actinolite-chlorite-epidote-albite to hornblende-actinolite-albite, the latter being prevalent in the southwest. This demonstrates upper greenschist metamorphic facies, which increases in grade to lower amphibolite in the southwest of the study area. This is consistent with previous regional geological studies that identified an increase in metamorphic grade towards the southwest (Watkins & Hickman, 1990). Sedimentary and volcaniclastic rocks contain quartz clasts that often exhibit granoblastic textures, consistent with metamorphic crystallisation, and contain minor amounts of actinolite.

Several units display textures and assemblages consistent with retrograde metamorphism. This is best displayed by the Honeycomb Gabbro, which contains fragmented hornblende breaking down into actinolite and chlorite. The cordierite-andalusite porphyroblast assemblage, preserved in a metasedimentary unit of the Willowbank Clastics near Rothsay, is consistent with relatively low pressure regional metamorphism, in the absence of higher pressure metamorphic minerals.

Variable amounts of alteration are displayed by rocks in the belt. In igneous rocks, plagioclase often displays a mottled appearance or is visibly subject to sericite alteration or saussuritisation. In the most extreme cases, plagioclase is completely replaced by a finer-grained saussurite alteration assemblage. In mafic intrusive rocks, ilmenite commonly possesses a leucoxene halo that in some instances entirely replaces ilmenite grains and composites. Furthermore, quartz present in many mafic-ultramafic igneous units is clearly secondary, due to its close association with quartz veinlets that crosscut units. Felsic volcaniclastic units are occasionally altered to clay. Serpentinisation of olivine bearing ultramafic rocks is ubiquitous and is occasionally accompanied by carbonate alteration.

Despite metamorphism and alteration, many primary textures are preserved in supracrustal rocks. Volcaniclastic and sedimentary rocks commonly preserve primary features including bedding, cross bedding and graded bedding. In mafic and ultramafic intrusive rocks, a variety of primary igneous textures are preserved including cumulate, porphyritic, poikilitic and ophitic textures, and extrusive igneous rocks conserve porphyritic, amygdaloidal, variolitic and spinifex textures. Additionally, primary olivine, orthopyroxene and clinopyroxene can be found in rare instances within rocks of the Warriedar Suite, however, these are much more commonly pseudomorphed by serpentine, tremolite and magnetite (olivine) and actinolite-hornblende (pyroxene). However, in samples displaying increased metamorphic grade (particularly in the far southwest), textures in metaigneous rocks gradually become more porphyroblastic or granoblastic, metasedimentary rocks develop a lepidoblastic texture and primary minerals and textures are rare.

The relatively low metamorphic grades (upper greenschist-lower amphibolite) and preservation of abundant primary igneous textures and rare primary igneous mineralogy suggests that the geochemistry of the volcanic and intrusive rocks has not been significantly modified by alteration (see Chapter 6).

CHAPTER 6

Geochemistry of supracrustal and mafic-ultramafic intrusive rocks

6.1 Introduction

The geochemistry of volcanic and intrusive rocks comprising the central Yalgoo-Singleton greenstone belt remains poorly constrained. Previous geochemical studies of supracrustal rocks in the Murchison Domain have either been undertaken on a regional scale with relatively sparse sampling (Watkins & Hickman, 1990), or have been focussed in the better studied northeastern part of the region (e.g., Wyman & Kerrich, 2012; Van Kranendonk et al., 2013). The latter is primarily due to the progression of ongoing GSWA 1:100,000 scale mapping from the northeast towards the southwest over the last decade. In recent years, the identification of so called boninite-like rocks in the Murchison Domain has led to a reinvigoration in petrogenetic geochemical work in the area (e.g., Wyman, 2019; Lowrey et al., 2020; Koutsoumbis, 2020). Despite this, rocks in the Yalgoo-Singleton belt have not been the subject of a detailed geochemical study, other than limited and localised sampling (Koutsoumbis, 2020) and so their petrogenesis and possible correlation with rocks in neighbouring greenstone belts is poorly understood.

In this chapter, whole rock major and trace element data are presented for volcanic, volcaniclastic and mafic-ultramafic intrusive rocks within the Yalgoo-Singleton greenstone belt. The lab methods used for sample preparation and analysis, in addition to standard data and an assessment of the accuracy and precision of geochemical data, are detailed in **Appendix B1.** Hydrous geochemical data including new data presented by this study and literature data, are presented in **Appendix E7**. Standard data is presented in **Appendix E8**, alongside accuracy and precision calculations. In this study, total iron is referred to as $Fe_2O_3^{(T)}$. $Fe_2O_3^{(EST)}$ and $FeO^{(EST)}$ are estimated compositions of ferric and ferrous iron respectively and are calculated using Equation 6.1. Mg-number (Mg#) is calculated using Equation 6.2 (Gill, 2011). All major element concentrations described in the text and used in classification diagrams have been recalculated to anhydrous values.

$$FeO^{(T)} = Fe_2O_3{}^{(T)} \text{ x } 0.8998$$

$$FeO^{(EST)} = FeO^{(T)} \text{ x } 0.9$$

$$Fe_2O_3{}^{(EST)} = (FeO^{(T)} - FeO^{(EST)}) \text{ x } 1.11$$

Equation 6.1

$$Mg\# = 100 \text{ x } \left(\frac{\frac{MgO}{40.3044}}{\frac{MgO}{40.3044} + \frac{FeO^{(T)}}{71.844}} \right)$$

Equation 6.2

In the following sections, the distribution of samples is first described, and the subdivision of geochemical groups used in this study is summarised. The effects of element mobility associated with secondary alteration are then assessed by plotting major and trace elements of three representative geochemical groups against the immobile element Zr. Elements that correlate well with Zr are considered to be relatively immobile and will be used to assess the petrogenesis of the rocks. Whereas, elements that display a poor correlation with Zr, which cannot otherwise be explained by petrogenetic processes or limited sampling, are considered to have been remobilised and will not be used in petrogenetic interpretations.

The major and trace element data of each geochemical group are then described and plotted against different differentiation indexes to assess the crystallisation history of the volcanic and magmatic rocks. The major and trace element data are also plotted to classify the rock types present in each group. Chondrite- and primitive mantle- normalised plots are used for rare earth elements (REE) and all trace elements, respectively, in order to assess the extent and nature of processes such as partial melting, fractional crystallisation and crustal contamination. On these multi-element diagrams, trace element anomalies occur as variable enrichments or depletions of the normalised elemental concentrations relative to adjacent elements. The nature (positive/negative) and size of these anomalies for the elements Eu, Zr, Ti and Nb are calculated using Equation 6.3, in which CN refers to chondrite-normalised concentrations and PM refers to primitive mantle-normalised concentrations. Plots of trace element ratios are used to identify differences between the geochemical groups and plotted with reference to various source compositions and fields for different tectonic settings. In the following chapter (Chapter 7), modelling is undertaken to calculate estimates of primary magma compositions and corresponding temperatures and pressures, for each of the magmatic groups studied. Furthermore, modelling of major and trace element trends is carried out to assess the roles

of fractional crystallisation and crustal contamination upon the main magmatic suites. In Chapter 7, the occurrence of boninite-like rocks within the study area is evaluated and geochemical comparisons are made between each group reported in this study and other volcanic and mafic intrusive rocks previously reported across the Murchison Domain and the wider Yilgarn Craton.

$$\frac{Eu}{Eu^*} = \frac{(Eu)_{CN}}{[(Sm)_{CN}\ X\ (Gd)_{CN}]^{0.5}}$$

$$\frac{Zr}{Zr^*} = \frac{(Zr)_{PM}}{[(Nd)_{PM}\ X\ (Sm)_{PM}]^{0.5}}$$

$$\frac{Ti}{Ti^*} = \frac{(Ti)_{PM}}{[(Sm)_{PM}\ X\ (Tb)_{PM}]^{0.5}}$$

$$\frac{Nb}{Nb^*} = \frac{(Nb)_{PM}}{[(Th)_{PM}\ X\ (La)_{PM}]^{0.5}}$$

Equation 6.3 *(where CN refers to chondrite-normalised measured values and PM- refers to primitive mantle-normalised measured values: normalising values from Sun & McDonough [1989]).*

6.2 Sampling and Stratigraphy

This chapter utilises whole rock major and trace element geochemical data from 135 samples of volcanic, volcaniclastic and mafic-ultramafic intrusive rocks from the central YSGB. This includes new data from 111 samples collected and analysed as part of this study, many of which have also been studied petrographically (Chapter 5). A table compiling details of all petrographic and geochemical samples including locations, descriptions and a checklist of the analysis undertaken on each sample is provided in **Appendix E5**. The sampling strategy followed for geochemical and petrographic samples is summarised in Section 5.1. In addition to new data, the geochemistry of a further 14 rock samples from within the study area has been obtained from an undergraduate thesis (Koutsoumbis, 2020) and geochemical data for 10 samples has been acquired from the GSWA WACHEM database.

The geochemical dataset presented in this study is considered to be representative of the exposed volcanic and intrusive stratigraphy of the YSGB, and includes samples from the Chulaar Group (n=69), Willowbank Clastics (n=6), Mougooderra Formation (Fm) (n=8) and Warriedar Suite (n=52). The geochemistry of the basement Gossan Hill Fm is beyond the scope of this study. Sample locations are displayed in Figure 6.1 and sample locations in the Rothsay area are shown in Figure 6.2. The division of geochemical groups and sources of geochemical data are summarised in Table 6.1.

Chulaar Group volcanic rocks have been divided into four subgroups (Subgroups 1-4) based on their stratigraphic position and geochemistry (Table 6.1). Detailed geological mapping in the Rothsay area

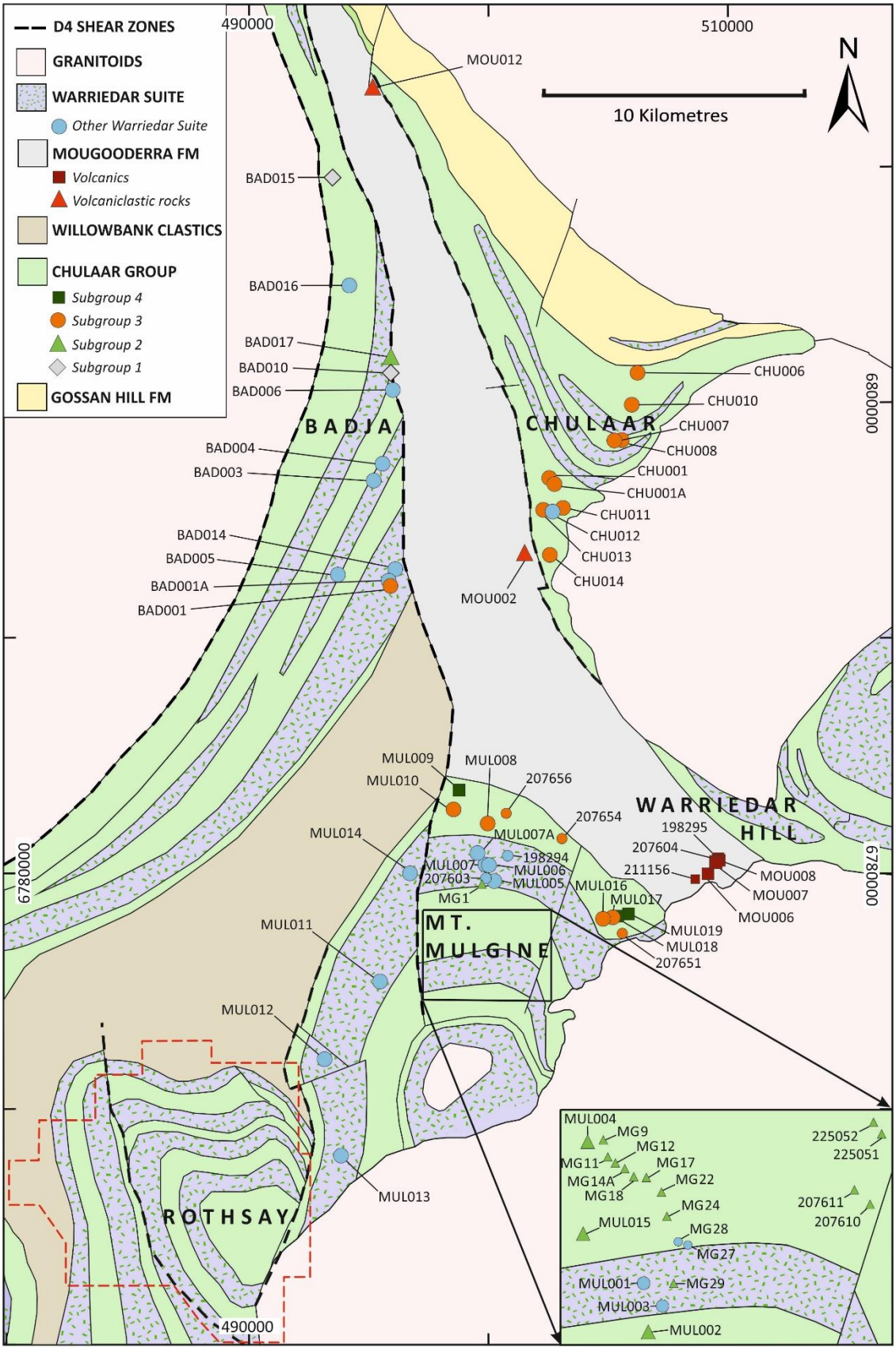

Figure 6.1: Simplified geological map of the central Yalgoo-Singleton greenstone belt showing the locations of geochemistry samples collected for this study, except for those in the far southwest (extent of Figure 6.2 outlined in dashed red). Each geochemical group is given a different symbol and labelled by sample number. Geology modified after Baxter & Lipple (1985), Zibra et al. (2016), Zibra et al. (2017a) and Ivanic (2018). Grid provided in the GDA94/MGA Zone 50 co-ordinate system.

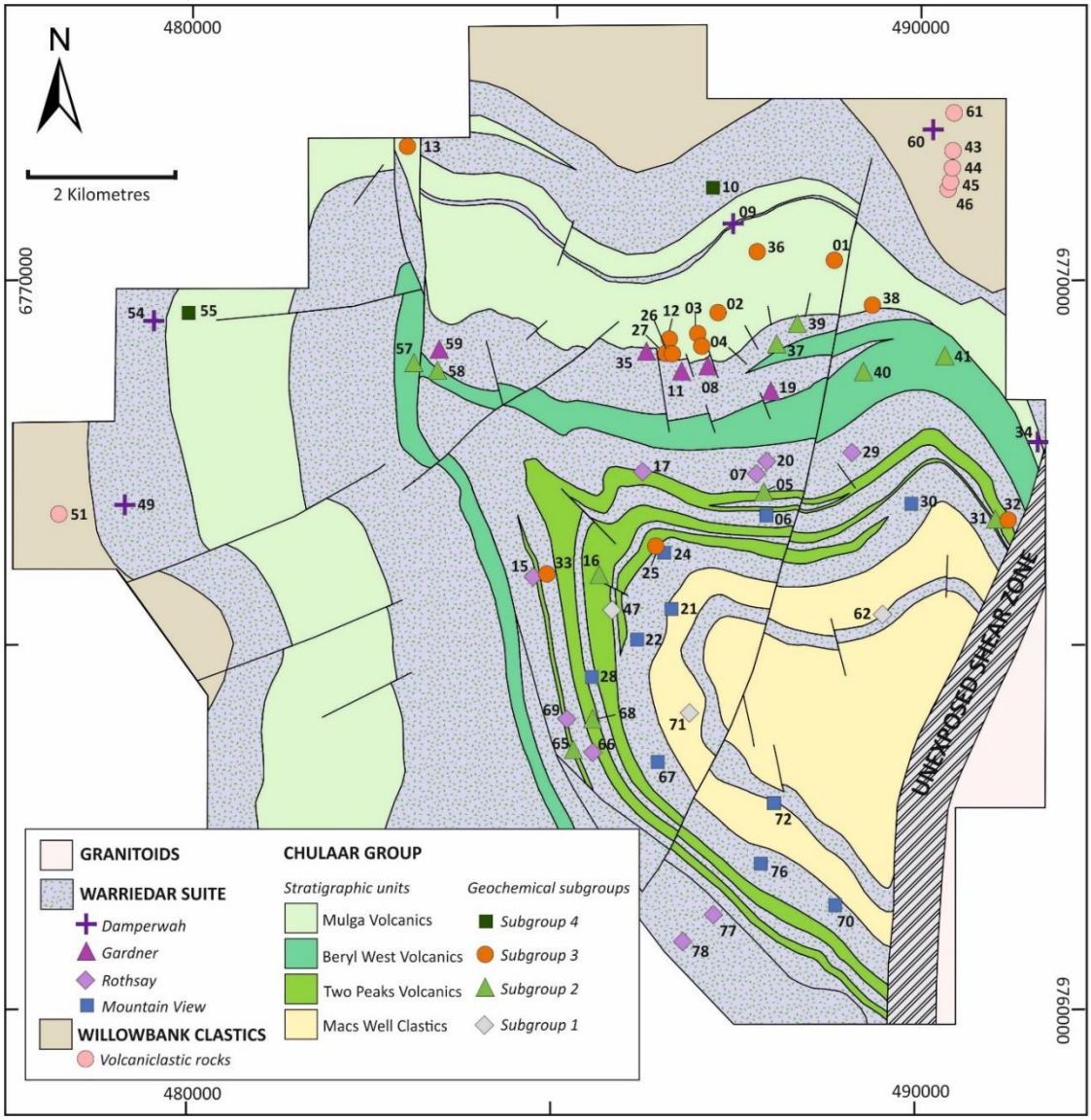

Figure 6.2: Simplified geological map of the Rothsay area in the southwest of the study area, showing the locations of geochemistry samples collected for this study. Each geochemical group is given a different symbol and labelled by sample number – the prefix ROTH0 is omitted for all samples. Grid provided in the GDA94/MGA Zone 50 co-ordinate system.

has defined four separate stratigraphic units within the Chulaar Group based on field relations and lithological associations: the Macs Well Clastics, Two Peaks Volcanics, Beryl West Volcanics and Mulga Volcanics (Section 3.4.1; Fig. 6.2). Volcanic rocks in the Chulaar Group comprise a ~2 km-thick conformable succession that contains only minor (1-10 m-thick) interflow BIF and volcaniclastic units (Fig. 3.9) and is therefore considered to represent an ongoing episode of volcanism. The four geochemical subgroups distinguished in this chapter do not correspond precisely with mapped units, and instead represent successive stratigraphic levels that are not readily differentiated in the field. The stratigraphic position of each of the Chulaar Group subgroups in relation to the stratigraphy at Rothsay is displayed on a simplified geological log in Figure 6.3.

Chulaar Subgroup 1 consist of porphyritic volcanic rocks (n=4) that represent the lowermost volcanic rocks in the Chulaar Group and cross the boundary between the upper Macs Well Clastics and the overlying Two Peaks Volcanics where they are defined in the Rothsay area (Fig 6.2). Elsewhere in the

Magmatic Suite		This study	WACHEM (WACHEM, 2020)	Koutsoumbis (2020)	Total no. of samples
CHULAAR GROUP	Subgroup 1	4	-	-	4
	Subgroup 2	16	2	12	30
	Subgroup 3	27	3	-	30
	Subgroup 4	5	-	-	5
MOUGOODERRA FORMATION	Volcanics	3	3	-	6
	Volcaniclastics	2	-	-	2
WILLOWBANK CLASTICS	Volcaniclastics	6	-	-	6
WARRIEDAR SUITE		48	2	2	52
All magmatic suites		*111*	*10*	*14*	*135*

Table 6.1: Table outlining the sources of geochemical data used in this study and the division of samples into geochemical groups described in this chapter.

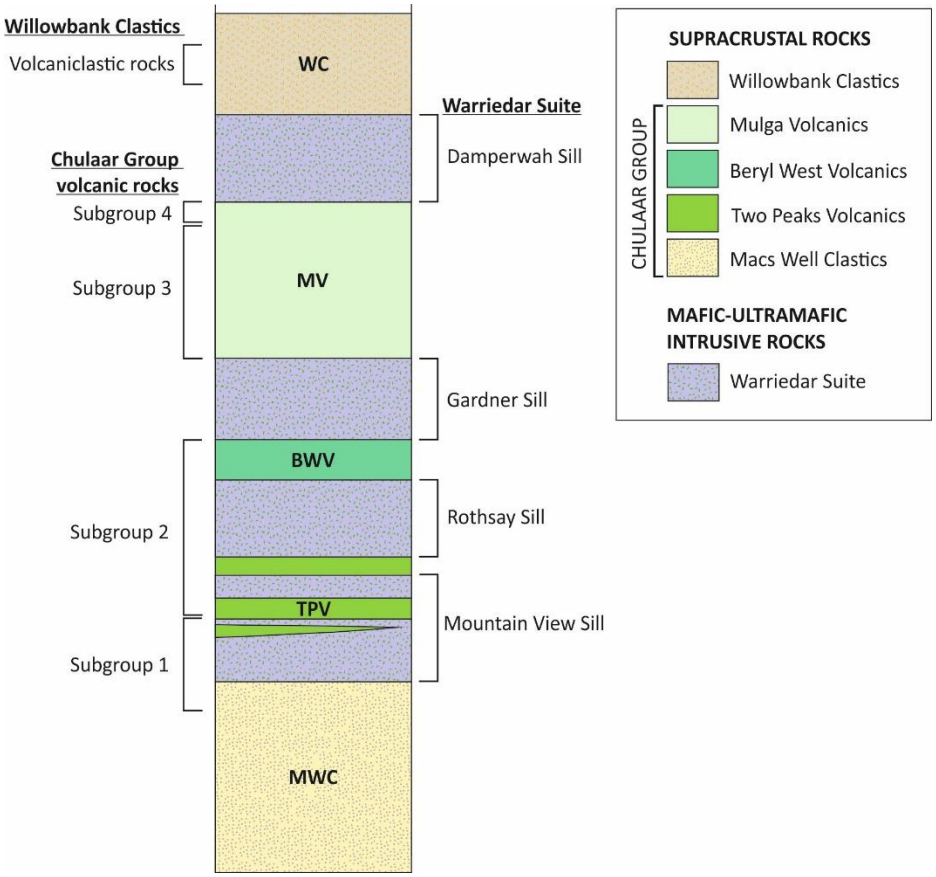

Figure 6.3: Simplified stratigraphic column of the stratigraphy in the Rothsay area (see Chapter 3), indicating the stratigraphic location of the four geochemical subgroups of Chulaar Group volcanic rocks, in addition to volcaniclastic rocks of the Willowbank Clastics, and the mapped sills of the Warriedar Suite referred to in this chapter.

belt, where stratigraphic units are not defined, Chulaar Subgroup 1 samples are located at the base of the Chulaar Group (Fig. 6.1). Chulaar Subgroup 1 are invariably porphyritic volcanic rocks with plagioclase phenocrysts and occasional amphibole phenocrysts, as described in Section 5.3.2. Chulaar Subgroup 2 rocks (n=30) consists of aphyric and minor spinifex-textured volcanic rocks from the Two Peaks Volcanics and the Beryl West Volcanics in the Rothsay area, and consistently overlie Subgroup 1 rocks (Fig. 6.3). Chulaar Subgroup 2 volcanics includes twelve samples reported by Koutsoumbis (2020) and two samples from the WACHEM database. Chulaar Subgroup 2 rocks are typically aphyric, although several samples exhibit either acicular or platy pyroxene spinifex textures (Section 5.3.5).

Chulaar Subgroup 3 rocks (n=30) correspond primarily to aphyric, acicular pyroxene spinifex-textured and variolitic volcanic rocks in the lower and middle portions of the Mulga Volcanics in the Rothsay area and elsewhere, occur stratigraphically above Chulaar Subgroup 2 rocks (Fig. 6.1). Three exceptions occur in the Rothsay area, where samples with a comparable geochemistry to Chulaar Subgroup 3 rocks occur at a stratigraphically lower level, principally in the upper portion of the Two Peaks Volcanics amongst Subgroup 2 rocks (Fig. 6.2). Subgroup 3 includes three samples from the WACHEM database. Chulaar Subgroup 4 consists of variably spinifex-textured volcanic rocks (n=5) that represent the uppermost volcanic rocks in the Chulaar Group and occur in the uppermost parts of the Mulga Volcanics in the Rothsay area and elsewhere, at the top of the Chulaar Group (Fig. 6.1). One sample from Chulaar Subgroup 4 (sample MUL009) exhibits a random 'platy acicular' spinifex texture that has not been identified elsewhere (Section 5.3.5.6).

The Mougooderra Fm overlies the Chulaar Group and is dominated by metasedimentary rocks, in addition to felsic volcaniclastic rocks and minor volcanic rocks (Watkins & Hickman, 1990). Geochemical samples collected from the Mougooderra Fm consist of six volcanic samples (herein Mougooderra Fm volcanics) collected from Warriedar Hill in the southeast of the study area, and two felsic volcaniclastic rock samples (herein Mougooderra Fm volcaniclastics) collected from the Chulaar area (Fig. 6.1). The petrography of these samples is described in Section 5.5. Three Mougooderra Fm volcanic samples were collected as part of this study and geochemical data for a further three samples are taken from the GSWA WACHEM database.

The Willowbank Clastics are an informal assemblage of metasedimentary and volcaniclastic rocks that overlies Chulaar Group rocks in the southwest of the study area (Section 3.4.1.5). Six felsic volcaniclastic rocks have been collected from the Willowbank Clastics for geochemical analysis (herein Willowbank volcaniclastics; Table 6.1). Owing to a similar stratigraphic position (i.e. overlying Chulaar Group rocks; Section 4.3), comparable lithologies and the similar petrographic features of felsic volcaniclastic units (Section 5.4), the Willowbank Clastics may be linked to rocks of the Mougooderra

Fm. Consequently, the Willowbank Clastics are maintained as a separate, informal unit in this thesis, to test whether this is the case.

The geochemistry of Warriedar Suite mafic-ultramafic layered intrusions is represented by 52 samples taken from intrusions across the study area (Fig. 6.1). This includes two samples reported by Koutsoumbis (2020) and two samples from the WACHEM database (Table 6.1). More dense sampling of Warriedar Suite intrusions has been undertaken in the Rothsay area, where a minimum of 5 samples has been taken from four major intrusions identified during lithostratigraphic mapping (Section 3.4.2). This includes samples from the Damperwah Sill (n=5), Gardner Sill (n=5), Rothsay Sill (n=9) and Mountain View Sill (n=9). For the purposes of this study, the Honeycomb Gabbro has been assigned to the Mountain View Sill. These four Warriedar Suite sills are plotted separately on geochemical plots and diagrams to distinguish and compare the geochemistry of individual Warriedar Suite intrusions. In these diagrams, samples from other Warriedar Suite intrusions in the Mt Mulgine, Badja and Chulaar areas are referred to collectively as 'Other Warriedar Suite' samples.

6.3 Element Mobility

Rocks comprising the Yalgoo-Singleton greenstone belt have been subject to variable amounts of secondary (hydrothermal) alteration. Petrographic analysis has demonstrated that supracrustal rocks in the belt have been subject to upper greenschist-lower amphibolite grade metamorphism (see Chapter 5), and some samples have also been subject to hydrothermal fluid flow due to proximity to major structures. However, the preservation of primary igneous textures and mineralogy in many samples suggests that the rocks have not been significantly modified by alteration. Thus, before geochemical data can be used for petrogenetic work, the effect of element mobility resulting from secondary alteration needs to be evaluated.

Sub-solidus element mobility is influenced by diagenetic processes, metamorphism, hydrothermal processes, and weathering, all of which can alter the geochemistry of a rock. Without accounting for element mobility resulting from these processes, incorrect geochemical interpretations may be made. Various elements frequently become mobile during sub-solidus alteration, particularly the Large-Ion Lithophile Elements (LILE; e.g., K, Rb, Ba). The mobility of an element is controlled primarily by its ionic potential (e.g., Pearce, 1996). Elements that form ions with a low ionic potential (<0.03 pm^{-1}) are easily removed in solution as hydrated cations, whereas ions with a high ionic potential (>0.10 pm^{-1}) readily enter solutions as hydrated oxyanions. Elements that form ions with an intermediate ionic potential (0.03-0.1 pm^{-1}) are typically immobile during secondary alteration (Pearce, 1996). Such elements include the REE (excluding La and Eu), Ti, Zr, Hf, Nb, Ta, Cr, Th, Sc and Ga (e.g., Pearce, 1996; Hastie et

al., 2007). These elements are considered to remain immobile to lower amphibolite metamorphic facies (Pearce, 1996). However, other studies have suggested that these so-called 'immobile' elements can be remobilised, particularly in the presence of carbonate-, hydrogen sulphide- or halogen-bearing fluids (e.g., Gieré, 1993; Fadda et al., 2012; Williams-Jones et al., 2012).

As rocks of this study have variable LOI values of 0-13 wt.% and show petrographic evidence of greenschist-amphibolite facies metamorphism and alteration (Chapter 5), an assessment of element mobility is crucial. To do so, the method established by Cann (1970) has been employed. The concentrations of each element from a cogenetic suite of rocks are plotted against Zr, which is incompatible during a wide range of magmatic fractionation and considered immobile at low metamorphic grade (Pearce, 1996). For an incompatible element in a cogenetic suite of igneous rocks, a linear trend would be expected with a good correlation between the two elements. If the element has been affected by secondary remobilisation, then a less well-defined trend with significant scatter would be displayed. However, a weak correlation between Zr and another incompatible and (typically) immobile element may not automatically signify secondary remobilisation and may instead be explained by petrogenetic processes such as crustal contamination or partial melting.

In order to quantify the correlation of an element with Zr, the square of the correlation coefficient (R^2) is calculated (Equation 6.4). R^2 is a measure of the strength of correlation between an element and Zr, thus gives an indication of the mobility of the element. An R^2 value approaching 1 demonstrates a very good correlation, whereas an R^2 value approaching 0 denotes a poor correlation. For this study, $R^2 > 0.6$ will be considered a good correlation with Zr, $0.3 \geq R^2 \geq 0.6$ will be considered a moderate correlation, and $R^2 < 0.3$ will be considered a poor correlation. The elements that display a poor correlation, with considerable scatter that cannot be explained by petrogenetic processes, will be regarded as remobilised during secondary alteration.

$$\boldsymbol{R^2} = \left(\frac{\boldsymbol{n}(\sum \boldsymbol{xy}) - (\sum \boldsymbol{x})(\sum \boldsymbol{y})}{\sqrt{[\boldsymbol{n}\sum \boldsymbol{x^2} - (\sum \boldsymbol{x})^2][\boldsymbol{n}\sum \boldsymbol{y^2} - (\sum \boldsymbol{y})^2]}} \right)^{\boldsymbol{2}}$$

Equation 6.4

All the rocks analysed in this study are part of a single supracrustal sequence and have been subject to the same degree of metamorphism. For this reason, the subgroups with the largest number of cogenetic samples are the best to use in order to assess element mobility. Accordingly, the Chulaar Group will be used for mafic-intermediate extrusive and intrusive lithologies, specifically Subgroup 2 *(n=16)* and Subgroup 3 *(n=27)*, and the Willowbank Clastics *(n=6)* will be used to assess element

mobility in the felsic volcaniclastic units. Note that only the samples analysed in this study will be used to assess element mobility.

6.3.1 Chulaar Group Volcanic Rocks

Volcanic rocks of the Chulaar Group have LOI values ranging from -0.22 to 4.51 wt.%, with most samples having values of < 1.7 wt.%. These values are typical for mafic-ultramafic volcanic and intrusive rocks in the area. The highest LOI value (4.51 wt.%) corresponds to a carbonate-altered cumulate olivine-bearing flow (ROTH026). Two further samples with elevated LOI values of 3.64 wt.% (BAD015) and 3.03 wt.% (BAD017) are of units that were sampled in drillcore proximal to shear zones, thus were likely subjected to a significant degree of hydrothermal alteration. The effect of alteration appears to be most significant in ultramafic units, however, the variation in LOI values in general indicates that secondary remobilisation of elements needs to be considered.

	Chulaar Subgroup 2	Chulaar Subgroup 3	Willowbank Volcaniclastics
SiO_2	0.01	0.13	0.80
TiO_2	0.76	0.60	0.38
Al_2O_3	0.24	0.14	0.86
Fe_2O_3 (T)	0.07	0.00	0.28
MnO	0.04	0.00	0.02
MgO	0.15	0.54	0.06
CaO	0.19	0.03	0.29
Na_2O	0.00	0.02	0.07
K_2O	0.18	0.06	0.00
P_2O_5	0.49	0.38	0.34
Cr_2O_3	0.19	0.42	0.78
Sc	0.04	0.00	0.01
V	0.43	0.16	0.28
Co	0.11	0.06	0.01
Ni	0.20	0.01	0.17
Cu	0.39	0.05	0.16
Zn	0.38	0.01	0.13
Ga	0.13	0.31	0.26
Rb	0.15	0.05	0.00
Sr	0.04	0.07	0.02
Y	0.69	0.36	0.33
Nb	0.55	0.46	0.92

	Chulaar Subgroup 2	Chulaar Subgroup 3	Willowbank Volcaniclastics
Cs	0.03	0.01	0.00
Ba	0.04	0.12	0.14
La	0.69	0.45	0.01
Ce	0.77	0.61	0.01
Pr	0.67	0.62	0.01
Nd	0.64	0.50	0.03
Sm	0.72	0.65	0.23
Eu	0.70	0.43	0.47
Gd	0.90	0.35	0.49
Tb	0.88	0.51	0.52
Dy	0.76	0.57	0.48
Ho	0.63	0.63	0.39
Er	0.67	0.54	0.39
Tm	0.73	0.40	0.63
Yb	0.55	0.48	0.63
Lu	0.63	0.52	0.56
Hf	0.86	0.83	0.97
Ta	0.58	0.65	0.96
Pb	0.29	0.03	0.04
Th	0.03	0.09	0.23
U	0.84	0.28	0.84

Table 6.2: Coefficient of determination (R^2) values for all major and trace elements versus Zr in Chulaar Subgroup 2 samples, Chulaar Subgroup 3 samples and Willowbank volcaniclastics samples. Elements with R^2 values > 0.6 (green) are considered to show a good correlation with Zr, those with $0.3 \geq R^2 \geq 0.6$ (yellow) show a moderate correlation with Zr and those with $R^2 < 0.3$ show a poor correlation with Zr.

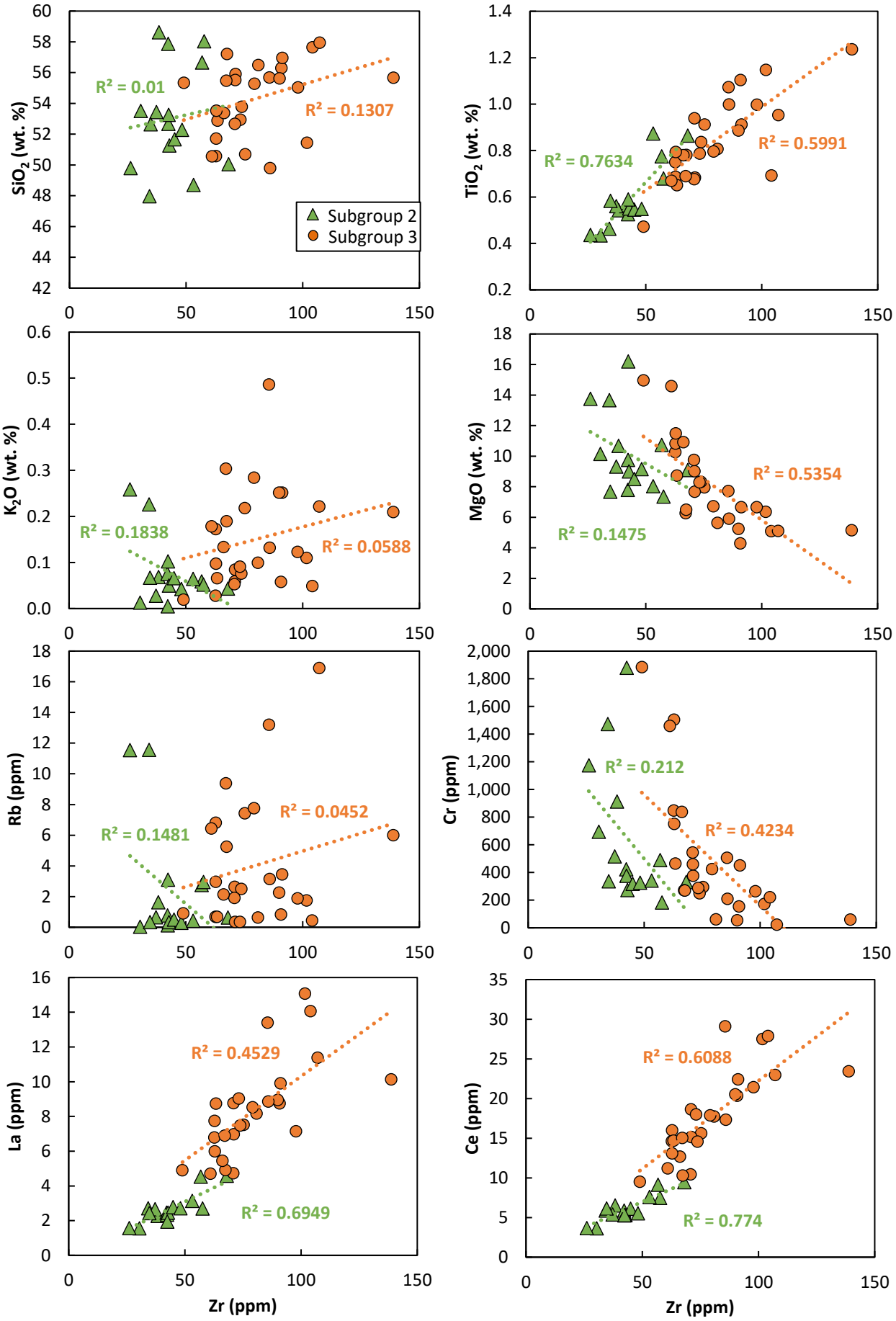

Figure 6.4: Bivariate diagrams of selected elements versus Zr for Chulaar Group volcanic rocks (Subgroup 2 and Subgroup 3).

A selection of major and trace element vs. Zr plots for the Chulaar Group are displayed in Figure 6.4, and correlations are quantified by R^2 values in Table 6.2. For Subgroup 2 rocks, good correlations against Zr are displayed by TiO_2, Y, Hf, U and all the REE (except Yb). Elements showing moderate correlation with Zr include P_2O_5, Cu, Zn, Nb, Ta and Yb. Poor correlations against Zr are shown by remaining elements, including Sc, Rb, Sr, Ba, Pb and Th. For Subgroup 3 rocks, elements that show good correlations with Zr include TiO_2, the Light Rare Earth Elements (LREE) (excluding La and Nd), Ho, Hf and Ta. Moderate correlations are present between Zr and P_2O_5, Cr, Ga, Y, Nb and the remaining REE, including La. Poor correlations with Zr are shown by Rb, Sr, Cs, Ba, Pb and U, in addition to the base metals (Co, Ni, Cu, Zn).

The correlations described above show that the High Field Strength Elements (HFSE) such as Nb, Ta, Hf and Y and the REE (except La) have not been significantly mobilised in Chulaar Group volcanic rocks. La displays a slightly weaker correlation and more scatter compared to other REE (Fig. 6.4), consistent with minor secondary remobilisation. Sporadic La depletion has been noted by others working in the Murchison Domain (e.g., Watkins & Hickman, 1990; Wyman & Kerrich, 2012) and has been attributed to an alteration effect in mafic rocks in the region. The good correlation of Ce and other LREE indicates that the rest of the REE in these samples were relatively immobile. In particular, the apparent immobility of Ce in Chulaar Group volcanic rocks is notable, as previous workers in the region have documented increased mobility of Ce that is attributed to hydrothermal alteration by oxygenated fluids (Kerrich et al., 2013). The incompatible LILE (Rb, Sr, Cs, Ba, K_2O) have been remobilised and will not be used to assess the petrogenesis of these rocks. Interestingly, the strength of correlations is not consistent across the two different subgroups, despite them containing very similar lithologies and belonging to the same volcanic group. This is likely due to the smaller sample size for Subgroup 2 and the fact that rocks of Subgroup 3 have a wider range of compositions compared to Subgroup 2.

6.3.2 Willowbank Clastics Volcaniclastic Rocks

Volcaniclastic rocks of the Willowbank Clastics have very variable LOI values that range from 2.1 to 7.0 wt.%, with an anomalous value of 10.7 wt.% for sample ROTH043. In general, these values are significantly higher than LOI values for surrounding mafic-ultramafic units and are consistent with the extensive clay alteration identified in several volcaniclastic samples. For this reason, there is a strong probability of secondary remobilisation of elements that needs to be assessed.

The volcaniclastic rocks of the Willowbank Clastics have similar geochemical features that suggest the samples are cogenetic and represent the products of a single fractionating magmatic suite. This can allow an assessment of element mobility in felsic volcaniclastic rocks. A subset of element

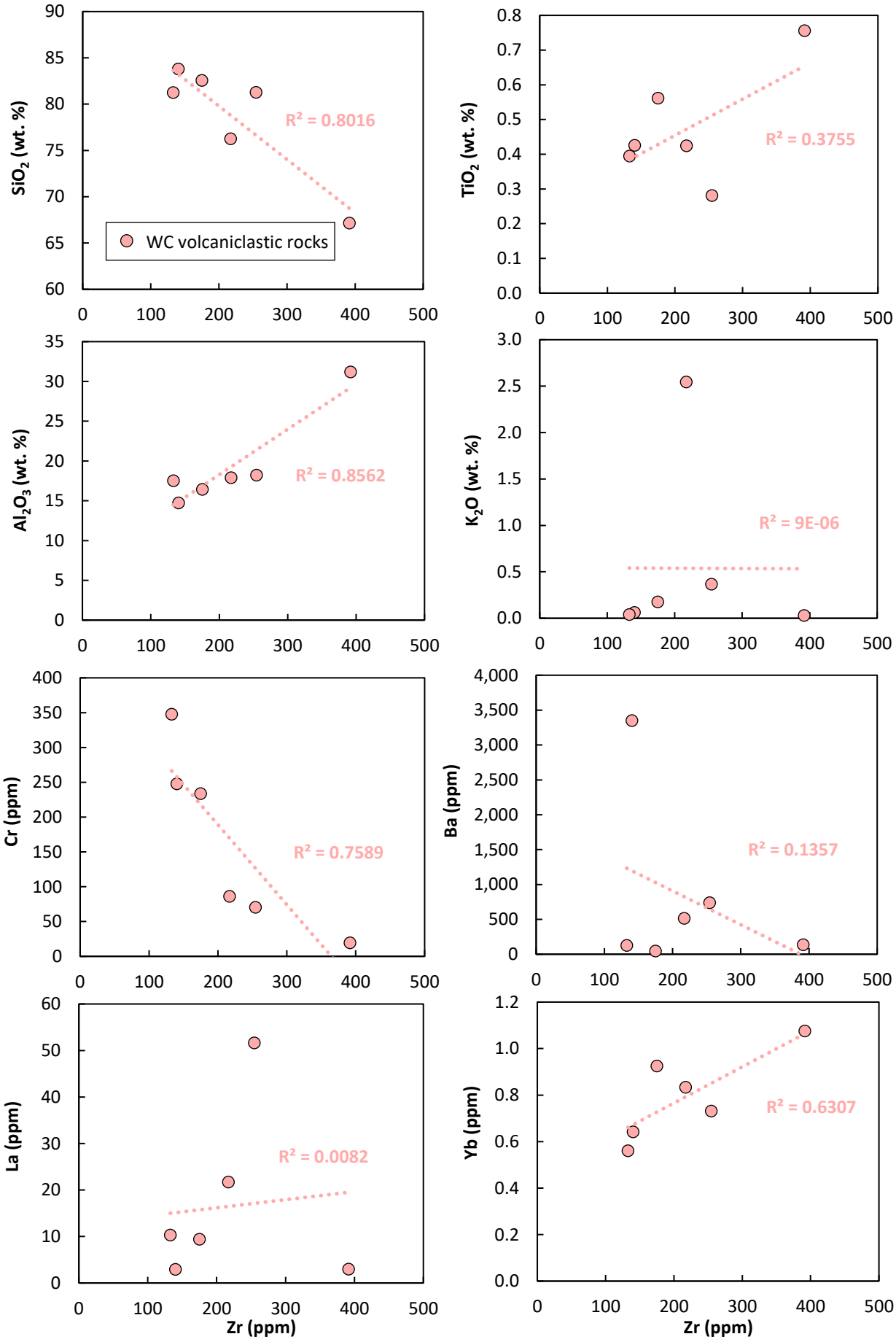

Figure 6.5: Bivariate diagrams of selected elements versus Zr for Willowbank Clastics volcaniclastic rocks.

concentrations vs. Zr plots are displayed in Figure 6.5 and correlations are quantified in Table 6.2. Willowbank Clastics volcaniclastic rocks show good correlations between Zr and Cr, Nb, Ta, Hf, U and the Heavy Rare Earth Elements (HREE), particularly Tm and Yb. Good correlations are also present between Zr and SiO_2 and Al_2O_3 (Fig. 6.5). Moderate correlations are present between Zr and TiO_2, P_2O_5, Mn, Y and the Middle Rare Earth Elements (MREE; Eu, Gd, Tb, Dy, Ho, Er). Poor correlations are present between Zr and the remaining elements, most notably the LREE and Th in addition to elements that are considered to be mobile under low metamorphic-grade conditions (e.g., Ba, Sr, Rb and K_2O).

The correlations outlined above indicate that whilst many of the incompatible trace elements appear to have remained immobile, the LREE (especially La) may have been affected by secondary remobilisation. This has been noted in other rocks in the Murchison Domain that have been subject to increased amounts of secondary alteration (e.g., Watkins & Hickman, 1990; Wyman & Kerrich, 2012). An alternative explanation is that heavy mineral layers within the volcaniclastic units may be affecting the correlation of Zr with the REE. Whereas HREE would be hosted by zircon in heavy mineral layers, and thus correlate with Zr, the LREE would more likely be hosted by other minerals such as monazite and allanite and would not correlate so well with Zr. As LREE mobilisation cannot be ruled out, care will be taken when interpreting REE data from these lithologies. Elements such as Ba, Sr, Rb, Cs, Pb and K_2O are considered mobile in these rocks and will not be used during petrogenetic analysis. Furthermore, whilst a good correlation is identified between SiO_2 and Zr ($R^2 = 0.80$), the correlation is negative as opposed to the anticipated positive correlation for a fractionating cogenetic sequence. This may suggest that some of the samples have been silicified because of hydrothermal fluid flow, or alternatively, zircon is fractionating as the magma evolves. Such interpretations are tentative considering the volcaniclastic nature of these samples and the relatively small sample size (n=6).

6.4 Geochemical Results

6.4.1 Chulaar Group

In this section, the geochemistry of the four geochemical subgroups of volcanic rocks comprising the Chulaar Group are described. Notably, Subgroup 2 Chulaar volcanics includes twelve samples reported by Koutsoumbis (2020) and two samples from the WACHEM database and Subgroup 3 Chulaar volcanics includes three samples from the WACHEM database. These published geochemical data are incorporated into the descriptions and ranges provided in this section and are plotted on diagrams using smaller symbols than the new data reported by this study.

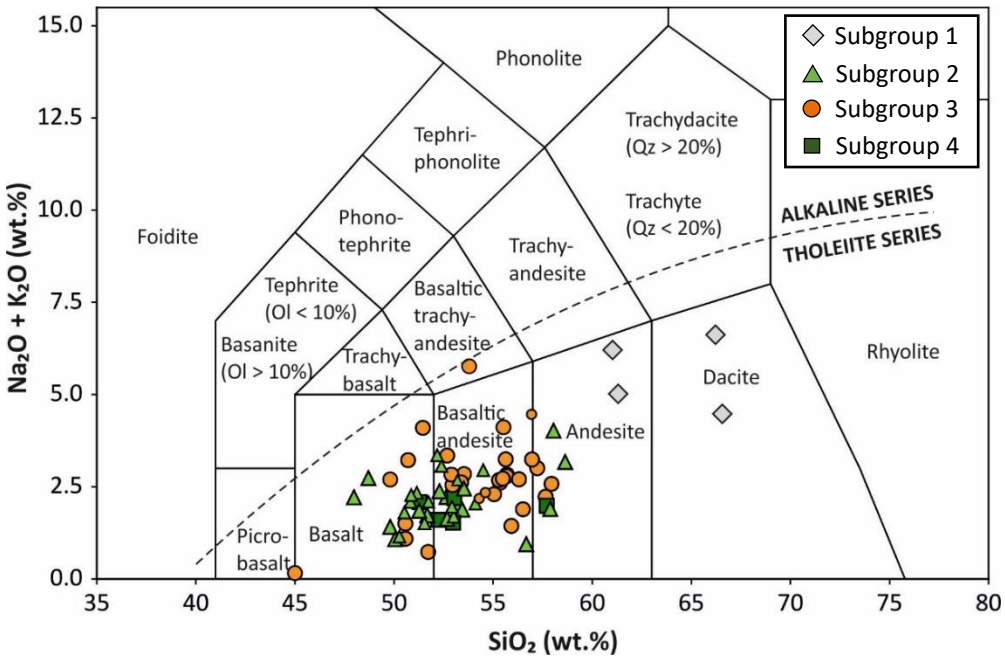

Figure 6.6: Total Alkali versus Silica (TAS) classification diagram for Chulaar Group volcanic samples. Field boundaries as defined by Le Maitre et al. (1989).

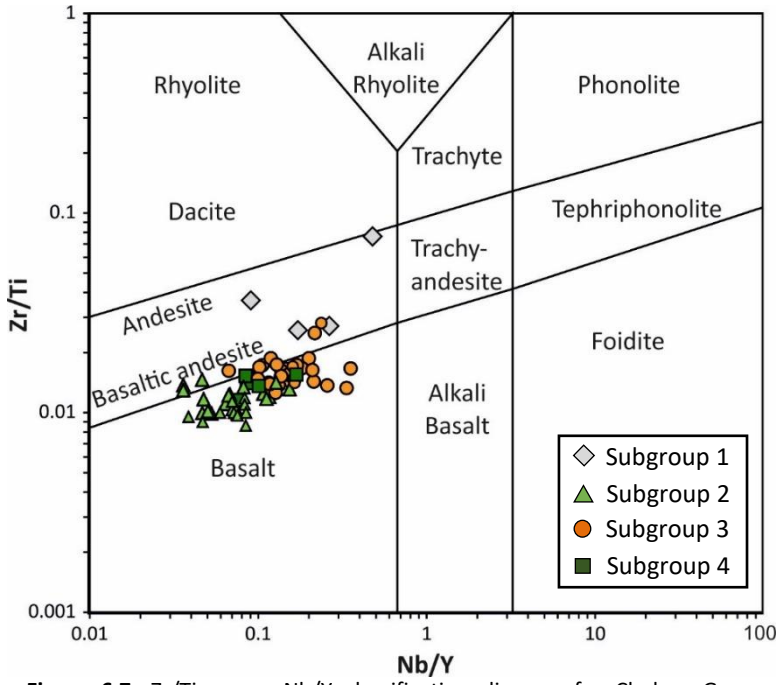

Figure 6.7: Zr/Ti versus Nb/Y classification diagram for Chulaar Group volcanic samples. Field boundaries as defined by Pearce (1996).

6.4.1.1 Classification

On the TAS diagram (Fig. 6.6), the Subgroup 1 Chulaar volcanics plot as andesites and dacites. The Subgroup 2 volcanic rocks plot as two clusters; most of the samples classify as basalts and basaltic andesites, and a subset of four samples plot as more evolved basaltic andesites and andesites. Subgroup 3 samples plot as a continuous trend largely in the tholeiitic basalt and basaltic andesite fields and show significant scatter. A further four Subgroup 3 samples plot as andesites, one sample

plots as a basaltic trachy-andesite and a cumulate-olivine bearing volcanic sample plots at the boundary between basalt and picro-basalt. Subgroup 4 Chulaar volcanics form a tight cluster that plots along the boundary between tholeiitic basalt and basaltic andesite fields (Fig. 6.6).

The poor correlation of K_2O, Na_2O and SiO_2 against Zr and the scatter in Figure 6.6 suggest that these elements may have been remobilised. Instead of the TAS diagram, the use of the Zr/Ti vs. Nb/Y

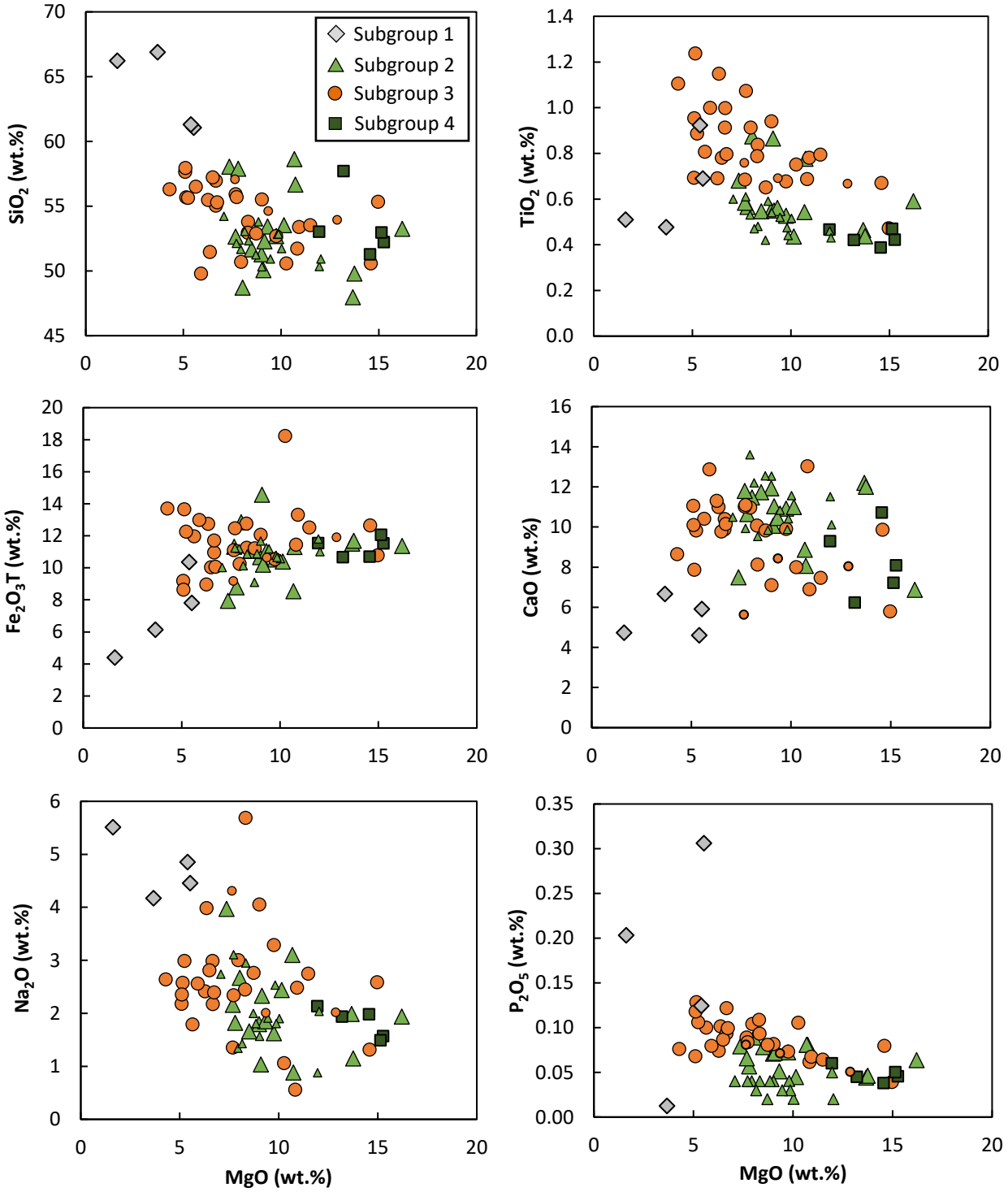

Figure 6.8: Bivariate diagrams of selected major elements versus MgO for Chulaar Group volcanic samples.

classification of Pearce (1996) may be more suitable for these rocks. In this diagram (Fig. 6.7), two Subgroup 1 volcanics are classified as basaltic andesite, one plots as andesite and one straddles the boundary between andesite and dacite. Subgroup 2 samples are classified primarily as basalt with three samples plotting in the basaltic andesite field. The Subgroup 3 volcanic samples are more tightly constrained compared to the TAS classification, mostly plotting as basalt with six samples in the basaltic andesite field. Subgroup 4 volcanics form a tight cluster in the basalt field, with one sample plotting on the boundary with basaltic andesite.

6.4.1.2 Major Elements

The Subgroup 1 volcanics range in MgO content between 1.6-5.5 wt.% and $Fe_2O_3^{(T)}$ content between 4.4-10.4 wt.%, corresponding to Mg# values between 42.1-58.3. SiO_2 and TiO_2 of Subgroup 1 volcanics ranges between 61.1-66.9 and 0.5-0.9 wt.% respectively and total alkali content ($Na_2O + K_2O$) varies between 4.4-6.6 wt.%. The Subgroup 2 volcanics exhibit a range in MgO content of 7.0-16.2 wt.% and $Fe_2O_3^{(T)}$ content of 7.9-14.6 wt.%, corresponding to Mg# values between 55.3-73.8 (average 63.4). The SiO_2 and TiO_2 content of Subgroup 2 volcanics ranges between 48.0-58.6 and 0.4-0.9 wt.% respectively and total alkali content ($Na_2O + K_2O$) varies between 0.9-4.0 wt.%. Subgroup 3 volcanics include a cumulate olivine-bearing volcanic sample with very high MgO (20 wt.%) and Mg# (79.9) and low SiO_2 (43.8 wt.%), which is excluded from bivariate diagrams to better display trends for the subgroup. The rest of the Subgroup 3 volcanics exhibit a range in MgO content of 4.3-15.0 wt.% and $Fe_2O_3^{(T)}$ content of 8.6-18.2 wt.%, corresponding to Mg# values between 38.2-73.3 (average 57.1). The SiO_2 and TiO_2 content of Subgroup 3 volcanics ranges between 49.8-58.0 and 0.5-1.2 wt.% respectively and total alkali content ($Na_2O + K_2O$) varies between 0.7-5.8 wt.%. Subgroup 4 volcanics range in MgO content between 12.0-15.3 wt.% and $Fe_2O_3^{(T)}$ content between 10.7-12.1 wt.%, corresponding to Mg# values between 67.2-72.9 (average 71.0). The SiO_2 and TiO_2 content of Subgroup 4 volcanics ranges between 51.3-57.7 and 0.4-0.5 wt.% respectively and total alkali content ($Na_2O + K_2O$) varies between 1.5-2.2 wt.%.

Most major elements in Subgroup 2 and 3 samples exhibit poor correlations with MgO, indicating that major elements may have been affected by secondary remobilisation in Chulaar Group rocks. Subgroups 2 and 3 show poor negative correlations between MgO and SiO_2, CaO and Na_2O and moderate negative correlation with Al_2O_3 (Fig. 6.8). In Subgroup 3, negative correlations are present for MgO versus TiO_2 and P_2O_5, whereas these negative correlations are poor for Subgroup 2 volcanics. Poor positive correlations are present between MgO and $Fe_2O_3^{(T)}$ in both Subgroups 2 and 3. Subgroup 1 volcanics show moderate to good negative correlations between MgO and SiO_2, Na_2O and Al_2O_3 and

moderate positive correlation between MgO and Fe_2O_3 (Fig. 6.8). In contrast to other subgroups, Subgroup 2 volcanics also show a positive correlation between MgO and TiO_2. Subgroup 4 volcanics show poor negative correlations between MgO and SiO_2, TiO_2, CaO and Al_2O_3, moderate negative correlations for MgO against Na_2O and P_2O_5 and no correlations between MgO and $Fe_2O_3^{(T)}$. All four subgroups display separate trends on plots of MgO against P_2O_5 and TiO_2 (Fig. 6.8), supporting their division into separate geochemical subgroups with distinct evolutionary paths.

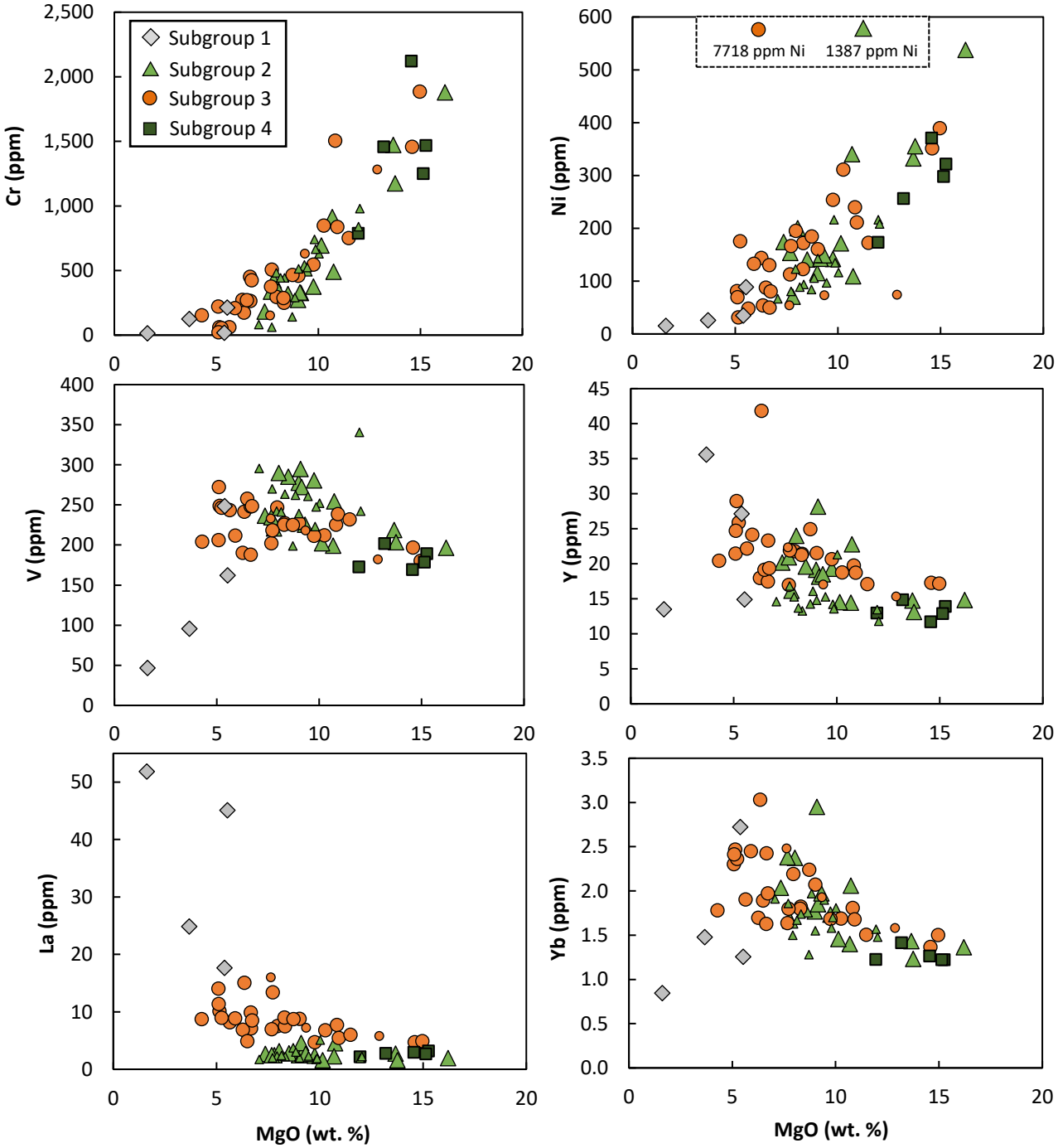

Figure 6.9: Bivariate diagrams of selected trace elements versus MgO for Chulaar Group volcanic samples.

6.4.1.3 Trace Elements

For all Chulaar Group volcanic rocks, elements that are compatible during early basaltic fractionation (e.g., Cr, Ni, Cu) display good positive correlations with MgO (Fig. 6.9). Cr abundance varies from 60-1879 ppm in Subgroup 2, 22-1884 ppm in Subgroup 3 and 789-2121 ppm in Subgroup 4, whilst Ni abundance varies from 66-537 ppm for Subgroup 2, 31-389 ppm for Subgroup 3 and 173-370 ppm for Subgroup 4. Two samples with Ni values of 1387 ppm and 7718 ppm for Subgroup 2 and Subgroup 3 respectively may represent mineralised samples or erroneous analyses. Subgroup 1 has consistently lower ranges of Cr (13-212 ppm) and Ni (15-88 ppm) compared to the other subgroups.

Poor negative correlations occur between MgO and most incompatible trace elements (e.g., V, Y, Sc) for Subgroups 2, 3 and 4 (Fig. 6.9). In contrast, Subgroup 1 volcanics have both broadly lower abundances and apparently positive correlations of elements such as V and Y against MgO. Moderate to good negative correlations are found between MgO and the REE for Subgroups 2, 3 and 4, except for La, which shows no correlation for Subgroup 2 and a moderate positive correlation for Subgroup 4. This may indicate secondary remobilisation of La, as has been suggested in mafic volcanic rocks in the area (e.g. Wyman & Kerrich, 2012; Wyman, 2019), or alternatively, demonstrate that La concentrations are low in these mafic magmas. Subgroup 1 volcanics exhibit moderate negative correlations between MgO and the LREE, but moderate positive correlations between MgO and HREE.

On chondrite-normalised REE diagrams (Fig. 6.10), Chulaar Subgroup 1 volcanics have steeply sloping REE patterns with variably strong LREE enrichment [average $(La/Sm)_{CN}$ = 4.10] up to 218 x chondritic values, pronounced HREE depletion [average $(Gd/Yb)_{CN}$ = 2.52] and minor negative Eu anomalies (average Eu/Eu* = 0.90). Subgroup 2 Chulaar volcanics have sub-parallel, generally flat REE patterns at concentrations 7-11x chondritic values. Minor LREE enrichment is shown by some Subgroup 2 samples [average $(La/Sm)_{CN}$ = 1.24], with distinct, slightly concave LREE-MREE patterns shown by all samples. Subgroup 2 volcanics also show flat to slightly negatively sloping HREE trends [average $(Gd/Yb)_{CN}$ = 0.92] and insignificant Eu anomalies (average Eu/Eu* = 1.0), although three samples have positive Eu/Eu* of ~1.2. Subgroup 3 volcanics are typified by moderately sloping REE patterns with consistent LREE enrichment [average $(La/Sm)_{CN}$ = 1.94] and slightly depleted HREE [average $(Gd/Yb)_{CN}$ = 1.29]. Variably negative Eu anomalies are present in most Subgroup 3 volcanics, and they have Eu/Eu* values between 0.67-1.06, consistent with the crystallisation of plagioclase from the parental magma. A cumulate olivine-bearing volcanic in Subgroup 3 (ROTH026) has a lower total REE abundance, but otherwise similar pattern to the rest of the samples. Subgroup 4 volcanics have flat to gently sloping REE patterns at 7-10.5x chondritic values and have a similar trend to Subgroup 2 volcanics albeit more closely spaced. Subgroup 4 has flat to slightly enriched LREE [average $(La/Sm)_{CN}$

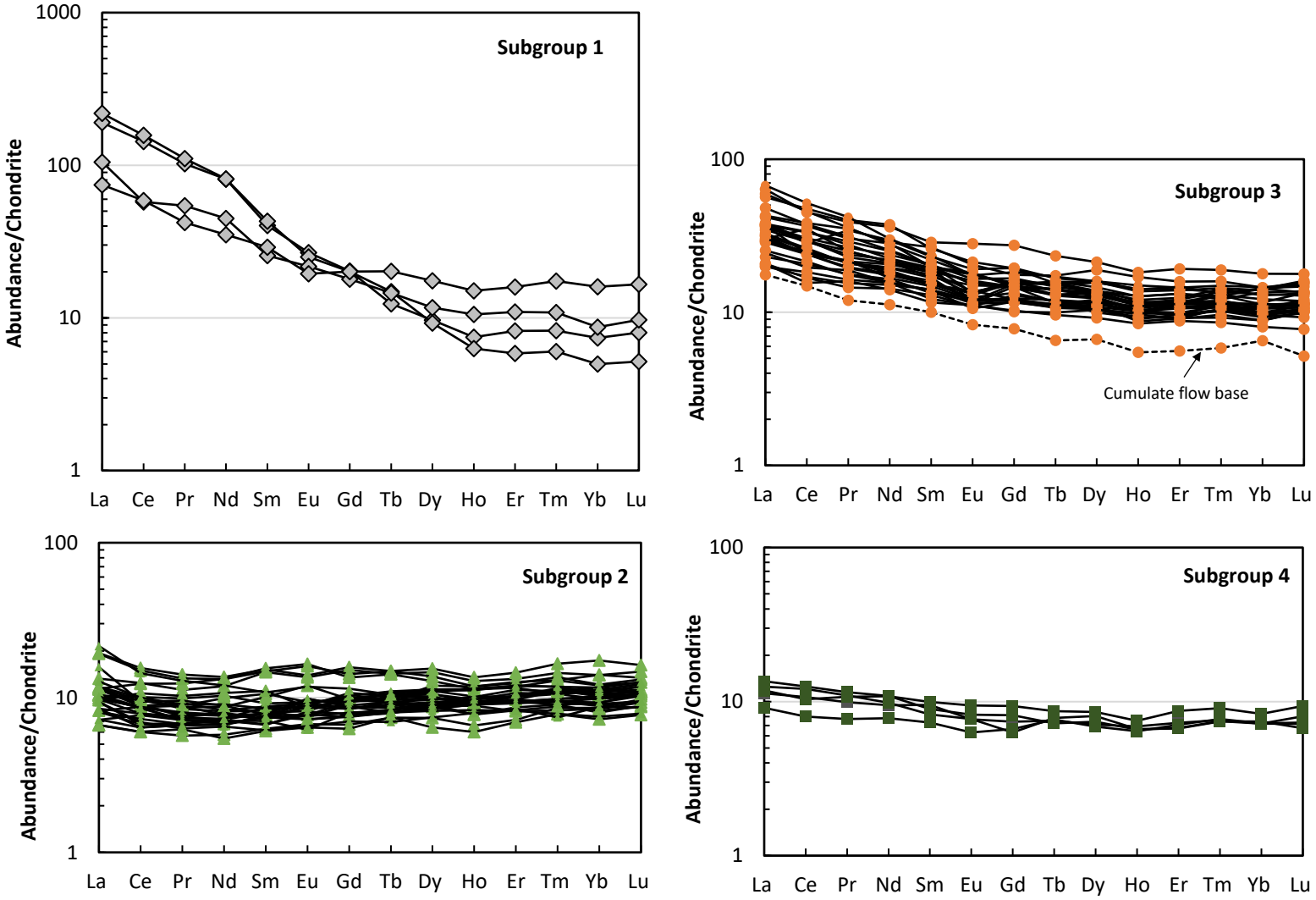

Figure 6.10: Chondrite-normalised REE plots for Chulaar Group volcanic samples. Normalising values from Sun & McDonough (1989).

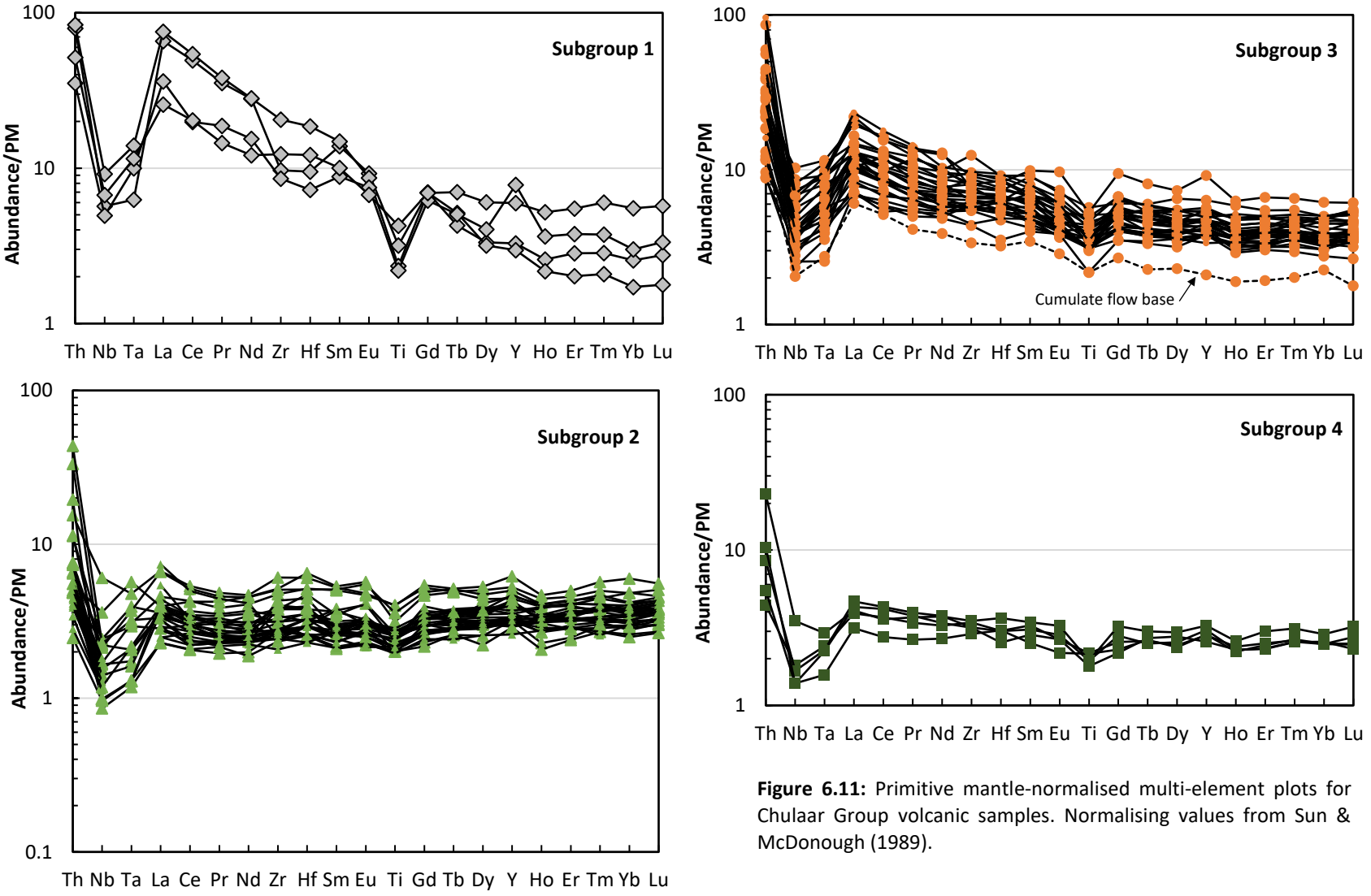

Figure 6.11: Primitive mantle-normalised multi-element plots for Chulaar Group volcanic samples. Normalising values from Sun & McDonough (1989).

= 1.33], flat HREE patterns [average $(Gd/Yb)_{CN}$ = 1.01] and negligible negative Eu anomalies (average Eu/Eu* = 0.97).

On primitive mantle-normalised multi-element plots (Fig. 6.11), Subgroup 1 volcanics have steeply sloping trace element patterns, with enrichment in the most incompatible elements compared to the less incompatible elements. Prominent negative Nb-Ta (Nb/Nb* = 0.07-0.18) and Ti (Ti/Ti* = 0.27-0.51) anomalies are present in all Subgroup 1 samples, and two samples possess a negative Zr-Hf anomaly, corresponding to Zr/Zr* values of 0.49-0.73. Subgroup 2 volcanics have sub-parallel, broadly flat patterns with most elements at concentrations at 2-7x primitive mantle values. All samples in Subgroup 2 show strongly negative Nb-Ta anomalies (Nb/Nb* 0.13-0.77, average 0.36) and minor negative Ti anomalies (Ti/Ti* 0.61-0.86, average 0.78), with subtle positive Zr-Hf anomalies in about half of the volcanic samples (Zr/Zr* 0.91-1.64, average 1.20) and slight positive Y anomalies. Subgroup 3 have sub-parallel, sloping trace element patterns, with enrichment in the most incompatible elements. As with other subgroups, Subgroup 3 have significant negative Nb-Ta anomalies (Nb/Nb* 0.12-0.50, average 0.29) and Ti anomalies (Ti = 0.51-0.95, average 0.80). Both positive and negative Zr-Hf anomalies (Zr/Zr* = 0.64-1.64) are shown by most Subgroup 3 samples and like Subgroup 2, minor positive Y anomalies are also present. Subgroup 4 volcanics have generally flat trace element profiles with very slight enrichment in the most incompatible elements and marked negative Nb-Ta (Nb/Nb* = 0.24-0.44, average 0.34) and less prominent negative Ti anomalies (Ti/Ti* = 0.61-0.83, average 0.70). Unlike the other three subgroups, Subgroup 4 samples show no obvious Zr-Hf anomalies (average Zr/Zr* = 1.01).

The Chulaar Group volcanics have been plotted on two ratio-ratio diagrams, in addition to end member compositions and field boundaries for different tectonic settings (Figs. 6.12 and 6.13). Chulaar Subgroup 1 samples have not been plotted due to their more highly fractionated nature. It must be stressed that considering the Archaean age of these rocks, these fields and compositions are plotted for reference and are not used to make direct inferences about the tectonic setting in which the rocks were formed (e.g., Condie, 2015). On a Nb/Y vs. Zr/Y diagram (Fig. 6.12), most Chulaar volcanics plot on the non-plume sources portion of the diagram, largely at the overlapping margins between normal mid-ocean ridge basalt (NMORB), oceanic plateau basalt (OPB) and arc-related basalt (ARC) fields of Condie (2005). Subgroup 2 volcanics cluster between the deep depleted mantle and shallow depleted mantle endmembers. Subgroup 3 volcanics plot on a trend from shallow depleted mantle towards an enriched component and upper continental crust end members, whilst Subgroup 4 volcanics are clustered between shallow depleted mantle and primitive mantle compositional endmembers. On a Zr/Nb vs. Nb/Th diagram (Fig. 6.13), all Chulaar volcanic samples plot at the

margins of the arc-related basalt and oceanic plateau basalt fields, close to the enriched component and upper continental crust compositional end members of Condie (2005).

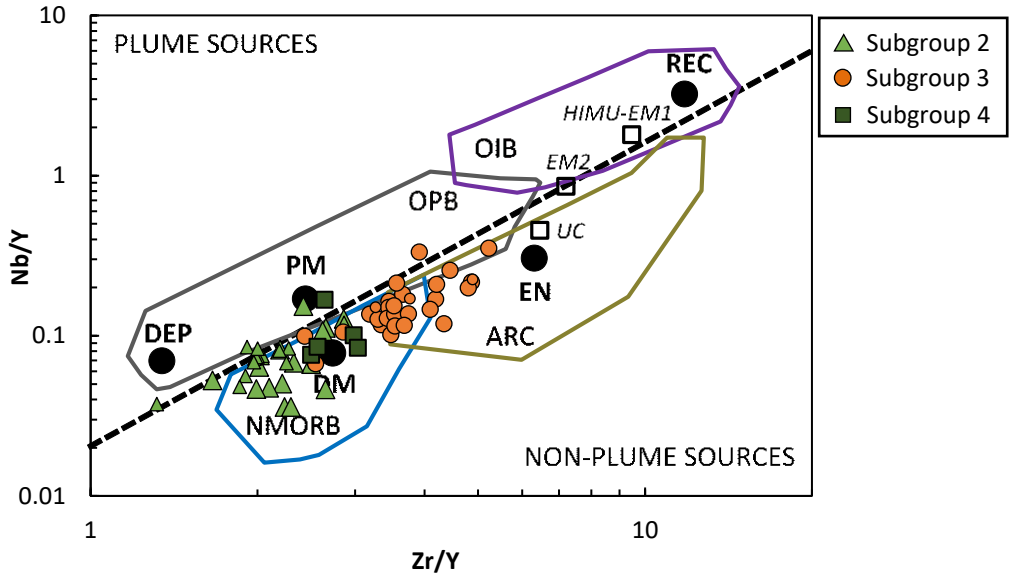

Figure 6.12: Nb/Y vs. Zr/Y diagram for Chulaar Group volcanic samples. Chulaar Subgroup 1 samples are not plotted due to their more highly fractionated compositions. End member compositions and field boundaries from Condie (2005). Abbreviations: NMORB = normal mid-ocean ridge basalt, OPB = oceanic plateau basalt, OIB = oceanic island basalt, ARC = arc-related basalts, DEP = deep depleted mantle, PM = primitive mantle, DM = shallow depleted mantle, EN = enriched component, REC = recycled component, HIMU = high mu (U/Pb) source, EM1 = enriched mantle source 1, EM2 = enriched mantle source 2, UC = upper continental crust.

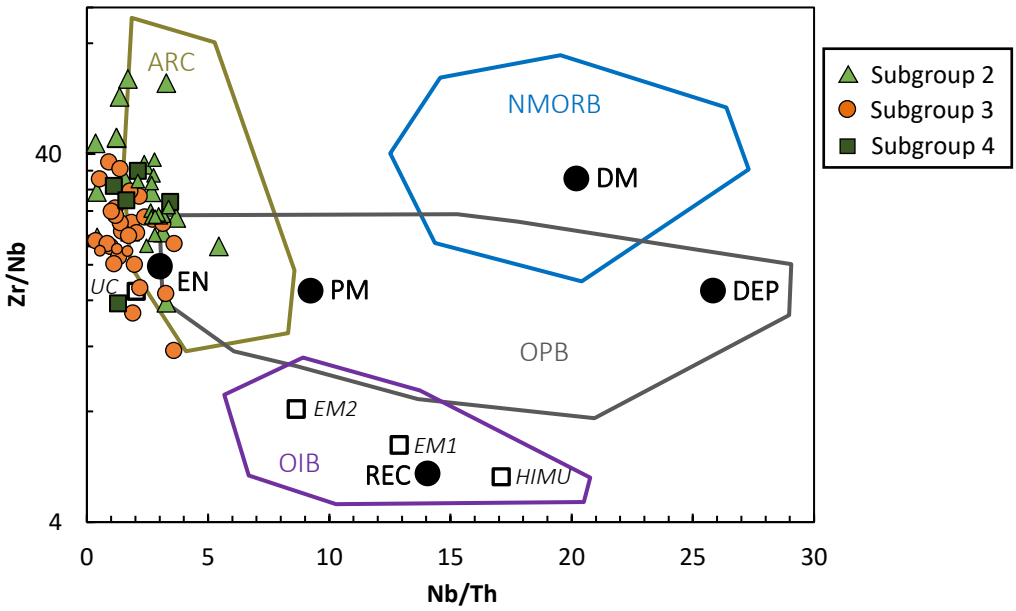

Figure 6.13: Zr/Nb vs. Nb/Th diagram for Chulaar Group volcanic samples. Chulaar Subgroup 1 samples are not plotted due to their more highly fractionated compositions. End member compositions and field boundaries from Condie (2005). Abbreviations as in Figure 6.11.

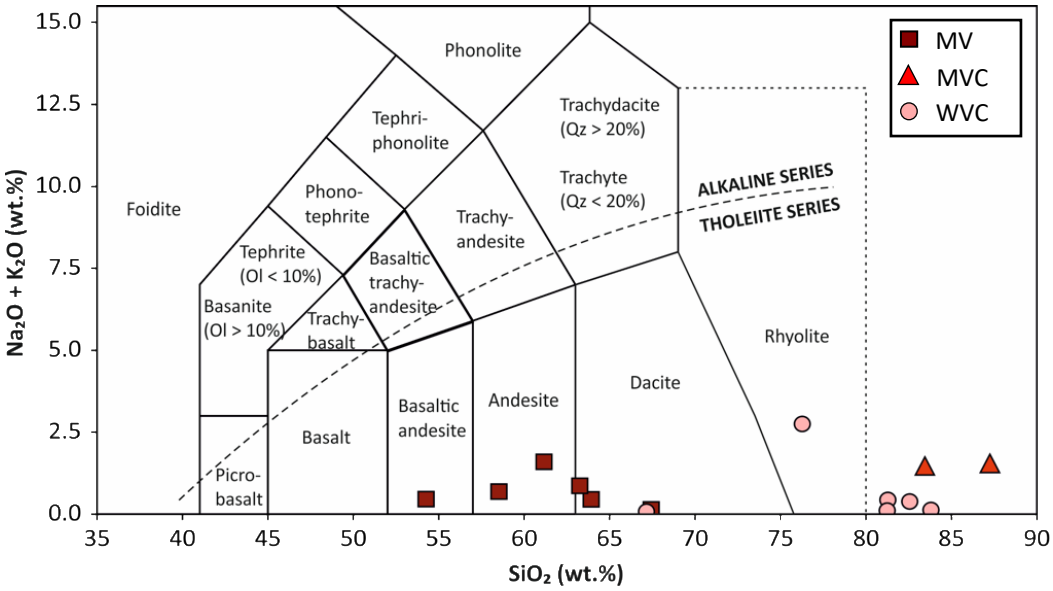

Figure 6.14: Total Alkali versus Silica (TAS) classification diagram for Mougooderra Fm volcanics (MV), Mougooderra Fm volcaniclastics (MVC) and Willowbank volcaniclastics (WVC). Field boundaries as defined by Le Maitre et al. (1989).

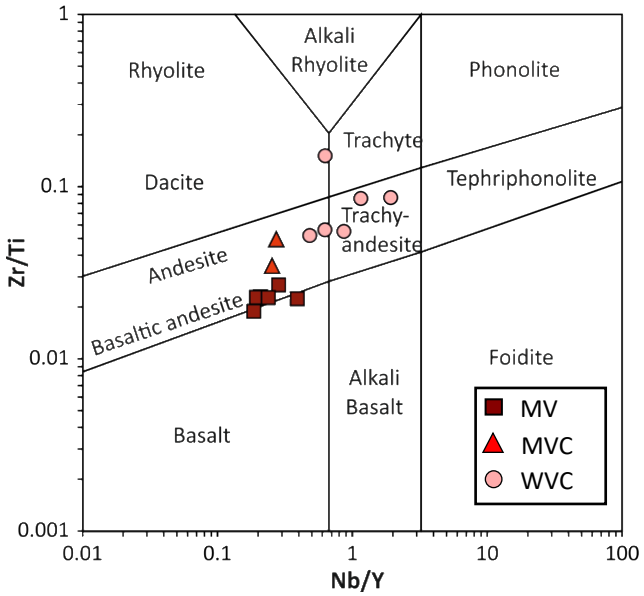

Figure 6.15: Zr/Ti versus Nb/Y classification diagram for Mougooderra Fm volcanics (MV), Mougooderra Fm volcaniclastics (MVC) and Willowbank volcaniclastics (WVC). Field boundaries as defined by Pearce (1996).

6.4.2 Mougooderra Formation and Willowbank Clastics

In this section, the geochemistry of mafic-intermediate volcanics and felsic volcaniclastic rocks of the Mougooderra Fm, and felsic volcaniclastic rocks of the Willowbank Clastics, are described. The geochemistry of three Mougooderra Fm volcanic rocks has been obtained from the WACHEM database.

6.4.2.1 Classification

On a TAS diagram (Fig. 6.14), Mougooderra Fm volcanics plot on a continuous trend from basaltic andesite to dacite, displaying a variation in SiO_2 content that is consistent with magmatic evolution. Mougooderra Fm volcaniclastics plot within the rhyolite classification on the TAS diagram, whilst

Willowbank volcaniclastics plot mostly in the rhyolite field, with a single sample in the dacite field. In contrast, on the Zr/Ti against Nb/Y incompatible trace element diagram of Pearce (1996) (Fig. 6.15), Mougooderra Fm volcanics plot as a tight cluster at the margin of the basaltic andesite field, with two samples classified as a basalt and crucially no clear evolution trend. Considering the likely mobile nature of SiO_2 and K_2O and the immobile character of the relevant incompatible elements, the latter diagram is a more reliable classification diagram and indicates that the Mougooderra Fm volcanics are

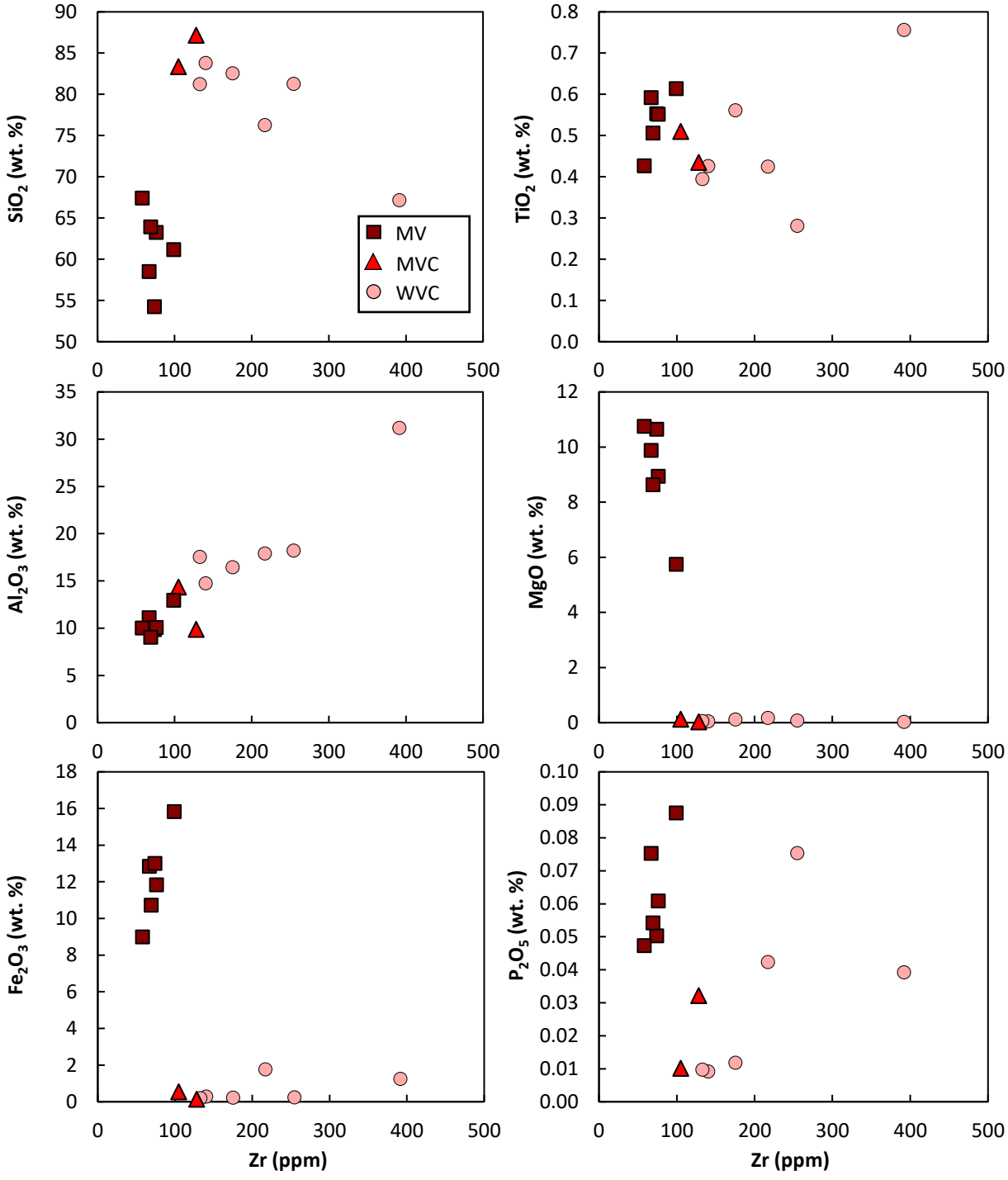

Figure 6.16: Bivariate diagrams of selected major elements versus Zr for Mougooderra Fm volcanics (MV), Mougooderra Fm volcaniclastics (MVC) and Willowbank volcaniclastics (WVC).

closer in composition than the TAS diagram suggests. On the Zr/Ti versus Nb/Y plot, Mougooderra Fm volcaniclastics plot as andesite, whereas Willowbank volcaniclastics plot largely in the andesite and trachy-andesite fields, with a single sample in the dacite field. Classification of these volcaniclastic rocks is made with caution not only because of the extent of the alteration evident in samples, but also because of the possibility of other (i.e. sedimentary) input additional to that of coeval volcanism.

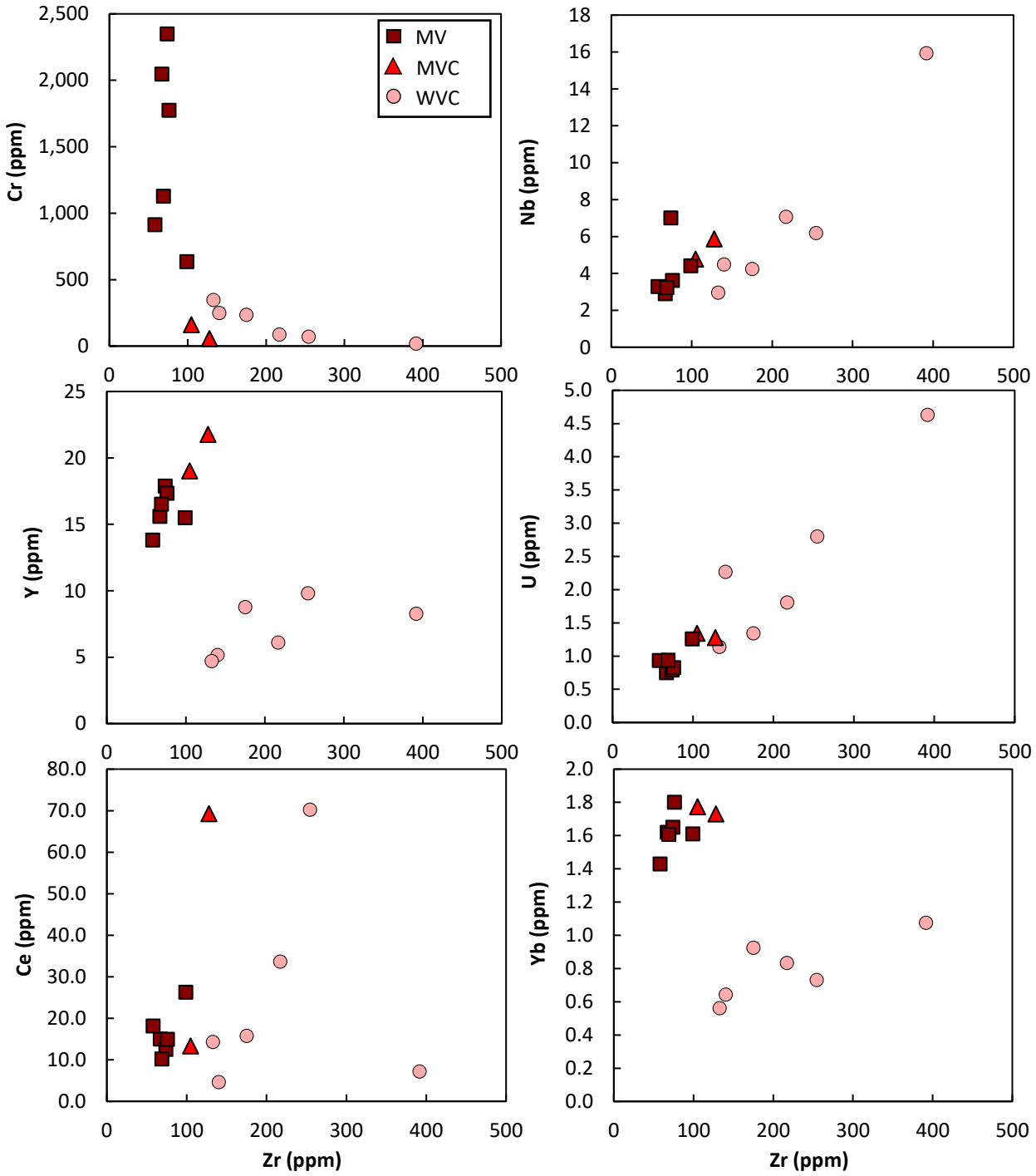

Figure 6.17: Bivariate diagrams of selected trace elements versus Zr for Mougooderra Fm volcanic rocks (MV) Mougooderra Fm volcaniclastics (MVC) and Willowbank volcaniclastics (WVC).

6.4.2.2 Major Elements

Mougooderra Fm volcanics range in MgO content between 5.8-10.8 wt.% and $Fe_2O_3^{(T)}$ content between 9.0-15.8 wt.%, corresponding to Mg# values between 41.8-70.3 (average 59.3). The SiO_2 content of Mougooderra Fm volcanics varies between 54.3-67.4 wt.% and TiO_2 ranges between 0.4-0.6 wt.%. The two Mougooderra Fm volcaniclastic samples have high SiO_2 contents ranging between 83.4-87.2 wt.%, TiO_2 in the range 0.4-0.5 wt.% and $Fe_2O_3^{(T)}$ ranging between 0.1-0.5 wt.%. In all Mougooderra Fm volcaniclastics, CaO and MgO are both <0.1 wt.% and total alkali content (Na_2O + K_2O) ranges between 0.1-0.4 wt.%. Willowbank volcaniclastics range in SiO_2 between 67.2-82.6 wt.%, TiO_2 between 0.3-0.8 wt.% and $Fe_2O_3^{(T)}$ 0.2-1.8 wt.%. Willowbank volcaniclastics contain only minor amounts of MgO and CaO at <0.17 wt.% and <0.15 wt.% respectively.

The Mougooderra Fm comprises both mafic-intermediate volcanics and evolved volcaniclastic rocks, for which MgO is a poor differentiation index. As the extent of SiO_2 remobilisation is not clear, Zr is used as a differentiation index in bivariate diagrams for the Mougooderra Fm and Willowbank Clastics (Fig. 6.16). Moderate to good positive correlations are present between Zr and TiO_2, Al_2O_3, Fe_2O_3 and P_2O_5, consistent with magmatic fractionation of the volcanic rocks and the source material for volcaniclastic rocks. A good negative correlation is present between Zr and MgO for the Mougooderra Fm volcanics (not replicated by volcaniclastic rocks due to negligible MgO content) and between Zr and SiO_2 for Willowbank volcaniclastics, contrary to the positive correlation expected for an evolving sequence. This may be further evidence supporting significant remobilisation of SiO_2 in these rocks. It is notable that volcaniclastic units from both the Mougooderra Fm and Willowbank Clastics plot on a similar path to Mougooderra Fm volcanics for Zr vs. Al_2O_3 but have distinct trends against all other major elements.

6.4.2.3 Trace Elements

Mougooderra Fm volcanics are characterised by relatively high Cr and Ni abundances of 636-2350 and 206-552 ppm, respectively, which combined with Zr abundances of 58-99 ppm, further supports a more mafic rather than felsic classification for these rocks. The volcanics have poor negative correlations between Zr and Cr, Ni and Co, whereas there are poor to moderate positive correlations between Zr and the HFSE (e.g., Nb, Y, U) as well as for the REE (Fig. 6.17). A poor correlation between Zr and Th is probably due to the narrow range in Zr content shown by the volcanic samples. Mougooderra Fm volcaniclastics have lower, but not insignificant, Cr abundances at 57-160 ppm and low Ni concentrations of 2-15 ppm. Similarly, Willowbank volcaniclastics have Cr abundances in the range 20-348 ppm and Ni abundances largely between 2-8 ppm, although a single sample contains

134 ppm Ni. Mougooderra Fm volcaniclastics have consistently lower Zr (105-128 ppm) than Willowbank volcaniclastics (140-392 ppm). Willowbank volcaniclastic samples have good positive correlations between Zr and HFSE and HREE but poor correlations between Zr and LREE. This may suggest LREE mobility in these rocks, or reflect varying heavy mineral concentrations affecting the LREE content of the volcaniclastic rocks. Unsurprisingly, the abundances and trends shown by Mougooderra Fm volcaniclastics better matches the Mougooderra Fm volcanics than Willowbank volcaniclastics.

On a chondrite-normalised REE diagram (Fig. 6.18), Mougooderra Fm volcanics have gently sloping patterns with variable LREE enrichment expressed by $(La/Sm)_{CN}$ values between 1.58 and 4.13. The volcanics consistently show flat HREE patterns [$(Gd/Yb)_{CN}$ = 1.02-1.20] and only one sample has a significant negative Eu anomaly (Eu/Eu* = 0.75). Mougooderra Fm volcaniclastic rocks also display trends with LREE enrichment [$(La/Sm)_{CN}$ = 4.69-6.86] and flat to gently sloping HREE at similar concentrations to Mougooderra Fm volcanics (~10x primitive mantle). Willowbank volcaniclastics show highly variable LREE enrichment [$(La/Sm)_{CN}$ = 1.19-11.07] and a u-shaped LREE pattern in two samples. Two Willowbank volcaniclastic samples display negative Eu anomalies with average Eu/Eu* 0.61 and HREE are flat to negatively sloping at ~4-6x primitive mantle abundances, lower than Mougooderra Fm volcaniclastic samples.

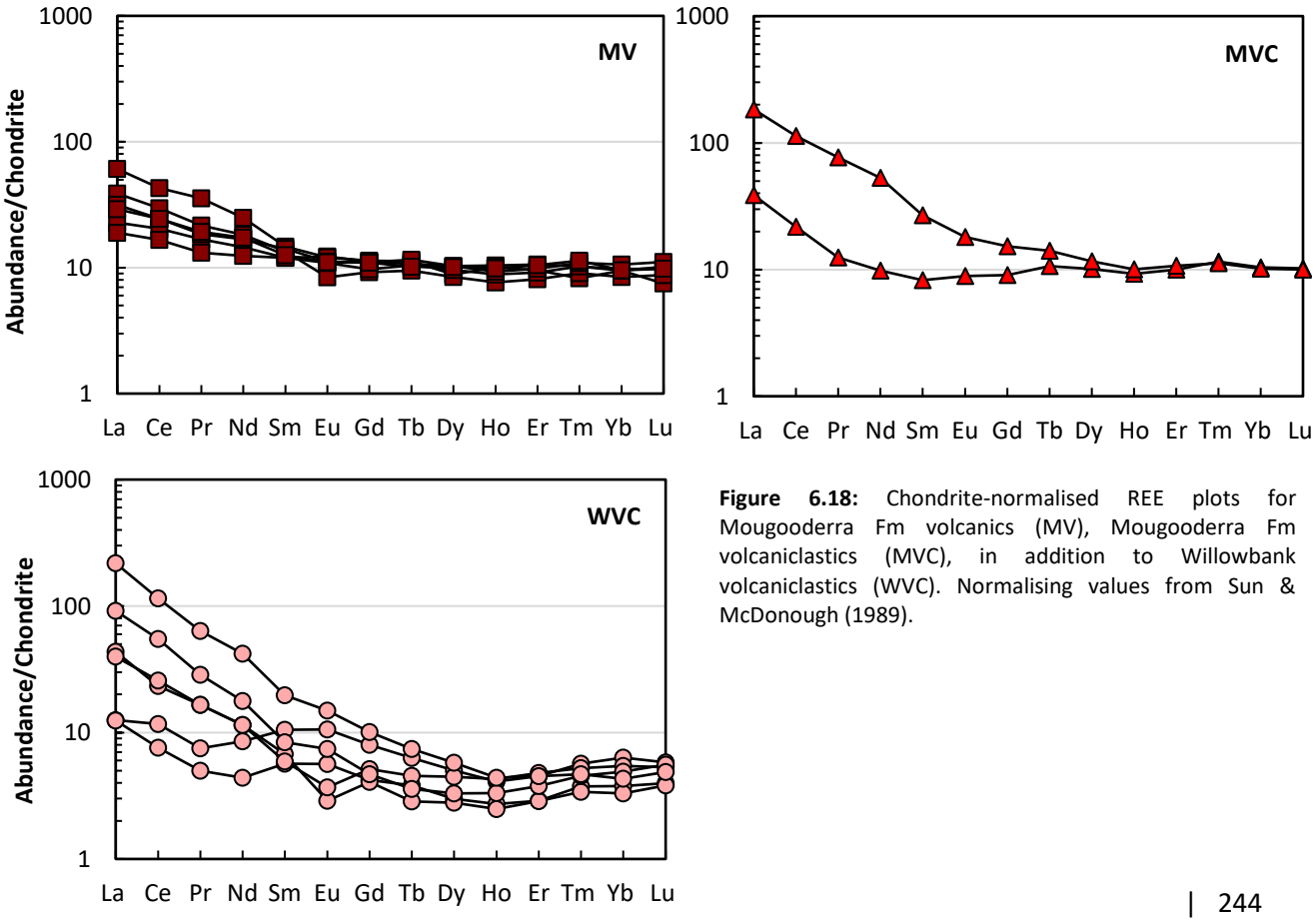

Figure 6.18: Chondrite-normalised REE plots for Mougooderra Fm volcanics (MV), Mougooderra Fm volcaniclastics (MVC), in addition to Willowbank volcaniclastics (WVC). Normalising values from Sun & McDonough (1989).

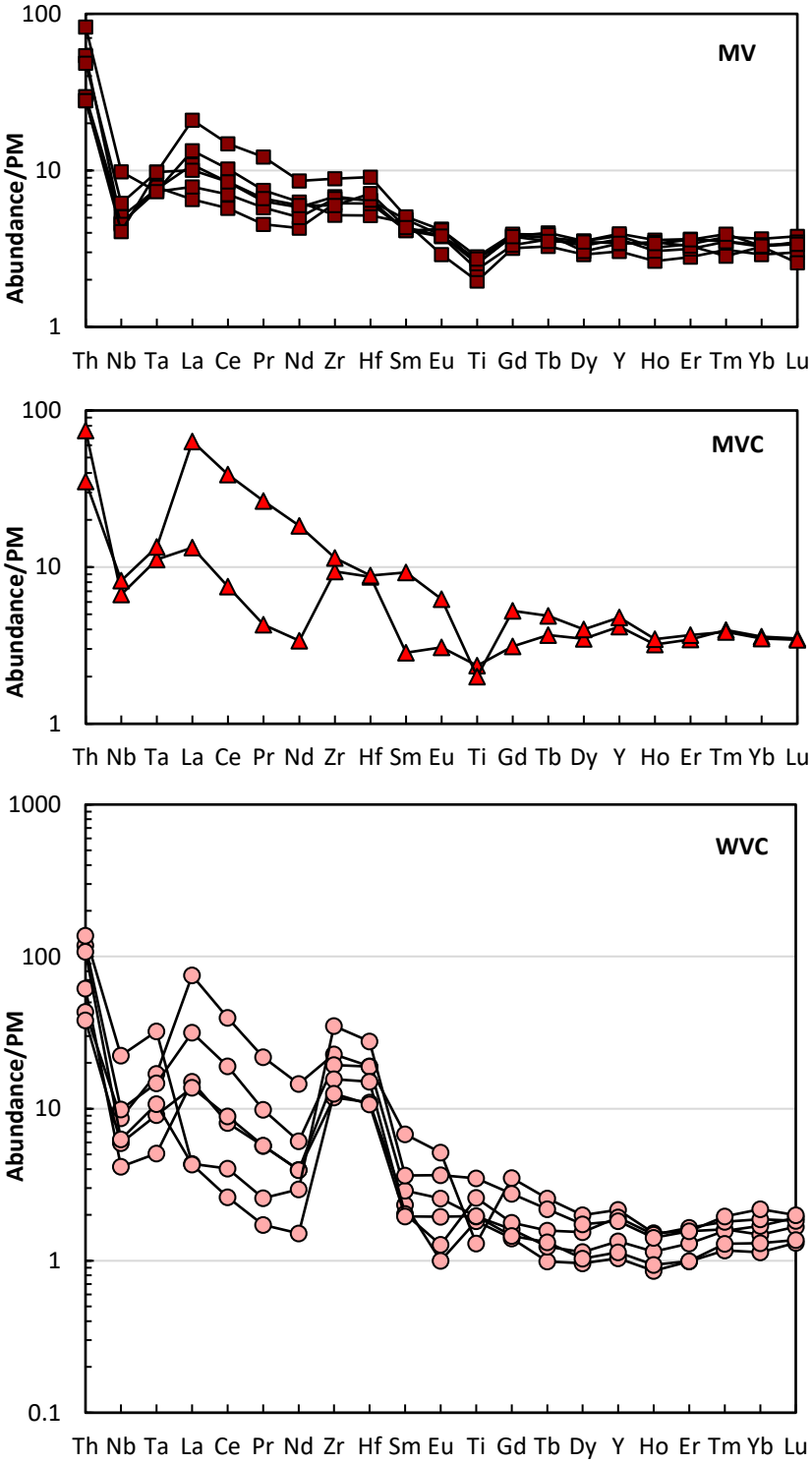

Figure 6.19: Primitive mantle-normalised multi-element plots for Mougooderra Fm volcanics (MV), Mougooderra Fm volcaniclastics (MVC) samples, in addition to Willowbank volcaniclastics (WVC). Normalising values from Sun & McDonough (1989).

On primitive mantle-normalised trace element diagrams (Fig. 6.19), Mougooderra Fm volcanics have sloping patterns with enrichment of the most incompatible elements. The volcanics show pronounced negative anomalies for Ti (average Ti/Ti* = 0.61) and Nb (average Nb/Nb* = 0.27) and five of the six samples show slight positive Zr anomalies at an average Zr/Zr* of 1.34. Mougooderra Fm volcaniclastic

rocks show two different trends: one sample (MOU012) is markedly enriched in the most incompatible elements with prominent negative Ti (Ti/Ti* = 0.30) and Nb (Nb/Nb* = 0.17) anomalies, whereas the other sample (MOU002) has a less-steep profile with less prominent negative Ti (Ti/Ti* = 0.73) and Nb (Nb/Nb* = 0.21) anomalies, and a distinctive positive Zr-Hf anomaly (Zr/Zr* = 3.02). Willowbank volcaniclastic are typified by sub-parallel sloping patterns with extreme positive Zr-Hf anomalies (Zr/Zr* = 2.29-10.69), comparable to sample MOU002 of the Mougooderra Fm volcaniclastics. These volcaniclastic rocks also show negative Nb anomalies (average Nb/Nb* = 0.3) and variable positive and negative Ti anomalies (Ti/Ti* range 0.31-1.45).

On a Nb/Y vs. Zr/Y diagram (Fig. 6.20), Mougooderra Fm volcanics straddle the boundary between plume and non-plume sources and plot in the overlapping areas of the arc-related basalt and oceanic plateau basalt fields. Sample GSWA 211156 plots directly at the enriched component endmember of Condie (2005). Mougooderra Fm volcaniclastics plot within the arc-related field trending away from the enriched component endmember and Willowbank volcaniclastics have very high Zr/Y values and mostly plot off the diagram. On a Zr/Nb vs. Nb/Th diagram (Fig. 6.21), Mougooderra Fm volcanics and volcaniclastics, and Willowbank volcaniclastics plot around the peripheries of the arc-related basalt field, with some clustering close to the enriched component and upper continental crust end members.

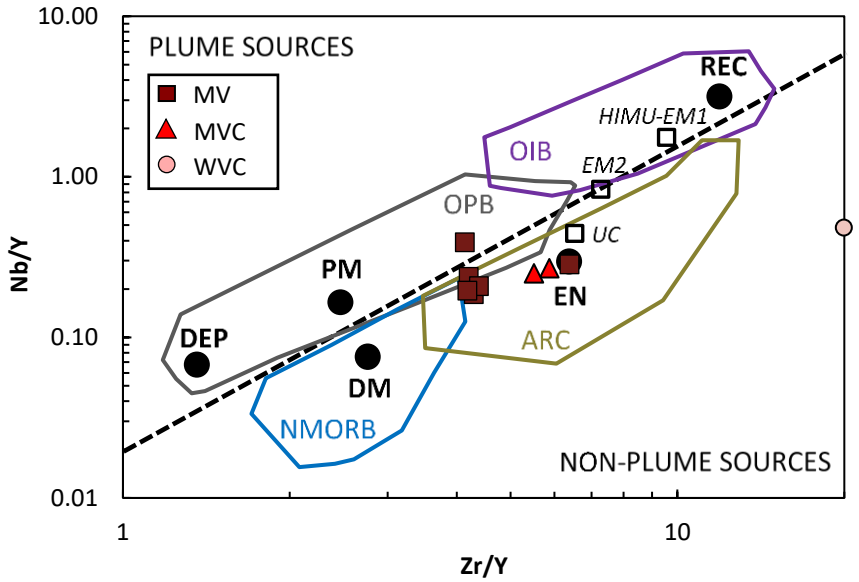

Figure 6.20: Nb/Y vs. Zr/Y diagram for Mougooderra Fm volcanics (MV), Mougooderra Fm volcaniclastics (MVC) and Willowbank volcaniclastics (WVC). End member compositions and field boundaries from Condie (2005). Note that five WVC samples plot off the diagram at > 20 Zr/Y. Abbreviations as in Figure 6.11.

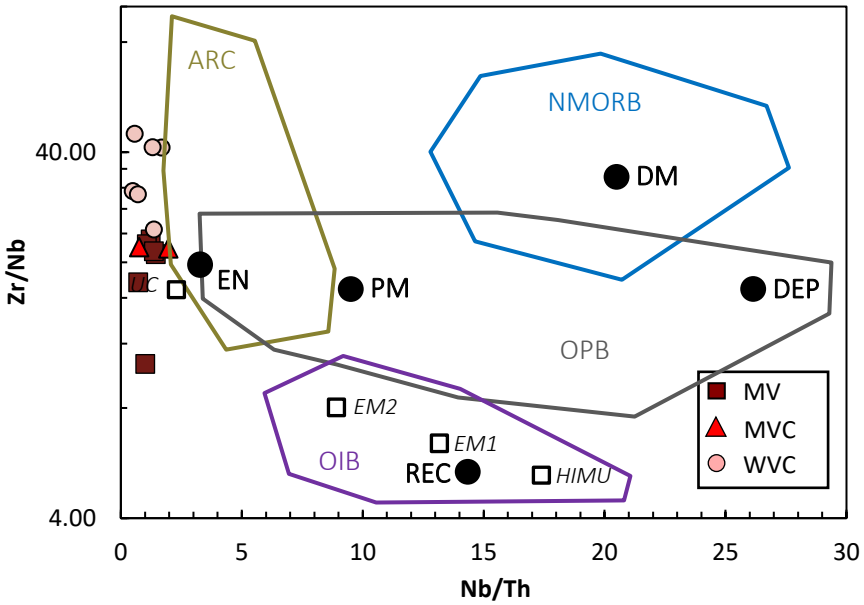

Figure 6.21: Zr/Nb vs. Nb/Th diagram for Mougooderra Fm volcanics (MV), Mougooderra Fm volcaniclastics (MVC), and Willowbank volcaniclastics (WVC). End member compositions and field boundaries from Condie (2005). Abbreviations as in Figure 6.11.

6.4.3 Warriedar Suite

In this section, the geochemistry of Warriedar Suite mafic-ultramafic sills is described. Four sills identified during lithostratigraphic mapping in the Rothsay area, the Mountain View, Rothsay, Gardner and Damperwah sills, are each represented by at least 5 samples. These four sills are each distinguished on diagrams to demonstrate the nature of individual intrusions, and the remaining samples from other Warriedar Suite intrusions across the belt are collectively referred to and plotted as 'Other Warriedar'. The Warriedar Suite geochemical dataset includes two samples report by Koutsoumbis (2020) in the Mt Mulgine area, and two samples from the WACHEM database (Table 6.1).

6.4.3.1 Classification

On a TAS diagram (Fig. 6.22), intrusive rocks of the Warriedar Suite form a group classified largely as gabbro, gabbroic diorite and diorite, with single outliers in the olivine-gabbro, alkali gabbro, granodiorite and quartz monzonite fields. Trends for individual intrusions are distinctive and indicate changes with stratigraphic height, consistent with in situ differentiation. The Mountain View Sill plots as two main clusters on the TAS diagram, within the gabbro and gabbroic dolerite fields and a single outlier plots as an alkali gabbro with >4.0 wt.% total alkalis. The Rothsay Sill forms a continuous trend from olivine-gabbro, through gabbro and gabbroic diorite and diorite; the olivine-gabbro corresponds to the olivine cumulate sampled at the base of the intrusion. The Gardner Sill intrusives plot as a tight

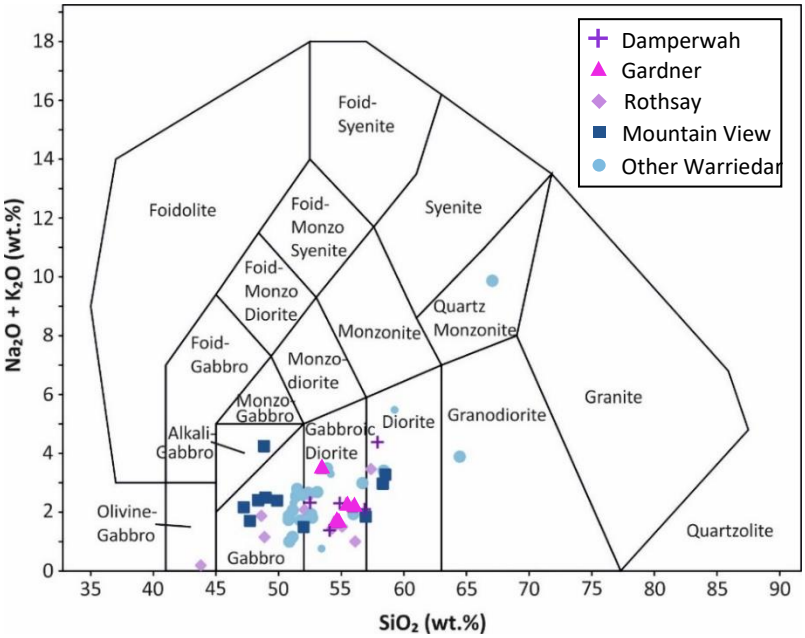

Figure 6.22: Total Alkali versus Silica (TAS) classification diagram for Warriedar Suite intrusive samples. Field boundaries as defined by Le Maitre et al. (1989).

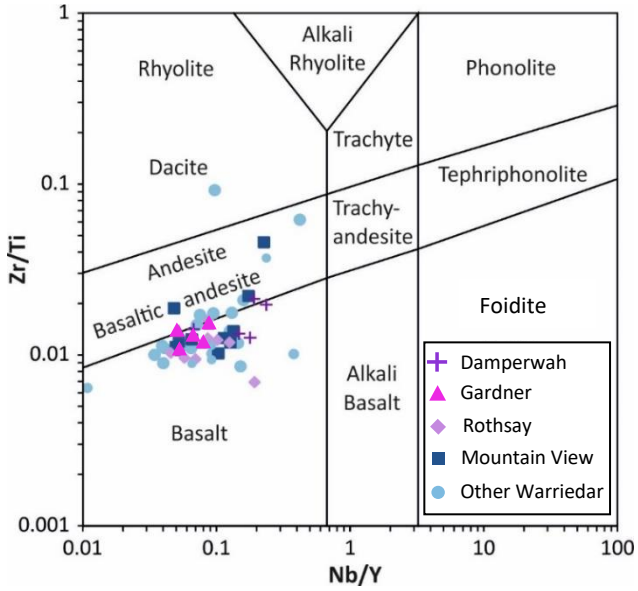

Figure 6.23: Zr/Ti versus Nb/Y classification diagram for Warriedar Suite intrusive samples. Field boundaries as defined by Pearce (1996).

cluster within the gabbroic diorite field and one sample has elevated alkali content. The Damperwah Sill samples largely classify as gabbroic diorite and a sample from the upper more evolved portion of the sill plots in the diorite field. The four samples classified as quartz monzonite, granodiorite and diorite from other Warriedar Suite intrusions in the belt all correspond to the evolved upper portions of sills, with primary quartz identified in the latter two samples.

Though some trends are identifiable, there is a significant amount of scatter on the TAS diagram. The diagram relies on Na_2O and K_2O content, which may not be entirely reliable as these elements have been shown to be mobile in these rocks. Alternatively, the Zr/Ti against Nb/Y trace element plot of Pearce (1996) may be more applicable (Fig. 6.23). In this classification, Warriedar Suite intrusions plot

mostly within the basaltic (equivalent to gabbro) and basaltic andesite (= gabbroic diorite) field, with less scatter than the TAS diagram. A further three samples plot in the andesite field (= diorite) and a single sample in the dacite field (= granodiorite), broadly consistent with the more evolved samples in the TAS diagram. The Rothsay and Gardner sill intrusives all plot as basalt and the Damperwah Sill intrusives mostly plot as basalt with one sample in the basaltic andesite field. The Mountain View Sill trends from basalt to basaltic andesite and an andesite classification for one sample.

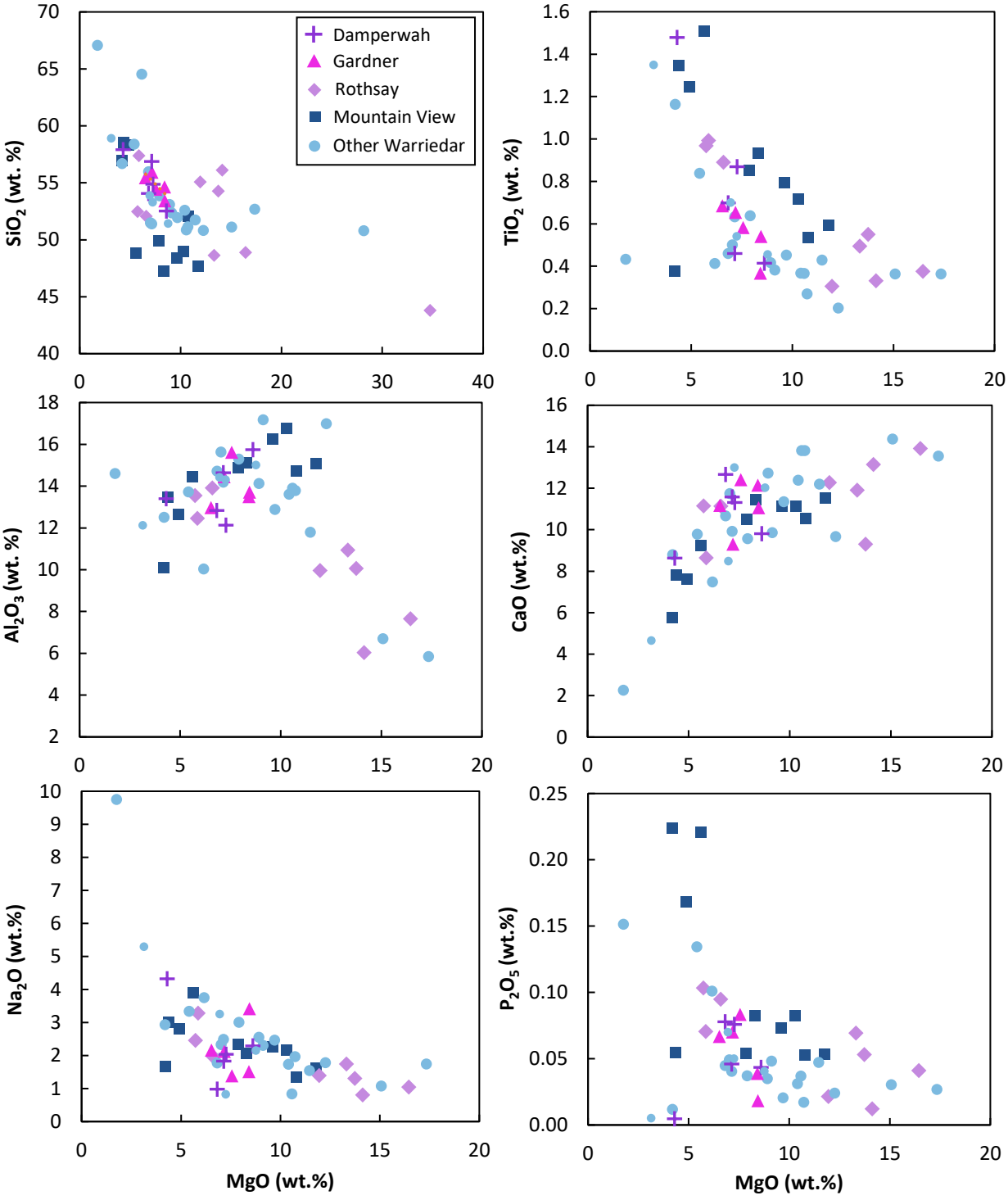

Figure 6.24: Bivariate diagrams of selected major elements versus MgO for Warriedar Suite intrusive samples.

6.4.3.2 Major Elements

Warriedar Suite intrusions show a significant variation in major element content (Fig. 6.24), consistent with the compositional magmatic layering observed in many of the larger intrusions. For example, MgO content varies between 28.17-34.73 wt.% for two cumulate olivine and pyroxene-bearing basal units, to 1.76 wt.% for an evolved, primary-quartz bearing sill top. In addition to highly elevated MgO contents, the two ultramafic cumulate samples (ROTH015, MUL006) display high Mg# values (83.9-84.1) and low SiO_2 (43.79-50.80 wt.%), TiO_2 (0.20-0.22 wt.%) and CaO (3.82-4.06 wt.%) contents compared to other intrusive samples. These cumulate samples will be omitted from further major element descriptions and bivariate plots (Fig. 6.24; except MgO vs. SiO_2) to better reflect the content of the rest of the suite. Non-cumulate Warriedar intrusive samples range in MgO between 1.76-17.35 wt.% and $Fe_2O_3^{(T)}$ between 3.22-19.60 wt.%, corresponding to Mg# values between 29.8-79.2. TiO_2 content of Warriedar intrusives ranges between 0.20-1.51 wt.%, SiO_2 between 47.22-67.06 wt.%, CaO between 2.26-14.37 wt.% and total alkali content between 0.86-9.87 wt.%.

The Mountain View, Rothsay, Gardner and Damperwah intrusive samples range in MgO contents between 4.2-11.8 wt.%, 5.7-16.4 wt.%, 6.5-8.4 wt.% and 4.3-8.6 wt.% respectively and range in $Fe_2O_3^{(T)}$ contents between 10.0-19.6 wt.%, 8.3-13.4 wt.%, 8.7-11.0 wt.% and 7.8-11.9 wt.% respectively. These values correspond to Mg# values ranging between 29.8-68.2 in Mountain View, 45.8-77.0 in Rothsay, 54.0-65.2 in Gardner and 45.8-64.4 in Damperwah. The SiO_2 content of Mountain View, Rothsay, Gardner and Damperwah intrusions ranges between 47.2-58.5 wt.%, 48.6-57.3 wt.%, 53.4-55.9 wt.% and 52.5-57.9 wt.% respectively and TiO_2 content ranges between 0.38-1.51 wt.%, 0.30-0.99 wt.%, 0.37-0.69 wt.% and 0.41-1.48 wt.% respectively. It is apparent that the uppermost Damperwah and Gardner sills are broadly lower in $Fe_2O_3^{(T)}$ and do not show such a wide compositional variation compared to the structurally lower Mountain View and Rothsay sills.

For all non-cumulate Warriedar Suite samples, there are moderate negative trends between MgO and SiO_2, TiO_2, P_2O_5 and Na_2O, and between MgO and Al_2O_3 for samples with > 9.5% MgO (Fig. 6.24). Positive correlations are observed between MgO and Al_2O_3 for samples < 9.5 wt.% MgO and between MgO and CaO, with no clear correlation between MgO and $Fe_2O_3^{(T)}$. The prominent inflection shown between MgO and Al_2O_3 at ~9.5 wt.% MgO reflects a change in the fractionating sequence with fractionation of Al_2O_3-bearing mineral, probably plagioclase feldspar. Less conspicuous inflections are shown between MgO and CaO at ~9 wt.% MgO, whereby CaO decreases more rapidly with decreasing MgO, and between MgO and P_2O_5 at ~7.5 wt.% MgO, whereby P_2O_5 seems to increase sharply with decreasing MgO, also indicating changes to the fractionating assemblage. The Mountain View and Rothsay intrusions have the same trends on bivariate diagrams as the whole suite (Fig. 6.24), including

inflections in Al_2O_3, CaO and P_2O_5 versus MgO. In contrast, the Gardner and Damperwah intrusions do not show such well-defined trends. Furthermore, the lowermost intrusions (Mountain View and Rothsay) have a lower Mg# for a given MgO content compared to the upper Gardner and Damperwah intrusions (Fig. 6.24), indicating lower relative $Fe_2O_3^{(T)}$ content for the latter two intrusions.

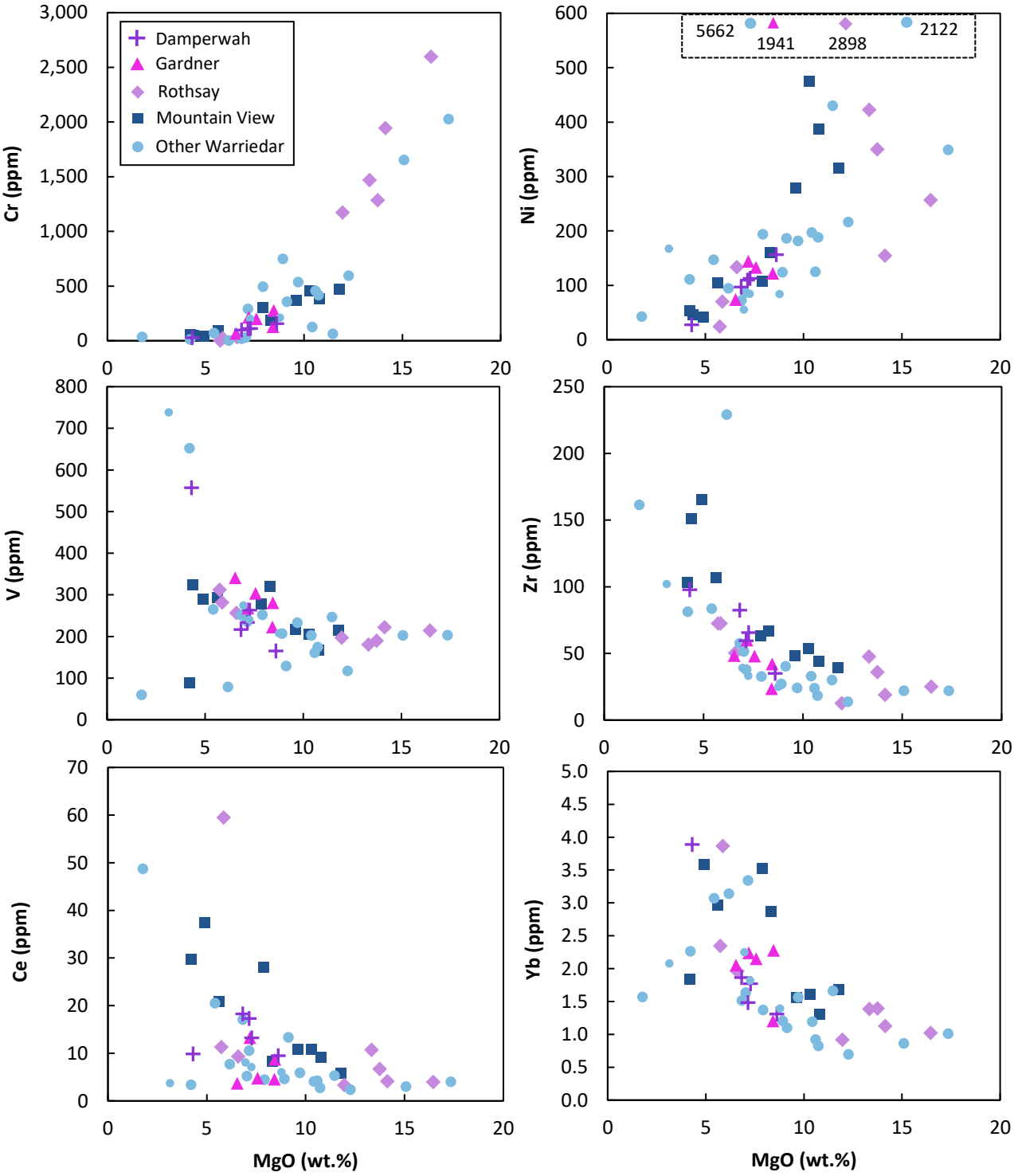

Figure 6.25: Bivariate diagrams of selected trace elements versus MgO for Warriedar Suite intrusive samples.

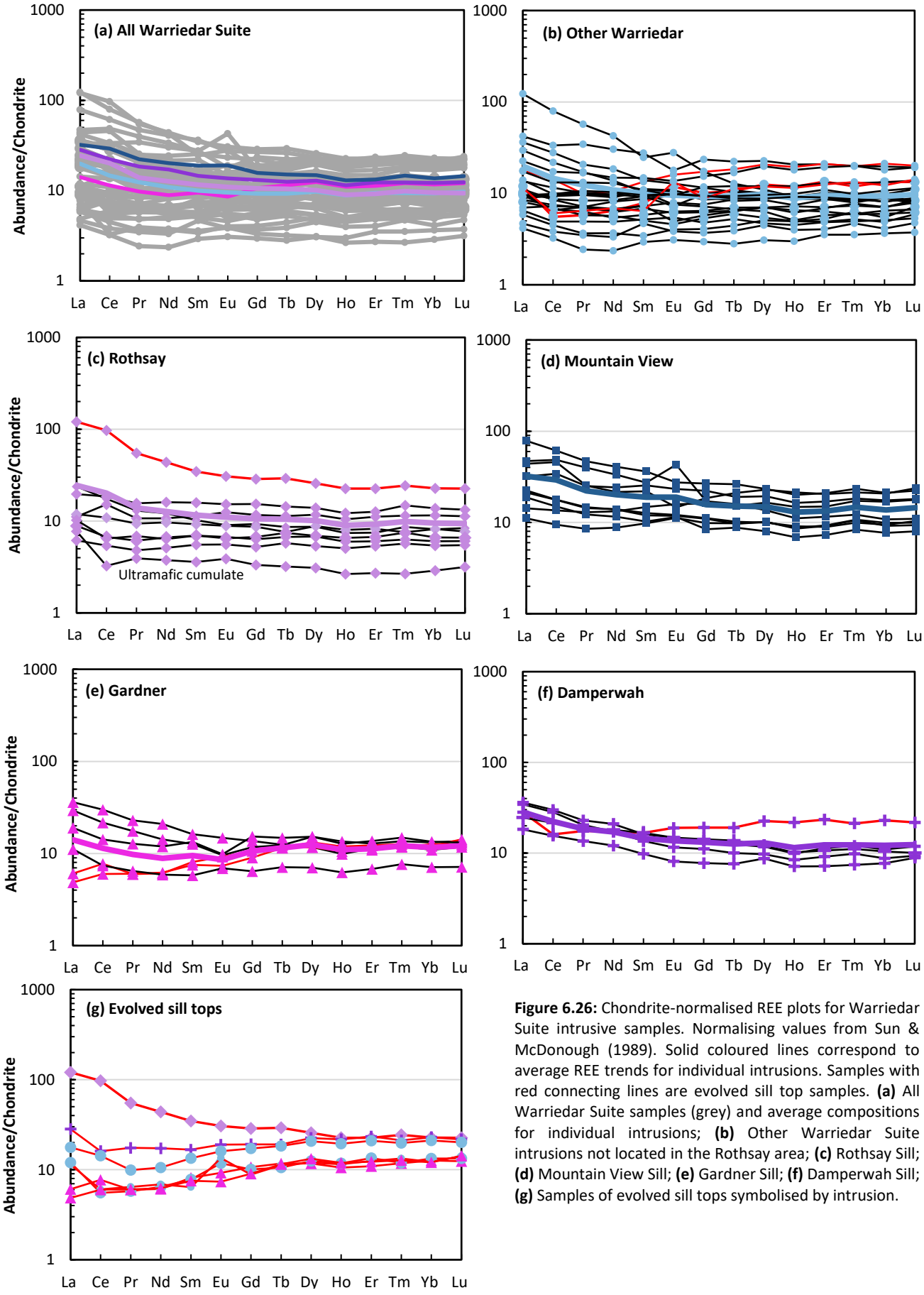

Figure 6.26: Chondrite-normalised REE plots for Warriedar Suite intrusive samples. Normalising values from Sun & McDonough (1989). Solid coloured lines correspond to average REE trends for individual intrusions. Samples with red connecting lines are evolved sill top samples. **(a)** All Warriedar Suite samples (grey) and average compositions for individual intrusions; **(b)** Other Warriedar Suite intrusions not located in the Rothsay area; **(c)** Rothsay Sill; **(d)** Mountain View Sill; **(e)** Gardner Sill; **(f)** Damperwah Sill; **(g)** Samples of evolved sill tops symbolised by intrusion.

6.4.3.3 Trace Elements

Elements highly compatible during mafic fractionation such as Cr and Ni show very marked positive correlations with MgO for Warriedar Suite intrusions (Fig. 6.25). The concentrations of these elements are highly variable, with Cr ranging between 1-3593 ppm, Ni ranging between 23-5662 ppm and Co ranging between 11-252 ppm. The presence of several highly elevated Cr and Ni-rich rocks (> 2000 ppm, above the scale of diagram) demonstrates the crystallisation and accumulation of chromite, olivine and sulphides in several Warriedar Suite intrusions (including the Rothsay and Gardner intrusions). Moderate to high amounts of V (250-738 ppm) are present in rocks with MgO content between 3.1-8.5 wt.% in most intrusions (Fig. 6.25). Warriedar Suite rocks show poor to moderate negative correlations between MgO and the HFSE (e.g., Nb, Y, U) and between MgO and the REE (Fig. 6.25), and curvilinear negative trends are present between Zr and Th against MgO. These correlations are also shown by some individual intrusions and are particularly evident in the Mountain View intrusion. A reasonably good negative correlation between TiO_2 and MgO combined with a poor to moderate negative correlation between V and MgO is consistent with the fractionation of magnetite and ilmenite during the late stages of crystallisation of Warriedar Suite intrusions (Fig. 6.25).

On chondrite-normalised REE plots (Fig. 6.26), Warriedar Suite intrusions have flat to negatively sloping, LREE-enriched patterns at highly variable concentrations ranging between 3-100x chondritic values. Enrichment in LREE generally increases with REE abundance and in some intrusions, corresponds directly to the magmatic layering present in the thickest sills. For example, in the Mountain View and Rothsay intrusions, cumulate peridotite/pyroxenite bases have flat trends [$(La/Sm)_{CN}$ = 1.1] at low REE abundance, overlying dolerite and gabbro shows slight LREE enrichment at increased REE abundance [$(La/Sm)_{CN}$ = 1.2-2.0] and the evolved dioritic upper portions have more extreme LREE enrichment [$(La/Sm)_{CN}$ = 2.2-3.0] (Fig. 6.26). However, in the Gardner, Damperwah and two other intrusions, evolved sill-tops have negative to positively sloping REE patterns with less significant LREE depletion to slight enrichment [$(La/Sm)_{CN}$ = 0.64-1.8] and HREE depletion [$(Gd/Yb)_{CN}$ = 0.68-0.83] (Fig. 6.26). Anomalously high La shown by the Rothsay Sill olivine cumulate sample (ROTH015) is likely due to the significant alteration that this sample has been subjected to (LOI = 8.1%).

Although samples from Warriedar intrusions have variable REE patterns, the average compositions of individual intrusions show similar gently sloping negative trends at concentrations between 10-30 x chondritic values (Fig. 6.26). Average compositions of individual Warriedar Suite intrusions all show slight to moderate LREE enrichment [$(La/Sm)_{CN}$ = 1.5-3.0], most prominent for the Rothsay intrusion, and flat HREE patterns [$(Gd/Yb)_{CN}$ = 0.9-1.1]. The Warriedar Suite intrusives have both minor positive and negative Eu anomalies, shown by a limited range of Eu/Eu* values between 0.69-1.35, apart from

two samples, which have prominent positive Eu anomalies (Eu/Eu* = 1.8-2.0). Furthermore, Eu anomalies do not form a clear trend with MgO and are largely restricted to MgO contents of < 4 wt.% (Fig. 6.27a), suggesting the limited extent of plagioclase fractionation in Warriedar intrusions.

On primitive mantle-normalised multi-element plots (Fig. 6.28), Warriedar Suite rocks have flat to gently negatively sloping patterns at concentrations mostly between 1-70x PM values. As with the REE plots, the most incompatible elements become progressively more enriched with increasing REE abundance, resulting in progressively steeper patterns. The Mountain View and Damperwah intrusions have gently sloping patterns, whereas the Rothsay and Damperwah intrusions typically have flat patterns, except for evolved sill tops (highlighted in red; Fig. 6.28). The Warriedar Suite displays abundant negative Nb-Ta anomalies with Nb/Nb* values between 0.10-0.76 (average 0.31), apart from a single sample which has a positive Nb anomaly (Nb/Nb* = 1.30), potentially due to secondary alteration. Warriedar Suite intrusives typically show a minor negative Ti anomaly and in three samples a slight positive Ti anomaly (average Ti/Ti* = 0.76, range 0.13-2.10). Ti/Ti* progressively becomes lower with decreasing MgO (Fig. 6.27b), particularly at MgO contents lower than 6.5 wt.% where the most negative Ti anomalies and only positive Ti anomalies are present, indicating the fractionation and accumulation of oxides (magnetite and/or ilmenite), respectively.

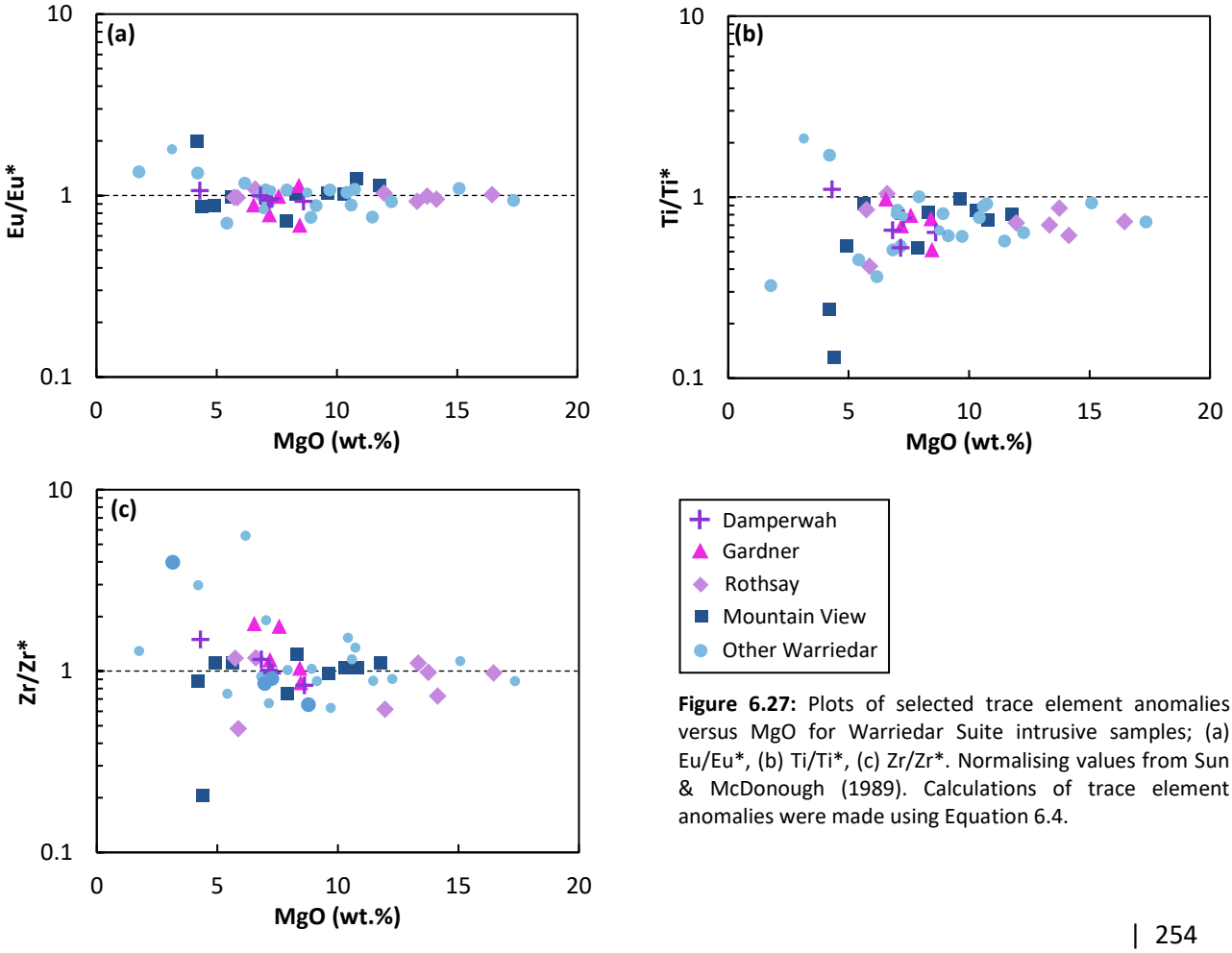

Figure 6.27: Plots of selected trace element anomalies versus MgO for Warriedar Suite intrusive samples; (a) Eu/Eu*, (b) Ti/Ti*, (c) Zr/Zr*. Normalising values from Sun & McDonough (1989). Calculations of trace element anomalies were made using Equation 6.4.

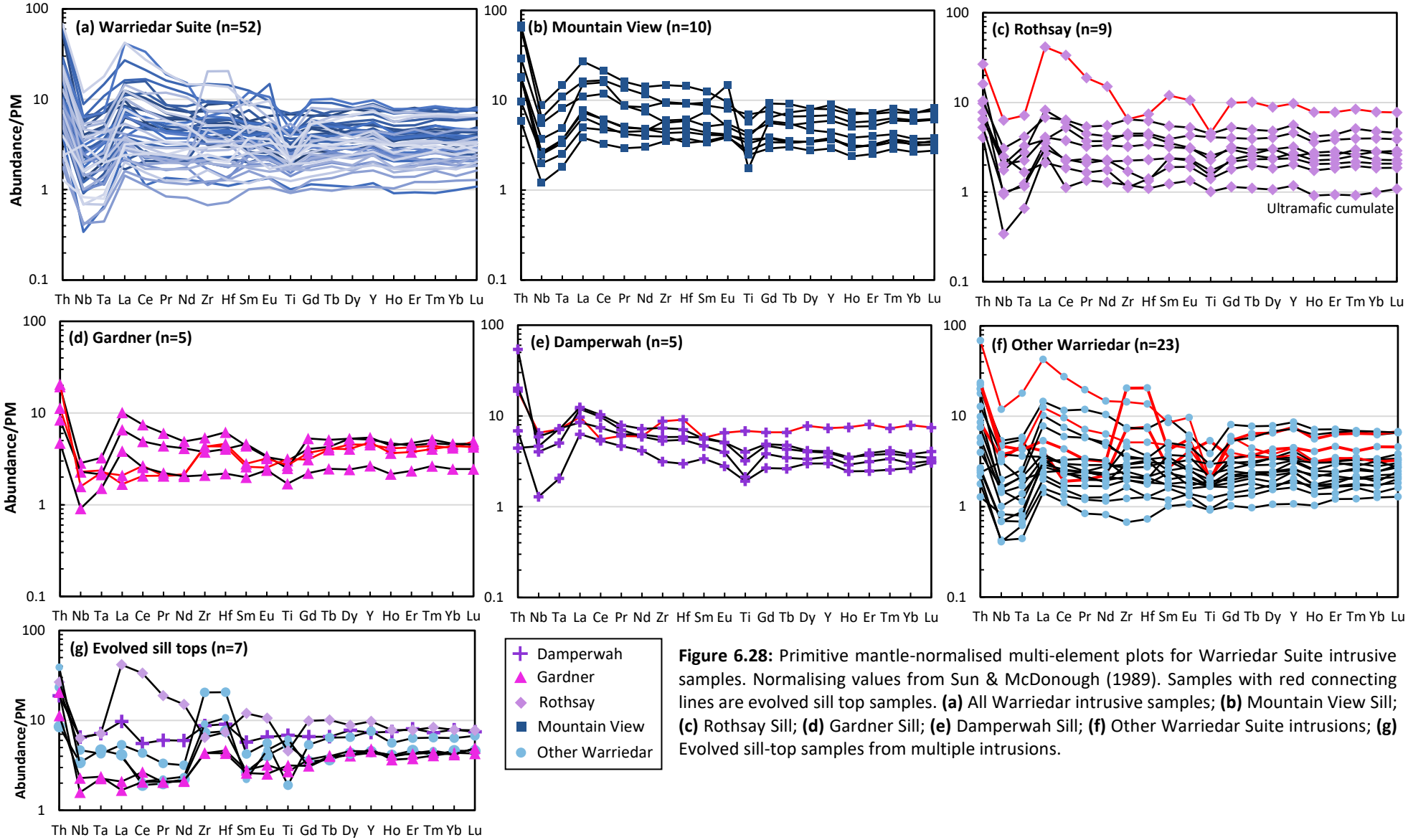

Figure 6.28: Primitive mantle-normalised multi-element plots for Warriedar Suite intrusive samples. Normalising values from Sun & McDonough (1989). Samples with red connecting lines are evolved sill top samples. **(a)** All Warriedar intrusive samples; **(b)** Mountain View Sill; **(c)** Rothsay Sill; **(d)** Gardner Sill; **(e)** Damperwah Sill; **(f)** Other Warriedar Suite intrusions; **(g)** Evolved sill-top samples from multiple intrusions.

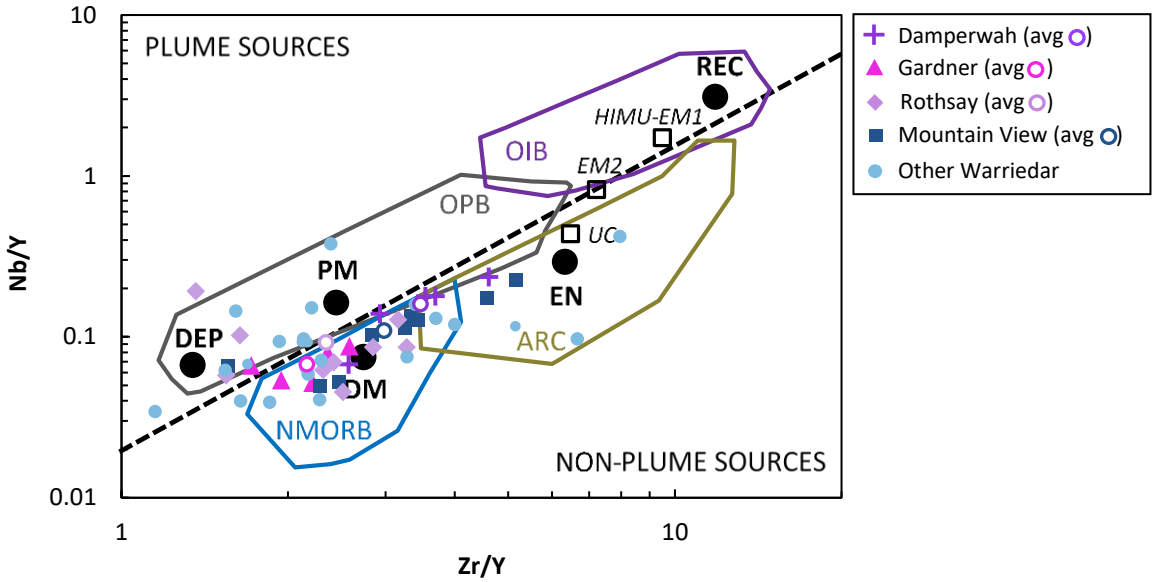

Figure 6.29: Nb/Y vs. Zr/Y diagram for Warriedar Suite intrusive samples. End member compositions and field boundaries from Condie (2005). Abbreviations as in Figure 6.11.

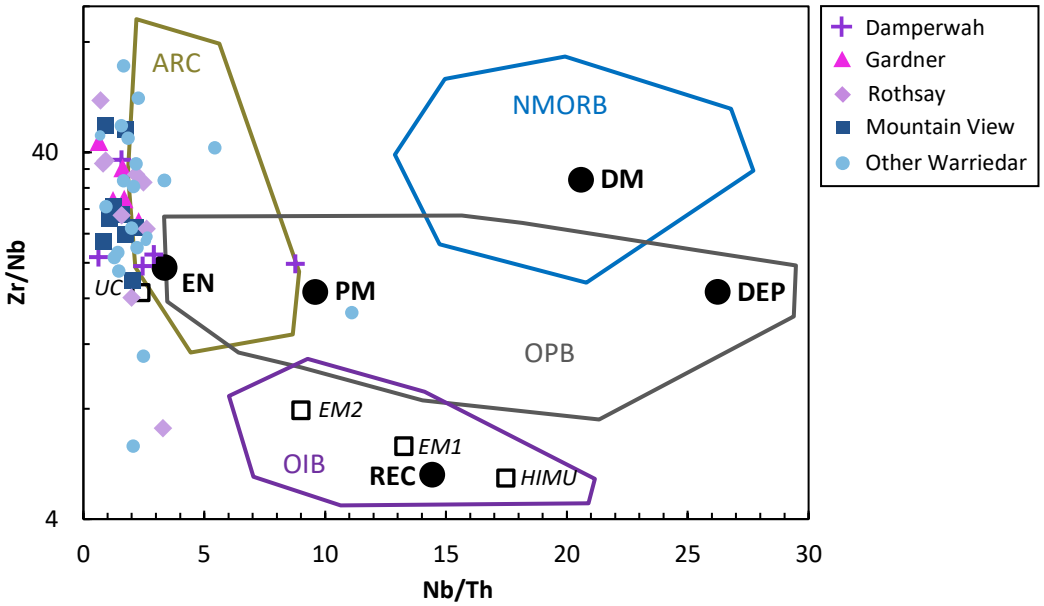

Figure 6.30: Zr/Nb vs. Nb/Th diagram for Warriedar Suite intrusive samples. End member compositions and field boundaries from Condie (2005). Abbreviations as in Figure 6.11.

The trace element pattern displayed by evolved sill tops, typically composed of (quartz) diorite or granophyric dolerite, is distinct from other samples in the Warriedar Suite, in that they have significant Zr-Hf anomalies (Fig. 6.27). Of the seven 'sill-top' samples (from 5 separate intrusions), six show positively sloping patterns with strongly positive Zr-Hf anomalies (at Zr/Zr* values of 1.49-5.58), combined with variable Ti anomalies (Ti/Ti* = 0.37-2.11) and relatively shallow negative Nb anomalies (Nb/Nb* = 0.24-0.57) (Fig. 6.28). In contrast, one sample displays a negatively sloping pattern with a prominent negative Zr-Hf anomaly (Zr/Zr* = 0.48), along with a negative Ti anomaly (Ti/Ti* = 0.41) and a more negative Nb-Ta anomaly (Nb/Nb* = 0.19).

On a Nb/Y vs. Zr/Y diagram (Fig. 6.29), most Warriedar Suite intrusive samples plot on an array of increasing Nb/Y with Zr/Y in the normal MORB field, with a few samples in the arc-related field. Twelve samples plot on the 'plume sources' portion of the diagram, within the oceanic plateau basalt field. The average compositions of the four individual Warriedar intrusions described in this study show less variation and define a linear trend that straddles the boundary between non-plume and plume sources and lie primarily in the normal MORB field. On a Zr/Nb vs. Nb/Th diagram (Fig. 6.30), Warriedar Suite samples generally plot to the left and at the margins of the arc-related basalt field, with two samples in the oceanic plateau basalt field. This distribution is like that for both Chulaar Group and Mougooderra Fm volcanic rocks.

6.4.4 Summary of Geochemical Results

This section has presented the geochemistry of the main geochemical groups that constitute the volcanic and intrusive stratigraphy of the YSGB, using a combination of data analysed by this study and collated from previous work.

Four distinct geochemical subgroups have been distinguished within volcanic rocks of the Chulaar Group, which also correspond to different stratigraphic levels. The geochemical features of each of these subgroups are summarised in Table 6.3. The stratigraphically lowermost Chulaar Subgroup 1 volcanic rocks are typically porphyritic and possess markedly enriched LREE and depleted HREE, corresponding to steep patterns on mantle-normalised multi-element plots. Subgroup 2 is typified by

	CHULAAR GROUP				MOUGOODERRA FORMATION		WILLOW-BANK CLASTICS	WARRIEDAR SUITE *(n=52)*
	Subgroup 1 *(n=4)*	**Subgroup 2** *(n=30)*	**Subgroup 3** *(n=30)*	**Subgroup 4** *(n=5)*	**Volcanics** *(n=6)*	**Volcanic-lastics** *(n=2)*	**Volcanic-lastics** *(n=6)*	
MgO (wt. %)	1.6-5.5	7.0-16.2	4.3-15.0	12.0-15.3	5.8-10.8	<0.1	<0.2	1.8-34.7
$Fe_2O_3^T$ (wt. %)	4.4-10.4	7.9-14.6	8.6-18.2	10.7-12.1	9.0-15.8	0.1-0.5	0.2-1.8	3.2-19.6
Mg#	42-58	55-74	38-73	67-73	42-70	-	-	30-84
SiO_2 (wt. %)	61.1-66.9	48.0-58.6	49.8-58.0	51.3-57.7	54.3-67.4	83.4-87.2	67.2-82.6	43.8-67.1
TiO_2 (wt. %)	0.5-0.9	0.4-0.9	0.5-1.2	0.4-0.5	0.4-0.6	0.4-0.5	0.3-0.8	0.2-1.5
Cr (ppm)	13-212	60-1879	22-1884	789-2121	636-2350	57-160	20-348	1-3953
Zr (ppm)	96-230	26-68	49-139	32-39	58-99	105-128	133-392	8-229
Av. $(La/Sm)_{CN}$	4.1	1.2	1.9	1.3	2.5	5.8	6.4	1.7
Av. $(Gd/Yb)_{CN}$	2.5	0.9	1.3	1.0	1.1	1.2	1.3	1.1
Av. Eu/Eu*	0.9	1.0	0.9	1.0	0.9	1.0	1.0	1.0
Av. Ti/Ti*	0.4	0.8	0.7	0.7	0.6	0.5	1.1	0.8
Av. Nb/Nb*	0.1	0.4	0.3	0.3	0.3	0.2	0.3	0.3

Table 6.3: Summary of the geochemical features of each of the geochemical groups studied.

low Zr contents, broadly flat trace element patterns and many samples display a slight convex pattern for LREE-MREE. In contrast, overlying Subgroup 3 Chulaar volcanics are characterised by LREE enrichment and more elevated Zr than Subgroup 2, and the uppermost Subgroup 4 volcanic rocks comprise flat trace element patterns, with consistently elevated MgO contents (12.0-15.3 wt. %) and low TiO_2 contents (0.4-0.5 wt. %). The dearth of rocks that geochemically classify as komatiite within the Chulaar Group (MgO up to 16.2 wt.%), despite the abundance of pyroxene spinifex in Subgroup 3 and Subgroup 4 rocks (see Chapter 5), is notable.

The Mougooderra Fm volcanic rocks, representing the uppermost volcanic rocks in the study area, differ from Chulaar Group volcanic rocks in that they have combined high MgO content (6-11 wt.%) and high SiO_2 content (54-67 wt. %), with elevated Cr (up to 2350 ppm) and variable LREE enrichment (Table 6.3). Mougooderra Fm volcaniclastic rocks plot on similar trends to Mougooderra Fm volcanics, consistent with them belonging to same cogenetic formation. Felsic volcaniclastic rocks of the Willowbank Clastics show consistent geochemical features and some compositional similarity with Mougooderra Fm volcaniclastic rocks.

Warriedar Suite intrusive samples show significant compositional variability in both major and trace elements, including MgO contents between 2-35 wt. % and SiO_2 contents between 44-67 wt. %, consistent with the layered and fractionated nature of many of the intrusions that comprise the group. Collectively, Warriedar Suite intrusions display similar geochemical trends and features, such as the flat to LREE-enriched trace element patterns and ubiquitous negative Ti and Nb-Ta anomalies. Despite the significant range in trace element concentrations corresponding to compositional layering within the sills, the average normalised patterns of individual intrusions remain remarkably consistent. Highly evolved sill tops display unusual positive Zr-Hf anomalies, combined with less negative Nb-Ta anomalies and LREE depletion.

CHAPTER 7

Interpretation of geochemical results

7.1 Introduction

In this chapter, the geochemical data presented in Chapter 6 are discussed and evaluated in order to establish the petrogenetic origin and evolution of volcanic and intrusive rocks in the Yalgoo-Singleton Greenstone Belt (YSGB). The discussion starts with an assessment of significant trace element anomalies, including negative Nb-Ta and Ti anomalies in all volcanic and intrusive rocks studied, and the markedly positive Zr-Hf anomalies exhibited by Warriedar Suite sill top samples.

The melting conditions (compositions, temperatures and pressures) of predicted primary magmas responsible for the magmatic groups reported in this study are then evaluated, using spreadsheet models developed by Herzberg & Asimow (2015; PRIMELT3) and Lee et al. (2009; FRACTIONATE-PT). Processes that may have affected the geochemistry of the rocks are then examined, initially focussing on the operation and prevalence of fractional crystallisation. Major and trace element variations exhibited by YSGB rocks are investigated using a range of petrogenetic models, to assess the conditions under which parental magmas evolved in the crust. For major element data, the rhyolite-MELTS program (Gualda et al. 2012; Ghiorso & Gualda, 2015) is used to produce fractional crystallisation models at different conditions, the results of which are used in part to undertake further modelling of trace element concentrations. Furthermore, assimilation-fractional crystallisation (AFC) modelling is undertaken using PETROMODELLER software of Ersoy (2013), to assess whether trace element trends display evidence of AFC processes.

This is followed by a more thorough assessment of crustal contamination in the magmatic suites studied, including the calculation of incompatible trace element ratios, plotting of ratio-ratio plots including the Th/Yb vs Nb/Yb diagram of Pearce (2008), and modelling of contamination. Volcanic rocks of the Chulaar Group and Mougooderra Fm are then classified according to the recent discrimination diagrams of Pearce & Reagan (2019). This allows a more thorough classification of high-Mg volcanic rocks and is used to evaluate whether boninite-like rocks occur in the study area, as has recently been reported elsewhere in the Murchison Domain (e.g., Wyman, 2019). A geochemical comparison is undertaken between the rocks studied and other magmatic suites in the Murchison

Domain, in order to identify comparable rocks and the potential extents of magmatism. Finally, the origin of the unusual highly positive Zr-Hf anomalies in Warriedar Suite sill top samples is discussed.

7.2 Overview of Trace Element Anomalies

Chulaar Group and Mougooderra Fm volcanic rocks, and intrusive samples from the Warriedar Suite, display ubiquitous negative Nb-Ta and Ti anomalies, relative to HFSE and LREE. For Chulaar Subgroup 2 and Subgroup 3 rocks, these anomalies are consistently exhibited by the most compositionally primitive samples, which on the basis of high MgO (>12.0 wt.%) contents and no petrographic evidence of pyroxene or plagioclase fractionation (Chapter 5), can be considered the closest approximation of the parental melts for these groups. Field and petrographic evidence indicate that Warriedar Suite intrusions represent fractionated magmatic bodies and that the layered portions of these intrusions correspond to the products of in situ fractional crystallisation. Notably, samples from all lithologies except from leucogabbroic sill tops, including olivine cumulates, pyroxenite, gabbro and dolerite, display negative Nb-Ta and Ti anomalies. Comparable anomalies have been recorded in differentiated layered sills of the 2.97 Ga Fiskenæsset Complex, western Greenland and are attributed to parental magma compositions rather than fractionation processes (Polat et al., 2009).

In Phanerozoic rocks, coupled negative Nb-Ta and Ti anomalies are widely regarded to be diagnostic features of subduction-related magmatism (Murphy, 2007; Pearce, 2008). In Archaean rocks, these signatures are also commonly attributed to magmas derived in a subduction-like setting, either synchronous with a subduction-like process, or from melting of a previously subduction-modified mantle source (Pearce, 2008; Van Hunen & Moyen, 2012). An alternative mechanism to explain these anomalies involves contamination of mantle-derived magmas by Archaean crust (which contains moderate negative Nb-Ta and Ti anomalies) (Moyen & Laurent, 2018). The manner in which the most primitive Chulaar Group and Warriedar Suite samples exhibit ubiquitous Nb-Ta and Ti depletions, and the absence of a systematic increase in the magnitude of these anomalies with decreasing MgO content, suggests that these anomalies did not result from extensive crustal contamination of mantle-derived magmas. Instead, these depletions were most likely inherent features of the source(s) of parental magmas(s) from which Chulaar Group and Warriedar Suite rocks were derived.

The uppermost portions of Warriedar Suite intrusions typically consist of a thin (<30 m) interval of leucogabbro or quartz diorite (Section 5.6.4). Primitive-mantle normalised trends of six sill top samples from four separate intrusions display Zr-Hf anomalies that are typically markedly positive ($Zr/Zr^* = 1.49$-5.58) and are accompanied by relatively flat to slight depletions in Nb-Ta and LREE, unlike ubiquitous Nb-Ta depletions and LREE enrichment in other Warriedar Suite units. There are several

potential explanations for these anomalies in sill top samples. Firstly, positive Zr-Hf anomalies could reflect intense secondary alteration, such as weathering and/or hydrothermal alteration, whereby residual zircon (host to Zr and Hf) enables the effective enrichment of Zr-Hf relative to the LREE (Nesbitt, 1979). However, sill top samples are relatively fresh and unaltered and contain upper greenschist to lower amphibolite facies metamorphic assemblages that typify Warriedar Suite rocks, suggesting that alteration is not responsible for these features.

An alternative, logical explanation is that the positive Zr-Hf anomalies signify enhanced zircon crystallisation in the late-stage, incompatible element-enriched and highly evolved magmas located at the top of the intrusions, derived from in situ fractional crystallisation. This is supported by petrographic analysis of sill top samples, several of which contain large (>200 μm), euhedral crystals of zircon (Section 5.6.4). Alternatively, positive Zr-Hf anomalies could reflect crustal contamination of Warriedar Suite magmas, as Archaean felsic crust is enriched in Zr & Hf (Rudnick & Fountain, 1995). Geochronological analysis of a Warriedar Suite sill top sample in the study area (Lu et al., 2016b) identified a single age population of primary magmatic zircon crystals, precluding the possibility of inherited zircon xenocrysts into magmas during crystal contamination accounting for Zr-Hf anomalies (e.g., Hansmann & Oberli, 1991). Modelling has been undertaken to assess the extents of fractional crystallisation (Section 7.4.4) and contamination (Section 7.5.4) in Warriedar Suite rocks, and to evaluate whether either process can adequately account for the Zr-Hf anomalies in sill top samples.

7.3 Primary Magma Characteristics

7.3.1 Introduction

In this section, the melting conditions of primary magmas for igneous rocks in the study area are determined. A primary magma refers to an undifferentiated magma that formed directly from melting of the upper mantle (e.g., O'Hara, 1965). The potential composition(s) of a primary magma provides crucial insights into the petrogenetic development of the resulting rocks. The *PRIMELT3* spreadsheet program (Herzberg & Asimow, 2015) and the *Fractionate-PT* spreadsheet program (Lee et al., 2009) are used to calculate primary magma compositions, in addition to estimations of the temperatures and pressures under which they formed.

PRIMELT3 is a spreadsheet program developed by Herzberg & Asimow (2015) that can be used to calculate primary magma compositions by inputting the composition of evolved lavas, using both batch and accumulated fractional melting of fertile peridotite and a combination of forward and inverse modelling (Herzberg & Asimow, 2015). Forward modelling uses mass balance solutions to calculate the composition and amount of partial melting required to form magmas from a fertile

mantle peridotite source at a range of temperatures and pressures [based on the composition of partial melts derived from fertile mantle peridotite KR-4003 (Walter, 1998)]. The inverse modelling attempts to produce estimated compositions of potential primary magmas from a primitive lava composition, through the sequential incremental addition and subtraction of olivine. PRIMELT3 presents a potential primary magma for an evolved lava when the composition derived from forward modelling matches a composition derived from inverse modelling of olivine addition and/or subtraction (Herzberg & Asimow, 2015). PRIMELT3 also calculates a mantle potential temperature (T_P) for successful solutions and gives an indication of the source rock residuum (Herzberg & Asimow, 2008).

The FRACTIONATE-PT program of Lee et al. (2009) uses a silica activity thermobarometer and calculations based on Si and Mg contents to calculate primary magma compositions. The program assumes that the melt is derived from an olivine- and orthopyroxene- bearing source and also undertakes a fractionation correction through the incremental addition of olivine to the input sample composition. FRACTIONATE-PT computes thermobarometric results for successful primary magma solutions in the form of T_P and pressure values (Lee et al., 2009).

Unfortunately, both PRIMELT3 and FRACTIONATE-PT programs are only applicable to rocks that formed from olivine-bearing sources and cannot compute reliable primary magma solutions for pyroxenite sources (Lee et al., 2009; Herzberg & Asimow, 2015). A further pitfall of both programs is that they can only successfully calculate solutions for rocks that have undergone olivine fractionation or accumulation, and cannot determine primary magmas for rocks that have fractionated or accumulated other phases (i.e., clinopyroxene or plagioclase). In general, mafic volcanic and intrusive rocks that constitute Archaean supracrustal belts are frequently shown to have fractionated clinopyroxene and plagioclase, in addition to olivine (e.g., Van Kranendonk et al., 2013; Lowrey et al., 2020). Consequently, it can be difficult to find primitive volcanic and intrusive rocks that have only fractionated olivine. Due to the significant range in MgO contents (1.6 to >16.0 wt. %), the occurrence of plagioclase and (pseudomorphed) clinopyroxene phenocrysts in some samples (Section 5.3.2), and petrographic evidence of cumulate plagioclase and clinopyroxene in some Warriedar Suite rocks (Section 5.6), only a fraction of samples in this study are suitable for the calculations described above.

Volcanic rocks from the Chulaar Group and intrusive rocks from the Warriedar Suite have been considered for analysis using PRIMELT3 and FRACTIONATE-PT programs. Samples that contain plagioclase and/or clinopyroxene phenocrysts, display Eu anomalies, exhibit cumulate textures or elevated amounts of secondary alteration (Chapter 5) have not been used as they are not suitable for analysis. As all Mougooderra Fm samples and Chulaar Subgroup 1 samples invariably contain plagioclase phenocrysts, it was not possible to calculate primary magma compositions for these rocks.

For all samples tested, an $Fe^{2+}/\Sigma Fe$ ratio of 0.9 has been used. In total, modelling using PRIMELT3 resulted in the calculation of primary magmas for 4 samples, whereas modelling using FRACTIONATE-PT successfully calculated primary magmas for 21 samples, including 3 of those modelled by PRIMELT3. Primary magma compositions and corresponding temperatures and pressures successfully calculated for Chulaar Subgroups 2-4 and Warriedar Suite rocks, are described below.

7.3.2 Chulaar Group

PRIMELT3 was only successful in calculating a primary magma for one Chulaar Group sample (Subgroup 2), using accumulated fractional melting, whereas FRACTIONATE-PT successfully calculated primary magmas for 14 Chulaar Group samples from Subgroups 2, 3 and 4, including the one sample for which PRIMELT3 obtained a primary magma (Table 7.1).

For Subgroup 2 samples, the MgO contents of calculated primary magmas varies between 15.9-18.3 wt. % for FRACTIONATE-PT and is more elevated at 20.4 wt. % for PRIMELT3 (Table 7.1). The single successful PRIMELT3 primary magma was derived from 34.6% melting of a fertile peridotite source, signifying extensive melting, in addition to 21.3% cumulate olivine addition. For Subgroup 3 samples, primary magmas have MgO contents between 17.0-19.9 wt.% MgO, which overlap with calculated Subgroup 4 primary magmas, which have MgO contents between 17.0-19.0 wt.% (Table 7.1).

Calculated T_P values for Chulaar Subgroup 2 rocks range between 1434-1538 °C for FRACTIONATE-PT solutions and is significantly higher at 1572 °C for the single PRIMELT3 solution (Table 7.3). Corresponding pressures for Subgroup 2 show considerable variation between 0.89-2.70 GPa. T_P values for Subgroup 3 rocks range between 1441-1558 °C and appear to be slightly more elevated than Subgroup 2, with calculated pressures in the range 1.1-2.5 GPa. The calculated T_P values for Subgroup 4 primary magmas are well constrained at 1472-1514 °C, corresponding to pressures of 1.58-1.69 GPa (Table 7.3). The calculated temperatures for Chulaar Group parental magmas are significantly higher than modern non-arc mantle potential temperatures (~1350 °C; Lee et al., 2009), but are in agreement with maximum mantle potential temperatures of 1500-1600 °C between 2.5-3.0 Ga (Herzberg et al., 2010). There is no consistent trend between calculated T_P and pressures of primary magmas and stratigraphic height within the succession, with the uppermost Chulaar Subgroup 4 volcanic rocks displaying T_P and pressures within the range of Chulaar Subgroup 3 and the stratigraphically lower Chulaar Subgroup 2 rocks.

Whereas compositions produced by the two models are broadly similar, MgO contents calculated by the FRACTIONATE-PT model are consistently ~2.3 wt.% lower than PRIMELT3, as noted in previous geochemical studies (e.g., Phillips, 2017). This results in the calculation of higher T_P values for samples entered into the PRIMELT3 model, compared to the same samples using the FRACTIONATE-PT model.

Sample	**MUL015**	**ROTH068**	**ROTH005**	**BAD015**	**BAD010**		**BAD001a**	**ROTH054**	**CHU001**	**MUL016**	**CHU001a**	**ROTH010**	**MUL009**	**MUL019**	**MUL018**
Rock type	Basalt	Spin-basalt	Basalt	Basalt	Basalt		Spin-basalt	Basalt	Basalt	Basalt	Basalt	Spin-basalt	Spin-basalt	Spin-basalt	Spin-basalt
Group	CG 2	CG 2	CG 2	CG 2	CG 2		CG 3	CG 3	CG 3	CG 3	CG 3	CG 4	CG 4	CG 4	CG 4
Program	*FRAC-PT*	*FRAC-PT*	*FRAC-PT*	*FRAC-PT*	*PRIMELT3 (FM)*	*FRAC-PT*	*FRAC-PT*	*FRAC-PT*	*FRAC-PT*	*FRAC-PT*	*FRAC-PT*	*FRAC-PT*	*FRAC-PT*	*FRAC-PT*	*FRAC-PT*
SiO_2 (wt. %)	51.66	53.63	47.47	52.60	47.68	48.27	53.91	49.99	50.78	48.58	50.00	50.95	51.04	51.38	51.29
TiO_2	0.37	0.64	0.41	0.55	0.35	0.38	0.44	0.57	0.63	0.56	0.58	0.36	0.39	0.38	0.41
Al_2O_3	9.78	9.53	9.23	8.36	9.09	9.75	9.78	8.51	8.73	9.09	9.07	8.37	9.36	9.14	9.40
FeO	10.14	10.88	11.04	10.80	10.23	11.02	10.16	11.11	11.90	11.78	12.55	10.26	11.06	10.96	11.33
Fe_2O_3	0.49	0.51	0.56	0.59	1.04	0.56	0.56	0.52	0.55	0.59	0.55	0.56	0.54	0.58	0.59
MnO	0.16	0.13	0.21	0.15	0.16	0.15	0.15	0.20	0.15	0.14	0.14	0.20	0.15	0.16	0.15
MgO	15.89	17.24	18.16	18.29	20.35	18.17	16.95	17.56	19.03	19.55	19.86	16.97	17.72	18.33	18.97
CaO	9.34	6.61	10.77	6.46	9.67	10.35	5.38	10.74	5.91	8.27	5.17	10.07	7.80	7.39	6.34
Na_2O	2.07	0.73	1.75	1.82	0.92	0.99	2.40	0.46	2.17	1.11	1.86	1.87	1.79	1.44	1.31
K_2O	0.01	0.05	0.20	0.10	0.21	0.22	0.02	0.14	0.08	0.15	0.10	0.09	0.05	0.02	0.03
X_{Fo}	90.0	90.0	90.0	90.0	92.1	90.0	90.0	90.0	90.0	90.0	90.0	90.0	90.0	90.0	90.0
%ol add					21.29										
%melt					34.60										

Table 7.1: Primary magma compositions calculated for volcanic rocks of the Chulaar Group (CG 2 = Subgroup 2, CG 3 = Subgroup 3, CG 4 = Subgroup 4) using PRIMELT3 software (Herzberg & Asimow, 2015) and FRACTIONATE-PT software (Lee et al., 2009). All major oxides are given in wt. %. FM corresponds to accumulated fractional melting in the PRIMELT3 software. X_{FO} represents the composition of liquidus olivine that coexists with the primary liquid. %ol add represents the mass fraction of olivine added to the original sample composition to find the primary magma composition and %melt corresponds to the calculated percentage of accumulated fractional melting; these values are only calculated by the PRIMELT3 software.

Sample	ROTH078	ROTH067	MUL011		ROTH059	MUL013	ROTH007	BAD003	ROTH017	
Group	Dolerite WS	Dolerite WS	Dolerite WS		Dolerite WS	Dolerite WS	Pyroxenite WS	Dolerite WS	Dolerite WS	
Program	*FRAC-PT*	*FRAC-PT*	*PRIMELT3 (FM)*	*FRAC-PT*	*PRIMELT3 (FM)*	*FRAC-PT*	*FRAC-PT*	*FRAC-PT*	*PRIMELT3 (FM)*	*FRAC-PT*
SiO_2	54.27	50.57	49.47	50.19	51.84	51.11	49.39	49.51	47.23	47.80
TiO_2	0.29	0.47	0.29	0.31	0.30	0.35	0.38	0.36	0.40	0.43
Al_2O_3	9.49	12.95	10.78	11.57	10.86	6.55	7.77	9.81	8.83	9.49
Cr_2O_3			0.02		0.02				0.18	
FeO	8.51	9.63	0.90	9.79	0.79	9.71	9.63	10.86	1.05	11.18
Fe_2O_3	0.47	0.49	9.29	0.48	8.62	0.55	0.57	0.53	10.35	0.56
MnO	0.14	0.13	0.16	0.14	0.15	0.16	0.16	0.14	0.16	0.15
MgO	13.54	15.15	17.60	15.33	16.16	16.17	16.45	17.21	20.45	18.26
CaO	11.69	9.26	9.84	10.53	9.80	14.03	14.11	10.14	9.63	10.32
Na_2O	1.33	1.19	1.37	1.47	1.21	1.05	1.06	1.29	1.41	1.51
K_2O	0.10	0.12	0.16	0.17	0.13	0.08	0.11	0.14	0.10	0.11
X_{Fo}	90.0	90.0	91.5	90.0	91.1	90.0	90.0	90.0	92.1	90.0
%ol add			21.78		22.14				22.36	
%melt			31.77		33.83				33.06	

Table 7.2: Primary magma compositions calculated for intrusive rocks of the Warriedar Suite (WS), using PRIMELT3 software (Herzberg & Asimow, 2015) and FRACTIONATE-PT software (Lee et al., 2009). All major oxides are given in wt. %. FM corresponds to accumulated fractional melting in the PRIMELT3 software. X_{FO} represents the composition of liquidus olivine that coexists with the primary liquid. %ol add represents the mass fraction of olivine added to the original sample composition to find the primary magma composition and %melt represents the calculated percentage of accumulated fractional/batch melting; these values are only calculated by the PRIMELT3 software.

Sample No.	Group	PRIMELT3 Temp. (°C)	FRACTIONATE-PT Temp. (°C)	FRACTIONATE-PT Pressure (GPa)
MUL015	CG 2		1434	1.30
ROTH068	CG 2		1452	0.89
BAD015	CG 2		1488	1.45
BAD010	CG 2	1572	1525	2.24
ROTH005	CG 2		1538	2.70
BAD001a	CG 3		1441	1.11
ROTH054	CG 3		1496	1.54
CHU001	CG 3		1521	2.01
CHU001a	CG 3		1549	2.26
MUL016	CG 3		1558	2.50
ROTH010	CG 4		1472	1.58
MUL009	CG 4		1486	1.65
MUL019	CG 4		1499	1.61
MUL018	CG 4		1514	1.69
ROTH078	WS		1359	0.50
ROTH059	WS	1465		
ROTH067	WS		1414	1.21
MUL011	WS	1502	1427	1.36
MUL013	WS		1459	1.15
ROTH007	WS		1478	1.55
BAD003	WS		1487	1.79
ROTH017	WS	1575	1535	2.52

Table 7.3: Pressures and temperatures of primary magmas of the Chulaar Group (CG 2 = Subgroup 2, CG 3 = Subgroup 3, CG 4 = Subgroup 4) and Warriedar Suite (WS), calculated by the PRIMELT3 software (Herzberg & Asimow, 2015) and FRACTIONATE-PT software (Lee et al., 2009). Note that pressures are not calculated directly by the PRIMELT3 software.

7.3.3 Warriedar Suite

PRIMELT3 was able to obtain primary magmas for 3 samples using accumulated fractional melting. FRACTIONATE-PT was able to generate primary magmas for 7 samples, including two of those for which primary magmas were calculated by PRIMELT3. The MgO contents of Warriedar Suite primary magmas vary between 16.2-20.5 wt. % for PRIMELT3 solutions, in contrast to 13.5-18.3 wt. % MgO for FRACTIONATE-PT solutions (Table 7.2). The two samples for which primary magmas were calculated by both PRIMELT3 and FRACTIONATE-PT display broadly similar compositions, however, the MgO content calculated by PRIMELT3 is consistently ~2.3 wt.% higher than that calculated by FRACTIONATE-PT (Table 7.2). For the PRIMELT3 solutions, the three primary magmas were calculated to have been derived from 21.8-22.4% olivine addition and 31.8-33.8 % partial melting.

Calculated T_P for Warriedar Suite primary magmas range between 1359-1535 °C for FRACTIONATE-PT and 1465-1575 °C for PRIMELT3 (Table 7.3). For samples that have calculated T_P values from both models, PRIMELT3 values are typically 40-75 °C higher than those calculated by FRACTIONATE-PT, consistent with the elevated MgO contents calculated by the former. Pressures calculated for Warriedar Suite primary magmas vary significantly between 0.5-2.52 GPa, although a significant majority of the samples have calculated pressures of 1.2-1.8 GPa (Table 7.3).

7.4 Fractional Crystallisation

7.4.1 Introduction

This section examines the significance of fractional crystallisation as a mechanism for producing the geochemical trends observed in YSGB volcanic and intrusive rocks. Several geochemical features described in the magmatic suites studied are consistent with fractional crystallisation; the process by which a cooling magma differentiates into crystals and compositionally evolving liquid. For example, negative Eu anomalies and Ti anomalies observed in Chulaar Group volcanic rocks are indicative of the fractionation of plagioclase and iron oxides, respectively. Similarly, curves and inflections in major and trace element geochemical trends are also demonstrative of fractional crystallisation.

Fractional crystallisation has been modelled using the rhyolite-MELTS program (Gualda et al. 2012; Ghiorso & Gualda, 2015), which, based on the original work of Ghiorso & Sack (1995) and Asimow & Ghiorso (1998), allows users to model a variety of phase relations over a range of temperatures (500-2000 °C) and pressures (0-2 GPa). The software can model fractional crystallisation paths in anhydrous and hydrous mafic magmatic systems and in contrast to its MELTS predecessors, is also calibrated to reliably model crystallisation in silicic magmatic systems (Gualda et al., 2012). The resulting models

can be used to assess the extent and conditions under which fractional crystallisation occurred in the magmatic suites described in this study.

Fractional crystallisation has been modelled for the three magmatic suites that are represented by the most samples: Subgroups 2 and 3 of the Chulaar Group and the Warriedar Suite. These subgroups represent the most voluminous components of the supracrustal stratigraphy and samples display a significant range in major and trace element content. Other geochemical groups representing smaller components of the succession only have a limited sample count (6 or less), which do not display sufficient compositional variation for modelling fractional crystallisation processes. Fractional crystallisation in Chulaar Group volcanic rocks (Subgroups 2 and 3) and Warriedar Suite rocks is modelled using the most primitive samples in each geochemical group (i.e., the sample with combined high MgO content and low incompatible trace element concentrations). The most primitive sample is unlikely to represent the actual composition of the primary magma of each group, however, it is assumed to be the closest estimation during modelling. High-Mg volcanic rocks of the Chulaar Group (MgO up to 15.0 wt. %) are particularly useful in this respect, as their major and trace element content is relatively close to their parental compositions.

Five alternative scenarios have been used to model the major element geochemical trends exhibited by each of the magmatic groups (Table 7.4), employing variable physical parameters as previously used in modelling of Precambrian mafic successions (e.g., Ciborowski, 2013). The conditions assigned to each model are as follows: *Model 1:* anhydrous fractional crystallisation at 1 kbar; *Model 2:* anhydrous fractional crystallisation at 3 kbar; *Model 3:* anhydrous fractional crystallisation at 7 kbar; *Model 4:* anhydrous fractional crystallisation at 10 kbar; *Model 5:* hydrous fractional crystallisation at 1 kbar. All models have used a quartz-fayalite-magnetite oxygen buffer and have calculated the liquid composition at 5 °C cooling intervals from the liquidus temperature.

The model that best fits the major element geochemical trends of each group is then tested further through incompatible trace element modelling. Trace element fractional crystallisation trends are determined using mineral proportions predicted to form by rhyolite-MELTS, literature mineral/melt partition coefficient data (Table 7.5) and equations for calculating bulk distribution coefficients (Equation 7.1) and fractional crystallisation (Equation 7.2).

Model no.	Pressure	H_2O content	Oxygen buffer
Model 1	1 kbar	0%	Quartz-fayalite-magnetite
Model 2	3 kbar	0%	Quartz-fayalite-magnetite
Model 3	7 kbar	0%	Quartz-fayalite-magnetite
Model 4	10 kbar	0%	Quartz-fayalite-magnetite
Model 5	1 kbar	1%	Quartz-fayalite-magnetite

Table 7.4: Physical parameters used during fractional crystallisation modelling of Chulaar Group and Warriedar Suite magmas.

$$D^i = \sum_{j=1}^{n} w_j . Kd_{ij}$$

Equation 7.1, where D^i = the bulk distribution coefficient for element i, w_j = weight proportion of mineral j in the solid assemblage, K_{d_i} = partition coefficient for element i in the mineral j.

$$C_l^i = C_0^i f^{D^i - 1}$$

Equation 7.2, where C_l^i = concentration of element i in evolving liquid, C_0^i = concentration of element i in parent magma, f = residual fraction of parent liquid, D^i = bulk distribution coefficient for element i.

Element	Olivine	Orthopyroxene	Clinopyroxene	Spinel	Plagioclase
Th	0.0000001	0.0004	0.014	0.013	0.3435
Nb	0.0001	0.002825	0.00605	0.01	0.09725
Ta	0.0001	0.002825	0.00605	0.01	0.0795
La	0.000007	0.0000535	0.05025	0.0006	0.0631
Ce	0.00001	0.0026	0.089	0.0006	0.0457
Pr	0.00004	0.0065	0.1335	0.0006	0.1375
Nd	0.00007	0.010267	0.178	0.0006	0.0478
Zr	0.0005	0.01775	0.1975	0.07	0.0094
Hf	0.0038	0.027225	0.2115	0.003	0.082
Sm	0.0007	0.018	0.3775	0.0006	0.06575
Eu	0.00095	0.0215	0.458	0.0006	0.3254
Ti	0.015	0.082	0.3955	0.15	0.0473
Gd	0.002	0.028	0.487	0.0009	0.07175
Tb	0.003	0.035	0.516	0.0012	0.084
Dy	0.004	0.041	0.5455	0.0015	0.057167
Y	0.007365	0.0935	0.412	0.002	0.00989
Ho	0.0065	0.05	0.603	0.00225	0.0592
Er	0.009	0.063917	0.66	0.003	0.07633
Tm	0.015	0.078	0.66	0.00375	0.072
Yb	0.023	0.093917	0.5165	0.0045	0.0903
Lu	0.03	0.1	0.536	0.00525	0.1175

Table 7.5: Mineral/melt partition coefficients for basaltic and basaltic andesitic liquids. Data compiled from the dataset presented by Bedard (2001). See Bedard (2001) for individual data sources.

Mineral/melt partition coefficient data, derived from the dataset presented by Bedard (2001), has been utilised in trace element geochemical modelling. This data has been used as it is applicable to mafic magmatic systems fractionating olivine, clinopyroxene and plagioclase, which on the basis of petrography and rhyolite-MELTS modelling, are understood to have fractionated from the parental magmas of the rocks studied. Partition coefficients in Table 7.5 are experimentally derived and based on anhydrous systems (Bedard, 2001). As such, the application of anhydrous partition coefficient data to the hydrous model used may introduce a source of error into the trace element modelling. However, for the purposes of comparison between alternative models in this study, this partition coefficient data will be used throughout, and results will be treated with a degree of caution.

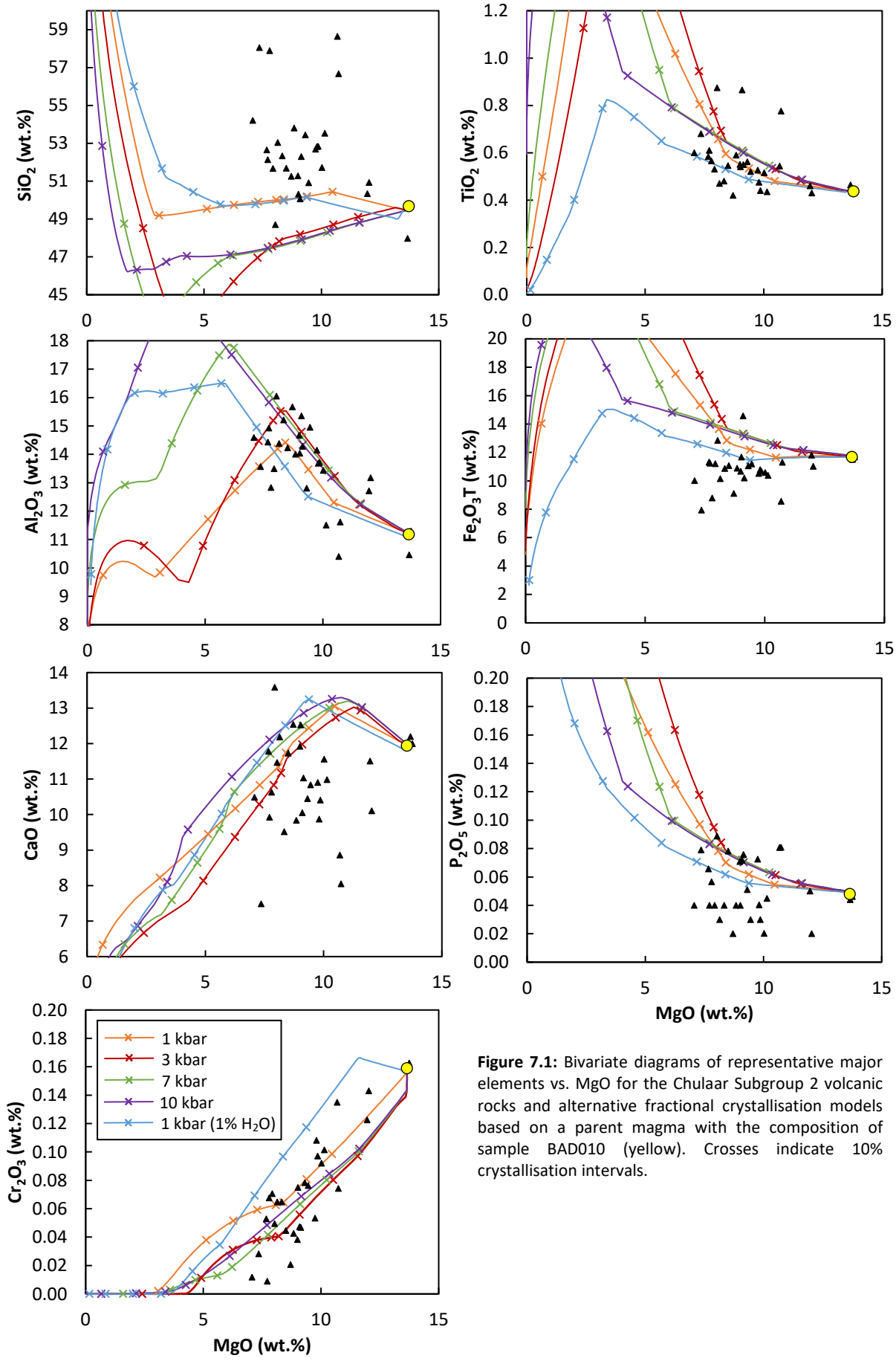

Figure 7.1: Bivariate diagrams of representative major elements vs. MgO for the Chulaar Subgroup 2 volcanic rocks and alternative fractional crystallisation models based on a parent magma with the composition of sample BAD010 (yellow). Crosses indicate 10% crystallisation intervals.

In addition to fractional crystallisation, modelling of assimilation-fractional crystallisation (AFC) has also been attempted for each of the modelled geochemical groups. These models attempt to predict the trace element geochemical evolution of a magma undergoing fractional crystallisation that is accompanied by assimilation of surrounding country rocks (DePaolo, 1981). AFC modelling has been undertaken using PETROMODELLER software (Ersoy, 2013) and utilises mineral proportions predicted to form by rhyolite-MELTS and the mineral/melt partition coefficient data in Table 7.5. The average composition of Archaean felsic crust (Rudnick & Fountain, 1995) is used as the contaminant in AFC modelling, which is a good approximation of the ca. 2.95 Ga felsic volcanic, volcaniclastic and intrusive rocks that outcrop in the study area and are considered to act as the basement to supracrustal rocks across the Murchison Domain (Van Kranendonk & Ivanic, 2009). The 'r value', which denotes the relative ratio of assimilated material to crystallised material, has been selected to best approximate the trace element trends shown by each magmatic suite and occur in the range 0.05-0.25, consistent with previous modelling of Archaean supracrustal rocks in the region (e.g., Lowrey et al., 2020).

7.4.2 Chulaar Subgroup 2

Fractional crystallisation of Chulaar Subgroup 2 volcanic rocks was modelled using a starting composition equivalent to sample BAD010. This sample is considered to be the closest estimate of the parent magma for the subgroup as it has the second highest MgO content (13.75 wt. %), combined with the lowest Zr content (26 ppm) and incompatible trace element content of the samples.

It is not immediately clear which of the models best fits the major element trends displayed by Chulaar Subgroup 2 Chulaar rocks, as no single model consistently replicates the geochemical data (Fig. 7.1). The anhydrous 1 kbar model best explains the trends shown by TiO_2 and Al_2O_3, although the latter is slightly more elevated in the samples than predicted. The hydrous 1 kbar model is the best approximation for the trend shown by Fe_2O_3 and the concentrations of P_2O_5, but does not fit the Cr_2O_3 or Al_2O_3 trends, which are better explained by the anhydrous models (Fig. 7.1). SiO_2 does not form a coherent trend against MgO but is consistently elevated relative to the models and closest to the 1 kbar models. The ambiguous nature of some trends, such as those shown by CaO, SiO_2 and P_2O_5, may be due to secondary alteration, as has been demonstrated both geochemically (Section 6.4.1) and petrographically (Section 5.3) in volcanic rocks in the area. Alternatively, the lack of trends may be due to the limited range in MgO content shown by Subgroup 2 samples (75% of samples in the range 7.1-10.1 wt.% MgO, with no samples < 7.0 wt. % MgO). However, the modelling does support fractional crystallisation at relatively low pressures, as the two models that best approximate the data are the 1 kbar models. On balance, anhydrous 1 kbar fractional crystallisation of a magma with a composition of sample BAD010 is considered to be the closest match for the major element trends as a whole.

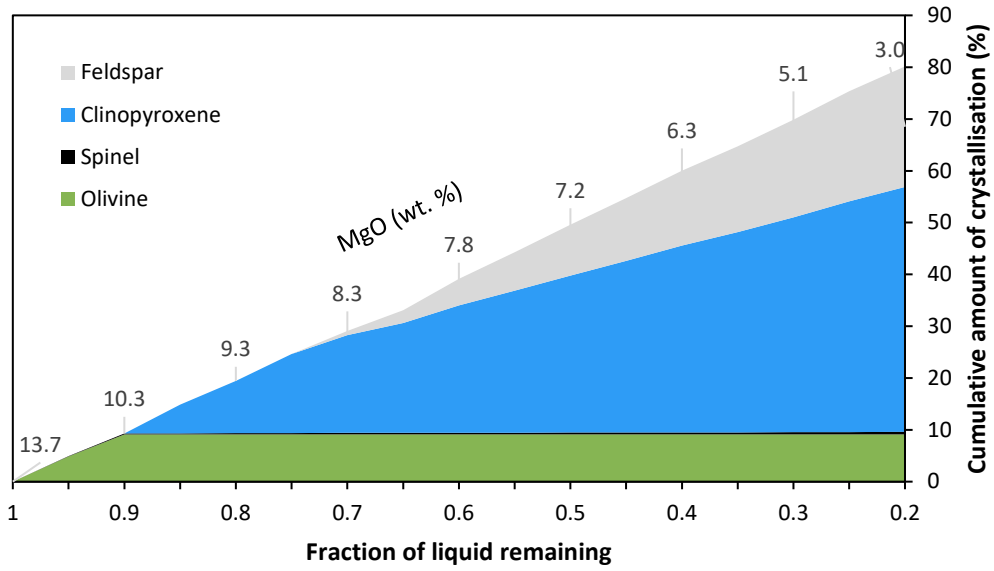

Figure 7.2: A plot of the cumulative crystal proportions predicted to form during fractional crystallisation of the Chulaar Subgroup 2 parental magma based on the BAD010 anhydrous 1 kbar model. The modelled MgO content of the remaining liquid is labelled at each 10% crystallisation interval.

According to the anhydrous 1 kbar model, crystallisation of a primary magma with the composition of sample BAD010 starts at 1315 °C with spinel being the first mineral to crystallise (Fig. 7.2). Olivine starts to fractionate soon after at 1313 °C, after just 0.3% crystallisation. At 1233 °C, olivine is replaced in the crystallising assemblage by clinopyroxene, after 11.2% crystallisation. The final mineral to crystallise is feldspar, at 1207 °C after 27.5% crystallisation. The assemblage comprising spinel, clinopyroxene and feldspar continues to fractionate until the model ends at 80% crystallisation and the magma contains ~2.8 wt. % MgO, which is lower than that of the most evolved Subgroup 2 sample (~7.0 wt. % MgO). The aphyric nature of Chulaar Subgroup 2 rocks means it is not possible to corroborate this fractionating assemblage.

Trace element FC and AFC models for the Chulaar Subgroup 2 samples, using the mineral proportions predicted to form by the 1 kbar anhydrous model and a starting composition equal to sample BAD010, are displayed in Figures 7.3 and 7.4. AFC modelling has utilised an r-value of 0.05 as this best approximates the trace element trends displayed by the subgroup. The Chulaar Subgroup 2 data is generally best replicated by the modelled FC trends, which predicts the increase in incompatible trace element content with progressing crystallisation, and indicates that most samples have undergone less than 40% fractional crystallisation, but several have experienced up to ~60%. The modelled AFC trends do not match the data as closely as FC, apart from Y, which is slightly overestimated by FC modelling and also the decrease in Ti/Ti* with crystallisation, absent in FC modelling (Fig. 7.3). Subgroup 2 samples do not show any systematic changes in $(La/Sm)_N$ or $(Gd/Yb)_N$ with increasing Zr content, but do show a slight increase in $(La/Yb)_N$ as crystallisation progresses, replicated by the FC modelling (Fig. 7.3).

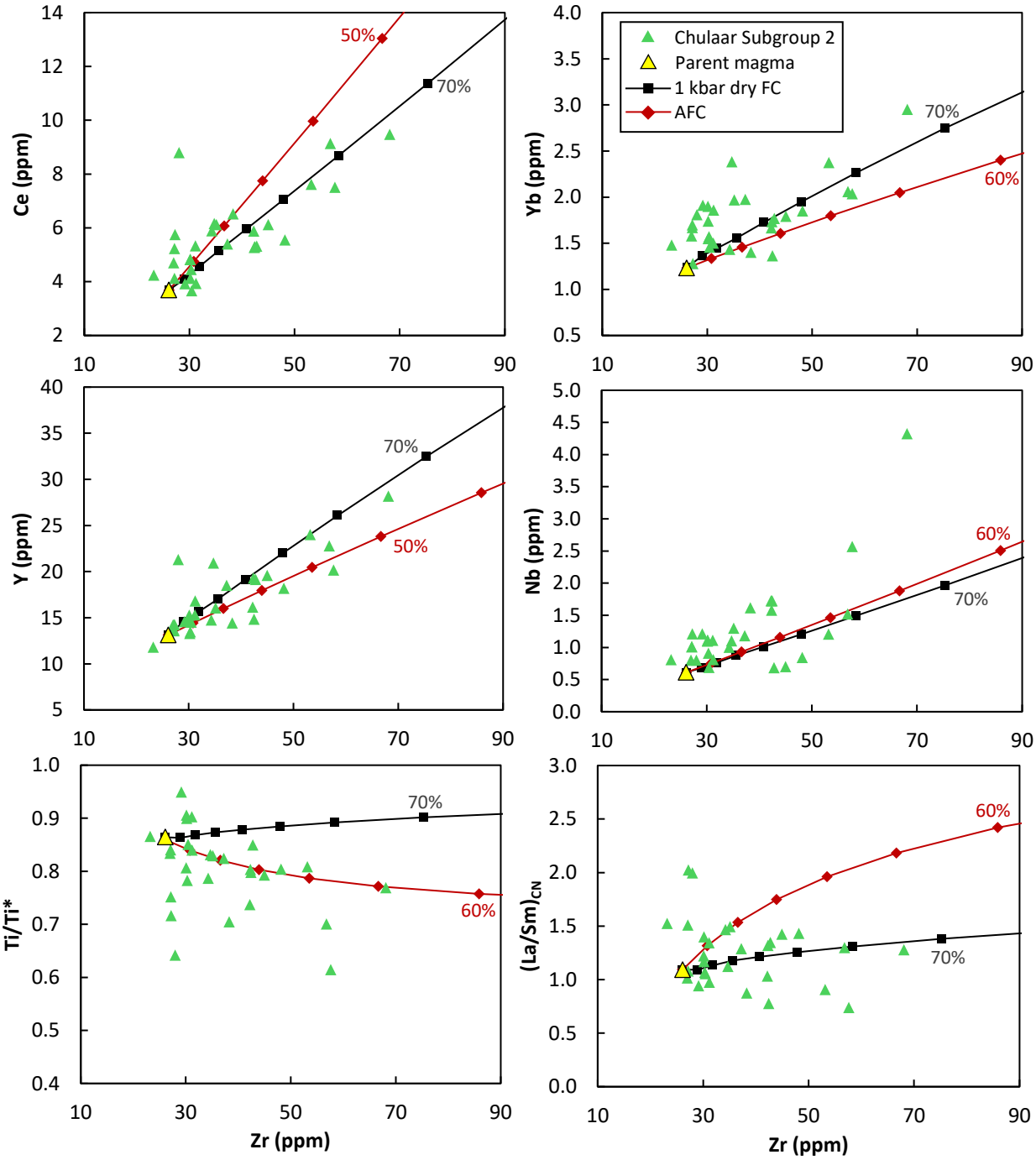

Figure 7.3: Bivariate diagrams of selected trace elements versus MgO for Chulaar Subgroup 2 volcanic rocks, in addition to predicted fractional crystallisation (FC) and AFC model lines for the 1kbar anhydrous model using the starting composition of sample BAD010 and the parameters described in the text. The $(La/Sm)_{CN}$ ratio is normalised to chondrite and Ti/Ti* is calculated using Equation 6.3; normalising values from Sun & McDonough (1989). Markers on model lines are plotted at 10% crystallisation intervals up to 80% crystallisation.

On a primitive mantle-normalised plot (Fig. 7.4), the characteristic flat trend shown by the most incompatible element-enriched Chulaar Subgroup 2 sample is broadly consistent with the ~60 % crystallisation interval predicted by the FC model, albeit with several exceptions. Negative Ti anomalies are more pronounced than predicted by the FC model, which may signify the fractionation of oxides, minor crustal contamination or the operation of AFC. Furthermore, slight positive Eu

anomalies shown by several samples are not predicted, likely attributed to minor plagioclase accumulation, and predicted Th concentrations are consistently elevated relative to Subgroup 2 samples, due to sample BAD010 (the assumed primary magma composition) possessing an anomalously high Th.

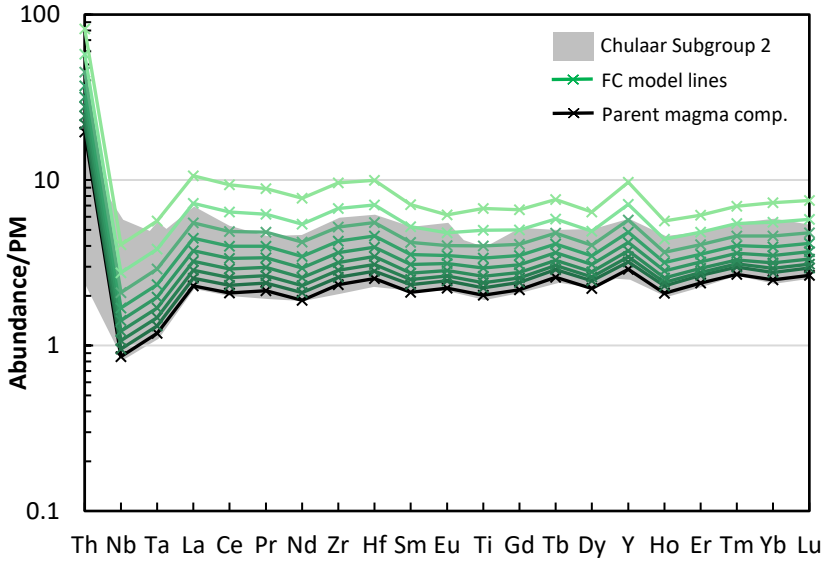

Figure 7.4: Primitive mantle-normalised trace element plot of Chulaar Subgroup 2 rocks (grey field), with model lines drawn based on 1 kbar anhydrous fractional crystallisation of a parent magma with the composition of sample BAD010 (black). Model compositional lines are plotted at 10% crystallisation intervals. Normalising values from Sun & McDonough (1989).

7.4.3 Chulaar Subgroup 3

Sample MUL016 is selected as the best estimate of the parent magma for Chulaar Subgroup 3 volcanic rocks, as it has the second highest MgO content (14.59 wt. %) and the lowest concentrations of incompatible trace elements of the Subgroup 3 rocks sampled. The fractional crystallisation model that best predicts the major element trends of Chulaar Subgroup 3 volcanics is the hydrous 1 kbar model (Fig. 7.5), which generally matches the abundances and trends shown by TiO_2, Al_2O_3, $Fe_2O_3^T$ and P_2O_5 versus MgO. The SiO_2 content of Subgroup 3 samples is consistently elevated relative to all of the models, however the 1 kbar hydrous model is the closest fit to the data. The only trend for which the 1 kbar hydrous model is not the best fit is Cr_2O_3 versus MgO, which generally show a better correlation with the anhydrous models (Fig. 7.5). Abundant variolitic features in Chulaar Subgroup 3 volcanic samples (lower Mulga Volcanics; Section 3.4.1.4) occur at a range of scales (Section 5.3.4) and have been interpreted to reflect H_2O saturation and derivation from a hydrous parental magma (Ballhaus et al., 2015; Lowrey et al., 2020).

According to the hydrous 1 kbar model, crystallisation is predicted to commence at 1329 °C with olivine as the first fractionating mineral (Fig. 7.6). This is followed by spinel crystallisation at 1287 °C after ~5% crystallisation and clinopyroxene replaces olivine in the crystallising assemblage at 1165 °C

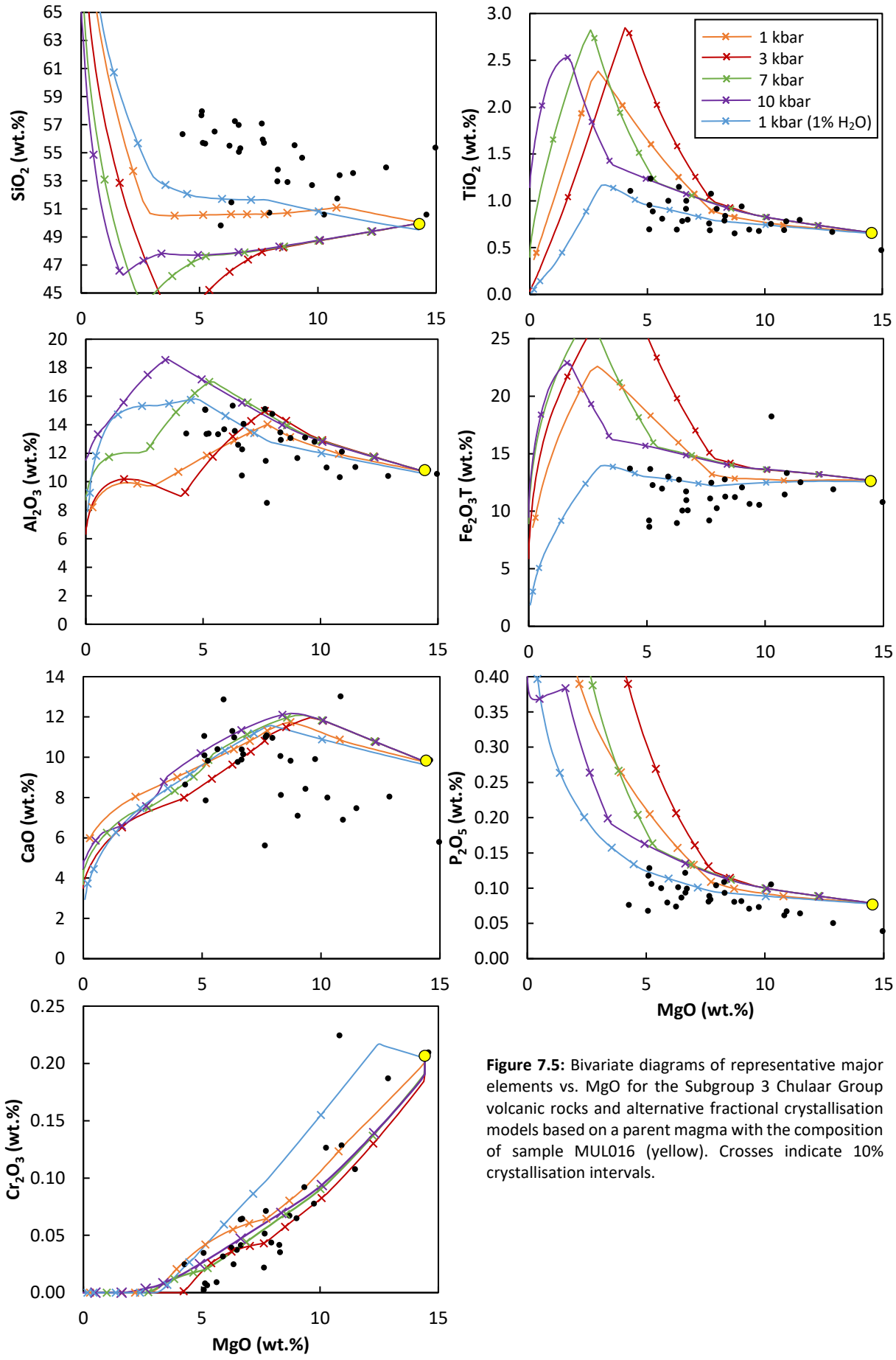

Figure 7.5: Bivariate diagrams of representative major elements vs. MgO for the Subgroup 3 Chulaar Group volcanic rocks and alternative fractional crystallisation models based on a parent magma with the composition of sample MUL016 (yellow). Crosses indicate 10% crystallisation intervals.

after ~18% crystallisation. The final mineral to crystallise is feldspar at 1101 °C after ~39% crystallisation. The combined assemblage of spinel, clinopyroxene and feldspar continues to crystallise to the end of the model at 80% crystallisation, at which point the MgO content of the remaining liquid is ~0.5 wt. %, which is significantly lower than the most evolved Subgroup 3 volcanic rock sampled (4.2 wt. % MgO). This fractionating assemblage is consistent with petrographic analysis (Section 5.3), which identified minor plagioclase phenocrysts and occasional acicular pyroxene phenocrysts within Chulaar Group volcanic rocks. The minor negative Eu anomalies (Eu/Eu* = 0.67-1.06) shown by many Chulaar Subgroup 3 samples are also indicative of plagioclase fractionation prior to eruption.

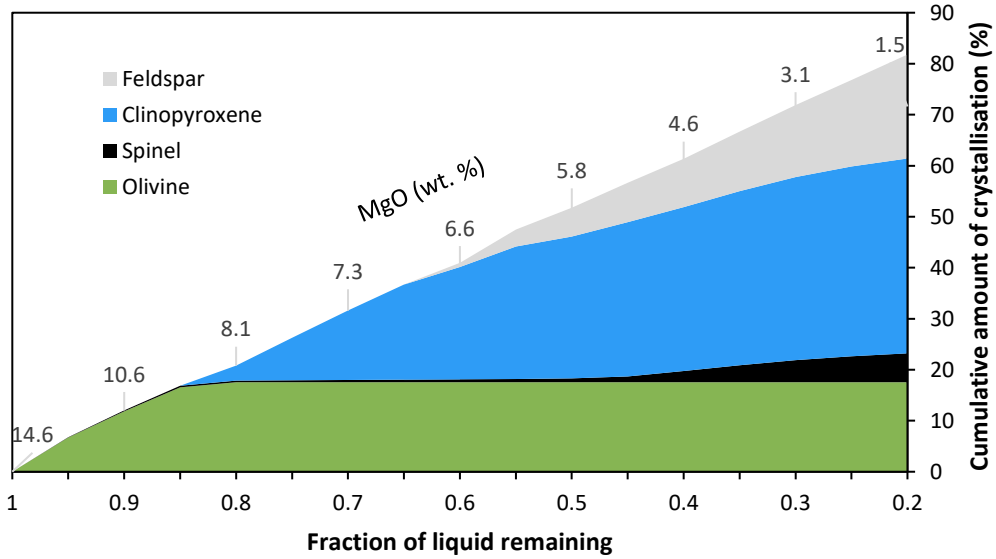

Figure 7.6: A plot of the cumulative crystal proportions predicted to form during fractional crystallisation of the Chulaar Subgroup 3 parental magma based on the MUL016 hydrous 1 kbar model. The modelled MgO content of the remaining liquid is labelled at each 10% crystallisation interval.

The modelled FC and AFC trends of trace elements in Chulaar Subgroup 3 rocks, using the predicted mineral proportions for the MUL016 1 kbar hydrous model, are displayed in Figure 7.7 and Figure 7.8. An r-value of 0.15 has been utilised in AFC modelling as this best approximates the trace element trends shown by Chulaar Subgroup 2 rocks. The modelling unequivocally supports the operation of AFC during evolution of Subgroup 3 rocks, rather than FC. Modelled AFC trends are able to replicate the trends shown by the REE, Y and Nb in Chulaar Subgroup 3 samples, indicating the progressive increase in incompatible trace element content with progressive crystallisation (Fig. 7.7). These successfully modelled trends indicate that up to ~45% AFC has been experienced by the most evolved Chulaar Subgroup 3 rocks. The modelled AFC trends also match the gradual increase in $(La/Sm)_{CN}$ and decrease in Ti/Ti* with further crystallisation, neither of which are displayed by FC trends (Fig. 7.7). However, the trends of several elements are not as closely matched by modelling, most notably Th, which is consistently underestimated by the model at all degrees of crystallisation (Fig. 7.7).

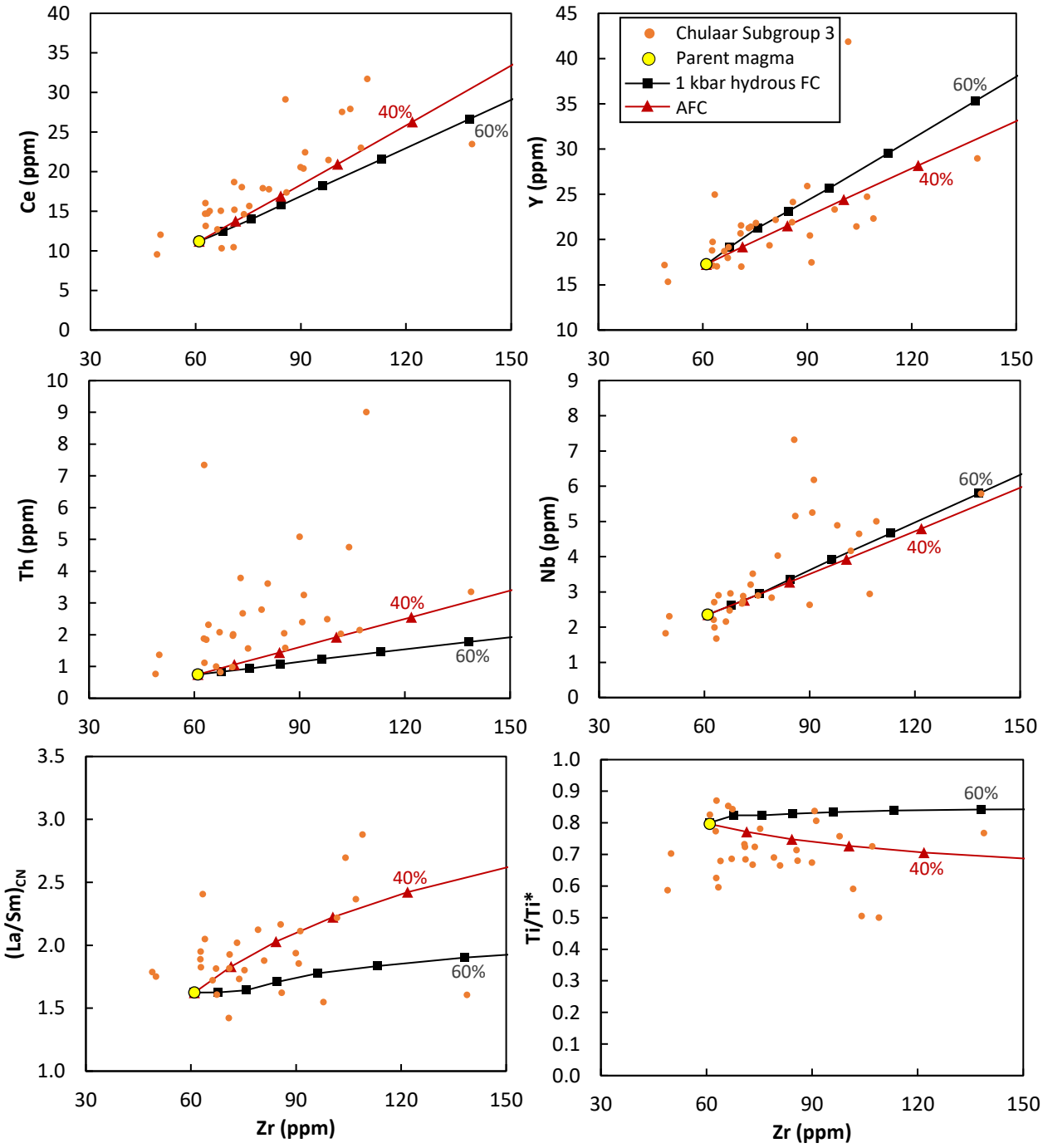

Figure 7.7: Bivariate diagrams of selected trace elements versus MgO for Chulaar Subgroup 3 volcanic rocks, in addition to predicted fractional crystallisation model lines for the 1kbar hydrous model using the starting composition of sample MUL016 and the parameters described in the text. Markers on model lines are plotted at 10% crystallisation intervals up to 80% crystallisation. $(La/Sm)_{CN}$ is normalised to chondrite using normalising values from Sun & McDonough (1989)

For primitive mantle-normalised trace element data, the modelled compositional line for ~50% AFC best matches the trend of the most evolved Chulaar Subgroup 3 samples for much of the REE and LREE enrichment, in addition to the negative Nb-Ta anomalies, elevated Th concentrations and apparent Y anomalies (Fig. 7.8). However, it only partially accounts for the ubiquitous negative Ti anomalies displayed by Chulaar Subgroup 3 samples.

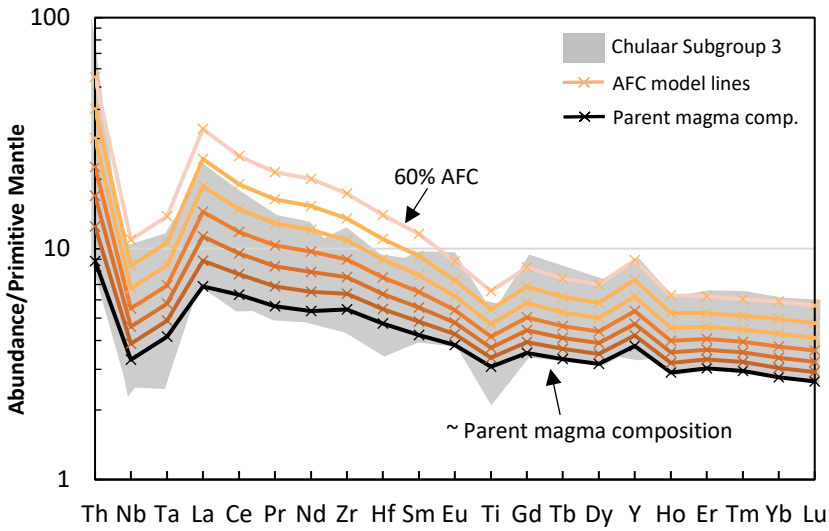

Figure 7.8: Primitive mantle-normalised trace element plot of Chulaar Subgroup 3 rocks (grey field), with model lines drawn based on 1 kbar hydrous AFC of a parent magma with the composition of sample MUL016 (black), using an r-value of 0.15 and the parameters described in the text. Model compositional lines are plotted at 10% crystallisation intervals. Normalising values from Sun & McDonough (1989).

7.4.4 Warriedar Suite

Layered intrusions, such as the Warriedar Suite intrusive sills, represent fractionated magmatic bodies, thus samples taken from their constituent units are unlikely to represent the composition of the parental magma. Instead, parent magma compositions can be estimated from the sampling of fine-grained chilled margins and cogenetic dykes associated with the layered intrusions (e.g., Barnes et al., 2010; Ivanic et al., 2017). Alternatively, parental compositions for an individual layered intrusion can be derived from systematic geochemical sampling of constituent units, followed by summing the compositions of each unit into a weighted average for the whole intrusion (e.g., Ciborowski et al., 2013). Unfortunately, no unaltered chilled margin or cogenetic dyke samples were obtained during fieldwork and as a strategy was employed to sample intrusions across a ~50 km length of the YSGB, a maximum of nine samples was retrieved from an individual Warriedar Suite layered intrusion; this is insufficient for a reliable weighted average composition based on the geometry of mapped intrusions (Section 3.4.2). For these reasons, an alternative method of estimating the parental magma composition is required.

Most non-cumulate Warriedar Suite samples lie on the same, relatively well-constrained geochemical trends on major and trace element diagrams (Section 6.5.3). For the purposes of modelling fractional crystallisation in this study, sample ROTH007 is selected as an estimate of the Warriedar Suite parental magma composition, because this sample has the highest MgO content of any non-cumulate Warriedar Suite rock and lies at the primitive end of geochemical trends on bivariate diagrams. Although sample ROTH007 contains rare actinolite microphenocrysts (pseudomorphing pyroxene) in the part of the sampled unit examined petrographically (Section 5.6.2), these features are considered

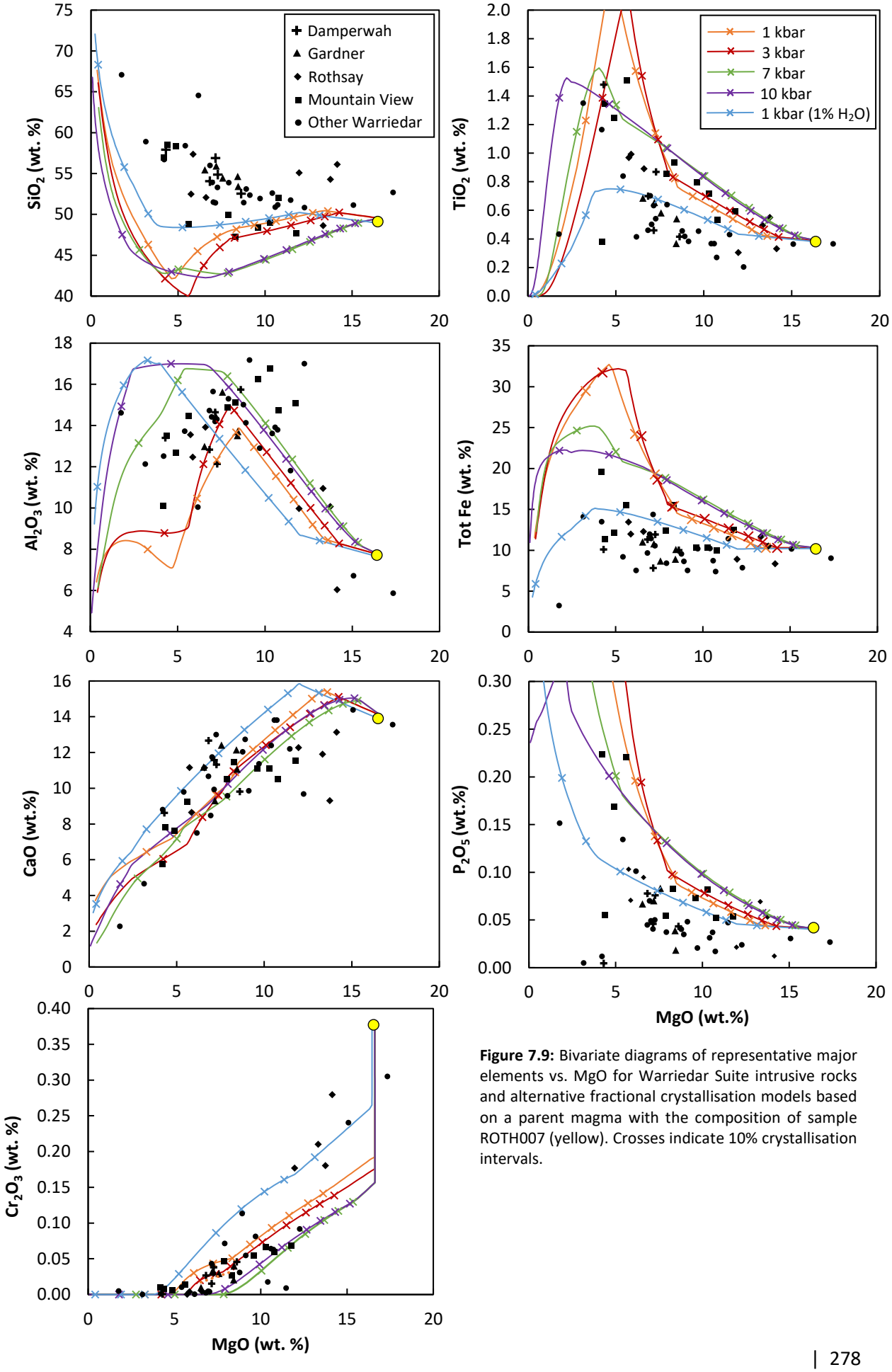

Figure 7.9: Bivariate diagrams of representative major elements vs. MgO for Warriedar Suite intrusive rocks and alternative fractional crystallisation models based on a parent magma with the composition of sample ROTH007 (yellow). Crosses indicate 10% crystallisation intervals.

to be volumetrically negligible in the geochemical sample analysed. Sample ROTH007 also contains high Cr (~2600 ppm), low Zr (25 ppm) and low incompatible trace element concentrations but does not demonstrate cumulate features.

The major element geochemical trends displayed by Warriedar Suite rocks are not fully explained by a single FC model but are instead partially replicated by two alternative models: the 1 kbar hydrous model and the 3 kbar anhydrous model (Fig. 7.9). The trends shown for $Fe_2O_3^T$ and P_2O_5 are best explained by the 1 kbar hydrous model and although the SiO_2 contents of Warriedar Suite samples are more elevated than all modelled trends, flat to increasing SiO_2 content with decreasing MgO content is only replicated by the 1 kbar hydrous model. Most samples follow the low TiO_2 trajectory of the hydrous 1 kbar model, however several samples, primarily from the Mountain View Sill, follow the more elevated TiO_2 trend of the anhydrous 3 kbar model. The inflection in the Al_2O_3 trend at ~8 wt. % MgO is replicated by the 3 kbar anhydrous model, and most Warriedar Suite samples follow the anhydrous modelled trends for Cr_2O_3, although a distinct portion of the samples (corresponding to 'Other Warriedar' intrusions) follow the hydrous 1 kbar modelled trend. On balance, the hydrous 1 kbar model is considered to be the best approximation of Warriedar Suite rocks, as a whole (Fig. 7.9). A hydrous parental melt is compatible with the identification of minor primary hornblende in the largest Warriedar Suite intrusion, the Gnanagooragoo Complex (Section 2.3.1; Ivanic, 2019). It has also been suggested that Warriedar Suite intrusions may be genetically associated with boninite-like rocks of the Meekatharra Fm, which are proposed to have been derived from hydrous, subduction-modified magmatism (Wyman, 2019; Ivanic, 2019).

The 1 kbar hydrous model predicts that crystallisation starts at 1407 °C with spinel as the first crystallising mineral (Fig. 7.10), followed by olivine at 1335 °C after just 0.5% crystallisation and

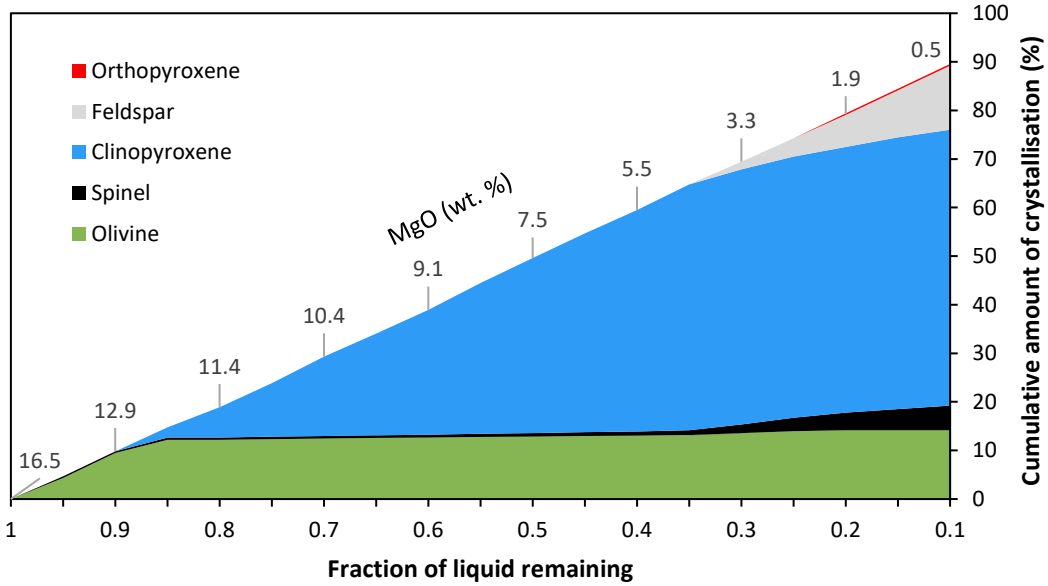

Figure 7.10: A plot of the cumulative crystal proportions predicted to form during fractional crystallisation of the Warriedar parental magma based on the ROTH007 hydrous 1 kbar model. The modelled MgO content of the remaining liquid is labelled at each 10% crystallisation interval.

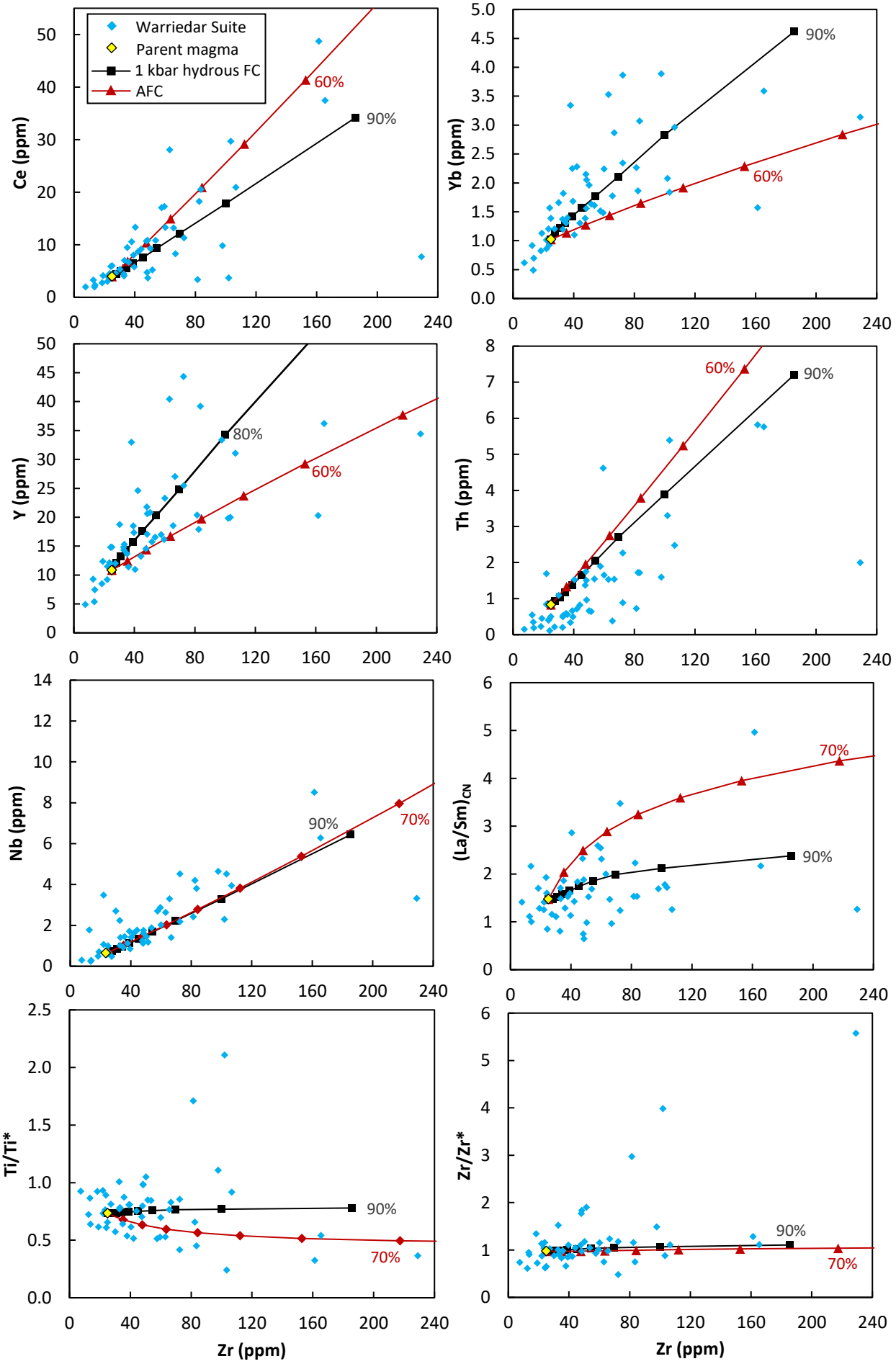
Warriedar Suite
Parent magma
1 kbar hydrous FC
AFC
Ce (ppm)
60%
90%
Yb (ppm)
90%
60%
Y (ppm)
80%
60%
Th (ppm)
60%
90%
Nb (ppm)
90%
70%
(La/Sm)CN
70%
90%
Ti/Ti*
90%
70%
Zr/Zr*
90%
70%
Zr (ppm)
Zr (ppm)

Figure 7.11 (previous page): Bivariate diagrams of selected trace elements and ratios versus MgO for Warriedar Suite rocks, in addition to predicted fractional crystallisation (FC) and AFC model lines for the 1kbar hydrous model using the starting composition of sample ROTH007 and the parameters described in the text. Markers on model lines are plotted at 10% crystallisation intervals up to 90% crystallisation. $(La/Sm)_{CN}$ is normalised to chondrite and Ti/Ti* and Zr/Zr* are calculated using Equation 6.3. Normalising values from Sun & McDonough (1989).

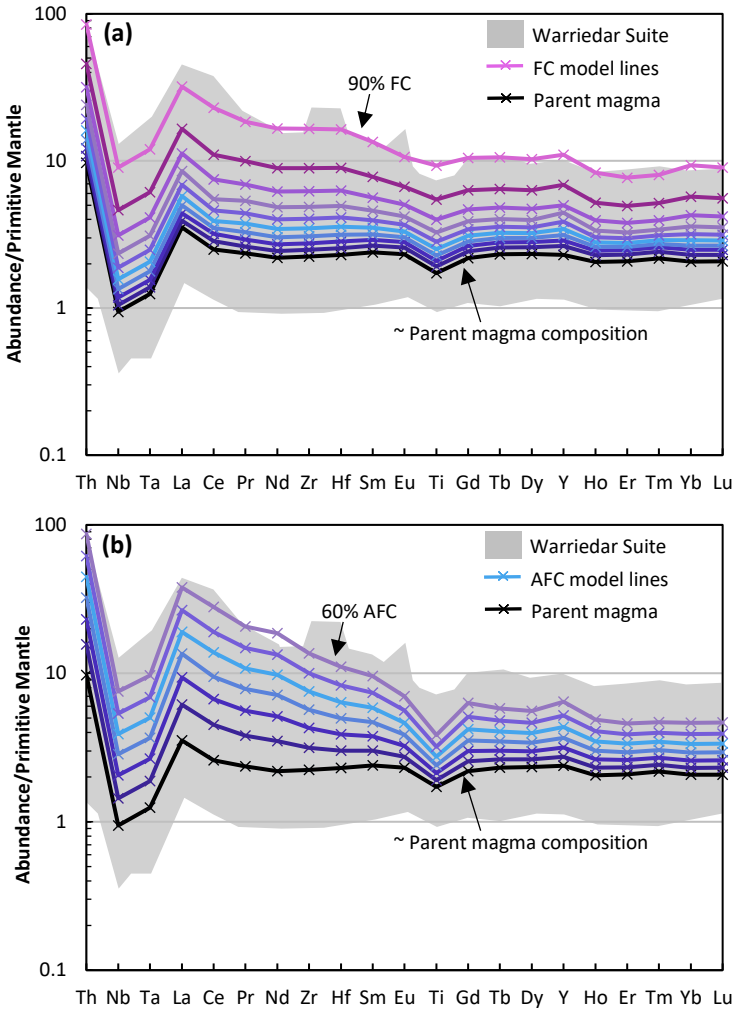

Figure 7.12: Primitive mantle-normalised trace element plots of Warriedar Suite rocks (grey field), with model lines drawn based on 1 kbar hydrous FC (a) and AFC (b), based on a parent magma with the composition of sample ROTH007 (black). Model compositional lines are plotted at 10% crystallisation intervals. Normalising values from Sun & McDonough (1989).

clinopyroxene at 1227 °C after ~15% crystallisation. Feldspar joins the crystallising assemblage at 1059 °C after ~65% crystallisation and orthopyroxene is predicted to briefly crystallise between 1013-1009 °C corresponding to ~77-78% crystallisation, at which point olivine stops crystallising (Fig. 7.10). This assemblage of spinel, clinopyroxene and feldspar continues to crystallise to the end of the model at 90% crystallisation, with the MgO content of the liquid containing 0.4 wt.% MgO, which is lower than observed in Warriedar Suite rocks. This predicted modal assemblage is consistent with petrographic descriptions (Section 5.5), in which cumulate olivine and pyroxene and, in some instances, plagioclase and clinopyroxene phenocrysts, have been observed in Warriedar Suite rocks. A single Warriedar Suite cumulate sample is dominated by cumulate orthopyroxene (sample MUL006; Section 5.6.1),

consistent with the brief crystallisation of orthopyroxene predicted by the model, and petrographic analysis also supports increased opaque mineral content (i.e., spinel) in the most evolved samples.

Trace element modelling for FC and AFC using the parameters and mineral proportions predicted by the 1 kbar hydrous FC model and the starting composition of sample ROTH007 are shown in Figure 7.11. AFC modelling has been undertaken using an r-value of 0.24, on the basis that this best fits the trace element trends shown by Warriedar Suite samples. The trace element content of Warriedar Suite samples displays two distinct trends with respect to modelling: approximately two thirds of samples follow the modelled FC trends, whereas a third of samples consistently follow the modelled AFC trends (Fig. 7.11). The split trends for the REE and Y are predicted by the FC and AFC models and demonstrate that AFC causes a steeper increase in LREE and more gradual increase in HREE and Y with crystallisation, relative to FC. In other instances where modelled FC and AFC trends are indistinguishable, such as Nb, samples follow the single modelled trend (Fig. 7.11). The modelling suggests that whilst most Warriedar Suite samples have been derived from FC (>80% for the most evolved samples), a significant proportion of the samples have undergone AFC processes (up to ~60%).

Several samples with lower Zr contents than the assumed parental magma composition lie on the liquid line of descent of the FC modelled trends and thus are consistent with cumulates derived from fractionation. Th content in the group is consistently overestimated by the modelled trends, potentially due to a slightly elevated initial Th concentration. Warriedar Suite samples do not display a good correlation between $(La/Sm)_{CN}$ and Zr, although an increase in $(La/Sm)_{CN}$ with crystallisation shown by some samples is predicted by the AFC model. Decreasing Ti/Ti* with progressive crystallisation is also replicated by AFC modelling, in contrast to the flat trend shown by FC models. A relatively flat Zr/Zr* trend is matched well by FC and AFC modelling, although a further trend of elevated Zr/Zr* values is apparent; these correspond to highly evolved sill tops (Section 5.5.4).

Primitive mantle-normalised trace element trends are reasonably well modelled by FC and demonstrate that significant amounts of FC (80-90%) are required for the more incompatible-element enriched samples of the Warriedar Suite (Fig. 7.12a). This is consistent with the layered, differentiated nature of most Warriedar Suite intrusions, interpreted as resulting from in situ fractionation (Section 3.4.2). However, several features such as LREE enrichment, Ti depletion and positive Zr-Hf anomalies are not fully accounted for based on modelled FC alone. In contrast, modelled AFC trace element trends of 50-60 % AFC match the most incompatible element enriched samples, and account for LREE enrichment and negative Ti anomalies (Fig. 7.12b). However, AFC modelling does not explain Zr-Hf anomalies displayed by sill top samples. It should be noted that the ubiquitous negative Nb-Ta

anomalies are considered to be a feature of the Warriedar Suite parental magma and are broadly comparable to Nb-Ta anomalies in the Archaean felsic crust contaminant used in AFC modelling.

7.4.5 Summary

In this section, the geochemical trends displayed by the three most prevalent magmatic suites in the study area have been investigated, to determine how the parental magmas of each suite evolved in the crust. For Chulaar Subgroup 2 volcanic rocks, no definitive model produced by rhyolite-MELTS replicated all of the major element geochemical trends shown by the subgroup, however, FC at low pressures (~1 kbar) best approximated the Subgroup 2 samples and in particular, the 1 kbar anhydrous model was considered the best fit. Trace element modelling of FC was able to successfully replicate trends for the REE, Y and Nb, but was not able to account for elevated Th and negative Ti anomalies shown by Subgroup 2 samples. AFC modelling using PETROMODELLER was able to partially replicate Ti anomalies, but otherwise did not fit the rest of the trace element geochemical trends. FC modelling indicates that up to ~60 % FC has occurred within the subgroup, although most samples can be attributed to < 40 % FC.

The major element trends of Subgroup 3 Chulaar volcanic rocks were matched by the modelled trends of the 1 kbar hydrous rhyolite-MELTS model. The fractionating assemblage predicted by this model assemblage matches petrographic descriptions of volcanic rocks from this group (Section 5.3). Trace element modelling using the parameters for this model and the PETROMODELLER program demonstrated that Chulaar Subgroup 3 trends are best approximated by AFC of up to 45-50%, which is able to account for REE, Y, Nb, negative Ti anomalies and LREE enrichment, whereas FC modelling consistently fails to replicate these trends

For Warriedar Suite intrusive rocks, two rhyolite-MELTS models were each able to partially replicate major element geochemical trends displayed by samples: the 3 kbar anhydrous model and the 1 kbar hydrous model. It was decided that on balance, the 1 kbar hydrous model was the best fit to the data, supporting previous suggestions of a hydrous parental magma for the suite (Wyman, 2019; Ivanic, 2019). The fractionating assemblage predicted by rhyolite-MELTS for the hydrous model is consistent with petrographic descriptions in Chapter 5. Trace element modelling of FC and AFC suggests that Warriedar Suite samples have undergone both FC and AFC; approximately two thirds of samples follow the modelled trends for FC and indicate that extensive FC has occurred (up to ~80 %), whereas the remaining samples follow the AFC modelled trends and display concentrations consistent with up to ~55 % AFC. Both FC and AFC modelling can replicate trends for the REE and the HFSE, including Nb and Y, although Th tends to be underestimated by the models. Furthermore, the AFC modelling can

replicate LREE enrichment and markedly negative Ti anomalies displayed by some samples. However, pronounced Zr-Hf anomalies exhibited by sill top samples are not accounted for by either process.

7.5 Contamination

7.5.1 Introduction

The supracrustal basement in the Murchison Domain consists of a sequence of felsic volcanic and volcaniclastic rocks, exemplified by the Gossan Hill Fm in the northeast YSGB (Van Kranendonk & Ivanic, 2009; Wang et al., 1998). The presence of older crust at depth beneath supracrustal rocks in the Murchison Domain is supported by recent isotopic studies (Ivanic et al., 2012; Smithies et al., 2018). In Section 7.4, AFC modelling was able to replicate the trends for two geochemical suites studied: Chulaar Subgroup 3 rocks and Warriedar Suite intrusive rocks. For these reasons, the effects of crustal contamination upon the magmatic suites described in the study area needs to be further evaluated.

Crustal contamination has previously been identified as an important process in the petrogenesis of extrusive and intrusive rocks in the Murchison Domain (e.g., Barley et al., 2000; Van Kranendonk et al., 2013; Wyman, 2019), using a combination of immobile and incompatible trace element ratios, modelling and radiogenic isotope analysis. However, many of the geochemical signatures used to distinguish crustal contamination, such as negative Nb-Ta anomalies, can also be interpreted as evidence favouring interaction of primary magmas with subduction-related material or metasomatism of the lithospheric mantle source by subduction-related fluids (e.g., Van Hunen & Moyen, 2012).

In this section, incompatible trace element ratios and ratio-ratio plots are first used to assess whether there is geochemical evidence in favour of crustal contamination and/or subduction-related interaction in the magmatic suites studied. Ubiquitous negative Nb-Ta and Ti anomalies in all volcanic subgroups and most Warriedar Suite rocks, are interpreted to be an inherent feature of parental magmas (Section 7.2), which may reflect a source that has been modified by subduction-related components. As a result, Nb-Ta and Ti anomalies are of limited use when assessing and modelling the potential effects of subsequent crustal contamination. To try and distinguish between crustal and subduction-related contamination, volcanic and intrusive samples are plotted on the Th/Yb vs. Nb/Yb plot of Pearce (2008), which is commonly used to distinguish between such processes. For groups that display evidence for crustal contamination, simple mixing modelling is undertaken to assess whether the trace element content of samples can be replicated through contamination with Archaean felsic crust and if so, determine the approximate amount of crustal contamination that may have occurred.

7.5.2 Trace Element Ratios

Certain immobile and incompatible element ratios, such as La/Nb, can be used to trace crustal contamination of magmas and/or interaction with subduction-related components (Condie, 2003). In basaltic rocks, La/Nb > 1.4 is typically considered to reflect a contaminated magma (Condie, 2003). The La/Nb ratio for all Chulaar Group volcanic rocks ranges between 1.1-11.1, with 94% of volcanic samples possessing La/Nb > 1.4, including rocks from all geochemical groups. Mougooderra Fm volcanics display La/Nb values between 0.8-3.3, whilst Warriedar Suite intrusive samples show La/Nb values ranging between 0.4-7.5, with 83% of samples possessing La/Nb > 1.4. An alternate trace element ratio that is indicative of subduction/crustal contamination of volcanic rocks is Nb/Th < 5 (Condie, 2003). All bar one of the Chulaar Group volcanic rocks display Nb/Th < 5, with over 50 % of samples with Nb/Th < 2, and all Mougooderra Fm volcanics possess Nb/Th ratios between 0.7-1.4.

In the Archaean Superior Province, Canada, the Th/Ce values of crustally-contaminated basalts are > 0.05 and $(La/Sm)_{CN}$ ratios are typically > 1.5 (Kerrich et al., 1999). For this study, Th/Ce values for Chulaar Group rocks invariably exceeds 0.05 (average ~0.14) and are relatively consistent between Subgroup 2 (average 0.13), Subgroup 3 (average 0.14) and Subgroup 4 (average 0.14), although Subgroup 1 displays a lower average Th/Ce of ~0.08. $(La/Sm)_{CN}$ values vary more considerably between each of the geochemical groups of Chulaar Group rocks, with Subgroup 1 possessing the most elevated $(La/Sm)_{CN}$ (average ~4.11), followed by Subgroup 3 (average ~1.94), Subgroup 4 (average ~1.33) and Subgroup 2 (average ~1.24). Mougooderra Fm volcanics have Th/Ce between 0.16-0.56 and $(La/Sm)_{CN}$ between 1.6-4.1, matching the criteria for crustally-contaminated volcanic rocks (Kerrich et al., 1999).

These incompatible element ratios indicate that Subgroup 1 and Subgroup 3 Chulaar Group volcanic rocks and Mougooderra Fm volcanic rocks have experienced crustal contamination, whereas the geochemistry of Chulaar Subgroup 2 and Subgroup 4 are less indicative of contamination, characterised by flat trace element patterns, but do appear to match the trace element criteria that favours interaction with subduction-related components.

On immobile incompatible element ratio/ratio plots (Figs. 6.11 and 6.12), Chulaar Subgroup 3 volcanic rocks exhibit a linear trend between depleted mantle composition and upper continental crust, consistent with variable amounts of crustal contamination. In contrast, Subgroup 2 and Subgroup 4 samples are more tightly clustered on these diagrams, supporting a lack of contamination within these subgroups. Similarly, Mougooderra Fm volcanic rocks do not display linear trends towards upper continental crust on these plots (Figs. 6.19 and 6.20), but are largely clustered, potentially a consequence of limited sampling. A minority of Warriedar Suite samples define a linear trend between depleted mantle and upper continental crust fields in Figure 6.28, including samples from the

Mountain View and Damperwah sills, suggesting that crustal contamination has affected some Warriedar Suite intrusions. Notably, the trends shown by samples from the Gardner and Rothsay sills are not consistent with contamination.

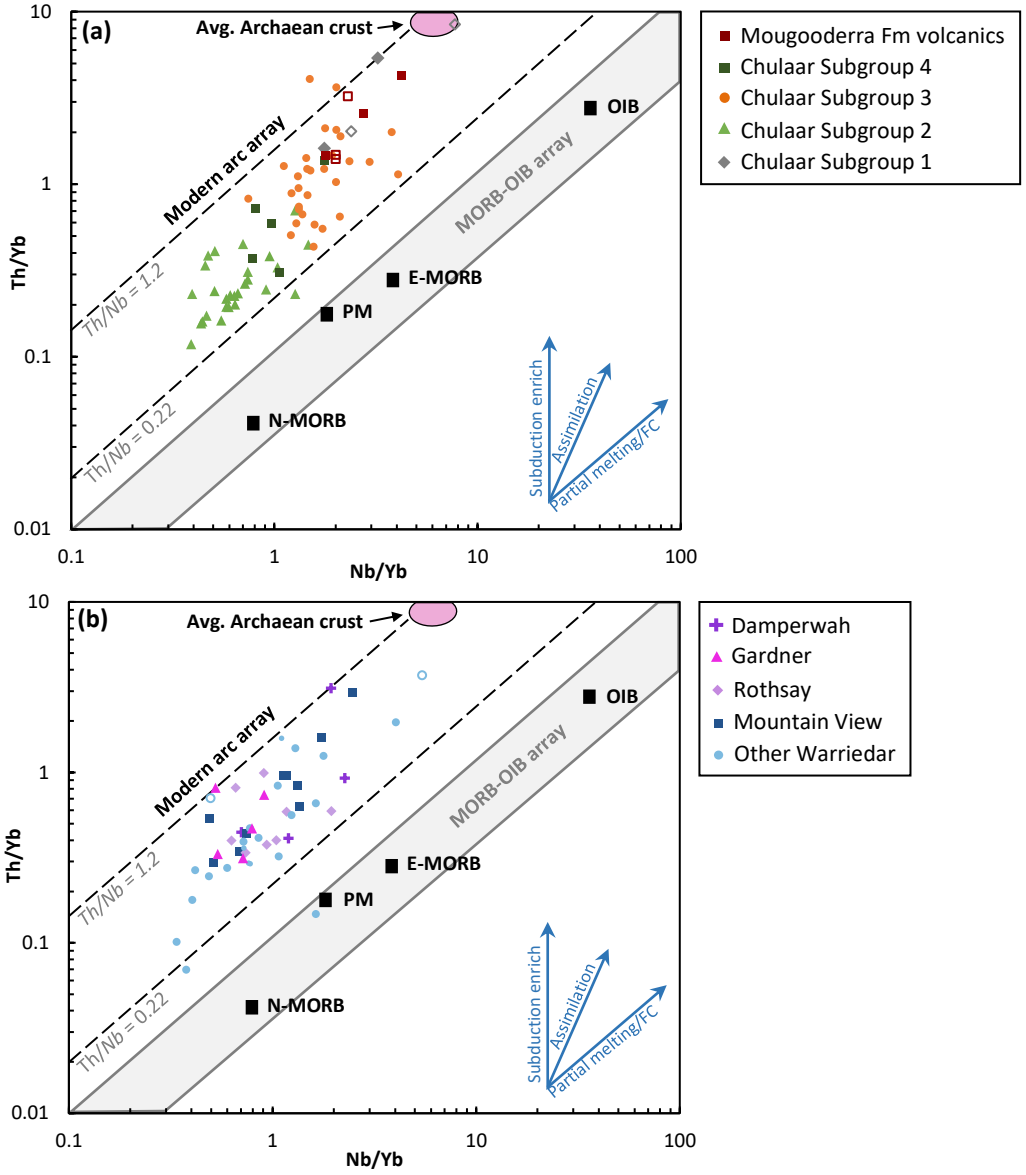

Figure 7.13: Nb/Yb vs. Th/Yb plot of Pearce (2008) for volcanic rocks of the Chulaar Group and Mougooderra Fm (a) and intrusive rocks of the Warriedar Suite (b), with some individual Warriedar Suite intrusions distinguished. The main fields and compositional vectors predicted for subduction-related enrichment, crustal assimilation, and partial melting and/or fractional crystallisation are drawn after Pearce (2008). Ratios for selected mantle reservoirs are based on values from Sun & McDonough (1989). The compositional field for average Archaean crust is from Smithies et al. (2018) and includes the average felsic Archaean crust composition of Rudnick & Fountain (1995). Analyses with > 63 wt.% SiO_2 are distinguished by open symbols, as saturation in accessory phases in high SiO_2 magmas may introduce additional influences on compositional trends (Smithies et al., 2018).

7.5.3 Th/Yb-Nb/Yb Systematics

The Th/Yb vs. Nb/Yb diagram of Pearce (2008) provides a useful means of assessing how the crust and mantle-derived magmas have interacted (Fig. 7.13). Geochemical trends displayed on this diagram can distinguish processes including crustal contamination and subduction-related interaction of

mantle derived magmas, as well as FC and partial melting (Pearce, 2008). Magmas formed from subduction-modified (Th-enriched) mantle display extended linear trends displaced vertically at elevated Th/Yb values within the modern arc array, but parallel to the modern mantle array (Pearce, 2008). These trends correspond to constant Th/Nb ratios and samples plotting along such trends are interpreted to represent variable FC of the subduction-modified magmas and/or partial melting of the source (Smithies et al., 2018). In contrast, mantle-derived magmas subject to variable amounts of crustal contamination plot along steep trends above and oblique to the MORB-OIB array, essentially defining a linear trend between the source composition and the crustal contaminant (Pearce, 2008), referred to as variable Th/Nb trends (Smithies et al., 2018). Chulaar Group and Mougooderra Fm volcanic rocks are plotted on the Th/Yb vs. Nb/Yb diagram in Figure 7.13a and Warriedar Suite samples are plotted on Figure 7.13b.

Despite almost all Chulaar Group volcanic rocks plotting within the modern arc array, samples from each geochemical group form distinct clusters and display some relatively well constrained trends (Fig. 7.13a). Subgroup 1 samples plot along an oblique trend towards and overlapping with the average Archaean crustal composition, although two of these samples contain elevated SiO_2 contents and should be treated cautiously. Subgroup 2 volcanic rocks plot at markedly lower Th/Yb and Nb/Yb ratios compared to the other subgroups. About two thirds of samples plot on a well-defined 'constant Th/Nb' trend sub-parallel to the MORB-OIB trend, including high Mg volcanic samples, and very few samples plot between this trend and the modern mantle array. This suggests that the elevated Th/Nb ratios of Subgroup 2 rocks were inherited from the mantle source, prior to the ascent of magmas through the crust.

Chulaar Subgroup 3 samples exhibit a diffuse, oblique trend at increasing Th/Nb ratios and directed towards the average Archaean crust compositional field (Fig. 7.13a). Several secondary trends at constant Th/Nb ratios parallel to the mantle array are accompanied by decreases in Mg# (from ~65 to ~38) and increases in incompatible trace element content, consistent with compositional changes resulting from melting and/or FC. Unfortunately, Subgroup 4 samples show moderate scatter and do not display a clear trend, but largely plot in a diffuse group between the trends of Subgroup 3 and Subgroup 2, partially overlapping with the linear trend shown by the latter. Mougooderra Fm volcanics plot at similar Nb/Yb and Th/Yb ratios to the Chulaar Subgroup 3 samples and display a linear trend of increasing Th/Nb ratios, at a shallow oblique angle to the MORB-OIB array.

Warriedar Suite samples form a diffuse pattern on the Th/Yb vs Nb/Yb diagram (Fig. 7.13b), which on first appearance, mirrors the distribution displayed by Chulaar Group volcanic rocks in Figure 7.13a. Only two Warriedar Suite samples plot outside the modern arc array, one of which plots close to

primitive mantle composition. Collectively, it is hard to differentiate between oblique and sub-parallel trends with respect to the MORB-OIB array. However, some individual intrusions, most notably the Mountain View Sill, exhibit oblique trends that are aligned with Archaean crustal composition, consistent with crustal assimilation. Along this trend, Mountain View samples exhibit a decrease in Mg#, which could be interpreted as progressive contamination with crystallisation and the pattern expected for AFC processes. Other intrusions (e.g., Gardner Sill and Rothsay Sill) do not display oblique trends, suggesting that contamination is not a ubiquitous feature throughout Warriedar Suite units.

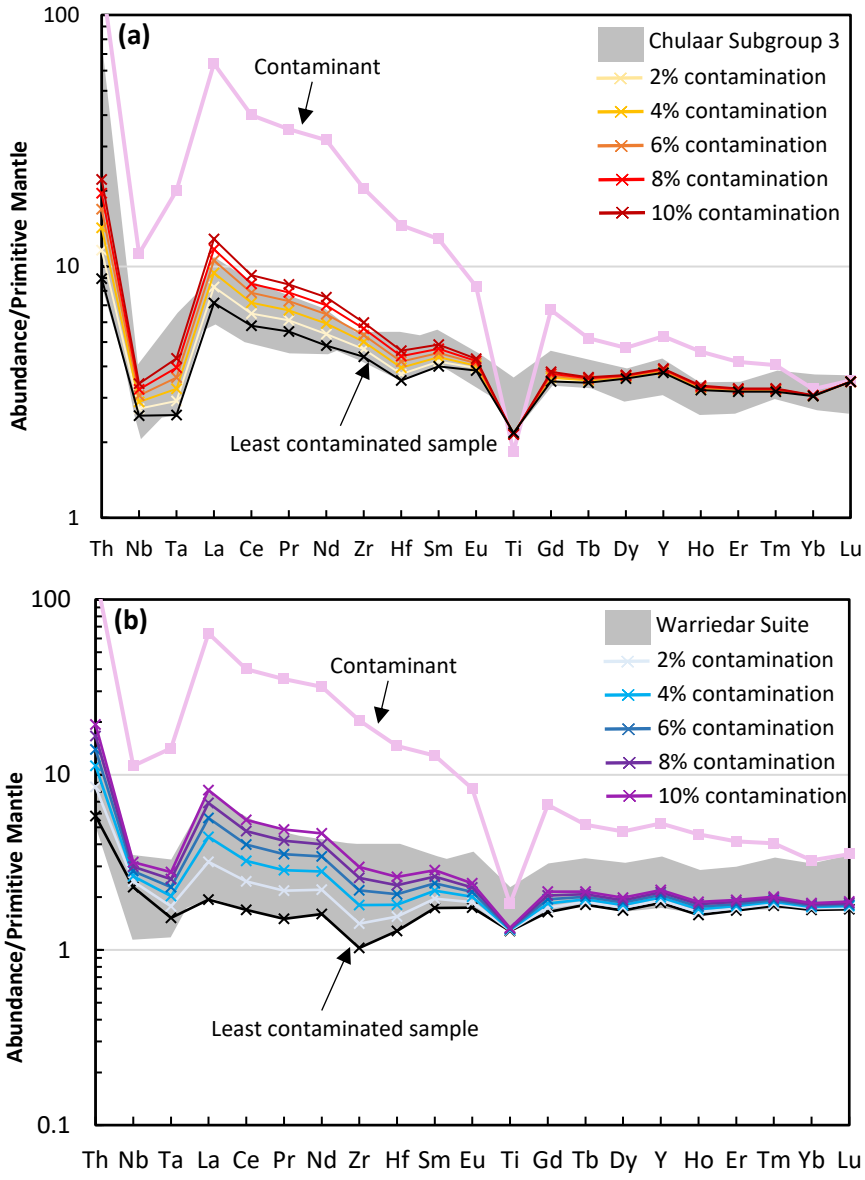

Figure 7.14: (a) Primitive mantle-normalised trace element plot of Chulaar Subgroup 3 rocks with >7.7 wt. % MgO that have been subject to incremental addition of olivine (Fo^{88}) until they reach ~15.0 wt. % MgO (grey field); **(b)** Primitive mantle-normalised plot of Warriedar Suite rocks with > 11.0 wt.% MgO that have been subject to incremental addition of olivine (Fo^{88}) until they reach ~ 15.1 wt. % MgO (grey field). In both plots, the least contaminated sample is symbolised in black and the modelled contaminant (average Archaean felsic crust; Rudnick & Fountain, 1995) is symbolised in pink. Modelled composition lines are drawn at 2% contamination intervals to 10% contamination. Normalising values from Sun & McDonough (1989).

7.5.4 Modelling

Incompatible trace element ratios suggest that Chulaar Subgroup 1 and Subgroup 3 volcanics, Mougooderra Fm volcanics and at least some Warriedar Suite intrusive rocks were derived from variable crustal contamination of parental magmas. This is also supported by AFC modelling (Section 7.3), which is able to replicate most trace element trends for Chulaar Subgroup 3 and Warriedar Suite rocks. To test this hypothesis, simple mixing modelling has been undertaken.

Prior to modelling contamination, the effects of FC need to be removed (Section 7.3). To do so, only the samples with MgO contents corresponding to olivine-only fractionation, as predicted by rhyolite-MELTS modelling, have been used. For Chulaar Subgroup 3 rocks, this corresponds to samples with >7.7 wt.% MgO, as this is the composition at which clinopyroxene is predicted to join olivine in the fractionating assemblage, and for Warriedar Suite rocks, samples with >11.0 wt.% MgO have been used. Olivine of Fo^{88} composition has been added incrementally to the composition of each of these samples until the MgO content reaches parity with the 'least contaminated' sample in each group, theoretically removing the effects of olivine fractionation. A contaminant has then progressively added to the 'least contaminated' sample using simple mixing, to try to replicate the trace element concentrations and trends of the 'most contaminated' sample. The average Archaean felsic crustal composition of Rudnick & Fountain (1995) is used as the contaminant during modelling, as it is considered to be broadly representative of the ~2.95 Ga basement felsic supracrustal and intrusive rocks in the Murchison Domain.

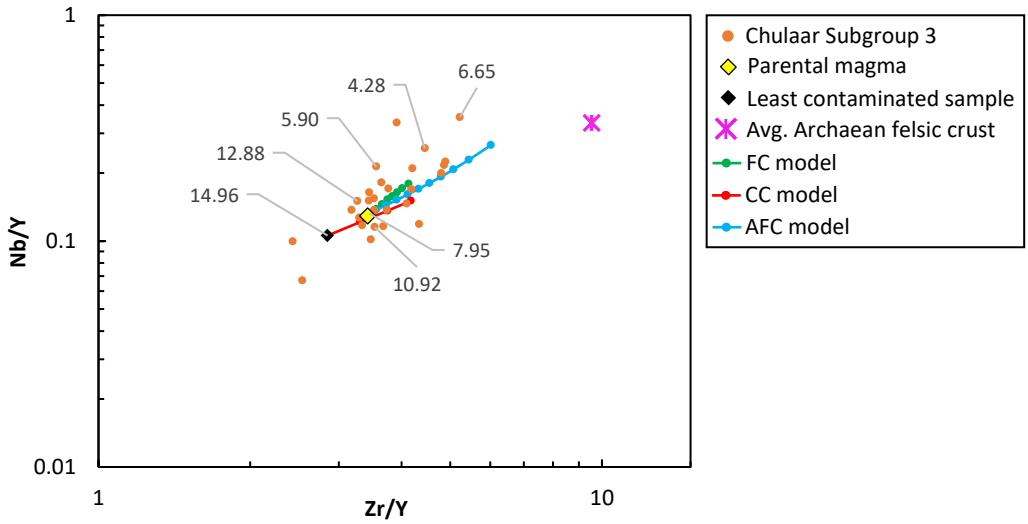

Figure 7.15: Nb/Y versus Zr/Y plots for Chulaar Subgroup 3 volcanic rock samples, labelled by their respective MgO content. The modelled trends for fractional crystallisation (FC; green) and assimilation-fractional crystallisation (AFC; blue) are also plotted, using the parameters described in Section 7.3.1 and with markers shown in 10% intervals to 80% crystallisation. Also plotted is the modelled trend for pure crustal contamination (CC; red), using the parameters described in this section, average Archaean felsic crust (Rudnick & Fountain, 1990) as the contaminant (pink) and with markers shown in 5% intervals to 15% contamination. The parental magma (yellow) is represented by sample MUL016.

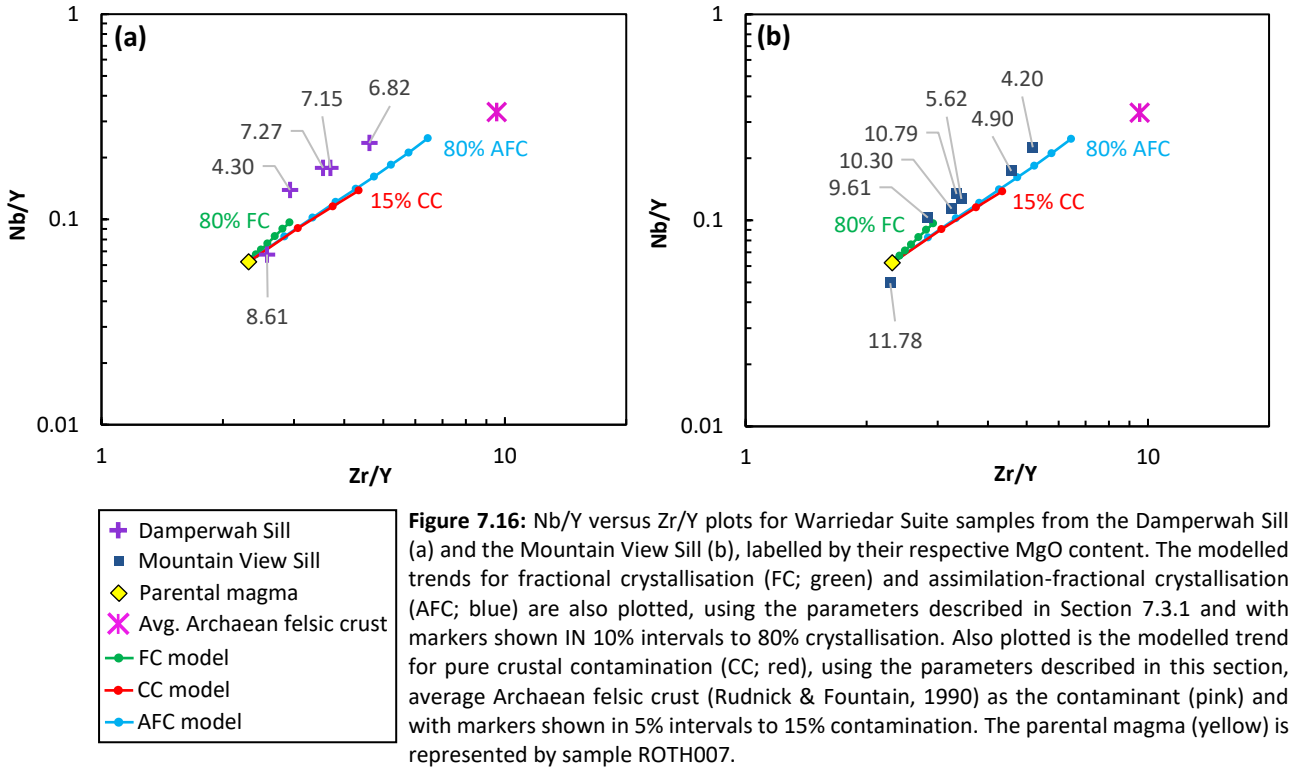

Figure 7.16: Nb/Y versus Zr/Y plots for Warriedar Suite samples from the Damperwah Sill (a) and the Mountain View Sill (b), labelled by their respective MgO content. The modelled trends for fractional crystallisation (FC; green) and assimilation-fractional crystallisation (AFC; blue) are also plotted, using the parameters described in Section 7.3.1 and with markers shown IN 10% intervals to 80% crystallisation. Also plotted is the modelled trend for pure crustal contamination (CC; red), using the parameters described in this section, average Archaean felsic crust (Rudnick & Fountain, 1990) as the contaminant (pink) and with markers shown in 5% intervals to 15% contamination. The parental magma (yellow) is represented by sample ROTH007.

For Chulaar Subgroup 3 volcanic rocks, contamination modelling is able to successfully account for the enrichment in LREE and Th shown by the samples after fractionation effects have been removed (Fig. 7.14). Increasing Nb content and slight enrichment in Zr-Hf and the MREE is also replicated by the model. The trace element trend for the sample with the highest incompatible trace element content corresponds to the modelled trend for ~8% contamination (Fig. 7.14a). Variation in Ti content and slight enrichment in HREE shown by Subgroup 3 samples is not fully attributed to contamination according to the modelling, as the rocks have similar concentrations of these elements as the contaminant used (Rudnick & Fountain, 1995). Contamination modelling of Warriedar Suite rocks also successfully reproduces the variation in LREE, Nb-Ta and partially accounts for Zr-Hf enrichment, with the modelled trend for ~10% contamination closely matching the trend of these elements for the most enriched sample (Fig. 7.14b). Slight variation in Ti and HREE shown by the samples is not fully accounted for by the modelling.

The modelling, trace element ratios and plots presented in this section demonstrates that the geochemistry of Warriedar Suite and Chulaar Subgroup 3 rocks has been modified through the assimilation of felsic crust. Chulaar Subgroup 3 rocks collectively show this trend (Fig. 7.15) whereas it is only exhibited by some Warriedar Suite intrusions, particularly the Damperwah (Fig. 7.16a) and Mountain View (Fig. 7.16b) sills. When modelled results for FC, AFC and crustal contamination are plotted on these diagrams, AFC is the only mechanism that is able to adequately fit the trends shown. For Chulaar Subgroup 3 rocks, the trend towards felsic crustal composition is accompanied by a progressive decrease in MgO content, consistent with the most evolved samples being the most

affected by combined assimilation and FC (Fig. 7.15), and indicates up to ~50-60% AFC has taken place, consistent with previous modelling (Section 7.3.4). The Damperwah and Mountain View intrusions also show a progressive decrease in MgO content along the AFC trends, whereby the evolved rocks at the tops of the intrusions plot closest to the composition of Archaean felsic crust (Fig. 7.16). A notable exception is the highly evolved sill top of the Damperwah Sill, which plots along the linear trend but further from felsic crustal composition than other samples (Fig. 7.16b). The modelled AFC trends indicate that the Damperwah Sill has undergone up to ~60% AFC and the Mountain View Sill up to ~65% AFC, within the range predicted by trace element modelling (Section 7.3.4).

7.6 Classification of Magnesian Volcanic Rocks

7.6.1 Introduction

Given that the volcanic rocks described in this study are part of an Archaean supracrustal sequence, exhibit spinifex textures and both komatiites (e.g., Barley et al., 2000) and so-called 'boninite-like' rocks (e.g., Lowrey et al., 2020) have been recorded in the region, further classification of magnesian extrusive rocks is necessary. Other Mg-rich volcanic rock classifications reported in the Murchison Domain include high-Mg basalt (also referred to as komatiitic basalt), siliceous high-Mg basalt (SHMB), picrite, low-Ti basalt and high-Mg andesite (Lowrey et al., 2020; Koutsoumbis, 2020).

Several of these rock types have important petrogenetic implications and have previously been used in support of geodynamic models for the Meso-Neoarchaean. Komatiites are classified in this study as spinifex-textured rocks with >18.0 wt.% MgO (Kerr and Arndt, 2001) and are widely recognised as being derived from mantle plume-related volcanism (e.g., Sossi et al., 2016). Conversely, boninites, classified as high MgO (>8 wt. %), high SiO_2 (>52 wt. %) and low TiO_2 (<0.5 wt. %) volcanic rocks according to the current IUGS classification, are considered to signify the initiation of subduction in Phanerozoic rocks (Pearce and Reagan, 2019). The recognition of boninite-like rocks in Archaean terranes have been used in support of subduction-related magmatism (e.g., Wyman, 2019). Alternatively, boninite-like rocks may be derived from crustal contamination of komatiitic magmas, as has also been suggested for SHMB and komatiitic basalts (Barnes et al., 2012; Lowrey et al., 2020). The three-stage classification scheme recently devised by Pearce & Reagan (2019) has been applied to Chulaar Group and Mougooderra Fm volcanic rocks. This scheme was constructed to provide a more thorough classification of boninitic rocks than the current IUGS classification, using mineral control lines to account for fractionation processes, and can also be used to classify other magnesian volcanic rocks, such as SHMB, picrite, low-Ti basalt and high-Mg andesite (Pearce & Reagan, 2019). Before geochemical data is plotted onto these discrimination diagrams, the major element data first

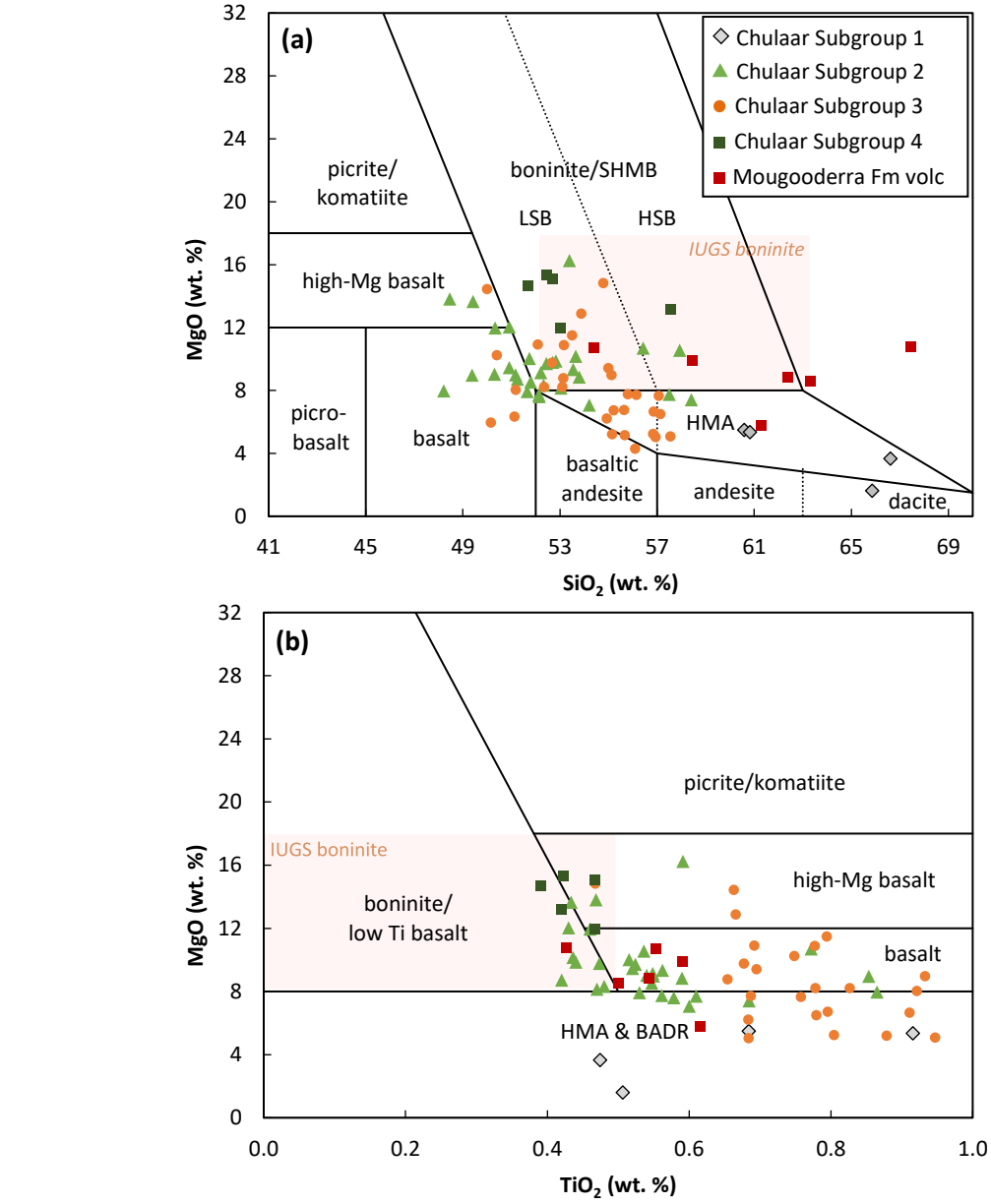

Figure 7.17: Volcanic rocks of the Chulaar Group and Mougooderra Fm plotted on a series of discrimination diagrams devised by Pearce & Reagan (2019) for classifying boninites and other similar rock types. **(a)** MgO-SiO_2 classification plot with the IUGS boninite criteria shaded in orange; **(b)** MgO-TiO_2 classification plot with the IUGS criteria for a boninite composition shaded in orange; **(c)** Discrimination diagram for rocks with compositions of MgO > 8 wt. %, using extrapolation to MgO = 8 wt. % for SiO_2 (Si8) and TiO_2 (Ti8), calculated using equations 7.3 and 7.4 in the text. BADR = basalt-andesite-dacite-rhyolite series; HMA= high-Mg andesite; SHMB = siliceous high-Mg basalt. Boninites with Si8 < 57 are referred to as low-Si boninites (LSB) and those with Si8 > 57 are classified as high-Si boninites (HSB).

needs to be converted to a volatile-free basis that totals 100%. The classification consists of three discrimination diagrams: MgO-SiO_2, MgO-TiO_2 and Si8-Ti8. The third discrimination plot involves the calculation of the extrapolated SiO_2 (Si8) and TiO_2 (Ti8) content at 8 wt.% MgO for those rocks with > 8 wt.% MgO, using equations 7.3 and 7.4, in order to satisfy the IUGS boninite criteria described above. For the purposes of classifying boninites, a sample needs to plot within the boninite field on all three discrimination diagrams (Pearce & Reagan, 2019).

$$Si8 = \frac{SiO_2 + (MgO - 8)}{3.83} \quad for\ MgO > 8\ wt.\%$$

Equation 7.3

$$Ti8 = \frac{42TiO_2}{(50 - MgO)} \quad for\ MgO > 8\ wt.\%$$

Equation 7.4

7.6.2 Chulaar Group

On the MgO vs. SiO_2 diagram, Subgroup 1 volcanics all plot as high magnesium andesites and dacites, whereas Subgroup 2 volcanics plot between the basalt and boninite/SHMB field, with two high-Mg basalts and three high-Mg andesites (Fig. 7.17a). Subgroup 3 volcanics plot on a trend from the high-Mg andesite field to the boninite/SHMB field, with four samples plotting as basalt and three as basaltic andesite. All Subgroup 4 volcanics plot in the boninite/SHMB field. On the accompanying SiO_2 vs. TiO_2 discrimination diagram (Fig. 7.17b), all Subgroup 1 and Subgroup 3 volcanics plot as basalt and part of basalt-andesite-dacite-rhyolite (BADR) evolutionary series, except for two Subgroup 3 volcanics in the high-Mg basalt field. Subgroup 2 volcanics plot as basalt and high-Mg basalt, with eight samples plotting at the margin of the boninite/low-Ti basalt field, whereas three Subgroup 4 volcanics plot as high-Mg basalt and two samples plot just inside the boninite/low-Ti basalt field.

On the third diagram (Si8 vs. Ti8), almost all Subgroup 3 volcanics plot in the SHMB field, with three samples in the BADR field (Fig. 7.17c). Three Subgroup 4 samples plot as SHMB and two samples plot just inside the boninite field; therefore, two Subgroup 4 samples fit the boninitic criteria on all three diagrams. Most Subgroup 2 samples form a cluster in the centre of the Si8 versus Ti8 diagram, with five plotting as boninite, three plotting as low-Ti basalt and the rest in the BADR or SHMB fields; thus five Subgroup 2 samples classify as boninite on all three discrimination plots.

In summary, Subgroup 1 volcanic rocks are classified primarily as high-Mg andesites, with one dacite. Subgroup 2 volcanics consists of several geochemical types owing to them plotting at the margins of

fields, including five boninites, three low-Ti basalts and the rest basalt or high-Mg basalt. Subgroup 3 samples plot primarily as basalt and high-Mg basalt, with several SHMB. Subgroup 4 samples comprise two samples classified as boninite and three that classify as SHMB. Notably, no Chulaar Group samples fall under the komatiite or picrite classification, due to the lack of samples with > 18 wt.% MgO.

7.6.3 Mougooderra Formation

On the MgO vs. SiO_2 plot (Fig. 7.17a), four Mougooderra Fm volcanic samples plot in the boninite/SHMB field, one plots as high-Mg andesite and one plots off the diagram with elevated SiO_2, possibly due to silicification. On the accompanying MgO vs. TiO_2 diagram (Fig. 7.17b), four Mougooderra Fm volcanic samples plot as basalt, one plots along a BADR series and one plots just inside the boninite/high-Ti basalt field, however, this sample does not plot as boninite/SHMB in the MgO vs. SiO_2 diagram. On the Si8 vs. Ti8 diagram (Fig. 7.17c), all Mougooderra Fm volcanic samples that plotted as boninite in one of the other diagrams plot in the SHMB field. It is therefore evident that most Mougooderra Fm volcanic samples are distinguished as (siliceous) high-Mg andesites and dacites based on the Pearce and Reagan (2019) classification, and one sample plots as a dacite.

7.7 Regional Geochemical Comparisons

7.7.1 Introduction

The greenstone stratigraphy in the central YSGB is poorly constrained and is yet to be fully integrated into the updated regional stratigraphic framework of the Murchison Domain (see Van Kranendonk et. al., 2013). This is largely due to incomplete GSWA regional mapping in the area and limited geochemical sampling undertaken to date. For this reason, the relationship between rocks in the study area and surrounding greenstone belts is not very well understood.

In this section, comparisons are made between the geochemistry of the groups of rocks studied and that of other volcanic and intrusive rocks in the Murchison Domain and the wider Youanmi Terrane. Identification of analogous rocks is important for evaluating the petrogenesis of the magmatic suites studied and for assessing wider geodynamic implications. In combination with lithological mapping (Chapter 3), structural mapping (Chapter 4) and geochronological analysis (Chapter 8), some of these geochemical comparisons may also assist in constraining the relationship between the stratigraphy in the YSGB and across the Murchison Domain.

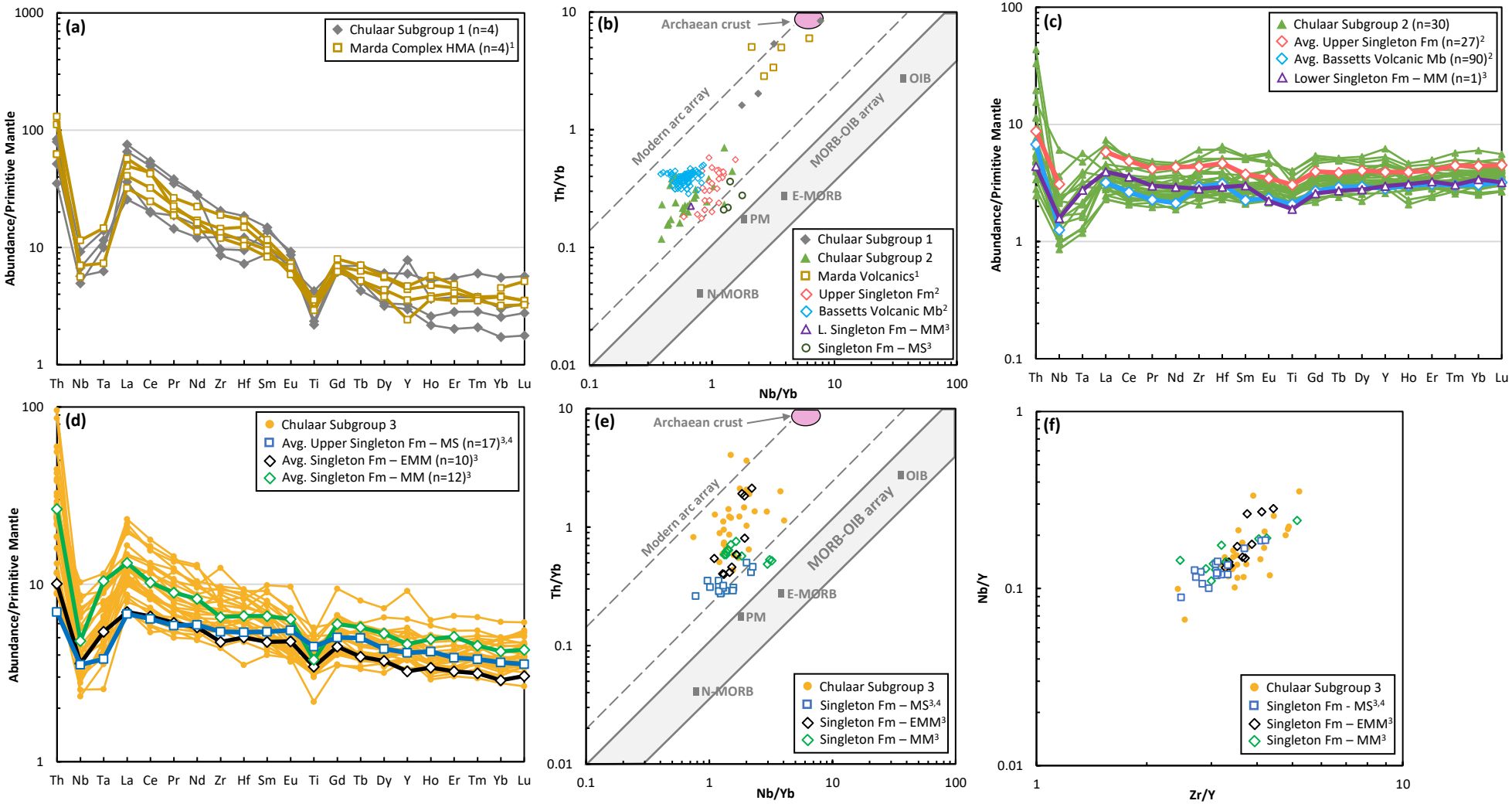

Figure 7.18: Trace element plots comparing the geochemistry of Chulaar Group volcanic rocks with other volcanic suites in the Youanmi Terrane. Superscript numbers refer to data sources – see below. **(a)** Primitive-mantle normalised trace element plot of Chulaar Subgroup 1 rocks and high-Mg andesitic rocks of the Marda Complex, Southern Cross Domain; **(b)** Th/Yb vs Nb/Yb plots of Chulaar Subgroup 1 and Subgroup 2 volcanic rocks, along with volcanic rocks comprising the Marda Complex, the Bassetts Volcanic Member (Meekatharra Fm, Polelle Syncline), the Upper Singleton Fm (Gabinintha mining district), the lower Singleton Fm (Mt Singleton; MS) and a single sample of the lower Singleton Fm at Mt Magnet (MM); **(c)** Primitive-mantle normalised plot of Chulaar Subgroup 2 volcanic rocks with averages of the Upper Singleton Fm at Gabanintha and the Bassetts Volcanic Member, and the single lower Singleton Fm sample from Mt Magnet (MM); **(d)** PM-normalised trace element plot of Chulaar Subgroup 3 rocks with averages of the Singleton Fm rocks from drillcore at Mt Magnet (MM), Singleton Fm rocks from East Mt Magnet (EMM) and the Upper Singleton Fm at Mt Singleton (MS); **(e)** Th/Yb vs Nb/Yb plot of the groups of rocks in (d); **(f)** Nb/Y vs Zr/Y ratio-ratio plot of the groups of rocks in (d). [1]Morris & Kirkland, 2014 [2]Lowrey et al. 2020 [3]Wyman, 2019 [4]WACHEM database, GSWA.

7.7.2 Chulaar Group

Chulaar Subgroup 1 rocks are characterised as porphyritic volcanic rocks of andesitic to dacitic composition, with elevated SiO_2 (61-67 wt.%), combined with moderately elevated MgO (1.5-5.5 wt.%), Cr (13-212 ppm) and steep REE profiles, consistent with a high-Mg andesitic classification. Rocks with a similar geochemistry to Subgroup 1 Chulaar Volcanics occur in the Marda Complex, Southern Cross Domain (Morris and Kirkland, 2014). These rocks comprise high-Mg andesites that like Subgroup 1 volcanic rocks, contain elevated MgO (3.4-6.3 wt.%), Cr (60-340 ppm) as well as enrichment in LREE and LILE. Trace element patterns for both Subgroup 1 Chulaar rocks and Marda Complex rocks have prominent Ti and Nb-Ta depletions and display remarkably similar trends at similar concentrations (Fig. 7.18a). The marked negative Zr-Hf anomaly displayed by one Chulaar Subgroup 1 sample is not displayed by Marda Complex high-Mg andesites. The two groups also plot in similar positions on incompatible element ratio-ratio plots, such as the Th/Yb vs. Nb/Yb plot of Pearce (2008; Fig. 7.18b). Marda Complex high-Mg andesites have been interpreted as direct partial melts of subduction-modified peridotitic mantle (Morris & Kirkland, 2014). However, it should be noted that the Marda Complex is approximately coeval with the Glen Group in the Murchison Domain and are therefore not temporally associated with Chulaar Subgroup 1 rocks, which occur towards the base of the supracrustal succession.

The Chulaar Subgroup 2 volcanic rocks are composed of basalt and basaltic andesite with high MgO contents (7.0-16.2 wt.%), high Mg# (55-74) and low Zr contents (26-68 ppm) and display characteristically flat to slightly concave LREE-MREE trace element patterns, also shown by the overlying, less extensive Chulaar Subgroup 4 volcanics. Two other volcanic units in the Murchison Domain also exhibit subtle concave mantle-normalised LREE patterns; the Bassetts Volcanic Member of the Meekatharra Fm (Polelle Group) and the upper part of the Singleton Fm (Norie Group), both in the northeast Murchison Domain (Lowrey et al., 2020). The Bassetts Volcanic Member consists of variable SiO_2 (51.8-56.7 wt. %), high MgO (8.1-17.2 wt.%), high Mg# (63-77) and low TiO_2 (0.39-0.60 wt.%) and some samples plot within the boninitic fields of Pearce & Reagan (2019). Mantle-normalised trace element patterns are typically flat, with common concave LREE, strongly negative Nb-Ta anomalies and positive Zr-Hf anomalies ($Zr/Zr^* = 1.3$-1.4). These trace element trends are broadly similar in shape to the most primitive Chulaar Subgroup 2 rocks, apart from the lack of positive Zr-Hf anomalies which are ubiquitous in Bassetts Volcanic Member samples (Fig. 7.18c). In contrast, the upper Singleton Fm in the northeast Murchison Domain comprises mostly basalt and lesser basaltic andesite, with moderately elevated MgO contents (6.1-12.6 wt.%), Mg# (63-77) and flat to concave normalised LREE patterns (Lowrey et al., 2020). Trace element trends are comparable to Chulaar Subgroup 2 rocks and do not display positive Zr-Hf anomalies (Fig. 7.18c). A Singleton Fm basaltic

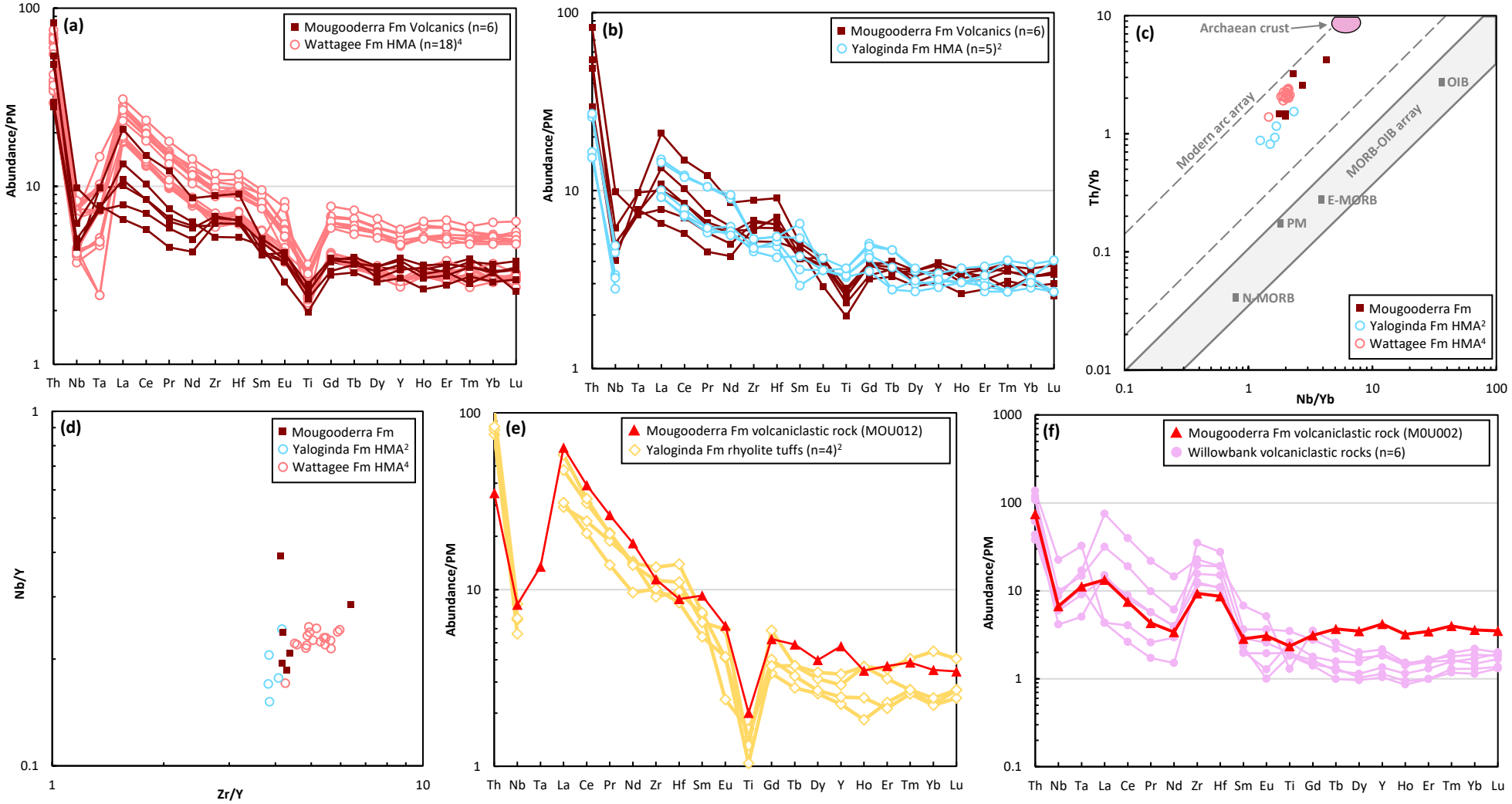

Figure 7.19: Trace element plots comparing the geochemistry of Mougooderra Fm volcanic rocks with other volcanic suites in the Youanmi Terrane. Superscript numbers refer to data sources – see below. **(a)** Primitive-mantle (PM) normalised trace element plot of Mougooderra Fm volcanic rocks and high-Mg andesitic rocks of the Wattagee Fm (Glen Group); **(b)** PM-normalised trace element plot of Mougooderra Fm volcanic rocks and high-Mg andesitic rocks of the Yaloginda Fm (Norie Group); **(c)** Th/Yb vs Nb/Yb plots of Mougooderra Fm volcanic rocks, along with high-Mg andesite rocks of the Wattagee Fm in (a) and the Yaloginda Fm in (b); **(d)** Nb/Y vs Zr/Y ratio-ratio plot of the rock groups in (c); **(e)** PM-normalised trace element diagram of sample MOU012 of Mougooderra Fm volcaniclastic rocks and rhyolitic tuffs of the Yaloginda Fm; **(f)** PM-normalised trace element diagram of sample MOU002 of Mougooderra Fm volcaniclastic rocks plotted with Willowbank volcaniclastic rocks. ²Lowrey et al. 2020 ⁴WACHEM database, GSWA.

unit at Mt Magnet (Wyman, 2019), closer to the study area, also displays the same flat normalised trace element patterns with concave LREE (Fig. 7.18c). On the Th/Yb vs Nb/Yb diagram, Subgroup 2 volcanic rocks overlap with the Upper Singleton Fm volcanic rocks from the northeast Murchison Domain (Lowrey et al., 2020), and a single depleted Singleton Fm sample from Mt Magnet (Wyman, 2019) (Fig. 7.18b). Notably, several depleted Singleton Fm samples from Mt Singleton with flat normalised REE patterns (the so-called 'flat boninitic' samples of Wyman, 2019) also plot closely to Chulaar Subgroup 2 volcanics and other Singleton Fm units (Fig. 7.18b).

Chulaar Subgroup 3 volcanic rocks are typified by aphyric, variolitic and spinifex-textured rocks with highly variable SiO_2 (50-58 wt.%) and MgO contents (4.3-15.0 wt.%), elevated Zr contents (49-139 ppm) and fractionated normalised REE patterns with variable LREE enrichment. To the south of the study area near Mt Singleton, Wyman (2019) reported LREE-enriched basaltic and basaltic andesite rocks ascribed to the Singleton Fm, including variolitic and spinifex-textured units. Further examples of LREE-enriched basaltic rocks were identified in the Mt Magnet area (Wyman, 2019). Both instances of LREE-enriched volcanic units display trace element patterns comparable to Chulaar Subgroup 3 volcanic rocks (Fig. 7.18d), at variable degrees of LREE enrichment. The rocks also plot at similar incompatible trace element ratios with similar trends to Chulaar Group 3 rocks (Fig. 7.18e, Fig. 7.18f).

7.7.3 Mougooderra Formation

The geochemistry of Mougooderra Fm volcanic rocks is consistent with high-Mg andesites, comprising high MgO (5.8-10.8 wt.%), combined with elevated SiO_2 (54-67 wt.%), Cr (636-2350 ppm), variable LREE enrichment and strongly negative Nb-Ta and Ti anomalies. These rocks form a minor component of the metasedimentary-dominated succession represented by the Mougooderra Fm. Several researchers have suggested that the Mougooderra Fm is coeval with the Glen Group in the northeastern Murchison Domain (Van Kranendonk & Ivanic, 2009; Van Kranendonk et al., 2013; Zibra et al., 2018). In the Glen Group, the Wattagee Fm comprises a sequence of high-Mg basalts and andesites, with elevated MgO (largely 5.5-7.6 wt.%) and SiO_2 (53.5-55.7 wt.%) and variably elevated LREE profiles (Van Kranendonk et al., 2013; WACHEM, 2020). Wattagee Fm high-Mg andesites also display prominent negative Ti and Nb-Ta anomalies (Fig. 7.19a) and have trace element trends that are broadly like Mougooderra Fm volcanics, but at higher REE concentrations.

Mougooderra Fm volcanic rocks also display compositional similarities with porphyritic high-Mg andesites of the Yaloginda Fm (Norie Group), sampled in the northeast Murchison Domain (Lowrey et al., 2020). The Yaloginda Fm andesites contain moderate SiO_2 (52.8-55.1 wt.%) and elevated MgO (8.9-11.7 wt.%), Cr (797-1092 ppm) and LREE enrichment in the range of Mougooderra Fm volcanic rocks.

Normalised trace element trends of the Yaloginda Fm match the elevated Th and LREE, and negative Nb anomalies shown by Mougooderra Fm volcanics, however, they only display weak negative Ti anomalies and show variable minor Zr-Hf anomalies (Fig. 7.19b). On trace element ratio-ratio plots, both the Wattagee Fm and Yaloginda Fm high-Mg andesites plot close to Mougooderra Fm volcanic samples, although the linear trends shown by Mougooderra Fm volcanics are marginally better approximated by the Yaloginda Fm (Fig. 7.19c, Fig. 7.19d).

Mougooderra Fm felsic volcaniclastic rocks display some compositional similarities with concurrent volcanic rocks, suggesting they are cogenetic (Section 6.5.2). One volcaniclastic sample (MOU012) displays a steep normalised REE profile with significantly elevated LREE and pronounced negative Nb-Ta and Ti anomalies. The trace element pattern of this sample is comparable to rhyolitic tuff units spatially associated with high-Mg andesitic units of the Yaloginda Fm (Lowrey et al., 2020) (Fig. 7.19e). The other felsic volcaniclastic rock sampled from the Mougooderra Fm (sample MOU002) displays very similar geochemical features and trends to Willowbank volcaniclastic rocks in this study, including variably elevated LREE, variable Eu anomalies and pronounced positive Zr-Hf anomalies (Fig. 7.19f).

7.7.4 Warriedar Suite

Warriedar Suite intrusive rocks are largely confined to the YSGB; in addition to the intrusions mapped and sampled in this study, Warriedar Suite intrusions have also been identified at Mt Singleton and Yalgoo, to the south and north of the study area, respectively (Ivanic, 2019; Wyman, 2019). Some intrusions in the Mt Magnet area have also been tentatively ascribed to the Warriedar Suite (Wyman, 2019). The 5 km-thick, 70 km-diameter Gnanagooragoo Igneous Complex mafic-ultramafic intrusion in the northeastern Murchison Domain, has also been assigned to the Warriedar Suite (Ivanic, 2019).

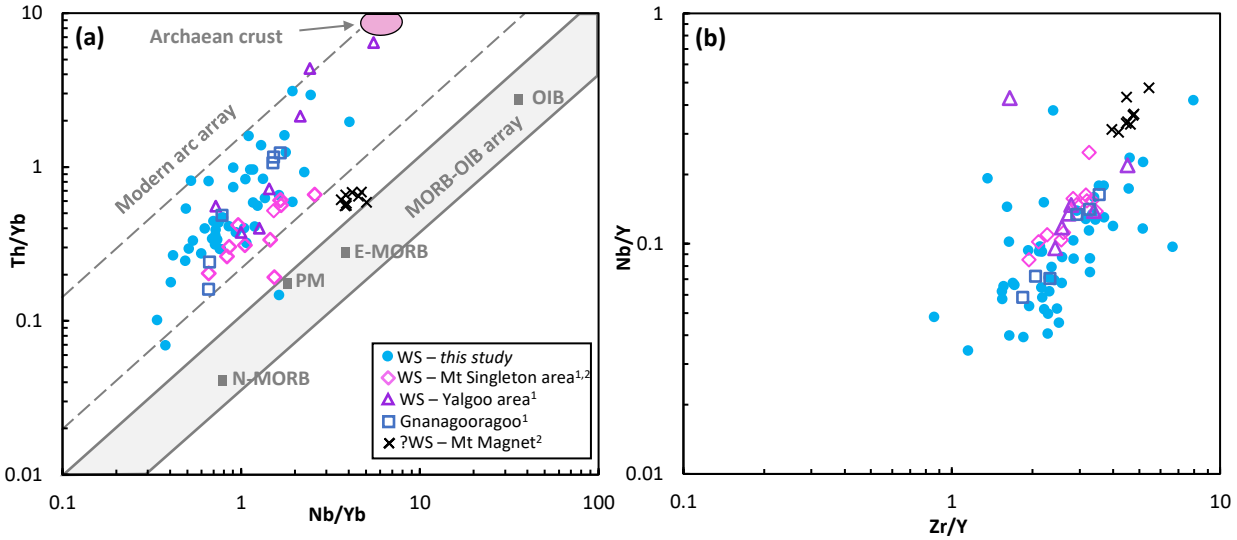

Figure 7.20: Trace element ratio-ratio plots of Warriedar Suite (WS) rocks from this study and from the literature. **(a)** Th/Yb vs Nb/Yb plot of Warriedar Suite rocks after Pearce (2008), comprising samples from this study, samples from the Mt Singleton area, samples from the Yalgoo area, samples from Mt Magnet, and samples from the Gnanagooragoo Igneous Complex, NE Murchison Domain; **(b)** Nb/Y vs Zr/Y plot for the samples in (a). [1]WACHEM database, GSWA, [2]Wyman (2019).

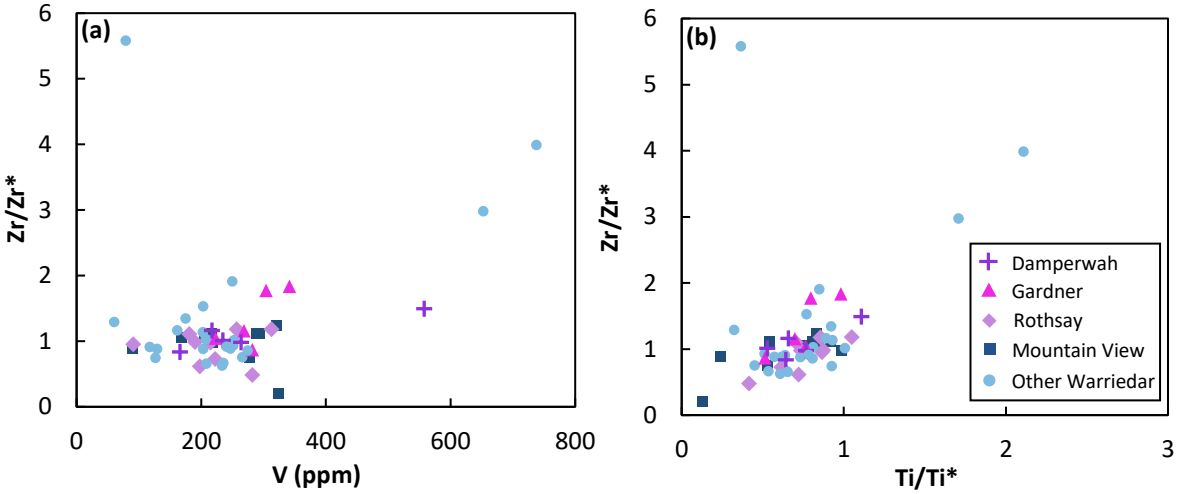

Figure 7.21: Bivariate plots for Warriedar Suite intrusive rocks. **(a)** Zr/Zr* versus V; **(b)** Zr/Zr* versus Ti/Ti*. Anomalies are relative to primitive mantle-normalised data and are calculated using Equation 6.3.

On a Th/Yb vs Nb/Yb diagram, Warriedar Suite samples from Mt Singleton and Yalgoo (Wyman, 2019; WACHEM, 2020) plot at similar ratios to Warriedar Suite samples of this study, and in particular, samples from the Yalgoo area exhibit a similar oblique trend towards Archaean crustal composition that is shown by some intrusions in the study area (Fig. 7.20a). Similarly, the limited number of samples from the Gnanagooragoo Igneous Complex (WACHEM, 2020) plot within the range of other Warriedar Suite rocks and demonstrate an oblique trend with respect to the mantle array (Fig. 7.20a). These trends and similarities in incompatible trace element ratios between Warriedar Suite rocks in the study area, Mt Singleton, Yalgoo and the Gnanagooragoo Igneous Complex are also displayed on a Nb/Y vs Zr/Y plot (Fig. 7.20b), and are consistent with them belonging to the same magmatic suite. However, the samples tentatively ascribed to the Warriedar Suite at Mt Magnet (Wyman, 2019) plot separate to all other Warriedar Suite rocks on both ratio-ratio plots, including a single cluster below the modern arc array on the Th/Yb vs Nb/Yb diagram (Fig. 7.20a).

7.8 Zr-Hf anomalies in Warriedar Suite rocks

The conspicuous positive Zr-Hf anomalies on primitive-mantle normalised diagrams exhibited by the Warriedar Suite sill top samples are not fully accounted for by FC, AFC or contamination modelling undertaken in this study. A logical explanation of these anomalies is that they reflect the late stage crystallisation and accumulation of zircon, host to the otherwise incompatible trace elements Zr and Hf, in the uppermost, most evolved portions of sills. This is supported by petrographic evidence of abundant zircon in sill top samples (Section 5.6.4) and is not precluded by modelling presented in this chapter as zircon crystallisation was not incorporated into FC modelling. However, zircon crystallisation and accumulation does not explain the consistent elevation in Nb and Ta (flat to slightly

negative anomalies) accompanying positive Zr-Hf anomalies in sill top samples, compared to the ubiquitous Nb-Ta depletions in concurrent Warriedar Suite rocks.

Positive HFSE anomalies, including Zr, Hf, Nb and Ta, have been identified in association with the crystallisation of Ti-magnetite (Howarth & Prevac, 2013). Experimental studies of Fe-Ti oxide-melt partition coefficients in hydrous mafic magmatic systems have demonstrated that the HFSE (Zr, Hf, Nb, Ta), along with the transition metals (e.g., V, Cr, Co), can be compatible in Fe-Ti oxides under certain conditions (Nielsen & Beard, 2000; Klemme et al., 2006). In these experiments, HFSE partition coefficients are comparable for any given magnetite/melt pair and correlate with temperature, pressure and the Ti- and Al- content of magnetite (Nielsen & Beard, 2000). Magnetite composition is shown to be the strongest controlling factor on partitioning behaviour, with HFSE preferably partitioning into Ti, Fe^{3+}-rich and Al, Cr-poor magnetite. Furthermore, the HFSE become more compatible relative to Ti at higher temperatures and lower pressures (Nielsen and Beard, 2000). Therefore, HFSE enrichment characterised by positive Zr-Hf and Nb-Ta anomalies is consistent with crystallisation of Ti-magnetite from hydrous magmas at high temperatures and/or low pressures (Howarth and Prevec, 2013; Nielsen and Beard, 2000).

Petrographic analysis in Section 5.6.4 demonstrates that Warriedar Suite sill top samples contain elevated Fe-Ti oxide mineral content and are commonly highly magnetic, unlike their less evolved counterparts. Positive Zr-Hf anomalies and reduced negative Nb-Ta anomalies in Warriedar Suite sill tops are typically associated with elevated TiO_2, V (Fig. 7.21a) and Ti/Ti* (Fig. 7.21b), and very low concentrations of Cr, which is consistent with the change in oxide composition required for increased HFSE compatibility in Ti-magnetite. The hydrous and low-pressure conditions required for increased HFSE compatibility according to Howarth & Prevac (2013) are supported by rhyolite-MELTS modelling of Warriedar Suite rocks (Section 7.4.4). However, fractionation of Ti-magnetite does not fully explain the LREE depletion in sill top samples, as REE are all consistently strongly incompatible in Fe-Ti oxides (Klemme et al., 2006).

On balance, positive Zr-Hf anomalies in sill top samples are attributed to zircon crystallisation and accumulation, potentially enhanced by changes in HFSE compatibility due to fractionation of Ti-magnetite from a hydrous magma at low pressures, which is supported by petrographic evidence and rhyolite-MELTS modelling.

7.9 Petrogenetic Synthesis

In this chapter, the geochemical data presented in Chapter 6 have been interpreted and evaluated. Modelling has been undertaken to estimate primary magma compositions and corresponding potential temperatures and pressures, the operation of FC and AFC, as well as crustal contamination. Limited sample numbers for Chulaar subgroups 1 and 4, and Mougooderra Fm rocks has prevented these geochemical groups from being successfully modelled. Volcanic rocks have been reclassified according to an updated classification scheme for high-Mg volcanic rocks and comparisons have been made between the geochemistry of the magmatic suites studied and other comparable suites in the region. The petrogenetic implications of the work presented in this chapter is summarised for each magmatic suite below.

7.9.1 Chulaar Group volcanic rocks

Four geochemically distinct volcanic subgroups have been identified within the stratigraphy of the Chulaar Group in the YSGB, corresponding to specific stratigraphic levels within the group. All volcanic samples contain pronounced negative Nb-Ta anomalies regardless of MgO content, interpreted as an inherited feature of the mantle source. The lowermost Chulaar Subgroup 1 comprises porphyritic, high-Mg andesites that represent a minor component at the base of the Chulaar Group volcanic succession. Although modelling has not been undertaken on this group, incompatible element characteristics suggest that the Subgroup 1 rocks have been affected by significant amounts of crustal contamination (Fig. 7.13a), in addition to FC.

The more extensive Chulaar Subgroup 2 comprises five samples that geochemically classify as boninites, in addition to low Ti basalts and high-Mg basalts (Section 7.6.2; Pearce & Reagan, 2019), which collectively exhibit distinctive flat to subtly concave LREE-MREE normalised trace element patterns. Modelling demonstrates that the geochemistry of Subgroup 2 rocks can be achieved by FC of up to ~40% at low pressures (~1 kbar), although it was not possible to distinguish the water content of the parental magma. The geochemistry of Chulaar Subgroup 4 rocks, which constitute a minor volcanic component at the top of the Chulaar Group, is remarkably similar to Subgroup 2 rocks. Subgroup 4 consists of pyroxene spinifex-textured rocks with relatively high MgO contents, including samples that geochemically classify as boninites and SHMB, and all samples of exhibit flat to subtly concave LREE-MREE patterns. The calculated primary magma characteristics for Chulaar subgroups 2 and 4 are also broadly comparable: The Subgroup 2 parental magma is calculated to have contained 16-20 wt.% MgO, corresponding to T_P of 1435-1535 °C and pressures of 0.9-2.7 GPa, whereas the

Subgroup 4 parental magma is better constrained at 17-19 wt.% MgO, and corresponds to T_P of 1470-1515 °C and pressures of 1.6-1.7 GPa.

Elevated Th/Nb ratios shown by all rocks in Subgroups 2 and 4 indicate that LILE enrichment was likely inherited from the mantle source, with no discernable evidence of crustal contamination or AFC processes (Fig. 7.13a). Lowrey et al. (2020) compared geochemically similar rocks comprising the Bassetts Volcanic Member and lower Singleton Fm in the northeast Murchison Domain with Cenozoic boninites rocks formed in modern subduction zone settings. The occurrence of dendritic pyroxene and platy pyroxene spinifex textures in these units, which notably have been identified within Chulaar Subgroup 4 rocks (Section 5.3.5) but appear to be absent in Subgroup 2 rocks, are also interpreted as evidence favouring a subduction-metasomatised mantle source (Lowrey et al., 2017; 2020).

Chulaar Subgroup 3 rocks constitute a significant proportion of the Chulaar Group volcanic succession and comprise pillowed, variolitic and pyroxene spinifex-textured basalt, high-Mg basalt and SHMB, with geochemical characteristics that are markedly different from underlying Subgroup 2 rocks. The invariably LREE-enriched geochemical characteristics of Subgroup 3 rocks are successfully modelled by AFC of up to 45-50%, most likely at low pressures (~1 kbar) and from a hydrous parental magma. Modelling supports the idea that the assimilation of crustal material was involved in the petrogenesis of Subgroup 3 rocks, despite the lack of macroscopic evidence of contamination in the field. Derivation from a hydrous magma is supported by abundant variolitic features within rocks of this subgroup (see Mulga Volcanics; Section 3.4.1.4), which has previously been interpreted as evidence of immiscibility between the silicate magma and exsolved, hydrous fluids (Ballhaus et al., 2015; Lowrey et al., 2020). The predicted primary magma characteristics for Subgroup 3 rocks are broadly within the range of surrounding Chulaar Group volcanic units (Section 7.3.2), including predicted MgO contents of 17-20 wt.%, T_P of 1440-1560 °C and pressures of 1.1-2.5 GPa. Based on stratigraphic relations and Th/Yb vs Nb/Yb systematics, LREE enriched Subgroup 3 could represent fractionated and crustally-contaminated equivalents of underlying Subgroup 2 rocks. However, this remains speculative, as the timescales represented by the Chulaar Group volcanic succession are not well constrained.

In contrast to previous geochemical studies that have identified *sensu stricto* komatiitic rocks in the Murchison Domain (including the YSGB), primarily on the basis of abundant spinifex textures (Watkins & Hickman, 1990; Barley et al., 2000), the results of this study suggest that komatiites are absent in the Chulaar Group volcanic succession. Spinifex-textured rocks invariably comprise pyroxene spinifex, rather than olivine spinifex, and geochemically classify as high-Mg basalts or even basalts (with < 12.0 wt.% MgO). As a result, estimates of parental magma temperatures are considerably lower than

previously inferred (e.g., Watkins & Hickman, 1990; Barley et al., 2000) and consequently, do not necessitate derivation from a mantle plume (e.g., Lowrey et al., 2017; 2020; Wyman, 2019).

7.9.2 Mougooderra Fm volcanic rocks

Mougooderra Fm volcanic rocks represent the uppermost volcanic rocks in the YSGB and consist primarily of siliceous high-Mg andesites and dacites. These rocks exhibit some similarities to underlying Chulaar Group volcanic rocks and also exhibit ubiquitous negative Nb-Ta and Ti anomalies. Although modelling has not been undertaken on these rocks, geochemically and petrographically similar rocks in the northeastern Murchison Domain and neighbouring Southern Cross Domain have been suggested to signify subduction-linked metasomatism of lithospheric mantle sources (Morris & Kirkland, 2014; Wyman, 2019). In the Murchison Domain, the geochemistry of Mougooderra Fm volcanic rocks is most comparable to high-Mg andesites of the Yaloginda Fm (Lowrey et al., 2020). Additionally, concurrent felsic volcaniclastic rocks plot on similar trends to Mougooderra Fm volcanic rocks, consistent with them belonging to the same cogenetic unit, and consistently exhibit geochemical similarities with similar felsic volcaniclastic rocks assigned to the Willowbank Clastics (Section 6.4.2).

7.9.3 Warriedar Suite intrusive rocks

Collectively, Warriedar Suite intrusions display consistent geochemical trends on bivariate diagrams (Figs. 6.24 and 6.25), plot as a single, albeit diffuse, group when plotted on a Th/Yb vs Nb/Yb diagram (Fig. 7.13b) and exhibit similar field (Section 3.4.2) and petrographic characteristics (Section 5.6). Together, this suggests that Warriedar Suite intrusions are cogenetic, with the implication that they were likely formed from the same, parental magmatic source. Modelling demonstrates that significant amounts of fractional crystallisation (up to 80%) are responsible for the geochemistry of the most evolved Warriedar Suite rocks, resulting in the compositionally layered configuration that characterises the thickest intrusions. This is corroborated by petrographic work (Section 5.6). In addition to the overarching geochemical trends displayed by all Warriedar Suite intrusive samples, independent fractionation trends for individual intrusions are discernible. This suggests that the primary magma underwent initial fractionation in a lower crustal magma chamber, followed by further, extensive fractional crystallisation after the emplacement of individual sills. Rhyolite-melts modelling indicates that sills were emplaced and underwent FC at relatively shallow depths (best modelled at a pressure of ~1 kbar), supporting previous suggestions that the Warriedar Suite intrusions represent sub-volcanic intrusions (Ivanic, 2019). Conspicuous positive Zr-Hf anomalies

coupled with relatively enriched (less negative) Nb-Ta anomalies in Warriedar Suite sill top samples, are attributed to zircon crystallisation and accumulation. This is potentially enhanced by changes in HFSE compatibility due to the fractionation of Ti-magnetite from a hydrous magma at low pressures.

Several Warriedar Suite intrusions, such as the Mountain View and Damperwah sills mapped in the Rothsay area (Section 3.4.2), exhibit distinct geochemical trends that are successfully modelled by AFC of up to 55%. These intrusions consistently display geochemical evidence in favour of crustal assimilation that is absent in most other Warriedar Suite sills. Contamination modelling indicates that the uppermost portions of these sills are typically the most contaminated, consistent with the manifestation of AFC processes.

Rhyolite-melts modelling indicates that Warriedar Suite major element trends are best approximated by fractional crystallisation of a hydrous parental magma. This concurs with a recent suggestion by Wyman (2019) that the Warriedar Suite intrusions are geometrically and lithologically comparable to Phanerozoic Alaskan type-intrusions (Himmelberg & Loney, 1995), which have been interpreted to represent subduction-related, hydrous magmatism (Yuan et al., 2017). Furthermore, primary hornblende has been identified in the Gnanagooragoo Complex (assigned to the Warriedar Suite), indicating a hydrous parental magma (Ivanic, 2019). Although primary amphibole has not explicitly been identified in Warriedar Suite rocks in this study (Section 5.6), it is possible that abundant metamorphic actinolite ± hornblende in Warriedar Suite rocks in the area may be obscuring any primary amphibole present in these rocks.

Warriedar Suite intrusions in the southwest Murchison Domain have been dated at ~2790-2801 Ma (Section 2.2) and are broadly coeval with the intrusions of the ca. 2800 Ma Boodanoo Suite, including the Narndee and Fields Find igneous complexes (Ivanic, 2019; Fig. 2.3). Both of these complexes contain abundant primary amphibole and have been interpreted to document a change from anhydrous magmatism at ca. 2820 Ma (Meeline Suite; Section 2.3.1) to predominantly hydrous magmatism) at c. 2800 Ma (Ivanic et al., 2015b; Ivanic, 2019). This is tentatively supported by the modelling presented in this study.

CHAPTER 8

Geochronology of supracrustal rocks in the Yalgoo-Singleton greenstone belt

8.1 Introduction

The stratigraphy of Archaean greenstone belts commonly consists of a succession of intercalated basaltic and komatiitic lavas with subordinate felsic volcanic products (e.g., Thurston, 2015). Such sequences are frequently cut by synvolcanic mafic-ultramafic intrusions (e.g., Anhaeusser, 2006; Ivanic et al., 2010). Though underlying basement is often obscured, basal unconformities overlying granite (e.g., Van Kranendonk et al., 2004), quartzite-carbonate platforms (e.g., Wilks and Nisbet, 1988) and older supracrustal units (e.g., Blenkinsop et al., 1993; Bickle et al., 1994) have been documented. Lower extrusive successions are commonly unconformably overlain by metasedimentary successions, known as 'late' or 'successor' basins (e.g., Krapez & Barley, 1987; Mueller & Corcoran, 2001). These sequences comprise alluvial-fluvial siliciclastic rocks and minor alkaline volcanic rocks (Thurston, 2015), and are widely interpreted as synorogenic, marking the termination of greenstone belt development (Krapež and Barley, 2008). The YSGB comprises such an archetypal greenstone stratigraphy, with a basement of felsic and felsic volcaniclastic rocks (Gossan Hill Fm), overlain by a thick succession of mafic-ultramafic volcanic rocks (Chulaar Group), in turn unconformably overlain by siliciclastic and minor felsic volcaniclastic and volcanic rocks (Willowbank Clastics & Mougooderra Fm).

The geodynamic setting of greenstone belt formation is very controversial. Some authors advocate allochthonous, accretionary models necessitating plate tectonic processes (e.g., Ludden and Hubert, 1986; de Wit et al., 1992; Kusky and Polat, 1999; Czarnota et al., 2010; Goscombe et al., 2019), whereas others provide evidence in favour of autochthonous models (e.g., Blenkinsop et al., 1993; Ayer et al., 2002; Stern, 2005; Hamilton, 2011; Van Kranendonk et al., 2013; Johnson et al., 2017). Numerical modelling provides further insights into Archaean geodynamics (Gerya, 2019). This modelling yields results that can be broadly subdivided into non-uniformitarian 'plume-lid' style models (e.g., François et al., 2014; Fischer and Gerya, 2016) and plate tectonic style models (e.g., Rosas and Korenaga, 2018).

Notwithstanding this debate, the formation of greenstone belts has been considered to occur over a period of many tens to hundreds of millions of years (e.g., Kamber, 2015). Recent analytical advancements and more widespread use of U-Pb geochronology, particularly in the Canadian, South African and Australian cratons, appears to support this protracted timeframe. Geochronology in the Canadian Superior Craton indicates that the Abitibi greenstone belt was created over ~75 Ma from 2750 Ma to 2675 Ma (Ayer et al., 2002; Thurston, 2002). Similarly, greenstone belts were constructed over ~60 Ma in the Kalgoorlie Terrane of the Australian Yilgarn Craton (2715-2655 Ma; Kositcin et al., 2008) and over ~110 Ma in the neighbouring Murchison Domain (2820-2710 Ma; Van Kranendonk et al., 2013). Geochronology of supracrustal rocks in the South African Barberton greenstone belt documents a protracted history spanning over 300 Ma (3550-3215 Ma; Heubeck et al. 2013; Drabon et al., 2017). However, recent high-resolution geochronological studies have suggested that extensive magmatic episodes in Archaean terranes may have occurred over discrete, relatively fast (<15 Ma) timescales (e.g., Schoene & Bowring, 2010) and that the rates of Archaean processes such as volcanism, sedimentation and deformation may be comparable to those of modern processes (e.g., de Wit et al., 2018).

New data from this study challenges the common picture of lengthy greenstone belt formation and lends support to a more rapid model of formation. This chapter reports the first robust U-Pb zircon depositional ages of the metasedimentary Mougooderra Fm, and an emplacement age of the upper part of the volcanic-dominated Chulaar Group. Geochronological results demonstrate that the Mougooderra Fm is considerably more extensive than previously recognised and incorporates the Willowbank Clastics described in the southwest YSGB in this study (Section 3.4.1.5). Whole rock geochemistry of volcanic rocks presented in Chapter 6 is used to make correlations with coeval units in neighbouring belts and reaffirm geochronological data. These results demonstrate that an entire greenstone belt, comprising a lower unit of mafic-ultramafic volcanic rocks and an unconformably overlying metasedimentary succession, was formed within 15 Ma, unlike the much longer periods of development observed and inferred elsewhere in Archaean cratons.

8.2 Summary of Published Geochronology

Current understanding, based on limited published geochemical and geochronological data, is that the YSGB comprises a protracted, autochthonous 2960-2740 Ma stratigraphy similar to the rest of the Murchison Domain (Van Kranendonk et al., 2013). Previous geochronological work in the belt is described in detail in Section 2.2 and is briefly summarised here. The location and ages of published geochronological samples are shown on Figure 8.1, and all ages referred to in this chapter correspond to SHRIMP U-Pb zircon $^{207}Pb/^{206}Pb$ ages. The age of Gossan Hill Fm basement rocks is well constrained

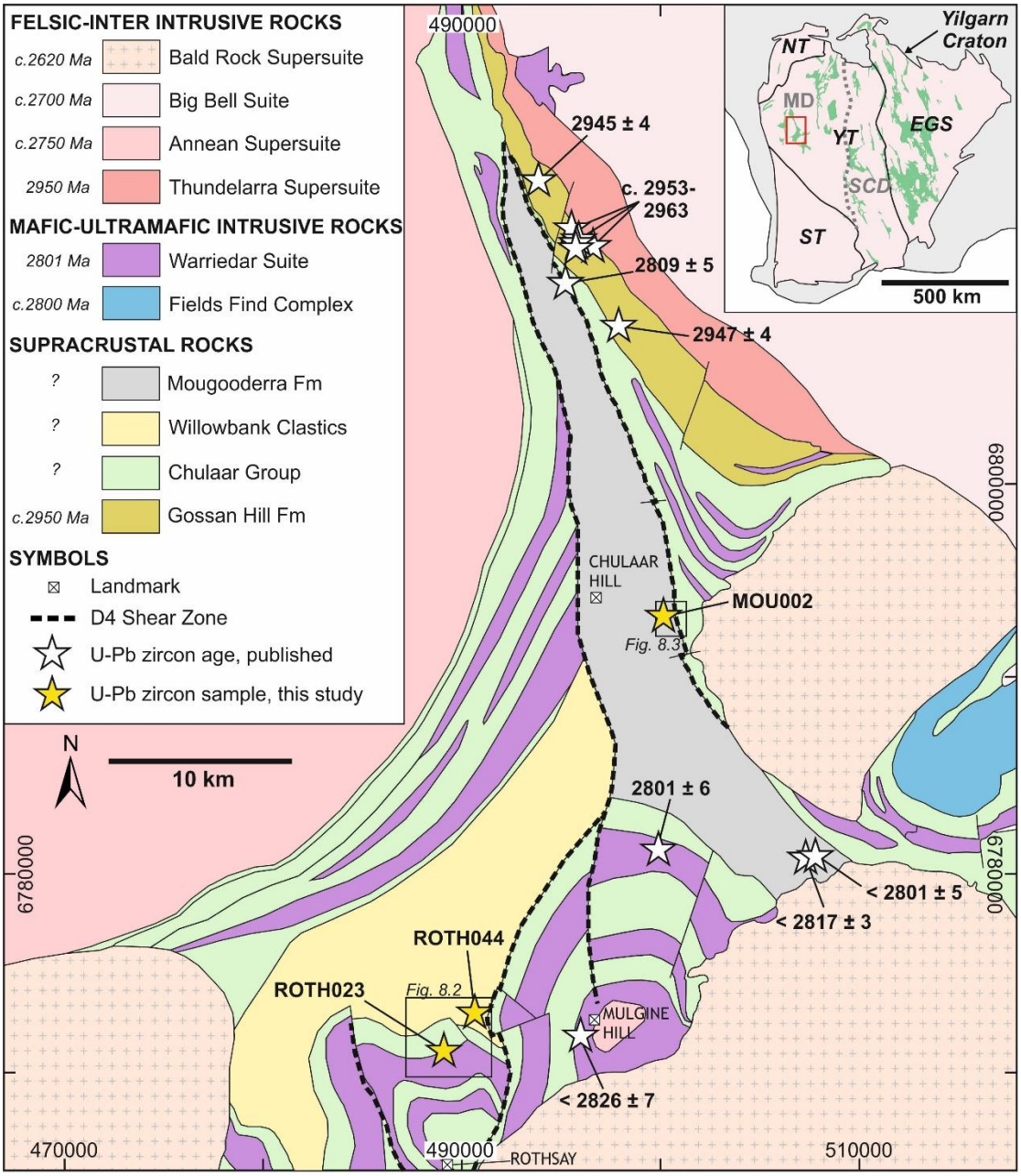

Figure 8.1: Geological map of the central Yalgoo-Singleton greenstone belt, showing the location of published U-Pb zircon ages (white stars) and U-Pb geochronology samples analysed in this study (yellow stars). NT= Narryer Terrane, YT = Youanmi Terrane, ST = Southwest Terrane, EGS = Eastern Goldfields Superterrane, MD = Murchison Domain, SCD = Southern Cross Domain. Geology after Geological Survey of Western Australia. Chulaar Group and Willowbank Clastics are informal names given to unassigned units. Inset map after Cassidy et al. (2006). < refers to maximum depositional/crystallisation ages. Published geochronology data is acquired from the GSWA geochemistry database. References referred to in the main text.

at 2940-2965 Ma from zircon U-Pb dating of several felsic volcanic and volcaniclastic samples (Wang et al., 1998; Wingate et al., 2015a; 2015b; 2015c; Fig. 8.1). In contrast, the age of the overlying Chulaar Group is poorly constrained; zircon U-Pb dating of a volcaniclastic sandstone near the base of the Chulaar Group gave an unreliable estimate of maximum depositional age, interpreted conservatively at 2894 ± 7 Ma based on five zircon analyses or more tentatively at 2826 ± 7 Ma, based on analysis of a single zircon crystal (Lu et al., 2016a). The crystallisation age of a mafic-ultramafic Warriedar Suite

sill intruding Chulaar Group volcanic rocks in the area has been constrained at 2801 ± 6 Ma, providing a minimum age for the host volcanic rocks (Lu et al., 2016b).

Rocks of the Willowbank Clastics have not previously been dated and their age remains unconstrained. Despite multiple attempts at dating the metasedimentary Mougooderra Fm, a conclusive depositional age is yet to be determined. In the study area, previous dating attempts have yielded a maximum depositional age of 2817 ± 3 Ma (quartz sandstone; Lu et al., 2018) and a maximum crystallisation age of 2801 ± 5 Ma from zircons that were interpreted as xenocrystic in a metadacite (Lu et al., 2016c). A volcanogenic sandstone sampled close to the sheared unconformable contact between the Mougooderra Fm and Chulaar Group returned a U-Pb zircon depositional age of 2809 ± 5 Ma (Wang et al., 1998). However, the stratigraphic unit to which this sample belongs is ambiguous. The angular unconformity at the base of the Mougooderra Fm is postulated to have formed during diapiric emplacement of ca. 2750 Ma granitic rocks in the region (Zibra et al., 2018). Zibra et al. (2018) suggest that a ca. 2750 Ma age is tentatively supported by U-Pb zircon dating of a Mougooderra Fm volcaniclastic siltstone sampled approximately ~50 km north of the study area. However, in addition to ca. 2750 Ma zircons, this sample also contains several populations ranging in age between 2953-2612 Ma. Analyses <2750 Ma are tentatively ascribed to hydrothermal activity, due to the close proximity of the sample to a major shear zone (Zibra et al., 2018). Therefore, owing to the uncertainties associated with the interpretation of these dates, the age of most of the supracrustal stratigraphy in the YSGB remains poorly known.

8.3 Methods Summary

Sensitive High Resolution Ion Microprobe (SHRIMP) U-Pb zircon isotopic analysis has been undertaken on three rock samples from undated units in the YSGB, namely the informal Chulaar Group and Willowbank Clastics, and the formal Mougooderra Fm. Sampling was targeted at lithologies within these units that were considered most likely to contain primary zircons. Sample preparation was undertaken at Cardiff University and zircon separation was carried out at the NERC Isotope Geoscience Laboratories in Keyworth, UK. Zircon separates were optically picked, mounted with reference materials, and imaged at Curtin University, Western Australia. Analysis was performed by SHRIMP II at the John de Laeter Centre, Curtin University. Full methods detailing sample preparation, analytical techniques, operating conditions, and standard data can be found in **Appendix B2**.

8.4 Results

A table summarising geochronological results for the three analysed samples can be found in **Appendix E9**. New U-Pb ages presented in this chapter are given with uncertainties at the 2SD level.

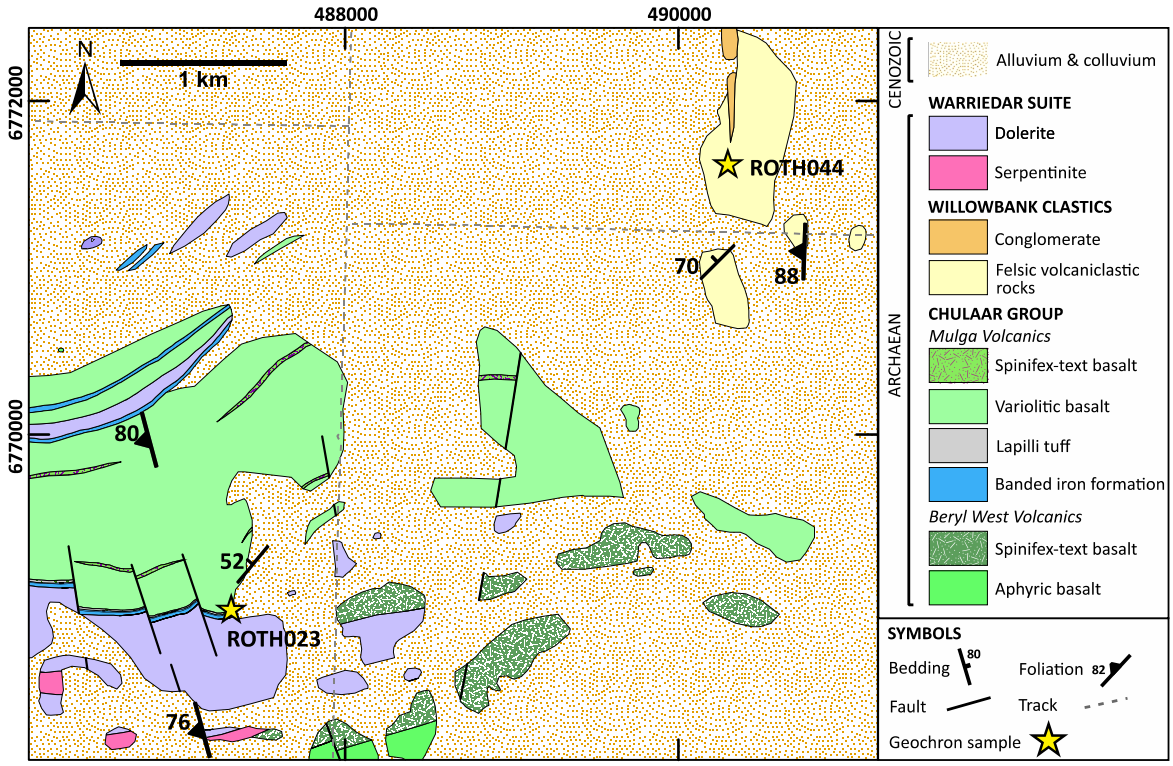

Figure 8.2: Geological map of the area surrounding the location of geochronology samples ROTH023 and ROTH044.

8.4.1 Chulaar Group SHRIMP analysis

8.4.1.1 Rationale for dating

Volcanic and interflow sedimentary rocks of the Chulaar Group represent a major proportion of the supracrustal sequence in the YSGB. However, the emplacement age of these rocks has not been determined. Owing to the prevalence of mafic-ultramafic volcanic units and the difficulty of separating zircons from these lithologies, the only previous attempt at U-Pb zircon analysis of a Chulaar Group volcanogenic sandstone yielded a detrital zircon spectrum and an unreliable maximum depositional age (Lu et al., 2016a). Regional stratigraphic comparison with comparable rocks in the well dated supracrustal succession of the northeast Murchison Domain has been difficult and limited to geochemical comparisons of volcanic rocks (Wyman, 2019; Koutsoumbis, 2020). A lapilli-bearing tuffaceous unit interbedded within the volcanic succession in the southwest of the YSGB has been targeted to better define the age of the Chulaar Group.

8.4.1.2 Sample description

Sample ROTH023 (116.8695° E, 29.2081° S) is a thinly bedded andesitic lapilli tuff collected from a patchy outcrop situated ~8.5 km north of Rothsay, in the southwest YSGB (Fig. 8.1). The 5 m-thick unit occurs at the base of the Mulga Volcanics in the upper part of the Chulaar Group (Section 3.4.1.4), underlying a >1.5 km pile of intercalated aphyric, variolitic and spinifex-textured volcanic rocks. The

tuff directly overlies a 10 m-thick cherty BIF unit, which in turn, overlies a >500 m-thick Warriedar Suite intrusion (Gardner Sill; Fig. 8.2).

Tuffaceous units at the base of the Mulga Volcanics occur as fine-grained, friable, light grey, finely bedded and ash-dominated rocks in hand specimen, which are characterised by rounded 1-3 mm volcanic clasts that are interpreted as lapilli (Section 3.4.1.4). Sample ROTH023 consists of 5-15 mm-thick beds dominated by fine, grey ash, comprising alternations between fine to medium-grained quartz-bearing beds, and very fine-grained lapilli-bearing beds. A detailed petrographic description of sample ROTH023 is given in Section 5.3.6. The presence of abundant lapilli, in addition to numerous ~0.2 mm rod-shaped fragments of quartz that possibly represent relic shards of volcanic glass, indicates proximal volcanism during deposition of the unit. Furthermore, features such as graded

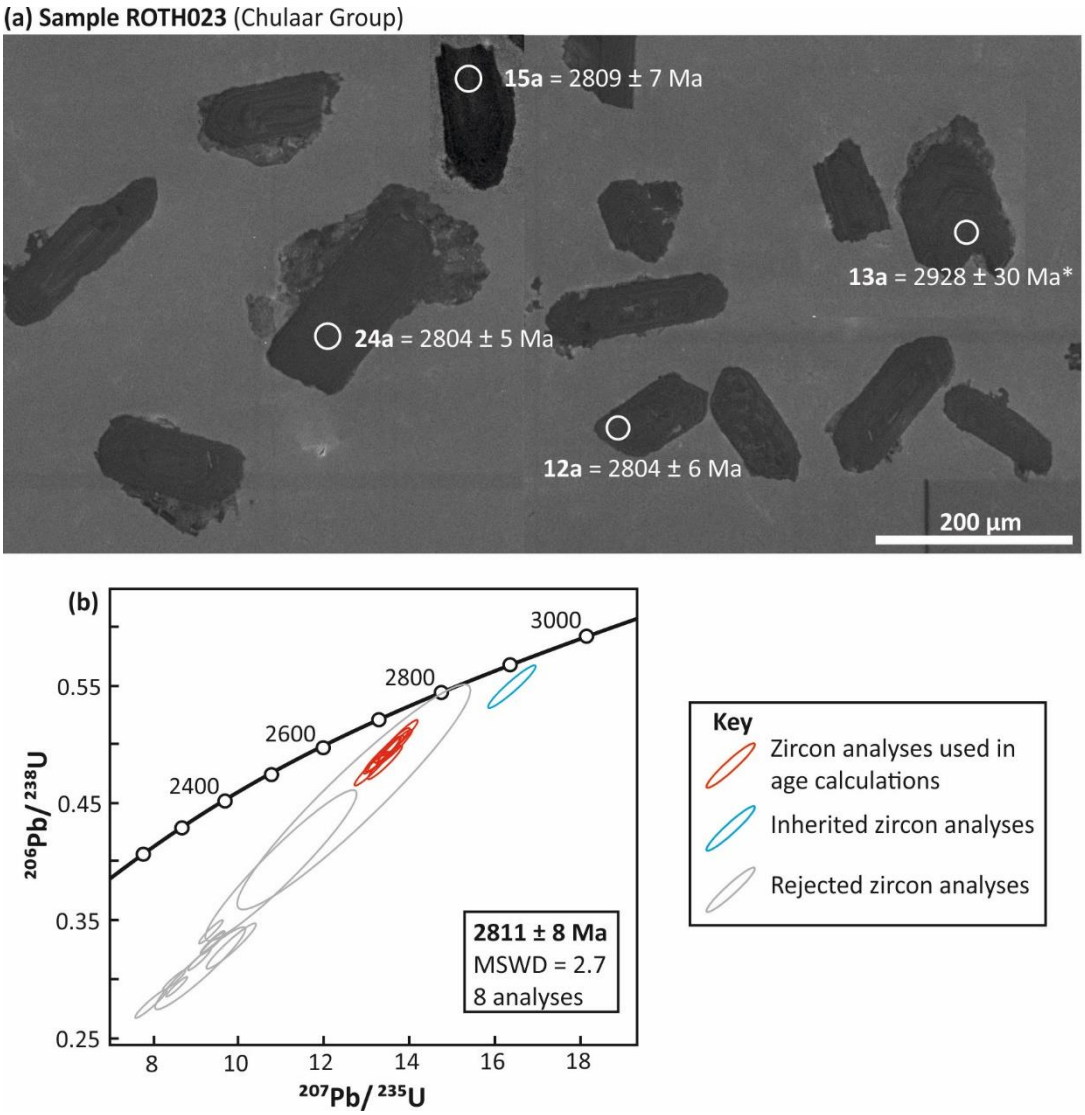

Figure 8.3: **(a)** Cathodoluminescence (CL) imagery of representative zircons, selected spot locations and zircon ages from sample ROTH023 of the Chulaar Group. * denotes analyses with >10% discordance that have been excluded from age calculations; **(b)** Concordia diagrams of all zircon analyses from sample ROTH023; red denotes analyses used in age calculations, blue denotes analyses of inherited zircon grains and grey denotes reject analyses. Error ellipses are shown at 1σ level.

bedding and erosive bases are indicative of periods of sedimentary re-working between eruptive episodes. Notably, zircon crystals have been identified both in the ash-dominated groundmass, where they commonly define graded bedding, and within lapilli clasts. Zircon crystals separated from sample ROTH023 are light brown in colour and range in size from 50 to 200 µm. Crystals largely consist of euhedral-subhedral tetragonal and prismatic grains or angular fragments of grains and display little to no compositional zoning (Fig. 8.3a).

8.4.1.3 SHRIMP U-Pb zircon analysis

Twenty analyses were undertaken on 20 zircon grains from sample ROTH023. Nine concordant analyses form two groups (**Appendix E9**). Eight analyses give a weighted mean $^{207}Pb/^{206}Pb$ age of 2811 ± 8 Ma (Mean Square Weighted Deviation [MSWD] = 2.7; Fig. 8.3b). This is interpreted as the age of deposition and coeval volcanism, due to the presence of zircon-bearing lapilli and features interpreted as volcanic glass shards. A single fragmented zircon grain is dated at ca. 2954 Ma, consistent with the age of underlying basement rocks and interpreted as an inherited grain. Eleven strongly discordant (> 17%) analyses with excessive Th/U ratios were rejected and excluded from age calculations (**Appendix E9**).

8.4.2 Willowbank Clastics SHRIMP analysis

8.4.2.1 Rationale for dating

The Willowbank Clastics represents an informal, undated succession of metasedimentary and volcaniclastic rocks in the southwest YSGB, overlying Chulaar Group volcanic rocks. The relationship between Willowbank Clastics and rocks of the Mougooderra Fm is ambiguous. The Willowbank Clastics may be related to, and thus form part of, the Mougooderra Fm, as suggested by their similar stratigraphic position (Section 4.2.1), in addition to comparable petrography (Chapter 5) and geochemistry of volcaniclastic rocks (Section 6.4.2). Alternatively, the Willowbank Clastics may represent an intermediate unit between the Chulaar Group and Mougooderra Fm that is only preserved in the southwest of the belt. To constrain the depositional age of the Willowbank Clastics, an outcrop of felsic volcaniclastic rocks north of the Rothsay area has been targeted for dating.

8.4.2.2 Sample description

Sample ROTH044 (116.9002° E, 29.1840° S) is a felsic metavolcaniclastic rock collected from a moderately well exposed, low lying outcrop situated 11.5 km north-northeast of Rothsay, in the southwest of the study area (Fig. 8.1). The unit forms part of a sequence of felsic volcaniclastic rocks

and conglomerate comprising the Willowbank Clastics, which stratigraphically overlies the Chulaar Group volcanic-dominated succession in this area (Fig. 8.2). Sample ROTH044 was collected ~4 km northeast of sample ROTH023 (Fig. 8.2).

Willowbank Clastics felsic volcaniclastic rocks are fine-grained, cream-white in colour, friable and weakly bedded to massive in hand specimen. The petrography of sample ROTH044 is described and illustrated in Section 5.4.4. The sampled volcaniclastic unit consists of ~20% sub-angular quartz crystals and ~30% sub-rounded, cherty lithic clasts in a fine-grained, weak to moderately clay-altered, quartzofeldspathic groundmass. A weakly to moderately developed foliation is shown by the alignment of lithic clasts and attributed to proximity (<500 m) to the concealed Enchanted Shear Zone to the east (Fig. 8.2). Zircon crystals separated from sample ROTH044 are pale to dark brown, 100-300

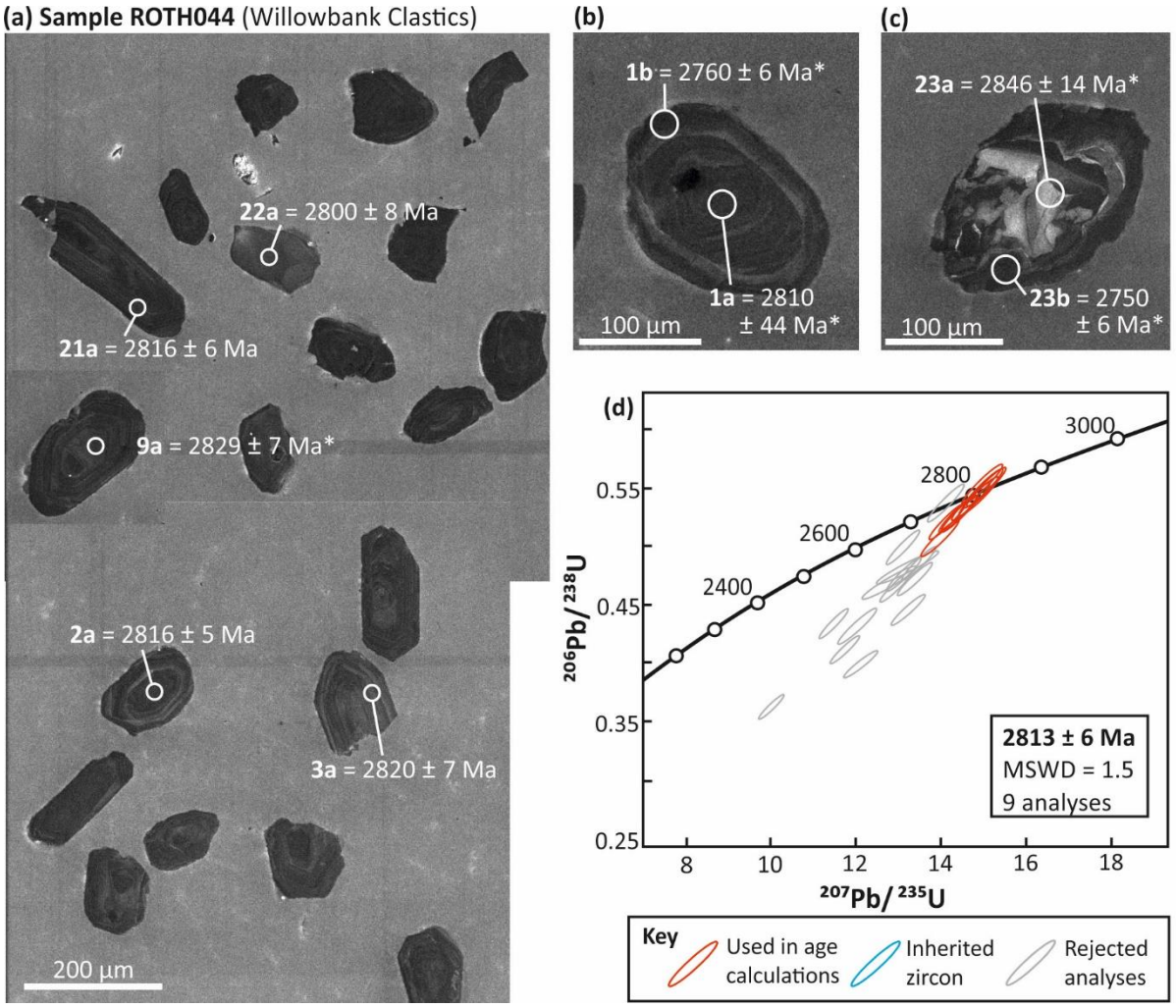

Figure 8.4: **(a)** Cathodoluminescence (CL) imagery of representative zircons, selected spot locations and zircon ages from sample ROTH044 of the Willowbank Clastics. * denotes analyses with >10% discordance that have been excluded from age calculations; **(b)** CL image of a ROTH044 zircon comprising a ca. 2810 Ma core surrounded by a <20 µm-thick rim aged returning a >10% discordant age of ca. 2760 Ma with a low U/Th ratio, interpreted as a late overgrowth related to fluid flow activity; **(c)** CL image of a ROTH044 zircon comprising an irregular core dated at ca. 2845 Ma, overprinted by a narrow rim returning a > 10% discordant age of ca. 2750 Ma and with a low U/Th ratio, interpreted as a late overgrowth as in (b); **(d)** Concordia diagrams of all zircon analyses from sample ROTH044; red denotes analyses used in age calculations, blue denotes analyses of inherited zircon grains and grey denotes reject analyses. Error ellipses are shown at 1σ level.

µm in size with 2:1-3:1 elongation and are prismatic euhedral-subhedral with pyramid terminations (Fig. 8.4a). A few grains are angular fragments of larger crystals. Well-developed oscillatory zoning is present and reveals rounded cores in a minority of zircon grains (Figs. 8.4a-c).

8.4.2.3 SHRIMP U-Pb zircon analysis

Twenty-three analyses were carried out on 21 zircons from sample ROTH044. Eleven concordant to slightly discordant analyses form two groups (Fig. 8.4d; **Appendix E9**). Nine analyses forming the main group give a weighted mean $^{207}Pb/^{206}Pb$ age of 2813 ± 6 Ma (MSWD = 1.5), interpreted as the depositional age of the rock and age of coeval felsic volcanism. Two analyses of irregular <20 µm rims surrounding 'main group' zircon cores yield ages of ca. 2750-2760 Ma (Figs. 8.4b, 8.4c), one of which is moderately discordant. These rims have markedly low U/Th ratios in comparison to main-group zircons and have ages that are broadly consistent with the age of c. 2750 Ma Annean Supersuite granitic intrusions adjacent to the YSGB, including the Yalgoo Dome and Mt Mulgine Dome (Chapter 4; Zibra et al., 2018) and thus are attributed to fluid flow activity related to this episode of magmatism. Eleven strongly discordant analyses (> 18%) and one analysis with a very high common Pb content were excluded from age calculations.

8.4.3 Mougooderra Fm SHRIMP analysis

8.4.3.1 Rationale for dating

Previous attempts at dating the Mougooderra Fm have either yielded maximum depositional and maximum crystallisation ages (Lu et al., 2016c; 2018), or have involved debatable interpretations of a hydrothermally altered sample containing 2960-2600 Ma zircons (Zibra et al., 2018). Consequently, the depositional age of Mougooderra Fm rocks remains unclear. The Mougooderra Fm represents the most extensive metasedimentary sequence in the southwestern Murchison Domain and exhibits a similar geometry to late clastic basins in the Eastern Yilgarn Craton (e.g., Krapež et al., 2008). However, this episode of clastic deposition in the southwestern Murchison Domain is essentially undated. An outcropping felsic volcaniclastic unit proximal to the inferred base of the Mougooderra Fm was selected for geochronological analysis. This unit was chosen as it was more likely to contain primary magmatic zircons from volcanism coeval with deposition, in contrast to the detrital zircon assemblages previously analysed in Mougooderra Fm metasedimentary rocks.

8.4.3.2 Sample description

Sample MOU002 (117.0145° E, 28.9840° S) is a felsic metavolcaniclastic rock collected from a slightly weathered, patchy outcrop located ~4.5 km southeast of Chulaar Hill (Fig. 8.1). The volcaniclastic unit

forms part of the metasedimentary-dominated Mougooderra Fm and is interbedded with pebbly sandstone and conglomerate (Fig. 8.5). The sample was collected ~350 m west of the sheared eastern contact of the Mougooderra Fm with Chulaar Group volcanic rocks, marked by the CSZ (Fig. 8.5). Notably, the unit does not display evidence of hydrothermal alteration observed along the CSZ.

The Mougooderra Fm felsic volcaniclastic unit is fine-grained, friable, light yellow to white and weakly bedded in hand specimen. The unit has an almost identical, albeit slightly less-altered, composition and appearance to felsic volcaniclastic rocks of the Willowbank Clastics, including sample ROTH044. A detailed petrographic description of sample MOU002 is given in Section 5.5.2. The volcaniclastic unit is dominated by a fine-grained (<0.1 mm) microcrystalline quartzofeldspathic groundmass comprising quartz, feldspar, sericite, actinolite and chlorite. The groundmass contains sub-angular quartz crystals up to 1 mm in size, sub-rounded felsic volcanic lithic clasts up to 1.5 mm in size and lithic clasts of chert up to 2 mm in size, interpreted as quartz-rich or recrystallised glassy lithic clasts (Section 5.5.2). The unit possesses a moderate foliation defined by elongate actinolite crystals and the alignment of lithic clasts. Zircons yielded from sample MOU002 are light to dark brown in colour, range in size from 100-300 µm and are typically prismatic with euhedral to subhedral crystal faces and some pyramidal

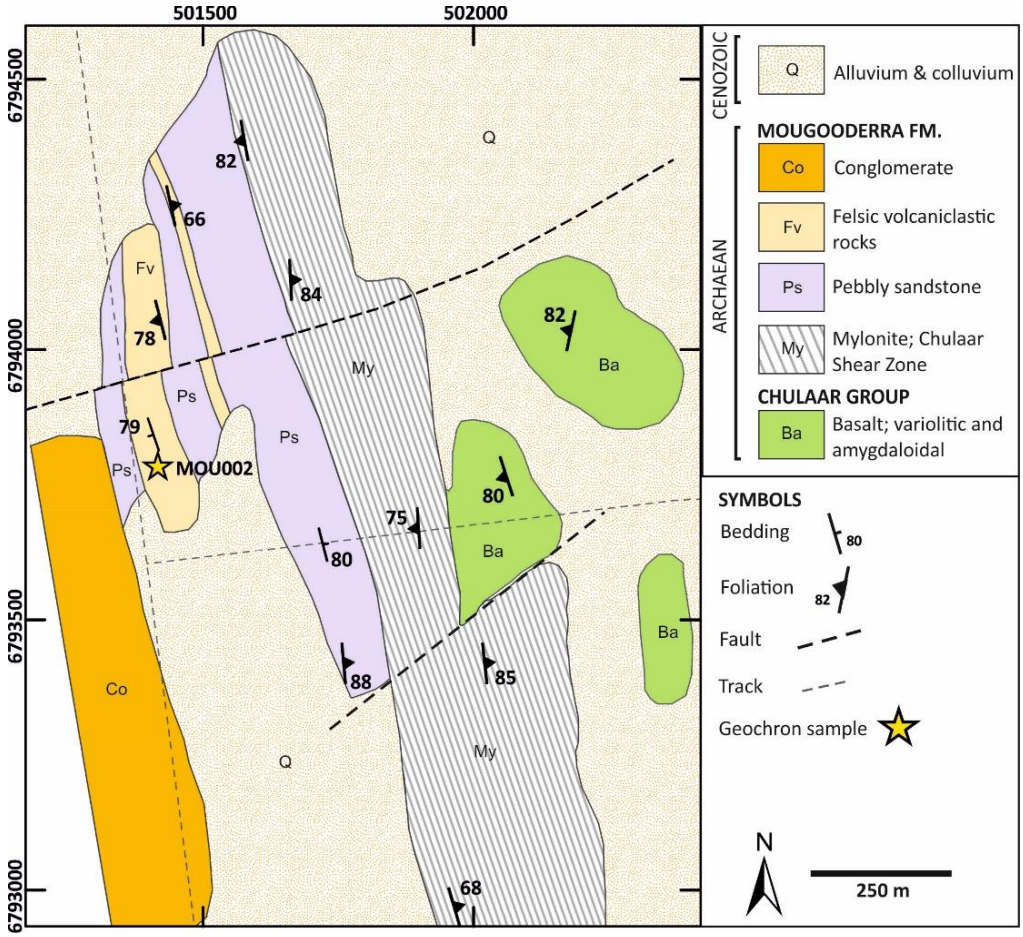

Figure 8.5: Simplified geological map of the area surrounding the location of geochronology sample MOU002. Representative structural measurements are shown.

terminations (Fig 8.6a). Oscillatory growth zoning is abundant and approximately half of the crystals exhibit visible, rounded, homogenous cores lacking zonation (Fig. 8.6b). One distinctive single grain consists of an oscillatory-zoned, angular zircon fragment, overprinted by a homogenous, irregular ~50 µm-thick rim (Fig. 8.6c). A few zircon grains also have very bright, irregular < 20 µm rims.

8.4.3.3 SHRIMP U-Pb zircon analysis

Thirty-five analyses were undertaken on 28 zircon crystals from sample MOU002. Twenty-eight concordant to slightly discordant analyses fall into two groups (Fig. 8.6d). A weighted mean $^{207}Pb/^{206}Pb$ age of 2818 ± 3 Ma (MSWD = 0.85; Fig. 8.6d) was calculated from 26 concordant to slightly discordant analyses in the first group, interpreted as the depositional age of the rock and age of coeval felsic volcanism. This group includes multiple analyses from grains that consist of homogenous cores and brighter, oscillatory-zoned rims, which yielded ages that are essentially indistinguishable (Fig. 8.6a,

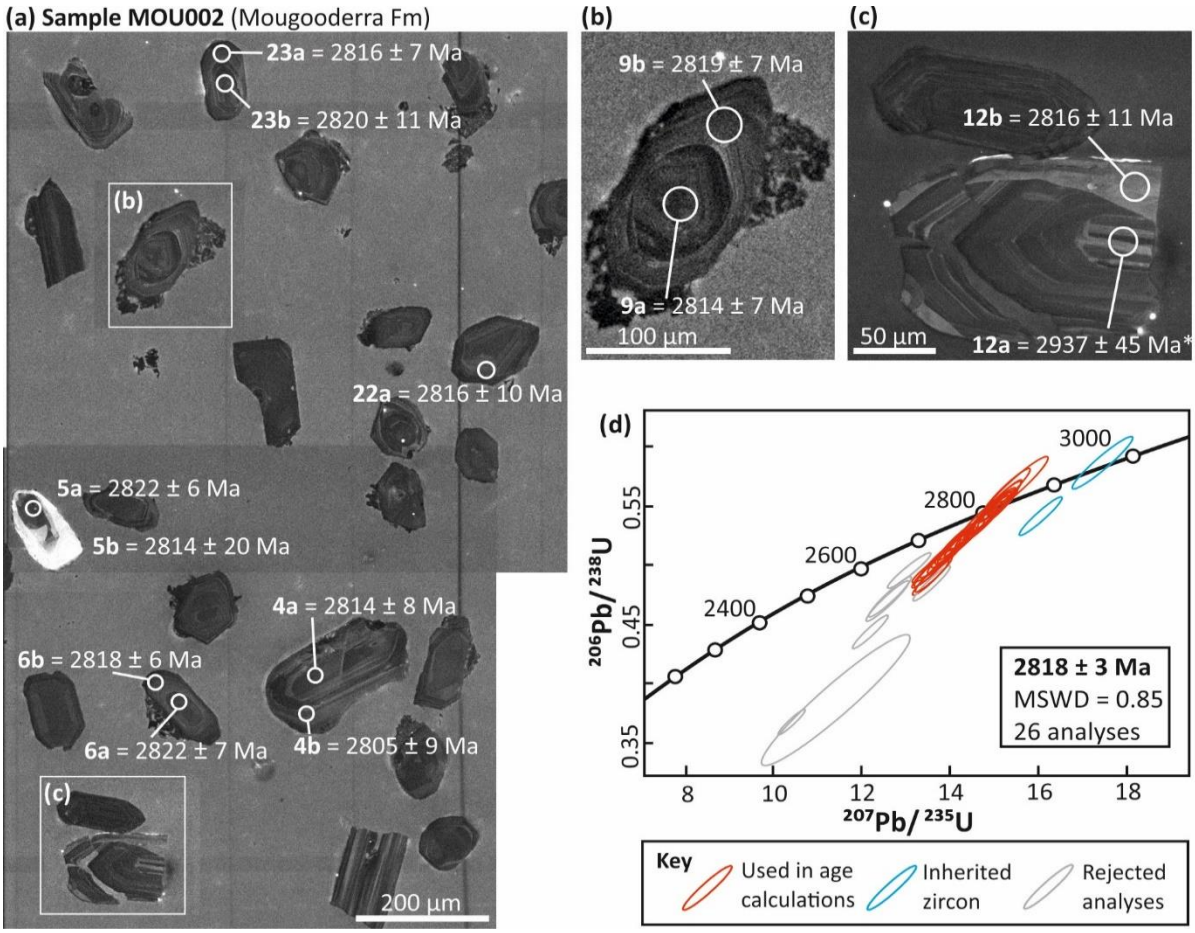

Figure 8.6: **(a)** Cathodoluminescence (CL) imagery of representative zircons, selected spot locations and zircon ages from sample MOU002 of the Mougooderra Fm. * denotes analyses with >10% discordance that have been excluded from age calculations; **(b)** CL image of a MOU002 zircon comprising a rounded core and oscillatory-zoned rim, both of which return comparable ages within error; **(c)** CL image of a MOU002 zircon comprising a ca. 2940 Ma core fragment, surrounded by a ca. 2815 Ma main-group rim, representing an overprinted inherited zircon crystal; **(d)** Concordia diagrams of all zircon analyses from sample MOU002; red denotes analyses used in age calculations, blue denotes analyses of inherited zircon grains and grey denotes reject analyses. Error ellipses are shown at 1σ level.

Fig. 8.6b). Two analyses of zoned cores yielded ca. 2950 Ma ages, both of which are surrounded by ca. 2815 Ma rims, consistent with inheritance and overprinting of zircons from basement lithologies. Five highly discordant (> 10%) analyses and two analyses with excessive Th/U, suggesting high common Pb, were rejected and excluded from age calculations. This includes a zircon rim that yielded a discordant age of ca. 2755 Ma, with a comparable geometry to the ca. 2750 Ma overgrowths in sample ROTH044 and is also attributed to late fluid flow associated with diapirism at ca. 2750 Ma.

8.5 Discussion

8.5.1 Correlations indicated by SHRIMP geochronology

The new geochronological data presented in this chapter has constrained the depositional ages of rocks assigned to the informal Willowbank Clastics, and the more extensive metasedimentary-dominated Mougooderra Fm. The relationship between these two units needs to be evaluated before the implications of new geochronological data can be discussed. SHRIMP U-Pb zircon analysis of similar felsic volcaniclastic samples from the Willowbank Clastics and Mougooderra Fm yield depositional ages of 2813 ± 6 Ma and 2818 ± 3 Ma, respectively. These ages are within error of one another, with the interpreted depositional age of the Mougooderra Fm slightly older than that of the Willowbank Clastics. In combination with equivalent stratigraphic positions, comparable lithologies and the strikingly similar petrography (Chapter 5) and geochemistry of volcaniclastic rocks (Section 6.4.2), this demonstrates that the Willowbank Clastics and Mougooderra Fm are coeval and belong to the same

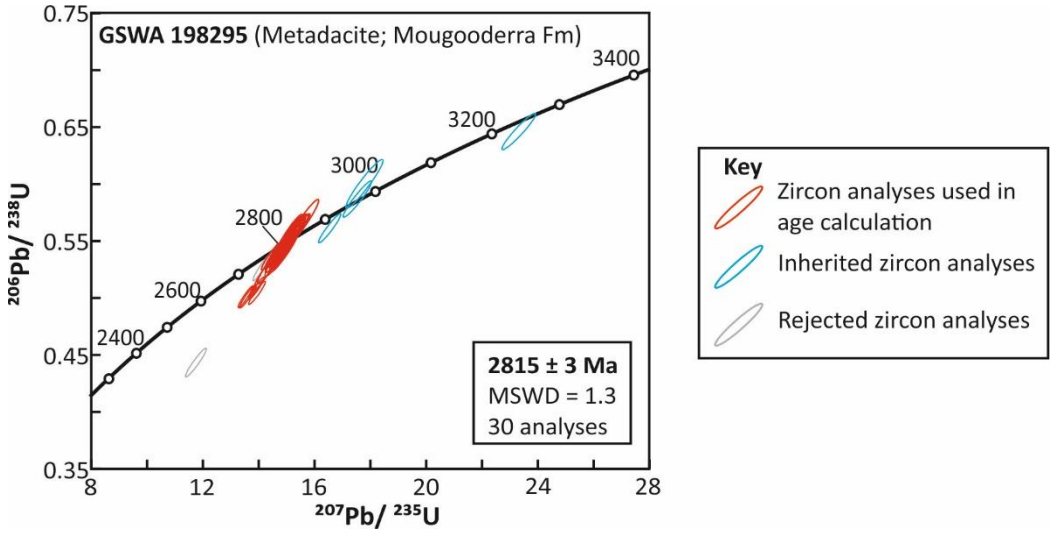

Figure 8.7: Concordia diagram displaying reinterpreted SHRIMP zircon U-Pb analyses from GSWA sample 198295. Data from (Lu et al., 2016c). A crystallisation age of 2815 ± 3 Ma is based on thirty concordant analyses, with the youngest two analyses rejected due to minor loss of radiogenic Pb. Error ellipses are shown at 1σ level. Red represents analyses used in age calculation, blue represents inherited zircon analyses and grey represents rejected analyses.

portion of the supracrustal succession. Consequently, the sequence defined as the Willowbank Clastics in this thesis should be assigned to the Mougooderra Fm. As such, the two ages described above will herein be considered as depositional ages for the Mougooderra Fm.

8.5.2 Comparison with previous geochronology

The U-Pb zircon ages from this study represent the first robust ages for the Mougooderra Fm and underlying Chulaar Group in the study area. The new depositional age of 2811 ± 8 Ma for an interflow lapilli bearing tuff in the upper part of the Chulaar Group (sample ROTH023) is slightly younger than the published maximum depositional age of 2826 ± 7 Ma near its base in the Mt Mulgine area (GSWA 198293; Lu et al., 2016a) (Fig. 8.1). The 2818 ± 3 Ma and 2813 ± 6 Ma depositional ages of the overlying Mougooderra Fm (encompassing the Willowbank Clastics) are supported by the existing maximum depositional age of 2817 ± 3 Ma (GSWA 198294; Lu et al., 2018) (Fig. 8.8). These ages also broadly correspond with the depositional age of 2809 ± 5 Ma for the ambiguous volcanogenic sandstone sample reported by Wang et al. (1998), indicating that this unit also belongs to the Mougooderra Fm.

However, the new age data are not supported by the 2801 ± 6 Ma maximum crystallisation age of a Mougooderra Fm metadacite, determined from analysis of ostensibly xenocrystic zircon crystals (GSWA 198295; Lu et al., 2016c). Zircons isolated from this sample are large (up to 300 µm), euhedral-subhedral and exhibit ubiquitous concentric zoning, and several zircon crystals contain discernible cores (Lu et al., 2016c). Unusually for such an evolved volcanic rock, none of the 36 concordant to moderately discordant analyses of zircon rims and cores were interpreted as primary, and the

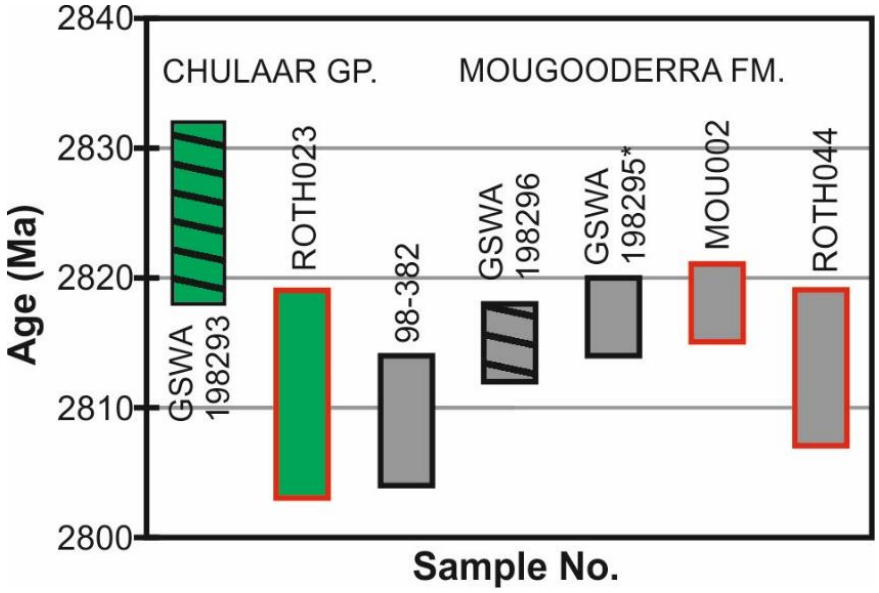

Figure 8.8: Age plot comparing the previously published U-Pb zircon ages from the YSGB to those presented in this study (outlined in red) from the Chulaar Group (green) and Mougooderra Fm (grey). Black hatch symbolises maximum depositional ages. References for published U-Pb crystallisation given in the main text. *reinterpreted magmatic crystallisation age in this study.

xenocrystic interpretation was based primarily on field relations and the presence of a few crystals with well-rounded and pitted outer surfaces (Lu et al., 2016c). Three zircon analyses in this sample yielded $^{207}Pb/^{206}Pb$ ages between ~2935-2957 Ma and a single zircon was dated at ~3259 Ma (Lu et al., 2016c), consistent with the age of inherited grains from basement rocks as identified in this study. The remaining 32 analyses include zircon cores and rims and form a single group of ages in the range 2780-2830 Ma, with 30 analyses between 2800-2830 Ma (Lu et al., 2016c). If the principal group of zircons isolated from this dacite sample (GSWA 198295) are instead considered to be primary magmatic (including rims overprinting older >2950 Ma inherited grains), then 30 concordant analyses give a crystallisation age of 2815 ± 3 Ma (MSWD = 1.3) for the host dacite, further supporting a ca. 2815 Ma age for the Mougooderra Fm (Fig. 8.7, Fig. 8.8). In this reinterpretation, the youngest two analyses are excluded from age calculations and are attributed to minor ancient loss of radiogenic Pb (Fig. 8.7).

The two new depositional ages, in addition to published maximum depositional ages and the reinterpreted crystallisation age (Fig. 8.8), therefore suggest that rocks of the Mougooderra Fm were emplaced at ca. 2818-2810 Ma. Considering that Chulaar Group rocks demonstrably underlie the Mougooderra Fm rocks (Section 4.2.1), the new 2811 ± 8 Ma depositional age for the upper Chulaar Group is difficult to reconcile with the ca. 2818-2810 Ma age of the overlying Mougooderra Fm. As the age data for the Chulaar Group is still limited, it is possible that the ~2811 Ma age determined in this study is marginally too young, and the older side of the error (c. 2818-2819 Ma) may represent the depositional age of the unit. Together with the 2826 ± 7 Ma maximum depositional age from the base of the group in the YSGB (Lu et al., 2016a), the new age data supports the emplacement of mafic-ultramafic volcanic rocks of the Chulaar Group at ca. 2825-2818 Ma. This timeframe for the eruption of a >3 km-thick sequence of dominantly basaltic volcanic rocks is broadly in line with previous age constraints in other Archaean greenstone belts. For example, a >2.7 km-thick sequence of mafic-ultramafic volcanic rocks comprising the Hooggenoeg Complex in the Barberton greenstone belt, South Africa, formed during a timespan of less than ~10 Ma (ca. 3472-3460 Ma; de Wit et al., 2011; de Wit et al., 2018).

An alternative interpretation of the new SHRIMP dating, in line with previous interpretations of Mougooderra Fm ages, is that all zircon crystals analysed in the Mougooderra Fm samples in this study are detrital and only constrain the maximum depositional age of the unit. As such, the actual depositional age of the Mougooderra Fm could be significantly younger, as anticipated by regional geological mapping and stratigraphic correlations (Van Kranendonk & Ivanic, 2009; Van Kranendonk et al., 2013; Zibra et al., 2018). Several lines of evidence challenge this contention. Firstly, according to this interpretation, all concordant to slightly discordant zircon analyses in the two felsic

volcaniclastic rocks in this study (n=39), the quartz sandstone at Warriedar Hill (n=63), the volcanogenic sandstone along the CSZ (n=17) and the dacite at Warriedar Hill (n=41) are considered to be detrital or xenocrystic, with not a single primary zircon crystal analysed derived from either concurrent felsic volcanism, crystallised directly from a dacitic magma, or overprinting zircon xenocrysts in a dacitic magma. This appears to be highly improbable considering the types of lithologies from which zircons have been separated.

Secondly, there is a distinct lack of suitable source rocks from which abundant 2820-2810 Ma detrital zircons may have been derived in the area. The Chulaar Group underlying the Mougooderra Fm is dominated by mafic-ultramafic volcanic rocks, with subordinate BIF and quartzite and rare, thin (<5 m) volcaniclastic units; none of which can suitably account for abundant 2820-2810 Ma detrital zircons. The Macs Well Clastics distinguished in the Rothsay area (Section 3.4.1.1) contains a 10 m-thick porphyritic dacite unit and an 80-180 m-thick banded felsic volcaniclastic unit, however, these units are not laterally extensive and have not yet been identified elsewhere in the belt. The most likely sources of abundant detrital zircons in the YSGB are felsic volcanic and volcaniclastic rocks of the Gossan Hill Fm, however, these units have been reliably dated at 2960-2940 Ma. Furthermore, recent geological mapping and geochronology of intrusive rocks has not distinguished any ca. 2820 Ma granitoid intrusions in the southwestern Murchison Domain, with the nearest identified felsic intrusions of this age (Mt Kenneth Suite) located > 100 km east of the study area. The typically sub-angular nature of zircons analysed in this study, combined with sub-rounded to sub-angular, zircon-bearing felsic lithic clasts in volcaniclastic rocks, is indicative of a proximal, rather than distal, zircon source.

For these reasons, the logical source of zircons in volcanogenic and volcaniclastic rocks is suggested to be proximal, concurrent volcanism, and the zircon crystals in the reinterpreted Mougooderra Fm dacite unit (GSWA 198295; Lu et al., 2016c) are considered to have crystallised directly from the parent magma. Thus, the depositional age of the analysed Mougooderra Fm rocks is interpreted to be ca. 2818-2810 Ma.

8.5.3 Stratigraphic Implications

New age constraints of previously undated supracrustal units in the YSGB have important stratigraphic implications and allow the geology of the study area to be placed within the revised stratigraphic framework of much of the rest of the Murchison Domain (Van Kranendonk et al., 2013; Lowrey et al., 2020). The current stratigraphic framework for the Murchison Domain is shown in Figure 2.2 and described in detail in Section 2.1.3.

Prior to this study, the greenstone sequence underlying the Mougooderra Fm in the study area (assigned to the Chulaar Group in this study) has been partially assigned to the Polelle Group due to lithological similarities encountered during regional geological mapping (Zibra et al., 2016; 2017a; Ivanic, 2018). A recent geochemical study focussing on a portion of Chulaar Group volcanic rocks north of Mt Mulgine has also drawn similarities to the Bassetts Volcanic Member of the Meekatharra Fm (Polelle Group) in the northeastern Murchison Domain (Koutsoumbis, 2020). Recent geological mapping has assigned the greenstone succession underlying the Mougooderra Fm to the south of the study area to the Singleton Fm of the Norie Group (Ivanic, 2018). The new depositional age of 2811 ± 8 Ma for base of the Mulga Volcanics defined in the Rothsay area, suggests that the Chulaar Group is temporally-equivalent to the Singleton Fm of the Norie Group in the current regional stratigraphic framework (Lowrey et al., 2020). This correlation is supported by geochemical comparisons of volcanic rocks in the Chulaar Group and Singleton Fm, described in Section 7.7.2. Specifically, Chulaar Subgroup 2 volcanic rocks exhibit major and trace element compositional similarities with the upper Singleton Fm defined in the northeastern Murchison Domain (Lowrey et al., 2020), and a single sample assigned to the lower Singleton Fm at Mt Magnet (Wyman, 2019) (Fig. 7.18c). Previous speculative correlations between exposed Chulaar Group rocks in the study area and the Polelle Group in the northeast Murchison Domain (e.g., Ivanic, 2018) are not supported by new geochronological data.

The Mougooderra Fm is provisionally assigned to the Glen Group in the current regional stratigraphic framework (Section 2.1.3.4) and has been suggested to represent the southwestern equivalent of the ca. 2735 Ma Ryansville Fm located in the northeast Murchison Domain (Ivanic et al., 2015a; Lowrey et al., 2020). However, the new interpreted ca. 2815 Ma depositional age for the Mougooderra Fm demonstrated by this study is inconsistent with previous correlations with the Glen Group, and instead indicate that the Mougooderra Fm is approximately time-equivalent with the ca. 2815-2805 Ma Yaloginda Fm of the Norie Group.

The Mougooderra and Yaloginda formations display stratigraphic and compositional similarities. Both formations comprise ~2-3 km-thick successions that contain felsic volcaniclastic rocks and andesitic-dacitic volcanic rocks near their bases, overlain by significant thicknesses of shale with lesser BIF and chert (Watkins & Hickman, 1990; Lowrey et al., 2020). The Mougooderra Fm contains units of conglomerate and quartz sandstone that are not as prevalent in the Yaloginda Fm. A temporal stratigraphic correlation is further supported by whole rock geochemistry of rocks from the Mougooderra Fm and Yaloginda Fm (Section 7.7.3). The major and trace element geochemistry of compositionally distinctive Mougooderra Fm high-Mg andesites and dacites described in this study (including geochronology sample GSWA 198295; Lu et al., 2016c) is remarkably similar to porphyritic high-Mg andesites of the Yaloginda Fm (Section 7.7.3; Fig. 7.19), although it is noted that high-Mg

andesites have also been identified in the Wattagee Fm of the Glen Group. Furthermore, a felsic volcaniclastic sample from the base of the Mougooderra Fm (sample MOU012) is geochemically identical to Yaloginda Fm rhyolitic tuffs spatially associated with high-Mg andesites in the northeastern Murchison Domain (Fig. 7.19; Lowrey et al. 2020)

In summary, the new geochronological data presented in this chapter and geochemical data presented in Chapter 6 indicates that supracrustal rocks in the YSGB are equivalent to Norie Group rocks elsewhere in the Murchison Domain; the informal Chulaar Group defined in this study is time-equivalent to the Singleton Fm, and the Mougooderra Fm is time equivalent with the overlying Yaloginda Fm. Consequently, the unconformity identified between the Mougooderra Fm and Chulaar Group (described in Section 2.4.3.4) indicates a ~2818 Ma hiatus and resulting unconformity that is not apparent in the northeastern Murchison Domain.

8.5.4 Short timescale for greenstone belt formation

The depositional ages for the Chulaar Group and Mougooderra Fm are all within error (Fig. 8.8), suggesting relatively rapid formation of supracrustal units over a period of < 15 Ma. This timeframe encompasses the eruption of mafic-ultramafic volcanic rocks, variably attributed to mantle-plume related volcanism (Van Kranendonk et al., 2013) or subduction-related volcanism in the region (Wyman & Kerrich, 2012; Wyman, 2019) followed by uplift and erosion, extension, and sedimentary deposition. Hence, the intervening unconformity represents only a few million years rather than the previously proposed ~80 Ma (Zibra et al., 2018). This < 15 Ma timescale between a lower mafic-ultramafic volcanic-dominated sequence and unconformably overlying clastic sedimentary rock, is significantly shorter than that typically inferred for other Archaean greenstone belts, including those of neighbouring granite-greenstone terranes (e.g., Van Kranendonk et al., 2013; Romano et al., 2014).

The north-south trending terranes comprising the Yilgarn Craton show a general supracrustal age progression from west (oldest) to east (youngest) (Cassidy et al., 2006; Fig. 8.1). This geometry has been used in part to support models invoking subduction-related accretion of successive terranes (e.g., Myers, 1995; Czarnota et al., 2010; Goscombe et al., 2019). Geochronology of supracrustal rocks within each of these terranes (summarised by Mole et al., 2019) consistently suggests a protracted formation timescale despite each having a distinct stratigraphy and history. In the eastern Kalgoorlie Terrane, two distinct supracrustal successions were deposited in > 60 Ma (Kositcin et al., 2008; De Joux et al., 2013). In the Southern Cross Domain, the Lake Johnstone belt appears to have been formed in > 45 Ma (Romano et al., 2014) and the stratigraphy of belts in the northeast Murchison Domain, in

the far west of the Yilgarn Craton, were largely developed over a ~110 Ma period (Van Kranendonk et al., 2013).

Kamber (2015) distinguishes two types of Archaean continental lithosphere based on the Pb isotope composition of hosted granitoids and the occurrence of inherited Eoarchaean (3.6-3.8 Ga) zircons: I) long-lived continental lithosphere that formed over timescales of > 1.0 Ga (e.g., Zimbabwe and Yilgarn Cratons) and II) juvenile continental lithosphere formed over < 300 Ma, for example the East Pilbara Craton and Abitibi terrane, Superior Craton (Kamber et al., 2003; Kamber, 2015). However, despite this dichotomy, the timeframe represented by greenstone belts on both long-lived (e.g., Yilgarn Craton, outlined above) and rapidly formed continental lithosphere such as the Abitibi (~76 Ma; Ayer et al., 2002; Thurston, 2002) is typically protracted and much longer than that distinguished in the YSGB. This raises the question of why greenstone belt formation, as suggested in this study, is contrary to the typically prolonged timescale indicated by other belts (e.g., Ayer et al., 2002; Romano et al., 2014).

It is possible that these other belts may also have experienced periods of rapid evolution, but supporting evidence has since been lost or remains ambiguous. The depositional rates of sedimentary-dominated Neoarchaean 'late basins' are sufficiently high to account for rapid greenstone belt formation, such as the 2.5 km/m.y. depositional rate has been calculated for late stage turbiditic basins of the Superior and Slave cratons, Canada (Bleeker, 2003; Goscombe et al., 2019). A similar depositional rate would account for the 2-3 km preserved thickness of the Mougooderra Fm within approximately ~1 m.y. More extensive burial within sedimentary basins, such as the 14 km of burial recorded in the Belches turbidite basin in the eastern Yilgarn Craton, could be achieved within ~5.5 Ma (Goscombe et al., 2019). Recent combined stratigraphic mapping and detailed geochronology in the Ora Banda Domain, eastern Yilgarn Craton, has demonstrated that a ~6 km volcano-sedimentary succession formed over ~30 Ma and contains at least two unconformities (Tripp, 2019). These unconformities document periods of uplift and erosion such as basin inversion events (Krapež and Barley, 2008). Krapež and Barley (2008) suggested that late basin development in the eastern Yilgarn Craton occurred during two extensional stages, separated by an inversion event. Inversion, caused by a change from transtension to transpression, resulted in uplift, localised tilting and erosion (Krapež and Barley, 2008; Krapež et al., 2008). The longer time periods recorded by many greenstone belts could therefore reflect the superposition of distinct cycles of greenstone belt formation separated and obscured by unconformities, thus explaining why rapid formation of greenstone belts has not been widely recognised, despite a recognition of quick episodes of magmatism and associated deformation (e.g., Schoene & Bowring, 2010; de Wit et al., 2018).

Timeframes form an important constraint in geodynamic modelling of the Earth's crust. The short timescales indicated by this study are similar to transient episodes of extensive magmatism constrained in the Kaapvaal Craton (e.g., Schoene & Bowring, 2010) and could be compatible with both non-uniformitarian plume-lid (e.g., Sizova et al., 2018) and plate tectonic-style models (e.g., Goscombe et al., 2019). Currently, most modelling approaches do not fully address the effects of eruption, sedimentation and erosion in the upper crust (Fischer and Gerya, 2016). Implementing rapid greenstone belt formation in more sophisticated models may therefore be an important step towards resolving Archaean geodynamic paradoxes.

CHAPTER 9

Lode-gold mineralisation along the Mougooderra and Winddine Well shear zones

9.1 Introduction

The Archaean Yilgarn Craton of Western Australia is recognised as one of the best-endowed geological terranes on Earth and is host to a diverse array of world-class orogenic-lode gold deposits. These lode-gold deposits commonly display a range of similar characteristics including a spatial association with regional structures, a distinct structural control and formation from low-salinity aqueous-carbonic fluids (e.g., Mole et al., 2015). Previous research into lode-gold deposits across the craton has focused on the largest and well renowned deposits of the Eastern Goldfields to the east, and have not fully investigated mineralisation in lesser endowed, but nevertheless highly prospective areas elsewhere.

The Yalgoo-Singleton Greenstone Belt (YSGB) has a similar stratigraphy and deformational history as the Eastern Goldfields (e.g., Czarnota et al., 2010), but is currently host to fewer discovered gold resources. This may be attributed to minimal (<5 %) outcrop, thick transported cover and a high degree of weathering, all of which make for a more difficult exploration environment (Watkins & Hickman, 1990). Currently, the belt is host to several mining operations exploiting lode-gold, Cu-Pb-Ag volcanogenic massive sulphide (VMS), intrusion-related W-Mo and BIF-related iron ore deposits. Most lode-gold deposits in the belt are characteristically hosted by D_4 shear zones, with a vast majority of discovered gold mineralisation situated along the unexposed, 50 km length, north-striking Mougooderra Shear Zone (MSZ; Fig. 9.1). Significant lode-gold deposits along the MSZ include the ~400 koz Silverstone deposit, in addition to the Bugeye and M1 deposits (Minjar, 2012). Other auriferous D_4 shear zones include the Rothsay Shear Zone (RSZ) in the southwest, host to the historical Rothsay gold mine, and the Winddine Well Shear Zone (WWSZ), located ~ 1.5 km west of, and parallel to, the MSZ and host to the ~100 koz Winddine Well deposit. A group of gold deposits in the south of the study area near Mt Mulgine, including the Black Dog, Trench and Ocean deposits, have previously been ascribed to the intrusion-related Mulgine Hill W-Mo-Au system, based principally on the spatial association of these gold deposits with the mineralised Mt Mulgine granite (Minjar, 2012).

Detailed structural analysis of oriented drillcore (Chapter 4) has demonstrated that the D_4 shear zones in the belt are steeply-dipping (65-85°) and comprise structural features that are consistent with a significant reverse component of shear. However, despite hosting a current gold resource in excess of ~1 Moz, little is known about the style and paragenesis of lode-gold mineralisation along the MSZ and WWSZ. Previous studies of mineralisation along these shear zones has been limited to undergraduate honours theses undertaken in collaboration with successive mining companies operating in the area (Thomas, 2003; Price, 2014; Wickham, 2014) involving preliminary drillcore logging, ore petrography and SEM analysis. Additionally, new aeromagnetic interpretations presented in this study (Chapter 4) indicate that gold deposits in the Mt Mulgine area may be located along or proximal to the southern extent of the MSZ.

In this chapter, the alteration assemblages, veining, ore parageneses and stable isotopic signatures of sulphides and quartz at lode-gold deposits along the MSZ and WWSZ are presented. Recent exploratory drilling beneath open cast pits has provided access to fresh, oriented drillcore intercepting mineralised zones at deposits along the length of these D_4 shear zones. Comparisons are made between new data from the primary focus of this study, the ~400 koz Silverstone deposit, and the M1, Bugeye, Black Dog deposits along a ~35 km strike length of the MSZ. This has allowed a comprehensive analysis of the ore forming processes along the extent of a gold mineralised D_4 shear zone. Additionally, new data is presented for the Winddine Well deposit, along the neighbouring WWSZ. The age of lode-gold mineralisation at the Silverstone deposit is determined, and this represents the first age for lode-gold mineralisation in the belt. A better understanding of the geometry, style, parageneses and age of lode-gold mineralisation along D_4 structures in the YSGB will provide a revised rationale to underpin and better target exploration in a highly prospective area suffering from extensive superficial cover.

The primary aims and objectives of this chapter are as follows:

- Assess the main style(s) of lode-gold mineralisation along D_4 shear zones in the YSGB
- Establish whether lode-gold deposits along the MSZ and WWSZ formed during the same deformational episode and as part of the same mineralising event.
- Determine the mineral paragenetic sequence associated with lode-gold mineralisation at Silverstone and assess whether this is comparable to other deposits along the MSZ
- Assess whether stable isotopes could be used as a reliable exploration vector towards mineralisation in a difficult exploration environment
- Compare the age of lode-gold mineralisation at the Silverstone deposit to the age(s) of mineralisation elsewhere across the Murchison Domain and Yilgarn Craton

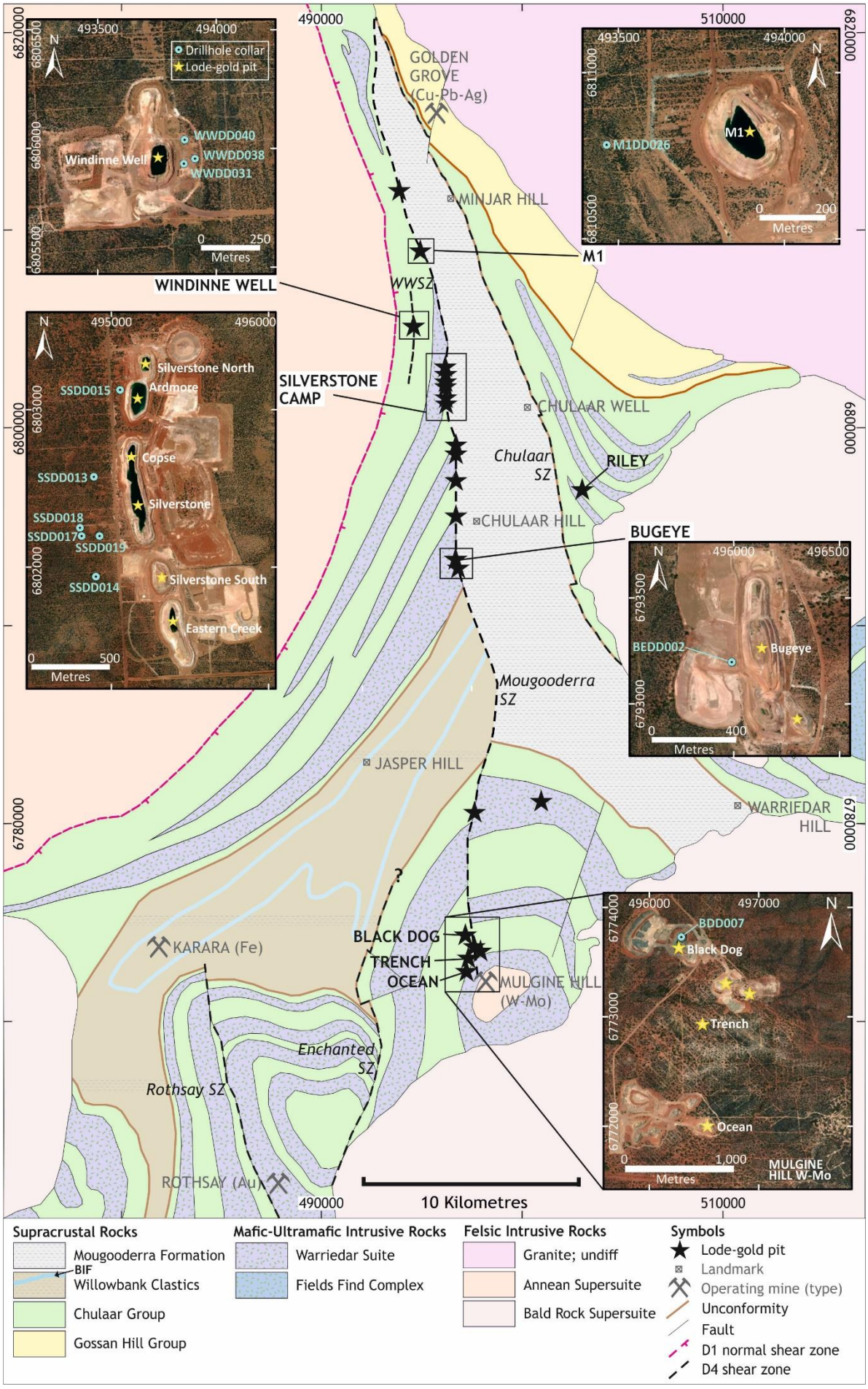

Caption on next page

Figure 9.1 (previous page): Simplified geological map of the central Yalgoo-Singleton greenstone belt showing the distribution of lode-gold deposits, D_4 shear zones and operating mines. Black stars denote individual open cast pits and key deposits referred to in this study are labelled. Satellite imagery of key deposits are shown, in addition to collar locations for drillholes studied. Satellite imagery courtesy of ESRI and Maxar; imagery taken in January 2019.

9.2 Deposit descriptions

Gold mineralisation in the central YSGB is widespread, with over 100 known gold prospects and historic workings. To date, nineteen separate gold deposits in the area have been mined or partially mined. Most of these deposits have been discovered over the past three decades and have been exploited as relatively shallow (<50 m depth) open-cast pits within the heavily oxidised and altered 'oxide' zone, with the exception of the historical Rothsay gold mine in the southwest, which also comprises underground workings. The locations of (partially) mined gold deposits in the area are shown in Figure 9.1. In this section, the geology at the deposits studied is summarised. The structural geology of the MSZ at the Silverstone, M1 and Bugeye deposits is described in Section 4.5.6.1 and the structural geology of the WWSZ at the Winddine Well deposit is described in Section 4.5.6.2.

9.2.1 Silverstone deposit

Silverstone is the largest discovered lode-gold deposit along the MSZ and occurs as six adjacent oxide pits covering a strike length of 2.0 km, located ~5.5 km west of Chulaar Well (Fig. 9.1). Silverstone occurs on a flexure of the MSZ, along which the strike of the shear zone progresses from north-northwest in the south, to north-northeast in the north. The pits at the surface of the Silverstone deposit consist of Silverstone North, Ardmore, Copse, Silverstone, Silverstone South and Eastern Creek, denoting zones of elevated gold content separated by intervals of lower grade gold mineralisation (Fig. 9.1). Lithological logging of drillcore intersecting mineralised rocks at Silverstone is shown in Figure 4.14 and described in Section 4.5.6.1. The MSZ at Silverstone dips 60-70° west, such that the footwall consists of Mougooderra Fm fine-grained metasedimentary rocks, in addition to minor chert and BIF. As hangingwall units intersect the MSZ obliquely, hangingwall lithologies in the south are dominated by Chulaar Group mafic volcanic rocks and interbedded tuffaceous and sedimentary rocks, whereas Warriedar Suite ultramafic intrusive rocks comprise hangingwall rocks in the north. Doleritic dykes partially intrude along the MSZ and are interpreted to be Proterozoic in age.

Mineralised rocks at Silverstone occur directly within the MSZ, primarily in the hangingwall mafic-ultramafic units situated immediately above the shear contact. The ore zone is characterised by intense silica-albite-carbonate alteration and typically varies in width between 12 and 25 metres (Minjar, 2012). A further, discrete mineralised zone occurs in sheared hangingwall units approximately ~30 m above the shear contact. Footwall metapelitic rocks at Silverstone are typically unmineralised

(Minjar, 2012). The entire Silverstone area is concealed by 10-15 metres of superficial cover and rocks are typically oxidised to approximately 80 m depth.

As part of an honours thesis, Thomas (2003) carried out a petrographic study of the vein and ore mineralogy at the mineralised zone beneath the Silverstone South pit. This study identified an arsenopyrite and pyrite-dominated sulphide assemblage, in addition to rare chalcopyrite and sphalerite. Two distinct forms of pyrite were identified, comprising large anhedral poikilitic aggregates and finer-grained, cubic crystals, although the paragenetic relationship between these two phases could not be resolved (Thomas, 2003). A strong association between carbonate alteration and gold grade was also highlighted by Thomas (2003).

9.2.2 M1 deposit

The M1 deposit is an oxide pit situated adjacent to the MSZ, ~8 km north of Silverstone. Lithological logging of a drillhole intersecting mineralised rocks at M1 is shown in Figure 4.19. Mineralisation is hosted by a ~20 m-thick talc-carbonate altered ultramafic unit that dips to the west at 50-75°. Hangingwall rocks to the west consist of variolitic and spinifex-textured basalt with interflow metapelitic and tuffaceous rocks, whereas footwall lithologies are dominated by mafic volcaniclastic rocks. Gold mineralisation at M1 consists of an overlying, flat lateritic zone and a steeply-west dipping 'main zone', oriented parallel to the principal shear fabric and both footwall and hangingwall units (Minjar, 2012). Additionally, minor, parallel gold-bearing shear zones occur 10-15 metres above the basal shear contact in the hangingwall of the main ore zone (Minjar, 2012). Rocks at M1 are extensively weathered to depths in excess of 90 m below the surface.

9.2.3 Bugeye deposit

The Bugeye deposit is located on the MSZ approximately 8.5 km south of the Silverstone deposit (Fig. 9.1). Lithological logging of drillcore intersecting mineralised rocks at Bugeye is shown in Figure 4.19. Hanging-wall rocks to the west comprise Warriedar Suite doleritic rocks, whereas the footwall rocks consist of magnetite BIF, chert and metapelitic rocks of the Mougooderra Fm. In contrast to Silverstone and M1, gold mineralisation at Bugeye is hosted by footwall lithologies, primarily BIF and chert, and the main ore body dips steeply to the west, consistent with the orientation of the MSZ and bedding in footwall units (Minjar, 2012). The base of oxidation at Bugeye is typically 50-60 m.

9.2.4 Winddine Well deposit

The Winddine Well deposit is located along the north-south striking, steeply- to vertically dipping

WWSZ, located ~3 km northwest of the Silverstone deposit. The geology at Winddine Well is summarised in Section 4.5.6.2 and illustrated by lithological logging of three drillholes in Figure 4.21. Unlike deposits along the MSZ, Winddine Well is situated within Chulaar Group rocks intruded by Warriedar Suite sills. Gold mineralisation is hosted by a 15-23 m-thick BIF unit and is bound by Warriedar Suite doleritic intrusive rocks to the east, and Chulaar Group felsic-mafic volcaniclastic rocks and minor metasedimentary rocks to the west. Gold mineralisation is present over a strike length of ~100 metres and is associated with multiple deformed zones of quartz-carbonate-pyrite veining within the mineralised BIF unit, separated by relatively undeformed intervals. On aeromagnetic imagery, the Winddine Well deposit is associated with a pronounced demagnetised zone within the host BIF unit. Oxidation of the bedrock at Winddine Well extends to depths in excess of 100 m.

Thomas (2003) undertook geological mapping of the Winddine Well deposit, paired with preliminary petrographic analysis of several mineralised samples. A sulphide assemblage comprising pyrrhotite, pyrite and lesser sphalerite and chalcopyrite was identified and found to be commonly associated with intense chlorite-carbonate alteration (Thomas, 2003). Furthermore, two separate stages of quartz veining were identified at Winddine Well: early, layer-parallel and deformed quartz-carbonate veins associated with minor gold and sulphide mineralisation, and subsequent cross-cutting carbonate-dominated veins with more prevalent sulphide mineralisation. It was interpreted that gold mineralisation occurred during emplacement of the early quartz-carbonate veins, and were later remobilised into dilatant sites and breccias, either as part of progressive deformation or a subsequent deformational event (Thomas, 2003). The relationship between the Winddine Well deposit and adjacent deposits along the MSZ is unclear.

9.2.5 Black Dog deposit

The Black Dog deposit is situated in the Mt Mulgine area proximal to the southern interpreted extremity of the MSZ, ~2 km north of Mulgine Hill and 29 km south of the Silverstone deposit. Lode-gold mineralisation at Black Dog is hosted by Warriedar Suite doleritic rocks and is truncated at depth by a feldspar porphyry intrusive. Gold mineralisation at Black Dog has previously been attributed to the Mt Mulgine intrusive-related W-Mo-Au system, along with neighbouring deposits such as Trench and Ocean (Minjar, 2012). Mineralised zones at Black Dog are typically discreet and comprise low sulphide contents (Minjar, 2012). The deposit has been exploited as an open cast pit and contains fresh rock, in contrast to the oxidised material present in most pits in the area.

As part of undergraduate theses in collaboration with Minjar Gold, Price (2014) and Wickham (2014) undertook SEM analysis of mineralised samples from the Black Dog deposit. These studies identified

pyrrhotite as the dominant sulphide phase at Black Dog, in addition to lesser pyrite, arsenopyrite, chalcopyrite and rare sphalerite and galena (Price, 2014; Wickham, 2014). Additionally, the antimony-bearing sulphides ullmannite (NiSbS) and gudmundite (FeSbS) were identified as minor phases within mineralised rocks (Price, 2014). Gold was identified as two alloys, electrum (AuAg) and aurostibite ($AuSb_2$), and was found to typically occur as free gold spatially associated with sulphides, commonly at the margins of quartz carbonate veins (Price, 2014).

9.2.6 Other notable lode-gold deposits

Samples from several other lode-gold deposits in the YSGB have been analysed as part of this study. The Ocean deposit is a small oxide pit situated ~0.5 km west of Mulgine Hill, on the flanks of the Mt Mulgine granite (Fig. 9.1). Gold mineralisation at Ocean is hosted by micaceous metasedimentary rocks and has been interpreted to form part of the Mt Mulgine intrusive-related W-Mo-Au system (Minjar, 2012). Similarly, the Trench deposit ~1.5 km northwest of Mulgine Hill also forms part of the group of deposits on the flanks of the Mt Mulgine granite (Fig. 9.1) and comprises gold mineralisation associated with highly altered and quartz veined mafic volcanic rocks (Minjar, 2012). The Riley deposit is situated 3.5 km southeast of Chulaar Well and currently represents the only discovered and mined deposit to the east of the CSZ (Fig. 9.1). The Riley deposit consists of one or more saddle reefs in a km-scale anticlinal fold hinge, hosted by a sequence of komatiitic ultramafic rocks and BIF that have been intruded by a felsic porphyry (Minjar, 2012). Notably, the Riley deposit is not located along a mapped shear zone, unlike most other deposits in the belt.

9.3 Sample Selection

A total of 130 drillcore samples have been collected from mineralised and unmineralized rocks at four lode-gold deposits across the MSZ: Silverstone, M1, Bugeye and Black Dog, in addition to the Winddine Well deposit along the WWSZ. These localities were selected as they exhibit a diverse range of lithological associations and are spatially distributed along the length of the D_4 shear zones. A further 20 hand samples have been taken from the Black Dog, Ardmore (Silverstone deposit), Winddine Well, Ocean, Trench and Riley pits, where exposure is relatively fresh in contrast to the oxidised and highly altered material exposed elsewhere. A majority of the samples have been collected from the Silverstone deposit (n=94), and these represent the primary focus of this study, in addition to samples from the Winddine Well deposit (n=21). Details of each of these samples, including location co-ordinates and drillcore depths, descriptions and a checklist for the analysis undertaken on each sample, can be found in **Appendix E10**. The gold grade of mineralised drillcore samples in this study is

indicated by assay data provided courtesy of Minjar Gold Pty, which typically represents one metre composite samples and is only used as a reference of the approximate gold grade.

From this sample suite, 70 polished thin sections have been prepared for samples that either display representative alteration assemblages or have been sampled from gold mineralised zones in each drillhole studied. Petrographic and SEM analysis has been undertaken on polished thin sections and five sections with exemplary textures and mineral associations were selected for element mapping.

A representative suite of 43 sulphide samples from eight deposits have been collected for $\delta^{34}S$ stable isotope analysis, with a particular focus on the Silverstone deposit. Sulphide samples have been collected from gold-mineralised zones and unmineralised samples distal to mineralisation. Samples have been collected from all drillholes studied as well as accessible pits, to provide a good spatial distribution. For $\delta^{18}O$ quartz analysis, 47 representative quartz samples have been collected from veins at the Silverstone, Winddine Well, Black Dog and Bugeye deposits. These samples comprise quartz from high-grade mineralised samples, lower-grade areas around the peripheries of mineralised zones and quartz from unmineralised rocks.

Four thin sections prepared from two samples along a ~60 cm interval of the high-grade intersection of drillhole SSDD019 at Silverstone have been selected for U-Pb geochronological analysis. These samples were selected due to the presence of abundant monazite crystals directly associated with gold mineralisation, which were of sufficient size for analysis.

9.4 Methods Summary

Structural logging of veining in oriented drillcore at Silverstone, M1, Bugeye and Winddine Well has been undertaken alongside structural and lithological logging presented in Section 4.5.6. The location of drillhole collars is displayed in Figure 4.13 and drillhole collar coordinates and details are provided in Table 4.1. Vein orientations have been measured following the α-β method described in Section 4.4.3. The Cor! Program (provided by T.G. Blenkinsop) utilises the methods described by Blenkinsop et al. (2015) and has been used to calculate the true orientation of structures from α-β measurements and hole orientation data. Structural logging data is detailed in **Appendix E4**. Transmitted and reflected light petrographic analysis of polished thin sections has been undertaken to study alteration minerals, veins and the mineralogy and textures of mineralised samples.

Back-scattered electron (BSE) imaging and semi-quantitative point analyses of mineralised samples has been carried out using an Environmental Scanning Electron Microscope (ESEM) at Cardiff University, to assist paragenetic studies. Element/mineral mapping of selected samples has been

undertaken using an Analytical Scanning Electron Microscope (ASEM) at Cardiff University. Full details of operating conditions and instruments used during ESEM and ASEM analyses are described in **Appendix B3**.

Conventional stable isotope analysis of sulphides ($\delta^{34}S$) and quartz ($\delta^{18}O$) was undertaken at the Natural Environmental Research Centre (NERC) stable isotope laboratory at the Scottish Universities Environmental Research Centre (SUERC), East Kilbride, Scotland. Details of the methods followed, standards used, and reproducibility data are provided in **Appendix B3**. Sulphur and oxygen isotope results are reported in standard notation as per mil (‰) deviations from the Vienna Canyon Diablo Troilite (V-CDT) and Vienna Standard Mean Ocean Water (V-SMOW) standards, respectively.

In-situ laser ablation inductively coupled plasma mass spectrometry (LA-ICP-MS) U-Pb monazite dating has been carried out at the Geochronology & Tracers Facility, British Geological Survey, Nottingham, UK, in order to constrain the age of lode-gold mineralisation at the Silverstone deposit. Monazite crystals were detected through automated mineral identification and subsequently imaged in BSE-mode using an ASEM at Cardiff University, UK. Full details of the methods used for identifying and imaging monazite crystals, in addition to methods, analytical instruments and standards used during geochronological analysis, are described in **Appendix B3**.

9.5 Results

9.5.1 Alteration

In this section, the alteration assemblages associated with mineralisation at the Silverstone, M1, Bugeye and Winddine Well deposits are described, following lithological logging of drillcore and petrographic analysis of selected samples.

9.5.1.1 Silverstone, M1 and Bugeye deposits

At Silverstone, the alteration assemblages in hangingwall rocks varies along strike owing to a progression from mafic-dominated lithologies in the south and central parts of the deposit, to ultramafic lithologies in the north. Alteration assemblages in mafic rocks comprise chlorite-epidote-albite-carbonate-sericite-quartz ± piemontite ± fuchsite ± garnet. In contrast, the alteration assemblages of ultramafic protoliths in the north comprise talc-magnesite-quartz-fuchsite ± chrysotile. The occurrence and intensity of alteration minerals varies as a function of distance to the main shear contact and the proximal mineralised ore zone. This is most clearly demonstrated by mafic rocks in the south.

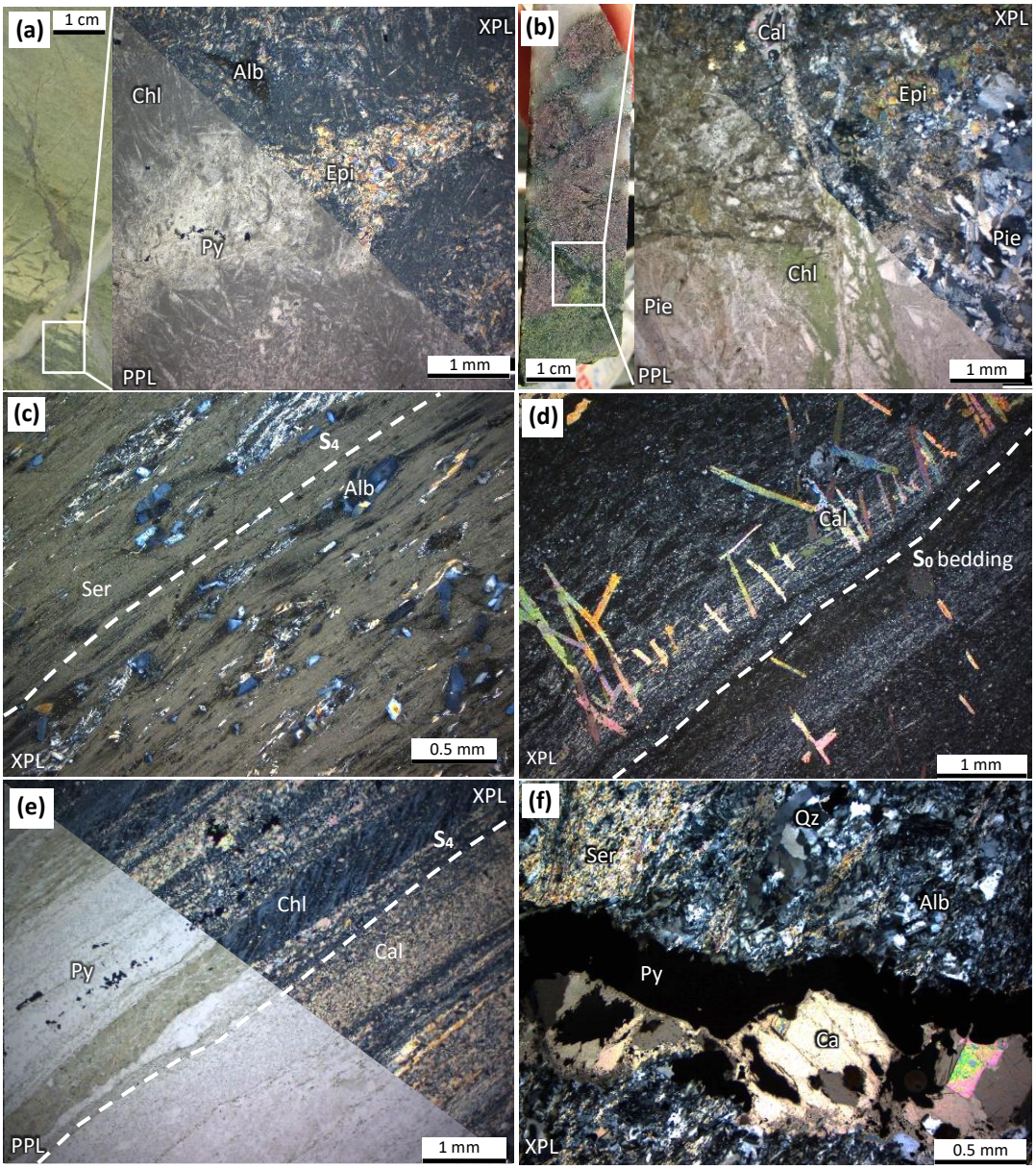

Figure 9.2: Drillcore photographs and photomicrographs of representative alteration assemblages at the southern and central parts of the Silverstone deposit. **(a)** Photograph and PPL/XPL view of epidote-chlorite-pyrite assemblage in a hangingwall basaltic unit distal to the MSZ (sample SS18A6); **(b)** Photograph and PPL/XPL view of a hangingwall chlorite-epidote-piemontite-carbonate altered mafic unit (sample SS18A8); **(c)** XPL view of albite crystals in a strongly foliated sericitic groundmass (sample SS18A3); **(d)** XPL view of euhedral laths of calcite focused along specific bedding horizons in a tuffaceous hangingwall unit (sample SS17A7); **(e)** PPL/XPL view of a mylonite comprising bands of chlorite and calcite, the latter containing pyrite (sample SS18A7); **(f)** PPL/XPL view of a typical gold mineralised sample in the ore zone comprising sulphides in a quartz-albite-sericite-calcite altered groundmass (sample SS19M4).

Distal to the MSZ, mafic rocks exhibit greenschist metamorphic mineral assemblages dominated by chlorite and actinolite, accompanied by tremolite in high-Mg units. This is consistent with petrographic descriptions of mafic volcanic rocks in the region (Chapter 5). On approach to the MSZ (within ~100 m), this metamorphic assemblage is joined by fine-grained epidote, which in turn progresses into coarser grained, more pervasive epidote alteration. Epidote commonly defines 0.5-2 cm deformed varioles in variolitic volcanic rocks proximal to quartz±carbonate veins (Fig. 9.2a) and is also associated

with minor brecciation and sparsely disseminated pyrite. Locally, in the central part of the deposit, epidote-chlorite-(carbonate) alteration is complemented by pink-red piemontite, occurring either as disseminated 1-5 mm crystals, or as cm-thick masses of interlocking piemontite crystals in the selvedge of quartz-carbonate veins (Fig. 9.2b). Garnet occurs as a rare accessory phase in association with chlorite-epidote alteration.

Albite occurs locally as subhedral-euhedral laths < 1 mm in size and becomes increasingly abundant towards the ore zone, particularly evident in more highly deformed intervals (Fig. 9.2c). Similarly, sericite typically occurs as a fine groundmass in strongly foliated and sheared units (Fig. 9.2c) and also becomes more abundant towards the centre of the MSZ. Carbonate alteration displays a close spatial relationship with increased deformation and with sulphide mineralisation, predominantly pyrite and less commonly, pyrrhotite. Carbonate minerals manifest as various textures including carbonate spotting, occasionally focussed as tabular, euhedral and aligned crystals in tuffaceous hangingwall rocks (Fig. 9.2d), as mm to cm-scale veinlets (Fig. 9.2b) or as disseminated carbonate alteration in the groundmass. Close to the centre of the MSZ, strongly deformed and mylonitic rocks are composed of bands of fine-grained calcite and chlorite, which are host to SC fabrics (Fig. 9.2e). The Silverstone ore zone displays the most intense alteration and comprises sericite-albite-chlorite-carbonate altered rocks (Fig. 9.2f), with rare fuchsite and abundant silicification coincident with stockwork quartz veining. The dominant carbonate mineral in the ore zone in the central and southern part of the deposit is ankerite, with lesser calcite.

In contrast, ultramafic hangingwall rocks in the northern part of Silverstone are invariably serpentinised, highly magnetic, locally talc-altered and occasionally contain fibrous, asbestiform veining, typically composed of chrysotile. Altered ultramafic rocks proximal to the MSZ are characterised by carbonate alteration accompanied by magnesite veining (Fig. 9.3a), both of which systematically increase in intensity towards the centre of the shear zone. Within the MSZ, carbonate-altered ultramafic rocks exhibit a striking beige-light green colour (Figs. 9.3b and 9.3c) and are characteristically resistant, in contrast to less-resistant, talcose serpentinite units elsewhere. The resistant nature of these units, combined with an abnormal light colour and localisation along the shear zone, has previously resulted in these intervals being logged as felsic intrusive rocks. However, petrographic analysis demonstrates that these units comprise a talc-magnesite-serpentine-fuchsite-quartz assemblage with pervasive carbonate alteration of the groundmass. Furthermore, abundant anhedral chromite crystals occur within the altered groundmass, consistent with listwaenite development from an ultramafic precursor (Fig. 9.3d). Listwaenitic units range in thickness between 10 cm and >5 m and are commonly silicified and dissected by quartz and carbonate veinlets. In several

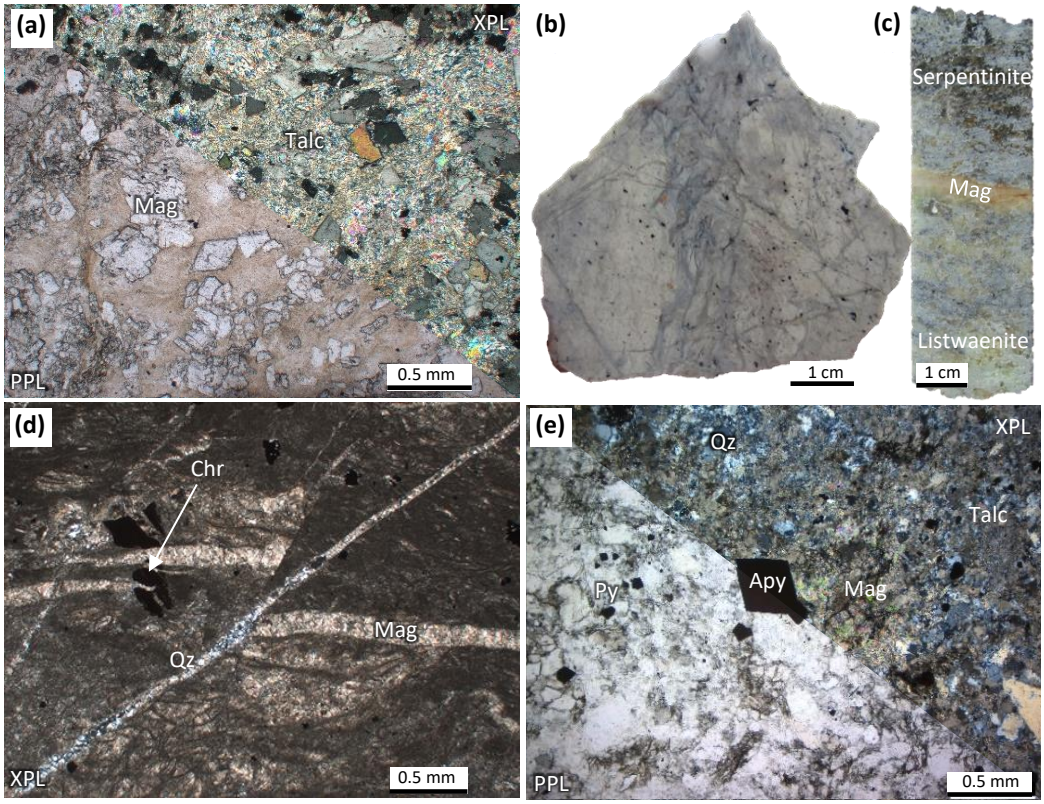

Figure 9.3: Drillcore photographs and photomicrographs of representative alteration assemblages at the northern part of the Silverstone deposit. **(a)** PPL/XPL view of talc-magnesite assemblage in a carbonate altered ultramafic protolith (sample SSDD15-3); **(b)** Photograph of a polished surface of listwaenite from the Ardmore pit, with a characteristic light green colour and interlocking quartz/magnesite veins (sample ARD005); **(c)** Photograph of drillcore displaying a progression from serpentinite to listwaenite over ~10 cm, dissected by a magnesite vein (SSDD015, 194.5 m); **(d)** XPL view of a thin section of the listwaenite in (b), displaying a fine grained, dusty groundmass of magnesite and silica, dissected by faulted magnesite veinlets, in turn dissected by a quartz veinlet. Note the fragmented crystals of chromite, signifying the ultramafic precursor (sample ARD005); **(e)** PPL/XPL view of a mineralised carbonate-altered ultramafic unit comprising talc, magnesite, quartz, pyrite and arsenopyrite (sample SS15M2).

instances, a gradation between serpentinite and listwaenite is evident in drillcore (Fig. 9.3c). Sulphide-mineralised rocks at north Silverstone either comprise silicified listwaenite (Fig. 9.3e), or less resistant, talc and magnesite-dominated assemblages, in which fuchsite occurs as a minor, locally abundant, phase. A metre-scale interval of gold-mineralised listwaenite with comparable features and mineralogy has also been identified in drillcore in the central portion of the deposit and represents the attenuation of ultramafic protoliths towards the south.

Metasedimentary rocks at Silverstone, including footwall units, exhibit chlorite and silica alteration that increases in intensity towards the centre of the shear zone. Magnetite horizons in BIF units are commonly sulphide-altered, resulting in disseminated pyrite and occasionally, pyrite bands replacing magnetite horizons. In contrast to all other rocks, dolerite dykes at Silverstone are unaltered to slightly chlorite altered and dissect strongly altered rocks, indicating they were intruded subsequent to significant hydrothermal activity.

The mineralogy and distribution of the alteration assemblages associated with mineralisation at Silverstone are directly comparable with those observed in single drillholes at the M1 and Bugeye deposits. Mafic units in the hangingwall at M1 are characterised by chlorite-epidote-albite-sericite-carbonate alteration, which progressively increases in intensity towards the shear contact. Ultramafic protoliths, including those units hosting mineralisation in the ore zone, are dominated by a talc-magnesite assemblage, but do not exhibit listwaenite development as present at Silverstone. Hangingwall doleritic units in drillcore at Bugeye exhibit chlorite-epidote±albite alteration, whereas mineralised footwall metapelitic rocks are silicified within the shear zone and BIF is locally sulphidised.

9.5.1.2 Winddine Well deposit

Mafic intrusive rocks situated to the east of the WWSZ at Winddine Well are typified by chlorite-epidote-calcite-tourmaline alteration, which typically occurs as alteration haloes around quartz-carbonate(-tourmaline) veins and becomes more pervasive towards the mineralised BIF unit to the west. Background chlorite-actinolite dominated metamorphic assemblages are overprinted by chlorite-epidote alteration in the selvedge of quartz-carbonate veins. The widths of these alteration haloes are typically <2 cm (Fig. 9.4a), however, intense epidote alteration occasionally occurs over intervals of up to 50 cm and occurs with abundant disseminated pyrite (Fig. 9.4b).

Calcite alteration is spatially associated with sulphide and gold mineralisation and exhibits several textures. Calcite locally replaces leucoxene in evolved mafic intrusive units, resulting in a mottled appearance. Commonly, the intensity of calcite alteration increases progressively in the selvedge of quartz-calcite(-tourmaline) veins over intervals of up to 20 cm. In some instances, calcite almost entirely replaces the dolerite groundmass adjacent to veins, encloses relict yellow leucoxene grains and is commonly accompanied by a green mineral, likely representing fine-grained fuchsite (Fig. 9.4c). Disseminated acicular crystals of tourmaline up to 1.5 cm in length occur in dolerite and diorite surrounding thicker (> 3 cm) quartz-calcite-tourmaline veins (Fig. 9.4d), where they are frequently oriented parallel to the S_4 shear fabric and exhibit boudinage.

The alteration assemblage in the ore zone at Winddine Well, hosted by BIF and interbedded metasedimentary rocks, comprises chlorite-carbonate-muscovite-quartz (Fig. 9.4e), accompanied by pyrite, pyrrhotite, minor chalcopyrite and gold. Chlorite and muscovite are invariably foliated and commonly wrap around masses of quartz and carbonate minerals (Fig. 9.4f), which comprise approximately equal proportions of ankerite and calcite. Metasedimentary and volcaniclastic rocks to the west of the WWSZ are characterised by chlorite alteration of variable intensity.

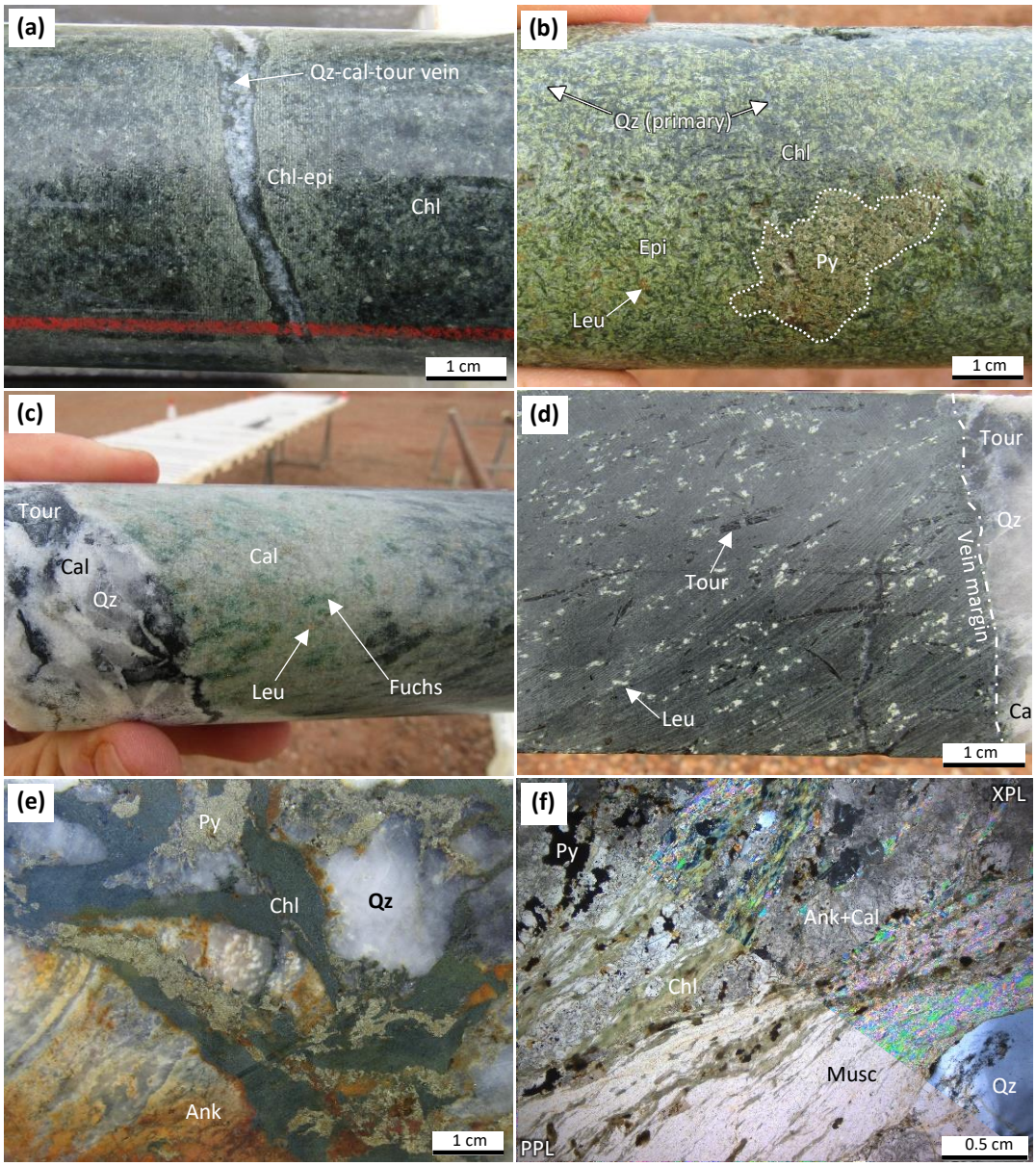

Figure 9.4: Drillcore photographs and photomicrographs of representative alteration at Winddine Well. **(a)** Photograph of chlorite-epidote alteration in the ~1 cm-thick selvedge of a quartz-calcite-tourmaline vein, in dolerite east of the WWSZ (WWDD031, 188.1 m); **(b)** Intense epidote-chlorite alteration of quartz diorite, enclosing primary quartz and leucoxene and associated with pyrite (WWDD038, 196.4 m); **(c)** Photograph of intense calcite alteration and replacement of dolerite at the margin of a thick quartz-calcite-tourmaline vein – note relict leucoxene and likely fuchsite (WWDD040, depth 208.8 m); **(d)** Disseminated acicular tourmaline at the margin of a quartz-calcite-tourmaline vein, overprinting leucoxene. Note the broad alignment of tourmaline crystals, parallel to the S_4 fabric in surrounding rocks (WWDD031, 196.3 m) **(e)** Photograph of a quartz-ankerite-chlorite-pyrite(-gold) assemblage characterizing mineralised rocks (WWDD040, 257.6 m); **(f)** PPL/XPL view of a quartz-ankerite-calcite-chlorite-muscovite-pyrite assemblage associated with gold mineralisation (sample WW31M2).

9.5.2 Vein orientations, textures and mineralogy

9.5.2.1 Silverstone deposit

Structural logging of oriented drillcore from six drillholes along the length of the Silverstone deposit has identified ten vein sets with contrasting mineralogy, textures and orientations (Table 9.1). A total

of 344 vein measurements occur in two principal orientations, with one group oriented approximately parallel to the S_4 shear fabric and the orientation of the MSZ at Silverstone, and another group of shallowly east-dipping to sub-horizontal veins (Fig. 9.5a). Based on cross cutting relations, the paragenesis of vein sets at Silverstone can be subdivided into three stages: early-, main- and late-stage veining, in relation to the temporal association of veins to lode-gold mineralisation. Early-stage veins of varying mineralogy denote the earliest, unmineralised veins emplaced at Silverstone, main-stage quartz-carbonate±sulphide veins are spatially and genetically associated with gold mineralisation, and late-stage calcite±pyrite veins represent subsequent veins that dissect and postdate gold mineralisation. Stereoplots summarising vein orientations are displayed in Figure 9.5 and representative photographs of veins from each stage are shown in Figure 9.6. The characteristics and orientations of each stage of veining are described successively below.

Early-stage veins

Early-stage veins at Silverstone comprise six vein sets with varying mineralogy, which largely dip towards the west to southwest at 50-75° and are predominantly oriented parallel to the local S_4 fabric. Where cross-cutting relationships are apparent, these veins are consistently overprinted by main-

STAGE	Vein Set	n	Typical orientation	Typical thickness (mm)	No. of cross cutting veins									
					Chlorite	*Talc-asbestiform*	*Calcite*	*Magnesite/ ankerite*	*K-Feldspar-quartz*	*Epidote ± piemontite ± calcite*	*Quartz-carb(-sulphide)*	*Quartz(-sulphide)*	*Sulphide veinlets*	*Calcite*
EARLY	Chlorite	9	variable	1-5										
	Talc-asbestiform	6	variable	1-8										
	Calcite	17	fol-parallel	1-35										
	Magnesite/ ankerite	23	fol-parallel	1-10				1						
	K-feldspar-quartz	21	fol-parallel	2-40					2					
	Epidote ± piemontite ± calcite	19	fol-parallel	1-15										
MAIN	Quartz-carbonate ±sulphide	157	fol-parallel **(I + IV)** or shallow E-dipping **(II)**	2-30	6	3				3	6			
	Quartz ±sulphide	43	variable - stockwork **(III)**	1-15	2									
	Sulphide veinlets	9	fol-parallel **(I)**	1-3										
LATE	Calcite	39	flat to shallow E-dipping	1-5	5	1					5	1	1	

Table 9.1: Summary of vein sets identified at the Silverstone deposit, including the number of each measured (n), typical orientations and vein thicknesses and the number of times veins in each set cross cut veins from other vein sets. Full logging data including all vein measurements can be found in Appendix E4.

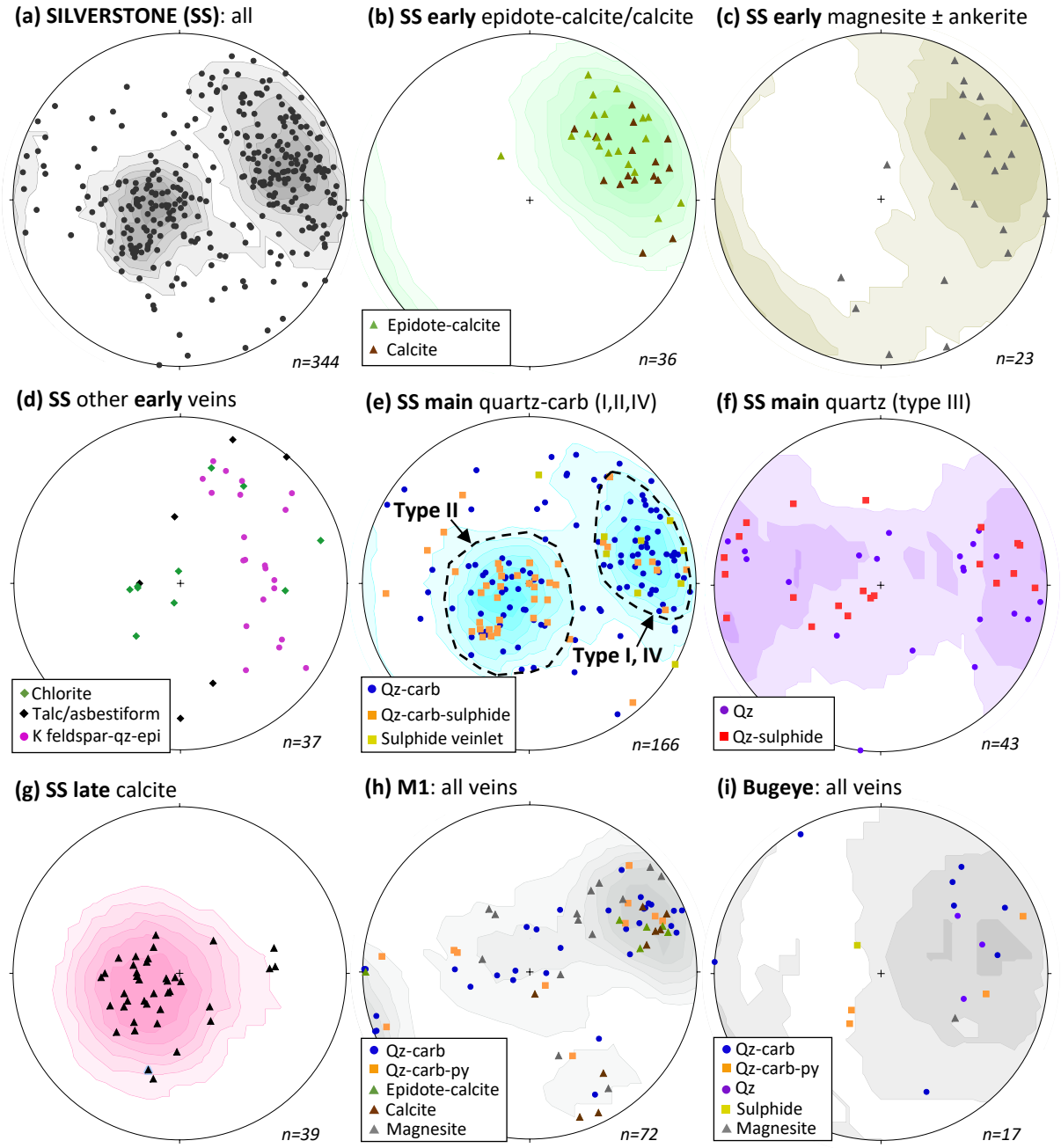

Figure 9.5: Lower hemisphere equal area stereonets summarising vein orientations measured in drillcore at the Silverstone (a-g), M1 (h) and Bugeye (i) deposits. In all stereonets, the poles to planes are displayed. Kamb contours are drawn at 2σ intervals. **(a)** All vein measurements from the Silverstone deposit; **(b)** Early epidote-calcite and calcite veins at Silverstone; **(c)** Early magnesite/ankerite veins at Silverstone; **(d)** Other vein sets at Silverstone, including chlorite, talc/asbestiform, quartz-K-feldspar; **(e)** Quartz-carbonate veins at Silverstone, subdivided according to sulphide content of veins. Sub-horizontal type II and foliation-parallel type I and type IV veins are indicated; **(f)** Quartz veins at Silverstone, with quartz-sulphide veins distinguished from quartz-only veins; **(g)** Late, cross cutting calcite veinlets at Silverstone; **(h)** All vein measurements at M1, subdivided by vein type; **(i)** All vein measurements at Bugeye, subdivided by vein type.

stage quartz-carbonate veins and late-stage calcite veins (Table 9.1; Fig. 9.6a). However, due to similar orientations and a lack of cross cutting relations, it is not possible to discern the relative order of early-stage vein sets.

Epidote-calcite veins typically vary in thickness between 1 and 15 mm, occasionally reaching 10 cm in

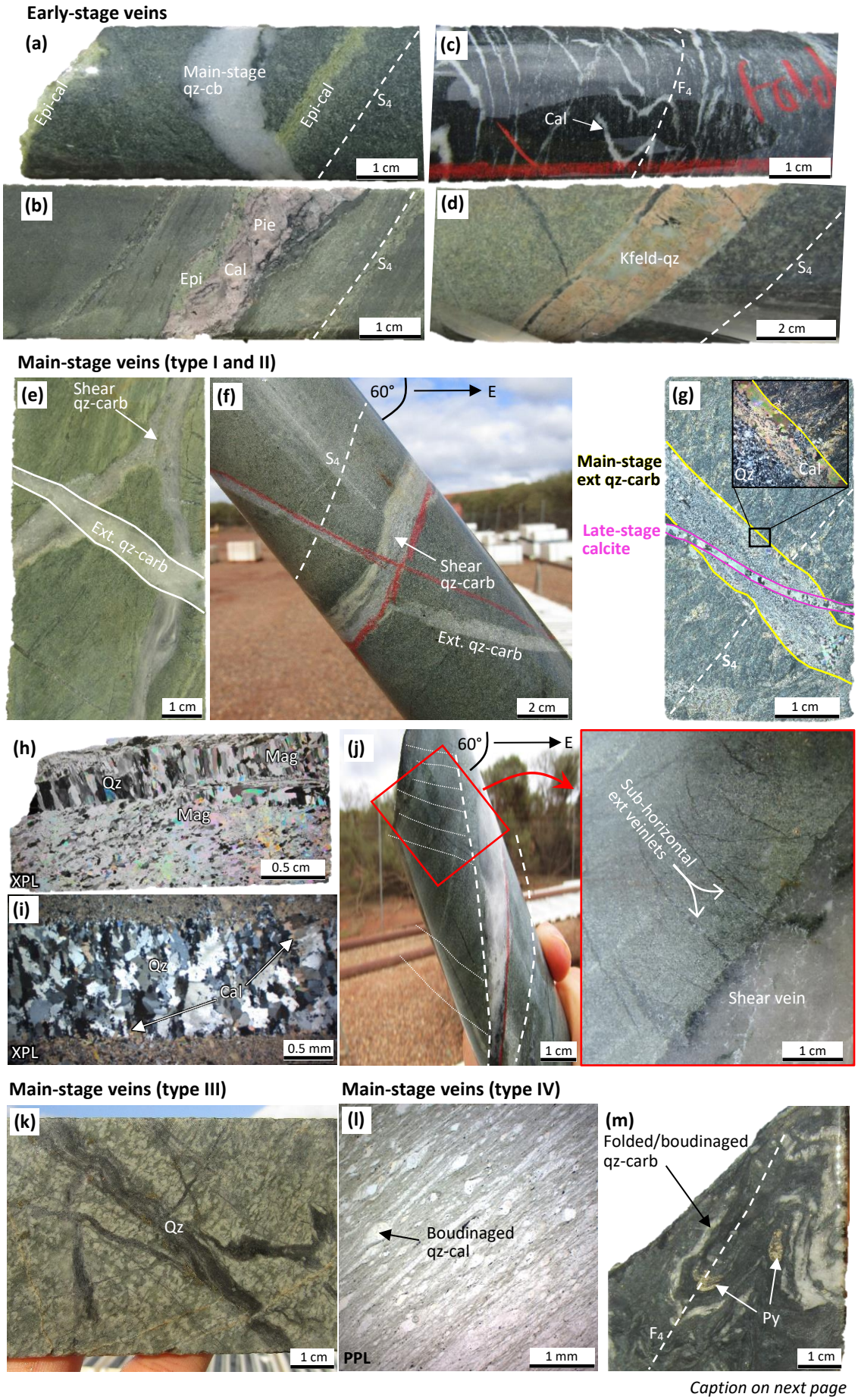

Caption on next page

Figure 9.6 (previous page): Drillcore photographs and thin section photomicrographs of representative veins at the Silverstone deposit. **(a)** Early stage foliation-parallel epidote-calcite veins, cross cut by main stage, sub-horizontal quartz-carbonate vein (SSDD019, 268.4 m); **(b)** Early-stage epidote-piemontite-calcite veining parallel to the S_4 shear fabric (SSDD019, 199.4 m); **(c)** Early stage calcite veining, folded as F_4 folds with hinge surfaces parallel to the S_4 fabric (SSDD018); **(d)** Early stage K-feldspar-quartz veining (SSDD014, 153.3 m); **(e)** Main stage assemblage of shear-textured quartz-carbonate vein (grey), dissected by a extensional textured quartz-carbonate vein (white) (SSDD018); **(f)** Drillcore oriented as it was in situ (plunging ~60° east) displaying a shear-textured main stage quartz-carbonate vein dissecting and displacing a sub-horizontal, extensional textured quartz-carbonate vein (SSDD019); **(g)** Thin section photomicrograph (XPL) of a main stage, sub-horizontal extensional quartz-carbonate vein, oriented perpendicular to the S_4 fabric, cross cut by a late stage calcite veinlet. Note the characteristic calcite margin at the margin of the extensional vein (sample SS18A4); **(h)** Photomicrograph (XPL) of a thin section comprising an extensional quartz-magnesite vein in a magnesite-talc dominated rock (sample SSDD15-1); **(i)** Photomicrograph displaying the internal structure of an extensional quartz-calcite vein (sample ARD001); **(j)** Drillcore oriented as it was in situ (plunging 60° east) displaying a foliation-parallel shear vein with multiple sub-horizontal extensional veinlets emanating from its margins (SSDD019); **(k)** Stockwork quartz veining in a carbonate altered ultramafic host rock, sampled from a high grade interval (SSDD017); **(l)** Photomicrograph (PPL) of deformed and sheared quartz-carbonate clasts in a mylonitic unit within the MSZ. Successive horizons with increased concentrations of quartz and carbonate clasts are considered to represent sheared and intensely boudinaged mm-scale veins (sample SS18A7); **(m)** Drillcore comprising boudinaged and folded quartz-carbonate veining in footwall metasedimentary rocks, deformed into F_4 folds and associated with pyrite (SSDD018).

width, and occur principally in mafic intrusive, volcanic and volcaniclastic lithologies (Fig. 9.6a). Locally in the central part of the deposit, epidote-calcite veins are accompanied by pink-purple coloured piemontite (Fig. 9.6b) and a minority of veins contain minor amounts of quartz. Epidote-calcite±quartz±piemontite veins commonly display laminated and sheared internal textures and consistently dip to the west to southwest at 45-80°, parallel to the local S_4 fabric (Fig. 9.5b). Calcite-only veins are present as 1-35 mm veinlets that occur in various hangingwall lithologies, increase in abundance towards the centre of the MSZ and are also consistently oriented parallel to the S_4 fabric (Fig. 9.5b). Locally, calcite veinlets are folded into F_4 folds, with hinge surfaces parallel to S_4 (Fig. 9.6c). Epidote-calcite and calcite-only veins are seldom associated with minor pyrite and rare pyrrhotite. In the north of the deposit, carbonate veins composed of magnesite±ankerite±chlorite occur in serpentinised ultramafic hangingwall rocks as 1-10 mm features that predominantly dip towards the west-southwest at 45-85° (Fig. 9.5c). Several shallowly dipping (20-40°) magnesite veins display extensional internal textures, with crystals oriented parallel to vein walls. Magnesite veins in hangingwall rocks are not associated with sulphide mineralisation.

In drillhole SSDD014, at the southernmost part of the Silverstone deposit, a quartz and K-feldspar-dominated vein set is present, variably associated with minor chlorite ± calcite ± epidote and ranging in thickness between 2 and 40 mm (Fig. 9.6d). These veins occur over a ~150 m interval in doleritic hangingwall rocks and are commonly associated with a sharp increase in the intensity of epidote-chlorite alteration (Fig. 9.6d). The orientation of K-feldspar-quartz veins varies between southwest and northwest dipping at angles of ~ 35-75° (Fig. 9.5d) and occasionally, veins cross cut one another. Unfortunately, no cross-cutting relations with other vein sets were observed. Based on orientations that are largely sub-parallel to the S_4 fabric in the south of the deposit, and a lack of a spatial relation with sulphide and gold mineralisation, K-feldspar-quartz veins are ascribed to early-stage veining.

Chlorite veinlets occur as narrow 1-5 mm-thick features in hangingwall mafic intrusive and volcanic units in the south and central parts of Silverstone, which contrary to other early-stage veins, exhibit variable orientations that range from steeply west-dipping to sub-horizontal (Fig. 9.5d). Chlorite veins are typically associated with fractures and minor faults and commonly occur in clusters, in association with cm-scale alteration haloes and disseminated pyrite. Talc±asbestiform±magnetite constitutes equivalent veins in ultramafic hangingwall lithologies in the north, and occur as 1-8 mm veins in variable orientations, comparable to chlorite veins further south (Fig. 9.5d). In contrast to other early-stage veins, chlorite and talc±asbestiform±magnetite veins occur distal to the MSZ and do not ostensibly increase in abundance towards the centre of the shear zone.

Main-stage veins

Main-stage veins at Silverstone consist of several types of quartz±carbonate±sulphide veins that are spatially and genetically associated with lode-gold mineralisation in mineralised rocks. These veins cross cut early-stage chlorite, talc and epidote-calcite veins, and are consistently dissected by late-stage calcite veins. Main-stage veins can be subdivided into four types (I-IV), based on their orientation, internal textures and deformation: shear veins (type I), extensional veins (type II), stockwork-like veins (type III) and strongly deformed, boudinaged and/or folded veins (type IV).

Type I shear veins and type II extensional veins commonly occur proximal to one another and typically have similar thicknesses in the range 1-30 mm. Several rare intervals of vein quartz in the hangingwall are up to several metres in thickness and are attributed as type I veins. Both type I and II veins are mainly composed of quartz (ca. 40-80 vol. %) in addition to variable amounts of carbonate minerals; veins in the south and central part of the deposit typically contain calcite and occasionally lesser ankerite, whereas veins in the north contain magnesite. Type I and type II quartz-carbonate veins have a variable sulphide content of 0-20 vol. %, which outside the ore zone is dominated by pyrite and lesser pyrrhotite, and within the ore zone also includes arsenopyrite, chalcopyrite, various Sb sulphides and gold.

Type I quartz-carbonate shear veins occur parallel or sub-parallel to the local S_4 fabric, mostly dipping to the west-southwest at 45-80° (Fig. 9.5e), and commonly have laminated appearance (Fig. 9.6e). Some type I veins exhibit ribbon textures defined either by discontinuous slithers of wall rock(s) or by alternations between quartz and bands of carbonate or fine sulphide minerals (Fig. 9.6f). In several mineralised veins, sulphides have pressure shadows infilled by comb-textured quartz. A set of 1-2 mm-thick sulphide veinlets measured within the main ore zone are principally composed of pyrite, pyrrhotite and arsenopyrite and are oriented parallel to type I veins, dipping at similar angles towards

the west to southwest (Fig. 9.5e). Rarely, type I veins display extensional internal fabrics. In contrast, type II quartz-carbonate±sulphide veins are hosted by flat to gently east-dipping (largely <30°; Fig. 9.5e) extensional fractures that dissect the S_4 fabric (Fig. 9.5g) and are typified by comb-textured quartz, in which crystals are oriented perpendicular to vein margins (Figs. 9.5h, 9.5i). These veins commonly display mineral zonation composed of carbonate margins and quartz cores (Fig. 9.5g) and quartz is locally recrystallised. Centimetre-scale flat-lying type II veins can be distinguished in several oxide pits at Silverstone and appear to be laterally continuous for several metres.

Type I and type II main-stage veins display ambiguous cross cutting relations. In several instances, foliation-parallel type I veins are dissected by sub-horizontal type II veins (Fig. 9.6e), whereas on other occasions other, type I shear veins cross-cut and occasionally displace type II extensional veins by several centimetres (Fig. 9.6f). Furthermore, some type I and type II veins cross-cut other veins of the same type at a small angle and contain differing amounts of quartz, carbonate and sulphides. Several examples of interconnected type I and II quartz-carbonate veins have been identified. In these instances, foliation-parallel quartz-carbonate veins (type I) are fringed on both sides by multiple mm-scale, sub-horizontal veins with extensional textures (Fig. 9.6j), comparable to type II veins elsewhere.

Type III veins are quartz-dominated, carbonate-poor (< 5 vol. %) veins that unlike type I and type II veins, do not exhibit a consistent orientation. Rather, the orientation of type III veins varies unsystematically from steeply west-dipping, to sub-horizontal and steeply east-dipping (Fig. 9.5f). Although these veins display a considerable variation in thickness between 0.5 mm and 80 mm, some are narrow, discontinuous and display irregular, stockwork-like geometries (Fig. 9.6k). Type III veins are variably mineralised with sulphide minerals, predominantly pyrite, and are commonly present within high-grade intersections. No clear relationship has been identified between type I-II veins and type III stockwork veins.

The fourth type of main-stage veining at Silverstone, type IV, consists of highly deformed quartz-carbonate veins that are spatially restricted to the strongly foliated and mylonitic portions of the MSZ, particularly within the ore zone. These veins are boudinaged on a mm- to cm-scale and in the most deformed intervals, are preserved as sheared, isolated clasts of recrystallised quartz and carbonate concentrated on successive foliation planes (Fig. 9.6l). Where type IV veins are still intact, they are locally folded into F_4 folds (Fig. 9.6m). Type IV features are interpreted as the deformed equivalents of the other three main-stage vein types, however, due to their deformed nature, it is not possible to resolve the original orientations and textures of these veins. In highly deformed portions of the main ore zone, type IV boudinaged quartz-carbonate veins are host to sulphide and gold mineralisation.

Late-stage veins

Late-stage veins at Silverstone consist of a single set of calcite ± pyrite veins, which cross cut all other vein sets described in the above sections (Fig. 9.6g). Calcite ± pyrite veins are typically sugary-textured, most commonly have thicknesses in the range 1-5 mm, but occasionally are up to 20 mm in thickness, and are characterised by sub-horizontal to gently east dipping (< 40°) orientations (Fig. 9.5g). These veins commonly comprise extensional internal fabrics with calcite crystals oriented perpendicular to vein walls and variably contain a pyrite content of up to ~5%. Crucially, late-stage calcite veins are not mineralised and dissect gold-bearing areas, including main-stage quartz-carbonate veins (Fig. 9.6g).

9.5.2.2 M1 deposit

Veins measured in a single drillhole intersecting the M1 deposit occur in two principal orientations, comprising a moderately to steeply west-southwest-dipping group that are broadly parallel to the S_4 shear fabric, and a shallowly-dipping to sub-horizontal group (Fig. 9.5h). A further cluster of several vein measurements is steeply north-northwest dipping (Fig. 9.5h). The earliest veins at M1 consist of 4-14 mm-thick epidote-calcite(-quartz) veins that occur in doleritic hangingwall rocks parallel to the local S_4 shear fabric. These veins typically comprise a sheared, laminated fabric that is comparable to similar veins at Silverstone and are occasionally boudinaged. Magnesite±talc veins ranging in thickness from 2-15 mm are focussed in ultramafic hangingwall rocks and the ore zone, and are largely oriented either parallel to the foliation, or sub-horizontal. A third early set of veins at M1 consists of variably sheared and/or boudinaged calcite veins that are also predominantly parallel to the principal fabric. Quartz-carbonate veins overprint epidote-calcite veins and display identical characteristics to two types of main-stage veins at the Silverstone deposit: type I shear quartz-carbonate veins oriented parallel to S_4, and type II sub-horizontal quartz-carbonate veins that display ubiquitous extensional features. Some quartz-carbonate veins contain up to 15 vol.% pyrite, whereas others do not contain sulphides. As is the case at Silverstone, cross-cutting relations between type I and type II veins at M1 are ambiguous. On multiple occasions, minor extensional type II veins border the margins of type I shear veins and are demonstrative of overpressure (Fig. 9.6j).

9.5.2.3 Bugeye deposit

Structural logging of veins in a single drillhole at Bugeye has identified several vein sets including quartz, quartz-carbonate±sulphide and magnesite veins (Fig. 9.6k). Quartz veins and quartz-carbonate veins vary in thickness between 2 and 40 mm and are principally oriented parallel to banding in footwall BIF units, and parallel to the local S_4 fabric (~55-80° southwest; Fig. 9.6k). Some of these veins

STAGE	Vein Set	n	Typical orientation	Typical thickness (mm)	No. of cross cutting veins					
					Boudinaged quartz-carb	*Quartz-carbonate (-sulphide)*	*Pyrrhotite breccia*	*Pyrite veinlets*	*Calcite*	*Colloform-textured calcite(-pyrite)*
EARLY	Boudinaged quartz-carb	10	Steep, bedding-parallel							
MAIN	Quartz-carbonate ±tourmaline±sulphide	52	Bedding-parallel or sub-horizontal		1	2				
	Pyrrhotite breccia	6	Steep, bedding-parallel							
	Pyrite veinlets	7	Bedding-parallel or sub-horizontal		2	1				
LATE	Calcite	30	Variable between steep and sub-horizontal		1	1			2	
	Colloform-textured calcite ±pyrite	7	Sub-horizontal		2				1	

Table 9.2: Summary of vein sets identified at the Winddine Well deposit, including the number of each measured (n), typical orientations and vein thicknesses and the number of times veins in each set cross cut veins from other vein sets. Full logging data including all vein measurements can be found in Appendix E4.

have sheared internal fabrics, akin to type I main-stage veins at Silverstone, and veins are seldom refolded into F_4 fold geometries. Two sulphide-bearing quartz-carbonate veins dip gently towards the northeast at 20-30°, dissecting BIF banding and the S_4 fabric, and exhibit comparable extensional features to type II quartz-carbonate veins at Silverstone (Fig. 9.6k). A sub-horizontal ~2 mm-thick pyrite veinlet was identified proximal to the gently dipping quartz-carbonate veins, and a single ~5 mm-thick magnesite vein was observed parallel to banding in BIF (Fig. 9.6k).

9.5.2.4 Winddine Well deposit

Structural logging of oriented drillcore from three drillholes intersecting the Winddine Well deposit has identified three stages of veining, early, main- and late-stage, sub-divided according to their relative timing compared to gold mineralisation. The characteristics of these vein sets are summarised in Table 9.2, stereoplots of vein orientations are displayed in Figure 9.7 and representative photographs and photomicrographs are shown in Figure 9.8.

The earliest veins at Winddine Well consist of a set of boudinaged quartz-carbonate veins emplaced parallel to layering in BIF (Fig. 9.8a). These veins are north-south striking and dip steeply to the east and west at 82-90° (Fig. 9.7b), consistent with the orientating of banding in BIF and bedding in volcaniclastic units to the west. Boudinaged quartz-carbonate veins vary in thickness between 2 and 10 mm and exhibit highly variable quartz:carbonate ratios. Calcite and ankerite are the most abundant carbonate minerals, in addition to minor magnesite present locally. Some boudinaged veins are

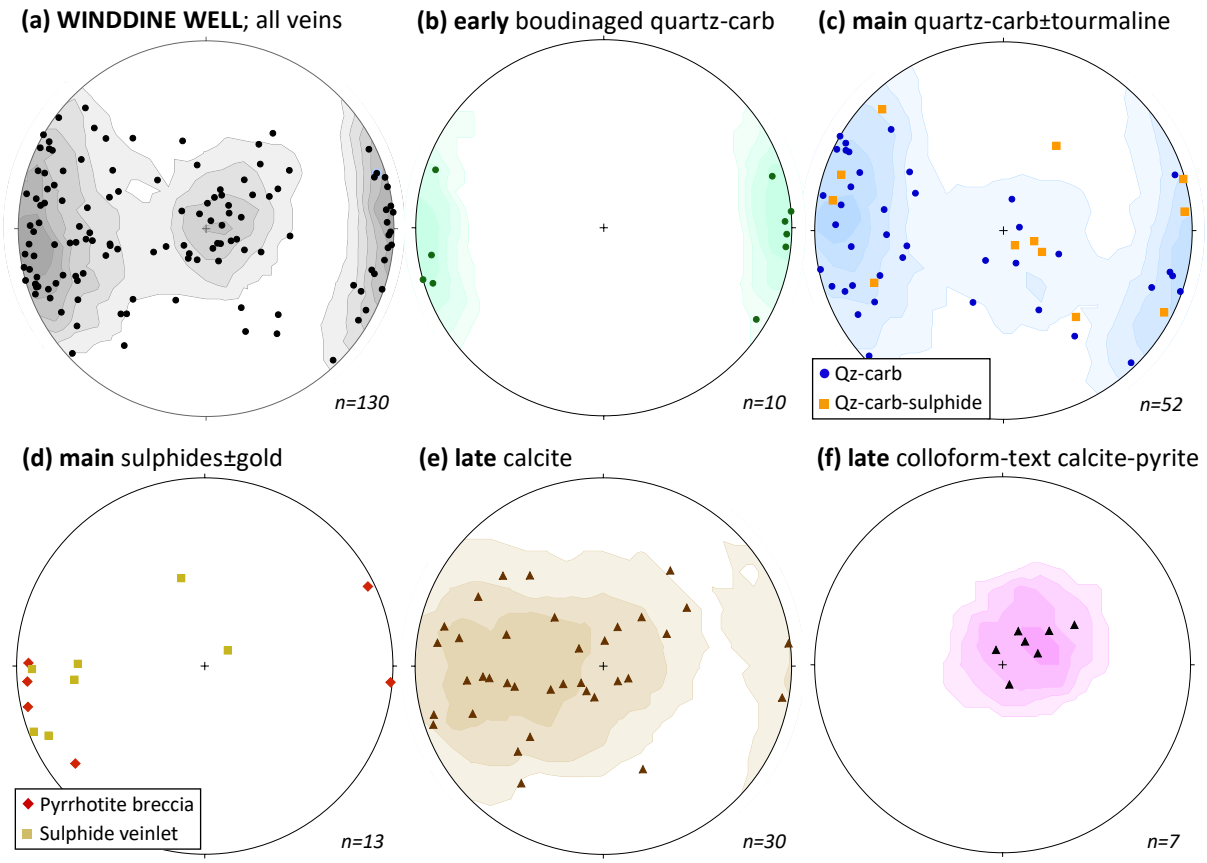

Figure 9.7: Lower hemisphere equal area stereonets summarising vein orientations measured in drillcore at the Winddine Well deposit. In all stereonets, the poles to planes are displayed. Kamb contours are drawn at 2σ intervals. **(a)** All vein measurements from the Winddine Well deposit; **(b)** Early, boudinaged quartz-carbonate veins; **(c)** Main stage quartz-carbonate and sulphide-bearing quartz-carbonate veins; **(d)** Main stage sulphide±gold orientations, including the margins of pyrrhotite breccia and sulphide veinlets; **(e)** Late-stage equigranular and massive calcite-only veins; **(f)** Late-stage, colloform-banded calcite-pyrite veins.

sheared, such that individual asymmetric boudins define shear sense indicators consistent with D_4 shearing, and other veins are folded alongside parallel BIF layers into F_4 folds.

Early, boudinaged quartz-carbonate veins are cross-cut by main-stage quartz-carbonate ± tourmaline ± sulphide ± gold veins. A majority of these veins occur parallel to sub-parallel with banding in BIF and the foliation in surrounding rocks (Fig. 9.7c). Other veins within this set occur in gently north-dipping (< 40°) to sub-horizontal orientations (Fig. 9.7c) and crosscut early boudinaged veins and bedding in BIF units (Fig. 9.8a). Main-stage veins are typically 1-50 mm in thickness, however, several veins up to 40 cm in thickness have been intersected in drillcore. A minority of veins contain black tourmaline as a constituent vein mineral, particularly within mafic intrusives towards the west where these veins are associated with disseminated tourmaline in calcite-altered vein selvedges. Main-stage quartz-carbonate veins within and proximal to the ore zone are mineralised with sulphides, including pyrite, arsenopyrite and pyrrhotite, and occasionally contain visible gold. In sub-horizontal veins, sulphides nucleate at the contacts with surrounding magnetite horizons in host BIF units (Fig. 9.8a).

The two contrasting orientations of main-stage quartz-carbonate veins exhibit different textural features. Some of the steeply-dipping, layer parallel veins have ribbon-textured, sheared internal fabrics, enclosing slithers of the wall rock (Fig. 9.8b). A single subvertical quartz-calcite-tourmaline vein in a strongly foliated volcaniclastic unit displays boudinage on a ~10 cm scale (Fig. 9.8c). In contrast, subhorizontal veins commonly display extensional textures comprised of comb-textured quartz and carbonate minerals oriented perpendicular to vein walls, and dissect steeply dipping main-

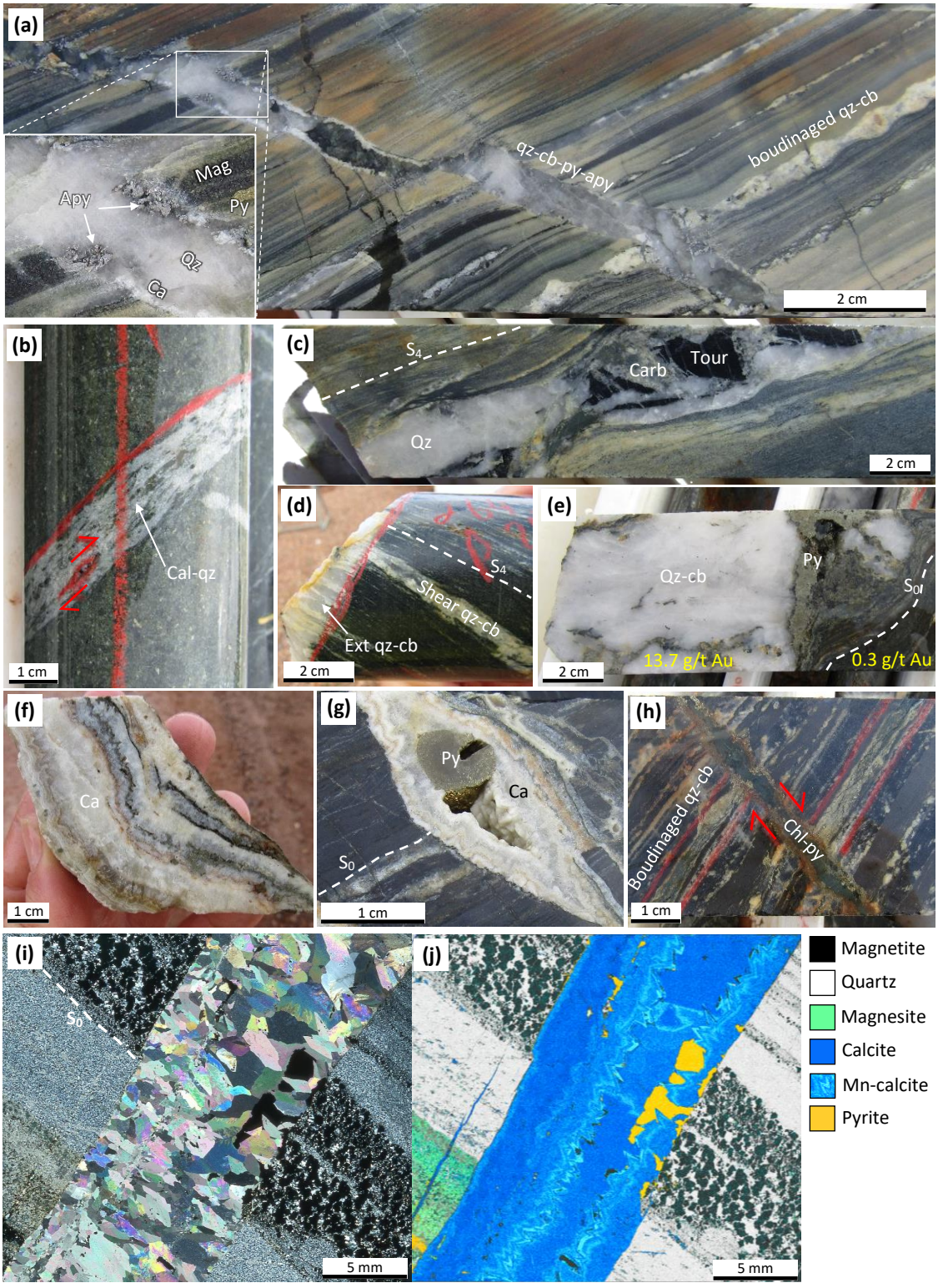

Caption on next page

Figure 9.8: Photographs (a-h), thin section photomicrograph (i) and mineral map (j) of representative veins identified in drillcore from the Winddine well deposit. **(a)** Boudinaged, layer-parallel quartz-carbonate veins in BIF, dissected by a shallowly-dipping quartz-calcite-pyrite-arsenopyrite vein. Note the nucleation of sulphides on magnetite bands in the inset image (WWDD040, 286.5 m); **(b)** Calcite-quartz shear vein enclosing bands of wall-rock, deformed as shear sense indicators (WWDD031, 170.2 m); **(c)** Boudinaged quartz-carbonate-tourmaline vein, parallel to the local S_4 shear fabric (WWDD031, 272.15 m); **(d)** Shear-textured quartz-carbonate vein, cross-cut by a extensional, sub-horizontal quartz-calcite vein (WWDD031, 235.9 m); **(e)** Thick, mineralised quartz-carbonate-pyrite-gold vein broadly parallel to layering in BIF, containing a significantly lower gold grade. Assay data provided by Minjar Gold (WWDD031, 248.2 m); **(f)** Colloform-textured banded calcite vein (WWDD038, 309 m); **(g)** Sub-horizontal, colloform-textured calcite vein enclosing pyrite and dissecting bedding and layer-parallel veins (WWDD031, 237.25 m); **(h)** Sub-horizontal chlorite-pyrite vein dissecting boudinaged qz-carb veins showing a displacement of ~3 cm. Displacement is top side towards the east (WWDD031, 242.0 m); **(i)** Thin section photomicrograph of a colloform-textured pyrite-calcite vein offsetting magnetite bands in the host BIF unit, taken in cross polarized light (sample WW38A3); **(j)** Mineral map of the calcite vein in (i). Note the zonation defined by Mn-enrichment, and localization of sulphides proximal to magnetite. An early, layer-parallel magnesite-bearing vein is evident in the bottom left, and dissected by the calcite-pyrite vein (sample WW38A3).

stage quartz-carbonate veins (Fig. 9.8d). These quartz-carbonate veins within sulphide and gold mineralised zones have margins that are typically parallel to the banding in host BIF (Fig. 9.8e). Pyrite and pyrrhotite veinlets that vary in thickness between 5 and 40 mm mirror the orientations of associated quartz-carbonate veins, with a minority sub-horizontal and a significant majority steeply-dipping towards the east (Fig. 9.7d). Similarly, the margins of pyrrhotite hydrothermal breccias within the ore zone (described below in Section 9.5.3.5) are consistently steeply- to vertically-dipping and broadly parallel to BIF banding and the S_4 fabric at Winddine Well (Fig. 9.7d).

Late-stage veins at Winddine Well consist of two sets of carbonate veins, principally composed of calcite, which cross-cut early boudinaged veins and main-stage veins. The most abundant set of calcite veins is typified by a white, equicrystalline and sugary textured calcite and exhibits inconsistent orientations that vary between vertical and sub-horizontal, predominantly dipping towards the east (Fig. 9.7e). Moderately to steeply-dipping calcite veins commonly show oblique internal fabrics, which constantly demonstrate east-side up sense of movement, which is consistent with all other shear sense indicators along the WWSZ (Section 4.5.6.2). Sub-horizontal veins comprise calcite crystals oriented perpendicular to vein walls, indicative of extension, and a minority of veins are brecciated. The other late-stage vein set at Winddine Well comprises sub-horizontal to shallowly southwest-dipping (< 35°) colloform and crustiform-textured calcite-pyrite veins, which crosscut bedding, the S_4 fabric and all other veins (Fig. 9.7f; Fig. 9.8f). These veins display complex zonation, are occasionally infilled by pyrite (Fig. 9.8g) and are associated with infilled fractures that indicate vertical extension (Section 4.5.6.2). Rare chlorite-pyrite infilled sub-horizontal fractures are associated with colloform-textured veins, and both frequently display offset of BIF banding of up to several centimetres (Fig. 9.8h, Fig. 9.8i). Element mapping of a colloform-textured calcite-pyrite vein demonstrates well developed, sawtooth compositional zonation within colloform-textured veins, defined by Mn -enriched calcite (Fig. 9.8j). Furthermore, pyrite with the veins nucleates in contact with, and proximal to, magnetite bands in the host BIF units (Fig. 9.8j). Crucially, both late-stage calcite vein sets dissect gold-mineralised veins and breccias and therefore post-date gold mineralisation.

9.5.3 Ore petrography and paragenesis

Reflected light microscopy and SEM imaging coupled with reconnaissance EDS analysis has been undertaken on 20 mineralised samples of variable gold grade, taken from four drillholes and one pit (Ardmore) along the ~1.5 km length of the Silverstone deposit. Furthermore, the ore mineralogy of mineralised drillcore samples from Bugeye (n=1), Winddine Well (n=5) and Black Dog (n=3), in addition to three pit samples from Black Dog, have also been assessed. ASEM element mapping has been carried out on selected ore samples from Silverstone, Black Dog and Winddine Well, in order to illustrate paragenetic relationships at these deposits. The ore petrography and mineral paragenesis at each of these deposits is described in this section.

9.5.3.1 Silverstone deposit

The main ore zone at Silverstone is typified by a relatively low sulphide content and in order of abundance consists primarily of pyrite, arsenopyrite, pyrrhotite, Sb-bearing sulphides and chalcopyrite. Gold grade displays a close spatial relationship with sulphide content, in particular arsenopyrite, pyrrhotite and Sb-sulphides, and the highest-grade samples at Silverstone have been assayed at ~20 g/t Au. Sulphides occur in in three settings: I) disseminated sulphides in the carbonate-sericite-albite-quartz altered groundmass (Fig. 9.9a), II) sulphides in main-stage veins (types I-IV; Section 9.5.2.1) composed of variable proportions of quartz and carbonate that are frequently zoned (Figs. 9.9b, 9.9c), and III) sulphides in the selvedge and alteration haloes surrounding quartz-carbonate veins (Fig. 9.9a). Close to the shear zone contact, quartz-carbonate veins in the ore zone are commonly highly deformed and are preserved as variably boudinaged and sheared clasts (type IV veins; Fig. 9.9d). The narrow mineralised zone in the hanging-wall in the southern portion of the Silverstone deposit consists of multiple narrow (<4 cm-thick), type I shear veins that are associated with the sulphides pyrrhotite, pyrite and minor arsenopyrite. Sulphides occur either as clasts in the shear veins, typically accompanied by pressure shadows, or as sulphides in the vein selvedge (Fig. 9.9a). The gold grade of this narrow mineralised zone is consistently lower than that of the main ore zone, with assays typically reaching ~2 g/t Au.

Following petrographic and SEM-EDS analysis, four successive stages of mineralisation (stages 1-4) have been identified in mineralised rocks at Silverstone, three of which are directly associated with discrete gold-bearing phases. The mineralogy, textural characteristics and features of minerals comprising each of these stages are summarised below and are illustrated in Figure 9.10 (stages 1-2) and Figure 9.11 (stages 3-4). A paragenetic table outlining the interpreted order of precipitation of ore and gangue minerals is shown in Table 9.3.

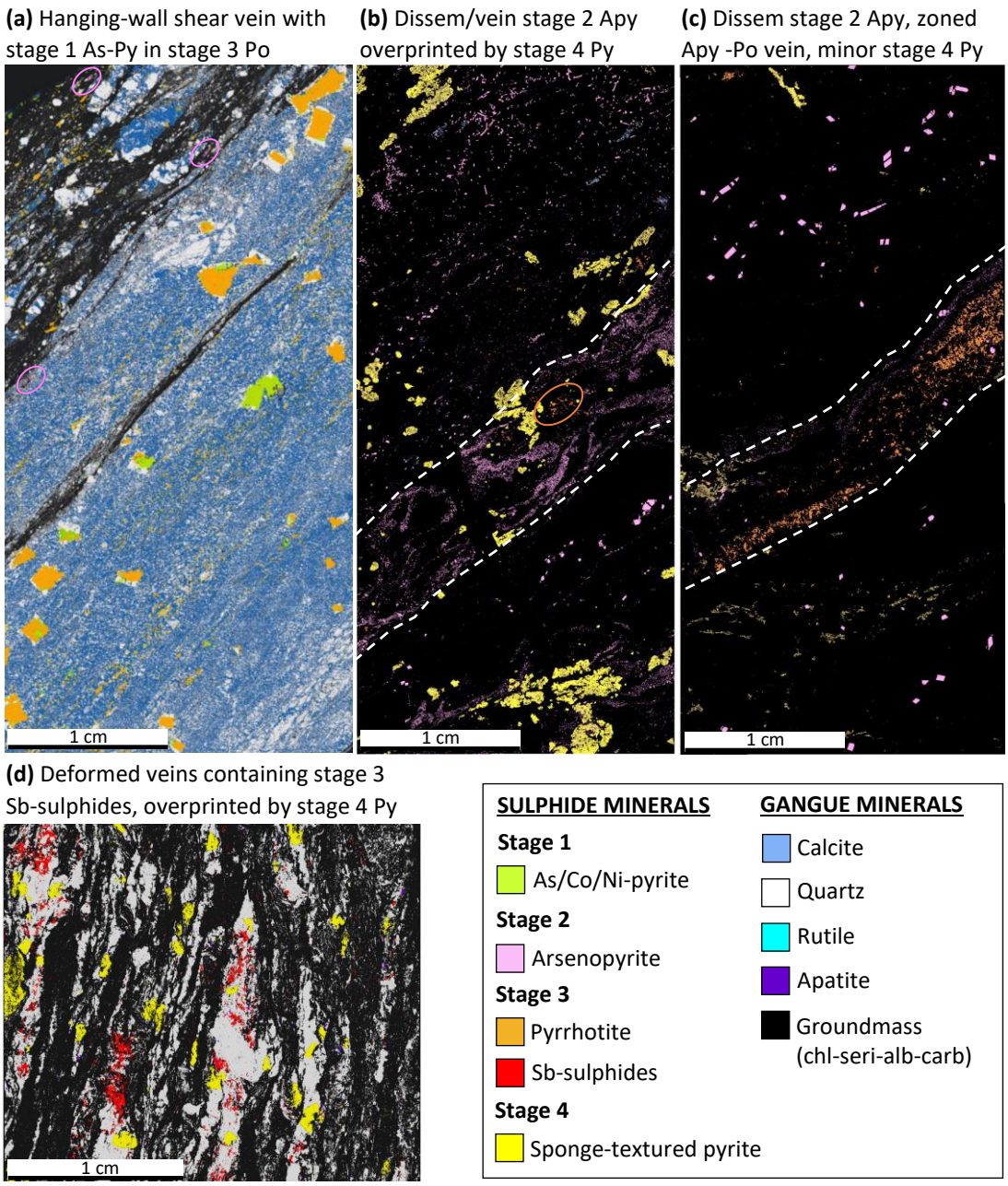

Figure 9.9: Mineral maps of high-grade ore samples from the Silverstone deposit, displaying the distribution of successive stages of sulphide mineralisation. (a) and (d) are element maps coloured to denote minerals, whereas (b) and (c) are colourised BSE maps showing sulphides only. **(a)** A hangingwall type I shear vein containing stage 1 As-bearing pyrite as inclusions within stage 3 pyrrhotite. Minor stage 2 arsenopyrite occurs at the margins of the vein, circled in pink (sample SS17M1); **(b)** Disseminated and vein stage 2 arsenopyrite and rutile, with minor stage 3 pyrrhotite at the core of the vein. All phases are overprinted by stage 4 sponge-textured pyrite (sample SS19M3); **(c)** Disseminated stage 2 arsenopyrite dissected by a zoned quartz-carbonate vein containing an arsenopyrite margin and stage 3 pyrrhotite core, overprinted by stage 4 pyrite (sample SS19M4); **(d)** Deformed type IV quartz veining containing various Sb-bearing sulphides, chiefly stibnite, berthierite and chalcostibite, overprinted by apatite and stage 4 pyrite (sample SS18M3).

Stage 1: As/Co/Ni-bearing pyrite-chalcopyrite-gold

The earliest sulphide mineralisation at Silverstone consists of an assemblage of trace element-enriched pyrite, in addition to chalcopyrite, electrum (AuAg) and rare sphalerite. The distribution of the stage 1 sulphide assemblage is predominantly limited to the selvedge of multiple discrete quartz-

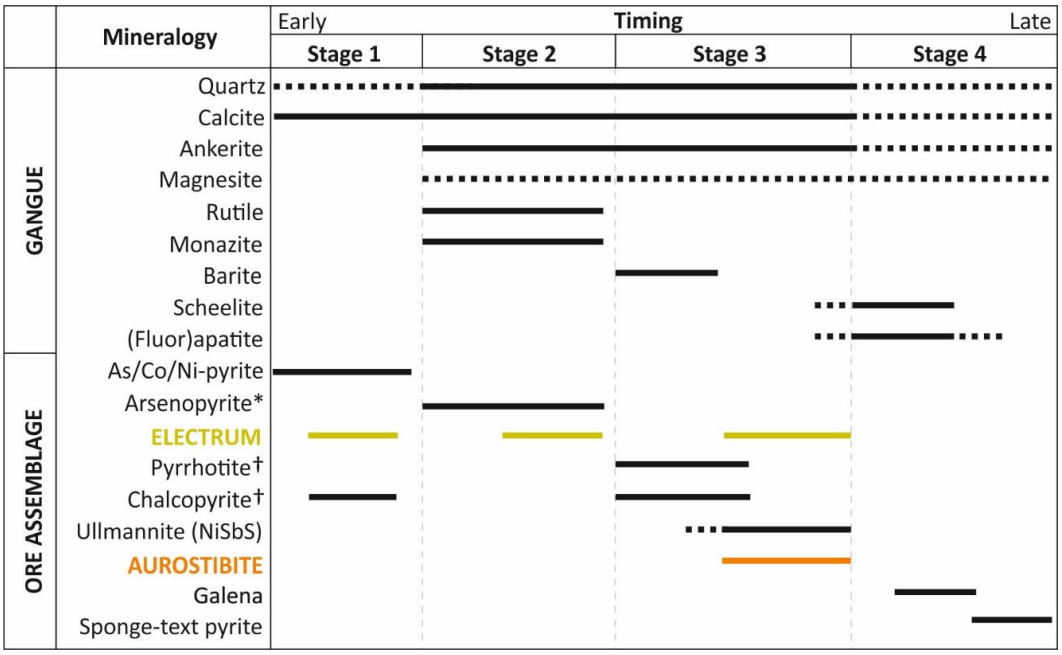

Table 9.3: Paragenetic table for the mineralised ore zone at the Silverstone deposit, outlining the mineral phases associated with each stage of mineralisation. The gold-bearing phases electrum (AuAg) and aurostibite ($AuSb_2$) are highlighted in yellow and orange, respectively. *In ultramafic rocks in the far north, stage 2 arsenopyrite is substituted by gersdorffite (NiAsS). †In localized Sb-rich/Fe-poor parts of the ore zone, these stage 3 minerals are substituted by the Sb sulphide minerals berthierite, tetrahedrite, chalcostibite, jamesonite and stibnite.

carbonate shear veins in the hangingwall of the deposit and is less common in the main ore zone. In the north of the deposit, stage 1 pyrite veinlets up 2 mm in width occur in the ore zone and are overprinted by subsequent episodes of sulphide mineralisation. Stage 1 pyrite crystals are idiomorphic, typically display hexahedral crystal shapes, and occur as aggregates of multiple crystals that range in size between 200 and 600 µm (Fig. 9.10a). Pyrite crystals variably contain up to several atomic % (0.5-2.5 at. %) of trace elements such as As, Co and Ni (Fig. 9.10b) and are spatially associated with calcite and minor < 30 µm crystals of sphalerite, both of which are occasionally present as inclusions. Stage 1 pyrite also contains irregularly shaped, allotriomorphic inclusions of chalcopyrite that vary in size from 10-60 µm (Fig. 9.10c).

Gold invariably occurs as 1-20 µm inclusions of electrum within stage 1 pyrite, commonly in contact with or proximal to chalcopyrite and/or sphalerite inclusions (Fig. 9.10a). Stage 1 electrum has a high gold content of 75-85 at. % (corresponding to a fineness of 750-850 ‰) and a minority of electrum grains contain detectable Fe content of < 5 %. In the main ore zone at Silverstone, stage 1 mineralisation is only evident as < 100 µm inclusions of arsenian pyrite within stage 2 arsenopyrite.

Stage 2: Arsenopyrite-gold-rutile

The second stage of mineralisation at Silverstone consists of an assemblage of arsenopyrite, electrum and rutile that typifies the high-grade areas of the main ore zone. Arsenopyrite typically occurs as

distinctive, idiomorphic, rhomb-shaped crystals that vary in size between ~20 and 800 µm and are located at the margins of massive veins or disseminated in the surrounding silicate groundmass (Fig.

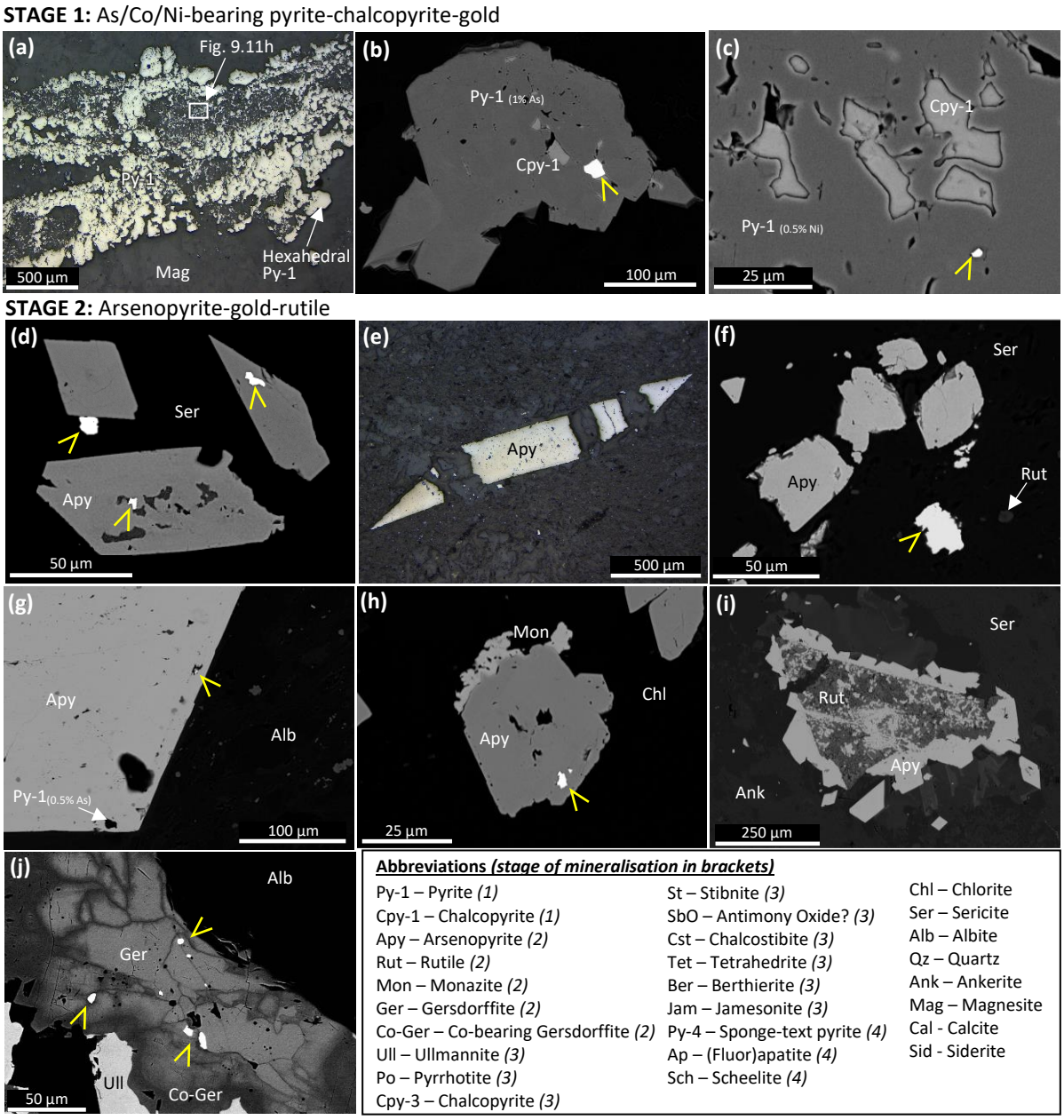

Figure 9.10: Back-scattered electron and reflected light images of mineralised drillcore samples from the Silverstone deposit, displaying the mineralogy, relationships and textures associated with stage 1 (a-c) and stage 2 (d-j) sulphide and gold mineralisation. Yellow arrows point towards electrum (AuAg). **(a)** Veinlet of stage 1 pyrite crystals in magnesite, enclosed by successive sulphide phases (see Fig. 9.11h) (sample SS15M5); **(b)** Hexahedral stage 1 arsenian pyrite crystals containing inclusions of chalcopyrite and electrum (sample SS18M1); **(c)** Magnified view of stage 1 Ni-bearing pyrite containing irregular inclusions of chalcopyrite and electrum (sample SS18M1); **(d)** Multiple stage 2 idiomorphic rhomb-shaped arsenopyrite crystals containing electrum as inclusions, or attached to crystal margins (sample SS17M5-1); **(e)** Microboudinaged elongate crystal of arsenopyrite (sample SS19M4); **(f)** 30 µm electrum grain hosted by sericite proximal to stage 2 arsenopyrite crystals (sample SS19M3); **(g)** Magnified view of the margin of a stage 2 arsenopyrite rhomb, containing <10 µm silicate, electrum and stage 1 As-bearing pyrite inclusions, aligned parallel to crystal margins (sample SS19M4); **(h)** Stage 2 arsenopyrite containing electrum inclusions and mantled by monazite crystals (sample SS19M3); **(i)** Rutile intergrown and bound by stage 2 idiomorphic arsenopyrite rhomb-shaped crystals (sample SS17M5-1); **(j)** Stage 2 mineralised ultramafic rocks in the northern part of Silverstone comprising electrum grains hosted by gersdorffite (NiAsS), with a Co-rich margin, in contact with stage 3 ullmannite (NiSbS) and albite (sample SSDD15-4a). Abbreviations and corresponding stage numbers for minerals are shown in the bottom right.

STAGE 3: Pyrrhotite-chalcopyrite-(Ni)Sb sulphides-gold

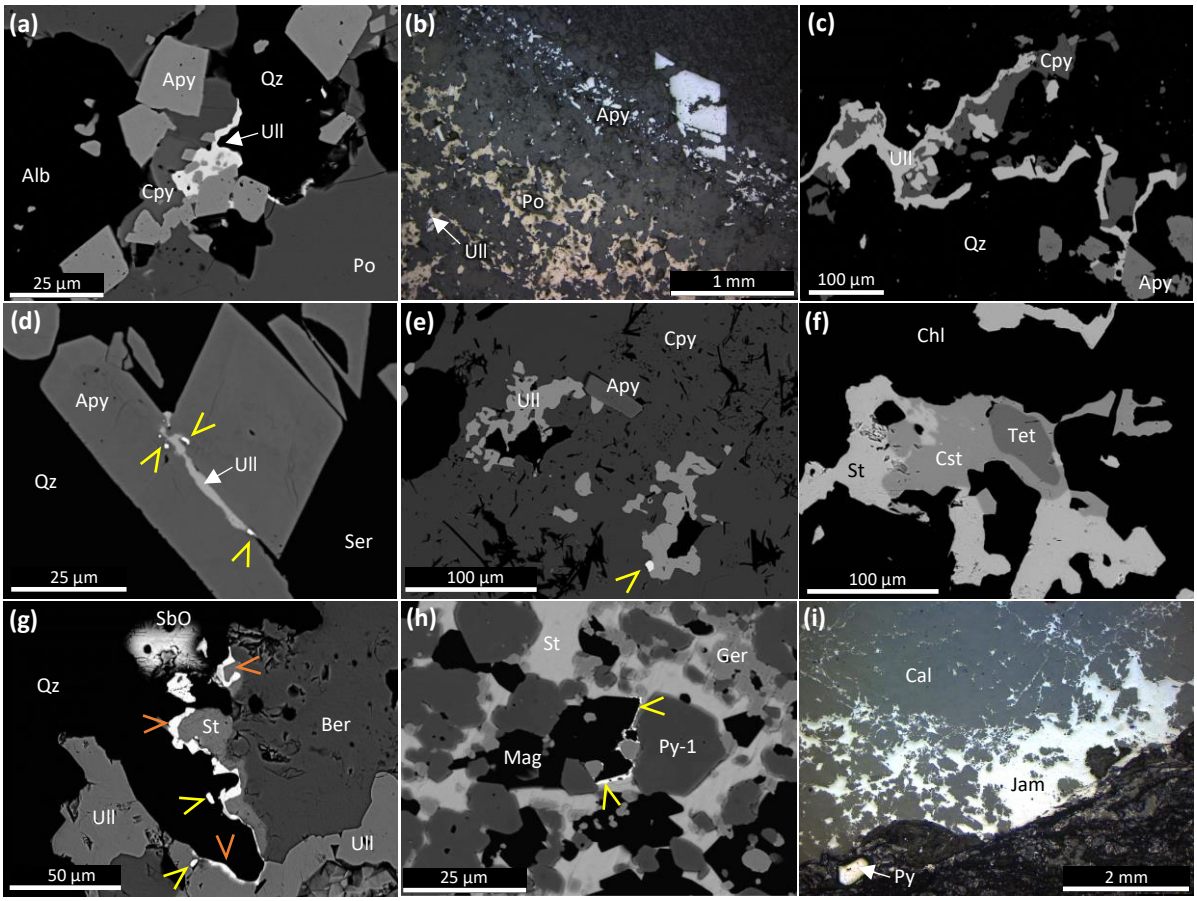

STAGE 4: Pyrite-scheelite-apatite-galena

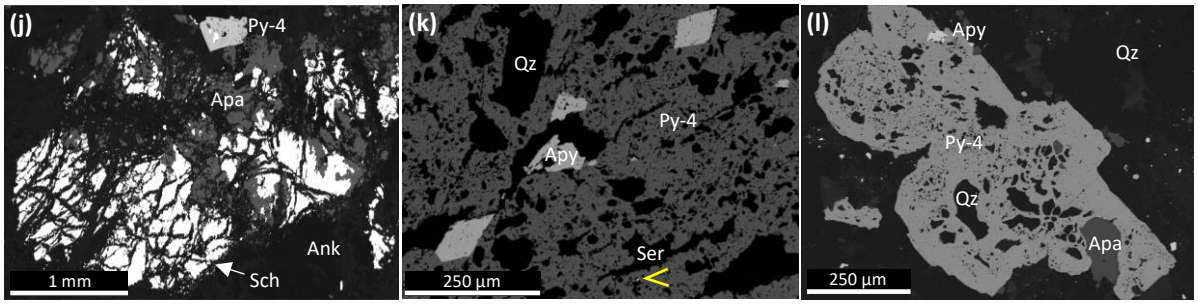

Figure 9.11: Back-scattered electron and reflected light images of mineralised drillcore samples from the Silverstone deposit, displaying the mineralogy, relationships and textures associated with stage 3 (a-i) and stage 4 mineralisation (j-l). **(a)** Stage 3 pyrrhotite, chalcopyrite and ullmannite overprinting stage 2 arsenopyrite crystals (sample SS19M3); **(b)** Magnified view of a zoned quartz carbonate vein in Fig. 9.9c, comprising a margin of arsenopyrite and poikilitic pyrrhotite in the core (sample SS19M4); **(c)** Stage 3 ullmannite at the margins of chalcopyrite, both overprinting stage 2 arsenopyrite (sample SS17M5); **(d)** Stage 3 ullmannite conjoining arsenopyrite crystals, with multiple 2-4 µm electrum grains at the margins (sample SS17M5-1); **(e)** Irregular inclusions of stage 3 ullmannite within chalcopyrite, one containing electrum. Note the inclusion of stage 2 arsenopyrite within chalcopyrite (sample SS17M5-1); **(f)** Assemblage of stage 3 Sb-bearing minerals comprising a core of tetrahedrite [$(Cu,Ag)_6(Cu_4(Fe,Zn)_2)Sb_4S_{13}$], chalcostibite ($CuSbS_2$) and a rim of stibnite (Sb_2S_3), hosted by chlorite (sample SS18M3-1); **(g)** An assemblage of stage 3 berthierite ($FeSb_2S_4$), ullmannite and stibnite surrounded by quartz, with aurostibite and minor electrum occurring along the sulphide margin (sample SS18M3-1); **(h)** Allotriomorphic stage 1 pyrite overprinted by stage 2 gersdorffite, both enclosed by stage 3 stibnite in the north Silverstone deposit. A narrow smear of electrum occurs between magnesite and stibnite (sample SS15M5); **(i)** Massive jamesonite ($Pb_4FeSb_6S_{14}$) at the margin of a calcite-quartz vein, containing calcite inclusions (sample SS19V3); **(j)** Large ~3 mm fragmented stage 4 assemblage of scheelite bound by apatite and infiltrated by ankerite veining. Minor stage 4 pyrite encloses scheelite and apatite inclusions (sample SS17M5-1); **(k)** Stage 4 'sponge-textured' pyrite containing abundant silicate and arsenopyrite inclusions, in addition to an isolated <10 µm inclusion of electrum attached to quartz, interpreted as an inherited inclusion (sample SS19M3); **(l)** Stage 4 sponge-textured pyrite containing rounded inclusions of apatite, quartz and minor stage 2 arsenopyrite, surrounded by quartz (sample SS19M3). Abbreviations as in Figure 9.10.

9.10d). Some elongate, acicular arsenopyrite crystals are boudinaged and broadly oriented parallel to the principal shear fabric (Fig. 9.10e). Less commonly, arsenopyrite occurs as cataclastic aggregates composed of smaller, fragmented crystals < 150 µm in size.

Gold is directly associated with arsenopyrite and invariably occurs as electrum, comprising grains ranging in size between 1 and 35 µm. Stage 2 electrum occurs in three alternative settings: I) most commonly, as <10 µm inclusions within arsenopyrite crystals (Fig. 9.10d); II) grains of variable size attached to the outer margins of arsenopyrite crystals (Figs. 9.10d), or III) larger (>10 µm) grains of 'free gold' in the sericite-quartz-albite groundmass, commonly proximal to arsenopyrite (Fig. 9.10f). Stage 2 electrum has a typical gold content of 65-85 at. % (650-850 ‰ fineness), with several grains containing elevated gold contents of > 90 at. %. A small amount of mercury was detected in a single electrum grain and approximately 20% of grains have an iron content of < 7%.

Inclusions within stage 2 arsenopyrite crystals comprise arsenian pyrite, considered to represent stage 1 pyrite, in addition to quartz, sericite, chlorite and locally, rutile. In several instances, oriented inclusions of silicate minerals, arsenian pyrite and electrum are located parallel to the margins of arsenopyrite crystals, indicative of growth zones (Fig. 9.10g). Monazite is directly associated with the stage 2 assemblage and occurs either as inclusions in arsenopyrite crystals, or more commonly, as overgrowths at the margin of arsenopyrite (Fig. 9.10h). In several instances, inclusions of arsenopyrite occur within monazite. Monazite is characterised by allotriomorphic crystals that range in size between 5-50 µm and commonly contain abundant <2 µm silicate inclusions (Fig. 9.10h). In some samples, arsenopyrite and rutile are intergrown and contain inclusions of one another (Fig. 9.10i).

Whereas the mineralogy of the stage 2 assemblage described above is consistent along the southern and central portions of the Silverstone deposit, ultramafic protoliths in the far north of the deposit contain a different stage 2 mineralogy. In this area, the dominant stage 2 sulphide mineral is gersdorffite (NiAsS), which occurs as hypidiomorphic, occasionally rhombic, crystals up to 400 µm in size that like arsenopyrite further south, contain < 10 µm inclusions of electrum (Fig. 9.10j). Gersdorffite surrounds and overprints stage 1 pyrite crystals but is itself overprinted by stage 3 Sb-bearing sulphides. The margins of some gersdorffite crystals are Co-rich and other inclusions are consistent with the surrounding magnesite-talc-sericite-albite-fuchsite groundmass (Fig. 9.10j).

Stage 3: Pyrrhotite-chalcopyrite-(Ni)Sb sulphides-gold

The third stage of mineralisation at Silverstone consists principally of pyrrhotite, chalcopyrite and ullmannite (NiSbS), all of which overprint stage 1 and 2 phases (Fig. 9.11a). These minerals have been identified along the length of the Silverstone deposit. The most abundant stage three phase is

pyrrhotite, which occurs as allotriomorphic crystals up to several mm in size, commonly displaying etched margins. Locally, poikilitic-textured pyrrhotite occurs in the centre of zoned quartz-carbonate-sulphide veins in the main ore zone (Fig. 9.11b), and contains inclusions of quartz, calcite and stage 2 arsenopyrite. Chalcopyrite is present as less abundant, 20-500 µm allotriomorphic crystals, sometimes occurring as inclusions within pyrrhotite. Ullmannite exhibits several distinctive textures, including coating other stage 3 minerals (Fig. 9.11c) or stage 2 arsenopyrite (Fig. 9.11d), in addition to irregular arrays of sub-rounded inclusions within other stage 3 minerals, principally pyrrhotite and chalcopyrite (Fig. 9.11e). Ullmannite typically is present at the margins of the stage 3 sulphide assemblage where the adjacent silicate mineral is albite or quartz (Fig. 9.11c). Ullmannite locally envelopes and conjoins ankerite crystals, and ragged barite crystals seldom up to 500 µm in size are associated with carbonate veining and considered coeval with pyrrhotite, based on textural relations.

The stage 3 sulphide assemblage in localised portions of the Silverstone ore zone display relative Sb-enrichment coupled with Fe-depletion, such that the typical assemblage present elsewhere is instead represented by Sb-bearing minerals, in addition to ullmannite. In order of abundance, these minerals include berthierite ($FeSb_2S_4$), stibnite (Sb_2S_3), tetrahedrite [$(Cu,Ag)_6(Cu_4(Fe,Zn)_2)Sb_4S_{13}$] and chalcostibite ($CuSbS_2$). Composite grains of these sulphides reach up to 1 mm in diameter and are commonly zoned: cores are typically composed of tetrahedrite, in turn surrounded by berthierite ± chalcostibite and outer rims are often composed of stibnite and ullmannite (Fig. 9.11f). Notably, stibnite consistently occurs at the interface between berthierite and quartz. Additionally, several rounded grains of an antimony oxide phase up to 100 µm in size occur proximal to stibnite and berthierite (Fig. 9.11g). Stage 3 Sb-bearing minerals are frequently associated and intergrown with carbonate minerals, exemplified by euhedral rhombic magnesite crystals within stibnite in the north of the deposit (Fig. 9.11h). Other minor phases associated with the Sb-rich stage 3 assemblage include jamesonite ($Pb_4FeSb_6S_{14}$), which occurs as inclusions in berthierite or at the margins of Sb-sulphides, as well as rare sphalerite and xenotime (YPO_4). Several carbonate-dominated veins contain large (up to 1 cm) poikilitic masses of jamesonite containing rounded inclusions of calcite (Fig. 9.11i). These veins are accompanied by an increase in gold grade (2.7 g/t Au in a 1 m composite sample); however, no discrete gold-bearing phases have been identified within them.

Gold associated with stage 3 sulphide mineralisation occurs in two different alloys, electrum and aurostibite ($AuSb_2$). Electrum is considerably more abundant, accounting for ~90% of stage 3 gold-bearing phases identified at Silverstone and occurs as 1-10 µm grains directly associated with ullmannite. Electrum is typically present either within ullmannite crystals (Fig. 9.11e), or at the contact between ullmannite and stage 2 arsenopyrite (Fig. 9.11d). The gold content of stage 3 electrum varies between 60 and 80 at. % (600-800 ‰ fineness). In contrast, aurostibite occurs in association with

stibnite and ullmannite, most frequently as markedly narrow (<3 µm) mantling features at the margins of these crystals where they are in contact with quartz (Fig. 9.11g). Aurostibite and electrum occur adjacent to one another at the margins of some Sb-sulphide composite grains (Fig. 9.11g). The gold content of aurostibite varies from 35-55 at. % and is considerably lower than the typical gold content of concurrent electrum. Both stage 3 gold-bearing phases occur predominantly as inclusions or at the margins of sulphides and are seldom present as free gold in the surrounding groundmass, in contrast to stage 2 electrum.

Stage 4: Pyrite-scheelite-apatite-galena

The stage 4 assemblage consists principally of the minerals pyrite, scheelite, (fluor)apatite and galena, which postdate all earlier phases and constitute the most recent stage of mineralisation at Silverstone. Contrary to the preceding three stages, the stage 4 assemblage is not directly associated with a gold-bearing phase. Scheelite typically occurs as allotriomorphic crystals up to 200 µm in size that are associated with calcite and ankerite and commonly exhibit etched crystal margins. Locally, scheelite crystals in ankerite veins reach up to 3 mm in size, are fragmented, mantled by fluorapatite and are pervaded by carbonate veining (Fig. 9.11j). Galena is present as a minor stage 4 phase and occurs as < 30 µm grains either disseminated in quartz or attached to the margins of pre-existing sulphide grains.

The most abundant stage 4 mineral is a distinctive sponge-textured pyrite phase that is disseminated throughout the ore zone and is typified by abundant inclusions of silicate, carbonate and sulphide minerals. Sponge-textured pyrite grains are consistently allotriomorphic, reach up to several centimetres in size and contain inclusions that reflect the local pre-existing stage 1-3 ore assemblage (Fig. 9.11k). Across much of the deposit, these are principally composed of sericite, quartz, ankerite, calcite, stage 2 arsenopyrite, stage 3 ullmannite and stibnite, and occasional chlorite and rutile. Sponge-textured pyrite also often contains inclusions of scheelite and apatite, indicating that these minerals precipitated prior to pyrite during the final stage of mineralisation (Fig. 9.11l). A minority of sponge-textured pyrite crystals contain up to ~0.8 at. % As and some crystals are deformed into the principal shear fabric.

9.5.3.2 Bugeye deposit

Mineralised rocks in the ore zone at the Bugeye deposit are dominated by arsenopyrite and pyrite, which are locally massive and form vein-like masses up to several centimetres in thickness. Arsenopyrite represents the earliest sulphide phase and occurs as rhomb-shaped, idiomorphic crystals that range in size between 50 and 600 µm, comparable to stage 2 arsenopyrite at Silverstone.

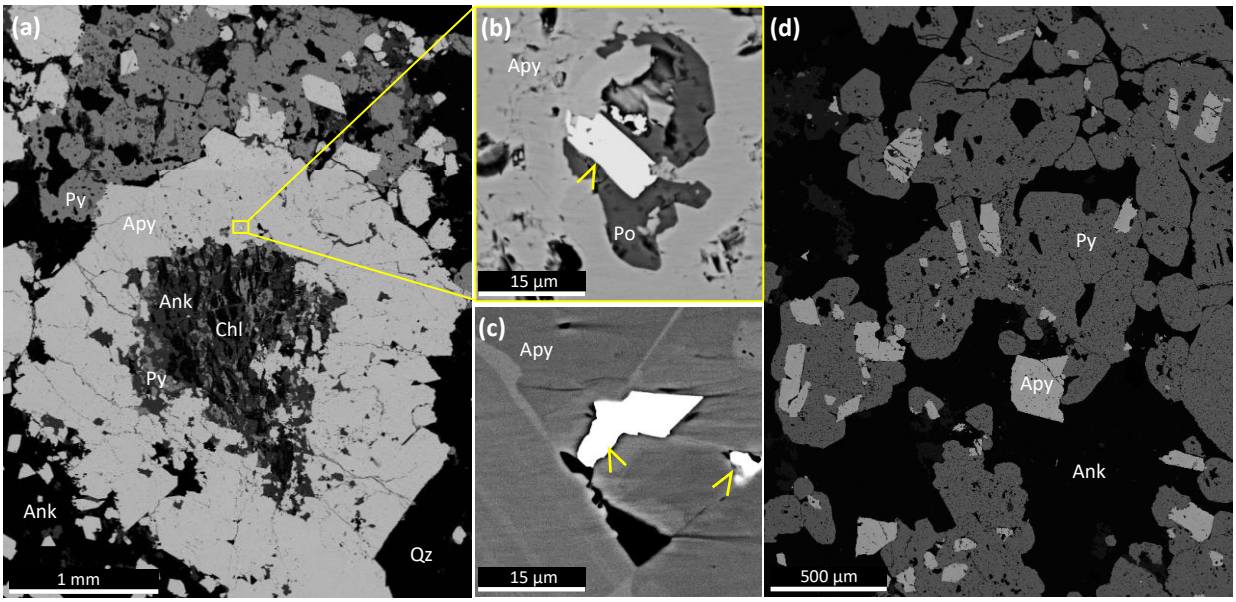

Figure 9.12: Back-scattered electron images of lode-gold mineralised drillcore samples from the Bugeye deposit (sample BE02M2. Yellow arrows point towards electrum (AuAg). **(a)** 3 mm spherical aggregate of arsenopyrite crystals with an irregularly shaped core composed of ankerite, chlorite and pyrite. The aggregate and isolated rhombs of arsenopyrite are overprinted by inclusion-rich pyrite, ankerite and quartz; **(b)** Magnified view of an idiomorphic electrum inclusion in arsenopyrite in (a), in contact with minor pyrrhotite; **(c)** Electrum inclusions in arsenopyrite, one of which displays the rhombic crystal shape that characterizes the host mineral; **(d)** Irregular mass of inclusion-rich 'sponge-textured' pyrite, containing inclusions of arsenopyrite, ankerite and quartz.

Arsenopyrite commonly forms peculiar, spherical aggregates of crystals that range in diameter between 1 and 3 mm and typically comprise cores of chlorite, ankerite and minor pyrite (Fig. 9.12a). Arsenopyrite is directly associated with electrum, which occurs as 3-20 µm idiomorphic inclusions, occasionally in contact with minor pyrrhotite inclusions (Fig. 9.12b), and less commonly attached to the outer margins of arsenopyrite. In one instance, an electrum inclusion inherits the rhombic crystal shape of the host arsenopyrite (Fig. 9.12c). Electrum has a gold content of approximately 70-75 at. % and a single electrum grain has an iron content of ~5 at.%. An inclusion-rich, sponge-textured pyrite occurs as massive, interlocking aggregates up to several cm in size and post-dates all other phases, as evidenced by abundant inclusions of arsenopyrite, electrum, ankerite and quartz (Fig. 9.12d).

9.5.3.3 Black Dog deposit

Sulphides in the ore zone at the Black Dog deposit comprise arsenopyrite, pyrrhotite, pyrite, chalcopyrite and lesser Sb-bearing sulphides. These minerals exhibit a variety of textures, including disseminated sulphides, sulphides within and/or in the selvedge of quartz-carbonate veins and as massive sulphide veins up to 5 cm in thickness. Gold is associated with each of these textural styles of sulphide mineralisation. The proportion of sulphide minerals in mineralised rocks at Black Dog is generally elevated relative to other lode-gold deposits along the Mougooderra Shear Zone. Commonly, massive or densely disseminated sulphides, such as arsenopyrite, are cross cut by

subsequent quartz-carbonate sulphide veins (Fig. 9.13). The highest-grade portions of the ore zone are dominated by arsenopyrite, exhibit visible gold, and have been assayed in excess of 100 g/t Au.

Petrographic and BSE-SEM analysis has demonstrated that the ore zone at Black Dog contains four distinct stages of mineralisation, which are directly comparable to the four stages of sulphide mineralisation at the Silverstone deposit described in Section 9.5.3.1. The earliest sulphide phase (Stage 1) consists of trace element-enriched pyrite, which typically occurs as hexahedral crystals up to 800 µm in diameter (Fig. 9.14a) and is overprinted by all other sulphide phases (Fig. 9.14b). A majority of crystals contain 0.1-0.3 at. % of trace elements such as As, Ni and Sb and occasionally, pyrite contains minor (<10 µm) inclusions of chalcopyrite or chalcostibite ($CuSbS_2$).

Overprinting Stage 2 sulphide mineralisation consists of idiomorphic, rhomb-shaped arsenopyrite crystals that range in size between 20 and 600 µm (Fig. 9.14c). Arsenopyrite occurs within quartz veins and as densely disseminated masses (Fig. 9.13). Locally, stage 2 arsenopyrite hosted by albite forms radiating masses of crystals on various scales up to ~1.5 mm in diameter, several of which appear to nucleate on ~100 µm magnetite crystals (Fig. 9.14d). Arsenopyrite is genetically associated with electrum, which occurs as < 5–50 µm grains present either as inclusions, at crystal margins or as free gold within the silicate groundmass proximal to arsenopyrite (Fig. 9.14c). Several electrum inclusions occur as idiomorphic rhombic crystals in crystallographic continuity with the host arsenopyrite (Fig. 9.14c). The gold content of stage 2 electrum varies between 90 and 97 at.%.

Subsequent Stage 3 sulphide mineralisation comprises pyrrhotite, chalcopyrite and ullmannite (Fig. 9.14e), in addition to various other Sb-bearing sulphides such as berthierite, stibnite, jamesonite and gudmundite (FeSbS). Stage 3 sulphides are commonly associated with calcite, and occur in veins that

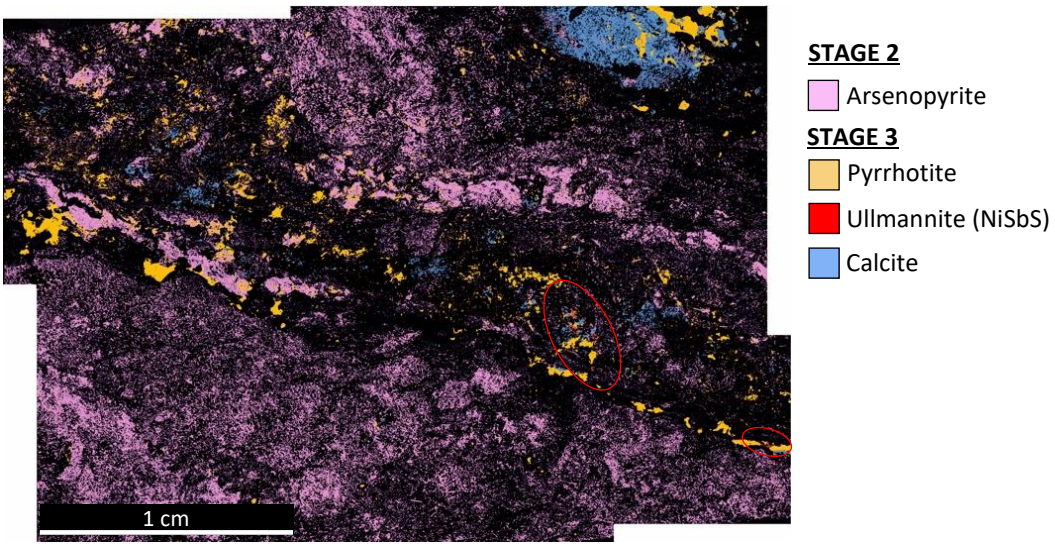

Figure 9.13: Mineral map of a high-grade ore sample (BD07M1) from the Black Dog deposit, showing massive stage 2 arsenopyrite dissected by a quartz vein comprising stage 3 pyrrhotite, minor ullmannite (circled) and calcite. Black represents quartz and other silicate gangue phases.

STAGE 1: As/Ni-bearing pyrite

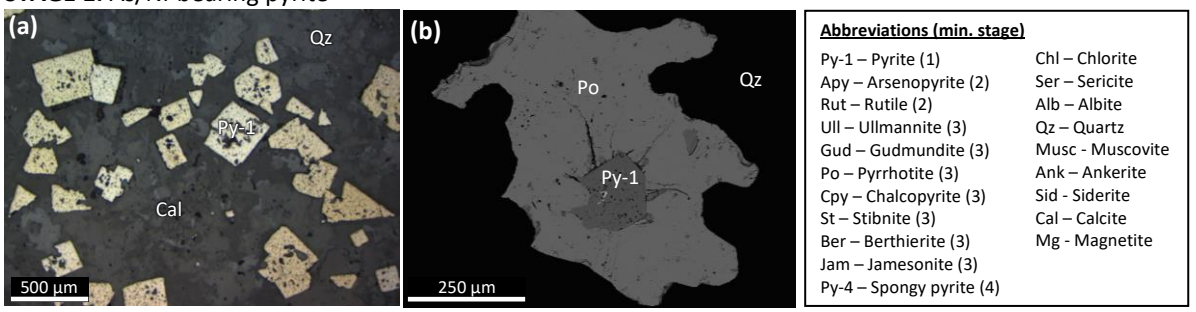

STAGE 2: Arsenopyrite-electrum

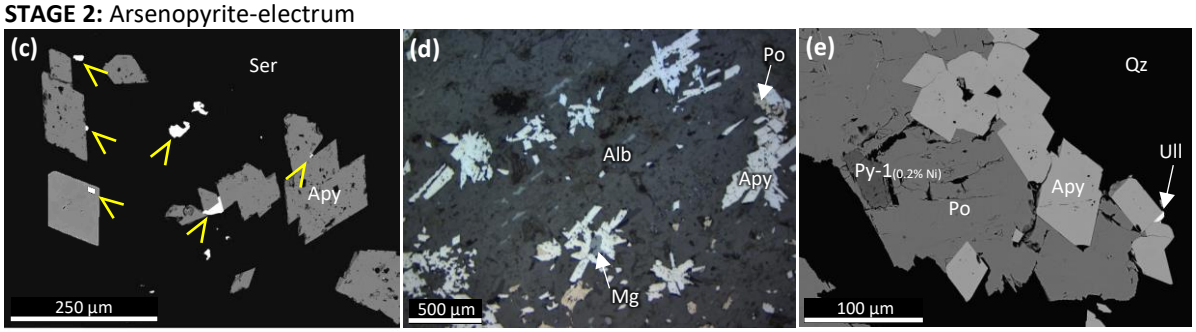

STAGE 3: Pyrrhotite-chalcopyrite-Sb sulphides-electrum-aurostibite

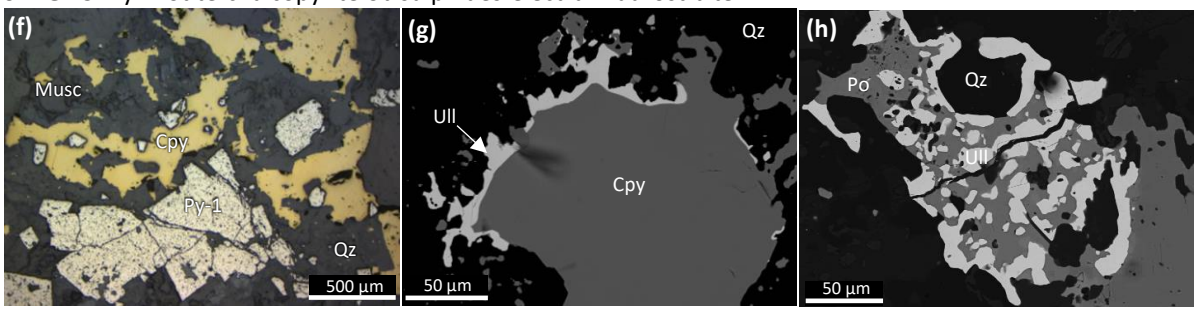

STAGE 4: Sponge-textured pyrite

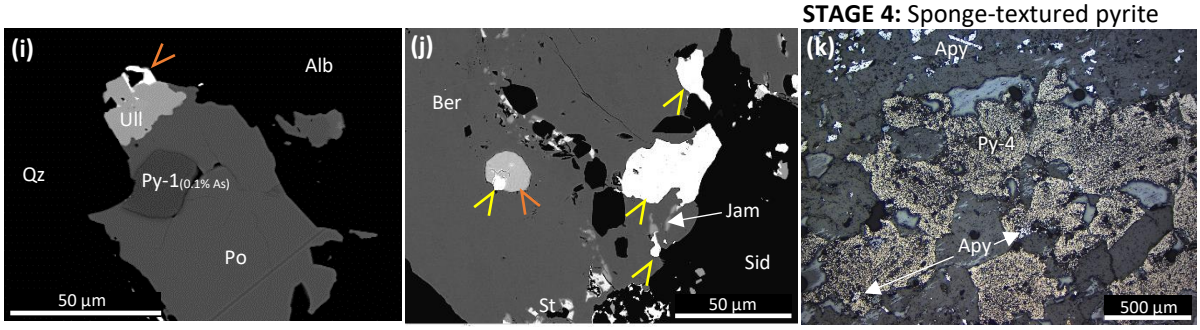

Figure 9.14: Back-scattered electron and reflected light images of lode-gold mineralised samples from the Black Dog deposit. Yellow arrows indicate electrum (AuAg) and orange arrows indicate aurostibite ($AuSb_2$). **(a)** Idiomorphic cubic and hexahedral crystals of stage 1 pyrite in a groundmass of quartz and calcite (sample BD002); **(b)** Quartz containing a hexahedral stage 1 pyrite enclosed in stage 3 pyrrhotite (sample BD07M3); **(c)** Idiomorphic rhombic crystals of stage 2 arsenopyrite containing electrum inclusions, at crystal margins and in the proximal silicate groundmass. Note the rhomb-shaped electrum inclusion in the bottom left (sample BD07M2); **(d)** Star-shaped radial aggregates of arsenopyrite in albite, overprinted by minor stage 3 pyrrhotite (sample BD07M2); **(e)** Stage 1 pyrite and stage 2 arsenopyrite, enclosed in stage 3 pyrrhotite, with minor ullmannite at the sulphide margin (sample BD07M2); **(f)** Stage 1 pyrite inclusions within chalcopyrite (sample BD002); **(g)** Stage 3 assemblage comprising ullmannite mantling an etched chalcopyrite crystal, in contact with quartz (sample BD003); **(h)** Stage 3 ullmannite present as inclusions and at the margins of pyrrhotite, in contact with quartz (sample BD003); **(i)** Aurostibite ($AuSb_2$) at the margin of ullmannite, in turn at the margin of pyrrhotite. Note the stage 1 pyrite inclusion within pyrrhotite (sample BD001); **(j)** Berthierite crystal containing inclusions of electrum and aurostibite, in addition to jamesonite, stibnite and galena. Note that one inclusion comprises both aurostibite and minor electrum (sample BD07M3); **(k)** Irregular, allotriomorphic aggregate of pyrite crystals, akin to sponge-textured pyrite at Silverstone, containing inclusions of quartz and arsenopyrite (sample BD07M2).

dissect massive to disseminated stage 2 arsenopyrite (Fig. 9.13). Pyrrhotite and chalcopyrite are by far the most prevalent stage 3 minerals, and locally form massive sulphide lenses up to 5 cm in thickness (Fig. 9.14f). Ullmannite and gudmundite are less abundant and occur as <300 µm mantling crystals around the margins of other sulphides (Figs. 9.14g, 9.14i), and as irregular arrays of rounded inclusions within pyrrhotite (Fig. 9.14h), as observed at Silverstone. Berthierite is locally present as allotriomorphic crystals up to 500 µm in size (Fig. 9.14j). Stage 3 sulphides are associated with two gold-bearing alloys, electrum and aurostibite. Electrum is most prevalent, typically occurring as 10-80 µm grains either as inclusions or most frequently as free gold surrounding stage 3 sulphides, with an approximate gold content of 92-94 at. % (Fig. 9.14j). In contrast, aurostibite is less common and occurs as irregular grains up to 25 µm in size, either as inclusions within or in direct contact with the Sb-bearing minerals ullmannite or berthierite (Fig. 9.14i). In one instance, an inclusion within berthierite consists of both electrum and aurostibite (Fig. 9.14j). The gold content of stage 3 aurostibite is consistently ~60 at. % and usually contains up to 4 at. % Ni.

The most recent stage of sulphide mineralisation at Black Dog (Stage 4) is represented by an inclusion-rich pyrite phase, which is texturally comparable to sponge-textured pyrite described at Silverstone. This phase of pyrite occurs as allotriomorphic crystals up to several mm in size and abundant inclusions consist of silicate groundmass minerals and all the sulphide minerals described above (Fig. 9.14k). Notably, this stage of sulphide mineralisation is less abundant at Black Dog than in mineralised rocks at Silverstone.

9.5.3.4 Winddine Well deposit

Lode-gold mineralisation at the Winddine Well deposit occurs in two distinct settings, associated with contrasting textures and sulphide assemblages. The most prevalent style consists of a pyrrhotite-infilled hydrothermal breccia, which is directly associated with high grade intersections of up to ~35 g/t in the drillholes studied (Fig. 9.15a). Hydrothermal breccia occurs as three to four steeply dipping units ranging in thickness between 1 cm and 50 cm, situated within and parallel to the sheared and deformed intervals of BIF described in Section 4.5.6.2. The margins of pyrrhotite breccias are locally folded, sheared and show evidence of ductile deformation. These deformed horizons are invariably separated by relatively undeformed, laminar BIF with negligible gold content.

The hydrothermal breccias at Winddine Well comprise a pyrrhotite matrix, accounting for approximately 25-70% of the breccias, and are typically matrix-supported, but locally grade into a clast-supported, crackle breccia (Fig. 9.16a). The dominant clast lithology is vein quartz, in addition to calcite and less common chalcopyrite and pyrite clasts (Fig. 9.16a). Quartz and calcite clasts are poorly

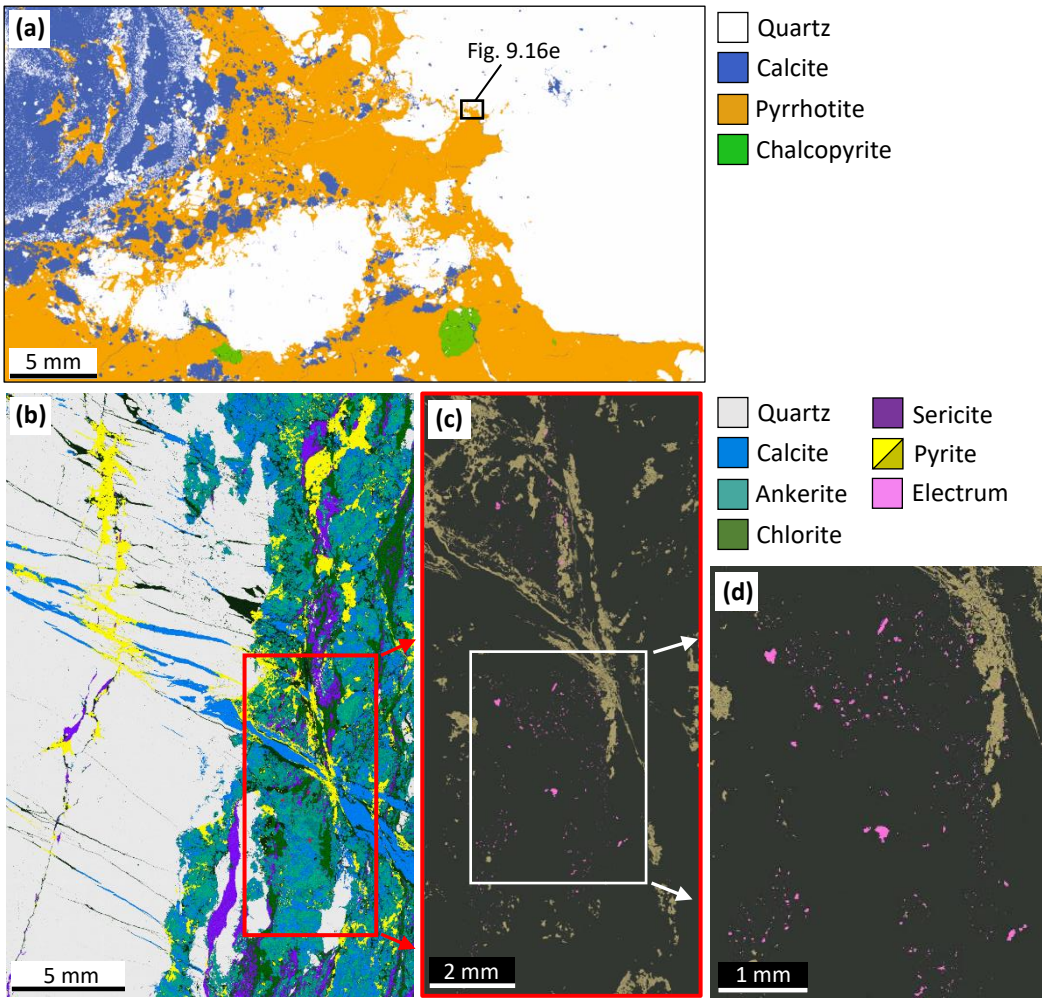

Figure 9.15: Mineral maps of high-grade ore samples from the Winddine Well deposit, displaying the two contrasting settings of lode-gold mineralization. (a) and (b) are element maps coloured to denote minerals, whereas (c) is a colourised BSE map, showing sulphides and gold only. **(a)** Mineral map of a typical mineralised hydrothermal breccia, comprising clasts of calcite, quartz and chalcopyrite in a pyrrhotite matrix (sample WW38M2); **(b)** Mineral map of pyrite and electrum in the altered selvedge of a thick, steeply dipping quartz vein (as shown in Fig. 9.16f), dissected by a late calcite-pyrite vein. The outline of the field of view in (c) is shown in red (sample WW31M2); **(c)** Colourised BSE map of part of the mineral map in (c) displaying the distribution of electrum (pink) and pyrite (yellow) in the vein selvedge. Note the lack of electrum within the dissecting calcite-pyrite vein; **(d)** Magnified view of electrum in (c).

sorted, display considerable variation in size between < 50 µm and > 5 cm, and are variably sub-angular to sub-rounded. Both quartz and calcite clasts are typically microcrystalline, indicating recrystallisation. Quartz clasts commonly have irregular, embayed margins that are invaded by the pyrrhotite matrix (Fig. 9.16b). Chalcopyrite clasts are typically sub-rounded and range in size between 1 and 5 mm (Fig. 9.16c), whereas rare pyrite clasts are well-rounded and are 0.5-1 cm in diameter (Fig. 9.16a). Pyrrhotite also encloses minor < 100 µm inclusions of sphalerite and 10-50 µm inclusions of monazite (Fig. 9.16d). The pyrrhotite breccia contains abundant visible gold, which is invariably located at the contact between quartz clasts and the pyrrhotite matrix (Fig. 9.16b). Gold occurs as electrum, present as allotriomorphic grains in the range 10-500 µm in size with an approximate gold content of ~70-74 at. % (Fig. 9.16e).

The second style of gold mineralisation at Winddine Well consists of an assemblage of pyrite and visible gold that occurs in the sericite-chlorite-ankerite-calcite altered selvedge of thick (>5 cm) steeply dipping, layer-parallel quartz veins (Fig. 9.15b; Fig. 9.16f). Less common gently-dipping quartz veins also are mineralised with pyrite and locally, minor arsenopyrite and are associated with the same alteration mineralogy as the steeply-dipping veins. In these zones, irregular, interlocking 1-50 mm masses of pyrite occur within 3-4 cm of quartz veins (Fig. 9.15c), although pyrite also occurs within some veins. Gold occurs as 10 µm to 1.5 mm allotriomorphic grains of electrum with a gold content of 78-82 at. %, consistently higher than electrum hosted by pyrrhotite breccias (Fig. 9.16g).

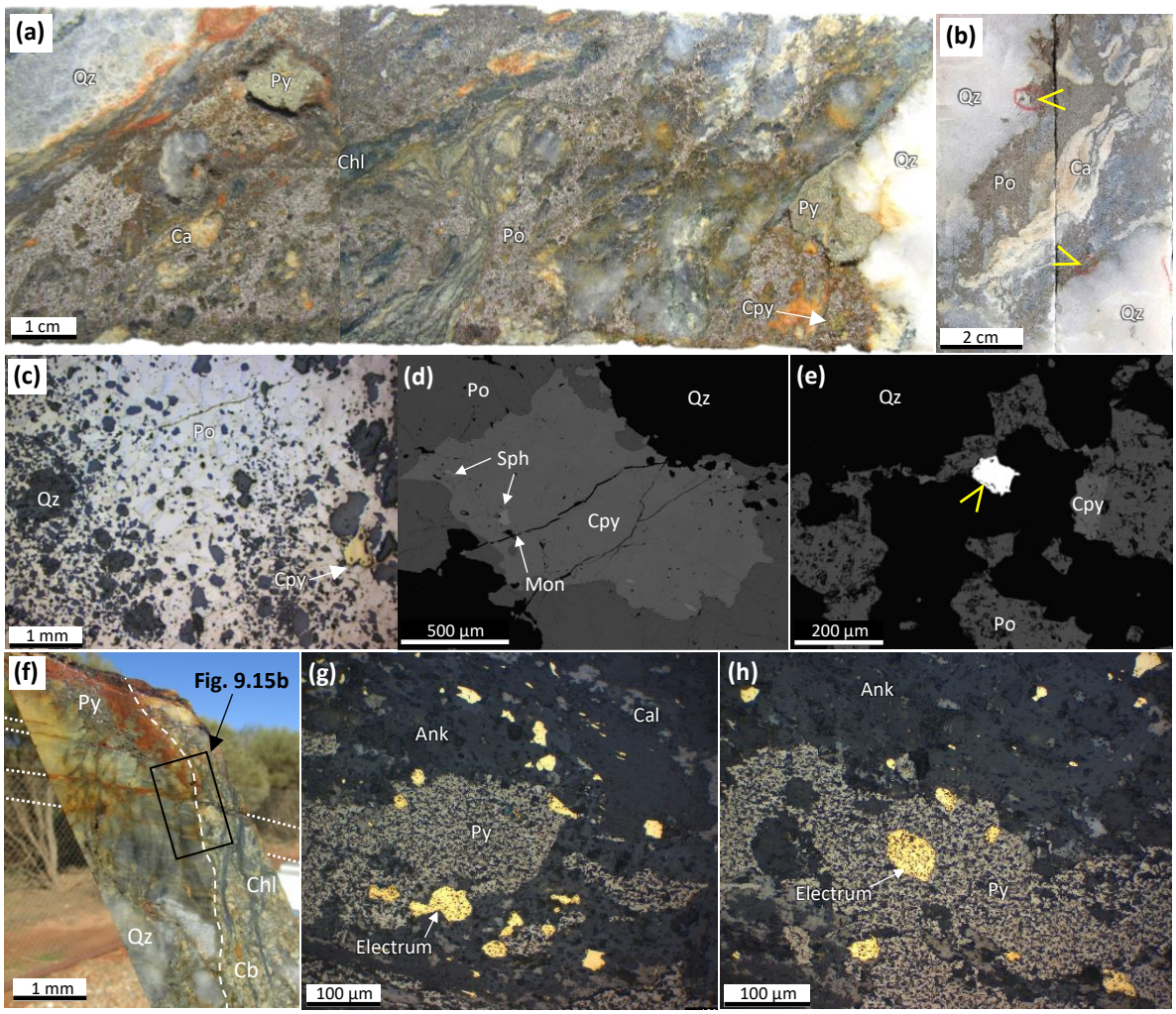

Figure 9.16: Photographs, reflected light photomicrographs and BSE images of high-grade ore samples from the Winddine Well deposit. Yellow arrows indicate electrum. **(a)** Drillcore comprising a ~12 cm interval of pyrrhotite hydrothermal breccia, containing clasts of quartz, calcite, chlorite, pyrite and chalcopyrite (WWDD031, 250.5 m); **(b)** Drillcore comprising a narrow ~3 cm interval of pyrrhotite hydrothermal breccia, with visible gold located quartz-pyrrhotite contacts (WWDD038; 299.5 m); **(c)** Reflected light photomicrograph of pyrrhotite breccia (sample WW38M2); **(d)** BSE image of a chalcopyrite inclusion hosted in a pyrrhotite breccia, associated with minor sphalerite and monazite, adjacent to clasts of quartz (sample WW38M2); **(e)** Electrum grain in pyrrhotite breccia, present at the contact between pyrrhotite and quartz, proximal to chalcopyrite (sample WW38M2); **(f)** Oriented drillcore sample of a steeply dipping quartz vein, with a gold-mineralised altered selvedge. The margin of the quartz vein is denoted by a dashed line, and late, cross-cutting carbonate veins are denoted by dotted lines. The position of sample WW31M2, as represented in Fig. 9.15b, is shown. The drillcore is oriented as it was in situ, facing south; **(g)** Reflected light photomicrograph of abundant electrum at the margins of pyrite and in proximal ankerite and calcite (sample WW31M2); **(h)** Reflected light photomicrograph of electrum inclusions within pyrite, surrounded by ankerite (sample WW31M2).

Approximately 20% of electrum grains occur as inclusions within pyrite (Fig. 9.16h), whereas the rest occur as clusters of free gold in the altered groundmass proximal to pyrite, most commonly hosted by ankerite and calcite (Fig. 9.15d). Locally, the steeply-dipping quartz veins and pyrite-electrum assemblage are dissected by subsequent, shallowly-dipping calcite-pyrite veins (Section 9.5.2.4). These veins are frequently colloform banded and display textures consistent with hydraulic fracturing. Crucially, these late calcite veins dissect the high-grade intersections comprising abundant electrum (Figs. 9.15b-d) and are not associated with gold-bearing phases.

9.5.4 Stable isotope analysis

Stable isotope analysis has been undertaken on sulphides ($\delta^{34}S$) and quartz ($\delta^{18}O$) from lode-gold deposits in the YSGB. A summary of stable isotope data is provided in Tables 9.4 and 9.5 and results are detailed in full in **Appendix E11** ($\delta^{34}S$ data) and **Appendix E12** ($\delta^{18}O$ data).

9.5.4.1 $\delta^{34}S$ sulphide analysis

Sulphur isotope analysis has been undertaken on sulphides from variably mineralised samples acquired from eight lode-gold deposits in the YSGB (Fig. 9.17; Table 9.4), including pyrite (n=23), pyrrhotite (n=8), arsenopyrite (n=6), chalcopyrite (n=2) and Sb-sulphides (stibnite/berthierite; n=4). Sampling for sulphur isotope analysis has been focussed primarily on the Silverstone deposit (n=21), in addition to the Winddine Well (n=9), Black Dog (n=5) and Bugeye (n=3) deposits. Two sulphide samples have been analysed from the Trench deposit, in addition to single samples from the M1, Riley and Ocean deposits.

The sulphide $\delta^{34}S_{V\text{-}CDT}$ (herein $\delta^{34}S$) data occupy the range -2.9 to +4.6 ‰ and the average $\delta^{34}S$ value irrespective of the analysed sulphide mineral is +1.7 ‰. Collectively, $\delta^{34}S$ values for pyrite vary considerably between -2.9 and +3.1 ‰ (Fig. 9.17a). Analyses of pyrrhotite and Sb sulphides yield values that are essentially indistinguishable from pyrite, with $\delta^{34}S$ values ranging between -1.4 and +3.6 ‰ and +0.9 to +3.5 ‰, respectively. Arsenopyrite $\delta^{34}S$ values are noticeably heavier than other sulphides at +1.8 to +4.6 ‰, whereas chalcopyrite is isotopically lighter at -0.8 to -1.7 ‰ (Fig. 9.17a). The values and distribution of $\delta^{34}S$ data are similar at Silverstone, Bugeye and Black Dog, as well as single samples from Riley and Ocean (Fig. 9.17b). In contrast, limited sampling from Winddine Well, Trench and M1 demonstrate more variable and isotopically lighter $\delta^{34}S$ values (Fig 9.17b).

Pyrite and arsenopyrite that are spatially associated with lode-gold mineralisation display $\delta^{34}S$ values that are distinct compared to equivalent sulphides sampled distal to the ore zone. Pyrite within the ore zone at Silverstone, Bugeye, Black Dog and M1 (stage 4 pyrite; Section 9.5.3.1) yield $\delta^{34}S$ values of +0.6 to +2.8 ‰, in contrast to unmineralized pyrite that typically have lighter $\delta^{34}S$ of < +1 ‰, but

$\delta^{34}S$ sulphide data (n=43)					
Deposit	***n***	**Min.**	**Max.**	**Average**	**σ**
SILVERSTONE	***n=21***				
Pyrite	9	+0.7	+2.6	+2.2	0.6
Pyrite - outside ore zone	4	-1.0	+2.7	+0.9	1.9
Arsenopyrite	2	+3.7	+4.3	+4.0	0.4
Pyrrhotite	1	+1.3	+1.3		
Sb-sulphides	4	+0.9	+3.5	+2.1	1.3
Chalcopyrite	1	-0.8	-0.8		
BUGEYE	***n=3***				
Pyrite - outside ore zone	1	+3.1	+3.1		
Pyrite	1	+2.9	+2.9		
Arsenopyrite	1	+4.6	+4.6		
BLACK DOG	***n=5***				
Pyrite	1	+0.6	+0.6		
Pyrrhotite	2	+1.3	+3.6	+2.5	1.6
Arsenopyrite	2	+3.5	+4.3	+3.9	0.6
WINDDINE WELL	***n=9***				
Pyrite - outside ore zone	3	-1.5	+2.8	+0.8	2.1
Pyrrhotite	4	+0.6	+3.1	+1.4	1.1
Arsenopyrite – outside ore zone	1	+1.8	+1.8		
Chalcopyrite	1	-1.7	-1.7		
M1	***n=1***				
Pyrrhotite	1	-1.4	-1.4		
OCEAN	***n=1***				
Pyrite	1	+2.6	+2.6		
RILEY	***n=1***				
Pyrite	1	+1.5	+1.5		
TRENCH	***n=2***				
Pyrite	2	-2.9	+1.3	-0.8	2.9
BACKGROUND VALUES	***n=4***				
Pyrite – FW shales, Silverstone	1	+2.7	+2.7		
Pyrite – Mt Mulgine Granite	2	-0.2	+0.1	-0.1	0.2
Pyrite - Golden Grove VMS	1	+1.5	+1.5		

Table 9.4: Table summarising sulphur isotope compositions for sulphides from lode-gold deposits in the YSGB, presented in per-mil $\delta^{34}S_{V\text{-}CDT}$. All sulphides are from gold mineralised ore zones, unless denoted as unmineralised. Background values from three sources are also given. The reproducibility of data is better than ± 0.7 ‰ (1σ). Full results can be found in Appendix E11.

occasionally range up to +2.9 ‰ (Fig. 9.17c). Gold-bearing arsenopyrite crystals at Silverstone, Black Dog and Bugeye (stage 2 arsenopyrite; Section 9.5.6.1) have $\delta^{34}S$ values of +3.5 to +4.7 ‰ (Fig. 9.17). These values are markedly heavier than an unmineralised (<0.1 g/t Au) arsenopyrite sample from Winddine Well, which yielded a $\delta^{34}S$ value of +1.8 ‰, and are also consistently heavier than coexisting stage 4 pyrite in mineralised samples (Fig. 9.17c-f). At Silverstone, a single mineralised pyrrhotite sample (stage 3 pyrrhotite; Section 9.5.6.1) has a $\delta^{34}S$ value of +1.3 ‰, within the range of coeval Sb-sulphides (+0.9 to +3.5 ‰; Fig. 9.17c). In an attempt to characterise background $\delta^{34}S$ values, four pyrite samples have been taken from various sulphide-bearing rocks in the YSGB that are considered to pre-date lode-gold mineralisation. Two pyrite samples from the W-Mo mineralised Mt Mulgine Granite yielded $\delta^{34}S$ values between -0.2 ‰ and +0.1 ‰, whereas a pyrite sample from a footwall sulphidic shale unit distal to mineralisation at Silverstone yielded a $\delta^{34}S$ value of +2.7 ‰ (Table 9.4). A pyrite

sample from the Scuddles VMS deposit at Golden Grove yielded a $\delta^{34}S$ value of +1.5 ‰ (Table 9.4).

9.5.4.2 $\delta^{18}O$ quartz analysis

Oxygen isotope analysis has been undertaken on quartz from variably mineralised samples acquired from five lode-gold deposits in the YSGB (Fig. 9.18; Table 9.5). Most samples analysed are from the Silverstone deposit (n=30), with additional quartz samples from the Winddine Well (n=9), Black Dog (n=4), Bugeye (n=2), M1 (n=2) and Ocean (n=1) deposits. The quartz $\delta^{18}O_{V\text{-}SMOW}$ (herein $\delta^{18}O$) data occupy the range +8.9 to +16.0 ‰ and the average $\delta^{18}O$ value across all deposits is +12.9 ‰. Whilst the data from the Silverstone deposit define the range of $\delta^{18}O$ values, several distinct populations are identified that correlate to individual deposits (Fig. 9.18a). For example, $\delta^{18}O$ values for quartz from

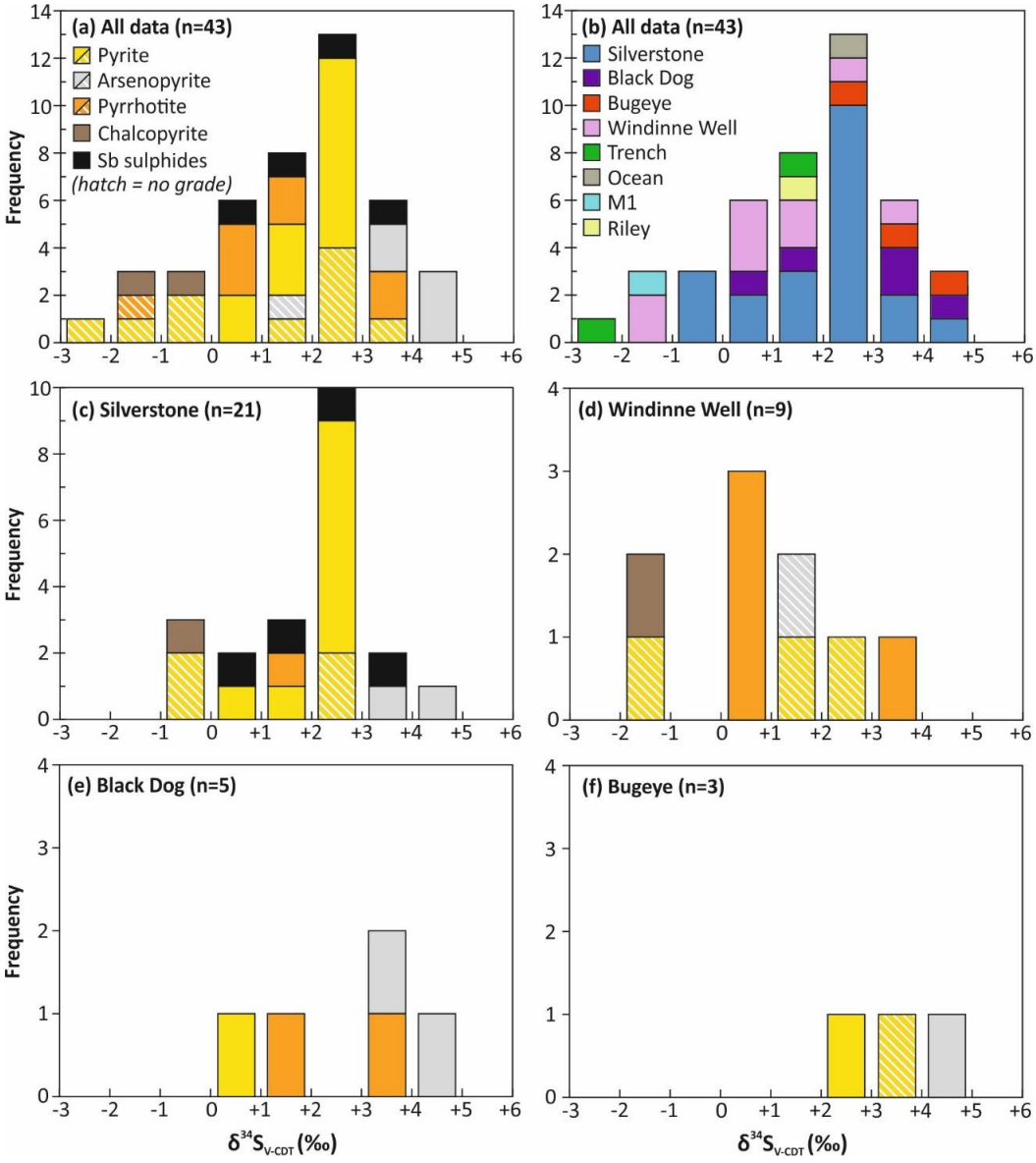

Figure 9.17: Histograms summarising sulphur isotope ($\delta^{34}S_{V\text{-}CDT}$) compositions of sulphides (n=43) from lode-gold deposits in the central YSGB, subdivided by sulphide type (a), deposit (b) and by sulphide type for individual deposits (c-f). Solid bars represent sulphides in gold mineralised samples, whereas crosshatching represents sulphides not spatially associated with gold mineralisation. Note the variable y axis for individual deposits in c-f.

$\delta^{18}O$ quartz data (n=48)					
Deposit	***n***	**Min.**	**Max.**	**Average**	**σ**
SILVERSTONE	***n=30***				
Main ore zone	11	+13.9	+15.0	+14.5	0.3
Hanging-wall ore zone	3	+10.7	+11.6	+11.1	0.5
Unmineralised	16	+8.9	+16.0	+12.7	2.3
BUGEYE	***n=2***				
Ore zone	1	+14.7	+14.7		
Unmineralised	1	+14.3	+14.3		
BLACK DOG	***n=4***				
Ore zone	4	+9.0	+12.6	+10.9	1.7
WINDDINE WELL	***n=9***				
Ore zone	7	+11.8	+12.7	+12.3	0.3
Unmineralised	2	+13.5	+13.6	+13.6	0.0
M1	***n=2***				
Unmineralised	2	+13.3	+13.3	+13.3	0.0
OCEAN	***n=1***				
Unmineralised	1	+12.4	+12.4		

Table 9.5: Table summarising oxygen isotope compositions for quartz from lode-gold deposits in the YSGB, subdivided by quartz in the gold-mineralised ore zones and quartz is surrounding, unmineralized rocks. The data is presented in per-mil $\delta^{18}O_{V\text{-}SMOW}$. The reproducibility of data is better than ± 0.3 ‰ (1σ). Full results can be found in Appendix E12.

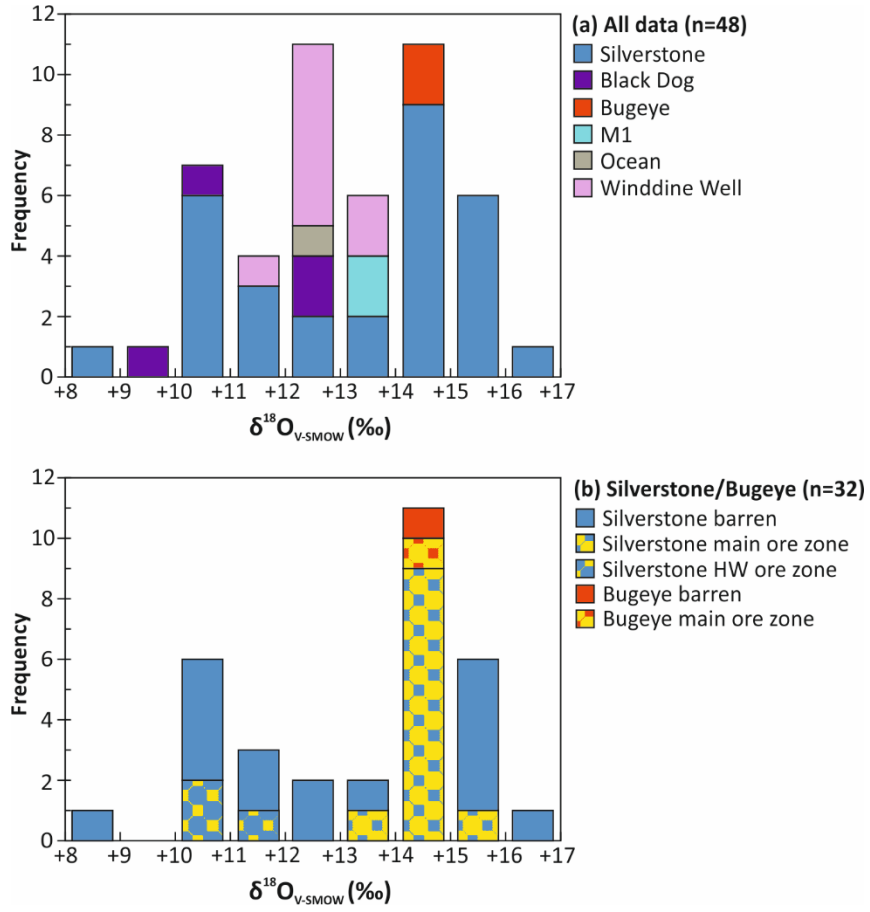

Figure 9.18: Histograms summarising oxygen isotope ($\delta^{18}O_{V\text{-}SMOW}$) compositions of quartz from lode-gold deposits in the central YSGB. **(a)** Oxygen isotope ($\delta^{18}O_{V\text{-}SMOW}$) compositions of quartz (n=48), subdivided by deposit; **(b)** Oxygen isotope ($\delta^{18}O_{V\text{-}SMOW}$) compositions of quartz (n=32) from the Silverstone and Bugeye deposits. Data are subdivided by quartz in the main ore zone, hanging wall (HW) ore zone and quartz not spatially associated with gold mineralisation.

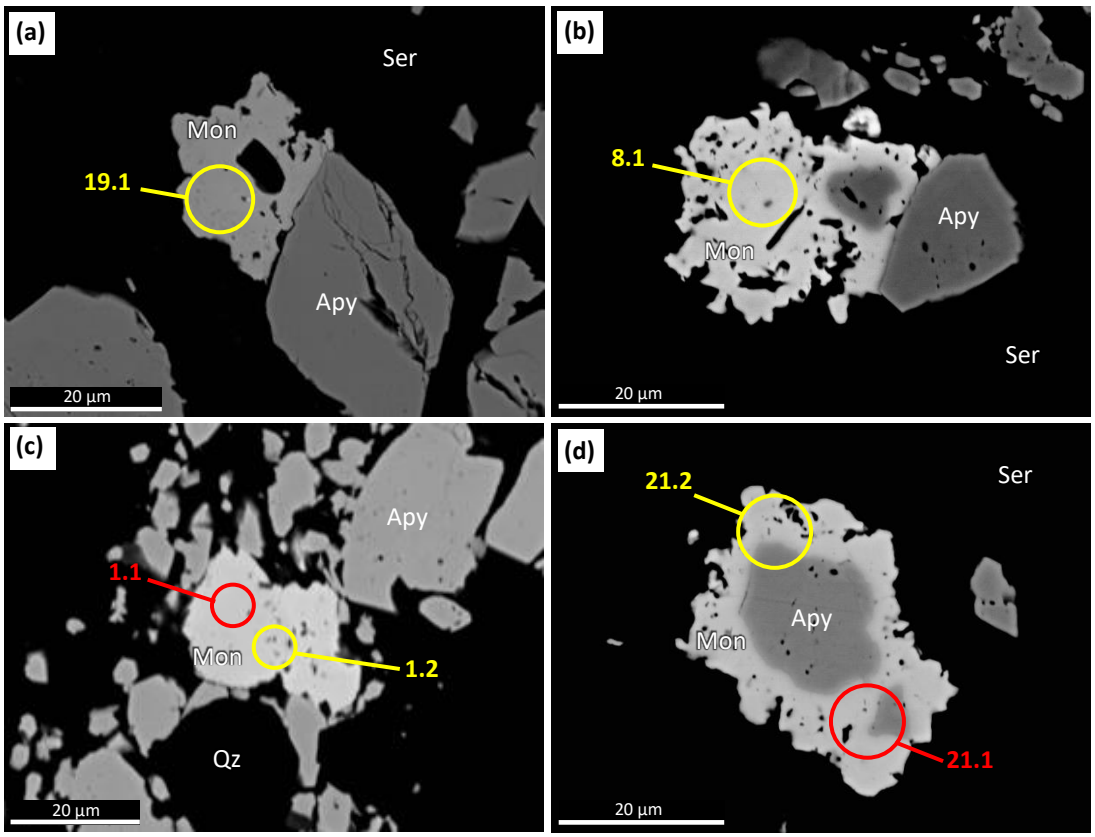

Figure 9.19: Back-scattered electron (BSE) images of representative monazite crystals targeted during LA-ICPMS isotopic analysis, displaying their association with gold-bearing arsenopyrite. Spots for analyses used in age calculations are shown in yellow and rejected analyses returning older ages are shown in red. Spot labels correspond to spot numbers (see Appendix E13). **(a)** Monazite (Mon) crystal in contact with arsenopyrite (Apy) and surrounded by sericite (Ser) (sample SS19M3); **(b)** Monazite attached to, and containing an inclusion of, arsenopyrite (sample SS19M3); **(c)** Monazite surrounded by arsenopyrite within a quartz (Qz) groundmass. Note that the two spots analysed in this crystal returned one main group age, and one significantly older age, despite the lack of zonation or a discernible inherited core (sample SS19M4); **(d)** Monazite with an irregular, embayed margin surrounding multiple arsenopyrite crystals. As in (c), one spot within this crystal returns a main group age, and the other, which includes significant arsenopyrite, returns a significantly older age (sample SS19M3).

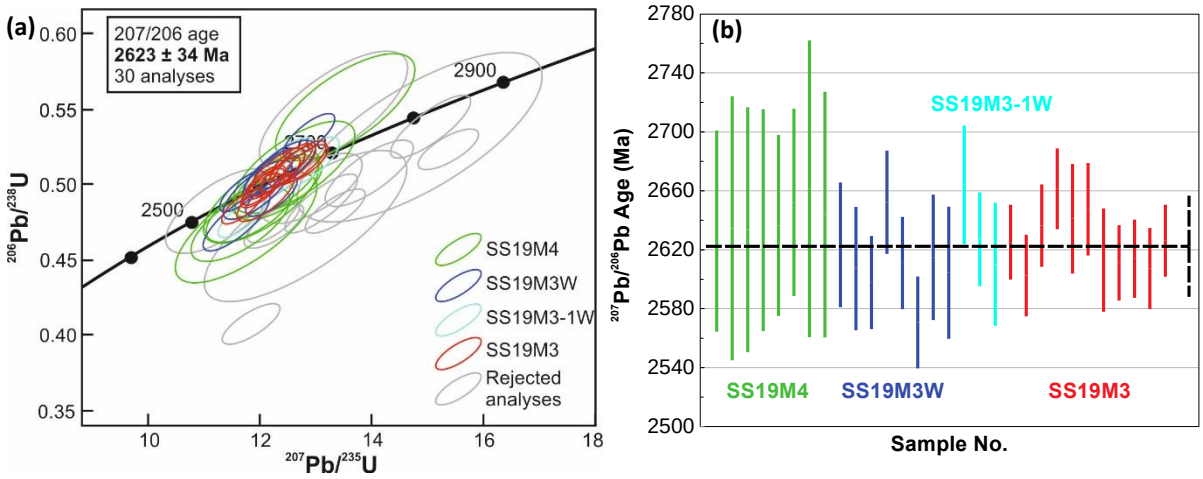

Figure 9.20: Summary of LA-ICP-MS U-Pb monazite geochronological data. **(a)** Concordia plot for U-Pb monazite analyses at the Silverstone deposit. Rejected analyses are denoted in grey and analyses used in age calculations are coloured according to the respective sample number. Error ellipses are shown at 2σ level; **(b)** Age plot summarising the age ranges corresponding to individual monazite U-Pb analyses used in age calculations, arranged and symbolized by sample. The calculated age and uncertainty for monazites at Silverstone is represented by the black dashed line.

the Black Dog deposit cluster between +9.0 and +12.6 ‰, whereas $\delta^{18}O$ values of quartz from the Winddine Well deposit cluster between +11.8 and +13.6 ‰. The limited number of samples from M1 and Bugeye most closely match the $\delta^{18}O$ distribution of quartz at Silverstone (Fig. 9.18a).

At Silverstone, the $\delta^{18}O$ values of quartz in gold-mineralised samples form two distinct clusters (Fig. 9.18b). Quartz samples from gold-bearing veins in the narrow mineralised hangingwall ore zone (n=3) have markedly lighter $\delta^{18}O$ values of +10.7 to +11.6 ‰. In contrast, the $\delta^{18}O$ values of all quartz samples within the main mineralised ore zone at Silverstone (n=12) invariably occur within the range +13.9 to +15.0 ‰ and are remarkably consistent over a strike length in excess of 1 km and to depths of at least 300 m. Notably, none of the analysed quartz veins from outside the ore zone have $\delta^{18}O$ values in this range. The single mineralised quartz sample from the main ore zone at Bugeye has a $\delta^{18}O$ value of +14.7 ‰, within the range of the main ore zone at Silverstone. The other sample from Bugeye, an unmineralized quartz vein in the hanging-wall, has a $\delta^{18}O$ value of +14.3 ‰, representing the only unmineralized quartz sample analysed in the belt that occurs in the range +13.9 to +15.0 ‰.

9.5.5 U-Pb monazite geochronology

In-situ LA-ICP-MS U-Pb monazite dating has been undertaken on four drillcore samples from a ~60 cm-interval of a high-grade (~20 g/t) quartz-carbonate-sericite-albite altered mafic unit, representing mineralised hanging-wall units at the southern end of the Silverstone deposit. This unit contains disseminated stage 2 arsenopyrite, zoned quartz-carbonate veins comprising stage 2 arsenopyrite and stage 3 pyrrhotite, chalcopyrite and ullmannite, in addition to overprinting stage 4 sponge-textured pyrite. Mineral maps illustrating the distribution of sulphides in two of the geochronological samples, SS19M3 and SS19M4, are displayed in Figure 9.9.

Automated scanning of polished sections identified approximately 830 monazite crystals across the four samples, the largest of which were imaged using a BSE detector. Monazite crystals display similar characteristics and are directly associated with lode-gold mineralisation, specifically stage 2 gold-bearing arsenopyrite, as demonstrated by the ore paragenesis described in Section 9.5.3.1. Monazite invariably occurs as allotriomorphic crystals with irregular, embayed margins, which range in size between ~5 and 50 µm, most frequently 10-30 µm (Fig. 9.19). Most monazite crystals contain micron-scale inclusions of surrounding silicate phases, such as sericite, quartz and albite. Monazite displays a close spatial association with arsenopyrite, occurring either as mantling crystals, as inclusions or in the silicate groundmass proximal to arsenopyrite (Fig. 9.19). Multiple monazite crystals also contain inclusions of arsenopyrite (Fig. 9.19b, d).

A total of 43 U-Pb analyses of 38 monazite grains form two groups (Fig. 9.20). The analyses are displayed on a concordia diagram in Figure 9.20a, representative monazite crystals and spot locations

are shown in Figure 9.19 and a table detailing results for all analyses is provided in **Appendix E13**. The main group consists of 30 concordant analyses of 29 grains within the four samples, which give a $^{207}Pb/^{206}Pb$ age of 2623 ± 34 Ma (2s), and a $^{206}Pb/^{238}U$ age of 2621 ± 66 Ma (2s) (Fig. 9.20). This group of analyses is interpreted as the age of crystallisation of hydrothermal monazite crystals in the mineralised samples, thus by association, the age of gold-bearing arsenopyrite at the Silverstone deposit. For these age assessments, a weighted mean of included points (from four samples) has been taken, and then the weighted mean uncertainty has been propagated by 2% (2s), to give the final uncertainty. Considering the Archaean age of these samples and the fact that the $^{207}Pb/^{206}Pb$ and $^{206}Pb/^{238}U$ mean ages are nearly identical, the more precise $^{207}Pb/^{206}Pb$ age of 2623 ± 34 Ma (2s) is quoted in this study (Fig. 9.20).

A second group consists of 13 moderately to strongly discordant analyses, most of which have calculated $^{207}Pb/^{206}Pb$ ages of >2800 Ma, including a single grain with a $^{207}Pb/^{206}Pb$ age of ~ 2929 Ma (Fig. 9.20). Notably, some of the calculated ages for this group are significantly older than the interpreted age of the volcanic host rocks at Silverstone (ca. 2820 Ma; Chapter 8). Many of these analyses correspond to spots located at the margins of monazite crystals that are in contact with arsenopyrite, or spots that encompass the contact between monazite and adjacent arsenopyrite. In several instances in which two spots were analysed in the same monazite grain, one analysed spot yielded a concordant main group age, whereas the other spot returned a highly discordant, older age (Fig. 9.19c-d). In these cases, monazite crystals do not exhibit growth zonation or a discernible core. Instead, the older, discordant analyses correspond to spots that breached the margin of the monazite crystal and incorporated arsenopyrite into the analysis (Fig. 9.19c-d). Thus, it is interpreted that the older, discordant analyses reflect the addition of common Pb from arsenopyrite into spot analyses, affecting the U-Pb count values and resulting in older, geologically unfeasible ages. These analyses are therefore rejected and consequently, are excluded from age calculations.

9.5.6 Fluid inclusion analysis

A preliminary reconnaissance study of fluid inclusions in gold mineralised quartz samples from the Silverstone deposit has been undertaken as part of this project. In all tested samples, fluid inclusions in quartz are invariably small, typically ranging in diameter between <1 µm and ~4 µm and rarely exceeding 5 µm in diameter. These inclusions are generally smaller than the typical size of fluid inclusions in hydrothermal quartz (~5-20 µm; Van den Kerkhof & Hein, 2001). Unfortunately, as fluid inclusions in quartz from the Silverstone deposit are of insufficient size for reliable analysis using conventional techniques and the analytical equipment available, further investigation of fluid inclusions has not been undertaken.

9.6 Discussion

9.6.1 Controls on lode-gold mineralisation

Lode-gold deposits in the YSGB display a ubiquitous structural control on a deposit to district-scale, which represents a characterising feature of orogenic lode-gold mineralisation (Groves et al., 2018; Blenkinsop et al., 2020a). A significant majority of discovered deposits in the YSGB are situated along a ~40 km length of the MSZ, effectively a first-order structure in the belt, whereas few deposits are located along less extensive structures, such as the WWSZ (Fig. 9.1). The MSZ and WWSZ are broadly parallel structures that display comparable kinematic and structural features, with the principal difference between the two being the steeper dip of the WWSZ (~85° E), relative to the MSZ (~65° W) (Fig. 9.21). This implies that these structures were active during the same episode of crustal shortening and according to their surface orientations, are likely connected at depth, thus the WWSZ is interpreted as a second-order structure in the hangingwall of the MSZ (Fig. 9.21). In contrast to the MSZ, there is a striking lack of lode-gold mineralisation along the parallel, NNW-striking first-order CSZ (Fig. 9.1).

World-class lode-gold deposits in Neoarchaean terranes are typically located in second-order structures proximal to major, crustal-scale faults and shear zones, which represent crucial, first-order fluid pathways (Groves et al., 2018). This is not the case in the YSGB, where most lode-gold deposits are located directly along the first-order MSZ, rather than associated second or third-order structures.

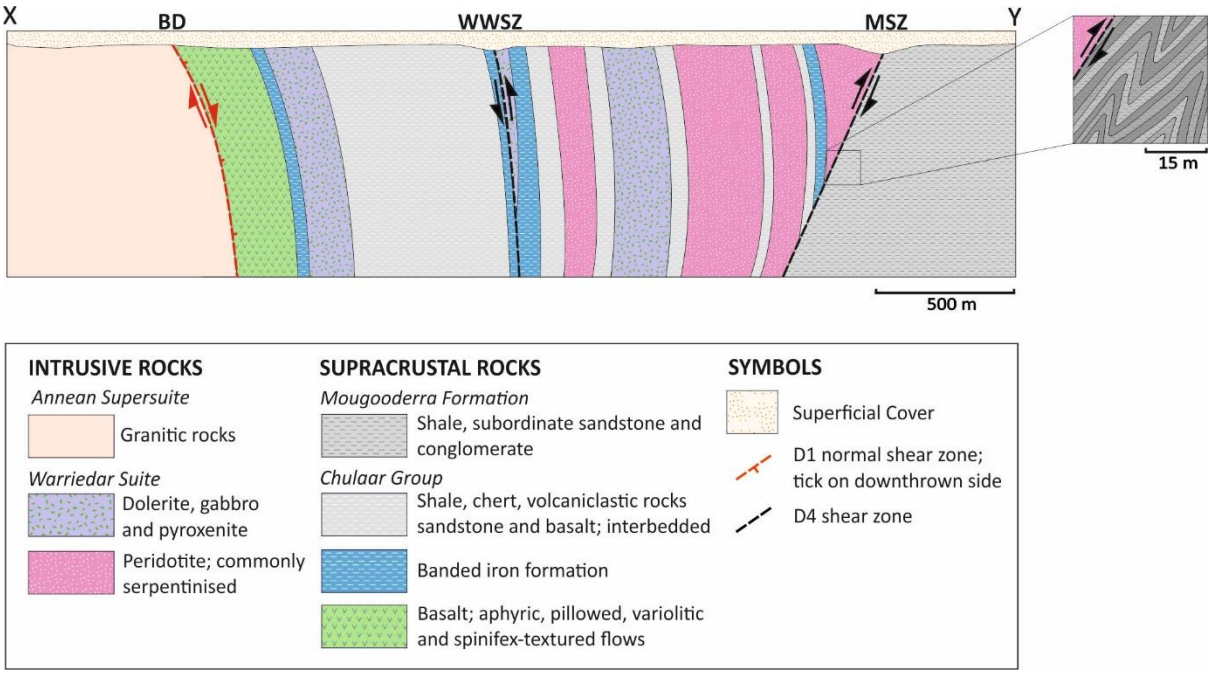

Figure 9.21: Schematic cross section X-Y along the fenceline indicated on Figure 4.11, showing the relative sub-surface geometries of two gold-mineralised D_4 shear zones in the central YSGB. BD = Badja Decollement; WWSZ = Winddine Well Shear Zone; MSZ = Mougooderra Shear Zone.

However, the MSZ does not form part of an extensive, first-order crustal to lithospheric-scale fault system that commonly represent tectonic sutures and are associated with significant lode-gold mineralisation, as is the case in most mineralised parts of the eastern Yilgarn Craton (Groves et al., 2016). To assess the distribution of lode-gold deposits in the YSGB and in particular, mineralisation along the well endowed MSZ, several potential controlling parameters need to be evaluated.

Large lode-gold deposits are commonly situated along or adjacent to curvilinear portions of first-order structures that jog into an anomalous orientation, typically at an angle of 10-25° to the main structural trend (Weinberg et al., 2004). Such jogs and bends are spaced at ostensibly regular intervals of tens of kilometres in some areas. For example, a series of jogs demonstrating angular discordance of 11-27° are associated with major gold deposits along the extremely well-endowed Boulder-Lefroy fault system in the Eastern Goldfields and are spaced at intervals of 30-35 km (Hodkiewicz et al., 2005). Notably, the jog with the greatest angular discordance relative to the dominant trend of this structure (~27°) is host to the giant Kalgoorlie Goldfield (Groves et al., 2018). There are two clear instances of jogs that are spatially associated with lode-gold deposits along the MSZ. The ~400 koz Silverstone deposit defines a curvilinear geometry and is situated along a conspicuous jog in the MSZ, which displays an angular discordance of ~24° from the principal trend (the 344° strike in the south is broadly parallel with the regional trend of the MSZ and progressively changes to ~008° in the north; Fig. 9.1). Similarly, the Bugeye deposit is situated at a jog along the MSZ, defined by a change in strike from 340° to the south, to 000° to the north (Fig. 9.1). However, no other deposits are located along clearly defined jogs in map view at the current structural level of the MSZ.

An alternative structural parameter suggested to influence in the distribution of gold in some areas are oblique cross faults at a high angle (~60-70°) to major first and second-order structures. Cross faults are frequently present adjacent to district-scale jogs, where they accommodate the deformation of more rigid lithological units and can allow the focussing of hydrothermal fluids and gold deposition (Groves et al., 2018). On aeromagnetic imagery, there is no clear evidence of subtle geophysical lineaments at a high angle to the MSZ or WWSZ (Fig. 4.2). Antiformal fold hinges are considered to be a robust parameter for the location of lode-gold deposits, as they represent sites of higher permeability induced by brittle-ductile failure (Robert et al., 2007). However, this is not the case in the YSGB, with the possible exception of the minor Riley deposit, representing the only mined deposit east of the CSZ located close to the hinge of an ~8 km-scale antiformal structure (Fig. 9.1).

In addition to structural controls, there are a number of potential lithological controls on the distribution of lode-gold deposits. The emplacement of lode-gold mineralisation is favoured in host rocks that are both competent and chemically reactive with auriferous fluids, to provide enhanced

fluid flow and facilitate reactions that precipitate gold (Groves et al., 2003). In general, competent, Fe-rich units, such as BIF, dolerite and tholeiitic basalt, are preferentially mineralised in Archaean terranes (Weinberg et al., 2004; Groves et al., 2018). Lode-gold deposits along the MSZ and WWSZ are predominantly hosted by Fe-rich host rocks, suggesting a strong lithological control on mineralisation. For example, the Silverstone and M1 deposits are hosted by Fe-rich ultramafic rocks (peridotite/serpentinite), the Black Dog deposit is hosted by magnetite-bearing granophyric dolerite and the Bugeye and Winddine Well deposits are hosted by BIFs (Section 9.2). Accordingly, most discovered deposits along the MSZ are located where Fe-rich hangingwall units intersect the shear zone at an oblique angle (Fig. 9.1). Unfortunately, it is not possible to fully test the lithological influence on the distribution of deposits along the MSZ, as the geology between mined deposits is poorly constrained, owing to an absence of exposure and extensive transported cover.

In summary, there is currently not enough data and geological mapping to accurately constrain the relative controls on the distribution of lode-gold deposits in the YSGB. Whereas it is evident that all significant deposits are located in Fe-rich host rocks, most of which are also competent units, the location of two deposits (Silverstone and Bugeye) coincides with district-scale jogs along the MSZ.

9.6.2 Style of lode-gold mineralisation

On a deposit-scale, the geometry and kinematics of host structures, and the orientation and characteristics of veining, is comparable at the Silverstone, Bugeye and M1 deposits along the MSZ, and the Winddine Well deposit along the WWSZ. Kinematic indicators consistently demonstrate ubiquitous reverse shear along the MSZ (Section 4.5.6.1) and the WWSZ (Section 4.5.6.2), such that these structures represent steeply-dipping, mis-oriented reverse faults according to Anderson theory (Anderson, 1905). Textural evidence indicates that some sulphide and related gold mineralisation at these deposits has been deformed by brittle-ductile deformation along the MSZ and WWSZ, consistent with mineralisation occurring in the late stages of reverse displacement.

The main stage of quartz-carbonate±sulphide±gold veining at the Silverstone deposit comprises two principal orientations, which display ambiguous cross-cutting relations (Section 9.5.2.1). Foliation-parallel veins commonly have a laminated, shear texture, whereas sub-horizontal veins typically have extensional internal fabrics. Crucially, some veins indicate evidence in favour of fluid overpressure. These characteristics are replicated by limited structural analysis at the Bugeye and M1 deposits, indicating a consistency in structural style along a ~20 km length of the MSZ, and at the Winddine Well deposit along the more steeply-dipping WWSZ.

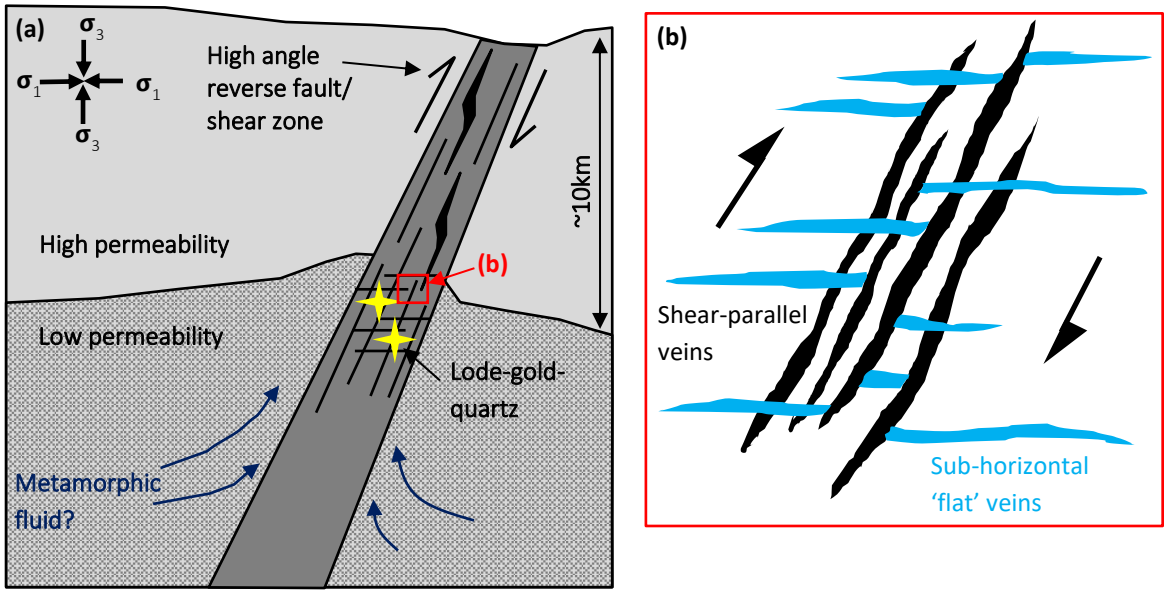

Figure 9.22: (a) Schematic cross section (not to scale) displaying the inferred tectonic setting of the fault-valve style of mesothermal lode-gold mineralisation. The shear zone is drawn at a similar angle to the MSZ; **(b)** Magnified view of the vein system within the reverse shear zone according to the fault-valve model, comprising shear-parallel veins and sub-horizontal 'flat' extensional veins, showing ambiguous cross cutting relations. Redrawn after Sibson et al. (1988).

Structural and kinematic analysis at the lode-gold deposits studied along the MSZ and WWSZ is compatible with fault-valve behaviour, suggested to operate in fault systems that are unfavourably oriented for frictional reactivation (Robert & Brown, 1986; Sibson et al., 1988; Sibson 1990; Cox, 2020). According to fault-valve theory, high pore fluid pressures at depths at or near the brittle-ductile transition are required to facilitate cyclic, reverse failure along a steeply-dipping, unfavourably oriented structure (Fig. 9.22a; Sibson et al., 1988; Sibson 1990).

Many orogenic lode-gold deposits in Archaean cratons have developed along high-angle reverse faults as a consequence of elevated fluid flux associated with fault-valve behaviour (e.g., Sibson et al., 1988; Faleiros et al., 2014). A characterising feature of vein arrays at many of these deposits is the co-occurrence of steeply-dipping 'fault' or 'shear' veins parallel to the shear fabric, and 'flat' subhorizontal extensional veins, as identified at the Sigma mine, Abitibi greenstone belt, Canada, where fault-valve behaviour was first distinguished (Robert & Brown, 1986; Sibson et al., 1988) (Fig. 9.22b). These vein sets invariably exhibit mutual cross-cutting relations (Sibson et al., 1988), as reflected by type I and type II main-stage quartz-carbonate veins at the Silverstone deposit (Fig. 9.22b). Sub-horizontal, extensional veins are interpreted to have formed in dilational zones during pre-failure stages, when fluid pressures below the seismogenic zone were at or exceeded lithostatic pressures (Sibson et al., 1988; Cox, 2020). For severely mis-oriented pre-existing structures (>53° to σ_1), such as the MSZ and WWSZ, shear failure could have been facilitated when fluid pressures exceeded the least principal compressive stress (σ_3) (Sibson, 1990). At this point, failure and associated seismogenic

activity resulted in increased fracture permeability, a rapid reduction in fluid pressures, and the ensuing emplacement of shear-parallel veins (Sibson et al., 1988). In turn, hydrothermal precipitation caused reduced permeability, in essence sealing the 'fault-valve' hydrothermal system and allowing fluid pressures to increase once again (Sibson, 1990). Deformed and boudinaged type IV veins at Silverstone can be suitably explained by progressive deformation of early-formed veins by repeated, cyclic episodes of fault-valve activity. The consistent geometry of vein arrays at lode-gold deposits along the MSZ and WWSZ reflects fault-valve behaviour in response to sub-horizontal east-west shortening and sub-vertical extension, in agreement with kinematic indicators along D_4 shear zones (Section 4.5.6). Fault-valve related lode gold mineralisation along steeply-dipping reverse structures has previously been suggested for several deposits in the Yilgarn Craton (e.g., Kenworthy & Hagemann, 2007).

Cyclic fluctuations in fluid pressure associated with fault-valve behaviour are considered to play an active role in promoting mineral precipitation from hydrothermal fluids (Sibson et al, 1988; Sibson, 1990; Faleiros et al., 2014). Fluid inclusion analyses at the Sigma mine have identified significant fluid pressure fluctuations of the order of 200-350 MPa (Robert et al., 1995), interpreted as variations between near-lithostatic to near-hydrostatic conditions. Repeated depressurisation of hydrothermal fluids is suggested to be the primary controlling factor on the precipitation of gold and associated gangue minerals during fault-valve events (e.g., Gaboury & Daigneault, 2000). Accordingly, phase separation is a commonly invoked mechanism for gold precipitation in fault-valve systems (Sibson et al., 1988; Section 9.6.3.5).

The pyrrhotite-infilled hydrothermal and crackle breccias that host gold mineralisation at the Winddine Well deposit are compatible with hydraulic fracturing and fluid overpressure (Chauvet, 2019). This, along with the almost perpendicular arrangement of shear-parallel veins and sub-horizontal veins, supports fluid overpressure and fault-valve activity at the Winddine Well deposit, as well as the MSZ. Hydrothermal vein breccias with similar features to those at Winddine Well are found in epithermal environments (Rhys et al., 2020). Additionally, the late-stage sub-horizontal colloform-textured calcite veins that dissect all other structures at Winddine Well are typical of extensional epithermal veins emplaced at shallower-crustal levels and are indicative of boiling and cooling of hydrothermal fluids (Rhys et al., 2020). Internal textures in some colloform-textured veins are defined by manganese-bearing calcite (Fig. 9.8), which is commonly paragenetically late in epithermal settings and indicates waning hydrothermal activity (Rhys et al., 2020). Crucially, late colloform-textured veins at Winddine Well are not auriferous, and are interpreted as overprinting features signifying subsequent, shallower hydrothermal activity along the WWSZ.

9.6.3 Lode-gold paragenesis

9.6.3.1 Paragenetic consistency along the MSZ

The mineral paragenesis associated with gold mineralisation at the Silverstone and Black Dog deposits, situated ~30 km apart along the MSZ, is remarkably consistent. At these deposits, the ore-forming process is subdivided into four paragenetic stages, based on mineral assemblages and cross-cutting relationships (Fig. 9.23) and the first three stages are directly associated with gold mineralisation. The minerals and textures associated with each stage are identical at both deposits, including several rare Sb-bearing sulphide minerals. Preliminary analysis of two samples from the Bugeye deposit indicates the presence of stage 2 and 4 assemblages. Notably, the Winddine Well deposit on the adjacent WWSZ does not exhibit part of the four-stage paragenesis observed along the MSZ. The paragenesis of lode-gold mineralisation along the MSZ is summarised in Figure 9.23 and described below.

Stage 1 mineralisation consists of pyrite commonly enriched in detectable concentrations of As, Co and Ni, containing inclusions of chalcopyrite and electrum. The stage 1 assemblage is more volumetrically abundant at Black Dog compared to Silverstone, where it occurs in a discrete zone in the hangingwall and only locally within the main ore zone. Stage 2 arsenopyrite-electrum is observed at all three deposits along the MSZ and is invariably associated with the highest-grade intersections, consistent with stage 2 being the main auriferous stage within the paragenetic sequence (Fig. 9.23). Stage 2 electrum most frequently occurs as <10 µm inclusions within arsenopyrite, but larger grains

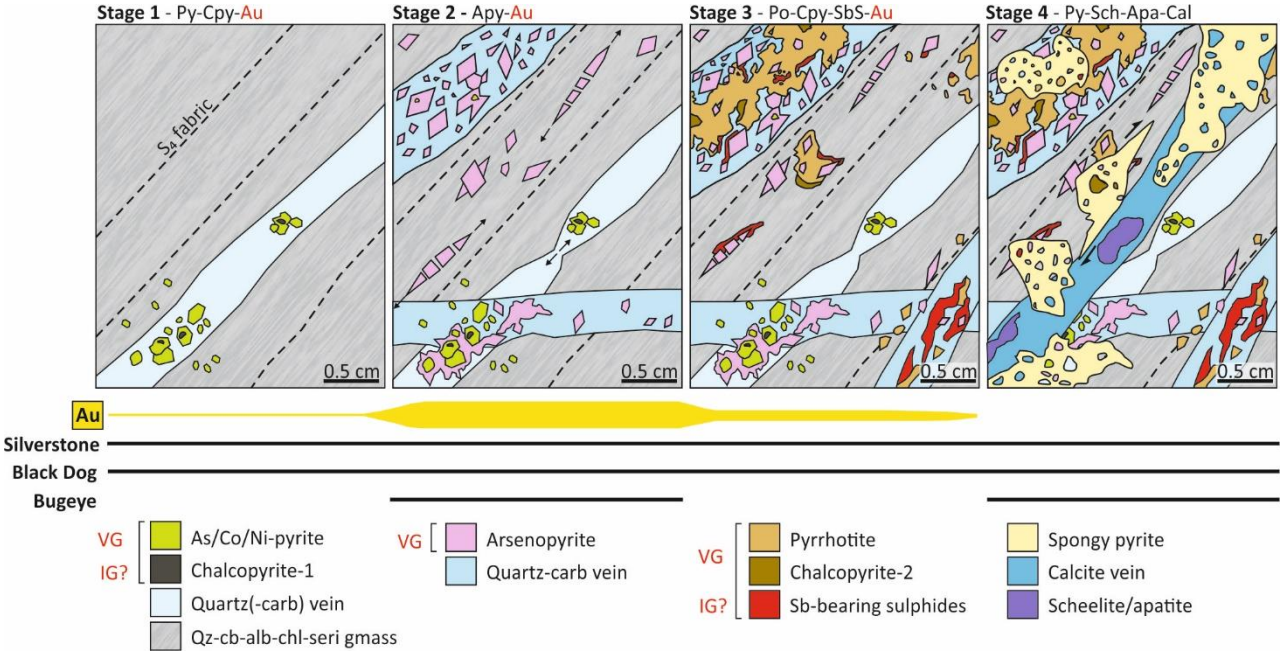

Figure 9.23: Schematic paragenetic sequence for lode-gold mineralisation along the Mougooderra Shear Zone. The paragenesis observed at each deposit is indicated: stages 1-4 are observed at Silverstone and Black Dog deposits, whereas stages 2 and 4 are observed at the Bugeye deposit. Images are oriented as cross sections, facing north with west to the left and east to the right. Abbreviations: VG = visible gold, IG? = inferred invisible gold. The mineralogy, textures and deformational features expressed by Figs. 9.9-9.14 are summarised here. *Arsenopyrite substituted for gersdorffite in ultramafic protoliths at the Silverstone deposit.

of free gold occur at crystal margins or in surrounding silicate phases. Stage 1 and stage 2 minerals reflect typical ore assemblages that characterise many orogenic lode-gold deposits, with arsenopyrite considered the most common sulphide mineral in metasedimentary host rocks and pyrite ± pyrrhotite typical in metaigneous host rocks (Groves et al., 1998).

The surprinting stage 3 assemblage at Silverstone and Black Dog comprises pyrrhotite-chalcopyrite-ullmannite-electrum-aurostibite, in addition to various locally abundant Sb-bearing sulphides, intimately associated with carbonate minerals. The mineralogy of the stage 3 assemblage at some parts of the Silverstone deposit includes more complex Sb-bearing sulphides including stibnite, berthierite, tetrahedrite, chalcostibite and jamesonite. The occurrence of several veins comprising margins of stage 2 arsenopyrite and cores of stage 3 sulphides (Fig. 9.9c) indicates a progression between stages 2-3, rather then two distinct, separate mineralising events. Whereas pyrrhotite is common in Archaean lode-gold deposits (Groves et al., 1998), the prevalence of Sb-sulphides associated with stage 3 mineralisation is a less common feature of some Archaean lode-gold deposits (e.g., Hagemann & Lüders, 2003; Section 9.6.3.2). Additionally, the paragenesis of lode-gold deposits along the MSZ displays a distinct lack of telluride minerals, which occur in the late mineralising stages at some Archaean deposits (e.g., Sung et al., 2007; 2009). A final, barren stage 4 assemblage comprising inclusion-rich 'sponge-textured' pyrite, locally associated with scheelite, apatite and calcite, overprints all other phases at Silverstone, Bugeye and Black Dog (Fig. 9.23) and represents the only non-auriferous paragenetic stage.

The minerals comprising paragenetic stages 2-4 at Silverstone locally demonstrate brittle-ductile deformation associated with displacement along the MSZ and where present, kinematic indicators consistently reflect a significant reverse shear component. For example, acicular stage 2 arsenopyrite crystals are commonly boudinaged and oriented parallel to the principal S_4 shear fabric (Fig. 9.9c), quartz veins containing stage 3 Sb-sulphide phases are locally highly deformed and sheared as σ-clasts (Fig. 9.9d), and stage 4 pyrite is deformed into the S_4 fabric and locally occurs as σ-clasts (Fig. 4.16d). This implies that mineralisation was emplaced during shearing or between episodes of shearing, likely as part of the same contractional episode. The paragenesis of mineralisation along the MSZ documents profound and significant mineralogical changes that are uniform over a strike length of ~30 km. This suggests that the Silverstone, Black Dog and Bugeye deposits were formed by equivalent hydrothermal fluids that evolved in the same manner, implying a connected fluid system over a strike length of at least ~30 km. Large Archaean lode-gold deposits commonly exhibit evidence of multiple separate episodes of mineralisation and associated fluid flow, that are separated by unconformities or discernible deformation events and are not part of a progressive mineralising event (Blenkinsop et

al., 2020b). However, an early mineralising event that is clearly distinct from the progressive paragenetic sequence at deposits along the MSZ has not been identified.

It has previously been suggested that the cluster of lode-gold deposits situated adjacent to the Mt Mulgine Granite, including the Black Dog deposit (Fig. 9.1), are spatially and genetically related to the W-Mo mineralised system at Mt Mulgine (e.g., Duuring et al., 2007). In turn, this has influenced the exploration strategies of successive mining companies operating in the area (Minjar, 2012). The paragenesis presented in this study contends this suggestion and demonstrates that mineralisation at Black Dog is unequivocally related to lode-gold mineralisation along the MSZ, and as such, overprints W-Mo mineralisation associated with the ca. 2750 Ma Mt Mulgine Granite. This also corroborates the aeromagnetic interpretations made in Section 4.5.2 and confirms the southern extent of the MSZ extends to the west margin of the Mt Mulgine Granite (Fig. 4.2). It is notable that the scattered nature of gold deposits in the Mt Mulgine area (Fig. 9.1) is not analogous to deposits further north along the MSZ, where mineralisation clearly delineates the broadly N-S strike of the shear zone. This could be attributed to the diapiric emplacement of the Mt Mulgine Granite (as part of D_1 diapirism; Section 4.3), which may have assisted in forming suitable structural traps that were later favourable hosts to gold mineralisation proximal to the MSZ in this area.

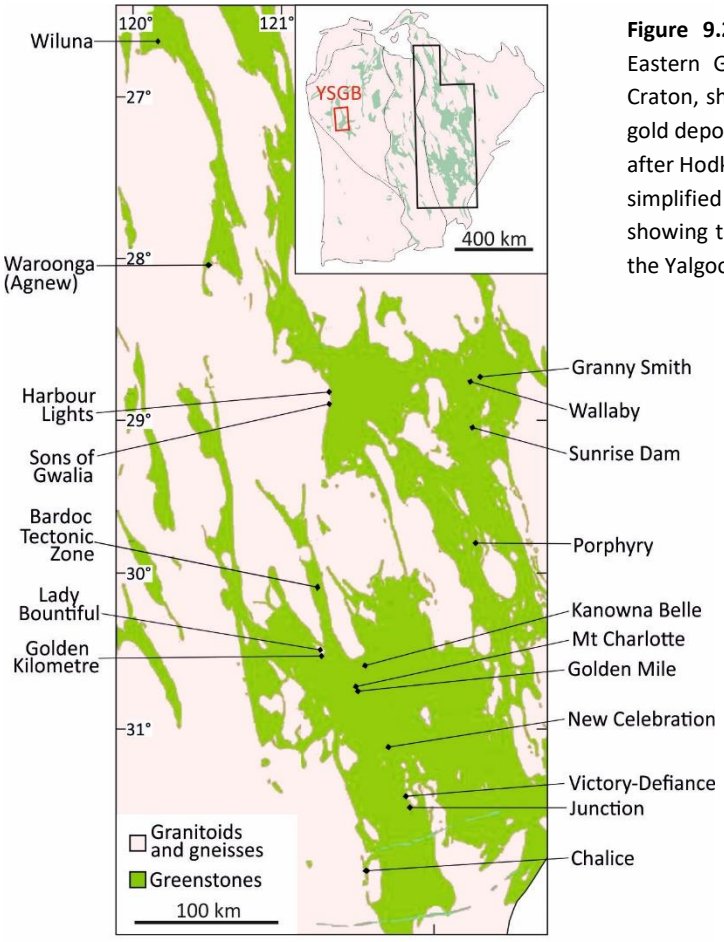

Figure 9.24: Simplified geological map of the Eastern Goldfields area of the eastern Yilgarn Craton, showing the locations of significant lode-gold deposits referred to in this chapter. Redrawn after Hodkiewicz et al. (2009). The inset image is a simplified geological map of the Yilgarn Craton, showing the map area relative to the location of the Yalgoo-Singleton greenstone-belt (YSGB).

9.6.3.2 Sb sulphide-gold association

The paragenetically-late stage 3 mineral assemblage at deposits along the MSZ include various Sb-bearing sulphide phases. The most common Sb-bearing phase at Black Dog is ullmannite, whereas significant amounts of stibnite, berthierite and other sulphosalt minerals also occur in some parts of the Silverstone deposit, and are directly associated with some high-grade gold intersections. Electrum and aurostibite have been identified with stage 3 Sb-sulphides in these intervals, providing further evidence of an Au-Sb metal association at this stage of mineralisation.

A metallogenic association between gold and antimony is common in hydrothermal ore deposits hosted in metasedimentary-dominated terranes (Williams-Jones & Normand, 1997; Hagemann & Lüders, 2003; An & Zhu, 2010; Kovalev et al., 2014). Many stibnite deposits contain recoverable quantities of gold and likewise, some hydrothermal gold deposits contain abundant antimony, typically in the form of stibnite (Krupp, 1988; Williams-Jones & Normand, 1997; Kovalev et al., 2014). In Archaean cratons, a spatial and genetic Au-Sb association has been described in some lode-gold deposits in the Superior Craton, Canada (e.g., Colvine et al., 1984), the well renowned antimony-gold deposits of the Murchison schist belt, South Africa (e.g., Jaguin et al., 2013), and the Wiluna deposit in the Eastern Goldfields Superterrane, Yilgarn Craton (Fig. 9.24; Hagemann & Lüders, 2003).

In Au-Sb deposits, stibnite and other Sb-sulphides typically occur in the later stages of complex paragenetic sequences (Williams-Jones & Normand, 1997). Decreasing temperature is considered to be a fundamental control on the precipitation of stibnite from a hydrothermal fluid (Krupp, 1988). At > 350°C, typical crustal fluids require concentrations of thousands of ppm Sb to saturate with stibnite, whereas at < 250°C, stibnite may precipitate from fluids containing as little as 1 ppm Sb (Williams-Jones & Normand, 1997; An & Zhu, 2010). Accordingly, the commonly late occurrence of stibnite and Sb sulphides is considered to reflect the progressive stages of cooling of an initially high temperature hydrothermal system (Krupp, 1988; Williams-Jones & Normand, 1997). At the Silverstone deposit, stage 3 Sb-sulphides occur late in the paragenetic sequence, commonly mantle earlier sulphides, and are only overprinted by late-stage barren pyrite, consistent with the late timing of Sb mineralisation at other lode-gold deposits (Hagemann & Lüders, 2003). Crucially, the co-occurrence of Sb-sulphides and gold, such as the stibnite-aurostibite-electrum assemblage identified at Silverstone, provides important constraints on the physiochemical conditions of the fluid from which these minerals were co-precipitated (Section 9.6.3.3). The rounded <100 μm antimony oxide phase situated proximal to stibnite and berthierite in auriferous samples from Silverstone is most likely senarmontite (Sb_2O_3), attributed to hypogene alteration of primary Sb sulphides, such as stibnite and berthierite, by oxidising hydrothermal fluids (Normand et al., 1996; Williams-Jones & Normand, 1997).

The paragenesis of gold mineralisation at the Wiluna deposit, eastern Yilgarn Craton (Fig. 9.24), is strikingly similar to that distinguished at the Silverstone deposit. Two stages of gold are distinguished at Wiluna, comprising stage 1 gold-pyrite-arsenopyrite disseminated in alteration haloes, succeeded by a stage 2 gold-stibnite assemblage in shear quartz veins and associated with extensive silicification (Hagemann & Lüders, 2003). Notably, the intimate stibnite-carbonate association and occurrence of aurostibite at Silverstone are not documented at Wiluna (Hagemann & Lüders, 2003).

9.6.3.3 Indications of invisible gold content

The ore petrography and mineral paragenesis presented in this study is focussed upon the assemblages associated with discrete, gold-bearing phases that are detectable during petrographic and SEM analysis. However, it is increasingly accepted that in some lode-gold deposits, significant amounts of so-called 'invisible' gold can occur in sulphides and can account for a variable proportion of the gold content of mineralised rocks. Invisible gold can occur as <1 µm, submicroscopic particles within sulphide minerals or in solid solution within the crystal lattice of sulphide minerals (Sung et al., 2009; Large & Maslennikov, 2020). Invisible gold is commonly referred to as refractory gold, owing to the increased difficulty and expense of separating and processing these ores compared to those comprising 'free gold' (Large & Maslennikov, 2020). An assessment of the prevalence of invisible gold therefore has crucial metallurgical implications and can affect the viability of an ore deposit.

Invisible gold in lode-gold deposits is most commonly hosted by pyrite and arsenopyrite, as is the case at the world class Sunrise Dam gold deposit in the eastern Yilgarn Craton (Fig. 9.24; Sung et al., 2007; 2009). LA-ICPMS analysis of sulphides at Sunrise Dam has recorded up to 3067 ppm Au in As-bearing pyrite and up to 5767 ppm Au in arsenopyrite (Sung et al., 2009). There are several indications of the presence of invisible gold within sulphide phases at the Silverstone deposit. Stage 1 pyrite crystals at Silverstone, which contain inclusions of native gold and chalcopyrite, typically contain detectable concentrations of the trace elements As, Co and Ni, which is considered to be indicative of invisible gold content (Large & Maslennikov, 2020). Furthermore, gold-bearing phases are markedly less common in stage 3 mineral assemblages at Silverstone and Black Dog compared to other auriferous stages, with analysis of some high-grade samples identifying no gold-bearing phases. This includes one vein sample (SS19V3) containing cm-scale crystals of jamesonite associated with a 1 m composite assay of 2.7 g/t Au, and a ~7 g/t Au intersection comprising abundant stage 3 Sb-sulphides, principally stibnite (sample SS18M3). It is therefore suggested that some Sb-bearing phases at Silverstone, such as stibnite and jamesonite, may contain invisible gold, which could account for the apparent lack of gold in these intervals. The occurrence of invisible gold in stibnite and associated Sb sulphides has previously been documented in Au-Sb deposits. For example, LA-ICPMS analysis of Sb-Au mineralised

quartz veins in the Schwarzwald, SW Germany, has demonstrated that stibnite contains up to 1800 ppm Au and coexisting berthierite contains up to 730 ppm Au (Epp et al., 2018).

In the few instances where aurostibite and electrum have been identified with stage 3 Sb sulphides, aurostibite typically occurs as intriguing, thin (1-10 µm) mantling feature at the outer contact of stibnite (Figs. 9.11g, h). This may resemble small-scale reaction fronts, in which elements have been released from the breakdown of some Sb sulphide minerals (i.e., stibnite) and are incorporated within other phases (Sung et al., 2007). In doing so, the presently inferred invisible gold within stibnite may have been released and subsequently precipitated in the intermediate area, either in the native form, or as aurostibite through reaction with Sb. This is supported by the presence of the oxide mineral senarmontite in contact with mantling aurostibite (Fig. 9.11g), which is considered to reflect alteration of stibnite by late, oxidising hydrothermal fluids (Normand et al., 1996). Alternatively, the rare, mantling aurostibite ± electrum features could reflect the partial recrystallisation of sulphides, which has long been recognised as a mechanism that can change the speciation of gold (i.e., the formation of visible gold from invisible gold) (Morey et al., 2008; Sung et al., 2009).

The presence and prevalence of invisible gold in stage 1 pyrite and stage 3 Sb sulphides indicated by the described features could be determined by systematic laser ablation analysis, which is beyond the scope of this study.

9.6.3.4 Temperature estimates

In the absence of fluid inclusion and geothermometry data, it is not possible to accurately constrain the temperatures associated with the emplacement of lode-gold mineralisation along the MSZ. A liberal maximum temperature constraint is provided by the peak metamorphic conditions for host rocks by calculated by Parmenter et al. (2020). Thermobarometry of Mougooderra Fm supracrustal rocks indicate peak metamorphic temperatures of 545-580 °C at 2.0-3.5 kbar (at ca. 2685 Ma; Section 9.6.5), whereas underlying Chulaar Group rocks sampled close to the Black Dog deposit in the south of the YSGB reached 610-650 °C at 4.0-7.2 kbar (Parmenter et al., 2020). These temperatures indicate upper greenschist to lower amphibolite peak metamorphic conditions, increasing to amphibolite facies in the south of the study area (Watkins & Hickman, 1990). The principal chlorite-epidote-albite-sericite-biotite-carbonate metamorphic alteration assemblage and lack of amphibolite and garnet associated with mineralisation along the MSZ is broadly indicative of greenschist metamorphic conditions (i.e., < 500°C).

Akin to the Silverstone deposit, the Sigma mine in the Abitibi greenstone belt, Canada, comprises fault-valve style lode-gold mineralisation and is hosted by greenschist facies metavolcanic and

metasedimentary rocks. Coupled fluid inclusion and oxygen isotope analyses of quartz veins and altered host rocks at the Sigma mine indicate temperatures in the range 270-450 °C for mineralisation and vein formation (Robert & Kelly, 1987). This provides a tentative indication of the potential temperatures associated with fault-valve behaviour at or near the brittle-ductile transition, as implied for deposits along the MSZ. Additionally, the occurrence of stibnite and associated Sb sulphides in the late stages of mineralisation at Silverstone is widely regarded as evidence of progressive cooling of an initially high temperature hydrothermal system (Krupp, 1988; Williams-Jones & Normand, 1997). Widespread precipitation of stibnite is facilitated by hydrothermal fluids that have cooled to <300 °C (Hagemann & Lüders, 2003).

9.6.3.5 Mechanisms for gold precipitation

Gold in orogenic-lode gold deposits is commonly closely associated with sulphide minerals and is widely understood to have been transported in low-salinity (0.4-0.65 wt. % NaCl), aqueous, carbonic fluids as reduced sulphur complexes at temperatures >200 °C, principally as a gold bisulphide complex ($Au(HS)_2^-$; Mikucki, 1998; Phillips & Evans, 2004; Garofalo et al., 2014). Potential depositional mechanisms for gold and associated sulphide mineralisation are varied and include changes in temperature, fluid pressure or fluid chemistry (i.e., fO_2, pH) as well as fluid-host rock reaction, boiling and fluid mixing (Groves et al., 2003, Garafalo et al., 2014; Gaboury, 2019).

Considering the robust structural evidence supporting fault-valve behaviour and related fluid pressure fluctuations at deposits along the MSZ and WWSZ, phase separation is a likely depositional mechanism for gold at these deposits. Phase separation is a commonly evoked mechanism for the precipitation of gold in lode-gold systems (e.g., Ridley and Diamond, 2000) and is likely initiated by lithostatic pressure fluctuations resulting from progressive deformation (e.g., fault-valve behaviour; Sibson et al., 1988; Cox, 2020). Because of decreasing fluid pressures through active fault movement, phase separation increases the acidity and oxygen fugacity of the fluid and decreases the reduced-sulphur content, affecting the solubility of contained gold (Wilkinson & Johnston, 1996). With sufficient separation of an Au-bearing fluid, gold mineralisation may occur. A significant majority of the Yilgarn lode-gold deposits that have undergone detailed fluid inclusion studies show evidence of phase separation of ore fluids (Hodkiewicz et al., 2009; Baker et al., 2010).

The conspicuous association between lode-gold deposits and iron-rich host rocks in the study area suggests that fluid-wall rock interaction may have also played an important role in the precipitation of gold. Wall rock interaction involves the reaction of an ore-bearing fluid with iron-rich rocks, causing the removal of H_2S, destabilising any gold complexes present and encouraging precipitation (Groves

& Mikucki, 1990). Pronounced localised interaction between fluids and host rocks at Silverstone is indicated by the variable mineralogy of some sulphide phases, such as the transition from stage 2 arsenopyrite in mafic host rocks in the south, to stage 2 gersdorffite in ultramafic host rocks in the north. In this instance, the Ni content in gersdorffite is likely sourced from surrounding ultramafic protoliths. Abundant fluid-host rock interaction at the BIF-hosted Winddine Well deposit, as previous suggested by Thomas (2003), is exemplified in Figure 9.8a, where arsenopyrite is nucleated at the vein contact with successive magnetite bands.

The co-precipitation of stibnite and gold at the Silverstone deposit (stage 3), as described in Section 9.6.3, gives further constraints on potential depositional processes at this stage. Two alternative mechanisms have been proposed for the contemporaneous precipitation of stibnite (and other Sb-bearing sulphides) and gold from a hydrothermal fluid. Williams-Jones & Normand (1997) suggest that a relatively alkaline and slightly reducing fluid would be favourable for the transport of both Au and Sb, which is broadly compatible with the abundant carbonate and pyrrhotite associated and in textural equilibrium with stage 3 Sb-sulphides at Silverstone. There is a distinct absence of minerals indicative of oxidising conditions, such as hematite and sulphates (Morey et al., 2007), at lode-gold deposits in the YSGB. Whereas stibnite precipitation is principally controlled by temperature decrease and reduction, and gold precipitation occurs due to various physiochemical changes, the coprecipitation of stibnite-gold is suggested to be restricted to acidification of the fluid, with or without reduction (Williams-Jones & Normand, 1997). The potential causes of such acidification include the precipitation of sulphide minerals such as pyrite and arsenopyrite, sulphidation reactions during fluid-wall rock interaction, phase separation triggered by pressure fluctuations and buffering of fluids by rocks rich in phyllosilicate minerals, such as shales (Normand et al., 1996; Williams-Jones & Normand, 1997). Notably, all four of these conditions are implied at Silverstone, considering the preceding arsenopyrite and pyrite, indications of fluid-wall rock interaction and phase separation, and the predominance of shales in the footwall of mineralisation.

Hagemann & Lüders (2003) contend that contemporaneous precipitation of stibnite-gold at the Wiluna deposit, eastern Yilgarn Craton, was fundamentally controlled by decreasing temperatures. According to their genetic model, fluid immiscibility triggered by cyclic pressure release during fault-zone movement, resulting in decompression and adiabatic cooling of ore fluids, reducing fluid temperatures, and causing stibnite precipitation (Hagemann & Lüders, 2003). In turn, stibnite precipitation reduced the H_2S concentration in the fluid, destabilising bisulphide complexes and triggering gold precipitation (Hagemann & Lüders, 2003). In a similar manner, the precipitation of ullmannite following stibnite and gold at the Baogutu gold deposit, NW China, has been attributed to further decreases in temperature and oxygen fugacity (An & Zhu, 2010).

A comprehensive fluid inclusion analysis of gold deposits along the MSZ is required to fully assess the composition and temperature of ore fluids, and the roles of the suggested mechanisms for precipitating gold and associated sulphide minerals.

9.6.4 Implications of stable isotope data

9.6.4.1 Consistency of stable isotope signatures

The uniformity of $\delta^{34}S$ sulphide data at deposits along the length of the MSZ, in conjunction with the striking similarity in structural setting, paragenesis and ore textures, suggests that mineralisation along the MSZ formed during a single mineralising event from similar ore fluids throughout the entire shear system. At the deposit scale, $\delta^{18}O$ values for gold-bearing quartz samples are remarkably consistent and can be reliably distinguished from unmineralised quartz from outside the ore zone. $\delta^{18}O$ values for auriferous quartz along a >1 km length and ~300 m depth of the Silverstone deposit invariably occurs within the range +13.9 to +15.0 ‰, in contrast to barren quartz that is either isotopically heavier or lighter. The lack of variation in the isotopic compositions of quartz and sulphides at Silverstone is consistent with deposition from a comparable ore fluid.

Additionally, $\delta^{18}O$ quartz analysis and $\delta^{34}S$ sulphide analysis show great potential for use as vectors towards mineralisation in a particularly challenging exploration environment. On a regional scale, the distinct $\delta^{34}S$ values for gold-bearing arsenopyrite (+3.7 to +4.6 ‰) relative to an unmineralised arsenopyrite sample (+1.8 ‰) could provide a means of targeting exploration. Similarly, the well-constrained and distinct $\delta^{18}O$ values for auriferous quartz on a deposit scale could provide a vector towards mineralised ore zones. These implications concur with the findings of Petrella et al. (2020), who suggested the use of in-situ sulphur stable isotope analysis as an exploration tool for orogenic gold mineralisation in the Northern Territory, Australia. Stable isotope data has not previously been routinely collected and utilised during mineral exploration, owing primarily to the cost per sample, the protracted time taken for analysis and uncertainty regarding the usefulness of stable isotope data (Barker et al., 2013). However, it is possible that recent analytical advancements (as described in Barker et al., 2013), could allow for more rapid and less expensive stable isotope analysis.

9.6.4.2 Implications for sulphur source

It is widely accepted that gold is mostly transported as bisulphide complexes in lode-gold deposits (e.g., Groves et al., 2003). Therefore, understanding the source of sulphur in these deposits is a crucial means of evaluating the source of gold, hydrothermal fluids, and the genesis of lode-gold mineralisation (Chang et al., 2008).

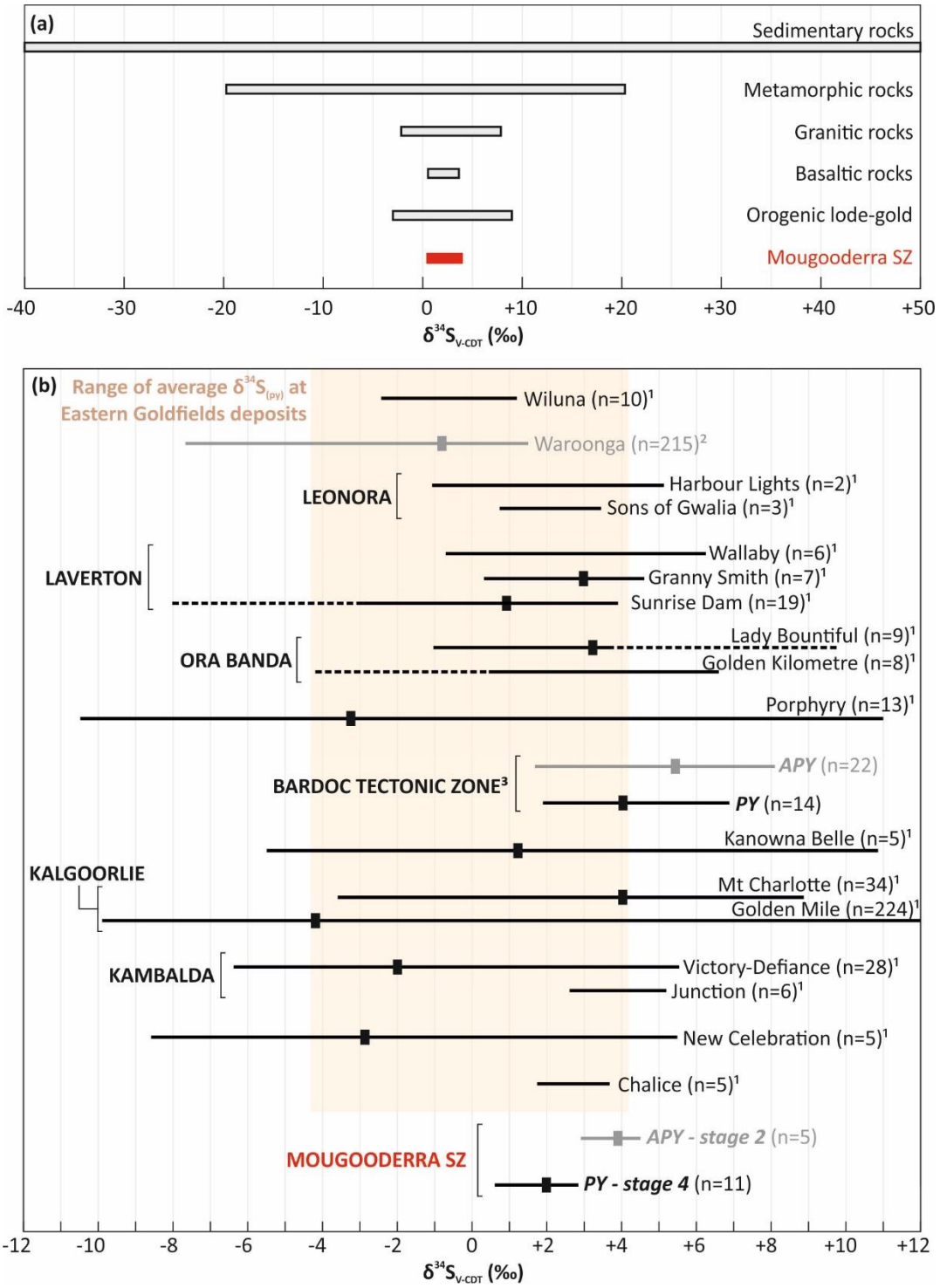

Figure 9.25: (a) Sulphur isotope ranges of common reservoirs in comparison with the range of sulphides along the Mougooderra Shear Zone. Fields are compiled by Bark et al. (2020) and Hodkiewicz et al. (2009); **(b)** Total range of $\delta^{34}S$ values of ore-related pyrite (black) and arsenopyrite (grey) at lode-gold deposits in the Eastern Goldfields Superterrane (grouped by mining district and arranged from north to south) compared to the range shown by deposits along the Mougooderra Shear Zone. Rectangles show average $\delta^{34}S$ values and dashed lines indicate ranges based on limited data (i.e., single sample). The yellow field represents the range of average $\delta^{34}S$ values at Eastern Goldfields lode-gold deposits, as defined by Hodkiewicz et al. (2009). The locations of all deposits are shown on Figure 9.24. n refers to the number of samples corresponding to each range. Data sources: [1]Hodkiewicz et al. (2009) and references therein; [2]LaFlamme et al. (2018); [3]Morey et al. (2007).

Sedimentary rocks generally exhibit a wide range of $\delta^{34}S$ compositions (-40 to +50 ‰; Fig. 9.25a), indicating either a combination of sulphur from different sources under reduced conditions, or sulphur precipitation from a single source under oxidising conditions (Ohmoto & Rye, 1979). In contrast, mantle-derived magmatic rocks have $\delta^{34}S$ compositions that occupy a narrow range around 0 ‰ (Ohmoto & Rye, 1979). A compilation of sulphur isotope data demonstrates a common range in $\delta^{34}S$ values between -3 and + 9 ‰ for lode-gold deposits globally (Fig. 9.25a; Bark et al., 2020; McCuaig & Kerrich, 1998). The sulphur isotope data from this study fall in this range, with $\delta^{34}S$ values between -1.7 and +4.6 ‰. This common range of $\delta^{34}S$ values in lode-gold deposits has been interpreted to reflect derivation of sulphur from several, alternative common reservoirs, including metamorphosed sedimentary sulphur, average crustal sulphur, and mantle-derived magmatic sulphur (Ridley & Diamond, 2000; Chang et al., 2008). However, mineralised pyrite and arsenopyrite from lode-gold deposits along the MSZ occupy significantly narrower ranges of +0.6 to +3.1 ‰ and +3.7 to +4.6 ‰, respectively. The uniformity of $\delta^{34}S$ values of gold-related sulphides at deposits along the MSZ suggests that sulphur likely originated from a single, uniform source reservoir.

A compilation of $\delta^{34}S$ data for ore-related pyrite and arsenopyrite at lode-gold deposits in the Eastern Goldfields, Yilgarn Craton, is shown in Figure 9.25b. Mineralised sulphides from the MSZ clearly fall within the $\delta^{34}S$ range shown by other deposits and display a strikingly narrow range of $\delta^{34}S$ values. Many world-class deposits in the Eastern Goldfields, such as the Sunrise Dam, Porphyry, Kanowna Belle and Golden Mile deposits, have a much broader range of mineralised pyrite $\delta^{34}S$ values reaching -10 to + 12 ‰ (Fig. 9.25b; Hodkiewicz et al., 2009). The larger variations in $\delta^{34}S$ values demonstrated by world-class gold deposits may be attributed to more oxidised environments during gold precipitation or reaction of reduced fluids with oxidised host rocks (Morey et al., 2007; Salier et al., 2005). The apparently restricted range of $\delta^{34}S$ values for sulphides along the MSZ does not seem to be an artefact of limited sampling, as other deposits with similar or lower sample numbers (e.g., New Celebration, Kanowna Belle) typically demonstrate a broader range of $\delta^{34}S$ values (Fig. 9.25b). Similar $\delta^{34}S$ values to sulphides along the MSZ, including isotopically heavier arsenopyrite relative to pyrite, are demonstrated by lode gold deposits in the Bardoc Tectonic Zone (Fig. 9.25; Morey et al., 2007). The lack of more significant variations in sulphide $\delta^{34}S$ values in this area is interpreted to reflect uniform hydrothermal conditions and dominantly reduced ore fluids (Morey et al., 2007).

Pyrite grains from the unmineralised Mt Mulgine granite (Fig. 9.1) yielded $\delta^{34}S$ values of -0.2 to +0.1 ‰, within the range expected for magmatic rocks and isotopically lighter than mineralised pyrite along the MSZ, precluding a single magmatic sulphur source for the samples analysed (Ohmoto & Rye, 1979). In contrast, unmineralised pyrite from footwall sulphidic shales at Silverstone yields a $\delta^{34}S$ value (2.7 ‰) within the range of mineralised pyrite along the MSZ. The $\delta^{34}S$ values of other unmineralised

sedimentary pyrite samples from comparable rocks in the Eastern Goldfields Superterrane range between 0 to +12 ‰ (average +5.5 ‰; Morey et al., 2007). If the sampled unmineralised pyrite is diagenetic, then sedimentary sulphur in footwall Mougooderra Fm shales may represent a viable sulphur source for mineralised pyrite and arsenopyrite along the MSZ. Alternatively, it remains possible that disseminated pyrite in the footwall units has a hydrothermal origin and is within the range of mineralised pyrite. Curiously, a pyrite sample from the Gossan Hill VMS deposit situated in exposed basement units in the YSGB has a $\delta^{34}S$ value of +1.5 ‰, also within the range of mineralised pyrite along the MSZ.

An interesting feature of the sulphur isotope data for mineralised sulphides along the MSZ is the distinctly different $\delta^{34}S$ values for auriferous arsenopyrite (stage 2: +3.7 to +4.6 ‰) and pyrite in the same mineralised samples (stage 4: +0.6 to +3.1 ‰). It is plausible that variations in pH/fO_2 is causing fractionation of sulphur isotopes as modelled and tested by Ohmoto & Rye (1979). Considering the homogeneity of this data along the length of the MSZ, it is unlikely that the variability in S isotope composition between earlier arsenopyrite and subsequent pyrite is due to the tapping of multiple reservoirs.

9.6.5 Age of lode-gold mineralisation along the Mougooderra Shear Zone

The new 2623 ± 34 Ma $^{207}Pb/^{206}Pb$ crystallisation age for gold-related monazite at the Silverstone deposit represents the first age determination for lode-gold mineralisation in the YSGB, and westernmost age for lode-gold mineralisation in the Yilgarn Craton. This age is younger than the ca. 2801 Ma age of Warriedar Suite intrusions in the hangingwall at Silverstone (Lu et al., 2016b), and the ca. 2815 Ma age of Mougooderra Fm footwall rocks (this study; Section 8.4). Although the new age specifically constrains the timing of stage 2 arsenopyrite-gold mineralisation at Silverstone, textural relations indicate that paragenetic stages 2 and 3, which account for most of the gold observed at the Silverstone, Black Dog and Bugeye deposits, were part of a single, progressive mineralising episode (Section 9.6.3.1). This age is interpreted as the age of lode-gold mineralisation along the length of the MSZ, due to the remarkable consistency of structural characteristics, mineral parageneses and stable isotope data at deposits along this structure. The deformed nature of some stage 2-4 sulphides at Silverstone suggests that the MSZ was active during and/or following the emplacement of mineralisation, providing additional time constraints on D_4 shearing in the area.

A minimum age constraint for lode-gold mineralisation along the MSZ is provided by the 2626 ± 6 Ma crystallisation age of the 50x25 km Seeligson Monzogranite (Walganna Suite) that dissects the belt and multiple D_4 shear zones, including the MSZ and Rothsay Shear Zone (Wingate et al., 2014).

Furthermore, felsic pegmatites attributed to ca. 2620 Ma low-Ca Walganna Suite magmatism (Section 3.4.3.2) cross-cuts the duplex structure along the RSZ and, crucially, dissects lode-gold mineralisation at the Rothsay gold mine (Egan Street Resources, 2019). Collectively, this indicates that Walganna Suite magmatism postdates, or at the very least is coeval with lode-gold mineralisation along D_4 shear zones, thus providing an inferred ca. 2620 Ma lower age constraint for the age of lode-gold mineralisation along the MSZ and RSZ.

Garnet Lu-Hf dating of metamorphic garnet in rocks of the Chulaar Group and Mougooderra Fm in the study area has yielded crystallisation ages of 2686 ± 18 Ma and 2685 ± 15 Ma, respectively, interpreted as the timing of late prograde metamorphism in the YSGB (Parmenter et al., 2020). The ca. 2623 Ma age for lode-gold mineralisation at Silverstone is markedly younger than the indicated ca. 2685 Ma age of late prograde metamorphism, consistent with the post-peak metamorphic timing that characterises many orogenic-lode gold deposits (Groves et al., 2003).

The new age for lode-gold mineralisation at Silverstone is plotted alongside the ages of other lode-gold deposits across the Yilgarn Craton in Figure 9.26, including ages determined by a variety of methods. Unfortunately, the ~68 Ma uncertainty associated with the presented age is greater than many other ages for mineralisation across the Yilgarn Craton, several of which are associated with uncertainties of < 10 Ma (e.g., Brown et al., 2002; Salier et al., 2005). This may be due to the relatively high proportions of common Pb in monazite and the addition of common Pb from arsenopyrite in contact with monazite, precluding a more accurate age determination.

Previous dating of ore components in lode-gold deposits across the Yilgarn Craton, including three deposits in the Murchison Domain, distinguishes a protracted ~45 m.y. window of significant lode-gold mineralisation between ~2665 Ma to ~2620 Ma (Robert et al., 2005; Czarnota et al., 2010) (Fig. 9.26). The age of lode-gold mineralisation at Silverstone broadly coincides with the Yilgarn-wide period of gold mineralisation, and in particular, correlates with the ~2620 Ma younger boundary of this window (Fig. 9.26) (with the caveat that the older bracket of the uncertainty in age corresponds to 2670 Ma, at the older margin of the Yilgarn-wide event). The apparent ca. 2623 Ma age of mineralisation at Silverstone is similar to two of the three published ages in the Murchison Domain (Figs. 2.23; 9.26), at the Reedy mining centre in the northwest (2639 ± 4 Ma; Wang et al., 1993) and the Mt Gibson mine to the south (2627 ± 13 Ma; Yeats et al., 1996), and contrasts with the older age for lode-gold mineralisation at Big Bell (2662 ± 5 Ma; Mueller et al., 1996) (Fig. 9.26). Several comparable ca. 2620 Ma ages for lode-gold mineralisation have been reported in the Eastern Goldfields (Fig. 9.26). This includes the Chalice deposit in the south (Bucci et al., 2002) and deposits in the north Eastern Goldfields including the Matilda deposit in the Wiluna gold camp (Kent & Hagemann;

1996), and the Agnew gold camp (Thébaud et al., 2018) (Figs. 9.24, 9.26). In particular, the comparable age of lode-gold mineralisation in the Wiluna area is notable, as structural (Section 9.6.2) and paragenetic (Section 9.6.3) similarities have also been highlighted between the Silverstone deposit and the Wiluna camp of deposits in this study.

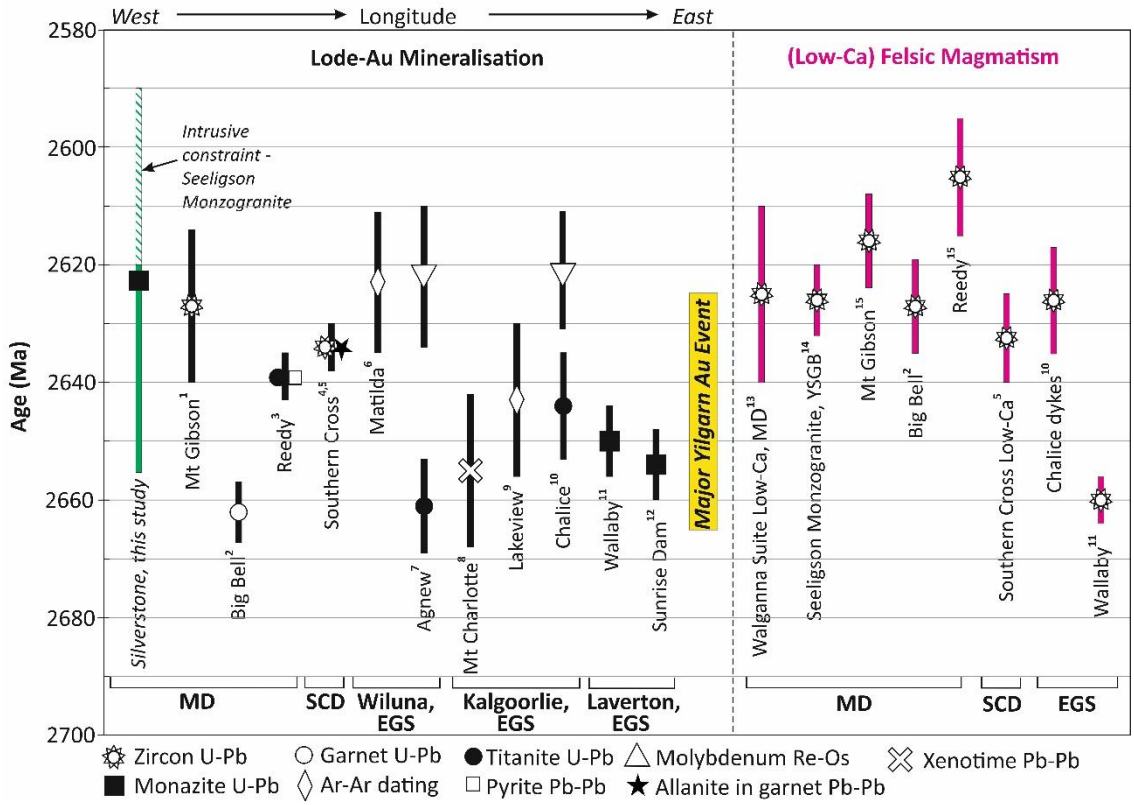

Figure 9.26: Diagram comparing the ages of lode-gold mineralisation at major gold deposits and the ages of late felsic magmatism across the Yilgarn Craton, plotted in order of increasing longitude from west to east. In each instance, the mineral and isotopic system used for dating is symbolised and bars represent the uncertainty associated with each age. All published lode-gold mineralisation ages for the Murchison Domain (MD) and Southern Cross Domain (SCD) are shown, in addition to representative ages from the Eastern Goldfields Superterrane (EGS). References: [1]Yeats et al. (1996), [2]Mueller et al. (1996), [3]Wang et al. (1993), [4]Mueller et al. (2004), [5]Doublier et al. (2014), [6]Kent & Hagemann (1996), [7]Thébaud et al. (2018), [8]Rasmussen et al. (2009), [9]Kent & McDougall (1995), [10]Bucci et al. (2002), [11]Salier et al. (2005), [12]Brown et al. (2002), [13]Van Kranendonk et al. (2013), [14]Wingate et al. (2014), [15]Wang (1998).

The new dating presented in this study indicates a close temporal relationship between lode-gold mineralisation and post-tectonic low-Ca felsic magmatism in the YSGB. The 2626 ± 6 Ma crystallisation age of the Seeligson Monzogranite (Walganna Suite) is comparable to the inferred ca. 2623 Ma age of lode gold mineralisation at the Silverstone deposit, although this intrusion and associated pegmatites dissect D_4 shear zones and mineralisation at the Rothsay gold mine (Egan Street Resources, 2019). Similar spatial and temporal correlations between lode-gold mineralisation and low-Ca felsic magmatism have been demonstrated elsewhere in the Yilgarn Craton. The ca. 2627 Ma Mount Gibson deposit to the south of the study area is also spatially and temporally associated with Walganna Suite intrusions (Fig. 9.26). This association, combined with high-salinity fluid inclusions with

homogenisation temperatures of up to 600 °C in gold-bearing quartz veins (Straub et al., 1995), has been interpreted as evidence of a magmatic-hydrothermal fluid source for at least part of this system (Duuring et al., 2007). In contrast, the Big Bell and Reedy deposits in the northeastern Murchison Domain are not temporally associated with low-Ca magmatism (Fig. 9.26).

An affinity between lode-gold and a late ~2630-2620 Ma granitic bloom has been implicated for deposits in Southern Cross Domain (Doublier et al., 2014). In this area, geochronological and isotopic analysis of multiple ca. 2635 Ma lode-gold deposits are consistent with contemporaneous low-Ca granitoids being a major source of hydrothermal fluids (Mueller et al., 2004; Doublier et al., 2014) (Fig. 9.26). At the Chalice deposit, Eastern Goldfields, a second stage of lode-gold mineralisation is spatially and temporally associated with monzogranitic dykes, although a genetic association between gold and magmatism has not been resolved (Bucci et al., 2002). Despite evidence for a close temporal relationship between lode-gold mineralisation and felsic magmatism, there remains significant controversy as to whether magmatism was the source of auriferous fluids, assisted in setting up hydrothermal systems, or whether pre-existing intrusions provided structural traps that controlled the location of lode-gold deposits (e.g., Wang et al., 1998; Salier et al., 2005; Wyman et al., 2016).

9.6.6 Summary

A series of small- to moderate-sized lode-gold deposits located in the YSGB display a ubiquitous structural control and are principally situated along the relatively discrete, first-order, 50 km-length MSZ, with a single lode-gold deposit located on the second-order WWSZ. Although a thorough assessment of the controlling factors upon mineralisation in the YSGB is not possible, there is a marked relationship between lode-gold deposits and Fe-rich, competent host rocks. Additionally, the largest deposit in the belt, the ~400koz Silverstone deposit, is located along a bend on the MSZ.

In contrast to the commonly diverse characteristics of many lode-gold deposits elsewhere in the Yilgarn Craton, structural, paragenetic and isotope data from representative lode-gold deposits along the MSZ exhibit remarkably uniform features. These consist of: I) quartz-carbonate-sulphide vein arrays consistent with fault-valve behaviour associated with fluid overpressure-related failure of steeply-inclined reverse structures; II) a distinctive four-stage paragenetic sequence comprising three auriferous phases and documenting profound mineralogical changes, starting with pyrite, succeeded by arsenopyrite, progressing to base metal sulphides associated with various Sb-sulphide minerals and finally overprinted by barren pyrite; III) a homogenous, narrow range of $\delta^{34}S$ sulphide data at deposits along the length of the MSZ, including auriferous arsenopyrite and pyrite; IV) exceptionally uniform

$\delta^{18}O$ values of mineralised quartz on a deposit-scale that can be readily distinguished from unmineralised quartz.

The uniformity of mineral assemblages, ore textures and $\delta^{34}S$ sulphide data at deposits along the length of the MSZ supports structural analysis and demonstrates that mineralisation across the belt formed as part of the same mineralising event during a progressive episode of crustal shortening and associated D_4 shearing. A new ca. 2623 Ma U-Pb monazite age for lode-gold mineralisation at the Silverstone deposit falls within the range of the 2665-2620 Ma Yilgarn-wide mineralising event, and distinguishes a temporal, but not necessarily genetic, relationship between lode-gold and post-tectonic low-Ca granitoids in the region.

A more thorough understanding of lode-gold mineralisation along the MSZ will ultimately provide a revised rationale to underpin exploration in a highly prospective area with significant transported cover.

CHAPTER 10

Synthesis & Conclusions

10.1 Introduction

In this chapter, the new geological mapping, structural data, and geochronology presented in this thesis are integrated with literature data to construct a time-constrained stratigraphic and structural model for the YSGB, which is compared with published models for the Murchison Domain. The geodynamic implications of the work presented are assessed and suggestions for future work are then presented. Finally, the conclusions of this thesis are summarised.

10.2 Structural Model

This study proposes a seven-stage deformational framework to account for the stratigraphic and structural features observed in the YSGB. The timing of these structural events, in addition to the emplacement of supracrustal rocks, intrusions, metamorphism and mineralisation in the YSGB, is summarised in Figure 10.1. This sequence records a progression from bulk extension (D_E), which accommodated initial volcanism, sedimentation, and the emplacement of mafic-ultramafic sills, to a period of extensive granite-related doming (D_1, D_2?), followed by bulk horizontal shortening and associated shearing (D_3, D_4), and successive episodes of late-stage brittle faulting (D_5, D_6). The stratigraphic and structural development of rocks in the YSGB is illustrated in Figure 10.2 and described below.

10.2.1 Emplacement of Chulaar Group rocks

The earliest event consists of bulk extension (D_E) and accounts for the emplacement of ca. 2825-2818 Ma volcanic, volcaniclastic and minor sedimentary rocks of the Chulaar Group onto pre-existing basement rocks (Figs. 10.1, 10.2a). The exposed basement in the northeast of the study area consists of ca. 2950 Ma Gossan Hill Formation felsic volcanic and volcaniclastic rocks, which are considered to represent the basement units across much of the Murchison Domain (e.g., Wang et al., 1998; Van

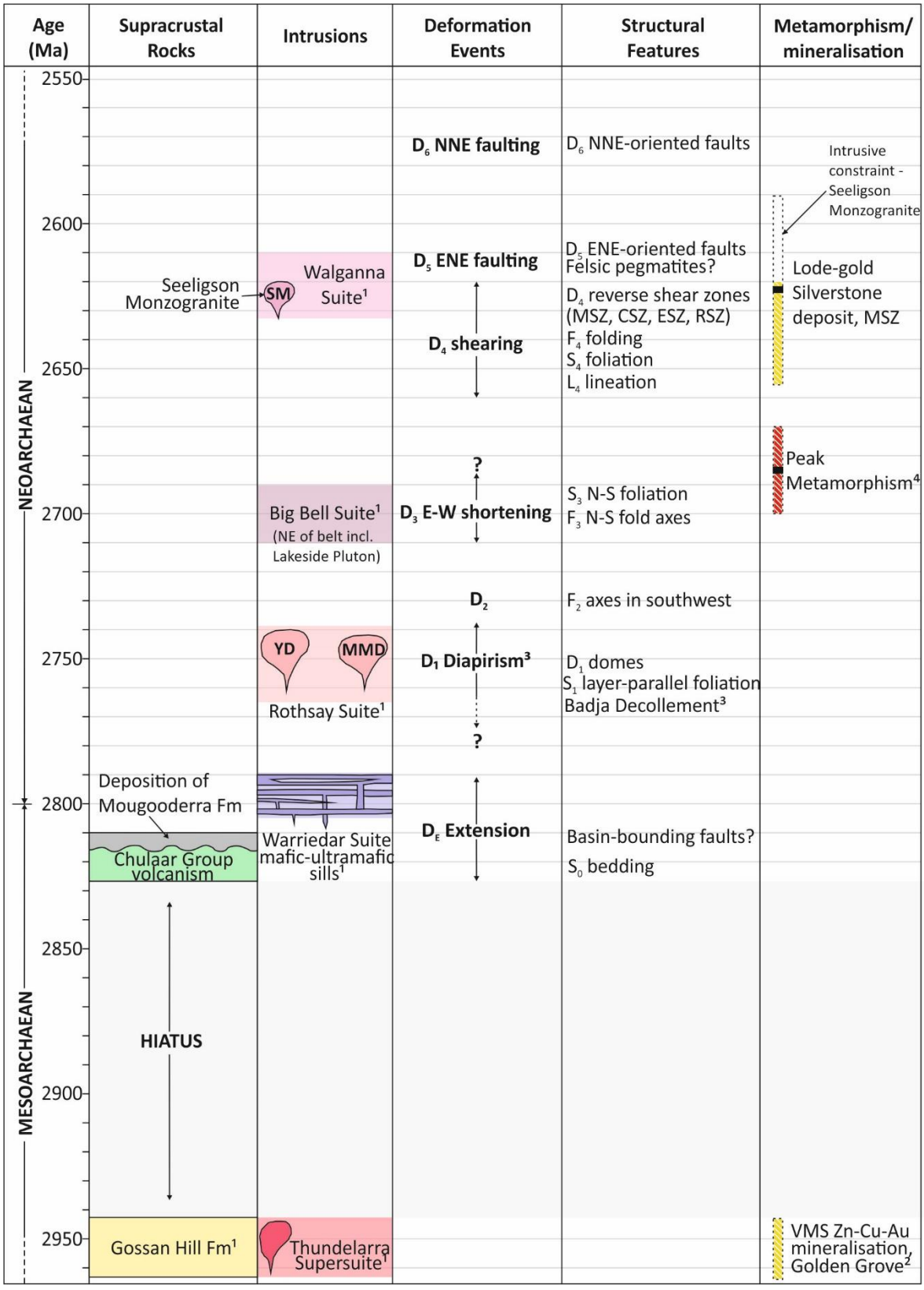

Figure 10.1: Synthesis diagram summarising the order and timing of geological events in the YSGB, including the emplacement of supracrustal rocks, intrusions, deformational events, structures associated with each deformation event, metamorphism and mineralisation. Uncertainties for the ages of mineralisation and peak metamorphism are shown. Abbreviations: YD: Yalgoo Dome; MMD: Mt Mulgine Dome; SM: Seeligson Monzogranite. Data sources for geochronological data as follows: [1] GSWA geochronology database (see Section 2.2 for further details); [2]Wang et al., 1998; [3]Zibra et al. (2018; 2020); [4]Parmenter et al. (2020).

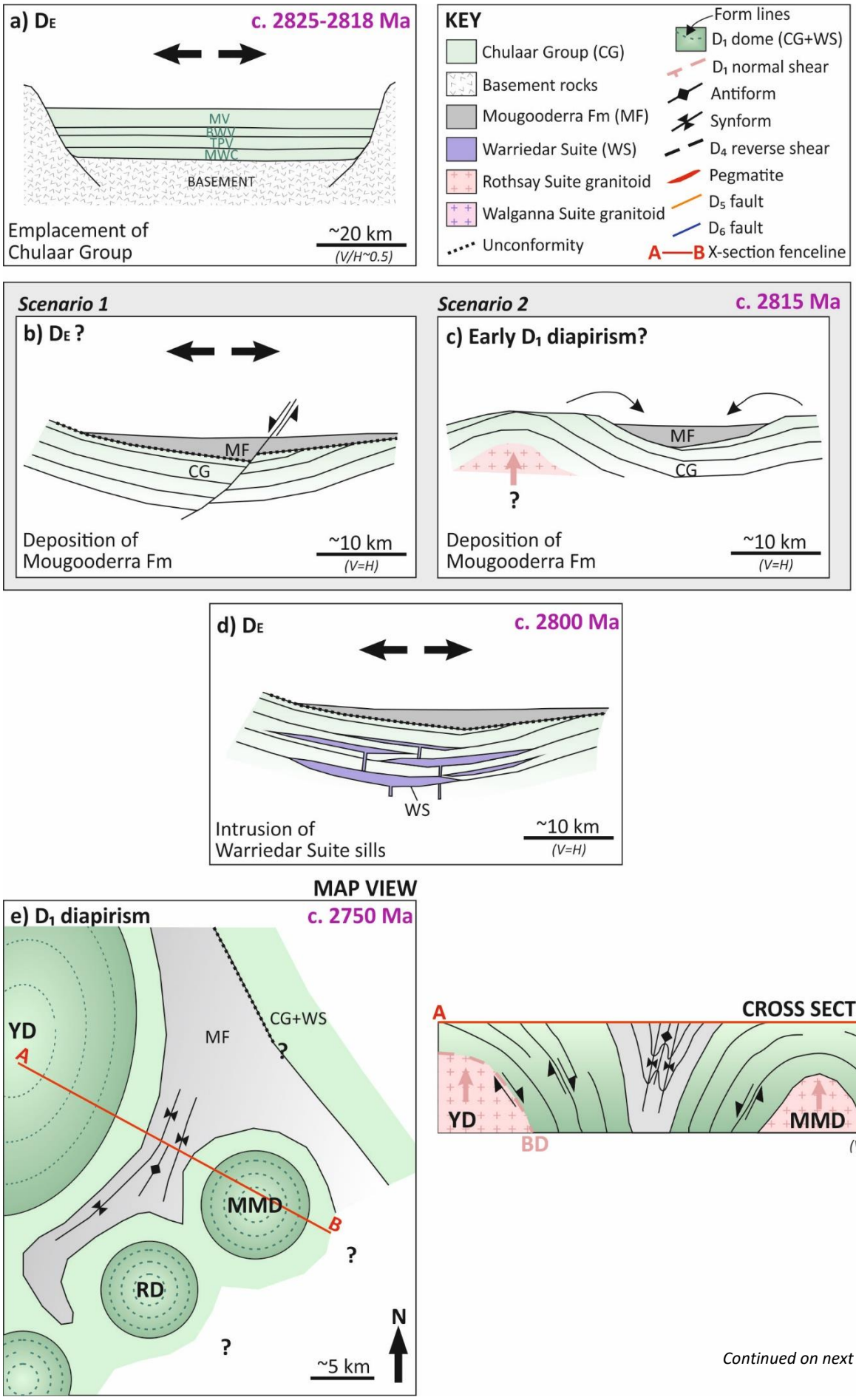

Continued on next page

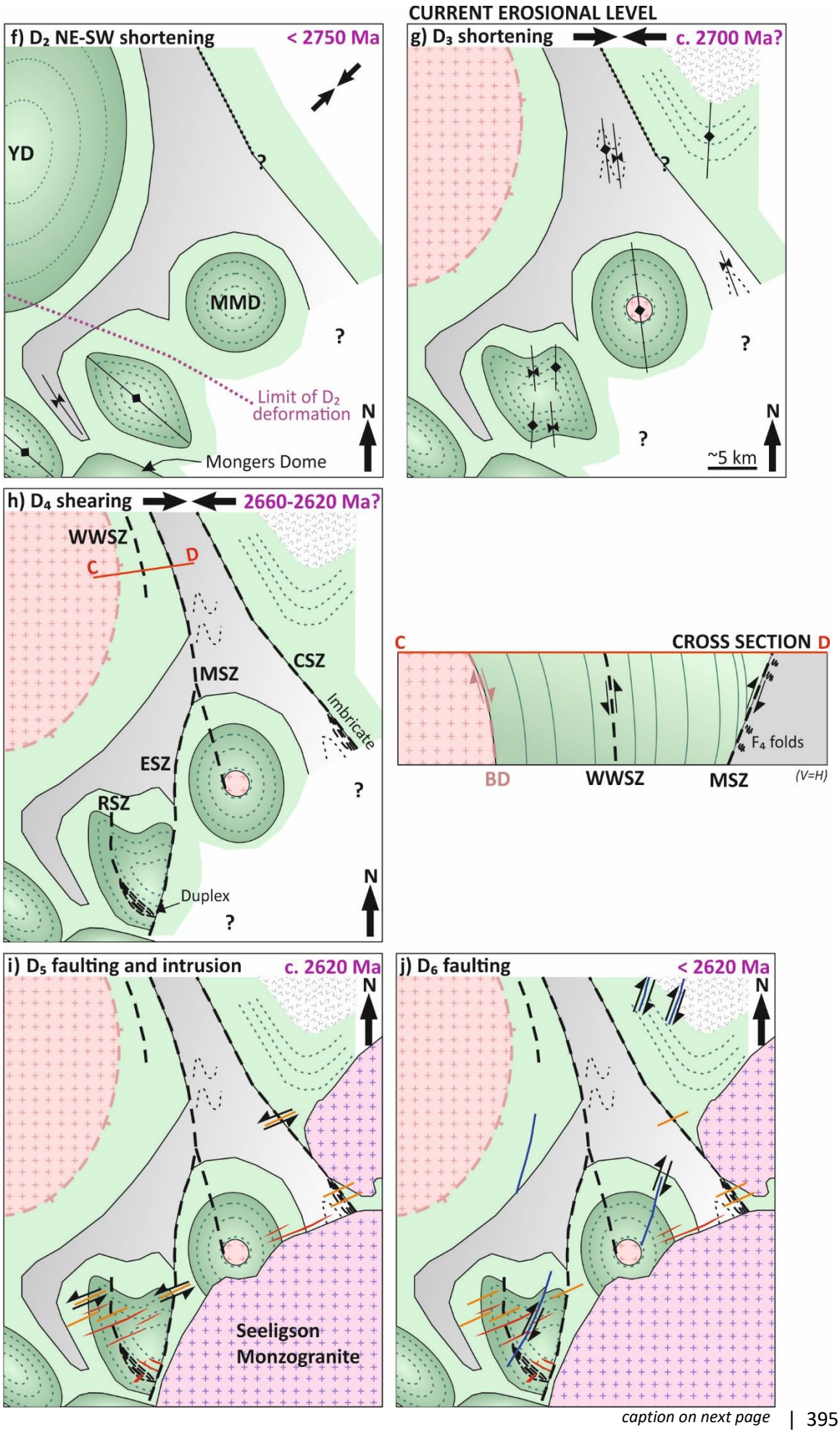

caption on next page

Figure 10.2 (previous two pages): A series of schematic sketch maps and cross sections illustrating the stratigraphic and structural development of the YSGB. **(a)**; D_E - emplacement of Chulaar Group rocks onto basement units during bulk extension. The sub-division of Chulaar Group rocks identified at Rothsay are shown (MWC = Macs Well Clastics; TPV = Two Peaks Volcanics; BWV = Beryl West Volcanics; MV = Mulga Volcanics); **(b)** Scenario 1 for the emplacement of Mougooderra Fm rocks, during bulk extension and associated normal faulting (D_E); **(c)**; Scenario 2 for the emplacement of Mougooderra Fm rocks, during the inferred early stages of a protracted period of diapirism (early D_1); **(d)**; D_E - emplacement of Warriedar Suite intrusions into the Chulaar Group, during inferred bulk extension; **(e)**; D_1 – sketch map and cross section illustrating granitic diapirism resulting in the formation of multiple, approximately coeval domes in overlying supracrustal units. A fan-shaped geometry of dominantly synclinal, km-scale F_1 folds formed in Mougooderra Fm rocks occupying the interstices between surrounding domes. The Badja Decollement (BD) developed at the granite-greenstone-contact of the Yalgoo Dome at this stage, and associated layer-parallel shearing in the supracrustal succession formed the S_1 layer-parallel foliation; **(f)** D_2 – localised NE-SW shortening in the southwest of the study area, preserved as F_2 axes refolding D_1 domes; **(g)** D_3 – regional E-W shortening resulting in the development of N-S trending fold axes at various scales in Chulaar Group and Mougooderra Fm units, locally refolding pre-existing folds, and accompanied by a pervasive N-S striking foliation; **(h)** D_4 – development of NNE- to NNW-striking shear zones during the later stages of continued E-W shortening, which show evidence of a significant vertical component of shear and locally comprise imbricate structures (MSZ = Mougooderra Shear Zone; CSZ = Chulaar Shear Zone; WWSZ = Winddine Well Shear Zone; ESZ = Enchanted Shear Zone; RSZ = Rothsay Shear Zone). The accompanying cross section displays the subsurface geometry and kinematics of the MSZ and WWSZ, and F_4 folding in footwall units; **(i)** D_5 - ENE-oriented faults with typical sinistral offsets and locally associated with folding (fault-drag), approximately coeval with the intrusion of parallel ENE-striking pegmatite dykes in the south, directly related to the intrusion of the Seeligson Monzogranite to the southeast; **(j)** D_6 - late-stage, brittle faults with typical dextral offsets, dissecting all pre-existing structures including D_4 shear zones.

Kranendonk et al., 2013). This is also supported by evidence of crustal contamination in some Chulaar Group volcanic rocks (Section 7.5) and the occurrence of ca. 2950 Ma zircon cores overprinted by ca. 2820 Ma zircon rims in the volcaniclastic geochronology samples analysed in this study (Section 8.4). Previous studies in the Murchison Domain have also suggested that early volcanism and deposition occurred during a period likely dominated by lithospheric extension (e.g., Van Kranendonk et al., 2013; Smithies et al., 2018; Zibra, 2020).

Chulaar Group rocks are interpreted to have accumulated in submarine depositional environments, characterised by bedded interflow BIF, volcaniclastic units and pillowed volcanic rocks towards the top of the succession. The micro-banded nature of BIF in the Chulaar Group is consistent with deposition at water depths in excess of 200 m (Klein, 2005). Coarse sandstone and occasional conglomeratic layers in the Macs Well Clastics at the base of the Chulaar Group in the Rothsay area are indicative of higher energy, shallow marine conditions (Section 3.4.1.1).

10.2.2 Deposition of Mougooderra Fm

New geochronological data indicates that the Mougooderra Fm (including the Willowbank Clastics; Section 8.5.1) was deposited upon underlying Chulaar Group rocks at ca. 2815-2810 Ma (Section 8.5.2). Conglomeratic units within the succession indicate that clasts were sourced locally, either from erosion of underlying Chulaar Group units or other Mougooderra Fm rocks. Crucially, the lack of clasts displaying internal deformation fabrics implies that no fabric-forming deformational events preceded deposition of the Mougooderra Fm. An angular unconformity has been identified along part of the

basal contact of the Mougooderra Fm (described in Section 2.4.3.4), however, much of the rest of the contact is either sheared (as D_4 shear zones; Section 10.2.7), or very poorly exposed. In some instances, such as in the Rothsay area, there is no angular discordance between Chulaar Group and Mougooderra Fm units, although the contact is invariably obscured.

Two alternative scenarios are proposed to account for the deposition of the Mougooderra Fm and the ostensibly local angular unconformity at its base. The first model invokes normal faulting and minor uplift associated with ongoing bulk lithospheric extension at this stage (Fig. 10.2b). Tilting and erosion of hangingwall units suitably accounts for the unconformity observed locally, whereas deposition in the footwall of an extensional fault would have resulted in the broadly conformable contact observed elsewhere (Fig. 10.2b). Tilting of the supracrustal succession was suggested for the formation of an angular unconformity at the base of the Glen Group in the northeastern Domain (Van Kranendonk et al., 2013), although a mechanism to account for tilting was not provided. A series of early extensional detachments, transfer faults and sediment-filled half grabens that predate regional folding have been recorded in the Margaret anticline, eastern Yilgarn Craton (McIntyre & Martyn, 2005). Unfortunately, extremely poor exposure and the dominantly sheared nature of the lower contact may preclude the identification of extensional structures underlying the Mougooderra Fm in the study area. In the Margaret anticline, early extension, uplift and sedimentary basin development has been attributed to a thermal anomaly in the crust, generated by the insulating effect of a thick (>10 km) mafic-ultramafic volcanic pile emplaced onto the crust (McIntyre & Martyn, 2005). The Mougooderra Fm is similarly underlain by a thick mafic-ultramafic volcanic pile (Chulaar Group).

Notably, there is a close temporal association between the ca. 2810-2815 Ma Mougooderra Fm and the emplacement of 2813-2819 Ma Meeline Suite mafic-ultramafic intrusions in the region, attributed to plume-related magmatism (Section 2.3.1; Ivanic et al., 2010; Czarnota et al., 2010; Ivanic et al., 2017). The Meeline Suite includes the vast 85 x 35 km Windimurra Igneous Complex situated ~100 km to the east, and the less extensive Buddadoo Complex ~30 km to the west of the study area (Ivanic, 2019). The impingement of a mantle plume at this time may have induced plume-related rifting in the western Yilgarn Craton (e.g., Mole et al., 2019) and may have promoted uplift associated with deposition of the Mougooderra Fm. Plume-related uplift, rifting and sedimentary deposition has previously been documented in the Belingwe greenstone belt, Zimbabwe (Hunter et al., 1998).

An alternative explanation is that the Mougooderra Fm was deposited in the early stages of a protracted episode of granite-related doming and associated uplift. Zibra et al. (2018) previously suggested that unconformable deposition of the Mougooderra Fm occurred at ca. 2730 Ma in response to a major episode of diapirism at ca. 2750 Ma (D_1; Section 10.2.4). Whereas this is

demonstrably incompatible with new age dating and the occurrence of major F_1 folds in Mougooderra Fm rocks, it is possible that the onset of gravitational stability and doming may have preceded the main diapiric episode (Zibra et al., 2018) by several tens of millions of years. For example, the gravitational overturn of 3600-3400 Ma rocks in the Pilbara Craton, Western Australia, occurred over a timescale of at least ~45 Ma (Wiemar et al., 2018). A prolonged episode of gravitational instability is supported by the presence of ca. 2950 Ma gneissose rocks at the cores of the deeply eroded Yalgoo and Gullewa domes (Zibra et al., 2018; 2020). However, early doming at ca. 2815 Ma is not currently supported by geochronology, as dated samples from granitic domes in the area occur in the interval 2740-2760 Ma, consistent with the main episode of granite-up greenstone-down tectonics (D_1; Section 10.2.4).

10.2.3 Emplacement of Warriedar Suite intrusions

Following the deposition of the Mougooderra Fm, Warriedar Suite mafic-ultramafic sills were intruded concordantly into the underlying Chulaar Group succession at ca. 2800-2790 Ma (Fig. 10.2d), based on zircon U-Pb crystallisation ages (e.g., Lu et al., 2016b). Warriedar Suite intrusions are invariably deformed in the same manner as Chulaar Group rocks, indicating a lack of deformation prior to their emplacement, and consistent with ongoing extension to at least ca. 2790 Ma.

10.2.4 D_1 deformation

Early formed D_1 structures and the inherent dome-and-keel architecture of the study area are compatible with an early episode of granite-up greenstone-down tectonics resulting from gravitational instability, such as the diapiric model advocated by Zibra et al. (2018; 2020), or a similar vertical tectonic process such as partial convective overturn (Collins et al., 1998; Jones et al., 2020). It can be difficult to determine between the principal mechanisms proposed for magma ascent and emplacement into the crust, diapirism and the 'ballooning' of inflated plutons, as resulting structures typically exhibit similar field relationships and data that do not exclusively support either model (Weinberg, 1996; 1997). In addition to diapirism, the 'ballooning' or inflation of plutons of granitic magma can also account for the magma ascent and emplacement in the crust, and the dome-and-keel pattern that typifies the southwest Murchison Domain (e.g., Weinberg, 1996; 1997). However, it is commonly difficult to distinguish between diapirism and 'ballooning' mechanisms, as the resulting domal structures exhibit features that are not exclusively to either model (Weinberg, 1996; 1997; McCarthy et al., 2015). In many cases, diapirism can be taken to indicate a combination of these processes (Weinberg, 1997).

In addition to the granite cored Yalgoo and Mt Mulgine domes, for which Zibra et al. (2018) documents robust structural evidence in favour of diapirism, geological mapping at Rothsay (Chapter 3) supports the formation of an additional 'Rothsay Dome' during D_1 (Fig. 10.2e). This structure has been refolded in multiple orientations and a granitic core is likely concealed and obscured by greenstone cover.

The vertical emplacement of D_1 granitic domes is supported by the Badja Decollement at the outer contact of the Yalgoo Dome, which demonstrates a 'granite-up, greenstone down' normal sense of shear (Zibra et al., 2018). Furthermore, the pervasive S_1 layer-parallel foliation observed in incompetent greenstone lithologies in the YSGB (Section 3.5.3) is attributed to layer-parallel shearing in the overlying supracrustal succession during D_1 diapirism. The laterally discontinuous nature of some supracrustal units can be fully accounted for based on intrusive relations, rather than an episode of early horizontal shortening (e.g., Swager & Griffin, 1990), which is not supported by field evidence (Section 3.6.4.1). There is insufficient structural evidence that domal structures formed due to the superposition of multiple sets of upright, orthogonal folds, as suggested by Myers & Watkins (1985) and Watkins & Hickman (1990).

Crucially, Mougooderra Fm (Willowbank Clastics) units located interstitial to D_1 domes in the southwest of the area have been deformed into a fan-shaped pattern of km-scale, dominantly synclinal F_1 folds, possessing curvilinear axes parallel to the margins of surrounding domes (Fig. 10.2e; Zibra et al., 2018). This demonstrates that Mougooderra Fm units were emplaced prior to D_1 deformation, consistent with the ca. 2815 Ma depositional age determined in this study and were deformed in the keels between ascending domes. Zibra et al. (2018) also noted the presence of folds in Mougooderra Fm rocks, with geometries comparable with other folds in the area that were directly attributed to emplacement of the Yalgoo Dome (F_2-like folds; Zibra et al., 2018). U-Pb zircon dating of granitic rocks from the Yalgoo and Mt Mulgine domes indicates that D_1 deformation occurred principally in the interval 2760-2740 Ma (Zibra et al., 2018). Similar granite-up greenstone-down tectonics (attributed to partial convective overturn) have recently been proposed to account for early (D_1) deformation in the Eastern Goldfields Superterrane (Jones et al., 2020), including a layer-parallel S_1 fabric accredited to doming-related layer-parallel shearing, as identified by this study.

10.2.5 D_2 deformation

D_2 deformation is localised in the southwest of the study area and comprises NW-SE oriented F_2 axes that refold multiple D_1 structures including the Rothsay Dome but is not associated with a fabric (Fig. 10.2f). There are two possible explanations for D_2 deformation. Firstly, D_2 may represent an episode of localised NE-SW horizontal shortening that is only manifested in rocks in the southwest of the study

area and is absent elsewhere. An alternative, preferred interpretation is that D_2 structures signify fold superposition related to the asynchronous emplacement of granitic domes, in which early formed D_1 structures formed during the main period of doming (i.e., the Rothsay Dome) have subsequently been refolded by the diapiric emplacement of an adjacent late-formed dome. This is supported by the orientation of F_2 axes, which are approximately parallel to the margin of the Mongers Dome to the southwest of the Rothsay area (Fig. 2.9). Although the Mongers Dome is currently undated, Zibra et al. (2018; 2020) attributed its emplacement to the same period of diapirism as other domal structures in the area, including the Rothsay, Mt Mulgine and Yalgoo domes (Zibra et al., 2018; 2020). This explanation may also account for the absence of an axial-planar fabric associated with D_2 and the spatially restricted nature of D_2 structures around the peripheries of the Mongers Dome.

10.2.6 D_3 deformation

The D_3 deformational event involved pervasive east-west horizontal shortening across the entire study area, reflecting a shift from dominantly vertical tectonics (D_1, D_2?) to dominantly horizontal tectonics. This shortening episode resulted in metre to map-scale F_3 folds in Chulaar Group and Mougooderra Fm rocks, including a major 10 km-scale fold in the northeast and refolding of F_1-F_2 folds in the Rothsay area. D_3 is characterised by a pervasive, steeply dipping and locally well-developed S_3 foliation that is axial planar to F_3 folds, where present, and overprints the D_1 dome-and-keel architecture of the area. The S_3 foliation corresponds with the 'orogenic fabric' described in the southwestern Murchison Domain by Zibra et al. (2020) and is sub-parallel to the north-striking fabric that typifies the western Yilgarn Craton.

Zibra (2020) attributes this episode of regional E-W shortening to the ca. 2730-2650 Ma Neoarchaean Yilgarn Orogeny and distinguishes four localised "pulses" of horizontal shortening during this orogenic episode, identified in the central and northeastern parts of the Murchison Domain. The S_3 foliation is sub-parallel to the Mulloo Shear Zone, situated to the northeast of the study area, which was active during the emplacement of the Lakeside Pluton (Big Bell Suite) at ca. 2700 Ma (D_3 event; Zibra, 2020). This provides a tentative indication of the timing of D_3 deformation (Fig. 10.1), although the duration of the D_3 event is not clear and may have persisted until the D_4 event described below. This is broadly similar to the ca. 2685 ± 15 Ma age calculated for peak metamorphism in Mougooderra Fm and Chulaar Group rocks (Parmenter et al., 2020). The change in tectonic style from vertical processes associated with gravitational instability, to regional bulk horizontal shortening, is considered to represent the progressive strengthening of continental lithosphere during the Neoarchaean (Zibra, 2020).

10.2.7 D_4 deformation

D_4 deformation involved the localisation of strain during the late stages of E-W shortening and is represented by a network of five NNE to NNW-striking, steeply-dipping (50-80°) reverse shear zones in the YSGB (Fig. 10.2h). These structures are commonly located along major lithological contacts, such as the contact between the Chulaar Group and Mougooderra Fm. The four principal D_4 shear zones comprise the Mougooderra Shear Zone (MSZ), Chulaar Shear Zone (CSZ), Rothsay Shear Zone (RSZ) and the unexposed Enchanted Shear Zone (ESZ), the latter of which may be connected to the MSZ along strike. A further less extensive D_4 structure, the Winddine Well Shear Zone (WWSZ) is interpreted to be a second order structure in the footwall of the MSZ (Fig. 10.2h). D_4 shear zones unequivocally display a significant reverse component of shear, including map-scale imbricate structures along the southern portions of the sub-parallel RSZ and CSZ (Fig. 10.2h), and exhibit oblique down-dip L_4 stretching mineral lineations and cm to metre-scale F_4 shear-parallel folds. Shearing along D_4 structures was not associated with magmatism, and several D_4 shear zones are host to lode-gold mineralisation, most notably the MSZ and RSZ.

The D_4 structures distinguished in the YSGB are markedly similar to a network of late-orogenic, upper crustal, west-dipping reverse shear zones in the northeastern Murchison, collectively identified as the "Cue shear zone network" by Zibra (2020). Structures comprising the Cue shear zone network truncate earlier N-S trending structures (equivalent to D_3 in this study) and are interpreted to coincide with the late stages of the Yilgarn Orogeny (Zibra et al., 2017b; Zibra, 2020). D_4 shear zones in the YSGB are also comparable to the north-striking gold-mineralised Salt River Shear Zone, located west of the Yalgoo Dome, and characterised by a steeply-dipping mylonitic fabric, steeply plunging mineral lineation and reverse kinematics (Zibra et al., 2020). The steeply east-dipping Salt River Shear Zone comprises Mougooderra Fm footwall rocks and stratigraphically lower, dominantly volcanic hangingwall rocks along much of its length (Zibra et al., 2020), ostensibly reflecting a mirror image of the west-dipping MSZ situated on the opposite flank of the Yalgoo Dome (Fig. 2.9).

The late stages of brittle-ductile deformation along the MSZ have been constrained at 2623 ± 34 Ma from U-Pb monazite dating of mineralisation deformed into the shear zone (Section 9.6.5). This age is at the lower margin of the postulated 2660-2624 Ma interval for deformation along the Cue shear zone network in the northeast Murchison Domain (Van Kranendonk et al., 2013; Zibra, 2020).

10.2.8 D_5 deformation

The D_5 event is represented by a series of ENE-trending, sub-vertical D_5 faults that dissect several D_4 shear zones in the study area, including the RSZ, ESZ and CSZ (Fig. 10.2i). These faults typically exhibit sinistral offsets, and some are accompanied by fault drag of surrounding units, best exemplified in the Rothsay area (Section 3.5.7). In the southern YSGB, ENE-striking felsic pegmatite dykes are commonly oriented parallel to D_5 faults and crosscut D_4 structures, thus are associated with D_5 deformation. In turn, a direct spatial association between pegmatite dykes and Walganna Suite granitoids in the Rothsay area indicates that the Seeligson Monzogranite intruded at this time and dissected the greenstone belt (Fig. 10.2i). The 2626 ± 6 Ma crystallisation age of the Seeligson Monzogranite (Wingate et al., 2014) provides an approximate time constraint on the age of felsic pegmatites and D_5 faults.

10.2.9 D_6 deformation

D_6 deformation in the YSGB is recorded by a group of NNE-oriented brittle faults that typically exhibit dextral offsets of the order of several hundred metres and dissect all earlier structures, including D_4 shear zones and D_5 faults (Fig. 10.2j). The sub-surface orientation of these faults is not clear due to an absence of outcrop along them. The timing of D_6 faulting is not constrained, although cross-cutting relations indicate that D_6 faults occurred after ca. 2620 Ma. D_6 faults are post-dated by a period of regional extension resulting in the intrusion of several orientations of sub-vertical dolerite dykes, which dissect all other lithologies and structures in the study area. Locally, dolerite dykes have intruded along pre-existing structural weaknesses, such as the MSZ at the Silverstone deposit. These dolerite dykes are prevalent across the Murchison Domain and Yilgarn Craton and are widely regarded as Proterozoic in age (e.g., Watkins and Hickman, 1990; Ivanic et al., 2010; Ivanic, 2019).

10.3 Implications for Geodynamic Models

The interpretation of geodynamic settings in which Archaean rocks formed is controversial (e.g., Cawood et al., 2018; Section 2.5), in particular regarding the application of uniformitarian processes, principally modern-style plate tectonics, to the Archaean. End-member Archaean tectonic models consist of plume-related models, commonly invoking vertical tectonic processes (e.g., Barnes et al., 2012; Van Kranendonk et al., 2013; Mole et al., 2019) and models implicating plate tectonic processes, typically subduction-accretion tectonics (e.g., Arndt, 2013; Hastie et al., 2016; de Wit et al. 2018; Goscombe et al., 2019). In addition to these there are various mixed tectonic models involving plume-plate interaction (e.g., Czarnota et al., 2010; Witt et al., 2018).

The Archaean geodynamic debate is epitomised by recent studies in the Murchison Domain (Section 2.5.2), which include the proposal of an autochthonous, plume-related model (Van Kranendonk et al., 2013), a subduction-related model (Wyman, 2019), and a mixed plate-plume model (Wyman & Kerrich, 2012). New data presented in this study have implications on the validity of existing endmember geotectonic models for the Murchison Domain.

According to the autochthonous model of Van Kranendonk et al. (2013), a major plume event triggered the onset of crust formation across the Murchison Domain at 2825-2820 Ma, which approximates to the age determined for Chulaar Group volcanic rocks in this study. Van Kranendonk et al. (2013) suggest that plume magmatism is indicated by the co-occurrence of komatiites and komatiitic basalts within the supracrustal succession, including ca. 2820 Ma Al-depleted komatiites at the base of the Norie Group (Barley et al., 2000), and the large, voluminous ca. 2815 Ma Meeline Suite of mafic-ultramafic intrusions. In line with recent petrographic and geochemical work in the northeast Murchison Domain (Wyman, 2019; Lowrey et al., 2020), the results presented in this study contradict several aspects of the plume model of Van Kranendonk et al. (2013).

Firstly, units previously mapped and described as komatiites in the YSGB, based on the apparent occurrence of olivine spinifex (Watkins & Hickman, 1990), have been reinterpreted as pyroxene spinifex-textured basalts (Section 5.3.5), with maximum MgO contents of ~16.2 wt. % (typically <12.0 wt.%; Section 6.4.1) that preclude a *sensu stricto* komatiite classification (e.g., Kerr & Arndt, 2001). As a result, estimates of parental magma temperatures are considerably lower than previously inferred (e.g., Watkins & Hickman, 1990; Barley et al., 2000). These findings concur with recent studies in the northeast Murchison Domain, where mapped komatiites and komatiitic basalts have likewise been reclassified as spinifex-textured basalts comprising various geometries of pyroxene spinifex (Lowrey et al., 2017; 2020). This includes the basal Al-depleted komatiites that Van Kranendonk et al. (2013) used to infer initial plume magmatism, which have been reclassified as picrites containing cumulate olivine (Wyman, 2019). Consequently, no *sensu stricto* komatiites are currently distinguished in the Murchison Domain, including the YSGB, invalidating a crucial piece of evidence used in favour of plume tectonics by Van Kranendonk et al. (2013). In contrast, locally abundant komatiites in supracrustal belts of the Eastern Goldfields Superterrane have been used as unequivocal evidence of Neoarchaean plume-related magmatism in the area (e.g., Arndt et al., 2008; Czarnota et al., 2010; Barnes et al., 2012).

The trace element geochemistry of Chulaar Group volcanic rocks is inconsistent with direct derivation from a plume-related source, as even the most compositionally primitive samples display ubiquitous, markedly negative Nb-Ta and Ti anomalies (Section 7.2). Some authors have attributed such anomalies

to crustal contamination of plume-derived magmas (e.g., Barnes & Van Kranendonk, 2014). However, trace element modelling indicates that many volcanic samples that exhibit these anomalies have undergone little to no crustal contamination (e.g., Chulaar Subgroup 2; Section 7.5). Negative HFSE anomalies are instead considered to be an inherent feature of parental magmas, potential reflecting metasomatism of mantle source rocks.

Despite limited evidence in supracrustal rocks, the emplacement of vast, anhydrous mafic-ultramafic intrusive complexes of the Meeline Suite in the Murchison Domain, including the extensive Windimurra Complex, is compatible with magmatism associated with impingement of a mantle plume (Ivanic et al., 2010; 2017; Van Kranendonk et al., 2013; Ivanic, 2019). The occurrence of komatiites and mafic-ultramafic complexes of the same age in the eastern Yilgarn Craton suggests a craton-wide, plume-related event at this time (Mole et al., 2019). Moreover, the interpreted early (pre-2730 Ma) deformational history of the Murchison Domain, including early extension and granite-up greenstone down tectonics, such as diapirism (Zibra et al., 2018; 2020; this study), is compatible with a plume-related geodynamic setting. The prevalence of early granite-up greenstone-down tectonics is less consistent with a subduction-accretion scenario, in which horizontal tectonic processes would be expected to dominate. The significance of diapirism in the YSGB could have implications on the early structural development, and thus interpreted geodynamic setting, of other parts of the Yilgarn Craton. Other areas may also have experienced early granite-up greenstone-down tectonics but have since been extensively overprinted and obscured by subsequent structures (e.g., Jones et al., 2020), in contrast to the well preserved early structural architecture of the YSGB.

Numerous pieces of evidence have been presented in support of post 2820 Ma subduction-related magmatism, and in turn, a subduction-accretion model for the Murchison Domain (Wyman, 2019). These include indications of a hydrated mantle source for ca. 2800 Ma mafic-ultramafic intrusions (Ivanic et al., 2015b; Wyman, 2019), and the proposed identification of boninite-like rocks that are considered geochemically and texturally comparable to modern boninites found in juvenile arc settings (Wyman & Kerrich, 2012; Lowrey et al., 2020). In this study, major and trace element modelling of fractional crystallisation trends tentatively indicates that the parental magmas of the Warriedar Suite intrusions and some Chulaar Group (Subgroup 3) volcanic rocks were hydrous in nature (Section 7.4). Furthermore, several ‘boninite-like’ rocks have also been identified in the Chulaar Group using the same classification schemes as Lowrey et al. (2020) (Section 7.6). Notably, in the case of this study and Lowrey et al. (2020), boninite-like samples predominantly plot at the margins of the boninite classification. The results presented in this thesis therefore indicates that the hydrous mantle sources and boninite-like rocks occur over a greater extent of the Murchison Domain than previously constrained.

Logically, the combination of hydrous parental magmas, unequivocal negative Nb-Ta and Ti anomalies, and the possible occurrence of boninite-like rocks, could suggest mantle source rocks that have been metasomatised by a subduction-derived fluid or melt (Smithies, 2002). However, a fundamental issue with the subduction-accretion model proposed by Wyman (2019) is that it is based entirely on geochemical data and lacks crucial structural and tectonic constraints. This sort of approach has been criticised by some Archaean researchers (e.g., Bédard, 2006; Hamilton, 2011) as geochemical fingerprinting is considered to be demonstrably equivocal and open to non-unique interpretations (Moyen & Laurent, 2018). For example, on a purely geochemical basis, it is plausible that the above signatures were derived from various other subduction-like processes that have previously been implicated in Archaean terranes, such as dripduction and subcretion (Moyen & Laurent, 2018). In specific regard to boninite-like rocks in Archaean terranes, Smithies (2002) advises that "the tectonic setting of rocks with boninite-like compositions must be interpreted with caution".

Definitive structural criteria supporting a subduction-accretion model are also lacking in the Murchison Domain (Van Kranendonk et al., 2013). For example, there is a distinct absence of major, crustal scale thrusts and regional scale faults in the Murchison Domain, as would be expected in subduction and modern-style plate tectonic scenarios (Van Kranendonk et al., 2013). This is particularly pertinent in the southwest Murchison Domain and the YSGB, where a dome-and-keel architecture dominates, unlike the more linear, fault-bounded terranes of the eastern Yilgarn Craton. This dome and keel architecture is attributed to diapirism during a period of tectonic quiescence at ca. 2750 Ma (Zibra et al., 2020). Crucially, no penetrative fabrics pre-dating this event have been identified in this study, as may be expected for a major episode of subduction and associated convergence at ca. 2820-2800 Ma. The short timescale for greenstone belt formation indicated by this study (Section 8.5.4) could be compatible with either non-uniformitarian plume-related models (e.g., plume-lid; Sizova et al., 2018) or plate tectonic-style subduction-accretion models (e.g., Goscombe et al., 2019).

In summary, the data presented in this study indicate that whilst existing plume-related (Van Kranendonk et al., 2013) or subduction-accretion (Wyman, 2019) models partly account for some features, there are also significant inconsistencies between the data and both models. In concluding this discussion, it is clear that existing geodynamic models do not fully account for, and adequately explain, the distinctive geochemistry, structure and distribution of rocks that characterise the Murchison Domain.

10.4 Future Work

This project documents the most complete synthesis of the stratigraphic, structural and geochemical development of rocks in the YSGB, and the formation of lode-gold deposits in the area, to date. However, there are several opportunities to build upon the work presented, and several questions raised by the findings of this study.

An aim for future work should be to constrain the nature of the unexposed contact at the base of the Willowbank Clastics in the southwest of the study area, following the recognition that this unit forms part of the Mougooderra Fm (Section 8.5.1). This may have crucial implications for mineralisation, as elsewhere in the belt, concealed, gold mineralised D_4 shear zones are localised along this basal contact. Alternatively, determining whether the contact is conformable or unconformable would provide further insights into the early development of the belt and deposition of the Mougooderra Fm. The location of the contact could be determined through systematic, detailed mapping in poorly exposed areas proximal to the base of the Willowbank Clastics, and subsequent drilling could determine the nature and geometry of the contact.

Further high-precision U-Pb zircon dating would be beneficial to better constrain the timescale represented by Chulaar Group volcanism. A unit at the base of the Chulaar Group would be a good target for dating, for example, the 10 m-thick porphyritic dacite unit in the Macs Well Clastics located in the Rothsay area. Geochemical and petrographic analysis of this unit (sample ROTH062) indicates a high zircon content that would likely yield abundant primary magmatic zircons for geochronological analysis. The hybrid platy-acicular geometry of pyroxene spinifex texture identified in this study (Section 5.3.5.6) has not previously been recorded and warrants further petrographic and geochemical investigation, following the recent discovery of platy pyroxene spinifex in the region (Lowrey et al., 2017). Detailed mapping and sampling of units exhibiting this texture would allow an assessment of the relationship between this and other forms of spinifex and give insights into its formation.

The proposed early episode of diapirism in the southwest Murchison Domain (e.g., Zibra et al., 2020) could be corroborated through diamond or reverse circulation (RC) drilling in the poorly exposed core of the Rothsay Dome. This would determine whether an unexposed granitic core occurs at depth, as predicted by this study and consistent with a diapiric model of formation. Moreover, the identification of a granitic stock at the core of the Rothsay Dome may have significant economic implications, as the exposed granitic core of the neighbouring Mt Mulgine Dome hosts significant W-Mo mineralisation, and is interpreted by this study to have provided abundant, favourable structural traps for subsequent lode-gold mineralisation (Section 9.3.6.1). The application of geophysical techniques, such as a gravity survey, could provide an indication of the location of the inferred intrusion, and an estimation of its

depth could be determined by geophysical inversion. Drilling in this area would also allow the stratigraphy of the poorly exposed lower Macs Well Clastics to be better constrained.

From a regional perspective, the recently recognised importance of early diapirism/ballooning in the southwest Murchison Domain (this study; Zibra et al., 2020) and the Eastern Goldfields (Jones et al., 2020) warrants a reinterpretation of early-formed structures in other parts of the Yilgarn Craton. In contrast to previous interpretations of early-formed fabrics involving D_1 thrusting or extension (e.g., Swager & Griffin, 1990), these structures may also be explained in terms of diapirism/ballooning and could give an indication of the prevalence of this style of deformation during the early Neoarchaean.

With regard to lode-gold mineralisation, an aim of future work should be to undertake further detailed paragenetic and stable isotope analysis at additional lode-gold deposits along the MSZ. This would enable the remarkable uniformity and lateral continuity of gold parageneses identified along the MSZ in this study to be further tested and potentially extrapolated along strike. Furthermore, a structural and paragenetic study of mineralisation at the unstudied Rothsay gold deposit, along the RSZ, would crucially allow an assessment of whether the style and paragenesis of lode-gold mineralisation present is comparable to other deposits along similar D_4 structures. This would help determine whether most, if not all, lode-gold mineralisation along D_4 shear zones in the belt formed as part of the same mineralising event, during the late stages of horizontal shortening and reverse shear.

A comprehensive fluid inclusion study of lode-gold mineralisation along the MSZ would be beneficial, to provide insights into the composition and temperatures of mineralising fluids and potential depositional mechanisms. Unfortunately, fluid inclusions in quartz from the Silverstone deposit were too small for analysis in this study, therefore further sampling from Silverstone or an alternative deposit is required. In combination with the quartz $\delta^{18}O$ data presented in this study, an estimation of fluid temperatures would allow the original $\delta^{18}O$ compositions of mineralising fluids to be calculated and a thorough evaluation of the source of hydrothermal fluids could be carried out (i.e., role of metamorphic vs. magmatic fluids). The new ca. 2625 Ma age for lode-gold mineralisation at Silverstone presented in Section 9.6.5 is consistent with an ostensibly young (ca. 2620-2630 Ma) age for lode-gold deposits in the western Yilgarn Craton, relative to the more variable and older ages of deposits in the east. Further dating of lode-gold deposits in the western Murchison Domain, such as the Deflector Au deposit to the west of the YSGB, is required to test the validity of the apparently young age for lode-gold deposits in the region and to evaluate the temporal association with low-Ca granitic magmatism.

10.5 Conclusions

The Yalgoo-Singleton greenstone belt (YSGB) consists of a typical Archaean supracrustal succession of volcanic, volcaniclastic and sedimentary rocks, extensively intruded by mafic-ultramafic layered sills and surrounded by successive generations of granitoid intrusions. A revised stratigraphy is proposed for the YSGB, comprising locally exposed Gossan Hill Fm basement rocks, overlain by dominantly mafic-ultramafic volcanic rocks assigned to the Chulaar Group, in turn overlain by the metasedimentary-dominated Mougooderra Fm.

The Chulaar Group is characterised by a succession of variably aphyric, porphyritic, variolitic and pyroxene spinifex-textured basaltic rocks, with interflow BIF, volcaniclastic and minor sedimentary units, largely emplaced in deep (>200 m) submarine conditions. Detailed geological mapping and petrography has locally subdivided the Chulaar Group into four distinct stratigraphic units in the better exposed Rothsay area: the lowermost Macs Well Clastics, Two Peaks Volcanics, Beryl West Volcanics and uppermost Mulga Volcanics. Float mapping used to correlate distinctive marker horizons across poorly exposed areas demonstrates significant lateral continuity of supracrustal units. The Chulaar Group succession is intruded by a network of Warriedar Suite mafic-ultramafic sills, the thickest of which (>250 m) are typified by well-developed compositional layering and occasionally contain map-scale rafts of supracrustal rocks. Many Warriedar Suite sills show remarkable lateral continuity of layering over distances > 20 km, signifying rapid emplacement of magma preceded extensive in-situ fractionation. Warriedar Suite intrusions comprise a significant component (~40%) of the lower supracrustal succession in the YSGB, expressing a characteristic trait of greenstone belts in the Murchison Domain (e.g., Ivanic, 2019). The Mougooderra Fm broadly consists of an upward-fining siliciclastic sequence occupying the centre of the YSGB that locally unconformably overlies Chulaar Group rocks. However, the basal contact is mostly unexposed or highly sheared. Petrographic, geochemical and geochronological data demonstrate that a previously unassigned portion of supracrustal rocks in the southwest of the YSGB (informally assigned to the Willowbank Clastics in this study) are attributed to the Mougooderra Fm, thus increasing the known extent of this formation.

Igneous rocks in the YSGB have invariably been subject to at least upper greenschist facies metamorphism, increasing to lower amphibolite facies in the southwest, and exhibit variable degrees of secondary alteration. Although there is geochemical evidence for remobilisation of the most mobile elements (e.g., K, Rb, Ba), the major and trace element geochemistry of volcanic and intrusive rocks has not been significantly modified by alteration.

Four geochemically distinct volcanic subgroups have been identified within the Chulaar Group and correspond to specific stratigraphic levels. The lowermost Chulaar Subgroup 1 rocks are porphyritic,

markedly LREE-enriched and exhibit trace element ratios that suggest they may have been affected by crustal contamination. Overlying Subgroup 2 rocks are typified by flat to concave LREE-MREE trace element patterns and some samples fit the criteria for boninite-like rocks (e.g., Lowrey et al., 2020). Modelling demonstrates that Subgroup 2 rocks were derived from up to ~40% crustal contamination at low pressures (~1 kbar), although the water content of the parental magma could not be discerned. The geochemistry of overlying Subgroup 3 volcanic rocks is characterised by marked LREE enrichment and are successfully modelled by up to 45% assimilation-fractional crystallisation of a hydrous magma at low pressures (~1 kbar). The uppermost Subgroup 4 volcanic rocks comprise flat to subtly concave trace element patterns, with consistently elevated MgO contents, and several samples that fit the criteria for boninites. Mougooderra Fm volcanic rocks consist of siliceous high-Mg andesites and dacites, which display similar trace element characteristics to cogenetic felsic volcaniclastic rocks. The pronounced negative Nb-Ta and Ti anomalies exhibited by all Chulaar Group and Mougooderra Fm samples, regardless of MgO content, suggests these features are inherited features of the mantle source, and are inconsistent with direct derivation from a plume-related source.

Geochemistry, petrography and field characteristics indicate that Warriedar Suite sills are cogenetic and were likely formed from the same parental magmatic source. Trace element modelling indicates that extensive (up to 80%) fractional crystallisation occurred in some intrusions, compatible with abundant compositional layering. Several Warriedar Suite sills exhibit distinct trends that reflect assimilation-fractional crystallisation of up to 55% and demonstrate that the uppermost portions of these sills are most affected by crustal contamination. Rhyolite-MELTS modelling indicates that sills were emplaced and underwent fractionation at relatively shallow depths (~1 kbar), and trends are best approximated by fractional crystallisation of a hydrous parental magma. This concurs with recent studies that indicate a switch from anhydrous to hydrous magmatism at ca. 2800 Ma (e.g., Wyman, 2019). Markedly positive Zr-Hf anomalies coupled with relatively enriched Nb-Ta anomalies in Warriedar Suite sill top samples are attributed to zircon crystallisation and accumulation. This is potentially enhanced by changes in HFSE compatibility resulting from Ti-magnetite fractionation from a hydrous magma at low pressures.

New SHRIMP U-Pb zircon dating, combined with an existing detrital zircon maximum depositional age (Lu et al., 2016a), indicates that Chulaar Group volcanic rocks were emplaced at ca. 2825-2818 Ma. The new age constraints indicate that the Chulaar Group is temporally equivalent to the Singleton Fm of the Norie Group in the current regional stratigraphic framework (e.g., Lowrey et al., 2020). This correlation is supported by the comparable geochemistry of volcanic rocks in the Chulaar Group and Singleton Fm. This study also documents the first robust age determination of the Mougooderra Fm. Two new SHRIMP U-Pb depositional ages of 2818 ± 3 Ma and 2813 ± 6 Ma for felsic volcaniclastic units,

combined with the reinterpreted 2815 ± 3 Ma crystallisation age of an interbedded dacite (Lu et al., 2016c), indicates that the Mougooderra Fm was deposited at ca. 2816-2810 Ma. The interpreted ca. 2815 Ma depositional age for the Mougooderra Fm is inconsistent with previous ca. 2730 Ma Glen Group correlations, and instead indicates that the Mougooderra Fm is temporally and lithologically comparable to the ca. 2815-2805 Ma Yaloginda Fm (Norie Group) in the northeastern Murchison Domain (cf. Van Kranendonk et al., 2013).

SHRIMP U-Pb zircon dating reveals that the formation of the YSGB occurred over a maximum period of ~15 Ma. This timeframe includes the eruption of a thick volcanic package and deposition of an unconformably overlying metasedimentary succession and is significantly shorter than the more protracted timescales recorded by most greenstone belts. This data implies that other greenstone belts may have formed over such short periods, but that evidence for such rapid development has commonly been removed and obscured by subsequent erosion, metamorphism and deformation.

Rocks in the YSGB record a seven-stage deformational history that details a progression from early bulk extension, to an episode of regional diapirism, followed by bulk shortening and multiple late faulting events:

- D_E: early bulk extension accommodated the emplacement of Chulaar Group volcanic rocks and Warriedar Suite sills. The (partly?) unconformable deposition of the Mougooderra Fm may have resulted from normal faulting during bulk extension or may represent the earliest stages of D_1 diapirism. The Gossan Hill Fm in the YSGB, which represents the local basement, was extended to allow the emplacement of the above units.
- D_1: period of granitic diapirism at ca. 2750 Ma responsible for the formation of multiple coeval domal structures and the prevailing dome-and-keel architecture of the YSGB, consistent with structural studies of neighbouring areas (e.g., Clos et al., 2019a; Zibra et al., 2020). The earliest layer-parallel fabrics in the YSGB, which are also common elsewhere in the Yilgarn Craton, are compatible with D_1 diapirism and do not require an early shortening deformation episode.
- D_2: localised NE-SW shortening in the southwestern YSGB that most likely represents fold superposition related to the asynchronous emplacement of granitic domes, during the late stages of a prolonged episode of diapirism.
- D_3: regional E-W shortening causing refolding of pre-existing structures, outcrop to map-scale folding and the impartation of a N-S trending tectonic fabric across the area. Diapiric doming and fold interference are typically considered to be exclusive processes; however, the Rothsay area demonstrates an example of a diapiric dome (D_1) that has been subjected to fold interference (D_2, D_3) on a comparable scale to that of the original dome.

- D_4: development of major NNE to NNW-striking, steeply-dipping (>60°) shear zones that consistently demonstrate reverse kinematics and reflect E-W shortening. D_4 structures are commonly focussed on major lithological contacts, such as the contact between Chulaar Group and Mougooderra Fm rocks.
- D_5: ENE-trending faulting coeval with the intrusion of the Seeligson Monzogranite and associated Li-bearing pegmatitic dykes.
- D_6: localised NNE-trending brittle faulting.
- Post-D_6: intrusion of cross-cutting doleritic dykes, likely in the Proterozoic, representing the most recent structures in the YSGB.

Gold deposits in the YSGB exhibit characteristics that are consistent with an orogenic-lode gold classification, including a ubiquitous structural control on mineralisation. Lode-gold deposits are principally hosted by D_4 shear zones, mostly along the first order MSZ, and were emplaced during the late stages of reverse displacement along host D_4 structures. Structural and kinematic analysis at lode-gold deposits in the YSGB demonstrates fault-valve behaviour, whereby high pore-fluid pressures facilitated cyclic, reverse failure along steeply-dipping, unfavourably oriented structures. Lode-gold deposits along the MSZ exhibit a progressive four-stage paragenetic sequence that documents profound mineralogical changes and comprises three auriferous phases: early pyrite-electrum, overprinted by arsenopyrite-electrum, succeeded by auriferous base metal sulphides associated with various Sb-sulphide minerals.

Lode-gold mineralisation in the YSGB was likely emplaced as part of a single mineralising event, as suggested by the striking consistency of structural style, ore paragenesis and stable isotope signature of ore and gangue minerals at deposits along the MSZ. In particular, the consistency of stable isotope data in mineralised rocks show great potential for use as vectors towards mineralisation in a particularly challenging exploration environment (e.g., Petrella et al., 2020). The 2623 ± 34 Ma $^{207}Pb/^{206}Pb$ age of gold-related monazite at the Silverstone deposit represents the first age for lode-gold mineralisation in the YSGB and falls within the 2660-2620 Ma interval comprising most dated lode-gold deposits across the Yilgarn Craton. The new dating discloses an apparent temporal, but not necessarily genetic, association between lode-gold mineralisation and post-tectonic low-Ca granitoids, such as the Walganna Suite intrusions that surround the YSGB.

Reference List

An, F. & Zhu, Y. (2010). Native antimony in the Baogutu gold deposit (west Junggar, NW China): Its occurrence and origin. *Ore Geology Reviews*, 37, p. 214-223.

Anderson, E.M. (1905). The dynamics of faulting. *Transactions of the Edinburgh Geological Society*, 8(3), p. 387-402.

Anhaeusser, C.R. (1981). Geotectonic evolution of the Archaean successions in the Barberton mountain land, South Africa. In: Kröner, A. (ed.) Precambrian Plate Tectonics, Elsevier Science, Amsterdam, p. 137-160.

Anhaeusser, C.R. (2006). Ultramafic and mafic intrusions of the Kaapvaal Craton. In: Johnson, M.R., Anhaeusser, C.R. & Thomas, R.J. (eds.) *Geology of South Africa*, Geological Society of South Africa, Johannesburg and Council for Geoscience, Pretoria, p. 95–134.

Anhaeusser, C.R. (2014). Archaean greenstone belts and associated granitic rocks – A review. *Journal of African Earth Sciences,* 100, p. 684-732.

Archibald, N.J., Bettenay, L.F., Bickle, M.J. & Groves, D.I. (1981). Evolution of Archaean crust in the Eastern Goldfields Province of the Yilgarn Block, Western Australia. In: Glover, J.E. & Groves, D.I. (eds.) *Archaean Geology, 2nd International Archaean Symposium, Perth, 1980, Geological Society of Australia Special Publication,* 7, p. 491-504.

Arndt, N.T., Naldrett, A.J. & Pyke, D.R. (1977). Komatiitic and iron-rich tholeiitic lavas of Munro Township, Northeast Ontario. *Journal of Petrology*, 18, p. 319–369.

Arndt, N.T. & Nisbet, E.G. (1982). What is a komatiite? In: Arndt, N.T. & Nisbet, E.G. (eds.) *Komatiites*, George Allen and Unwin, London, p. 19-27.

Arndt, N.T. & Fowler, A. (2004). Textures in komatiites and variolitic basalts. In: Eriksson, P.G., Altermann, W., Nelson, D.R., Mueller, W.U. & Catuneanu, O. (eds.) *The Precambrian Earth: tempos and events*, Elsevier Science, p. 298-311.

Arndt, N.T., Lesher, C.M. & Barnes, S.J. (2008). *Komatiite*. Cambridge University Press, 488 pp.

Arndt, N.T. (2013). Formation and Evolution of the Continental Crust. *Geochemical Perspectives*, 2(3), p. 405–533.

Asimow, P.D. & Ghiorso, M.S. (1998). Algorithmic modifications extending MELTS to calculate subsolidus phase relations. *American Mineralogist*, 83(9–10), p. 1127–1132.

Ayer, J., Amelin, Y., Corfu, F., Kamo, S., Ketchum, J., Kwok, K. & Trowell, N. (2002). Evolution of the southern Abitibi greenstone belt based on U–Pb geochronology: autochthonous volcanic construction followed by plutonism, regional deformation and sedimentation. *Precambrian Research*, 115, p. 63–95.

Baker, T., Bertelli, M., Blenkinsop, T., Cleverley, J. S., McLellan, J., Nugus, M. & Gillen, D. (2010). P-T-X Conditions of Fluids in the Sunrise Dam Gold Deposit, Western Australia, and Implications for the Interplay between Deformation and Fluids. *Economic Geology*, 105(5), p. 873–894.

Ballhaus, C., Fonseca, R.O.C., Munker, C., Kirchenbaur, M. & Zirner, A. (2015). Spheroidal textures in igneous rocks—textural consequences of H_2O saturation in basaltic melts. *Geochimica et Cosmochimica Acta*, 167, p. 241–252.

Bark, G., Boyce, A., Fallick, A. & Weihed, P. (2020). Fluid and metal sources in the Fäboliden hypozonal orogenic gold deposit, Sweden. *Mineralium Deposita*, 16 pp.

Barker, S. L. L., Dipple, G. M., Hickey, K. A., Lepore, W. A. & Vaughan, J. R. (2013). Applying stable isotopes to mineral exploration: Teaching an old dog new tricks. *Economic Geology*, 108(1), p. 1-9.

Barley, M.E., Kerrich, R., Reudavy, I. & Xie, Q. (2000). Late Archaean Ti-rich, Al-depleted komatiites and komatiitic volcaniclastic rocks from the Murchison Terrane in Western Australia. *Australian Journal of Earth Sciences*, 47, p. 873–883.

Barnes, S.-J. & Often, M. (1990). Ti-rich komatiites from northern Norway. *Contributions to Mineralogy and Petrology*, 105, p. 42-54.

Barnes, S.-J., Maier, W.D. & Curl, E.A. (2010). Composition of the marginal rocks and sills of the Rustenburg Layered Suite, Bushveld Complex, South Africa: implications for the formation of the platinum-group element deposits. *Economic Geology*, 105, p. 1491–1511.

Barnes, S.J., van Kranendonk, M.J. & Sonntag, I. (2012). Geochemistry and tectonic setting of basalts from the Eastern Goldfields Superterrane. *Australian Journal of Earth Sciences*, 59, p. 707–735.

Barnes, S.J. & Van Kranendonk, M.J. (2014). Archean andesites in the east Yilgarn craton, Australia: Products of plume-crust interaction? *Lithosphere,* 6(2), p. 80-92.

Bateman, R. & Hagemann, S. (2004). Gold mineralisation throughout about 45 Ma of Archaean orogenesis: protracted flux of gold in the Golden Mile, Yilgarn craton, Western Australia. *Mineralium Deposita,* 39, p. 536-559.

Baxter, J.J., Lipple, S.L. & Marston, R.J. (1983). Kirkalocka, Western Australia: Geological Survey of Western Australia, 1:250,000 Geological Series Explanatory Notes.

Baxter, J.L. & Lipple, S.L. (1985). Perenjori, Western Australia. Geological Survey of Western Australia, 1:250,000 Geological Series SH/50-6 Explanatory Notes.

Bédard, J.H. (2001). Parental magmas of the Nain Plutonic Suite anorthosites and mafic cumulates: a trace element modelling approach. *Contributions to Mineralogy and Petrology*, 141, p. 747-771.

Bédard, J.H. (2006). A catalytic delamination-driven model for coupled genesis of Archaean crust and sub-continental lithospheric mantle. *Geochimica et Cosmochimica Acta*, 70, p. 1188–1214.

Bédard, J.H. (2010). Falsification of the plate tectonic hypothesis for genesis of Archaean volcanic and plutonic rocks, and an outline of possible alternative mechanisms. In: Tyler, I.M. & Knox-Robinson, C.M. (eds.) *Fifth International Archaean Symposium Abstracts*, Geological Survey of Western Australia, Record 2010/18, p. 151-152.

Bédard, J.H., Harris, L.B. & Thurston, P.C. (2013). The Hunting of the SnArc. *Precambrian Research*, 229, p. 20–48.

Begg, G.C., Griffin, W.L., O'Reilly, S.Y. & Napatov, L.M. (2010). Archean cratonic architecture: implications for the Yilgarn and Superior Provinces. *Yilgarn-Superior Workshop – Abstracts, Fifth Archean Symposium, 10 September 2010*. Geological Survey of Western Australia Record 2010/20, p. 1–3.

Belousova, E.A., Griffin, W.L., Begg, G. & O'Reilly. (2010). The TerraneChron® approach to crustal evolution studies and implications for continental growth. In: Tyler, I.M. & Knox-Robinson, C.M. (eds.) *Fifth International Archaean Symposium Abstracts*, Geological Survey of Western Australia, Record 2010/18, p. 44-46.

Bickle, M.J., Bettenay, L.F., Boulter, C.A., Groves, D.I. & Morant, P. (1980). Horizontal tectonic interaction of an Archaean gneiss belt and greenstone terrain involving horizontal tectonics: evidence from the Pilbara Block, Western Australia. *Geology*, 8, p. 525-529.

Bickle, M.J., Nisbet, E.G. & Martin, A. (1994). Archean greenstone belts are not oceanic crust. *Journal of Geology*, 102, p. 121–138.

Binns, R.A., Gunthorpe, R.J. & Groves, D.I. (1976). Metamorphic patterns and development of greenstone belts in the Eastern Yilgarn Block, Western Australia. In: B.F. Windley (ed.) *The Early History of the Earth*, John Wiley & Sons, London, UK, p. 303–313.

Bleeker, W. (2003). The late Archean record: A puzzle in ca. 35 pieces. *Lithos,* 71, p. 99–134.

Blenkinsop, T.G., Fedo, C.M., Bickle, M.J., Eriksson, K.A., Martin, A., Nisbet, E.G. & Wilson, J.F. (1993). Ensialic origin for the Ngezi Group, Belingwe greenstone belt, Zimbabwe. *Geology*, 21, p. 1135–1138.

Blenkinsop, T.G., Doyle, M. & Nugus, M. (2015). A unified approach to measuring structures in orientated drill core. In: Richards, F. L., Richardson, N. J., Rippington, S. J., Wilson, R.W. & Bond, C. E. (eds), *Industrial Structural Geology: Principles, Techniques and Integration*. Geological Society, London, Special Publications, 421, 10 pp.

Blenkinsop, T.G., Oliver, N.H.S., Dirks, P.G.H.M., Nugus, M., Tripp, G. & Sanislav, I. (2020a). Structural geology applied to the evaluation of hydrothermal gold deposits. *Reviews in Economic Geology*, 21, p. 1-23.

Blenkinsop, T.G., Tripp, G.I., Price, J.J. & Nugus, M. (2020b). Stratigraphic and structural controls on Archean lode-gold deposits. *Geological Society of America Conference 2020*, Abstract, in press.

Blewett, R.S. (2002). Archaean tectonic processes: a case for horizontal shortening in the North Pilbara granite–greenstone terrane, Western Australia. *Precambrian Research*, 113, p. 87–120.

Blewett, R.S., Cassidy, K.F., Champion, D.C., Henson, P. A., Goleby, B.R., Jones, L. & Groenewald, P. B. (2004a). The Wangkathaa Orogeny: an example of episodic regional 'D2' in the late Archaean Eastern Goldfields Province, Western Australia. *Precambrian Research,* 130, p. 139-159.

Blewett, R.S., Shevchenko, S. & Bell, B. (2004b). The North Pole Dome: a non-diapiric dome in the Archaean Pilbara Craton, Western Australia. *Precambrian Research,* 133, p. 105-120.

Borradaile, G.J. (1976). “Structural facing” (Shackleton’s rule) and the Palaeozoic rocks of the Malaguide Complex near Velex Rubio, SE Spain. In: *Proceedings of the Koninklijke Nederlandse Akademie van Wetenschappen*, Amsterdam, Series B, 79(5), p. 330-336.

Bradley, D.C. (2011). Secular trends in the geologic record and the supercontinent cycle. *Earth-Science Reviews*, 108, p. 16-33.

Brown, S.M., Fletcher, I.R., Stein, H.J., Snee, L.W. & Groves, D.I. (2002). Geochronological constraints on pre-, syn- and post- mineralization events at the Cleo deposit, Eastern Goldfields Province, Western Australia. *Economic Geology*, 97, p. 541-559.

Brown, M. (2010). When did one-sided subduction begin on Earth? The metamorphic record and modelling. In: Tyler, I.M. & Knox-Robinson, C.M. (eds.) *Fifth International Archaean Symposium Abstracts*, Geological Survey of Western Australia, Record 2010/18, p. 176-179.

Brown, M. & Johnson, T.E. (2018). Secular Change in Metamorphism and the Onset of Global Plate Tectonics. *American Mineralogist*, 103 (2), p. 181–196.

Bucci, L.A., Hagemann, S.G., Groves, D.I. & Standing, J.G. (2002). The Archean Chalice gold deposit: a record of complex, multistage, high-temperature hydrothermal activity and gold mineralisation associated with granitic rocks in the Yilgarn Craton, Western Australia. *Ore Geology Reviews*, 19, p. 23-67.

Butt, C.R.M. (1981). The nature and origin of the lateritic weathering mantle, with particular reference to Western Australia. In: Doyle, H.A., Glover, J.E. & Groves, D.I. (eds.) *Geophysical prospecting in deeply weathered terrains*, University of Western Australia, Geology Department and Extension Service, Publication No. 6, p. 11-29.

Cann, J. R. (1970). Rb, Sr, Y, Zr and Nb in some ocean floor basaltic rocks. *Earth and Planetary Science Letters*, 10, p. 7-11.

Cassidy, K.C., Champion, D.C., Krapez, B., Barley, M.E., Brown, S.J.A., Blewett, R.S., Groenewald, P.B. & Tyler, I.M. (2006). A revised geological framework for the Yilgarn Craton, Western Australia. *Geological Survey of Western Australia,* Record 2006/8, p. 1-8.

Cawood, P.A. & Hawkesworth, C.J. (2015). Temporal Relations between Mineral Deposits and Global Tectonic Cycles. *Geological Society, London, Special Publications*, 393 (1), p. 9–21.

Cawood, P.A., Hawkesworth, C.J., Pisarevsky, S.A., Dhuime, B., Capitanio, F.A. & Nebel, O. (2018). Geological Archive of the Onset of Plate Tectonics. *Philosophical Transactions.* Series A, Mathematical, Physical, and Engineering Sciences, 376, (2132).

Champion, D.C. & Cassidy, K.C. (2002). Granites of the northern Murchison Province: their distribution, age, geochemistry, petrogenesis, relationship with mineralisation, and implications for tectonic environment. *AMIRA P482/MERIWA M281 - Yilgarn Granitoids*, p. 5.1–5.54.

Chang, Z., Large, R.R. & Maslennikov, V. (2008). Sulfur isotopes in sediment-hosted orogenic gold deposits: Evidence for an early timing and a seawater sulfur source. *Geology*, 36, p. 971-974.

Chauvet, A. (2019). Structural control of ore deposits: The role of pre-existing structures on the formation of mineralised vein systems. *Minerals*, 9(56), 22 pp.

Ciborowski, T.J.R., Kerr, A.C., McDonald, I., Ernst, R.E. & Minifie, M.J. (2013). The geochemistry and petrogenesis of the Blue Draw Metagabbro. *Lithos*, 174, p. 271–290.

Ciborowski, T.J.R. (2013). The Geochemistry and petrogenesis of the early Proterozoic Matachewan Large Igneous Province. *Unpublished PhD thesis*, Cardiff University, 332 pp.

Clarke, E.D. (1925). The Geology and Mineral Resources of the Yalgoo Goldfield Part II - The Mining Centres of Rothesay and Goodingnow (Payne's Find). *Geological Survey of Western Australia*, Bulletin 86, 41 pp.

Clifford, B.A. (1992). Facies and palaeoenvironment analysis of the Archean volcanic-sedimentary succession hosting the Golden Grove Cu-Zn massive sulphide deposits, Western Australia. Unpublished PhD Thesis, Monash University.

Clos, F., Weinberg, R. & Zibra, I. (2018). Building the Archean continental crust: 300 Ma of felsic magmatism in the Yalgoo dome (Yilgarn Craton). *Geological Survey of Western Australia*, Report 186, 23 pp.

Clos, F., Weinberg, R., Zibra, I. & Fenwick, M. (2019a). Archean diapirism recorded by vertical sheath folds in the core of the Yalgoo Dome, Yilgarn Craton. *Precambrian Research*, 320, p. 391–402

Clos, F., Weinberg, R.F., Zibra, I. & Schwindinger, M., (2019b). Magmatic and anatectic history of a large Archean diapir: Insights from the migmatitic core of the Yalgoo Dome, Yilgarn Craton. *Lithos*, 338–339, p. 18–33.

Collins, W.J. (1989). Polydiapirism of the Archaean Mt. Edgar Batholith, Pilbara Block, Western Australia. *Precambrian Research*, 43, p. 41–62.

Collins, W.J., Van Kranendonk, M.J. & Teyssier, C. (1998). Partial convective overturn of Archaean crust in the east Pilbara Craton, Western Australia: Driving mechanisms and tectonic implications. *Journal of Structural Geology*, 20, p. 1405–1424.

Colvine, A.C., Andrews, A.J., Cherry, M.E., Durocher, M.E., Fyon, A.J., Lavigne, M.J. Jr., Macdonald, A.J., Marmont, S., Poulsen, K.H., Springer, J.S. & Troop, D.G. (1984). An integrated model for the origin of Archean lode gold deposits. *Ontario Geological Survey Open File Report,* 5524, 84 pp.

Condie, K.C. (1986). Origin and early growth rate of continents. *Precambrian Research,* 32, p. 261-278.

Condie, K.C. (1997). Plate Tectonics and Crustal Evolution (Fourth Edition). Oxford, Butterworth Heinemann, p. 99-104.

Condie, K.C. (2003). Incompatible element ratios in oceanic basalts and komatiites: Tracking deep mantle sources and continental growth rates with time. *Geochemistry, Geophysics, Geosystems,* 4, p. 1–28.

Condie, K.C. (2005). High field strength element ratios in Archean basalts: a window to evolving sources of mantle plumes? *Lithos*, 79, p. 491-504.

Condie, K.C. & Kroner, A. (2008). When did plate tectonics begin? Evidence from the geologic record. In: Condie, K.C. & Pease, V. (eds.) When Did Plate Tectonics Begin on Planet Earth? *Geological Society of America Special Paper*, 440, p. 281-294.

Condie, K.C. (2015). Changing tectonic settings through time: Indiscriminate use of geochemical discriminant diagrams. *Precambrian Research,* 266, p. 587-591.

Condie, K.C. (2018). A Planet in Transition: The Onset of Plate Tectonics on Earth between 3 and 2 Ga? *Geoscience Frontiers*, 9 (1), p. 51–60.

Cox, S.F. (2020). The dynamics of permeability enhancement and fluid flow in overpressured, fracture-controlled hydrothermal systems: *Reviews in Economic Geology*, 21, p. 25–82.

Czarnota, K., Champion, D.C., Goscombe, B., Blewett, R.S., Cassidy, K.F., Henson, P.A. & Groenewald, P.B. 2010. Geodynamics of the eastern Yilgarn Craton. *Precambrian Research,* 183, p. 175–202.

Davis, B.K., Blewett, R.S., Squire, R., Champion, D.C. & Henson, P. A. (2010). Granite-cored domes and gold mineralisation: Architectural and geodynamic controls around the Archaean Scotia-Kanowna Dome, Kalgoorlie Terrane, Western Australia. *Precambrian Research,* 183, p. 316–337.

De Joux, A., Thordarson, T., Denny, M., Hinton, R.W. & De Joux, A.J. (2013). U-Pb dating constraints on the felsic and intermediate volcanic sequence of the nickel-sulphide bearing Cosmos succession, Agnew-Wiluna greenstone belt, Yilgarn Craton, Western Australia. *Precambrian Research,* 236, p. 85–105.

de Wit, M.J., Roering, C., Hart, R.J., Armstrong, R.A., de Ronde, C.E.J., Green, R.W.E., Tredoux, M., Peberdy, E. & Hart, R.A. (1992). Formation of an Archaean continent. *Nature*, 357, p. 553–562.

de Wit, M.J. (1998). On Archean granites, greenstones, cratons and tectonics: does the evidence demand a verdict? *Precambrian Research,* 91, p. 181-226.

de Wit, M.J., Furnes, H. & Robins, B. (2011). Geology and tectonostratigraphy of the Onverwacht suite, Barberton Greenstone Belt, South Africa. *Precambrian Research*, 186, p. 1-27.

de Wit, M.J, Furnes, H., MacLennan, S., Doucoure, M., Schoene, B., Weckmann, U., Martinez, U. & Bowring, S. (2018). Paleoarchean bedrock lithologies across the Makhonjwa Mountains of South Africa and Swaziland linked to geochemical, magnetic and tectonic data reveal early plate tectonic genes flanking subduction margins. *Geoscience Frontiers*, 9, p. 603-665.

de Vries, P.W. (2015). Gold and tectonic evolution of the southern end of the Yalgoo-Singleton greenstone belt, Murchison Domain, Western Australia. *Unpublished honours thesis*, University of New South Wales, Australia, 103 pp.

Deng, H., Kusky, T., Polat, A., Wang, C., Wang, L., Li, Y. & Wang, J. (2016). A 2.5 Ga fore-arc subduction-accretion complex in the Dengfeng Granite-Greenstone Belt, Southern North China Craton. *Precambrian Research*, 275, p. 241–264.

DePaolo, D.J. (1981). A neodymium and strontium isotopic study of the Mesozoic calc-alkaline granitic batholiths of the Sierra Nevada and Peninsula Ranges, California. *Journal of Geophysical Research,* 86, p. 10470–10488.

Dewey, J. & Spall, H. (1975). Pre-Mesozoic plate tectonics: How far back in the Earth history can the Wilson Cycle be extended? Penrose Conference Report, *Geology*, 3, p. 422-425.

Dilek, Y., Moores, E.M., Elthon, D. & Nicolas, A. (2000). Ophiolites and oceanic crust: new insights from field studies and the Oceanic Drilling Program. *Geological Society of America Special Papers*, 349, 552 pp.

Dilek, Y. & Polat, A. (2008). Suprasubduction Zone Ophiolites and Archean Tectonics. *Geology*, 36(5), p. 431–432.

Dirks, P.H.G.M. & Jelsma, H.A. (1998). Silicic layer-parallel shear zones in a Zimbabwean greenstone sequence: horizontal accretion preceding doming. *Gondwana Research,* 1, p. 177–193.

Dirks, P.H.G.M., Jelsma, H.A. & Hofmann, A. (2002). Thrust-related accretion of an Archaean greenstone belt in the Midlands of Zimbabwe. *Journal of Structural Geology,* 24, p. 1707-1727.

Doublier, M.P., Thébaud, N., Wingate, M.T.D., Romano, S.S., Kirkland, C.L., Gessner, K., Mole, D.R. & Evans, N. (2014). Structure and timing of Neoarchean gold mineralization in the Southern Cross district (Yilgarn Craton, Western Australia) suggest leading role of late Low-Ca I-type granite intrusions. *Journal of Structural Geology*, 67, p. 205-221.

Drabon, N., Lowe, D. R., Byerly, G. R. & Harrington, J. A. (2017). Detrital zircon geochronology of sandstones of the 3.6–3.2 Ga Barberton greenstone belt: No evidence for older continental crust. Geology, 45(9), p. 803–806.

Duuring, P., Cassidy, K.F. & Hagemann, S.G. (2007). Granitoid-associated orogenic, intrusion-related, and porphyry style metal deposits in the Archean Yilgarn Craton, Western Australia. *Ore Geology Reviews*, 32, p. 157-186.

Egan Street Resources. (2019). Quarterly activities report December 2018, ASX/Media Release 31 January 2019, *Egan Street Resources*, 17 pp.

Epp, T., Walter, B.F., Scharrer, M., Lehmann, G., Henze, K., Heimgartner, C., Bach, W. & Markl, G. (2018). Quartz veins with associated Sb-Pb-Ag±Au mineralization in the Schwarzwald, SW Germany: a record of metamorphic cooling, tectonic rifting, and element remobilization processes in the Variscan belt. *Mineralium Deposita*, 54, p. 281-306.

Ernst, W.G. (2009). Archean plate tectonics rise of Proterozoic supercontinentality and onset of regional episodic stagnant-lid behavior. *Gondwana Research,* 15, p. 243-253.

Ersoy, E.Y. (2013). PETROMODELER (Petrological Modeler): a Microsoft Excel spreadsheet program for modelling melting, mixing, crystallization and assimilation processes in magmatic systems. *Turkish Journal of Earth Sciences*, 22, p. 115-125.

Fadda, S., Fiori, M., Grillo, S. M. & Prochaska, W. (2012). REE Mobilization in Complex Hydrothermal–Metasomatic Systems: Fluid Chemistry Evidence of Albitite And Chlorite-Talc Mineralisation in Central Sardinia, Italy. *Proceedings of the 10th International Congress for Applied Mineralogy* (ICAM), p. 171-178.

Faleiros, A.M., da Cruz Campanha, G.A., Faleiros, F.M. & da Silveira Bello, R.M. (2014). Fluid regimes, fault-valve behaviour and formation of gold-quartz veins -The Morro do Ouro mine, Ribeira Belt, Brazil. *Ore Geology Reviews*, 56, p. 442-456.

Fetherston, J.M., Stocklmayer, S.M. & Stocklmayer, V.C. (2017). Gemstones of Western Australia, Second Edition. *Geological Survey of Western Australia*, Mineral Resources Bulletin 25, 356 pp.

Fischer, R. & Gerya, T. (2016). Regimes of subduction and lithospheric dynamics in the Precambrian: 3D thermomechanical modelling. *Gondwana Research*, 37, p. 53–70.

Forsyth, D. & Uyeda, S. (1975). On the Relative Importance of the Driving Forces of Plate Motion. *Geophysical Journal of the Royal Astronomical Society*, 43, p. 163–200.

Fowler, A.D., Berger, B., Shore, M., Jones, M.I. & Ropchan, J. (2002). Supercooled rocks: development and significance of varioles, spherulites, dendrites and spinifex in Archaean volcanic rocks, Abitibi Greenstone belt, Canada. *Precambrian Research,* 115, p. 311-328.

François, C., Philippot, P., Rey, P. & Rubatto, D. (2014). Burial and exhumation during Archean sagduction in the East Pilbara Granite-Greenstone Terrane. *Earth & Planetary Science Letters*, 396, p. 235–251.

Frisch, W., Meschede, M. & Blakely, R.C. (2011). Plate Tectonics: Continental Drift and Mountain Building. Springer-Verlag Berlin Heidelberg, 212 pp.

Gaboury, D. & Daigneault, R. (2000). Flat vein formation in a transitional crustal setting by self-induced fluid pressure equilibrium—an example from the Geant Dormant gold mine, Canada. *Ore Geology Reviews*, 17(3), p. 155-178.

Gaboury, D. (2019). Parameters for the formation of orogenic gold deposits. *Applied Earth Science*, 128(3), p. 124-133.

Garofalo, P.S., Fricker, M.B., Gunther, D., Bersani, D. & Lottici, P.P. (2014). Physical-chemical properties and metal budget of Au-transporting hydrothermal fluids in orogenic deposits. From: Garofalo, P. S. & Ridley, J. R. (*eds*) *Gold-Transporting Hydrothermal Fluids in the Earth's Crust.* Geological Society, London, Special Publications, 402.

Gee, R.D., Baxter, J.L., Wilde, S.A. & Williams, I.R. (1981). Crustal development in the Archaean Yilgarn Block, Western Australia. In: Glover, J.E. & Groves, D.I. (eds.) *Archaean Geology, 2nd International Archaean Symposium, Perth, 1980*, Geological Society of Australia Special Publication 7, p. 43-56.

Gerya, T. (2019). Geodynamics of the early Earth: Quest for the missing paradigm. *Geology*, 47, p. 1006–1007.

Ghiorso, M.S. & Sack, R.O. (1995). Chemical mass transfer in magmatic processes IV. A revised and internally consistent thermodynamic model for the interpolation and extrapolation of liquid-solid equilibria in magmatic systems at elevated temperatures and pressures. *Contributions to Mineralogy and Petrology*, 119(2–3), p. 197–212

Ghiorso M.S. & Gualda, G.A.R. (2015). An H_2O-CO_2 mixed fluid saturation model compatible with rhyolite-MELTS. *Contributions to Mineralogy and Petrology*, 169, p. 1-30.

Gieré, R. (1993). Transport and deposition of REE in H_2S-rich fluids: evidence from accessory mineral assemblages. *Chemical Geology*, 110, p. 251-268.

Gill, R. (2011). Igneous Rocks and Processes: A Practical Guide. Wiley. 438 pp.

Glover, J.E. & Groves, D.I. (1981). Archaean Geology, *2nd International Archaean Symposium, Perth, 1980*, Geological Society of Australia Special Publication 7, 515 pp.

Goldfarb, R.J., Snee, L.W., Miller, L.D. & Newberry, R.J. (1991). Rapid dewatering of the crust deduced from ages of mesothermal gold deposits. *Nature*, 354, p. 296-298.

Goldfarb, R.J., Groves, D.I. & Gardoll, S. (2001). Orogenic gold and geologic time: a global synthesis. *Ore Geology Reviews*, 18, p. 1-75.

Goldfarb, R.J. & Groves, D.I. (2015). Orogenic gold: common or evolving fluid and metal sources through time. *Lithos*, 233, p. 2–26.

Goscombe, B., Foster, D.A., Blewett, R., Czarnota, K., Wade, B., Groenewald, B. & Gray, D. (2019). Neoarchaean metamorphic evolution of the Yilgarn Craton: A record of subduction, accretion, extension and lithospheric delamination. *Precambrian Research*, 335, p. 1–74.

Gosselin, P. & Dubé, B. (2005). Gold deposits of the world: distribution, geological parameters and gold content. *Geological Survey of Canada*, Open File 4895, 271 pp.

Groenewald, P.B., Morris, P.A. & Champion, D.C. (2003). Geology of the Eastern Goldfields and an overview of tectonic models. *Geoscience Australia Record 2003/28*, p. 63-84.

Groves, D.I. & Phillips, G.N. (1987). The genesis and tectonic control on Archaean gold deposits of the Western Australian shield – A metamorphic replacement model. *Ore Geology Reviews*, 2, p. 287-322.

Groves, D.I. & Mikucki, E.J. (1990). Gold transport and depositional models. In: Groves, D.I. & Bennett, J.M. (eds.) *Gold deposits of the Yilgarn Block, Western Australia: Nature genesis and exploration guides*, 20, p. 277-298.

Groves, D.I. (1993). The crustal continuum model for late-Archaean lode gold deposits of the Yilgarn block, Western Australia. *Mineralium Deposita*, 28, p. 366-374.

Groves, D.I. & Foster, R.P. (1993). Archaean lode gold deposits. In: Foster, R.P. (ed.) *Gold Metallogeny and Exploration* (1st edition). Chapman & Hall, London, p. 63-103.

Groves, D.I., Goldfarb, R.J., Gebre-Mariam, M., Hagemann, S.G. & Robert, F. (1998). Orogenic gold deposits: A proposed classification in the context of their crustal distribution and relationship to other gold deposit types. *Ore Geology Reviews*, 13, p. 7-27.

Groves, D.I., Goldfarb, R.J., Knox-Robinson, C.M., Ojala, J., Gardoll, S., Yun, G.Y., Holyland, P. (2000). Late-kinematic timing of orogenic gold deposits and significance for computer-based exploration techniques with emphasis on the Yilgarn Block, Western Australia. *Ore Geology Reviews*, 17, p. 1-38.

Groves, D.I., Goldfarb, R.J., Robert, F. & Hart, C.J.R. (2003). Gold deposits in metamorphic belts; overview of current understanding, outstanding problems, future research and exploration significance. *Economic Geology*, 98, p. 1-29.

Groves, D.I., Goldfarb, R.J. & Santosh, M. (2016). The conjunction of factors that lead to formation of giant gold provinces and deposits in non-arc settings. *Geoscience Frontiers*, 7, p. 303-314.

Groves, D.I., Santosh, M., Goldfarb, R.J. & Zhang, L. (2018). Structural geometry of orogenic gold deposits: Implications for exploration of world-class and giant deposits. *Geoscience Frontiers*, 9(4), p. 1163-1177.

Groves, D.I. (2019). Orogenic gold deposits: part of a global dynamic conjunction between subduction and gold. *Australian Exploration Geoscience Conference (AEGC) 2019 Extended Abstracts*, p. 1-3.

Gualda G.A.R., Ghiorso M.S., Lemons R.V. & Carley T.L. (2012). Rhyolite-MELTS: A modified calibration of MELTS optimized for silica-rich, fluid-bearing magmatic systems. *Journal of Petrology*, 53, p. 875-890.

Guice, G.L. (2019). Origin and geodynamic significance of ultramafic-mafic complexes in the North Atlantic and Kaapvaal Cratons. *Unpublished PhD thesis*, Cardiff University, 289 pp.

GSWA. (2018). Compilation of Geochronology Information: Geological Survey of Western Australia, Digital Data Package.

Hagemann, S.G. & Lüders, V. (2003). P-T-X conditions of hydrothermal fluids and precipitation mechanism of stibnite-gold mineralization at the Wiluna lode-gold deposits, Western Australia: conventional and infrared microthermometric constraints. *Mineralium Deposita*, 38(8), p. 936–952.

Hallberg, J.A. (1976). A petrochemical study of a portion of the Yilgarn Block, Australia. *Australia CSIRO Mineral Resource Laboratory Report No. FP13*, 35 pp.

Hallberg, J. A. (1983). Geology and mineral deposits of the Leonora Laverton area, northeastern Yilgarn Block, Western Australia*. Geological Survey of Western Australia*, Record 1983/8, 218 pp.

Hamilton, W.B. (1998). Archean magmatism and tectonics were not products of plate tectonics. *Precambrian Research,* 91, p. 143-179.

Hamilton, W.B. (2011). Plate tectonics began in Neoproterozoic time, and plumes from deep mantle have never operated. *Lithos*, 123, p. 1-20.

Hamilton, W.B. (2019). Toward a myth-free geodynamic history of Earth and its neighbours. *Earth Science Reviews*, 198, p. 1-49.

Hansmann, W. & Oberli, F. (1991). Zircon inheritance in an igneous rock suite from the southern Adamello batholith (Italian Alps) - Implications for petrogenesis. Contributions to Mineralogy and Petrology, 107, p. 501–518.

Hastie, A.R., Kerr, A.C., Pearce, J.A. & Mitchell, S.F. (2007). Classification of Altered Volcanic Island Arc Rocks using Immobile Trace Elements: Development of the Th–Co Discrimination Diagram. *Journal of Petrology*, 48, p. 2341-2357.

Hastie, A.R., Fitton, J.G., Bromiley, G.D., Butler, I.B. & Odling, N.W.A. (2016). The Origin of Earth's First Continents and the Onset of Plate Tectonics. *Geology*, 10, p. 855–858.

Herzberg, C. & Asimow, P.D. (2008). Petrology of some oceanic island basalts: PRIMELT2.XLS software for primary magma calculation. *Geochemistry Geophysics Geosystems*, 9(9), p. 1-25.

Herzberg, C., Condie, K. & Korenaga, J. (2010). Thermal history of the Earth and its petrological expression. *Earth and Planetary Science Letters*, 292, p. 79-88.

Herzberg, C. & Asimow, P.D. (2015). PRIMELT3 MEGA. XLSM software for primary magma calculation: Peridotite primary magma MgO contents from the liquidus to the solidus. *Geochemistry, Geophysics, Geosystems*, 16 (2), p. 563-578.

Heubeck, C., Engelhardt, J., Byerly, G. R., Zeh, A., Sell, B., Luber, T. & Lowe, D. R. (2013). Timing of deposition and deformation of the Moodies Group (Barberton Greenstone Belt, South Africa): Very-high-resolution of Archaean surface processes. *Precambrian Research*, 231, p. 236–262.

Himmelberg, G.R. & Loney, R.A. (1995). Characteristics and petrogenesis of Alaskan-type ultramafic-mafic intrusions, southeastern Alaska. *US Geological Survey Professional Paper 1564*. 47 pp.

Hodkiewicz, P.F., Weinberg, R.F., Gardoll, S.J. & Groves, D.I. (2005). Complexity gradients in the Yilgarn Craton: fundamental controls on crustal-scale fluid flow and formation of world-class orogenic gold deposits. *Australian Journal of Earth Sciences*, 52, p. 831-841

Hodkiewicz, P.F., Groves, D.I., Davidson, G.J., Weinberg, R.F. & Hagemann, S.G. (2009). Influence of structural setting on sulphur isotopes in Archean orogenic gold deposits, Eastern Goldfields Province, Yilgarn, Western Australia. *Mineralium Deposita*, 44, p. 129-150.

Hofmann, A., Dirks, P.H.G.M. & Jelsma, H.A. (2001). Late Archaean foreland basin deposits, Belingwe greenstone belt, Zimbabwe. *Sedimentary Geology*, 141-142, p. 131–168.

Hollis, S.P., Yeats, C.J., Wyche, S., Barnes, S.J., Ivanic, T.J., Belford, S.M., Davidson, G.J., Roache, A.J. & Wingate, M.T.D. (2015). A review of volcanic-hosted massive sulphide (VHMS) mineralization in the Archaean Yilgarn Craton, Western Australia: Tectonic, stratigraphic and geochemical associations. *Precambrian Research*, 260, p. 113-135.

Howarth, G.H. & Prevec, S.A. (2013). Trace element, PGE, and Sr-Nd isotope geochemistry of the Panzhihua mafic layered intrusion, SW China: Constraints on ore-forming processes and evolution of parent magma at depth in a plumbing-system. *Geochimica et Cosmochimica Acta,* 120, p. 459–478.

Hunter, M.A., Bickle, M.J., Nisbet, E.G., Martin, A. & Chapman, H.J. (1998). Continental extensional setting for the Archean Belingwe Greenstone Belt, Zimbabwe. *Geology*, 26(10), p. 883-886.

Isacks, B., Oliver, J. & Sykes, L.R. (1968). Seismology and the New Global Tectonics. *Journal of Geophysical Research,* 73, p. 5855–5899.

Ivanic, T.J., Wingate, M.T.D., Kirkland, C.L., Van Kranendonk, M.J. & Wyche, S. (2010). Age and significance of voluminous mafic-ultramafic magmatic events in the Murchison Domain, Yilgarn Craton. *Australian Journal of Earth Sciences,* 57, p. 597–614.

Ivanic, T.J., Van Kranendonk, M.J., Kirkland, C.L., Wyche, S., Wingate, M.T.D. & Belousova, E.A. (2012). Zircon Lu–Hf isotopes and granite geochemistry of the Murchison Domain of the Yilgarn Craton: Evidence for reworking of Eoarchean crust during Meso-Neoarchean plume-driven magmatism. *Lithos*, 148, p. 112–127.

Ivanic, T.J., Li, J., Meng, Y., Guo, L., Yu, J., Chen, S.F., Wyche, S. & Zibra, I. (2015a). Yalgoo 1:100 000 Geological Series Sheet 2241 (First edition). Geological Survey of Western Australia, map.

Ivanic, T.J., Nebel, O., Jourdan, F., Faure, K., Kirkland, C.L. & Belousova, E.A. (2015b). Heterogeneously hydrated mantle beneath the late Archean Yilgarn Craton. *Lithos*, 238, p. 76–85.

Ivanic, T.J., Nebel, O., Brett, J. & Murdie, R.E. (2017). The Windimurra Igneous Complex: an Archean Bushveld? In: Gessner, K., Blenkinsop, T.G. & Sorjonen-Ward, P. (eds.) Characterization of Ore-Forming Systems from Geological, Geochemical and Geophysical Studies. *Geological Society, London, Special Publications*, 453.

Ivanic, T.J. (2018). Ninghan, WA Sheet 2339. Geological Survey of Western Australia, 1:100 000 Geological Series.

Ivanic, T.J., Nebel, O., Brett, J. & Murdie, R.E. (2018). The Windimurra Igneous Complex: An Archean Bushveld? *Geological Society Special Publications*, 453, p. 313–348.

Ivanic, T.J. (2019). Mafic–ultramafic intrusions of the Youanmi Terrane, Yilgarn Craton. *Geological Survey of Western Australia*, Report 192, 121 pp.

Jaguin, J., Boulvais, P., Poujal, M., Bosse, V., Paquette, J-L. & Vilbert, D. (2013). Albitization in the Antimony Line, Murchison Greenstone Belt (Kaapvaal Craton): A geochemical and geochronological investigation. *Lithos*, 168-169, p. 124-143.

Jelsma, H.A., van der Beek, P.A. & Vinyu, M.L. (1993). Tectonic evolution of the Bindura-Shamva greenstone belt (northern Zimbabwe): Progressive deformation around diapiric batholiths. *Journal of Structural Geology*, 15, p. 163–176.

Johnson, T.E., Brown, M., Gardiner, N.J., Kirkland, C.L. & Smithies, R.H. (2017). Earth's First Stable Continents Did Not Form by Subduction. *Nature*, 543, p. 239-242.

Johnson, T.E., Kirkland, C.L., Gardiner, N.J., Brown, W., Smithies, R.H. & Santosh, M. (2019). Secular change in TTG compositions: Implications for the evolution of Archaean geodynamics. *Earth and Planetary Science Letters*, 505, p. 65-75.

Jones, S.A., Cassidy, K.F. & Davis, B.K. (2020). Unravelling the D1 event: evidence for early granite-up, greenstone-down tectonics in the Eastern Goldfields, Western Australia. *Australian Journal of Earth Science. DOI: 10.1080/08120099.2020.1755364.*

Kamber, B.S., Collerson, K.D., Moorbath, S. & Whitehouse, M.J. (2003). Inheritance of early Archaean Pb-isotope variability from long-lived Hadean protocrust. *Contributions to Mineralogy and Petrology*, 145, p. 25–46.

Kamber, B.S. (2015). The Evolving Nature of Terrestrial Crust from the Hadean, through the Archaean, into the Proterozoic. *Precambrian Research*, 258, p. 48–82.

Kent, A.J.R. & McDougall, I. (1995). 40Ar/39Ar and U–Pb age constraints on the timing of gold mineralization in the Kalgoorlie gold field. Economic Geology, 90, p. 845-859.

Kent, A.J.R. & Hagemann, S.G. (1996). Constraints on the timing of lode-gold mineralisation in the Wiluna greenstone belt, Yilgarn Craton, Western Australia. Australian Journal of Earth Sciences, 43, p. 573-588.

Kenworthy, S. & Hagemann, S.G. (2007). Fault and vein relationships in a reverse fault system at the Centenary orebody (Darlot gold deposit), Western Australia: Implications for gold mineralisation. *Journal of Structural Geology*, 29, p. 712-735.

Kerr, A.C., Marriner, G., Arndt, N., Tarney, J., Nivia, A., Saunders, A. & Duncan, R. (1996). The Petrogenesis of Gorgona Komatiites, Picrites and Basalts New Field, Petrographic and Geochemical Constraints. *Lithos*, 37, p. 245–260.

Kerr, A.C. & Arndt, N.T. (2001). A note on the IUGS reclassification of the high-Mg and picritic volcanic rocks. *Journal of Petrology*, 42, p. 2169-2171.

Kerrich, R., Wyman, D., Hollings, P. & Polat, A. (1999). Variability of Nb/U and Th/La in 3.0 to 2.7 Ga Superior Province ocean plateau basalts: application for the timing of continental growth and lithosphere recycling. *Earth and Planetary Science Letters,* 168, p. 101-115.

Kerrich, R., Said, N., Manikyamba, C. & Wyman, D. (2013). Sampling oxygenated Archean hydrosphere: Implications from fractionations of Th/U and Ce/Ce* in hydrothermally altered volcanic sequences. *Gondwana Research,* 23, p. 506-525.

Klein, C. (2005). Some Precambrian banded iron-formations (BIFs) from around the world: Their age, geologic setting, mineralogy, metamorphism, geochemistry, and origins. *American Mineralogist*, 90(10), p. 1473–1499.

Klemme, S., Günther, D., Hametner, K., Prowatke, S. & Zack, T. (2006). The partitioning of trace elements between ilmenite, ulvospinel, armalcolite and silicate melts with implications for the early differentiation of the moon. *Chemical Geology*, 234, p. 251–263.

Kokelaar, P. (1988). Tectonic controls of Ordovician arc and marginal basin volcanism in Wales. *Journal of the Geological Society*, 145, p. 759-775.

Korenaga, J. (2013). Initiation and Evolution of Plate Tectonics on Earth: Theories and Observations. *Annual Review of Earth and Planetary Sciences*, 41 (1), p. 117–151.

Korsch, R.J., Blewett, R.S., Smithies, R.H., Quentin de Gromard, R., Howard, H.M., Pawley, M.J., Carr, L., Hocking, R., Neumann, N.L., Kennett, B., Aitken, A., Holzschuh, J., Duan, J., Goodwin, J.A., Jones, T., Gessner, K. & Gorczyk, W. (2013). Geodynamic implications of the Yilgarn craton – Officer Basin – Musgrave Province (YOM) deep seismic reflection survey: part of a 1800 km transect across Western Australia from the Pinjarra Orogen to the Musgrave Province. In: Neumann, N.L. (ed.) Yilgarn craton – Officer Basin –Musgrave Province (YOM) Seismic and MT workshop. *Geoscience Australia Record 2013/28*, p. 169–97.

Kositcin, N., Brown, S.J.A., Barley, M.E., Krapež, B., Cassidy, K.F. & Champion, D.C. (2008). SHRIMP U-Pb zircon age constraints on the Late Archaean tectonostratigraphic architecture of the Eastern Goldfields Superterrane, Yilgarn Craton, Western Australia. *Precambrian Research*, 161, p. 5-33.

Koutsoumbis, I. (2020). The geodynamic context of Archean volcanism in the western Yilgarn Craton: *Geological Survey of Western Australia*, Record 2020/3, 114 pp.

Kovalev, K.R., Kalinin, Y.A., Naumov, E.A. & Myagkaya, M.K. (2014). Relationship of antimony with gold mineralization in the ore districts of Eastern Kazakhstan. *Russian Geology and Geophysics*, 55, p. 1170-1182.

Krapež, B. & Barley, M.E. (1987). Archaean strike-slip faulting and related ensialic basins: Evidence from the Pilbara Block, Australia. *Geological Magazine*, 124, p. 555–567.

Krapež, B. & Barley, M.E. (2008). Late Archaean synorogenic basins of the Eastern Goldfields Superterrane, Yilgarn Craton, Western Australia. Part III. Signatures of tectonic escape in an arc-continent collision zone. *Precambrian Research*, 161, p. 183–199.

Krapež, B., Barley, M.E. & Brown, S.J.A. (2008). Late Archaean synorogenic basins of the Eastern Goldfields Superterrane, Yilgarn Craton, Western Australia. Part I. Kalgoorlie and Gindalbie Terranes. *Precambrian Research*, 161, p. 135–153.

Krupp, R.E. (1988). Solubility of stibnite in hydrogen sulfide solutions, speciation, and equilibrium constants, from 25 to 350 °C. *Geochimica et Cosmochimica Acta*, 52, p. 3005–3015.

Kusky, T.M. & Polat, A. (1999). Growth of granite-greenstone terranes at convergent margins, and stabilization of Archean cratons. *Tectonophysics*, 305, p. 43–73.

Kwelwa, S.D., Dirks, P.H.G.M., Sanislav, I,V., Blenkinsop, T.G. & Kolling, S.L. (2018). Archaean gold mineralisation in an extensional setting: The structural history of the Kukuluma and Matandani deposits, Geita greenstone belt, Tanzania. Minerals, 8 (171), p. 1-33.

LaFlamme, C., Sugiono, D., Thebaud, N., Caruso, S., Fiorentini, M., Selvaraja, V., Jeon, H., Voute, F. & Martin, L. (2018). Multiple sulfur isotopes monitor fluid evolution of an Archean orogenic gold deposit. *Geochimica et Cosmochimica Acta*, 22, p. 436-446.

Lallemand, S. & Funiciello, F. (2009). Subduction Zone Geodynamics. Springer-Verlag Berlin Heidelberg. 275 pp.

Large, R.R. & Maslennikov, V.V. (2020). Invisible gold paragenesis and geochemistry in pyrite from orogenic and sediment-hosted gold deposits. *Minerals*, 10, 339.

Le Bas, M.J. (2000). IUGS reclassification of the high-Mg and picritic volcanic rocks. *Journal of Petrology,* 41, p. 1467-1470.

Le Bas, M.J. (2001). Reply to comment by Kerr and Arndt. *Journal of Petrology*, 42, p. 2173-2174.

Le Maitre, R.W., Bateman, P., Dudek, A., Keller, J., Lameyre, J., Le Bas, M., Sabine, P.A., Schmid, R., Sorensen, H., Streckeisen, A., Woolley, A.R. & Zanettin, R. (1989). A Classification of Igneous Rocks and Glossary of Terms: Recommendations of the International Union of Geological Sciences Subcommission on the Systematics of Igneous Rocks. Oxford: Blackwell Scientific.

Lee, C.T.A., Luffi, P., Plank, T., Dalton, H. & Leeman, W.P. (2009). Constraints on the depths and temperatures of basaltic magma generation on Earth and other terrestrial planets using new thermobarometers for mafic magmas. *Earth and Planetary Science Letters*, 279, (1-2), p. 20-33.

Lipple, S.L., Baxter, J.J & Marston, R.J. (1983). Ninghan, Western Australia: Western Australia Geological Survey, 1:250,000 Geological Series Explanatory Notes.

Lowrey, J.R., Ivanic, T.J., Wyman, D.A. & Roberts, M.P. (2017). Platy pyroxene: New insights into spinifex texture. *Journal of Petrology*, 58, p. 1671–1700.

Lowrey, J.R., Wyman, D.A., Ivanic, T.J., Smithies, R.H. & Maas, R. (2020). Archean Boninite-like Rocks of the Northwestern Youanmi Terrane, Yilgarn Craton: Geochemistry and Genesis. *Journal of Petrology,* 60, p. 2131–2168.

Lu, Y., Wingate, M.T.D., Kirkland, C.L. & Ivanic, T.J. (2016a). 198293: volcaniclastic metasandstone, Mulgine Hill; Geochronology Record 1331: *Geological Survey of Western Australia*, 6 pp.

Lu, Y., Wingate, M.T.D., Kirkland, C.L. & Ivanic, T.J. (2016b). 198294: metamorphosed quartz diorite, Mugs Luck mine; Geochronology Record 1332: *Geological Survey of Western Australia*, 4 pp.

Lu, Y., Wingate, M.T.D., Kirkland, C.L. & Ivanic, T.J. (2016c). 198295: metadacite, Warriedar Hill; Geochronology Record 1333: *Geological Survey of Western Australia*, 4 pp.

Lu, Y., Wingate, M.T.D., Kirkland, C.L. & Ivanic, T.J. (2016d). 211102: felsic volcaniclastic rock, Mougooderra Hill; Geochronology Record 1338: *Geological Survey of Western Australia*, 4 pp.

Lu, Y., Wingate, M.T.D., Kirkland, C.L. & Ivanic, T.J. (2016e). 211101: volcaniclastic mudstone, Wadgingarra Hill; Geochronology Record 1337: *Geological Survey of Western Australia*, 6 pp.

Lu, Y., Wingate, M.T.D., Kirkland, C.L. & Ivanic, T.J. (2016f). 198298: metadacite, Wadgingarra Well; Geochronology Record 1334: *Geological Survey of Western Australia*, 4 pp.

Lu, Y., Wingate, M.T.D., Kirkland, C.L. & Ivanic, T.J. (2016g). 207686: volcaniclastic metasandstone, Barry No 2 Well; Geochronology Record 1336: *Geological Survey of Western Australia*, 7 pp.

Lu, Y., Wingate, M.T.D., Kirkland, C.L. & Zibra, I. (2017). 155858: metamonzogranite, Mac Well; Geochronology Record 1393: *Geological Survey of Western Australia*, 3 pp.

Lu, Y., Wingate, M.T.D &, Ivanic, T.J. (2018). 198296: quartz sandstone, Warriedar Hill. Geochronology Record 1501: *Geological Survey of Western Australia*, 5 pp.

Ludden, J. & Hubert, C. (1986). Geologic evolution of the Late Archaean Abitibi greenstone belt of Canada. *Geology*, 14, p. 707–711

Marjoribanks, R.W. (2010). Geological Methods in Mineral Exploration and Mining, Second Edition. *Springer, Berlin*, 368 pp.

McCarthy, W., Petronis, M.S., Reavy, R.J. & Stevenson, C.T. (2015). Distinguishing diapirs from inflated plutons: an integrated rock magnetic fabric and structural study on the Roundstone Pluton, western Ireland. *Journal of the Geological Society*, 172, p. 550-565.

McCuaig T.C. & Kerrich, R. (1998). P-T-t deformation-fluid characteristics of lode gold deposits: evidence from alteration systematics. *Ore Geology Reviews*, 12, p. 381-453.

McCuaig, T.C., New, B. & Gardner, P. (2002). Geological interpretation of the Minjar Project, Western Australia. *Minjar Gold - Unpublished Company Report*, 37 pp.

McIntyre, J.R. & Martyn, J.E. (2005). Early extension in the Late Archaean northeastern Eastern Goldfields Province, Yilgarn Craton, Western Australia. *Australian Journal of Earth Sciences*, 52(6), p. 975–992.

McKenzie, D. & O'Nions, R.K. (1991). Partial melt distributions from inversion of rare-earth element data. *Journal of Petrology,* 32, p. 1021–1091.

Means, W.D., Hobbs, B.E., Lister, G.S. & Williams, P.F. (1980). Vorticity and non-coaxiality in progressive deformation. *Journal of Structural Geology*, 2, p. 371–378.

Mikucki, E.J. (1998). Hydrothermal transport and depositional processes in Archean lode-gold systems: A review. *Ore Geology Reviews*, 13, p. 307-321.

Minjar. (2012). Minjar Visitor Information Booklet: Exploration and Development Information. *Minjar Gold Unpublished Company Report,* 100 pp.

Mole, D.R., Fiorentini, M.L., Thebaud, N., Cassidy, K.F., McCuaig, T.C., Kirkland, C.L., Romano, S.S., Doublier, M.P., Belousova, E.A., Barnes, S.J. & Miller, J. (2014). Archean komatiite volcanism controlled by the evolution of early continents. *Proceedings of the National Academy of Sciences of the United States of America*, 111(28), p. 10083-10088.

Mole, D.R., Fiorentini, M.L., Cassidy, K.F., Kirkland, C.L., Thebaus, N., McCuaig, T.C., Doublier, M.P., Duuring, P., Romano, S.S., Maas, R., Belousova, E.A., Barnes, S.J. & Miller, J. (2015). Crustal evolution, intra-cratonic architecture and the metallogeny of an Archaean craton. In: Jenkin, G.R.T., Lusty, P.A.J., McDonald, I., Smith, M.P., Boyce, A.J. & Wilkinson, J.J. (eds.) Ore deposits in an evolving Earth. *Geological Society, London, Special Publications*, 393, p. 23-80.

Mole, D.R., Kirkland, C.L., Fiorentini, M.L., Barnes, S.J., Cassidy, K.F., Isaac, C., Belousova, E.A., Hartnady, M. & Thebaud, N. (2019). Time-space evolution of an Archean craton: A Hf-isotope window into continent formation. *Earth Science Reviews*, 196, p. 1-46.

Morey, A.A., Weinberg, R.F., Bierlein, F.P. & Davidson, G.J. (2007). Gold deposits of the Bardoc Tectonic Zone: a distinct style of orogenic gold in the Archaean Eastern Goldfields Province, Yilgarn Craton, Western Australia. *Australian Journal of Earth Sciences*, 54, p. 783-800.

Morey, A.A., Tomkins, A.G., Bierlein, F.P., Weinberg, R.F. & Davidson, G.J. (2008). Bimodal distribution of gold in pyrite and arsenopyrite: examples from the Archean Boorara and Bardoc shear systems, Yilgarn Craton, Western Australia. *Economic Geology*, 103, p. 599–614.

Morris, P.A. & Kirkland, C.L. (2014). Melting of a subduction-modified mantle source: a case study from the Archean Marda Volcanic Complex, central Yilgarn Craton, Western Australia. *Lithos*, 190–191, p. 403–419.

Moyen, J.-F. (2010). Archaean granitoids record a range of geodynamical sites for crustal growth or recycling. In: Tyler, I.M. & Knox-Robinson, C.M. (eds.) *Fifth International Archaean Symposium Abstracts*, Geological Survey of Western Australia, Record 2010/18, p. 12-14.

Moyen, J.-F. & van Hunen, J. (2012). Short-term episodicity of Archaean plate tectonics. *Geology*, 40, p. 451–454.

Moyen, J.-F. & Laurent, O. (2018). Archaean tectonic systems: A view from igneous rocks. *Lithos*, 302-303, p. 99-125.

Mueller, A.G., Campbell, I.H., Schiøtte, L., Sevigny, J.H. & Layer, P.W. (1996). Constraints on the age of granitoid emplacement, metamorphism, gold mineralization, and subsequent cooling of the Archean greenstone terrane at Big Bell, Western Australia. *Economic Geology,* 91, p. 896–915.

Mueller, W.U. & Corcoran, P.L. (2001). Volcano-sedimentary processes operating on a marginal continental arc: The Archean Raquette Lake Formation, Slave Province, Canada. *Sedimentary Geology*, 141–142, p. 169–196.

Mueller, A.G., Nemchin, A.A. & Frei, R. (2004). The Nevoria gold skarn deposit, Southern Cross greenstone Belt, Western Australia: II. Pressure-Temperature-Time path and relationship to postorogenic granites. *Economic Geology*, 99, p. 453-478.

Muhling, P.C. & Low, G.H. (1977). Yalgoo, Western Australia: Western Australia Geological Survey, 1:250,000 Geological Series Explanatory Notes.

Murphy, J.B. (2007). Igneous rock associations 8. Arc magmatism II: geochemical and isotopic characteristics. *Geoscience Canada*, 34(1), p. 7-35.

Myers, J.S. & Watkins, K.P. (1985). Origin of granite-greenstone patterns, Yilgarn Block, Western Australia. *Geology*, 13, p. 778–780.

Myers, J.S. (1995). The generation and assembly of an Archaean supercontinent: evidence from the Yilgarn craton, Western Australia. *Geological Society of London Special Publications*, 95, p. 143–154.

Nelson, D.R. (1997). Evolution of Archaean granite-greenstone terranes of the Eastern Goldfields, Western Australia: SHRIMP U-Pb zircon constraints. *Precambrian Research,* 83, p. 57-81.

Nelson, D.R., Robinson, B.W. & Myers, J.S. (2000). Complex geological histories extending for ≥4.0 Ga deciphered from xenocryst zircon microstructures. *Earth and Planetary Science Letters,* 181, p. 89–102.

Nelson, D.R. (2001). 169003: Vesicular Rhyolite, Carron Hill; Geochronology Dataset 170. In: Compilation of Geochronology Information, 2009 update. *Geological Survey of Western Australia.*

Nesbitt, R.W. (1971). Skeletal crystal forms in the ultramafic rocks of the Yilgarn Block, Western Australia: evidence for an Archaean ultramafic liquid. *Geological Society of Australia Special Publication*, 3, p. 331-347.

Nesbitt, H.W. (1979). Mobility and fractionation of rare earth elements during weathering of granodiorite. *Nature*, 279, p. 206-210.

Nielsen, R.L. & Beard, J.S. (2000). Magnetite – melt HFSE partitioning. *Chemical Geology*, 164, p. 21–34.

Normand, C., Gauthier, M. & Jébrak, M. (1996). The Quebec Antimony deposit: An example of gudmundite-native antimony mineralization in the ophiolitic mélange of the southeastern Quebec Appalachians. *Economic Geology*, 91, p. 149—163.

O'Hara, M.J. (1965). Primary magmas and the origin of basalts. *Scottish Journal of Geology*, 1, p. 19-40.

Oliver, B. (1999). Granitoids of the Mount Mulgine and Noongal Areas, Murchison Province, Western Australia: Origin and relationship with granitophile and gold mineralisation. Unpublished BSc Honours thesis, The University of Western Australia, 98pp.

O'Neil, J., Maurice, C., Stevenson, R.K., Larocque, J., Cloquet, C., David, J. & Francis, D. (2007). Chapter 3.4: The Geology of the 3.8 Ga Nuvvuagittuq (Porpoise Cove) Greenstone Belt, Northeastern Superior Province, Canada. *Dev. Precambrian Geology*, 15, p. 219–250.

O'Neill, C., Lenardic, A., Moresi, L., Torsvik, T.H. & Lee, C.-T.A. (2007). Episodic Precambrian subduction. *Earth and Planetary Science Letters*, 262, p. 552-562.

Ohmoto, H. & Rye, R.O. (1979). Isotopes of sulfur and carbon. In: Geochemistry of hydrothermal ore deposits, 2nd ed. *Holt Rinehart and Winston*, New York.

Palin, R.M. & Santosh, M. (2020). Plate tectonics: What, where, why, and when? *Gondwana Research*, in press, 22 pp.

Parmenter, S., Ivanic, T.J., Korhonen, F.J., Bouvier, A., Kendrick, J.L. & Yakymchuk, C. (2020). Metamorphism of the Mougooderra Formation: Implications for Neoarchean tectonics in the western Youanmi Terrane, Yilgarn Craton. *Precambrian Research*, 350, p. 1-17.

Pearce, J.A. & Peate, D.W. (1995). Tectonic implications of the composition of volcanic arc magmas. *Annual Review Earth Planetary Sciences,* 23, p. 251–285.

Pearce, J. A. (1996). A user's guide to basalt discrimination diagrams. In: Wyman, D. (ed.) Trace element geochemistry of volcanic rocks: application for massive sulphide exploration, Winnipeg. *Geological Association of Canada, Mineral Deposits Division*, p. 79-113.

Pearce, J.A. (2008). Geochemical fingerprinting of oceanic basalts with applications to ophiolite classification and the search for Archean oceanic crust. *Lithos*, 100, p. 14–48.

Pearce, J.A. & Reagan, M.K. (2019). Identification, classification, and interpretation of boninites from Anthropocene to Eoarchean using Si-Mg-Ti systematics. *Geosphere*, 15, p. 1008–1037.

Pearson, D.G. & Wittig, N. (2008). Formation of Archaean continental lithosphere and its diamonds: the root of the problem. *Journal of the Geological Society, London*, 165, p. 895-914.

Percival, J.A., Stern, R.A. & Skulski, T. (2001). Crustal growth through successive arc magmatism: Reconnaissance U-Pb SHRIMP data from the northeastern Superior Province, Canada. *Precambrian Research*, 109, p. 203-238.

Percival, J.A. (2010). A 4-D Craton-scale framework for the Superior Province, Canada. In: Tyler, I.M. & Knox-Robinson, C.M. (eds.) *Fifth International Archaean Symposium Abstracts*, Geological Survey of Western Australia, Record 2010/18, p. 145-147.

Petrella, L., Thébaud, N., Laflamme, C., Martin, L., Occhipinti, S. & Bigelow, J. (2020). In-situ sulfur isotopes analysis as an exploration tool for orogenic gold mineralization in the Granites-Tanami Gold Province, Australia: Learnings from the Callie deposit. *Journal of Geochemical Exploration*, 214, p. 106542.

Phillips, G.N. & Groves, D.I. (1983). The nature of Archaean gold-bearing fluids as deduced from gold deposits of Western Australia. *Journal of the Geological Society of Australia*, 30, p. 25-39.

Phillips, G.N., & Evans, K.A. (2004). Role of CO_2 in the formation of gold deposits. *Nature*, 429, p. 860-863.

Phillips, G.N. (2013). Australian and global setting for gold in 2013. In: Proceedings World Gold 2013, Brisbane, Australia, 26–29 September, 2013. *Australian Institute of Mineralogy and Metallurgy*, p. 15–21.

Phillips, B.A. (2017). The origin and evolution of the Siletz Terrane in Oregon, Washington and Vancouver Island. *Unpublished PhD thesis*, Cardiff University, 361 pp.

Pidgeon, R.T. & Wilde, S.A. (1990). The distribution of 3.0 Ga and 2.7 Ga volcanic episodes in the Yilgarn Craton of Western Australia. *Precambrian Research*, 48, p. 309-325.

Pidgeon, R.T. & Hallberg, J.A. (2000). Age relationships in supracrustal sequences of the northern part of the Murchison Terrane, Archaean Yilgarn Craton, Western Australia: a combined field and zircon U-Pb study. *Australia Journal of Earth Sciences,* 47, p. 153–165.

Platten, I.M. & Dominy, S.C. (1999). Re-evaluation of quartz vein history in the Dolgellau Gold Belt, North Wales, United Kingdom. *Geological Journal*, 34(4), p. 369-391.

Polat, A., Appel, P.W.U., Fryer, B., Windley, B., Frei, R., Samson, I.M. & Huang, H. (2009). Trace element systematics of the Neoarchean Fiskenæsset anorthosite complex and associated meta volcanic rocks, SW Greenland: evidence for a magmatic arc origin. *Precambrian Research*, 175, p. 87–115.

Poulsen, K.H., Robert, F. & Dube, B. (2000). Geological classification of Canadian gold deposits. *Geological Survey of Canada Bulletin,* 540, 106 pp.

Price, J.J. (2014). Gold exploration in the Yalgoo-Singleton Greenstone Belt, Western Australia. *Unpublished BSc Thesis*, School of Earth and Ocean Sciences, Cardiff University, 123 pp.

Price, J.J., Blenkinsop, T.G., Goodenough, K.M. & Kerr, A.C. (2020). Stratigraphy, petrography and structure of Archaean rocks in the Rothsay Mining Area, Western Yilgarn Craton. *Geological Survey of Western Australia Record 2020/13*, 109 pp.

Rao, Y.J.B. & Babu, E.V.S.S.K. (2011). Plate Tectonics, Precambrian. In: Gupta, H.K. & Kole, S. (eds.) *Encyclopaedia of Solid Earth Geophysics*, Springer Publishers, Amsterdam, Netherlands, p. 991-998.

Rasmussen, B., Mueller, A.G. & Fletcher, I.R. (2009). Zirconolite and xenotime U-Pb age constraints on the emplacement of the Golden Mile Dolerite sill and gold mineralization at the Mount Charlotte mine, Eastern Goldfields Province, Yilgarn craton, Western Australia. *Contributions to Mineralogy & Petrography*, 157, p. 559-572

Rhys, D.A., Lewis, P.D. & Rowland, J.V. (2020). Structural controls on ore localisation in epithermal gold-silver deposits: a mineral systems approach. *Reviews in Economic Geology*, 21, p. 83-145.

Ridley, J.R. & Diamond, L.W. (2000). Fluid chemistry of orogenic lode gold deposits and implications for genetic models. *Society of Economic Geologists Reviews*, 13, p. 141–162.

Robb, L.J. (2005). Introduction to ore-forming processes. Oxford (Blackwell Publishing), 373 pp.

Robert, F. & Brown, A.C. (1986). Archean gold-bearing quartz veins at the Sigma Mine, Abitibi greenstone belt, Quebec; Part I, Geologic relations and formation of the vein system. *Economic Geology*, 81(3), p. 578-592.

Robert, F. & Kelly, W.C. (1987). Ore-forming fluids in Archean gold-bearing quartz veins at the Sigma Mine, Abitibi greenstone belt, Quebec, Canada. *Economic Geology*, 82(6), p. 1464-1482.

Robert, F., Boullier, A.-M. & Firdaous, K. (1995). Gold–quartz veins in metamorphic terranes and their bearing on the role of fluids in faulting. *Journal of Geophysical Research*, 100, p. 12861–12879.

Robert, F., Poulsen, K.H. & Dubé, B. (1997). Gold deposits and their geological classification. In: Gubins, A.G. (ed.*) Proceedings of Exploration '97: Fourth Decennial International Conference on Mineral Exploration*, p. 209-220.

Robert, F., Poulsen, K.H., Cassidy, K.F. & Hodgson, C.J. (2005). Gold metallogeny of the Superior and Yilgarn cratons. *Economic Geology 100th Anniversary Volume*, p. 1001-1034.

Robert, F., Brommecker, R., Bourne, B.T., Dobak, P.J., McEwan, C.J., Rowe, R.R. & Zhou, X. (2007). Models and Exploration Methods for Major Gold Deposit Types. In: Milkereit, B. (ed.) *Proceedings of Exploration 07: Fifth Decennial International Conference on Mineral Exploration,* p. 691-711.

Romano, S.S., Thébaud, N.J.M., Mole, D.R., Wingate, M.T.D., Kirkland, C.L. & Doublier, M.P. (2014). Geochronological constraints on nickel metallogeny in the Lake Johnston belt, Southern Cross Domain. *Australian Journal of Earth Sciences*, 61, p. 143–157.

Rosas, J.C. & Korenaga, J. (2018). Rapid crustal growth and efficient crustal recycling in the early Earth: Implications for Hadean and Archean geodynamics. *Earth and Planetary Science Letters*, 494, p. 42–49.

Rudnick, R.L. & Fountain, D.M. (1995). Nature and composition of the continental crust: a lower crustal perspective. *Reviews of Geophysics*, 33, p. 267-309.

Saji, N.S., Larsen, K., Wielandt, D., Schiller, M., Costa, M.M., Whitehouse, M.J., Rosing, M.T. & Bizzarro, M. (2018). Hadean Geodynamics Inferred from Time-Varying $^{143}Nd/^{144}Nd$ in the early Earth rock record. *Geochemical Perspectives Letters*, 7, p. 43-48.

Salier, B.P., Groves, D.I., McNaughton, N.J. & Fletcher, I.R. (2005). Geochronological and stable isotope evidence for widespread orogenic gold mineralisation from a deep-seated fluid source at ca 2.65 Ga in the Laverton Gold Province, Western Australia. *Economic Geology*, 100, p. 1363-1388.

Sanislav, I.V., Brayshaw, M., Kolling, S.L., Dirks, P.H.G.M., Cook, Y.A. & Blenkinsop, T.G. (2017). The structural history and mineralisation controls of the world-class Geita Hill gold deposit, Geita Greenstone Belt, Tanzania. *Mineralium Deposita,* 52, p. 257-279.

Saunders, A. & Tarney, J. (1991). Back-Arc Basins. In: Floyd, P.A. (ed.) *Oceanic Basalts.* Springer, Boston, USA, p. 219-263.

Schiøtte, L. & Campbell, I.H. (1996). Chronology of the Mount Magnet granite-greenstone terrain, Yilgarn Craton, Western Australia: implications for field based predictions of the relative timing of granitoid emplacement. *Precambrian Research,* 78, p. 237–260.

Schoene, B. & Bowring, S.A. (2010). Rates and mechanisms of Mesoarchean magmatic arc construction, eastern Kaapvaal Craton, Swaziland. *Geological Society of America Bulletin*, 122 (3/4), p. 408-429.

Schofield, D.I., Thomas, R.J., Goodenough, K.M., De Waele, B., Pitfield, P.E.J., Key, R.M., Bauer, W., Walsh, G.J., Lidke, D.J., Ralison, A.V., Rabarimanana, M., Rafahatelo, J.M. & Randriamananjara, T. (2010). Geological evolution of the Antongil Craton, NE Madagascar. *Precambrian Research*, 182, p. 187-203.

Scowen, P. (1991). The geology and geochemistry of the Narndee intrusion. *Unpublished PhD thesis.* Australian National University, Canberra Australia, 225 pp.

Sharpe, R. & Gemmell, J.B. (2001). Alteration characteristics of the Archean Golden Grove Formation at the Gossan Hill Deposit, Western Australia: Induration as a focusing mechanism for mineralising hydrothermal fluids. *Economic Geology*, 96, p. 1239-1262.

Shirey, S.B., Carlson, R.W., Richardson, S.H., Menzies, A.H., Gurney, J.J., Pearson, D.G., Harris, J.W. & Wiechert, U. (2001). Archean emplacement of eclogitic components into the lithospheric mantle during formation of the Kaapvaal Craton. *Geophysical Research Letters*, 28, p. 2509-2512.

Shirey, S.B., Kamber, B.S., Whitehouse, M.J., Mueller, P.A. & Basu, A.R. (2008). A review of the isotopic and trace element evidence for mantle and crustal processes in the Hadean and Archean: Implications for the onset of plate tectonic subduction. In: Condie, K.C. & Pease, V. (eds.) When Did Plate Tectonics Begin on Planet Earth? *Geological Society of America Special Paper,* 440, p. 1-29.

Shirey, S.B. & Carlson, R.W. (2010). Isotopic constraints on formation of Hadean-Archean mantle and crust. In: Tyler, I.M. & Knox-Robinson, C.M. (eds.) *Fifth International Archaean Symposium Abstracts*, Geological Survey of Western Australia, Record 2010/18, p. 25-28.

Sibson, R.H., Robert, F. & Poulsen, K.H. (1988). High-angle reverse faults, fluid-pressure cycling, and mesothermal gold-quartz deposits. *Geology*, 16(6), p. 551-555.

Sibson, R.H. (1990). Conditions for fault-valve behaviour. Geological Society, London, *Special Publications*, 54(1), p. 15-28.

Sizova, E., Gerya, T., Brown, M. & Perchuk, L. (2010). Subduction styles in the Precambrian: Insight from numerical experiments. *Lithos*, 116, p. 209-229.

Sizova, E., Gerya, T., Brown, M. & Stüwe, K. (2018). What drives metamorphism in early Archean greenstone belts? Insights from numerical modeling. *Tectonophysics*, 746, p. 587–601.

Smith, M.P., Storey, C.D., Jeffries, T.E. & Ryan, C. (2009). In situ U–Pb and trace element analysis of accessory minerals in the Kiruna district, Norrbotten, Sweden: new constraints on the timing and origin of mineralization. *Journal of Petrology*, 50(11), p. 2063-2094.

Smithies, R.H. & Champion, D.C. (1999). Late Archaean felsic alkaline igneous rocks in the Eastern Goldfields, Yilgarn Craton, Western Australia: a result of lower crustal delamination? *Journal of the Geological Society of London*, 156, p. 561-576.

Smithies, R.H. & Champion, D.C. (2000). The Archaean high-Mg diorite suite: Links to Tonalite-Trondhjemite-Granodiorite magmatism and implications for early Archaean crustal growth. *Journal of Petrology*, 41, p. 1653-1671.

Smithies, R.H. (2002). Archaean boninite-like rocks in an intracratonic setting. *Earth and Planetary Science Letters*, 197, p. 19-34.

Smithies, R.H., Champion, D.C. & Sun, S. (2004). The case for Archaean boninites. *Contributions to Mineralogy and Petrology*, 147, p. 705-721.

Smithies, R.H., Ivanic, T.J., Lowrey, J.R., Morris, P.A., Barnes, S.J., Wyche, S. & & Lu, Y. (2018). Two Distinct Origins for Archean Greenstone Belts. *Earth and Planetary Science Letters*, 487, p. 106–116.

Snowden, P.A. & Bickle, M.J. (1976). The Chinamora Batholith: diapiric intrusion or interference fold? *Journal of the Geological Society*, 132 (2), p. 131-137.

Sossi, P.A., Eggins, S.M., Nesbitt, R.W., Nebel, O., Hergt, J.M., Campbell, I.H., O'Neill, H.S.C., Van Kranendonk, M. & Davies, D.R. (2016). Petrogenesis and geochemistry of Archean Komatiites. *Journal of Petrology*, 57, p. 147–184.

Stern, R.J. (2005). Evidence from ophiolites, blueschists, and ultrahigh-pressure metamorphic terranes that the modern episode of subduction tectonics began in Neoproterozoic time. *Geology*, 33, p. 557-560.

Stern, R.J. (2008). Modern-style plate tectonics began in Neoproterozoic time: an alternative interpretation of Earth dynamics and history. In: Condie, K.C. & Pease, V. (eds.) When Did Plate Tectonics Begin on Planet Earth? *Geological Society of America Special Paper,* 440, p. 265-280.

Straub. K.T., Yeats, C.J., Brown, P.E. & Hagemann, S.G. (1995). Preliminary fluid inclusion investigation of the composite volcanic-hosted massive sulfide and lode-gold style Archaean deposit at Mount Gibson, Western Australia. *Geological Society of America Abstracts with Programs*, 27(6), p. A-66.

Sun, S.-S. & McDonough, W. F. (1989). Chemical and isotopic systematics of oceanic basalts: implications for mantle composition and processes. *Geological Society, London, Special Publications*, 42(1), p. 313–345.

Sung, Y.-H., Ciobanu, C.L., Pring, A., Brügger, J., Skinner, W., Cook, N.J. & Nugus, M. (2007). Tellurides from Sunrise Dam gold deposit, Yilgarn Craton, Western Australia: a new occurrence of nagyagite. *Mineralogy & Petrology*, 91, p. 249-270.

Sung, Y.-H., Brügger, J., Ciobanu, C.L., Pring, A., Skinner, W. & Nugus, M. (2009). Invisible gold in arsenian pyrite and arsenopyrite from a multistage Archaean gold deposit: Sunrise Dam, Eastern Goldfields Province, Western Australia. *Mineralium Deposita*, 44, p. 765-791.

Swager, C., Witt, W.K., Griffin, T.J., Ahmat, A.L., Hunter, W.M., McGoldrick, P.J. & Wyche, S. (1990). A Regional Overview of the Late Archaean Granite Greenstones of the Kalgoorlie Terrane. In: Ho, S.E., Glover, J.E., Myers, J.S. & Muhling, J.R. (eds.) *Third International Archaean Symposium, Perth 1990 - Excursion Guidebook,* University of Western Australia, Perth, Australia, p. 205–303.

Swager, C. & Griffin, T.J. (1990). An early thrust duplex in the Kalgoorlie-Kambalda greenstone belt, Eastern Goldfields Province, Western Australia. *Precambrian Research,* 48, p. 63-73.

Thébaud, N., Hollingsworth, D. & Vearncombe, J. (2007). Locality 20b: Prohibition gold. In: Wyche, S. (compiler), A Geological Transect Across the Northern Yilgarn Craton – A Field Guide. *Geological Survey of Western Australia*, Record 2007/20, p. 40–42.

Thébaud, N., Sugiono, D., LaFlamme, C., Miller, J., Fisher, L., Voute, F., Tessalina, S., Sonntag, I. & Fiorentini, M. (2018). Protracted and polyphased gold mineralisation in the Agnew District (Yilgarn Craton, Western Australia). *Precambrian Research*, 310, p. 291-304.

Thomas, B.D. (2003). The Geology of the Minjar Project, Western Australia. *BSc Honours Thesis*, School of Earth Sciences, University of Tasmania, Australia, 87 pp.

Thurston, P.C. (2002). Autochthonous development of Superior Province greenstone belts? *Precambrian Research*, 115, p. 11–36.

Thurston, P.C. (2015). Igneous rock associations 19. Greenstone Belts and granite−greenstone terranes: Constraints on the nature of the Archean world. *Geosciences Canada*, 42, p. 437–484.

Tomkins, A.G. (2013). On the source of orogenic gold. *Geology,* 41(12), p. 1255-1256.

Tripp, G.I. (2000). Structural geology and gold mineralisation of the Ora Banda and Zuleika districts, Eastern Goldfields, Western Australia. *Unpublished MSc thesis*, Curtin University of Technology, Australia, 378 pp.

Tripp, G.I. (2019). Stratigraphy and structure in the Neoarchaean of the Kalgoorlie district, Australia: Critical controls on greenstone-hosted gold deposits. *Geological Survey of Western Australia Report 199*, 476 pp.

Tripp, G.I., Tosdal, R.M., Blenkinsop, T.G., Rogers, J.R. & Halley, S. (2020). Neoarchaean Eastern Goldfields of Western Australia. *Society of Economic Geologists Special Publications*, in press, 26 pp.

Tyler, I.M. & Knox-Robinson, C.M. (2010). *Fifth International Archaean Symposium Abstracts*, Geological Survey of Western Australia, Record 2010/18, 400 pp.

Van den Kerkhof, A.M. & Hein, U.F. (2001) Fluid inclusion petrography. *Lithos*, 55, p. 27-47.

van Hunen, J. & Moyen, J-F. (2012). Archean subduction: fact or fiction? *Annual Review of Earth & Planetary Sciences*, 40, p. 195-219.

Van Kranendonk, M.J., Hickman, A.H., Smithies, R.H., Nelson, D. & Pike, G. (2002). Geology and Tectonic Evolution of the Archaean North Pilbara Terrain, Pilbara Craton. Western Australia. *Economic Geology*, 97, p. 695–732.

Van Kranendonk, M.J., Collins, W.J., Hickman, A.H., & Pawley, M.J. (2004). Critical tests of vertical vs horizontal tectonic models for the Archaean East Pilbara Granite–Greenstone Terrane, Pilbara Craton, Western Australia. *Precambrian Research,* 131, p. 173–211.

Van Kranendonk, M.J. (2008). New evidence on the evolution of the Cue–Meekatharra area of the Murchison Domain, Yilgarn Craton. *Geological Survey of Western Australia*, Annual Review 2006-07, p. 39–49.

Van Kranendonk, M.J. & Ivanic, T.J. (2009). A new lithostratigraphic scheme for the northeastern Murchison Domain, Yilgarn Craton. *Geological Survey of Western Australia*, Annual Review 2007-08, p. 34-53.

Van Kranendonk, M.J., Ivanic, T.J., Wingate, M.T.D., Kirkland, C.L. & Wyche, S. (2013). Long-lived, autochthonous development of the Archean Murchison Domain, and implications for Yilgarn Craton tectonics. *Precambrian Research,* 229, p. 49-92.

Vielreicher, N.M., Groves, D.I. & McNaughton, N.J. (2016). The giant Kalgoorlie Gold Field revisited. *Geoscience Frontiers*, 7(3), p. 359-374.

Viljoen, M.J. & Viljoen, M.J. (1969). The geology and geochemistry of the Lower Ultramafic Unit of the Onverwacht Group and a proposed new class of igneous rocks. In: Upper Mantle Project, *Geological Society of South Africa Special Publication 2*, p. 55-85.

WACHEM, (2020). Geological Survey of Western Australia, Western Australian Geochemistry database (WACHEM). http://www.dmp.wa.gov.au/GeoChem-ExtractGeochemistry-1559.aspx

Walter, M.J. (1998). Melting of garnet peridotite and the origin of komatiite and depleted lithosphere. *Journal of Petrology*, 39 (1), p. 29-60.

Wang, L.G., McNaughton, N.J. & Groves, D.I. (1993). An overview of the relationship between granitoid intrusions and gold mineralisation in the Archean Murchison Province, Western Australia. *Mineralium Deposita,* 28, p. 482–494.

Wang, L.G., McNaughton, N.J. & Groves, D.I. (1995). New geochronological data for granitoid intrusions in the Reedy's area, Murchison Province, Western Australia: constraints on genesis of gold mineralization. In: *Australian Conference on Geochronology and Isotope Geoscience*, Perth, Western Australia, Workshop Programme and Abstract, p. 37.

Wang, Q. (1998). Geochronology of the granite-greenstone terranes in the Murchison and Southern Cross Provinces of the Yilgarn Craton, Western Australia. *Unpublished PhD thesis*, Australian National University, Canberra, Australia, 186 pp.

Wang, Q., Schiøtte, L. & Campbell, I.H. (1998). Geochronology of supracrustal rocks from the Golden Grove area, Murchison Province, Yilgarn Craton, Western Australia. *Australian Journal of Earth Sciences,* 45, p. 571–577.

Watkins, K.P. & Hickman, A. H. (1990). Geological Evolution and Mineralization of the Murchison Province, Western Australia. *Geological Survey of Western Australia Bulletin 137*, 267 pp.

Watkins, K.P., Fletcher, I.R. & de Laeter, J.R. (1991). Crustal evolution of Archaean granitoids in the Murchison Province, Western Australia. *Precambrian Research*, 50, p. 311-366.

Weidenbeck, M. & Watkins, K.P. (1993). A time scale for granitoid emplacement in the Archean Murchison Province, Western Australia, by single zircon geochronology. *Precambrian Research*, 61, p. 1-26.

Weinberg, R.F., Hodkiewicz, P.F. & Groves, D.I., (2004). What controls gold distribution in Archean terranes? *Geology*, 32, p. 545-548.

Weinberg, R.F. (1996). The ascent mechanism of felsic magmas: news and views. *Transactions of the Royal Society of Edinburgh: Earth Science*, 87, p. 95-103.

Weinberg, R.F. (1997). Diapir-driven crustal convection: decompression melting, renewal of the magma source and the origin of nested plutons. *Tectonophysics*, 271, p. 217-229.

Wickham, D. (2014). Gold exploration in the Murchison Province, Western Australia, with Minjar Gold. *Unpublished BSc Thesis*, School of Earth and Ocean Sciences, Cardiff University, 69 pp.

Wiemer, D., Schrank, C.E., Murphy, D.T., Wenham, L. & Allen, C.M. (2018). Earth's oldest stable crust in the Pilbara Craton formed by cyclic gravitational overturns. *Nature Geoscience*, 11, p. 357-361.

Wilkinson, J.J. & Johnston, J.D. (1996). Pressure fluctuations, phase separation and gold precipitation during seismic propagation. *Geology*, 24(5), p. 395-398.

Wilks, M.E. & Nisbet, E.G. (1988). Stratigraphy of the Steep Rock Group, northwest Ontario: a major Archaean unconformity and Archaean stromatolites. *Canadian Journal of Earth Sciences*, 25, p. 370-391.

Williams-Jones, A.E. & Normand, C. (1997). Controls of mineral parageneses in the system Fe–Sb–S–O. *Economic Geology*, 92, p. 308–324.

Williams-Jones, A.E., Migdisov, A.A. & Samson, I.M. (2012). Hydrothermal Mobilisation of the Rare Earth Elements - a Tale of “Ceria” and “Yttria.” *Elements*, 8(5), p. 355–360.

Wilson, A.H. & Versfeld, J. A. (1994). The early Archaean Nondweni Greenstone Belt, southern Kaapvaal Craton, South Africa, Part II. Characteristics of the volcanic rocks and constraints on magma genesis. *Precambrian Research*, 67, p. 277–320.

Windley, B.F. (1995). The Evolving Continents, Third Edition. Chichester: John Wiley & Sons, p. 343-376.

Wingate, M.T.D., Bodorkos, S. & Kirkland, C.L. (2009a). 183975: metarhyolite, Wattagee Hill; Geochronology Dataset 785. In: Compilation of Geochronology Information, 2009 Update. *Geological Survey of Western Australia*.

Wingate, M.T.D., Bodorkos, S. & Van Kranendonk, M.J. (2009b). 178197: Biotite Monzogranite, Milliewarrie Well; Geochronology Record 790. *Geological Survey of Western Australia*, 4 pp.

Wingate, M.T.D., Kirkland, C.L. & Van Kranendonk, M.J. (2011). 183953: felsic metavolcaniclastic rock, Five Mile Well Mine; Geochronology Record 969. *Geological Survey of Western Australia*, 4 pp.

Wingate, M.T.D., Kirkland, C.L. & Ivanic, T.J. (2012). 193972: metarhyolite clast in volcaniclastic breccia, Weld Range; Geochronology Record 1011. *Geological Survey of Western Australia*, 4 pp.

Wingate, M.T.D., Kirkland, C.L., Guilliamse, J.N., Van Kranendonk, M.J. & Wyche, S. (2013a). 155569: metarhyolite, Weld Range; Geochronology Record 1096. *Geological Survey of Western Australia*, 4 pp.

Wingate, M.T.D., Kirkland, C.L. & Ivanic, T.J. (2013b). 198228: volcaniclastic metasandstone, Mount Singleton; Geochronology Record 1105. *Geological Survey of Western Australia,* 4 pp.

Wingate, M.T.D., Kirkland, C.L. & Ivanic, T.J. (2014). 207630: porphyritic monzogranite, Garden Pool Well; Geochronology Record 1215. *Geological Survey of Western Australia*, 4 pp.

Wingate, M.T.D., Kirkland, C.L., Ivanic, T.J. & Wyche, S. (2015a). 203702: metadacite, Golden Grove mine; Geochronology Record 1259. *Geological Survey of Western Australia*, 4 pp.

Wingate, M.T.D., Kirkland, C.L., Ivanic, T.J. & Wyche, S. (2015b). 203703: metarhyolite, Golden Grove mine; Geochronology Record 1260. *Geological Survey of Western Australia*, 4 pp.

Wingate, M.T.D., Kirkland, C.L., Ivanic, T.J. & Wyche, S. (2015c). 203704: metarhyolite, Golden Grove mine; Geochronology Record 1261. *Geological Survey of Western Australia*, 4 pp.

Wingate, M.T.D., Kirkland, C.L. & Zibra, I. (2015d). 155879: granodiorite gneiss, Toben Bore; Geochronology Record 1245. *Geological Survey of Western Australia*, 4 pp.

Wingate, M.T.D., Kirkland, C.L., Zibra, I. & Wyche, S. (2015e). 155822: monzogranite gneiss, Three Mile Well; Geochronology Record 1247: *Geological Survey of Western Australia*, 3 pp.

Witt, W. K., Cassidy, K. F., Lu, Y.-J. & Hagemann, S. G. (2018). The tectonic setting and evolution of the 2.7 Ga Kalgoorlie–Kurnalpi Rift, a world-class Archean gold province. *Mineralium Deposita*, 55, p. 601-631.

Wyche, S. (2010). Tectonic implications of recent advances in Yilgarn stratigraphy. In: Tyler, I.M. & Knox-Robinson, C.M. (eds.) *Fifth International Archaean Symposium Abstracts*, Geological Survey of Western Australia, Record 2010/18, p. 165-167.

Wyche, S., Pawley, M., Chen, S.F., Ivanic, T.J., Zibra, I., Van Kranendonk, M.J., Spaggiari, C.V. & Wingate, M.T.D. (2013). Geology of the Northern Yilgarn Craton. In: Wyche, S., Ivanic, T.J. & Zibra, I. (eds.) Youanmi and Southern Carnarvon Seismic and Magnetotelluric (MT) Workshop 2013, *Geological Survey of Western Australia Record 2013/6*, p. 33-65.

Wyman, D.A., Kerrich, R. & Groves, D.I. (1999). Lode gold deposits and Archean mantle plume-island arc interaction, Abitibi subprovince. *Canadian Journal of Geology*, 107, p. 715-725.

Wyman, D.A. & Kerrich, R. (2010). Geochemical characteristics of the NE Murchison Terrane, Western Australia. In: Tyler, I.M. & Knox-Robinson, C.M. (eds.) *Fifth International Archaean Symposium Abstracts*, Geological Survey of Western Australia, Record 2010/18, p. 242-243.

Wyman, D.A. & Kerrich, R. (2012). Geochemical and isotopic characteristics of Youanmi terrane volcanism: the role of mantle plumes and subduction tectonics in the western Yilgarn Craton. *Australian Journal of Earth Sciences*, 59 (5), p. 671-694.

Wyman, D.A., Cassidy, K.F. & Hollings, P. (2016). Orogenic gold and the mineral systems approach: Resolving fact, fiction and fantasy. *Ore Geology Reviews*, 78, p. 322–335.

Wyman, D.A. (2018). Do cratons preserve evidence of stagnant lid tectonics? *Geoscience Frontiers*, 9, p. 3-17.

Wyman, D.A. (2019). 2.8 Ga subduction-related magmatism in the Youanmi Terrane and a revised geodynamic model for the Yilgarn Craton. *Precambrian Research*, 327, p. 14–33.

Yardley, W.D. & Cleverley, J.S. (2015). The role of metamorphic fluids in the formation of ore deposits. In: Jenkin, G.R.T., Lusty, P.A.J., McDonald, I., Smith, M.P., Boyce, A.J. & Wilkinson, J.J. (eds.) *Ore deposits in an evolving earth, vol. 393*, Geological Society Special Publications, London, p. 117-134.

Yeats, C.J., McNaughton, N.J. & Groves, D.I. (1996). SHRIMP U-Pb geochronological constraints on Archaean volcanic-hosted massive sulphide and lode gold mineralization at Mount Gibson, Yilgarn Craton, Western Australia. *Economic Geology*, 91, p. 1354–1371.

Yuan, L., Zhang, X., Yang, Z., Lu, Y. & Chen, H. (2017). Paleoproterozoic Alaskan-type ultramafic–mafic intrusions in the Zhongtiao mountain region, North China Craton: petrogenesis and tectonic implications. *Precambrian Research*, 296, p. 39–61.

Zegers, T.E., White, S.H., de Keijzer, M. & Dirks, P. (1996). Extensional structures during deposition of the 3460 Ma Warrawoona Group in the eastern Pilbara Craton, Western Australia. *Precambrian Research,* 88, p. 233-248.

Zhao, J.H. & Zhou, M.F. (2007). Geochemistry of Neoproterozoic mafic intrusions in the Panzhihua district (Sichuan Province, SW China): Implications for subduction-related metasomatism in the upper mantle. *Precambrian Research*, 152, p. 27–47.

Zibra, I., Ivanic, T.J., Chen, S., Clos, F., Li, J., Gu, P., Meng, Y., Yu, J. & Wang, C. (2016). Badja, WA Sheet 2240: Geological Survey of Western Australia, 1:100 000 Geological Series.

Zibra, I., Chen, S., Ivanic, T.J., Li, J., Gu, P., Meng, Y., Yu, J. & Wang, C. (2017a). Thundelarra, WA Sheet 2340. Geological Survey of Western Australia, 1:100 000 Geological Series.

Zibra, I., Clos, F., Weinberg, R.F. & Peternell, M. (2017b). The ~2730 Ma onset of the Neoarchean Yilgarn Orogeny. *Tectonics*, 36, p. 1787–1813.

Zibra, I., Peternell, M., Schiller, M., Wingate, M., Lu, Y.-J. & Clos, F. (2018). Tectono-magmatic evolution of the Neoarchean Yalgoo dome (Yilgarn Craton): Diapirism in a pre-orogenic setting. *Geological Survey of Western Australia*, Report 176, 43 pp.

Zibra, I., Lu, Y., Clos, F., Weinberg, R.F., Peternell, M., Wingate, M.T.D., Prause, M., Schiller, M. & Tilhac, R. (2020). Regional-scale polydiapirism predating the Neoarchean Yilgarn Orogeny. *Tectonophysics*, 779, p. 1–26.

Zibra, I. (2020). Neoarchean structural evolution of the Murchison Domain (Yilgarn Craton). *Precambrian Research*, 343, 105719.

APPENDIX A

GEOLOGICAL MAPS OF THE ROTHSAY MINING AREA (CHAPTER 3)

1) 1:25,000 Scale Surface Bedrock Geology of the Rothsay Mining Area, Western Australia (PDF)

2) 1:25,000 Scale Interpreted Bedrock Geology of the Rothsay Mining Area, Western Australia (PDF)

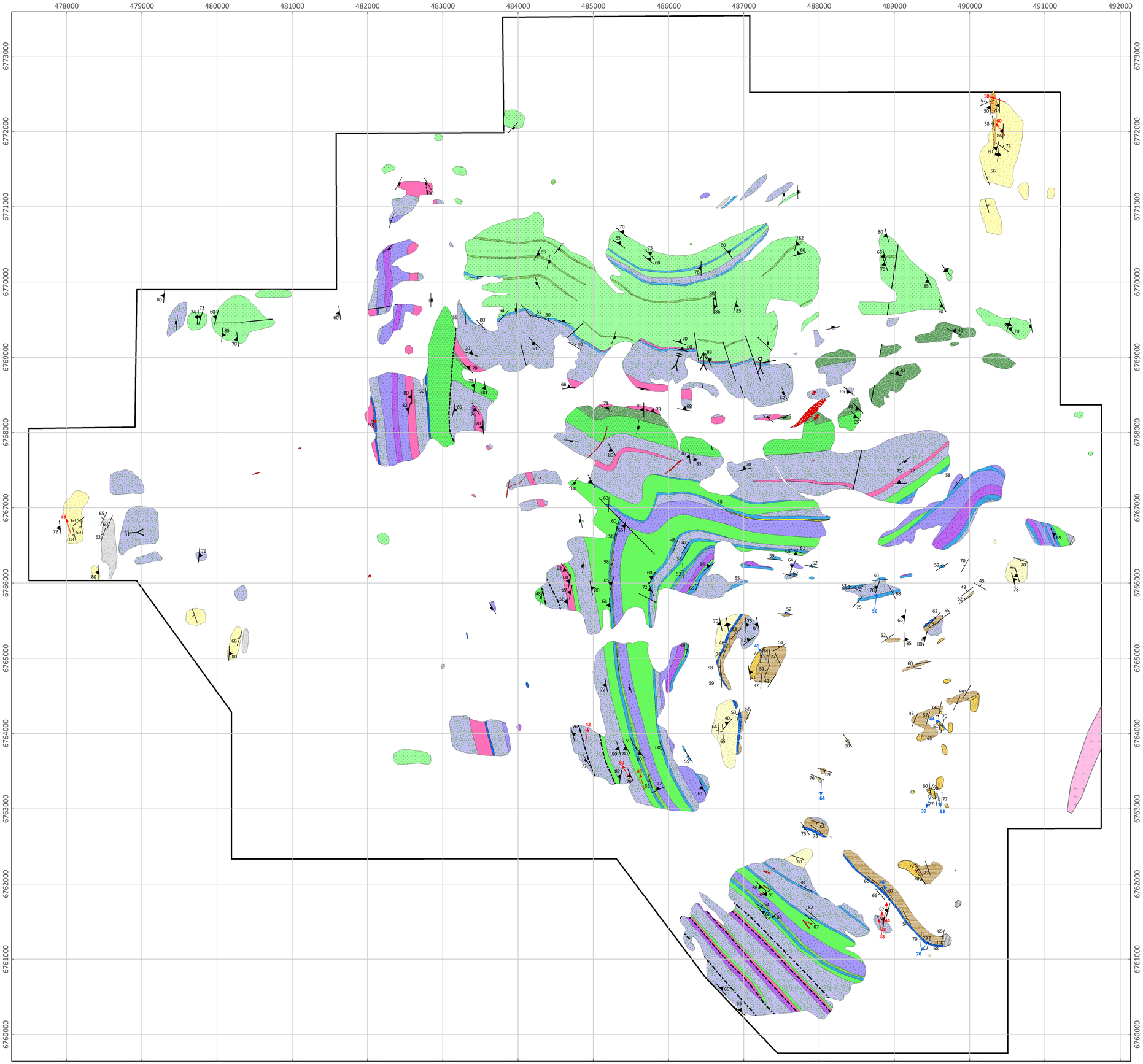

PROTEROZOIC

Mafic Intrusive Rocks

Dolerite dyke; fine to medium-grained, moderately magnetic.

Felsic Intrusive Rocks

WALGANNA SUITE

Seeligson Monzogranite

Monzogranite; equicrystalline, medium to coarse-grained, undeformed; metamorphosed.

Felsic pegmatite; coarse-grained quartz-feldspar-mica, locally Li-bearing, granophyric textures.

Mafic-Ultramafic Intrusive Rocks

WARRIEDAR SUITE

Dolerite; medium-grained, massive, non-magnetic, minor gabbro interleaved; metamorphosed.

Gabbro; coarse-grained, massive to weakly foliated, locally leucogabbroic; metamorphosed.

Pyroxenite; medium to coarse-grained, massive to weakly foliated; locally porphyritic; metamorphosed.

Peridotite; serpentinised with relict olivine ± pyroxene cumulate texture, often strongly foliated; metamorphosed.

Supracrustal Rocks

ARCHAEAN

Willowbank Clastics

Conglomerate, pebbly sandstone and volcanogenic sandstone, strongly foliated, locally silicified; metamorphosed.

Felsic volcaniclastic rocks, locally lapilli-bearing, laminated and welded, conglomeratic pebbly sandstone near base; metamorphosed.

CHULAAR GROUP

Mulga Volcanics

Pyroxene spinifex-textured basalt including random acicular and oriented acicular spinifex, locally strongly foliated; metamorphosed.

Spherulitic basalt; containing spherules 0.5-12 mm in diameter, locally pillowed and spinifex-textured, often foliated; metamorphosed.

Peridotite, moderately serpentinised, relict olivine cumulate textures, highly magnetic, basal portion of spinifex-textured units; metamorphosed.

Lapilli-brearing andesitic bedded tuff; locally massive, minor interbedded pelitic units; metamorphosed.

Metamorphosed banded iron formation and banded chert; magnetite, hematite, quartz.

Beryl West Volcanics

Metamorphosed banded iron formation and banded chert; magnetite, hematite, quartz.

Pyroxene spinifex-textured basalt; includes randomly oriented platy pyroxene and acicular pyroxene spinifex; metamorphosed.

Basalt; typically aphyric, featureless; metamorphosed.

Two Peaks Volcanics

Quartzite; medium-grained, white-pink in colour and typically massive, sugary-textured; metamorphosed.

Pyroxene spinifex-textured basalt including random and oriented acicular forms, locally strongly foliated; metamorphosed.

Basalt; typically aphyric, featureless; metamorphosed.

Metamorphosed banded iron formation and banded chert; red-black, magnetite, hematite, quartz.

Macs Well Clastics

Felsic volcaniclastic rocks, bedded, locally lapilli-bearing, minor interleaved dacitic volcanics, conglomeratic pebbly sandstone near base; metamorphosed.

Metamorphosed banded iron formation and banded chert; magnetite, hematite, quartz, minor interbedded ferruginous siltstone.

Siltstone; ferruginous, locally interbedded with BIF, minor quartzite; metamorphosed.

Quartzite and metamorphosed quartz-rich sandstone; minor volcanogenic content.

Structural Symbols

- Project area
- Inclined bedding, showing strike and dip (70)
- Vertical bedding
- Inclined foliation, showing strike and dip (70)
- Vertical foliation
- Inclined fracture, showing strike and dip
- Fold axial surface, small-scale, showing strike and dip (56)
- Fold axes, small-scale, showing trend and plunge (53)
- Mineral lineation, showing trend and plunge (60)
- Way-up structure, graded bedding
- Way-up structure, igneous differentiation
- Way-up structure, spinifex branching
- Shear zone
- Fault
- Strongly foliated rocks mostly beneath cover - concealed shear zone

Surface Bedrock Geology of the Rothsay Mining Area, Western Australia

SCALE 1 : 25 000

CO-ORD: GDA_1994_MGA_Zone_50

0 0.5 1 2 3 4

Kilometres

N

Geology by J Price 2014-2018

CARDIFF UNIVERSITY / PRIFYSGOL CAERDYDD

MINJAR GOLD

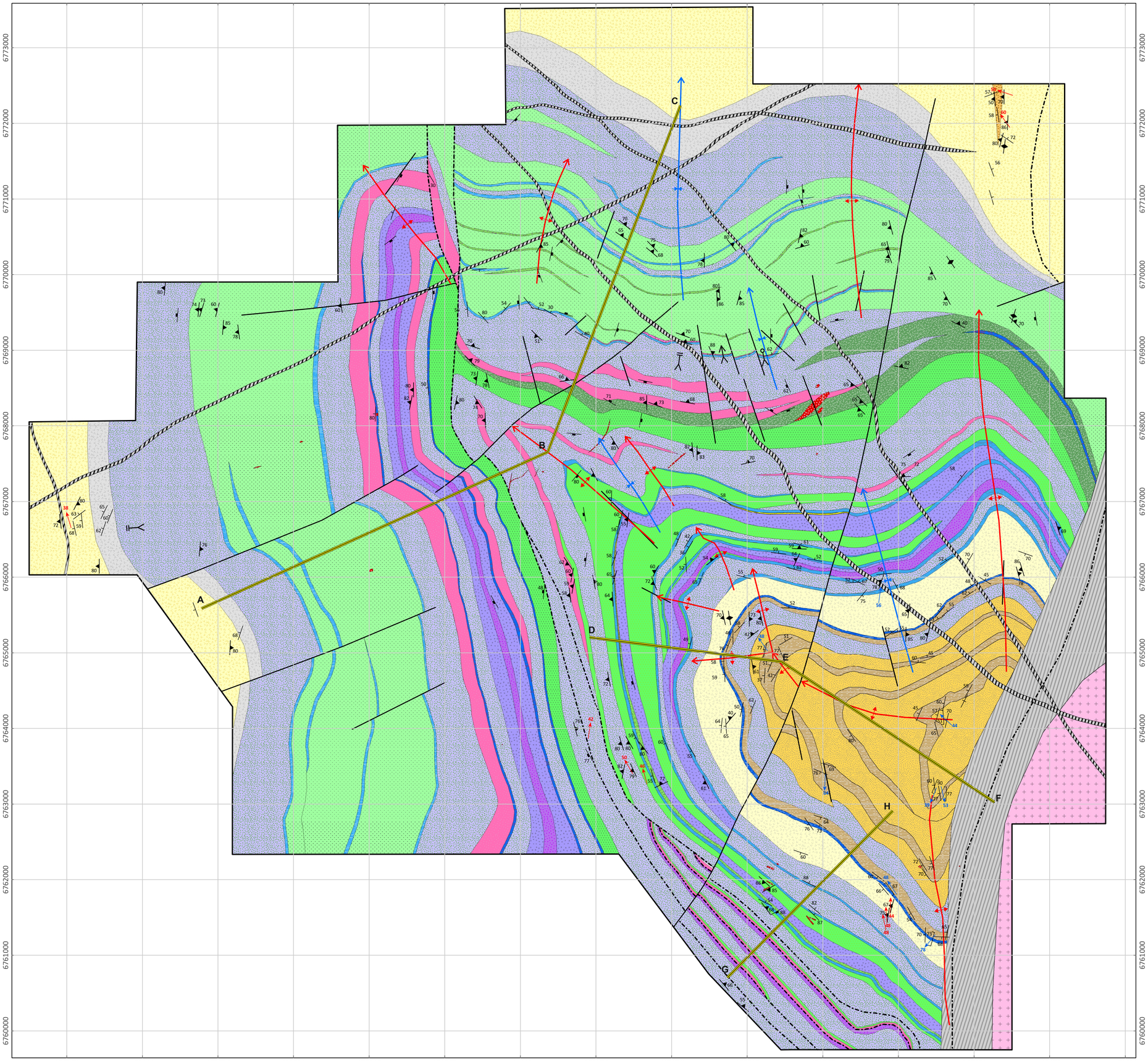

PROTEROZOIC

Mafic Intrusive Rocks

Dolerite dyke; fine to medium-grained, moderately magnetic.

Felsic Intrusive Rocks

WALGANNA SUITE

Seeligson Monzogranite

Monzogranite; equicrystalline, medium to coarse-grained, undeformed; metamorphosed.

Felsic pegmatite; coarse-grained quartz-feldspar-mica, locally Li-bearing, granophyric textures.

Mafic-Ultramafic Intrusive Rocks

WARRIEDAR SUITE

Dolerite; medium-grained, massive, non-magnetic, minor gabbro interleaved; metamorphosed.

Gabbro; coarse-grained, massive to weakly foliated, locally leucogabbroic; metamorphosed.

Pyroxenite; medium to coarse-grained, massive to weakly foliated; locally porphyritic; metamorphosed.

Peridotite; serpentinised with relict olivine ± pyroxene cumulate texture, often strongly foliated; metamorphosed.

Supracrustal Rocks

ARCHAEAN

Willowbank Clastics

Conglomerate, pebbly sandstone and volcanogenic sandstone, strongly foliated, locally silicified; metamorphosed.

Felsic volcaniclastic rocks, locally lapilli-bearing, laminated and welded, conglomeratic pebbly sandstone near base; metamorphosed.

CHULAAR GROUP

Mulga Volcanics

Pyroxene spinifex-textured basalt including random acicular and oriented acicular spinifex, locally strongly foliated; metamorphosed.

Spherulitic basalt; containing spherules 0.5-12 mm in diameter, locally pillowed and spinifex-textured, often foliated; metamorphosed.

Peridotite, moderately serpentinised, relict olivine cumulate textures, highly magnetic, basal portion of spinifex-textured units; metamorphosed.

Lapilli-brearing andesitic bedded tuff; locally massive, minor interbedded pelitic units; metamorphosed.

Metamorphosed banded iron formation and banded chert; magnetite, hematite, quartz.

Beryl West Volcanics

Metamorphosed banded iron formation and banded chert; magnetite, hematite, quartz.

Pyroxene spinifex-textured basalt; includes randomly oriented platy pyroxene and acicular pyroxene spinifex; metamorphosed.

Basalt; typically aphyric, featureless; metamorphosed.

Two Peaks Volcanics

Quartzite; medium-grained, white-pink in colour and typically massive, sugary-textured; metamorphosed.

Pyroxene spinifex-textured basalt including random and oriented acicular forms, locally strongly foliated; metamorphosed.

Basalt; typically aphyric, featureless; metamorphosed.

Metamorphosed banded iron formation and banded chert; red-black, magnetite, hematite, quartz.

Macs Well Clastics

Felsic volcaniclastic rocks, bedded, locally lapilli-bearing, minor interleaved dacitic volcanics, conglomeratic pebbly sandstone near base; metamorphosed.

Metamorphosed banded iron formation and banded chert; magnetite, hematite, quartz, minor interbedded ferruginous siltstone.

Siltstone; ferruginous, locally interbedded with BIF, minor quartzite; metamorphosed.

Quartzite and metamorphosed quartz-rich sandstone; minor volcanogenic content.

Structural Symbols

- Project area
- A — B Cross-section fence line
- 70 Inclined bedding, showing strike and dip
- Vertical bedding
- 70 Inclined foliation, showing strike and dip
- Vertical foliation
- Inclined fracture, showing strike and dip
- 56 Fold axial surface, small-scale, showing strike and dip
- 53 Fold axes, small-scale, showing trend and plunge
- 60 Mineral lineation, showing trend and plunge
- Way-up structure, graded bedding
- Way-up structure, igneous differentiation
- Way-up structure, spinifex branching
- Shear zone
- Fault
- Strongly foliated rocks mostly beneath cover - concealed shear zone
- Plunging antiform, typically concealed
- Plunging synform, typically concealed

Interpreted Bedrock Geology of the Rothsay Mining Area, Western Australia

SCALE 1 : 25 000

CO-ORD: GDA_1994_MGA_Zone_50

0 0.5 1 2 3 4

Kilometres

N

Geology by J Price 2014-2018

CARDIFF UNIVERSITY
PRIFYSGOL CAERDYDD

MINJAR GOLD

APPENDIX B: LABORATORY METHODS

APPENDIX B1 – METHODS FOR WHOLE ROCK GEOCHEMISTRY

B1.1 Major and trace element analysis

B1.1.1 Preparation of powdered samples

Preparation for whole rock major and trace element analysis has been undertaken using the rock preparation facilities at Cardiff University, UK. Two kilograms of each sample were collected and all weathered surfaces, veining and alteration was removed using a diamond-bladed rock saw. Samples were then crushed to < 0.5 cm size using a steel jaw crusher and ground to a fine powder using an agate disc mill. Approximately 2 g of each powdered sample was first heated at 103 °C for 30 minutes to remove moisture introduced during preparation, and then weighed to give an original mass of powder. Each sample was then ignited at 900 °C for 2 hours, allowed to cool to room temperature and then weighed once again to give an ignited mass of powder. The loss on ignition (LOI) of each sample was calculated using Equation B1.1.

$$Loss\ on\ ignition\ (LOI; wt.\%) = \frac{Original\ mass\ of\ powder - Ignited\ mass\ of\ powder}{Original\ mass\ of\ powder}\ x\ 100$$

Equation B1.1

Sample Batch	No. of samples	Solution preparation method	Analytical instrument		External standards		
			ICP-OES	ICP-MS	JB1-A[1]	MRG-1[2]	JR-1[1]
Jul-17	31	Fusion method 1	Jobin Yvon Horiba Ultima 2	Thermo Elemental X7 series	✓	✓	
Aug-18	44	Fusion method 1	Thermo iCAP 7000	Thermo iCAP RQ	✓ ✓	✓	
Jul-19	37	Fusion method 2	Thermo iCAP 7000	Thermo iCAP RQ	✓	✓	✓

Table B1.1: Details for each batch of geochemical samples analysed in this study including the number of samples in each batch, preparation methods, analytical instruments used and standards run with each batch. Further details of external standards are provided in the text. [1] Imai et al. (1995). [2] Abbey (1981).

B1.1.2 Preparation of solutions and ICP-OES and ICP-MS analysis

Geochemical samples presented in this study were prepared for ICP geochemical analysis in three batches, corresponding to groups of samples analysed in July 2017, August 2018 and July 2019 (Table

B1.1). The methods followed to prepare solutions for analysis varied slightly between these batches. Samples in the July 2017 and August 2018 batches were prepared using the lithium metaborate fusion method (*fusion method 1*). Following this method, 0.1 ± 0.001 g of each ignited powdered sample and 0.6 ± 0.006 g of lithium metaborate flux were measured in a platinum crucible. 5-6 drops of the wetting agent, lithium iodide, were added to each sample, which was then fused using an automated Claisse FLUXY fusion system. Each fused mixture was dissolved in a 50 ml solution comprising 20 ml of 10 % HNO_3 and 30 ml of 18 Mohm deionised water, the latter obtained from a Milli-Q purification system. Following dissolution, a 1 ml 100 ppm Rh spike was added to each solution, which was then made up to a volume of 100 ml using 18 Mohm deionised water.

Samples in the July 2019 batch were prepared for ICP geochemical analysis using a lithium metaborate/tetraborate fusion method (*fusion method 2*). Following this method, 0.1 ± 0.001 g of each ignited powdered sample was measured in a platinum crucible, in addition to 1.0 ± 0.010 g of a lithium metaborate/lithium tetraborate flux containing 0.5% integrated lithium iodide. Samples were then fused using an automated Claisse M4 FLUXY fusion system. Each fused mixture was then dissolved in a 50 ml solution comprising 20 ml of 10 % HNO_3 and 30 ml of 18 Mohm deionised water, the latter obtained from a Milli-Q purification system. Following dissolution, a 1 ml 50 ppm Rh spike was added to each solution, which was then made up to a volume of 100 ml using 18 Mohm deionised water.

Solutions were analysed at Cardiff University for major element and selected trace element (Sc, V, Cr, Co, Ni, Cu, Zn, Sr, Y, Zr, Ba) abundances using Inductively Coupled Plasma Optical Emission Spectrometry (ICP-OES), and for trace element abundances using Inductively Coupled Plasma Mass Spectrometry (ICP-MS). ICP-OES analysis was undertaken on approximately 20 ml of each sample solution. An aliquot of 1 ml of each solution were added to 1 ml solutions of In and Tl and 8 ml of 2% HNO_3, then analysed by ICP-MS. The analytical instruments used for each batch of whole rock geochemical analysis are outlined in Table B1.1. The July 2017 batch of samples was analysed using a Jobin Yvon Horiba Ultima 2 ICP-OES and a Thermo Elemental X7 series ICP-MS. Subsequent batches of samples (August 2018 and July 2019) were analysed using the Thermo iCAP 7000 ICP-OES and Thermo iCAP RQ ICP-MS systems (Table B1.1). Samples were run on the mass spectrometers by Dr. Iain McDonald at Cardiff University. A compilation of new hydrous whole rock major and trace element geochemical data presented by this study, in combination with literature data used in this study, are presented in **APPENDIX E7**.

B1.2 Evaluation of accuracy and precision of geochemical data

B1.2.1 Standards

External standards were used to assess the accuracy and precision of elemental data obtained from ICP-OES and ICP-MS analysis. The external standards used during analysis were JB1-A, JR-1 and MRG-1. JB1-A is a basalt standard and JR-1 is a rhyolite standard, both issued by the Geological Survey of Japan. The elemental data for both standards are reported by Imai et al. (1995). MRG-1 is a gabbro standard issued by the Canadian Certified Reference Materials Project (CCRMP) of the Canada Centre for Mineral and Energy Technology (CANMET). Elemental data for this standard is reported by Abbey (1981). JB1-A and MRG-1 standards were run with every batch of analysed samples, and JR-1 was also analysed for a single batch of samples (July 2019) that included felsic rocks (Table B1.1).

B1.2.2 Accuracy

The geochemical results for each run of the standards JB1-a, MRG-1 and JR-1 are given in **APPENDIX E8**, in addition to percentage errors for measured concentrations relative to the certified elemental concentrations of each standard. Percentage errors are calculated using Equation B1.2.

$$\%\ error = \frac{Measured\ value - certified\ value}{Certified\ value}\ x\ 100$$

Equation B1.2

A majority of elements in all standards have percentage errors of < 5%, for both ICP-OES and ICP-MS analyses. This suggests that the geochemical data acquired from all batches can be considered accurate and can be reliably used for petrogenetic assessment and interpretation. For those elements analysed by both ICP-OES and ICP-MS methods (Section B1.1.2), abundances in the analysed standards are broadly similar. However, as the ICP-MS analyses of these elements more closely match the certified values of standards, these data are used in this study.

B1.2.3 Precision

The precision of geochemical data can be assessed through comparing multiple analyses of the external standards run with each batch of samples. The precision of a given elements concentration in a standard is represented here by the relative standard deviation (RSD). RSD values for a given element are calculated using equations B1.3-B1.5 below:

$$x_a = \frac{\sum x}{n}$$

Equation B1.3

Where x_a is the average element concentration, x is the element concentration and n is the number of analyses.

$$S = \frac{\sqrt{\sum (x - x_a)^2}}{n - 1}$$

Equation B1.4

Where S is the standard deviation, x is the element concentration, x_a is the average element concentration and n is the number of measurements.

$$RSD\ (\%) = \frac{100S}{x_a}$$

Equation B1.5

Where RSD is the relative standard deviation, S is the standard deviation and x_a is the average element concentration.

(Note that these equations are also used in Appendix B3 for S and O isotope analyses).

RSD values for all elements analysed for external standards are given in **APPENDIX E8**. These values demonstrate that the analyses of most elements in standard JB1-a are precise, as the majority of elements have RSD < 5%. The only analyses of the JB1-a standard that could be considered as imprecise are P_2O_5, Zr (ICP-OES only), Rb and Pb, as these elements have RSD of just over 10%. Similarly, the vast majority of analyses of the MRG-1 standard have RSD < 5%. The only analyses of the MRG-1 standard that could be considered imprecise are K_2O, Zn (both ICP-MS and ICP-OES), Nb, Hf, Pb and Th, as these elements have RSD >10%.

In summary, repeated analyses of standards generally display low RSD values and thus the geochemical data presented in this study can be considered precise. Repeat analyses of standards also demonstrates that precision levels are comparable between the ICP-MS and ICP-OES analytical methods, and between the results from the two ICP-OES instruments and two ICP-MS instruments used for separate sample batches in this study (Table B1.1).

B1.3 References

Abbey, S. (1981). The search for the 'best values' – A study of three Canadian Rocks. *Geostandards Newsletter, 5 (1)*. p. 13-26.

Imai, N., Terashima, S., Itof, S. & Ando, A. (1995). 1994 Compilation values for GSJ reference samples, "Igneous Rock Series". *Geochemical Journal, 29(1).* p. 91-95.

APPENDIX B2 – METHODS FOR U-Pb ZIRCON GEOCHRONOLOGY

B2.1 Sample preparation

SHRIMP U-Pb zircon geochronological analysis has been undertaken on three samples taken from previously unconstrained units in the Yalgoo-Singleton Greenstone Belt. The procedure followed for sample preparation prior to analysis was as follows.

Between 5-7 kg of fresh material was collected for each sample and all alteration and weathered surfaces removed using a diamond bladed rock saw, prior to preparation and separation at the NERC Isotope Geoscience Laboratories in Keyworth, UK. Jaw crushing was undertaken to reduce sample size to <1 cm diameter, followed by milling to a coarse powder using a Fritsch Pulverisette disc-mill, and then sieving to separate grains < 355 µm in diameter. Heavy minerals were concentrated using a Rogers shaking table, followed by magnetic separation using a Franz separator, and density separation using di-iodomethane to isolate grains with a density greater than 3.3 g/cm^3.

Zircon crystals were picked from the separate and cast in an epoxy mount along with zircon reference materials BR266 (559 Ma 6/38 age, 909 ppm U; Stern, 2001) and OGC1 (3465 Ma 7/6 age; OG1; Stern et al., 2009), and then polished to expose the interior of the crystals. Secondary electron (SE) and cathodoluminescence (CL) imaging was carried out on the mounted crystals at the John de Laeter Centre, Curtin University, using a TESCAN Mira3 scanning electron microscope.

B2.2 SHRIMP U-Pb zircon geochronological analysis

Zircon U-Pb analyses were performed using a sensitive high resolution ion microprobe (SHRIMP II) at the John de Laeter Centre, Curtin University, Perth, between 21st-22nd August 2018. The SHRIMP was operated at a primary beam current of approximately 2 nA, with a spot size between 20-25 µm and a mass resolution in excess of 5000 (m/Δm). Data were collected from each sample in six cycles of sequential field-stepping covering the mass range of Zr_2O, ^{204}Pb, background, ^{206}Pb, ^{207}Pb, ^{208}Pb, ^{238}U, ^{248}Th and ^{254}UO, after which the data from the cycles were combined. Ratios and abundances of U-Pb-Th were deduced relative to the BR266 standard, which was analysed after every six analyses of unknown grains. Radiogenic ^{207}Pb/^{206}Pb ratios were compared to analyses of the OGC1 standard taken twice per day. Corrections for common Pb have been made using measured ^{204}Pb for each analysis, with the common Pb component modelled on the composition of Pb ore from Broken Hill. Data reduction was undertaken using SQUID2 and Isoplot 3 programs (Ludwig, 2001; 2003). Uncertainties for isotopic ratios and dates provided in the data table are given at the 1σ level, and for calculated

weighted mean values are at the 95% confidence (2SD) level. Generally, analyses >10 % discordance were rejected and are not included in age calculations.

B2.3 References

Ludwig, K.R., (2001). User's guide to SQUID 2. 2. Berkeley Geochronology Center, Berkeley.

Ludwig, K.R., (2003). User's manual for ISOPLOT 3, A Geochronological Toolkit for Microsoft Excel. Berkeley Geochronology Centre, Berkeley, CA. *Special Publication No. 4.*

Stern, R.A., (2001). A new isotopic and trace-element standard for the ion microprobe: preliminary thermal ionization mass spectrometry (TIMS) U–Pb and electron-microprobe data: *Geological Survey of Canada, Radiogenic Age and Isotopic Studies, Report 14, Current Research 2001-F1*, 11pp.

Stern, R.A., Bodorkos, S., Kamo, S.L., Hickman, A.H. and Corfu, F. (2009). Measurement of SIMS instrumental mass fractionation of Pb isotopes during zircon dating: *Geostandards and Geoanalytical Research*, 33, p. 145–168.

APPENDIX B3 – METHODS FOR SEM ANALYSIS, STABLE ISOTOPE ANALYSIS AND U-Pb MONAZITE GEOCHRONOLOGY

B3.1 SEM Analysis

B3.1.1 Back-scattered electron (BSE) imaging and mineral identification

Back-scattered electron (BSE) imaging and semi-quantitative mineral point analyses of polished thin sections has been undertaken using an FEI XL30 Field Emission Gun Environmental SEM (ESEM) at Cardiff University, fitted with a secondary electron (SE) and BSE detector, in addition to an Oxford Instruments Inca energy dispersive X-ray spectrometer (EDS) analysis system. Polished thin sections were sputtered with a carbon coating of 10-15 nm thickness and then analysed in BSE-mode. The operating conditions used for BSE imaging comprised an accelerating voltage of 20 kV, a 50 µm aperture and spot size 4. The BSE detector allows the imaging of mean atomic mass variations in a sample and can detect elements with an atomic number greater than 4 (i.e., B and heavier elements). Through adjusting the contrast and brightness settings, BSE imaging was able to distinguish the mineral phases present in a sample and in some instances, elemental variation within a given phase. When searching for gold-bearing minerals or other such atomically-heavy phases, brightness and contrast settings were adjusted using a pre-identified grain to more easily distinguish the phase and then samples were manually and systematically scanned. The EDS detector fitted to the ESEM has been used for semi-quantitative point analyses that are purely utilised for mineral identification purposes and has not been used in conjunction with standards.

B3.1.2 Element/mineral mapping

Element maps have been constructed to assess the relationship between sulphide phases and surrounding silicate and carbonate minerals, as well as the zonation of elements in carbonate veins (Chapter 9). Element mapping has also been used to assess the mineralogy of variolitic volcanic rocks and quartz dioritic vein features (Chapter 5). Element maps were acquired using a Zeiss Sigma Field Emission Gun Analytical SEM (ASEM) equipped with two Oxford Instruments 150 mm^2 X-MaxN silicon drift detector energy dispersive X-ray spectrometers (EDS), at Cardiff University. Operating conditions consisted of an accelerating voltage of 20 kV, a nominal beam current of ~5 nA, a 120 µm aperture and a fixed working distance of 8.9 mm. Aztec software (Oxford Instruments) was used to set up and acquire element maps and the resolution used varied slightly depending on the map area and the time available, with a magnification of between 154-215x and a step size of 5-7 µm. Additional parameters used during element mapping include a dwell time of 500 ms, a dead time of 40-50% and a process

time of 0.5 µs. Aztec software was used for spectra deconvolution, element map construction and identification of mineral phases. Spectral cross-referencing from EDS spot analysis was used to confirm the identification of mineral phases present.

B3.1.3 Automated mineral identification

Automated scanning of four polished thin sections was used to search for discrete (typically <50 µm) monazite crystals, in preparation for geochronological analysis (Section B3.3). A Zeiss Sigma Field Emission Gun Analytical SEM (ASEM) at Cardiff University, equipped with two Oxford Instruments 150 mm^2 X-MaxN silicon drift detector energy dispersive X-ray spectrometers (EDS), was used for automated scanning of polished thin sections. Automated scans utilised the point and ID feature of Aztec software for preselection of elements of interest, primarily the constituent elements of monazite and other atomically heavy discrete phases that were likely to occur in the samples, such as S, Fe, Cu, As, Au, Ag, Sb, Zr, Pb, La, Ce, Nd and P. BSE maps were acquired using an accelerating voltage of 20 kV, a fixed working distance of 8.9 mm and a 60 µm aperture. A magnification of 200x, dwell time of 20 µs and image scan size of 1024 pixels were used in order to achieve an optimal balance between analytical resolution and time taken. These settings were able to identify monazite crystals down to ~2 µm in diameter, which was significantly less than the spot size used in subsequent geochronological analysis (Section B3.3). The brightness and contrast of the BSE image was adjusted for each sample analysed, with the aim of setting the threshold just below that of a pre-identified monazite crystal in each sample. Consequently, the software was able to distinguish monazite, in addition to several other rare phases that were atomically heavier than monazite (and thus brighter in BSE), such as galena and electrum. Following the automated scans, the feature analysis tool in Aztec software was used to classify the identified features by chemistry. Monazite crystals >10 µm in diameter were then re-analysed using EDS, to verify the results of automated scans, and subsequently imaged in BSE mode to assess the suitability of individual grains for geochronological analysis.

Additionally, BSE maps of thin sections have been montaged using Aztec software, and colourised using ImageJ software, in order to demonstrate the relationship between various sulphide phases within these samples.

B3.2 Stable Isotope Analysis

Analysis of sulphur and oxygen stable isotopes was undertaken at the Scottish Universities Environmental Research Centre (SUERC) in East Kilbride, Scotland, UK. This analysis was supported by the NERC Isotope Geoscience Facilities Steering Committee grant IP-1858-1118.

B3.2.1 Conventional sulphur isotope analysis

Samples analysed by conventional sulphur isotope ($\delta^{34}S$) extraction consisted of sulphide grains that were optically picked from crushed separates and inspected for impurities using a stereomicroscope. Approximately 4-8 mg of each sample was measured and subsequently converted to SO_2 through combustion with 200 mg of cuprous oxide at 1070 °C, following the method outlined by Robinson & Kusakabe (1975). A VGA SIRA II gas source mass spectrometer was used to analyse each combusted sample. All sulphur isotope values are calculated relative to the Vienna Canyon Diablo Troilite (V-CDT) standard, and are reported in per mil (‰) using the conventional delta ($\delta^{34}S$) notation. Data quality was assessed through the repeated combustion and analysis of the international standards NBS-123 (+17.1 ‰) and IAEA-S-3 (-31.5 ‰) and an internal standard, CP1 (-4.6 ‰). The results for standard analyses, in addition to calculated accuracy and precision measurements such as percentage errors, mean values, standard deviations and the relative standard deviations are shown in Table B3.1. These values are calculated using the equations shown in Appendix B1. The reproducibility of all analyses of standards was consistently better than ± 0.7 ‰ (1σ).

Standard	CP1	NBS123	IAEA S3
Certified value	-4.6	17.1	-31.5
Run 1	-4.7	16.4	-32.5
% Error	2.2	-4.1	3.2
Run 2	-4.2	17.5	
% Error	-8.7	2.3	
Run 3	-4.4	17.6	
% Error	-4.3	2.9	
Run 4	-4.4		
% Error	-4.3		
Mean	-4.4	17.2	-32.5
Standard Deviation	0.2	0.7	
RSD	-4.7	3.9	

Table B3.1: Summary of analyses of the CP1, NBS-123 and IAEA-S3 standards analysed by conventional sulphur isotope extraction. Results are reported in standard notation relative to V-CDT, in ‰.

B3.2.2 Conventional oxygen isotope analysis of quartz

Samples of quartz were hand-picked from crushed separates using a stereomicroscope and separated from impurities where present. Oxygen isotope analysis was undertaken following the conventional laser fluorination methodology described by Sharp (1990). Following this method, approximately 1 mg of quartz crystals were measured for each sample and prefluorinated in a chamber with ClF_3 for approximately 16 hours. Each sample was then reacted with excess ClF_3, using a CO_2 laser as a heat source (temperatures exceeding 1500 °C; following Sharp, 1990), to release oxygen. The liberated oxygen was converted to CO_2 by reaction with hot graphite and the resultant yield was measured using a capacitance manometer. The oxygen isotope composition of CO_2 was analysed on-line by a VG Isotech SIRA II mass spectrometer. Results are reported in standard notation ($\delta^{18}O$) as per mil (‰) deviations relative to the Vienna Standard Mean Ocean Water (VSMOW) standard. Data quality was monitored through the repeat analysis of two international standards, GP147 (+7.2 ‰) and UWG2 (+5.8 ‰), as well as the internal standard YP2 (+16.4 ‰). The results for standard analyses, in addition

Standard	**YP2**	**GP147**	**UWG2**
Certified value	16.4	7.2	5.8
Run 1	16.4	7.0	6.0
% Error	0.0	-2.8	3.4
Run 2	16.3	7.6	5.5
% Error	-0.4	5.5	-4.8
Run 3	16.8	7.4	5.7
% Error	2.6	2.6	-2.0
Run 4	16.4	6.9	6.1
% Error	0.2	-4.3	5.7
Run 5	16.4	6.9	6.0
% Error	0.2	-4.1	4.2
Run 6	16.4	7.4	5.9
% Error	-0.2	3.1	1.2
Run 7	16.5	7.2	5.7
% Error	0.3	0.5	-2.5
Run 8	16.4	7.3	5.8
% Error	0.0	1.0	0.2
Run 9	16.4	7.3	5.8
% Error	0.0	1.4	-0.3
Run 10			5.7
% Error			-1.7
Mean	16.45	7.22	5.82
Standard Deviation	0.15	0.24	0.19
RSD	0.9	3.4	3.3

Table B3.2: Summary of analyses of the YP2, GP147 and UWG2 standards repeatedly analysed during oxygen isotopic analysis of quartz. Results are reported in standard notation relative to V-SMOW, in ‰.

Laboratory & Sample Preparation	
Laboratory name	Geochronology & Tracers Facility, British Geological Survey
Sample type/mineral	Monazites in thin section
Sample preparation	Conventional 30µm thin section
Imaging	Automated scanning and BSE imaging of suitable monazite grains undertaken using a Zeiss Sigma Field Emission Gun Analytical SEM (ASEM) at Cardiff University, equipped with two Oxford Instruments energy dispersive X-ray spectrometers (EDS).
Laser ablation system	
Make, model & type	ESL NWR193UC
Ablation cell & volume	TV2 two-volume cell, ~1cm^3 inner-cup volume
Laser wavelength (nm)	193 nm
Pulse width (ns)	4 ns
Fluence (J.cm^{-2})	1 J.cm^{-2}
Repetition rate (Hz)	10 Hz
Ablation duration (secs)	10 secs
Ablation pit depth / ablation rate	Estimated 5 µm pit depth assuming ablation rate of 0.05 µm/pulse.
Spot diameter (µm)	5-10 µm
Sampling mode / pattern	Static spot ablation
Carrier gas	100% He in the cell, Ar make-up gas combined using a Y-piece 50% along the sample transport line to the torch.
Cell carrier gas flow (l/min)	0.8 l/min
ICP-MS Instrument	
Make, Model & type	Nu Instruments, Attom, SC-SF-ICP-MS
Sample introduction	laser
RF power (W)	1300W
Make-up gas flow (l/min)	Sourced from Nu Instruments DSN-100 desolvating nebulizer. Neb pressure 24psi (estimated at 0.7l/min) Ar. Aspirating air during ablation
Detection system	Pulse-counting ion counter with attenuation system
Masses measured	202, 204, 206-208, 232, 238
Integration time per peak/dwell times; switch delay between mass jumps (ms)	200, 200, 600, 1000, 200, 200, 800, switch delay 40
Total integration time per output datapoint (secs)	~0.46 secs
'Sensitivity' as useful yield (%, element)	n.d.
IC Dead time (ns)	12 ns
Data Processing	
Gas blank	Iolite on-peak baseline subtracted
Calibration strategy	'Stern' used as primary reference material, Moacyr & Manangotry used for validation
Reference Material info	'Stern', Moacyr & Manangotry (Horstwood et al., 2016)
Data processing package used / Correction for LIEF	Iolite v.3.71
Mass discrimination	Sample-standard bracketing to primary reference material
Common-Pb correction, composition and uncertainty	No common-Pb correction applied to the data.
Uncertainty level & propagation	Ages are quoted at 2*s* absolute, propagation is by quadratic addition. Repeatability (excess variance) of reference material and inter-session reproducibility (2% 2s) propagated into data points and sample ages as appropriate.

Table B3.3 (continued on next page)

Quality control / Validation	Moacyr – Wtd ave $^{206}Pb/^{238}U$ age Day 1 = 506.6 ± 5.6 (95% conf., MSWD = 1.4, n=18) Day 2 = 513.7 ± 2.6 (95% conf., MSWD = 1.6, n=24) Manangotry – Wtd ave $^{206}Pb/^{238}U$ age Day 1 = 553.7 ± 5 (95% conf., MSWD = 1.11, n=18) Day 2 = 569.6 ± 3.2 (95% conf., (MSWD = 1.8, n=24) Systematic uncertainty for propagation is 2% (2*s*).

Table B3.3: Metadata for LA-ICP-MS analysis, including details for the laboratory used, analytical instruments, operating conditions and data processing. Reporting template modified after Horstwood et al. (2016).

to calculated accuracy and precision measurements using the equations in Appendix B1, are shown in Table B3.2. Reproducibility of the oxygen isotopic data was consistently better than ±0.3 ‰ (1σ), based on repeat analyses of standards.

B3.3 LA-ICPMS geochronological analysis

In-situ laser ablation inductively coupled plasma mass spectrometry (LA-ICP-MS) geochronological analysis was undertaken at the Geochronology & Tracers Facility, British Geological Survey, Keyworth, Nottingham, UK. This analysis was supported by the NERC Isotope Geoscience Facilities Steering Committee grant IP-1858-1118. Monazite crystals were identified during automated scanning and suitable crystals were subsequently imaged in BSE, using the ASEM at Cardiff University (Section B3.1.3). LA-ICP-MS U-Pb analyses were performed using a Nu Instruments Attom single-collector sector field (SC-SF-)ICP-MS coupled to an Elemental Scientific Lasers NWR193UC 193nm excimer laser ablation system. A Nu Instruments DSN-100 desolvating nebuliser provided Ar make-up gas for the 0.8l /min He sample gas, with the two combined approximately halfway between the ablation cell and the plasma torch. $^{254}UO/^{238}U$ was around 0.1% across two analytical sessions. A variable 5 or 10 µm ablation spot size was utilised at 10Hz, 1 $J.cm^{-2}$ for a duration of 10 seconds. Multiple spot analyses of minerals surrounding monazite grains, such as sericite, albite, quartz and arsenopyrite, indicate that these phases have negligible common Pb content. The 'Stern' monazite (Bananeira 1 pegmatite, sample 8153, Geol. Surv. Can.) was used as primary reference material, with Moacyr and Manangotry monazites used for validation [see Horstwood et al. (2016) for further details of standards]. Sample data were filtered for apparent common-Pb components with the resulting single age population weighted mean propagated by 2% (2s) for both Pb/Pb and Pb/U, to reflect long-term reproducibility. Pb/Pb and Pb/U weighted mean ages are nearly identical, so in this study, the more precise Pb/Pb age of 2623 ± 34 Ma (2s) is quoted. All data are presented in **APPENDIX E13**.

B3.4 References

Horstwood, M.S.A., Košler, J., Gehrels, G., Jackson, S.E., McLean, N.M., Paton, C., Pearson, N.J., Sircombe, K., Sylvester, P., Vermeesch, P., Bowring, J.F., Condon, D.J. & Schoene, B. (2016). Community-derived standards for LA-ICP-MS U-(Th-)Pb geochronology – uncertainty propagation, age interpretation and data reporting. *Geostandards and Geoanalytical Research*, 40, p. 311-332.

McCrea, J.M. (1950). On the isotopic chemistry of carbonates and a paleotemperature scale. *Journal of Chemical Physics*, 18, p. 849-857.

Robinson, B.W. & Kusakabe, M. (1975). Quantitative preparation of sulfur dioxide, for $^{34}S/^{32}S$ analyses, from sulfides by combustion with cuprous oxide. *Analytical Chemistry*, 47, p. 1179-1181.

Sharp, Z.D. (1990). A laser-based microanalytical method for the in situ determination of oxygen isotope ratios of silicates and oxides. *Geochimica et Cosmochimica Acta,* 54, p. 1353–1357. °